Precision Background Stability And Response Calibration in Borexino:

Prospects For Wideband, Precision Solar ν Spectroscopy and BSM ν Oscillometry Through a Deeper Detector Understanding

David Bravo Berguño

Dissertation submitted to the Faculty of the
Virginia Polytechnic Institute and State University
in partial fulfillment of the requirements for the degree of

Doctor of Philosophy in Physics

Robert Bruce Vogelaar, Chair
Jean Heremans
Mark Pitt
Eric Sharpe
Tatsu Takeuchi

November 16th, 2016

Keywords: *Borexino, neutrino, fluidodynamics, calibration, particle, Sun*

Precision Background Stability And Response Calibration in Borexino: Prospects For Wideband, Precision Solar ν Spectroscopy and BSM ν Oscillometry Through a Deeper Detector Understanding

David Bravo Berguño

Abstract

This work sets out to be a description of the initiatives utilizing the Borexino liquid scintillator neutrino observatory to perform the first direct, high-precision, wideband solar neutrino spectroscopy measurement of the the solar neutrino spectrum's main components, as well as its next-generation short-baseline source program (SOX). Its original scope revolved around the creation of a $\mathcal{O}$(MCi) ^{51}Cr source to be inserted under the detector, intended to explore the small region of the anomaly-favored $sin^2(\theta_{14})/\Delta m^2_{14}$ phase space where sterile neutrinos may lie –or otherwise unambiguously measure or disprove signs of anomalous oscillatory behavior in low L/E ν_es and $\overline{\nu}_e$s. Investigating the feasibility and optimization of producing such a large amount of ^{51}Cr for the source, by irradiating chromium material in a high-flux reactor, required extensive simulative work with the MCNP-5 neutronics code.

With the switch of pace toward a ^{144}Ce-^{144}Pr $\overline{\nu}_e$ source, this work was re-oriented toward the efforts to re-calibrate the detector after the 2009-10 campaign, improving and expanding upon it by the introduction of new source fabrication techniques, a source positioning LED device, and a re-evaluation of the objectives sought after, fitting the needs of Borexino's Phase 2 priorities. Indeed, the detector's unprecedented and record-setting background levels are tightening its requirement for background stability. Aiming to reduce fluctuations in 210Po levels that remain problematic in Borexino's quest to lower the upper limit of the solar CNO neutrino flux (or even measure it), among other components, a new Temperature Monitoring and Management System was deployed and associated tools necessary to fully utilize it were developed as part of the present work. *Computational Fluid Dynamics* (CFD) simulations in 2D and 3D, conductive and fully convective, were also developed in collaboration with Dr Riccardo Mereu of Milan's Polytechnic Institute in order to model, characterize and ultimately predict the subtle fluid currents ($\sim$$10^{-7}$ m/s) that may be of concern for the required background stability. A brief discussion of the recent $>5\sigma$ measurement of geo-neutrinos by Borexino, a complementary part of the work for this thesis, is presented as well.

Precision Background Stability And Response Calibration in Borexino: Prospects For Wideband, Precision Solar ν Spectroscopy and BSM ν Oscillometry Through a Deeper Detector Understanding

David Bravo Berguño

General Audience Abstract

Neutrinos are one of the few distinct probes we have to observe the large-scale features of the world around us. Together with photons, some charged leptons, and the dense conglomerates of quarks and gluons we call atomic nuclei, they are the only fundamental particles with large enough a range to travel from distant objects to reach us. In contrast with any of the other particles though, they are the only ones solely bound by one of the fundamental non-gravitational forces alone: the weak nuclear force. This makes them the most penetrating radiation currently known, but consequently the one whose detectable effects are the subtlest. Observing our environment through neutrinos, we transcend the boundaries imposed by electromagnetic interactions: most objects, even astronomical ones, are no longer opaque, but mostly transparent. Further, the only luminous objects (in neutrinos) are those where some nuclear reactions take place, which release them.

Being the only known particle with such properties, they can be used as an extraordinarily versatile tool to observe and understand Nature in its most fundamental and far-reaching realm –in addition to opening a whole new array of possible future practical uses, some closer to feasibility than others, that our early and still incomplete understanding of neutrinos barely scratches the surface of: from ultra-penetrating communication links to tomographies of whole planets, targeted quickened radioactive decay (for example, for medical purposes) or unshieldable monitoring of nuclear material for non-proliferation purposes.

The Borexino neutrino observatory is a detector located under the Gran Sasso massif in central Italy, whose objective is to precisely measure the neutrinos emitted in nuclear processes such as the nuclear fusion chains powering the our Sun. In fact, the main subject of study for Borexino is solar neutrinos, which travel mostly unimpeded at close to the speed of light from their generation areas inside the Sun to Earth. Three known types of neutrinos exist, defined depending on the way they interact with matter, producing other particles. These types intermix among themselves, as the neutrino propagates through space, and the behavior of this transmutation (known technically as *oscillation*) is influenced by areas with high density of matter, such as the Sun itself. The study of neutrino fluxes and their oscillation is a very recent topic of research, and one which offers a crucial handle on physical processes in Nature that we still do not know of, or do not fully understand: the so-called *Beyond Standard Model* processes. The Sun is the largest neutrino emitter at low energies we can detect from Earth, and the study of the precise amounts it produces is crucial to understand how it (and, by extension, other similar stars) work in detail. Furthermore, just like with light, the Sun produces neutrinos at different energies (akin to sunlight's different colors, or wavelengths), depending on the nuclear reaction which produced them –and their relative contributions can be separated by Borexino. All solar neutrino components (except two very faint ones) have been directly observed by Borexino,

many for the first time, with varying levels of precision, since it started operations in 2007, by disentangling against the backgrounds the very feeble contribution of the <200 neutrinos that leave a signal every day in Borexino.

Borexino's unique sensitivity lies in its unprecedented and extreme radiopurity: the levels of radioactive elements in its innermost, most pristine materials it is composed of are much below typical natural values, and have been steadily improving for the last 10 years, in some cases to record-setting lows. The data accumulation since 2012, when a purification campaign brought down the background levels dramatically, has yielded extremely high-quality datasets. However, since Borexino's active material is liquid, small temperature upsets in the detector's environment have caused fluid shifts that brought less radiopure material into the cleanest area. This dissertation details the work devoted to monitoring, managing, stabilizing and improving Borexino's temperatures with the aim to reduce background fluctuations that are obstructing efforts to measure the CNO solar neutrino component, which has never been observed before, having a small contribution in our Sun, but holds the key to understanding how many other stars work (in particular, larger ones, where the CNO process is much more dominant), as well as having profound implications on our own.

The insulation of Borexino's exterior, paired with the precise determination of its exterior and interior temperatures, has also enabled the development of Computational Fluid Dynamics (CFD) simulations that shed light into how the fluids inside Borexino respond to recorded past temperature changes, or to possible thermal distributions in the future –which is crucial to limit the penetration of backgrounds that may hinder a CNO measurement, or the improvement in the precision with which other previously-detected solar neutrino components can be measured. Furthermore, in order to reach such accurate results, a careful calibration of the detector is needed, so that its signals can be correctly interpreted: this dissertation explains the upgrade and improvement work carried out in order to perform a new calibration campaign in 2017, after the very successful one completed at the beginning of Borexino's life in 2009-10. Additionally, this dissertation explains the latest measurement, to a high statistical precision, of other naturally-occurring type of neutrinos: geo-neutrinos, that is, those emitted by radioactive components inside Earth, which allow us to understand the composition, evolution and thermal power output of our planet.

Finally, this dissertation details the simulation work performed for the SOX-A experiment, which intends to utilize a man-made neutrino source, located in a tunnel under the detector, as a way to understand these particles' oscillatory behavior, which may have shown characteristics we do not yet understand in the past. One of such hypothesis is the existence of practically-undetectable, *sterile* neutrinos, into which the three known types can oscillate –effectively making a given neutrino flux appear weaker than expected. The SOX source would serve as a reference "candle" which could be probed for deficits in the flux of the known neutrinos (those Borexino can detect) as a smoking gun for the existence of others. In particular, the creation in ORNL's HFIR of a high-intensity neutrino source based on radioactive ^{51}Cr is discussed here. Confirming or disproving the existence of these type of unknown oscillatory behavior is critical for the understanding the core framework of Particle Physics, as well as expand its frontiers to unexplored areas we know exist, but have not yet been probed.

"Without experimentalists, theorists tend to drift. Without theorists, experimentalists tend to falter."

T. D. Lee

"It is best not to think about it, like the new taxes."

P. Debye

Acknowledgements

Rarely, if ever, are accomplishments solely –or even mainly– the piece of work of a single individual. Not being an exception to the rule, this Thesis was made possible by the support, encouragement and positive influence of many people I have the privilege of having in my life. The (long, but bear with me) gratitude messages that follow intend to acknowledge beyond the mere production of this material –which is but the small, visible "tip of the iceberg" of the extraordinary, life-defining experience of pursuing a Graduate Degree while adding, in my case, learning to live in two countries other than my own.

Like someone special said once, this goes to *who believes in me, more than I do.*

Professionally and personally, I will always be grateful and indebted to my mentor and adviser Dr R. Bruce Vogelaar, who recruited me as a Graduate Student when I was just an exchange student in his Nuclear and Particle Physics class preparing to return home, and opened before me a wide array of academic and professional development possibilities that were probably only limited by the restrictions I chose to set. The opportunity to participate under his wing in not one, but two international particle physics collaborations, meet some of the best minds and personalities in my field both through them and in renowned conferences, as well as his continued support, flexibility and understanding while in Virginia Tech and traveling alike, made the Graduate School experience one for the books. This work, and the positive consequences stemming from it, would never have been possible without him.

Although formally not academically linked to me, I would like to express my gratitude to the extraordinary professionals I had the honor of establishing professional contact with through the Borexino Collaboration / family. In particular, my sincere "thank you" goes to Drs. Gioacchino Ranucci, Barbara Caccianiga, Livia Ludhova, Marco Pallavicini, Gianpaolo Bellini, Alessandra Re, Lino Miramonti, Sandra Zavatarelli and Emanuela Meroni for their warm backing, mentoring and company during my long –and sometimes unstructured– stays in Milan, and for strongly supporting me as a candidate for the unique new upcoming period in their University. Vi ringrazio profondamente e di tutto cuore, e spero saprete che siete stati una influenza decisiva nell'inizio della mia vita "veramente adulta", sia professionale che personale.

Without the strong support by the Virginia Tech University and, originally, my *alma mater* the Universidad de Oviedo, none of this academic experience would have existed, and I would have never met some of my best friends and colleagues – for that I am truly grateful to both institutions, but particularly to the people that make them and strive to improve them to ever new heights. Furthermore, even though it seems like ages in the past, I will never express enough gratitude toward the educational community whose knowledge, ethics and personal fruits I am, and I expect to continue to be for maybe all my life, reaping every day. Thank you, Dominicas Oviedo. Aunque parece que haya pasado una eternidad, nunca llegaré a expresar suficiente gratitud para con la comunidad educativa cuyos frutos, en cuanto a enseñanza en conocimientos, ética y valores, recojo cada día –y seguramente seguiré recogiendo toda mi vida: gracias, Dominicas Oviedo.

Borexino and LNGS are inseparable, and so is my experience in the Collaboration. I am truly grateful to the many and excellent people affiliated in one way or another to this extraordinary institution, although I would like to especially mention some of the people I had the fortune to pre-eminently work with: Paolo Cavalcante for all the (huge) help during sometimes not so pleasant tasks and his company during (high-speed) Italian road trips; Marco Carlini, for always having a helpful hand and for always having his conversation and demeanor ready to make even the most stressful situations suddenly become alright; Laszlo Papp, who although living in Virginia and Baviera during my PhD research period, he's known like a local even in the most remote Abruzzese villages (so I'm listing him here), and patiently taught me so many secrets about real craftsmanship and good technical practices I might need to write an extra appendix just to list them; Giorgi "George" Korga, who showed me what an outstanding person, professional and teammate looks like when mixed in a single individual, and saved my legs many trips up the hill; Francesco di Eusanio, for always providing solutions and gentle help; Andrea

Ianni, for making me understand that "tajalápiz" sounds Arabic to Italians; Chiara Ghiano, for the best multi-year Parmesan introduction to Abruzzo I ever had, Nicola Rossi for patiently explaining me his data analysis techniques... and of course Augusto Goretti, Giuseppe "Pino" Bonfini, Federico Gabriele, Massimo Orsini, Yuri Suvorov, Stefano Davini, Pablo Mosteiro, and the many others my forgetful mind is leaving out of this list but have made my many visits to Gran Sasso something to remember. Also my hat off to Riccardo Mereu, for his unending energy supply, incredible spirits and general life approach; and to Dr Vincenzo Roca, for his help, patience, local culinary tours and excellent personality. Grazie a tutti ragazzi! Non potrei menzionare il Gran Sasso ed Assergi senza pensare al pazientissimo e straordinario padrone del "appartamento VT" (prima noto come "casa di Laszlo"), Domenico Sacco, grazie alla cui personalità, affabilità e simpatia sempre avevo vicino una persona cara in Abruzzo.

Thank you to my fellow Graduate Students, Xinjian, for sharing with me my first year of Master's in the UCNA project and our first trip to New Mexico; and Zach, for his knowledge, good company and great times visiting and working in Italy. Thank you to my non-Graduate Student colleagues too, Tristan, for his huge help installing thermometers everywhere and long, short, but always pleasant chats in the office and in Italy; and Derek, for his experienced and helpful advice. To all those wonderful "youngsters" and "not-so-youngsters" I have the fortune to work with, mainly in Borexino but also elsewhere, thank you.

Gracias, thank you, grazie, danke, spasibo, obrigado, shakar and merci to the ones I am privileged to call my friends. Without you, be it through direct intervention or just by being there and yourselves, the road to this conclusion would have been a trek through the desert, if not impossible. I am so fortunate as to not be able to count on my fingers (or even with the help of my toes) the true friends I can thank for positive contributions in this period of my life. My forgetful mind will again leave some names in the inkwell, some maybe even so crucial I will only be able to dumbfoundedly mumble when reminded of them... but I trust they will know me well enough to attribute that to my "special" mind! Thank you to the 6 Nativos, Xabel, Íñigo, Viti, Rubio and Santi, because going around the Department with that tape was a glorious enterprise still bearing fruits today; Éder, because *Punch!* is all we need to say, and digressing about the decadence of the Roman Empire next to a cliff drinking *calimotxo* is perfectly normal for us; Leti, for the Italian, Milan, Virginia, Spain and beyond, because you think you didn't contribute much to who I am, and you couldn't be more mistaken; Ana, for being THE roommate and confident; Francho and Javi, because you gave me the best year of my life and showed me what awesome looks like (and a different view on what the Duckpond is truly for); David, for complimenting me on my English and buying a microwave in my company when I was weird, and the "few" adventures and conversations thereafter; Guillaume, for always being there even when I could be more myself; Lindsay, for making me learn programming when all seemed lost, and for everything that accompanied it; Chus, because crápulas tend to group together... and Ricardo, Pilar, Jess, Yen, Clea, Olatz, Daniela, Mirs, Mònica, Juli, Annelies, Mercedeh, Karen, Sandra, Chris, Sheldon, Aníbal, Giulia, Marissa, Deni, Miguel, César "Assun", Sultan... and still many others. Thank you also to those aforementioned, ellipsed or implied "extra"-friends who, maybe not even consciously or even willingly, have made me who I am today and been my inspiration and solace. And thank You, because life is wonderful when we are allowed to embrace it.

Sometimes, the most precious and cherished is reserved for last, and this is one of such occasions. These lines will inevitably read empty, crude and withered compared to the concepts they barely reach to scratch, but such is the necessary fate of words aiming for such heights. Thank you to my family, always giving their everything and reaching much farther beyond: without you, not this work, not these years, not these experiences, not any positive or negative influence I could have had, not a single sidelined dot in the tale of my life within yours would have been possible, or worth happening. You have been my inspiration and my strength, my consolation and my model.

Thank you mom and dad, for everything that doesn't fit in these lines, for the little things, for the great ones, for taking me by the hand, for making me spread my wings wide and fly, for burning Skype, for the distant birthdays, for the noisy airport/bus/train welcomings, for the home luxuries and making me feel like I never left during those too brief visits, for the understanding and the telling-offs, the arguments and the laughter, the lazy

TV nights and the world travels, the morning orange juices and the goodnights. Thank you tita and tuto, for always being there, for your unmeasurable and selfless love, for my whole life around you, for the love of nature, the name of plants and the leaves collections; for the impeccable half-table meals that were always ready, for the rides to study English in "el motorín", for your unwavering support and encouragement, for your hugs and kisses: this thesis is for you. Thank you abuelo, abuela and Roberto, for your visits and love, for your travel adventures and your questions and support, for your pastries and coffee evenings, for your evenings in El Prao, for your encouragement in studies, travels and love. Thank you Geli and Iñaki, for your Whatsapps and Skypes, for visiting Virginia with me (and enjoying carrying "la neverina"), for sharing unique memories in Castro for so long, for being always just a call away, for the paintings and the laughs. Thank you Tía María and Tío Pepe, even if you aren't here for this time of my life, your legacy is imprinted in me. To all of you, I love you.

Gracias papi y mami, por todo lo que no cabe en estas líneas, por las pequeñas cosas, por las grandes, por llevarme de la mano, por hacer que extienda mis alas y vuele, por quemar Skype, por los cumpleaños en la distancia, por los recibimientos con algarabía en las estaciones de bus, tren y aeropuertos, por los lujos caseros y hacerme sentir como si nunca me hubiese ido durante esas visitas tan cortas; por entenderme y por regañarme, por las riñas y las risas, las noches perezosas frente a la tele y los viajes por el mundo, por los zumos de naranja mañaneros y las buenas noches. Gracias tita y tuto, por estar siempre ahí, por vuestro incontable y desprendido amor, por toda mi vida con y al lado de vosotros, por el amor a la naturaleza, los nombres de las plantas y las colecciones de hojas; por las impecables comidas que ocupan media mesa y siempre estaban a punto, por llevarme en "el motorín" para que estudiase inglés, por vuestro apoyo y ánimo inquebrantables, por vuestros besos y abrazos: esta tesis es para vosotros. Gracias abuelo, abuela y Roberto, por vuestras visitas y amor, por contarme las aventuras viajeras, por vuestras preguntas y apoyo, por los pasteles y las veladas de café, por las tardes en El Prao, por vuestro estímulo en los estudios, en los viajes y en el amor. Gracias Geli e Iñaki, por vuestros Whatsapps y Skypes, por visitar Virginia conmigo (y disfrutar de "la neverina"), por compartir recuerdos únicos en Castro durante tanto tiempo, por estar siempre a una sola llamada de distancia, por la pintura y las risas. Gracias Tía María y Tío Pepe, aunque no estéis aquí en esta etapa de mi vida, vuestro legado está grabado en mí. A todos vosotros, os quiero con locura.

Contents

List of Figures

List of Tables

Abbreviations

IBD	**I**nverse **B**eta **D**ecay
SM	**S**tandard **M**odel
CKM	**C**abibbo-**K**obayashi-**M**askawa
PMNS	**P**ontecorvo-**M**aki-**N**akagawa-**S**akata
QCD	**Q**uantum **C**hromo-**D**ynamics
SNA	**S**olar **N**eutrino **A**nomaly
ANA	**A**tmospheric **N**eutrino **A**nomaly
R(N)A	**R**eactor (**N**eutrino) **A**nomaly
m$_\nu$SM	**m**assive/**m**inimal ν **S**tandard **M**odel
VEV	**V**acuum **E**xpectation **V**alue
BSM	**B**eyond (the) **S**tandard **M**odel
C(P(T))	**C**harge (**P**arity (**T**ime))
FWHM	**F**ull **W**idth **H**alf-**M**aximum
SSM	**S**tandard **S**olar **M**odel
DB	**D**aya **B**ay
RENO	**R**eactor **E**xperiment (for) **N**eutrino **O**scillations
MINOS	**M**ain **I**njector **N**eutrino **O**scillation **S**earch
NOνA	NuMI **O**ff-axis ν_e **A**ppearance
NH/IH	**N**ormal/**I**nverted **H**ierarchy
WMAP	**W**ilkinson **M**icrowave **A**nisotropy **P**robe
MSW-LMA	**M**ikheev **S**mirnov **W**olfenstein-**L**arge **M**ixing **A**ngle
NSI	**N**on-**S**tandard **I**nteractions
LSND	**L**iquid **S**cintillator **N**eutrino **D**etector
KARMEN	**KA**rlsruhe **R**utherford **M**edium **E**nergy **N**eutrino experiment
SAGE	**S**oviet-**A**merican **G**allium **E**xperiment

GALLEX	**GALL**ium **EX**periment
(Mini/Sci/Micro)BooNE	(Mini/Sci/Micro) **Boo**ster **N**eutrino **E**xperiment
ICARUS	**I**maging **C**osmic **A**nd **R**are **U**nderground **S**ignals
OPERA	**O**scillation **P**roject with **E**mulsion-t**R**acking **A**pparatus
CDHSW	**C**ern **D**ortmund **H**eidelberg **S**aclay **W**arsaw
NOMAD	**N**eutrino **O**scillation **MA**gnetic **D**etector
LUCIFER	**L**ow-background **U**nderground **C**ryogenic **I**nstallation **F**or **E**lusive **R**ates
LNGS	***L**aboratori **N**azionali (del) **G**ran **S**asso*
PMT	**P**hoto-**M**ultiplier **T**ubes
p.e.	**p**hoto-**e**lectrons
ID	**I**nner **D**etector
OD	**O**uter **D**etector
I/OB	**I**nner/**O**uter **B**uffer
FV	**F**iducial **V**olume
SSS	**S**tainless **S**teel **S**phere
WT	**W**ater **T**ank
IV	**I**nner **V**essel / Volume (depends on context)
MOE	**M**ach4-**o**n-top-of-**E**chidna
FADC	**F**ast **A**nalog-to-**D**igital **C**onverter
PSD	**P**ulse **S**hape **D**iscrimination
MLP	**M**ulti-**L**ayer **P**erceptron
TFC	**T**hree-**F**old **C**oincidence
LAKN	**L**ow **A**rgon/ **K**rypton **N**itrogen
LTPS	**L**atitudinal **T**emperature **P**robes **S**ystem
TIS	**T**hermal **I**nsulation **S**ystem
AGSS	**A**ctive **G**radient **S**tabilization **S**ystem
CFD	**C**omputational **F**luid **D**ynamics
SOX	**S**hort-distance/baseline **O**scillations with Bore**X**ino
ANG	**A**nti-**N**eutrino **G**enerator
IRED	**I**nfra**R**ed-**E**mitting **D**evice
HFIR	**H**igh **F**lux **I**sotope **R**eactor
MCNP	**M**onte**C**arlo **N**-**P**article

Symbols

ν / ℓ	neutrino / lepton
$\overline{\nu}$ / $\overline{\ell}$	antineutrino / antilepton
p^+	Proton
n^0	Neutron
e^- / e^+	Electron / positron
μ	Muon
π	Pion
K	Kaon
γ	Gamma/photon

$SU(n)$	Unitary Special Group (order n)
$U(n)$	Unitary Group (order n)
I	Weak isospin
Y	Hypercharge
Q	Charge operator (=I_3+Y/2)
Ra	Rayleigh number
Pr	Prandtl number
Nu	Nusselt number

For those who taught and allowed me to enjoy the journey while descrying the destination.

Introduction and outline

This thesis describes some of the efforts associated with the project to measure the flux of the CNO component of the solar neutrino spectrum and a wideband, precision spectroscopy of all solar neutrinos accessible to the Borexino observatory. In particular, it focuses on the techniques associated with making its flux determination a reality including, but not limited to, the temperature determination and control strategies implemented to limit scintillator movement in the fiducial volume of the detector and the second calibration campaign that will take place in 2017. Also highlighted are the feasibility studies made for the realization of a ~ 6 MCi ^{51}Cr source to be inserted in the SOX pit as part of the SOX-A program (SOX-Cr) revolving around the search for anomalous neutrino oscillations –mostly focused on exploring the existence of $\sim$1 eV sterile neutrinos–, specifically the irradiation simulations and activity estimates in the Oak Ridge National Laboratories' (ORNL) High Flux Isotope Reactor (HFIR).

0.1 Part I: Active and sterile neutrinos in Borexino

In **Chapter** 1 the background theoretical framework for neutrino physics, masses and extensions into sterile states is reviewed. **Chapter** 2 will describe the Borexino detector, emphasizing the experimental challenges overcome during its long history, particularly background control, leading to a brief outline of its past achievements. A description on Borexino's immediate capabilities for the completion of the measurement of the major solar neutrino flux component (CNO νs) and the improvement of limits in previously-determined fluxes are discussed. The detection of Beyond-Standard Model (BSM) phenomena in the context of the *Short-distance Oscillations with BoreXino* (SOX) program is also investigated, concentrating mostly on the SOX-A phase, where the (anti)neutrino flux from external sources will be scrutinized for BSM effects.

0.2 Part II: Borexino's Solar Neutrino Program and CNO determination efforts

Chapter 3 will focus on the temperature determination and control strategies implemented to stabilize the detector's background levels in the critical area needed for CNO analysis, as well as the background stability measurements that motivated, and later verified the positive impact of, the thermal management and study strategies, and contextualizes the significance of the results. Chapter 4 will instead describe the fluidodynamical simulations performed in conjunction with the aforementioned hardware strategies, as an effort to fully understand, manage and predict the thermal stability of Borexino. Chapter 5 will instead focus on the second pillar of this measurement, namely the critical calibration campaign to be performed during 2017, detailing both the experimental techniques employed and the upgrades on Borexino's calibration hardware, as well as the significance of its analysis on the *NuSol* measurements.

0.3 Part III: Sources in Borexino for Anomalous Neutrino Oscillation detection: SOX

Chapter 6 will explain the efforts performed in the context of the SOX program, more specifically on the SOX-Cr part of the experiment, for which extensive feasibility and sensitivity studies were performed. Additional comments are devoted to the SOX-Ce source and calorimeter.

0.4 Conclusions and perspectives

Finally, Chapter 7 summarizes and highlights the most important points of the present thesis, and outlines the future perspectives for the detector and the next, most promising steps that build on the present results.

Part I

Active and Sterile Neutrinos in Borexino

Chapter 1

Neutrino physics and phenomenology

Neutrinos were taken by their intellectual father, W. Pauli, to be a last-resort solution[1] for the continuous energy spectrum of electrons ejected from beta decays in radioactive nuclei, discovered by J. Chadwick in 1914[2]. They were devised in order to avoid N. Bohr's proposal that conservation of energy is a principle relevant only *statistically* in nuclear decay processes. This followed the realization by L. Meitner[3], C. D. Ellis and W. A. Wooster[4] in separate, independent experiments, that the study of the heat released during the decay of the then-called *radium-E* (really ^{210}Bi) ruled out their theories postulating that the continuity of the beta spectrum was due to the so-called "primary origin" hypothesis (emission of a continuous gamma spectrum from the nucleus) or to a "secondary origin" hypothesis (emission of outer shell electrons by elastic scattering with the decay electron). These *"new, neutral particles"* would be far more penetrating than Pauli's initial estimate in his famous letter to the *Radioactives* group[1], where he called them "neutrons" (it was then still hypothesized they could be nucleons and clarify the spin-statistics problem –which was eventually solved by the actual neutron discovery in 1932[5]).

1.1 Neutrinos as a fermionic piece of the Standard Model

As unconventional as the origin of neutrino theory might be, its importance in particle physics did nothing but grow since the antineutrino discovery in the inverse beta decay (IBD) (see equation 1.1) experiment by F. Reines and C. L. Cowan[6] in 1956. This was so in spite of the negative result (complicated further because of its large cosmic ray background) obtained by R. Davis[7] in his Brookhaven radiochemical C_2Cl_4 detector for reactor antineutrinos –whose non-detection is precisely a consequence of the helicity conservation of the parity-violating weak interaction, even if $\nu = \overline{\nu}$.

[1] In fact, he was off by 16 orders of magnitude!

$$\overline{\nu} + p^+ \rightarrow n^0 + e^+ \tag{1.1}$$

By the late 1960s and early 1970s, the Weinberg-Salam electroweak theory was well established and started being referred to as the ***Standard Model***[2]. Since then, experimental discoveries (including the recent Higgs boson discovery[9]) have only strengthened it –with some exceptions, like the ones coming from certain neutrino observations (see Section 1.4).

FIGURE 1.1: 1933 Solvay Conference, where Pauli first publically proposed his ideas on the neutrino. Courtesy of the Archives, California Institute of Technology.

The Standard Model (SM) is a Lorentz-invariant field theory describing the electroweak and strong interactions at energies of at least ∼TeV scales, exhibiting a $U(1)_Y$ x $SU(2)_L$ x $SU(3)_C$[3] gauge symmetry that is spontaneously broken via the Higgs mechanism[10]. The $SU(3)_C$ group carries an underlying *unbroken* symmetry that allows it to be treated separately to the other, mixed electroweak groups $SU(2)_L$x$U(1)_Y$. The SM requires the empirical input of 19 independent parameters (9 *Yukawa coefficients*: 6 for quarks and 3 for leptons; the *Higgs mass* and its *vacuum expectation value* –which determines fermionic masses when multiplied by their Yukawa coefficients–; the 3 *quark mixing angles* and *one phase* for the Cabibbo-Kobayashi-Maskawa (CKM) matrix; the *quantum chromodynamic (QCD) phase*; and 3 *coupling constants* (g_1, g_2 and g_3) of the gauge group)[11]. An as-of-yet unknown underlying physical principle may justify the naturalness of these experimental assignments.

[2] Responsibility for the name has been traced back to S. Treiman[8] in his 1975 paper combining the electroweak model with the 4-quark theory.

[3] Y=weak hypercharge, L=left-handed chirality, C=color

As illustrated in figure 1.2, the SM encompasses a *bosonic* and a *fermionic* group. The fermionic group is divided into the quark and the lepton sector. At the same time, it is arranged in three weak generations (with corresponding antiparticles for each particle) where both left-handed quarks and leptons are members of weak isospin doublets, and right-handed quarks and *charged* leptons are members of weak isospin singlets[4]. Neutrinos are massless and, therefore, only of left-handed chirality in this minimal model: right-handed neutrinos would be decoupled[5]. All other fermions have both chiralities. Table 1.1 summarizes the fermionic contents of the SM.

		I	**I_3**	**Y**	**Q**
Lepton doublet	$L_L = \begin{pmatrix} \nu_{eL} \\ e_L \end{pmatrix}$	1/2	1/2 -1/2	-1	0
Lepton singlet	e_R	0	0	-2	-1
Quark doublet	$Q_L = \begin{pmatrix} u_L \\ d_L \end{pmatrix}$	1/2	1/2 -1/2	1/3	2/3 -1/3
Quark singlets	u_R d_R	0	0	4/3 -2/3	2/3 -1/3

TABLE 1.1: Weak isospin I, 3^{rd}-component weak isospin I_3, hypercharge Y and charge operator Q(=I_3+Y/2) eigenvalues for the fermion tuples in the weak isospin base[14]

The bosonic force carriers mediate the electromagnetic (self-interacting, massless photons), the weak (self-interacting, massive Z^0, W^+ and W^-) and the strong interactions (massive, self-interacting gluons). Finally, the interactions with the Higgs field are mediated by the (massive, self-interacting) Higgs boson, whose coupling with the Yukawa coefficients of each particle endows them with their observed masses.

All fermions in the SM are Weyl spinors (see [16] for a detailed discussion): a two-component object that behaves under rotations and boosts as indicated in equation 1.2 and has definite chirality. These chiral spinors are the smallest irreducible representations of the Lorentz group. Neutrinos are *massless*, because their description involves the two-component theory included in the SM by Landau, Lee and Yang and Salam in 1957, with one Weyl spinor each. Once masses are added to account for experimental observations of neutrino mixing, as described in the next Section 1.2, a four-component object composed of one (two) of these SM Weyl fermions will need

[4]These weak isospin tuples do **not** have definite masses, but rather are linear combinations of eigenstates with definite masses – which causes mixing in the quark and leptonic sectors. Note **no** qualifier is written before the word *leptonic*: both charged and neutral leptons can in principle undergo oscillations between weak states – charged lepton oscillations however are suppressed because of the combination of the decay width of the parent particles that produce them and their large masses (relatively so as compared to neutrinos), which causes incoherent mass eigenstates mixtures in any charged lepton production process. In addition, practical considerations concerning the detection process (unless the neutrino mass is measured directly), and the fact that both the charged and the neutral leptons from a *single* decay have to be detected, make it impossible for a charged lepton oscillation measurement to take place. Heavy sterile neutrinos, however, could produce observable charged lepton oscillations. See [12] and [13] for further discussions on this topic.

[5]This gives rise to *sterile* neutrinos, which do not interfere with the renormalizability condition of one-loop perturbative anomaly cancellations.

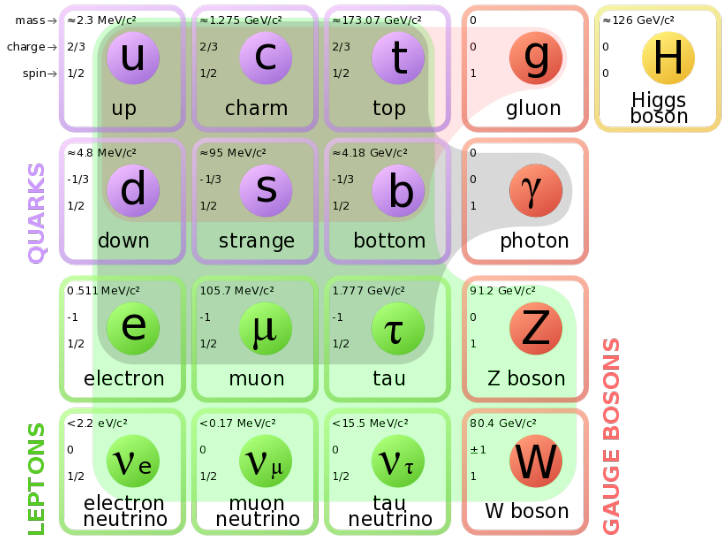

FIGURE 1.2: SM particle field content (not showing corresponding fermionic antiparticles) and couplings[15]

to be constructed via the Majorana (Dirac) spinor schemes, which behave under θ rotations and η boosts as seen in equation 1.2.

$$
\begin{aligned}
\chi &\rightarrow e^{-\frac{i}{2}\sigma\theta}\chi \\
\chi &\rightarrow e^{-\frac{1}{2}\sigma\eta}\chi
\end{aligned}
\tag{1.2}
$$

Being electrically neutral Q=0, (active) neutrinos will only couple through the charged and neutral current Lagrangians 1.3 (ϑ_W is the Weinberg angle, j_W and j_Z are the charged and neutral current densities respectively):

$$
\begin{aligned}
\mathcal{L}_I^{(CC)} &= -\frac{g}{2\sqrt{2}} j_W^{\rho} W_{\rho} + h.c. \\
\mathcal{L}_I^{(Z)} &= -\frac{g}{2cos\vartheta_W} j_Z^{\rho} Z_{\rho}
\end{aligned}
\tag{1.3}
$$

The radiochemical technique proposed by Pontecorvo and used by Davis in his pioneering experiment in Brookhaven would still have its time to shine when it was moved to the Homestake mine and started consistently obtaining[17] lower solar neutrino rates than those calculated[6] by his collaborator J. Bahcall[18]. Here was a direct indication that the minimal formulation for neutrinos in the SM was incomplete, and some other mechanism had to be incorporated in order to account for this *Solar Neutrino Anomaly* (SNA)[19]: **neutrino masses**.

[6]The modelling of solar fusion reactions and their neutrino output, as well as the underlying physics governing their behavior, is a central topic in Borexino's research and will be further discussed in Section 1.3.

1.2 Leptonic mixing and m_νSM

Although first proposed by Pontecorvo and Gribov as early as 1957[20][21] (but missing the important matter effect explained in section 1.3), and already evidenced by the Homestake experiment from 1964, neutrino oscillations had to endure a tortuous path before being considered proven by KamiokaNDE's Čerenkov measurements[22], further confirmed by GALLEX/GNO and SAGE's low-threshold (233.2 keV) gallium[7] count-rates[23][24] in the early 90s. This was indeed the most important phenomenon underlying the SNA. Definitive proof was attained by the SNO Collaboration[25] in 3 channels with different sensitivities, as well as in the antineutrino sector by the reactor analysis of KamLAND[26].

Additionally, the *Atmospheric Neutrino Anomaly* (ANA) also showed a consistent deficit between downcoming neutrinos produced in the atmosphere through collisions of cosmic rays with air molecules, as compared to upcoming neutrinos that had to traverse the Earth before arriving at the detector. This was explained thanks to the SuperKamiokaNDE Collaboration's zenith-angle analysis of $\nu_\mu \to \nu_\tau$ oscillations in 1998[27], for which this experiment was recently awarded the Nobel Prize in Physics, together with SNO.

Formally, the m_νSM extends the SM with the addition of 7 more independent parameters (3 masses and four PNMS matrix elements). It is based on the addition of a mass factor to the SM Lagrangian. A brief outline of the basic formalism is presented here; for in-depths discussions see [28] and [16]'s Appendix A2. Because of the spontaneous (hidden) breaking of gauge symmetry through the Higgs boson's vacuum expectation value (VEV) v, a fermion mass term must involve a coupling of left-handed and right-handed helicity fields (see equation 1.5) – since neutrinos don't exhibit right-handed components in the SM, they are massless: they do not couple with the Higgs boson. Incidentally, this also would mean lepton number L is conserved. However, this would imply the mass eigenstates coincide with the flavor eigenstates (and L is conserved), which in light of the experimental observation of neutrino flavor oscillations, is not the way Nature works.

$$f\overline{f} = \overline{f_L} f_R + \overline{f_R} f_L \tag{1.5}$$

There are two schemes by which we can add a mass term to the neutrino fields:

[7] The reaction observed by these detectors was jokingly referred to as the "Alsace-Lorraine" reaction due to its scheme of gallium → germanium → gallium:

$$\nu_e +^{71} Ga \to e^- +^{71} Ge \Rightarrow^{71} Ge \to^{71} Ga + \gamma \tag{1.4}$$

1.2.1 Majorana mass term

This is the simplest fermionic mass term, but is actually less flexible that the other possible scheme (Dirac mass, Section 1.2.2), because it is forbidden in any fermion that carries an electromagnetic charge. Further, only a Weyl spinor χ is needed to construct a Majorana mass term (equation 1.6).

$$\begin{aligned} &\mathcal{L} \supset \frac{1}{2}(\chi^T \epsilon \chi + h.c.) \\ &(\epsilon = i\sigma_2) \end{aligned} \tag{1.6}$$

A mass term is a chirality-flipping interaction, a mass term can be constructed for a single Weyl spinor by allowing the particle to change into its antiparticle, which has the opposite chirality. Neutrinos interact only through weak interactions in the SM, and considering the maximal symmetry violation of the charged-current V-A weak interactions[14], we can choose an arbitrary charge parity for neutrino fields, so $\psi_L^C = \mathcal{C}\overline{\psi_L}^T$, which implies the *Majorana condition*: a Majorana particle is equal to its antiparticle. Here we get the explanation for the fact that only (electrically) chargeless fermions can be Majorana particles:

$$\psi = \psi^C \tag{1.7}$$

where ψ is a two-component Weyl spinor composed of two Weyl fields χ, ξ. Lepton number L would not be conserved with these particles. Majorana neutrinos with negative helicity are customarily called "neutrinos", while "antineutrinos" are interpreted as Majorana neutrinos with positive helicity.

1.2.2 Dirac mass term

The same Higgs mechanism that gives rise to charged lepton and quark masses in the SM would be responsible for the m$_\nu$SM extension, just by including right-handed helicity components of the neutrino fields[8], which would be sterile.

Formally, a Dirac mass term would make use of a Dirac spinor, which is composed of two Weyl spinors to create a 4-component object, since two opposite-chirality Weyl spinors can be allowed

[8] The so-called *minimally-extended Standard Model* considers three right-handed neutrinos (one for each flavor generation), even though the theory doesn't constrain the number of extra neutrinos, since their presence is irrelevant for the cancellation of quantum anomalies: a single right-handed neutrino could also be possible.

to transition into each other in order to create a mass term:

$$\begin{aligned} &\mathcal{L} \supset -m((\psi^c)^T_L \mathcal{C}\psi_L + h.c.) = -m(\overline{\psi}\psi) = -\frac{1}{2}(\overline{\psi}\psi + \overline{\psi^C}\psi^C) \\ &\psi = \begin{pmatrix} \chi \\ \epsilon\xi^* \end{pmatrix} \end{aligned} \tag{1.8}$$

The two Weyl spinors that are collected into the Dirac spinor (the upper two components and the lower two components) can be considered anti-particles of each other.

The Majorana mass terms for the Weyl spinor can also be rewritten in a form similar to the Dirac mass term by re-expressing the 2-component Weyl spinor as a 4-component Majorana spinor (equation 1.9). The origin of this mass term may come from a coupling to a *different* Higgs boson than the scalar field recently discovered, or from a different mechanism (i.e. see-saw schemes, see Section 1.4).

$$\begin{aligned} &\mathcal{L} \supset -\frac{1}{2}m(\overline{\psi^C_{M,L}}\psi_{M,L} + \overline{\psi}_{M,L}\psi^C_{M,L}) \\ &\psi_M = \begin{pmatrix} \chi \\ \epsilon\chi^* \end{pmatrix} \end{aligned} \tag{1.9}$$

The naturalness of this model is controversial, and indeed many models bet on the neutrino mass coming from the Majorana mechanism, due to the extremely small coupling constant ($y \sim 10^{-12}$)[9]. Majorana neutrinos provide a more natural explanation for the small neutrino masses (given by the ratio $v^2/\mathcal{M}$) through see-saw mechanisms in which a heavier sterile neutrino would imply lighter active neutral leptons. This would consider the SM as an effective field theory for a broader theory at high energy: the latter would manifest itself through non-renormalizable effective Lagrangian terms, whose heavy mass coupling constant $\mathcal{M}$ is characteristic of the symmetry-breaking scale of this *Beyond Standard Model* (BSM) theory.

As can be deduced from the Majorana $\nu = \overline{\nu}$ condition, a Dirac neutrino has twice the amount of degrees of freedom as a Majorana one. Equation 1.7 is the condition that needs to be imposed on a four-component spinor to obtain a Majorana spinor, in order to halve the number of degrees of freedom, equating in the process the two Weyl spinors that went into its construction.

In addition, Dirac neutrinos can present an electric dipole moment due to the emission of a photon in a virtual W-charged lepton loop. Both Majorana and Dirac neutrinos could have transition dipole moments, but SM predictions would have to vastly underestimate their amplitudes in order for them to be observable.

[9] $\mathcal{L}_{SM} = y\overline{H_0}\overline{\nu_L}\nu_R \Rightarrow y = \frac{m_\nu}{\langle \overline{H_0} \rangle} \sim \frac{0.1eV}{174GeV} \sim 10^{-12}$

A *Dirac-Majorana mass term*, which would allow for active-sterile oscillations (see Section 1.4), can also be considered: pure Dirac masses do not allow for oscillation between these *flavorful* (e,μ,τ) and *flavorless* (sterile) states.

1.2.3 Oscillation formalism

Whatever the mechanism for neutrino mass generation is, it will not affect its best-studied and most-famous implication: neutrino oscillations. From the above, it is clear that flavor states do not coincide with the mass *eigenstates*. Neutrinos are detected through their weak current interaction with charged leptons, which constrains their nature. This causes the physical particle generated in a given process to be defined as a coherent quantum superposition of mass eigenstates[10]:

$$\mid \nu_\alpha\rangle = \sum_k U^*_{k\alpha} \mid \nu_k\rangle \quad \text{(k=1,2,3)} \tag{1.10}$$

In practice, since neutrinos are both produced and detected through certain reactions or channels, an extra normalizing multiplicative factor should be included next to the U parameter, but is in general ommitted for brevity. The *light ray* assumption (time=distance), as well as the colinearity of momentum and propagation length are unphysical too, but prove to be irrelevant for oscillation probabilities[14].

Flavor states must be orthogonal to one another (although not necessarily form a basis), because otherwise a CC interaction could create a charged lepton of a different flavor than the parent neutrino, which contradicts experimental evidence. Mass eigenstates must be orthogonal because they are eigenstates of the Hamiltonian, a Hermitean operator. We can then form 3 orthogonal linear combinations that pass from one representation to the other. The amplitudes governing the relative weight of each flavor state in each mass eigenstate are given by the Pontecorvo-Maki-Nakagawa-Sakata (PMNS) unitary leptonic mixing matrix. For the case of the three active neutrinos, U takes the form:

$$U_{PMNS} = \begin{pmatrix} U_{e1} & U_{e2} & U_{e3} \\ U_{\mu 1} & U_{\mu 2} & U_{\mu 3} \\ U_{\tau 1} & U_{\tau 2} & U_{\tau 3} \end{pmatrix} \tag{1.11}$$

[10]The special cases that involve flavor-blind interactions, such as neutral currents or Z^0 decays, involve superpositions of both mass and flavor eigenstates.

usually parameterized as a product of an *atmospheric*, a *reactor* and a *solar* part, multiplied by a diagonal Majorana phase matrix which doesn't intervene in oscillatory behaviors:

$$U_{PMNS} = \begin{pmatrix} 1 & 0 & 0 \\ 0 & c_{23} & s_{23} \\ 0 & -s_{23} & c_{23} \end{pmatrix} \begin{pmatrix} c_{13} & 0 & s_{13}e^{-i\delta_{CP}} \\ 0 & 1 & 0 \\ -s_{13}e^{i\delta_{CP}} & 0 & c_{13} \end{pmatrix} \begin{pmatrix} c_{12} & s_{12} & 0 \\ -s_{12} & c_{12} & 0 \\ 0 & 0 & 1 \end{pmatrix} \begin{pmatrix} e^{i\alpha_1/2} & 0 & 0 \\ 0 & e^{i\alpha_2/2} & 0 \\ 0 & 0 & 1 \end{pmatrix} \tag{1.12}$$

where, for brevity, $c(s)_{ij} = cos(sin)\theta_{ij}$, θ_{ij} being the mixing angles rotating in flavor space. Note this is only unitary if there are 3 types of neutrinos that mix among each other; otherwise the unitary matrix would be larger.

It is instructive to look at how the PMNS matrix can be roughly estimated from a few experimentally-determined parameters: $U_{e2} \sim \sqrt{0.3}$ has been ascertained thanks to the measurement of the flux deficit in the SNA ($\frac{\phi_{\nu_e}}{\sum \phi_{\nu_\alpha}}$); $U_{e3} \sim 0$ comes from long-baseline reactor experiments (E∼3 MeV; L∼1.5 km); $U_{\mu 3} \sim 1/\sqrt{2}$ comes from atmospheric neutrino analysis (upgoing vs downgoing fluxes). Since U_{e3} is very small, unitarity considerations give us the value of $U_{e1} \sim \sqrt{2/3}$ and $U_{\tau 3} \sim 1/\sqrt{2}$. Finally, orthogonality and unitarity impose the necessary conditions to arrive at $U_{\mu i}$, $U_{\tau i}$ (i=1,2).

Over time, the neutrino state will evolve according to its Hamiltonian, which in the case of a *plane wave* neutrino mass eigenstate with definite momentum but infinite spatial distribution corresponds to:

$$\mid \nu(\overrightarrow{L}, T)\rangle = e^{-PT + i\overrightarrow{P}\overrightarrow{L}} \mid \nu_\alpha^P\rangle \tag{1.13}$$

Being ultrarrelativistic, we can approximate for a given mass eigenstate with definite momentum $p_i = \sqrt{E^2 - m_i^2} \sim E - \frac{m_i^2}{2E}$. There are several derivations valid for *ultrarrelativistic* neutrinos: both the canonical, simplified one (see, for instance [14][30][31] and many others), which makes use of the *plane-wave approximation*; and the realistic *wave packet*[32][33][34] treatment arrive at the same general formula, which only has two experimentally-tunable parameters (E and L):

$$\begin{aligned} \mathcal{P}(\nu_\alpha \to \nu_\beta) = \delta_{\alpha\beta} - 4\sum_{i>j} \mathcal{R}(U_{\alpha i}^* U_{\beta i} U_{\alpha j} U_{\beta j}^*) sin^2\left(\Delta m_{ij}^2 \frac{L}{4E}\right) + \\ +2\sum_{i>j} \mathcal{I}(U_{\alpha i}^* U_{\beta i} U_{\alpha j} U_{\beta j}^*) sin\left(\Delta m_{ij}^2 \frac{L}{2E}\right) \end{aligned} \tag{1.14}$$

where $\Delta m_{ij}^2 \equiv m_i^2 - m_j^2$. The last "+" sign is a "−" for the antineutrino oscillation probability, so there would be an $\nu - \overline{\nu}$ asymmetry for the Dirac or Majorana phases $\delta_{CP}, \alpha_{j1} \neq 0, \pi$ causing CP violation, or other CP-violating effects.

There are many situations in which the experimental neutrino composition can be approximated with a great deal of precision to a 2-neutrino scenario. In this case, the formula 1.14

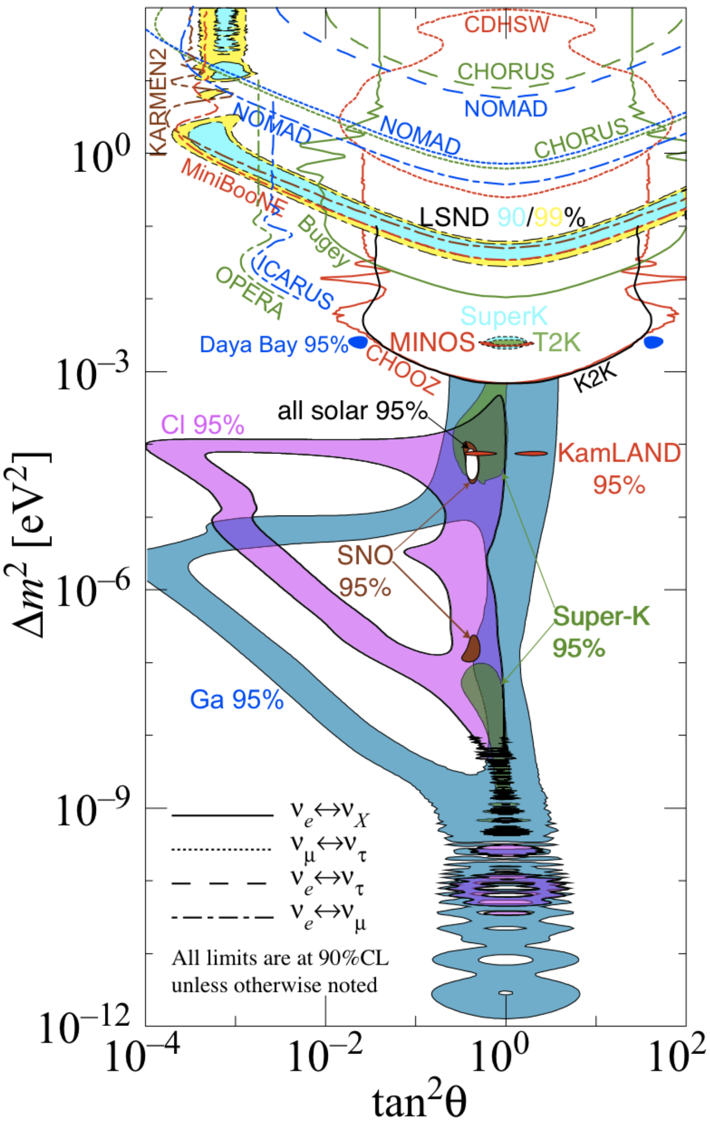

FIGURE 1.3: Allowed phase space for neutrino oscillations, for all experimental data[29]

simplifies to:

$$\begin{aligned}\mathcal{P}^{2\nu}_{\nu_\alpha \to \nu_\beta}(L,E) &= \frac{1}{2} sin^2 2\vartheta \left[1 - cos^2 \frac{\Delta m^2 L}{4E}\right] = \\ &= sin^2 2\vartheta sin^2 \left(\frac{\Delta m^2 L}{4E}\right)\end{aligned} \tag{1.15}$$

The survival probability $\mathcal{P}^{2\nu}_{\nu_\alpha \to \nu_\alpha}(L,E)$ is just $1 - P^{2\nu}_{\alpha\beta}$, by unitarity.

Care has to be exercised to make sure the coherency argument by which real neutrinos oscillate is mantained. Real neutrino sources are described by wave packets of massive neutrinos, whose group velocities are different because of their different masses, and which have a certain central momentum p_0 at production and a minimum localization dispersion of half an oscillation length $2E/\Delta m^2$[34]. At production, they overlap and interfere giving rise to neutrino oscillations (as

Measured parameter	Probe
$\mid U_{e2} \mid^2$	Solar
$\mid U_{\mu 2} \mid^2 + \mid U_{\tau 2} \mid^2$	Solar
$\mid U_{e2} \mid^2 \mid U_{e1} \mid^2$	KamLAND
$\mid U_{\mu 3} \mid^2 (1- \mid U_{\mu 3} \mid^2)$	Atmospheric, K2K, MINOS
$\mid U_{e3} \mid^2 (1- \mid U_{e3} \mid^2)$	DoubleChooz, DayaBay, RENO
$\mid U_{e3} \mid^2 \mid U_{\mu 3} \mid^2$	MINOS, T2K
Δm^2_{23}, Δm^2_{13}	Several

TABLE 1.2: Current channels for neutrino oscillation parameters, from [35]

long as neutrinos have sufficient space to evolve its oscillatory behavior from the production site to the detector ($\Delta m^2 L \gtrsim 2E$)), but they will drift over time. For non-continuous sources such as neutrino pulses, incoherency will develop, causing the interference to disappear over long propagation distances greater than the coherence length L^{coh}_{kj} (σ_x is the FWHM of the Gaussian wave packet):

$$L^{coh}_{kj} = \frac{4\sqrt{2}E^2}{\mid \Delta m^2_{kj} \mid}\sigma_x \tag{1.16}$$

If this incoherency develops for some reason, for example if the physical dimensions of the detector or the production site are not much smaller than the oscillation length $L^{osc}_{kj} = 4\pi E/\Delta m^2_{kj}$ (or the energy resolution of the detector is too broad), oscillations will smear out and the oscillation probability will only depend on the mixing angle, which is the case for sub-MeV solar neutrinos where matter effects (see Section 1.3) are not relevant:

$$\begin{aligned} \mathcal{P}^{incoh}_{\nu_\alpha \to \nu_\beta} &= \sum_k \mid U_{\alpha k} \mid^2 \mid U_{\beta k} \mid^2 \underset{2\nu}{\sim} \\ &\underset{2\nu}{\sim} \mathcal{P}^{2\nu}_{\nu_\alpha \to \nu_\beta} = \frac{1}{2} sin^2 2\vartheta \end{aligned} \tag{1.17}$$

In table 1.2 a summary of the channels that have been used so far to probe neutrino masses[11] and angles is offered, and in table 1.3 the best available values for the physical oscillation parameters are presented.

1.3 Solar neutrinos and SSM

Neutrinos can be produced in a wealth of natural or human-induced processes, as shown in Figure 1.4, of which Borexino's specialties (solar, reactor and geo-neutrinos) are only a few.

[11]Although regarded as unlikely, one of the neutrinos, namely ν_1, could have $m_1 = 0$ without contradicting observations.

Parameter	Value	Experimental probe
$sin^2 2\theta_{13}$	0.093 ± 0.008	Reactor data (DB, RENO, Chooz)
$sin^2 2\theta_{12}$	0.0846 ± 0.021	Solar, reactor, accelerator data
$sin^2 2\theta_{23}$	$0.92(90\% c.l.) \leftrightarrow \theta_{23} = 45 \pm 7.1°$	Atmospheric ν data
Δm^2_{21}	$7.53 \pm 0.18x10^{-5}eV^2$	Solar data
$\mid \Delta m^2_{31} \mid \approx \mid \Delta m^2_{32} \mid$	$2.44 \pm 0.06x10^{-3}eV^2$	Sign unknown, NOνA favors NH.
$\sum_j m_j$	$< 0.66eV; (95\% c.l.)$	Planck+WMAP+ACT (+BO $< 0.23eV$)
δ_{CP}	Unknown ($3\pi/2$?)	Newest: NOνA
α_{j1}	Unknown ($\nu = \overline{\nu}$?)	-

TABLE 1.3: Best neutrino oscillation parameter values, from [36].

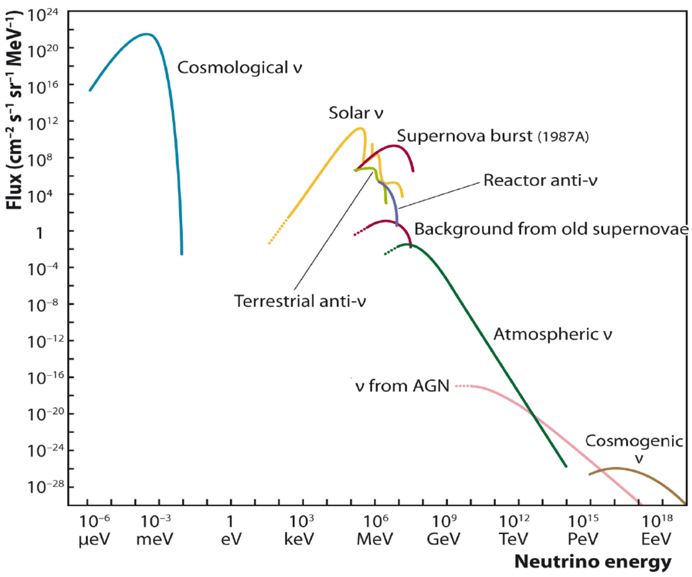

FIGURE 1.4: Major neutrino flux contributors on Earth and their energy spectra, from [37]. Not included are very localized neutrino beam sources such as accelerators, since by their nature they are just detectable in very particular areas.

Not taking into account the as-of-yet undetectable relic cosmic neutrinos, and localized man-made sources, solar neutrinos are the most important contributor to the neutrino flux on Earth. Stars are systems held in equilibrium by their gravitational and radiation pressures, and the nuclear fusion processes taking place in their interior produce copious amounts of neutrinos. As illustrated in Section 1.2, its study led to the smoking gun for neutrino oscillations, and its later discovery.

1.3.1 MSW effect and its influence in solar ν production

Neutrino oscillations, as described in the last section 1.2, were the key model that solved the SNA and ANA –however, in the case of solar neutrinos there were a few loose ends:

1. They exhibit a broad spectrum, so they shouldn't oscillate with the same frequency. The smearing of the oscillation probability would give the same survival probabilities for all neutrinos independent of energy (see equation 1.17), which is not the case in reality with solar neutrinos with E$\gtrsim$1 MeV.

2. The eccentricity in the Earth's orbit would cause a noticeable change in baseline L, which would produce a seasonal survival probability oscillation, which is not observed beyond the $\sim 7\%$ geometrical modulation of the flux[38].

An interesting concept was put forward by Wolfenstein[39] in 1978 when he postulated that, because of coherent forward elastic scattering[12] –which makes this relevant only in extremely dense matter environments (neutron stars, supernova cores...)– with the particles in the matter that neutrinos traverse (notably, electrons and nucleons), a potential[13] will modify their oscillatory behavior as compared to when they travel through vacuum, although the correct expression wasn't finalized until 1983[40]. In 1985, a special case of this matter effect by S. P. Mikheev and A. Yu. Smirnov[41] was identified when neutrinos travel in matter with varying density, reaching a resonant effect when the mixing angle reaches $\pi/4$: this is know as the *Mikheev-Smirnov-Wolfenstein* (MSW) effect.

The net effect is the addition of a helicity-conserving *interaction Hamiltonian* to the H_0 Hamiltonian for vacuum propagation, caused by charged-current interactions with electrons and neutral-current interactions with neutrons (proton and electron NC interactions cancel each other out):

$$\overline{\mathcal{H}_{eff}}(x) = \sum_{\alpha=e,\mu,\tau} V_{CC}\delta_{\alpha e} + V_{NC} = 7.63 \cdot 10^{-14} \frac{\text{eV} \cdot \text{cm}^3}{N_A} \left(N_e \delta_{\alpha e} - \frac{1}{2} N_n\right) \tag{1.18}$$

The NC part, as well as eventual Majorana phases, are eventually found to be irrelevant for the spatio-temporal *active* neutrino oscillations, which are governed by the Schrödinger-like equation:

$$\begin{gathered} i\frac{d}{dx}\psi_{\alpha\beta}(x) = \sum_{\eta} \left(\sum_k U_{\beta k} \frac{\Delta m^2_{k1}}{2E} U^*_{\eta k} + \delta_{\beta e}\delta_{\eta e} V_{CC} \right) \psi_{\alpha\eta}(x) \leftrightarrow \\ \leftrightarrow i\frac{d}{dx}\psi_{\alpha} = \mathcal{H}_F \psi_{\alpha}; \mathcal{H}_F = \frac{1}{2E}(U\mathbb{M}^2 U^\dagger + \mathbb{A}) \end{gathered} \tag{1.19}$$

Experimental bounds on short-distance oscillations of reactor $\overline{\nu_e}$ show that a 2ν approximate mixing expression is useful to describe matter effects, since only ν_1 and ν_2 are significantly

[12] Incoherent scattering also can take place, but is exceedingly rare: the mean free path of a neutrino is inversely dependent on its energy in GeV: $\ell_{matter} \sim \frac{10^{14} cm}{E(GeV)}$[14]

[13] Indeed, equivalent to an index of refraction

involved in the evolution of solar neutrinos (or, in the flavor basis, ν_e and a linear combination of ν_μ and ν_τ (ν_x)). In this case, the effective mixing angle becomes $\tan 2\vartheta_M = \frac{\tan 2\vartheta}{1-\frac{A_{CC}}{\Delta m^2 \cos 2\vartheta}}$; $(A_{CC} = 2\sqrt{2}EG_F N_e)$, which presents a resonance condition (mixing angle $\vartheta = \pi/4$) when $A^R_{CC} = \Delta m^2 \cos 2\vartheta$; that is, when the matter density is $N^R_e = \frac{\Delta m^2 \cos 2\vartheta}{2\sqrt{2}EG_F}$.

Furthermore, in the case of smooth matter density gradients, the adiabatic condition holds ($\nu^M_1 \leftrightarrow \nu^M_2$ transitions are negligible in that case):

$$\gamma = \frac{\Delta m^2_M}{4E \mid d\vartheta_M/dx \mid} \ggg 1 \tag{1.20}$$

For neutrino sources with smooth matter density variations in which the adiabaticity condition holds, and which are separated from the detector by a large vacuum distance, the survival probability averages out and is independent of the distance:

$$\overline{\mathcal{P}^{adiab}_{\nu_e\to\nu_e}} = \frac{1}{2} + \frac{1}{2}\cos 2\vartheta^{(i)}_M \cos 2\vartheta \tag{1.21}$$

This effect incidentally explains the fact that solar neutrinos exit the Sun in a practically-pure mass eigenstate $\mid \nu_2\rangle$[30], even if all of them are produced in the ν_e flavor state (electron-flavor neutrinos arise from all nuclear fusion reactions powering stars, see next subsection 1.3.2): since the propagation of a neutrino from the Sun's central regions to its surface fulfills the adiabaticity condition in the matter density variation, the ν_e created in a fusion reaction will be created in radius-dependent eigenstates of the effective Hamiltonian ($\mathcal{H}_T = \mathcal{H}_{vacuum} + \mathcal{H}_{matter}(r)$), which do not cross each other for any r. Furthermore, when matter density $N_e \ggg N^R_e$, the presence of matter supresses ν_e oscillations, and the heaviest mass eigenstate coincides with this flavor state[14]. In the opposite limit, oscillations trivially proceed as in vacuum. On the other hand, $\nu_\mu \leftrightarrow \nu_\tau$ oscillations proceed in a vacuum-like fashion also in dense matter.

The solar neutrino will continue to be in that eigenstate of $\mathcal{H}_T$ until matter effects are no longer valid (that is, until the solar surface). But being created in the heaviest of the total Hamiltonian $\mathcal{H}_T$ eigenstates, means it will continue to be in the heaviest of the *vacuum* Hamiltonian $\mathcal{H}_v$, which is precisely $\nu_2 = \nu_e sin\vartheta + \nu_x cos\vartheta$. Since this is a mass eigenstate, it will not suffer any oscillations during its trip through the vacuum of space.

The applicability of this solution has been strengthened over the years, notably by the precision measurement of the rates from the different parts of the solar neutrino spectrum, in particular the difference in oscillation between the high and low energy neutrino rates, as illustrated in Figure 1.5. Other measurable effects, like the regeneration of ν_e (by which the Sun shines more

[14] CP or CPT invariance does not hold in this case ($\mathcal{P}^{2\nu}_{m,ee} \neq \mathcal{P}^{2\nu}_{m,\overline{ee}}$) since normal matter is not charge-symmetric: most astrophysical objects, including the Solar System bodies, do not hold relevant amounts of antimatter.

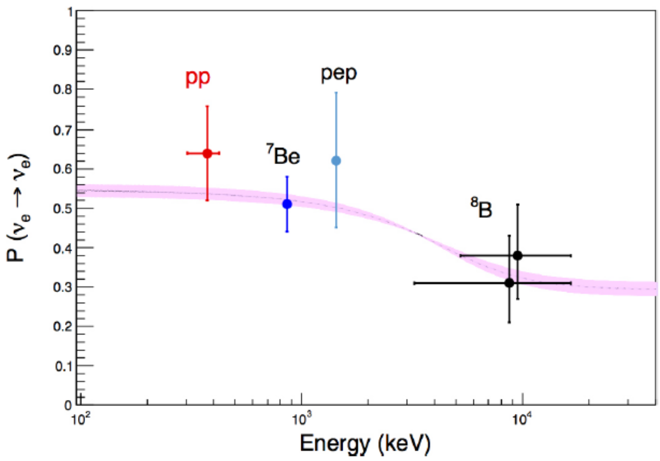

FIGURE 1.5: Survival probability according to the MSW effect (1σ band) and experimental measurements from Borexino for all observed solar neutrinos, from [42]

strongly at night than during the day if "seen" in neutrinos) giving rise to the day-night asymmetry in high solar neutrino energy ranges[43] (or its absence in lower-energy regimes[44]), or the absence of seasonal modulation[38] have backed up the LMA solution to very high statistical significance, even without external assumptions like CPT symmetry. Reactor $\overline{\nu_e}$ disappearance measurements[45] also back this solution independently. It implies the following survival probabilities (the resonance matter density is not reached in the Sun for sufficiently low-energy ($\leq$2MeV) neutrinos):

$$\begin{aligned} \overline{\mathcal{P}_{ee}} \simeq \mathcal{P}_{ee}^{vac} = 1 - \frac{1}{2}\sin^2 2\vartheta; E \leq 2 \text{ MeV} \\ \overline{\mathcal{P}_{ee}} \simeq \frac{1}{2}(1 + \cos 2\vartheta_M \cos 2\vartheta); E \geq 2 \text{ MeV} \\ \overline{\mathcal{P}_{ee}} \simeq \sin^2 \vartheta; E \ggg 2 \text{ MeV} \end{aligned} \tag{1.22}$$

For a model that fully accounts for all 3 active neutrinos in the Sun, the survival probability reduces to: $\mathcal{P}_{ee}^{3\nu} \simeq \sin^4 \theta_{13} + \cos^4 \theta_{13} \mathcal{P}_{ee}^{2\nu}(\Delta m_{21}^2, \theta_{12}; N_e \cos^2 \theta_{13})$, since the oscillatios due to Δm_{13}^2 are strongly suppressed because of the averaging of the oscillations ($L_{31}^{osc} \lesssim 10km$) over the ν_e production regions inside the Sun ($\Delta R \ggg L_{31}^{osc}$).

Other historically seriously-considered matter oscillation solutions were the Small Mixing Angle (SMA), the low mass-squared difference / low probability (LOW), the Quasi-Vacuum (QVO) and clearly the Vacuum Oscillations (VO)[46], whose phase spaces in the $\tan^2 \vartheta - \Delta m^2$ are shown in Figure 1.6. Non-Standard Interactions may still be present, but their phase space has been much constrained.

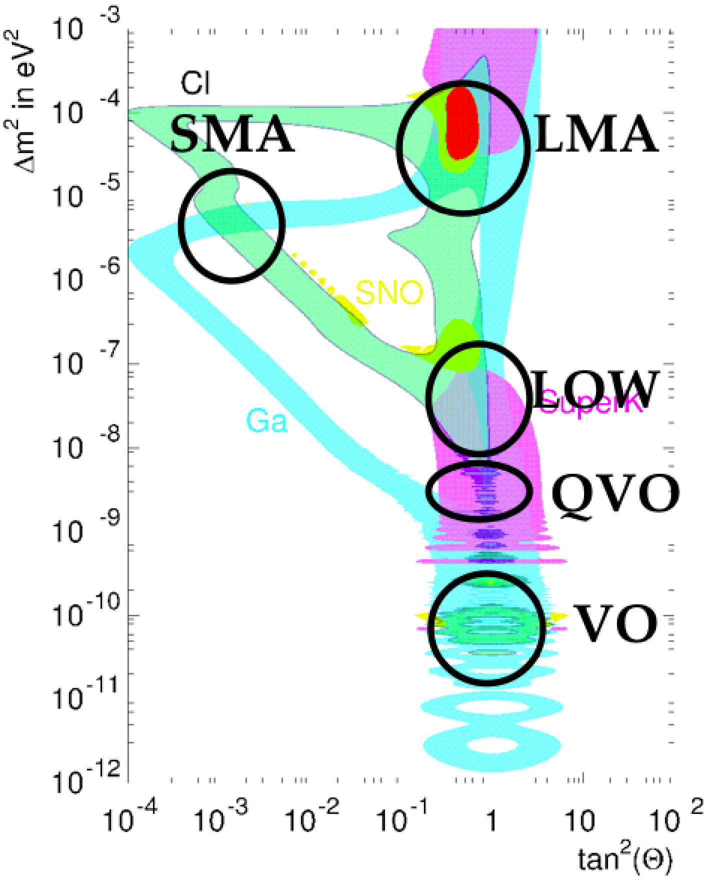

FIGURE 1.6: Historically-considered MSW solutions –nowadays all the non-LMA phase space is strongly disfavored. Adapted from [14] and [29]

1.3.2 Solar models

Stars are understood to be self-supported thermonuclear reactors, where gravitational pressure allows nuclear fusion processes to take place in their core, while radiation and particle pressure from these reactions prevents it from collapsing, arriving at a *steady-state hydrostatic and thermal equilibrium*. In fact, Solar Models consider our Sun to be a *spherically-symmetric collection of gas in different ionization states*, where energy is transported to the exterior by photonic transport (sunlight), convective magnetohydrodynamical phenomena in the outer layers and, to a lesser extent, neutrinos produced during the nuclear reactions. It is neutrinos that fusion reactions mainly produce, due to the transforming of protons into neutrons ($p^+ \to n^0 + e^+ + \nu_e$) that needs to take place in order to create stable nuclei (which, in general, have N>Z).

Stellar fusion drives four protons to become a helium-4 nucleus, accompanied by two positrons and two electron neutrinos, with the emission of ~26.7 MeV from the mass difference in binding energy. This energy is imparted mainly in the form of kinetic energy, most of which ($\sim$ 98%)

FIGURE 1.7: Video frame of the solar surface during a Coronal Mass Ejection (CME) event, as seen from NASA's Solar Dynamics Observatory (SDO)'s vantage point in the geosynchronous belt (GEO). The photons radiating from the Sun are emitted $10^4 - 10^5$ years since the fusion energy was produced, due to the multiple scatterings it will suffer inside the dense plasma –while neutrinos will majoritarily pass through, unimpeded, in ~2 seconds.

escapes in the form of photons as the positrons promptly annihilate with plasma electrons:

$$4p^+ \rightarrow^4 He + 2e^+ + 2\nu_e \Leftrightarrow 4p^+ + 2e^- \rightarrow^4 He + 2\nu_e + 26.731 \text{ MeV} \tag{1.23}$$

The completion of this process until termination, *i.e.*, until the production of a ^4He nucleus, can proceed by 2 main mechanisms in the Sun: the *pp* and the *CNO* chains, further explained below.

A Standard Solar Model is an iterative model that considers the Vogt-Russel theorem[47] to determine the radius, luminosity, internal structure and evolution of the Sun in a steady-state equilibrium by its mass and compositional structure. It is constrained by the assumption of homogeneity at the start of the Sun's lifetime (after the collapse of the protostellar nebula, just after fusion reactions started to account for most of its luminosity), and an approximately exponential matter density (see equation 1.24). Energy transport is accomplished via radiation (98% by mass, or 71% by radius) and convection (outer layers); and the initial composition of the $1M_\odot$ is fixed to primordial meteorites ratios. Its evolution after 4.6x10^9 years is then imposed to match several present-day observables ($L_\odot$, elemental abundance, $R_\odot$, density and structure derived from *p*-mode *sunquake* oscillations studied with helioseismology...), through the numerical calculation of the equations of state for pressure, opacity and energy generation rate.

$$N_e(d) = N_e(t_0)e^{-\frac{d-d_0}{r_0}}, N_e(0) = 245N_A/cm^3;\ r_0 = \frac{R_\odot}{10.54}\ (0.1 < r/R_\odot < 0.904) \\ N_e(d) = 18.9/R_\odot\ (r > 0.904R_\odot) \tag{1.24}$$

The solutions to these equations give information about the inital values of hydrogen, helium and *metals* (heavier than helium), the distribution of physical variables inside the Sun, the spectrum of acoustic oscillation frequencies measured through helioseismological processes and the neutrino fluxes[48].

Thanks to quantum tunneling, the Coulomb barrier between nuclei, that for two protons classically could not be overcome until $E \gtrsim 550$ keV, yields a probability for the reaction to occur given by the *Gamow factor* $\mathcal{P}_C \approx e^{-2\pi\frac{Z_A Z_B \alpha}{\sqrt{2}}\sqrt{\frac{\mu}{e}}}$ (μ is the reduced mass and E the center-of-mass energy), from which the cross section $\sigma(E) = \frac{1}{E}\mathcal{P}_C S(E)$ is derived. $S(E)$ is the astrophysical S-factor, and is extrapolated out of Earth-based cross section experiments for low energies, since it is weakly and smoothly affected by energy changes, away from resonance areas. The reaction rate is then, in terms of the Gamow energy $E_G = 2\mu(\pi\alpha Z_A Z_B)^2$:

$$\langle\sigma_v\rangle_{AB} = \sqrt{\frac{8}{\pi\mu(k_B T)^3}}\int_0^\infty dES(E)e^{-\frac{E}{k_B T}-\sqrt{\frac{E_G}{E}}} \simeq \\ \simeq 4\sqrt{\frac{2}{3\mu}S(E_0)\frac{\sqrt{E_0}}{k_B T}e^{-3\frac{E_0}{k_B T}}};\ E_0 = \sqrt[3]{\frac{\mu}{2}(\pi\alpha Z_A Z_B k_B T)^2} \tag{1.25}$$

This expression gives a "Gamow peak" that enhances fusion cross sections for light nuclei at low energies. Reaction 1.23, as mentioned, will occur through two mechanisms:

SSM pp

The *pp chain* accounts for the majority (∼99%) of the Sun's hydrogen burning. It is divided in three branches: pp-I, pp-II and pp-III. Regardless of the actual termination process, which is what defines these branches, the pp chain always proceeds via two initial reactions (Q values[15] shown to the right of each reaction):

pp reaction This process accounts for the vast majority (99.6%) of the *pp* chain onset, and as such, also for the vast majority of the Sun's energy production. It combines two protons to form a deuteron, plus a positron and the lowest-energy solar neutrino: the *pp neutrino*, which has a continuous spectrum from 0 to the Q-value of 420 keV.

$$p^+ + p^+ \rightarrow^2 H + e^+ + \nu_e;\ Q = 0.42\text{MeV} \tag{1.26}$$

[15] $\Delta m_{initial-final} = E_k^{final\_particles}$ (natural units)

Its rate at low energies is too low to be accurately measured in Earth-based laboratory conditions, but can be deduced from weak interaction theory and scattering data for proton-proton interactions. It is also very well determined by the solar luminosity constraint 1.27:

$$\Phi_\nu = \frac{2L_\odot}{4\pi r^2 26.7 \text{ MeV}} \tag{1.27}$$

The Earth-arriving flux for this reaction has been directly determined for the first time by Borexino[42] to be $(6.6 \pm 0.7)\text{x}10^{10} cm^{-2} s^{-1}$ with a survival probability $\mathcal{P}_{ee} = 0.64 \pm 0.12$; more details can be found in Section 2.5.

pep reaction The remaining ∼0.4% of pp chain initiations comes from the three-body fusion of two protons and an electron to form a deuteron and yield the *pep neutrino* at a monochromatic energy of 1.44 MeV:

$$p^+ + e^- + p^+ \rightarrow^2 H + \nu_e;\ Q = 1.44 \text{ MeV} \tag{1.28}$$

Since the ratio of *pep/pp* reactions is practically independent of the considered SSM (∼0.004), a measurement of one flux is an automatically very good constraint on the other. Borexino also performed the first direct measurement of this flux[49]: $(1.6 \pm 0.3)\text{x}10^8 cm^{-2} s^{-1}$ with a survival probability of $\mathcal{P}_{ee} = 0.67 \pm 0.17$; more details can be found in Section 2.5.

These two reactions provide the main restriction on the hydrogen burn-up rate inside the Sun, since they are determined via weak interaction processes. Both of them continue with the fusion of a further, third proton with the deuteron to form ^3He:

$$^2H + p^+ \rightarrow^3 He + \gamma;\ Q = 5.49 \text{ MeV} \tag{1.29}$$

From there, the pp chain branches out to its four termination reactions:

pp-I The pp-I branch accounts for the majority (∼85%) of the terminations in the pp chain. It doesn't involve the emission of any neutrinos, as two helium-3 nuclei combine to create an α particle (^{4}He nucleus) and release two free protons:

$$^3He +^3 He \rightarrow^4 He + 2p^+;\ Q = 12.86 \text{ MeV} \tag{1.30}$$

pp-II Both the pp-II and pp-III chains commence with the fusion of a ^{3}He and ^{4}He nucleus in the ^{7}Be-producing reaction accounting for 15% of continuations of reaction 1.29:

$$^3He +^4 He \rightarrow^7 Be + \gamma;\ Q = 1.59 \text{ MeV} \tag{1.31}$$

From here, the pp-II chain proceeds onwards through the electron-capture decay of ^{7}Be (which is the preferred (99.87%) continuation of the 15%-likely ^{7}Be creation process), producing the doubly-monochromatic ^{7}*Be neutrino*[16], whose precise flux determination was the primary objective for Borexino since its inception. Its world-first direct determination was its first main result in 2008[50], and an updated measurement with an unprecedented precision was performed in 2011[51]: $(4.84 \pm 0.24)\text{x}10^9 cm^{-2}s^{-1}$, for a survival probability $\mathcal{P}_{ee} = 0.51 \pm 0.07$; more details can be found in Section 2.5.

$$^7Be + e^- \rightarrow ^7 Li + \nu_e;\ Q = 0.862 \text{ MeV} \tag{1.32}$$

This branch is terminated with the subsequent transmutation of lithium-7 into a pair of termination ^{4}He nuclei:

$$^7Li + p^+ \rightarrow 2^4He;\ Q = 17.34 \text{ MeV} \tag{1.33}$$

pp-III This is the smallest branch (0.13%), yet extremely important, set of reactions that can also terminate the ^{7}Be creation; and also the chain that gives rise to the most energetic[17] detected solar neutrinos (continuous spectrum with endpoint at 17.98MeV). It is based on the creation of ^{8}B from ^{7}Be, which subsequently decays into metastable ^{8}Be (which itself rapidly –67as– double-alpha-decays into two termination ^{4}He products):

$$\begin{aligned} ^7Be + p^+ \rightarrow ^8 B + \gamma;\ Q = 140 \text{ keV} \\ ^8B \rightarrow ^8 Be^* + e^+ + \nu_e;\ Q = 17.98 \text{ MeV} \\ 8Be^* \rightarrow 2^4He;\ Q = 140 \text{ keV} \end{aligned} \tag{1.34}$$

This solar neutrino was the among the first one detected by the pioneering Homestake experiment as part of its integral measurement, and provided the first clear evidence towards neutrino oscillations in SNO[25]. Borexino provided the first measurement of the low-energy part of the ^{8}B neutrino spectrum in 2008[52], with a flux of $(2.4 \pm 0.4_{stat} \pm 0.1_{syst})\text{x}10^6 cm^{-2}s^{-1}$ for a survival probability of $\mathcal{P}_{ee} = 0.29 \pm 0.10$; more details can be found in Section 2.5.

hep Finally, the pp chain can also proceed through the fusion of a ^{3}He nucleus with a fourth proton directly, generating the termination ^{4}He nucleus (plus a positron and the *hep neutrino*):

$$^3He + p^+ \rightarrow ^4 He + e^+ + \nu_e;\ Q = 19.79 \text{ MeV} \tag{1.35}$$

[16] The resulting ^{7}Li nucleus can be created in an excited state at 487 keV (10% b.r.), which means the energy of the emmited ^{7}Be-ν is not the Q value of 862 keV, but its difference 384 keV.

[17] hep neutrinos have a slightly higher endpoint energy (∼1.8 MeV higher), but their flux is several orders of magnitude smaller, so they have never been detected yet.

This reaction has a vanishingly small importance inside the Sun (accounting for $\sim$ 2x10^{-5}% of the pp chain terminations) and therefore, its neutrinos will be exceedingly difficult to detect. Its best limit has been set in 2001 by SuperKamiokaNDE at <4x$10^4 cm^{-2}s^{-1}$[53], or 4.3 times the BP00 SSM prediction.

SSM CNO

The remaining $\sim$ 1% of helium-4 production in the Sun is due to the *carbon-nitrogen-oxygen cycle* (CNO), where four protons combine with a carbon-12 nucleus to catalytically give rise to the same reaction products as the pp chain (the aforementioned ^{4}He nucleus, two positrons and two electron-neutrinos), leaving behind another ^{12}C nucleus. The energy release is the same as in the pp chain. This process, although subdominant in small stars such as our Sun, is expected to account for ever larger percentages of energy production in larger ones (dominant for stars above $1.3M_{\odot}$). It is entirely dependent on the metallicity content of a star, which is constrained by its opacity and primordial abundances.

$$^{12}C + 4p^+ \rightarrow ^{12}C + ^4He + 2e^- + 2\nu_e;\ Q = 26.7 \text{ MeV} \tag{1.36}$$

The catalytic ^{12}C is generated through the *triple-alpha* process. This only happens assuming a ^{4}He nucleus will find its way to fuse with the metastable $^8Be^*$ before it decays in the termination of the pp-III chain in reaction 1.34; that is, when beryllium-8 nuclei can fuse at a faster rate than they decay ($^8Be + ^4He \rightarrow ^{12}C$;Q=7.367 MeV). Since this condition only prevails at temperatures beyond 10^8K, thanks to the parallel creation of ^{8}Be through the fusing of two helium-4 nuclei ($^4He + ^4He \rightarrow ^8Be^*$;Q=-93.7 keV), it is very rare in the Sun, whose core temperature is $\sim$10 times lower.

The CNO cycle is divided in two sub-cycles; namely, the CNO-I (CN cycle, or Bethe-Weiszäcker cycle) and CNO-II (NO cycle):

CN cycle Once believed to be the dominant energy-producing cycle in the Sun (because of wrong elemental abundances pointing to the sun being composed of $\sim$ 10% nitrogen[54]), this process is limited by the proton capture in nitrogen-14. The generated neutrinos have a continuous energy spectrum. It is the overwhelmingly preferent process for CNO termination (99.9%) and produces two neutrinos, one of which (in reaction 1.41) is common with the NO cycle.

$$^{12}C + p^+ \rightarrow ^{13}N + \gamma;\ Q = 1.94 \text{ MeV} \tag{1.37}$$

$$^{13}N \rightarrow ^{13}C + e^+ + \nu_e;\ Q = 1.19 \text{ MeV} \tag{1.38}$$

$$^{13}C + p^+ \rightarrow ^{14}N + \gamma;\ Q = 7.55 \text{ MeV} \tag{1.39}$$

$$^{14}N + p^{+} \rightarrow ^{15} O + \gamma;\ Q = 7.30 \text{ MeV} \tag{1.40}$$

$$^{15}O \rightarrow ^{15} N + e^{+} + \nu_{e};\ Q = 1.73 \text{ MeV} \tag{1.41}$$

$$^{15}N + p^{+} \rightarrow ^{16} O^{*} \rightarrow ^{12} + ^{4}He;\ Q = 4.97 \text{ MeV} \tag{1.42}$$

NO cycle This subdominant, $\sim 0.1\%$ termination relies on the small branching ratio of the decay in reaction 1.42, whose α decay is far more likely than a de-excitation through γ emission. This, however, can occur and will give rise to a different neutrino coming from the ^{17}F decay:

$$^{15}N + p^{+} \rightarrow ^{16} O^{*} \rightarrow ^{16} O + \gamma,\ Q = 12.13 \text{ MeV} \tag{1.43}$$

$$^{16}O + p^{+} \rightarrow ^{17} F + \gamma;\ Q = 0.60 \text{ MeV} \tag{1.44}$$

$$^{17}F \rightarrow ^{17} O + e^{+} + \nu_{e};\ Q = 1.74 \text{ MeV} \tag{1.45}$$

$$^{17}O + p^{+} \rightarrow ^{14} N + ^{4} He \tag{1.46}$$

The ^{14}N produced in the termination reaction 1.46 will re-integrate in the environment to potentially initiate another of the CN/NO-common proton capture reaction 1.40. For this reason, the neutrino coming from the oxygen-15 decay is produced in 100% of the cases a CNO cycle is initiated. However, ^{13}N neutrinos are produced both in cooler areas around the core (T$\lesssim 10^{7}$K) and in the deepest, hottest inner areas, while ^{15}O neutrinos are only produced in the latter.

Slightly different *hot CNO cycles* are also possible in novae and x-ray bursts.

The CNO neutrino flux has never been directly detected, although the Borexino *pep* neutrino rate measurement has provided its best available lower limit[49]. It is one of the objectives of this thesis to demonstrate the progress made and the efforts dedicated to the first-ever direct measurement of CNO neutrinos.

The most refined and trusted solar models currently available are the AGSS09[55] and the GS98[56] (although many others are available, such as the BP00, BP04, AGSS05...) which yield the solar neutrino fluxes shown in Figure 1.8.

1.3.3 Metallicity problem

As illustrated in table 1.4, even if the SNP has been solved, there remains an equally formidable, yet subtler problem: the elemental abundance in the Sun, or the Solar Composition Problem (SCP)[60][61].

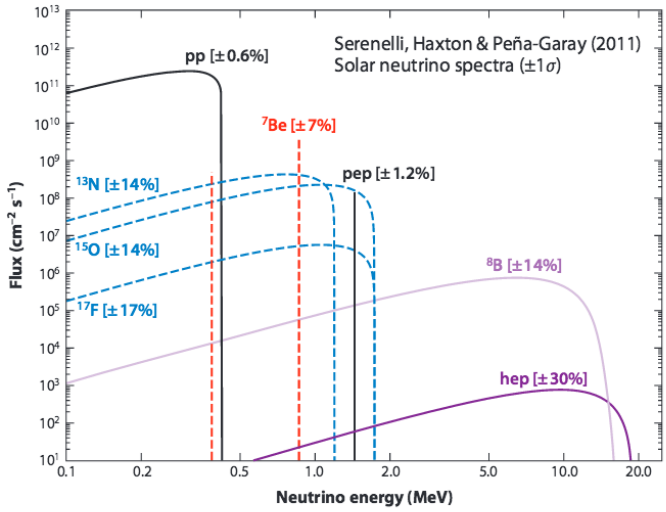

FIGURE 1.8: Neutrino flux spectrum at 1 AU for the different components stemming from the *pp* and *CNO* cycles in the latest SSM by Bahcall and Serenelli, adapted from [57]. It should be noted the "monochromatic" ^{7}Be and *pep* are thermally broadened in reality and the EC branching ratios have been omitted for the CNO fluxes (which would yield two monochromatic lines at 2-3 MeV of $\sim 10^5 cm^{-2}s^{-1}$[58]). Not shown either is a $\sim 10^9 cm^{-2}s^{-1}$ MeV^{-1} multi-flavor neutrino flux below 90 keV due to neutrino pair production[59].

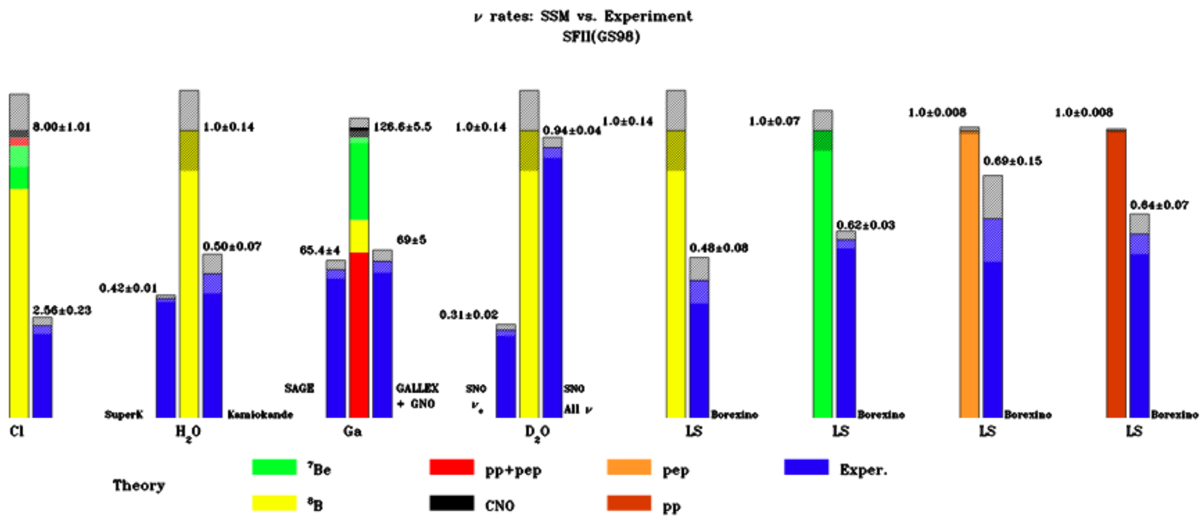

FIGURE 1.9: Predictions for neutrino fluxes at production and detected, with their uncertainties in shaded gray. The noticeable difference is well-explained by neutrino oscillations in all cases.

The metallic (C, N, O and Ne) and refractory (Mg, Si, S, Fe) elemental composition of the Sun is constrained through the photospheric study of the spectral emission lines, as well as from the homogeneity assumption from the protosolar nebula at first sustained thermonuclear reactions. The *low-metallicity* AGSS05 and AGSS09 models have lowered the metal-to-hydrogen ratio $(Z/X)_\odot$ from ~0.023 to ~0.018. They were considered to be an improvement over the

Reaction	ν energy (MeV)	GS98	AGS05	AGSS09	AGSS09ph	exp
pp	0 - 0.42	5.98(0.6%)	6.04	6.03(0.6%)	6.01	10^{10}
pep	1.44	1.44(1.2%)	1.41	1.47(1.2%)	1.43	10^{8}
hep	0-19.79	8.04(30%)	8.24	8.31(30%)	8.1	10^{3}
^{7}Be	0.862+0.383	5.00(7%)	4.54	4.56(7%)	4.79	10^{9}
^{8}B	0-17.98	5.58(14%)	4.66	4.59(14%)	5.22	10^{6}
^{13}N	0-1.19	2.96(14%)	1.85	2.17(14%)	2.15	10^{8}
^{15}O	0-1.73	2.23(15%)	1.29	1.56(15%)	1.55	10^{8}
^{17}F	0-1.74	5.52(17%)	3.14	3.40(16%)	3.70	10^{8}
CNO	0-1.74	5.24(84%)	-	3.76(60%)	-	10^{8}

Table 1.4: Earth-measured solar neutrino flux predictions according to the best SSMs available, organized by name and energy. Uncertainties for the most relevant models for CNO flux determination are noted in parentheses, as a percentage of the flux. Note the CNO cycle discrepancy is around $\sim 30\%$. ^{7}Be and ^{8}B discrepancies between models could, in principle, tilt the scale towards one of the models, but experimental measurements fall in the 1σ overlap seen in Figure 1.10. Adapted from [57] and [55]

high-metallicity GS98 model, thanks to its more careful selection of spectral lines, 3D hydrodynamical treatment of the Sun's convective envelope and relaxation of the local thermodynamic equilibrium condition in line formation. However, while this modification took into account the improved photospheric description, its results turned out to be in important tension with the helioseismically-deduced interior composition. While solutions to this puzzle can be as "trivial" as a technical re-tuning of the abundance or opacities parameters[57] or statistical combination of different channels[62]; or as far-reaching as the repeal of the homogeneity assumption[18] (Non-Standard Solar Models –NSSMs– study these scenarios[63]), its resolution will determine our understanding of the core composition of the Sun, its temperature ($\sim$ 1% lower in the low-metallicity models) as well as its convective zone boundary radius.

The CN fluxes have a linear dependence on presolar abundances of C and N, which do not affect solar opacity[60]. Late accretion models are extremely constrained by the solar neutrino flux, and indeed most of them don't account for the currently-known limits of neutrino fluxes yet. CNO fluxes vary by $\sim$ 30% between high- and low-metallicity models, and it seems likely the solution to the SCP will come from the CNO flux measurement. The importance of clearing this tension cannot be understated, since the proper modelling of our best-understood star has implications to understand all main sequence stars and planet formation itself.

[18] Indeed, inhomogeneities in the proto-solar nebula, and their persistence over time in the protoplanetary disk, is the reason planets exist: 40-90$M_{\odot}$ of metallic content was removed from the nebular gas when it collapsed into the Sun. This metal scouring might have meant the resulting metal-depleted remnants of the protostellar nebula could have accreted into the Sun, diluting its primordial composition. Alternatively, this gas could also have been blown away into interstellar space by the protosolar wind.

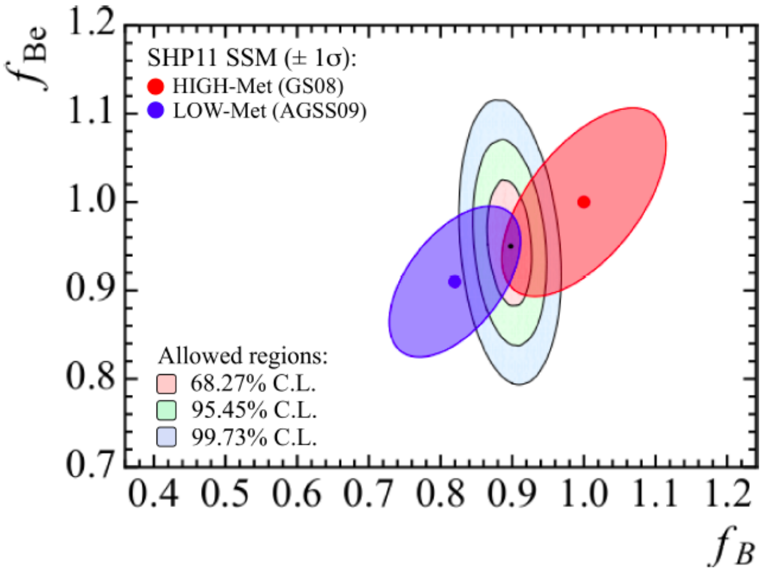

FIGURE 1.10: Current best ^{7}Be and ^{8}B flux measurements, superimposed on the predictions at 1σ from the two main competing metallicity models GS98 and AGSS09[64]. A refinement AGSS09ph brings the model's preferred region closer to the overlap.

1.4 Neutrino anomalies

Undiscovered types of neutrinos may exist beyond the three known active families, as mentioned already during the theoretical outline in Section 1.2. These hypothesized neutrinos would have the particularity of not coupling to neither the $W^{\pm}$ bosons (because there is no fourth generation of charged leptons), nor to the Z^0 boson because of its measured decay width: thefore, they would not exhibit weak interactions except through the leptonic mixing mechanism.

While the bestiary of models for sterile neutrinos is vast and varied, and indeed very heavy sterile neutrinos are being actively studied as a favorite component of dark matter particles, this section will review the experimental and theoretical grounds for *light* sterile neutrinos with a mass of ∼1eV, and in general non-standard neutrino oscillations. There are controversial experimental hints that may point toward the existence of 1, 2 or more sterile neutrinos that mix more or less rarely with the known ones.

1.4.1 Experimental anomalies

All the experiments which are typically held as (for now, circumstancial) proof of anomalous neutrino oscillations so far rely on the $e-\mu$ neutrino or antineutrino appearance or disappearance channels at a short baseline (L/E<10 m/MeV), which would depend in the most-studied models (see Section 1.4.2) on:

- A mass-squared difference between the first mass eigenstate and a mostly-sterile flavor, fourth mass eigenstate (Δm^2_{14}), which because of the large scale difference between the mostly-active three known mass eigenstates, can be considered equivalent to Δm^2_{42} or Δm^2_{43}. Therefore, the oscillation probability can be approximated (for both ν and $\overline{\nu}$) as:

$$\mathcal{P}_{\nu_\alpha \to \nu_\beta} = \delta_{\alpha\beta} - 4 \mid U_{\alpha 4} \mid^2 (\delta_{\alpha\beta} - \mid U_{\beta 4} \mid^2) sin^2 \Big(\frac{\Delta m^2_{41} L}{4E} \Big) \tag{1.47}$$

- The amplitude of the transitions, determined by the mixing angle of electron/muon (anti)neutrino disappearence $\vartheta_{ee/\mu\mu}$ or electron-to-muon (anti)neutrino transitions $\vartheta_{e\mu}$, given by $sin^2 2\vartheta_{e\mu} = 4 \mid U_{e4} \mid^2 \mid U_{\mu 4} \mid^2$, $sin^2\vartheta_{ee} = 4 \mid U_{e4} \mid^2 (1 - \mid U_{e4} \mid^2)$ and $sin^2 2\vartheta_{\mu\mu} = 4 \mid U_{\mu 4} \mid^2 (1 - \mid U_{\mu 4} \mid^2)$.

These models of course would not allow for CP violation, for which a minimum of 2 sterile neutrinos is needed (and, consequently: mixing angles, mass-squared differences *and* a CP-violating phase $\eta = arg[U^*_{e4} U_{\mu 4} U_{e5} U^*_{\mu 5}]$ for the fifth neutrino).

The best-regarded experimental hints are:

LSND Pion decay ($\pi^+ \to \mu^+ + \nu_\mu; \mu^+ \to e^+ + \overline{\nu_\mu}\nu_e$) $\overline{\nu_\mu} \to \overline{\nu_e}$ oscillation experiment with a L=30 m baseline and $E_\nu \in [20, 200] MeV$. It recognizes $\overline{\nu_e}$ by IBD. It is considered the first, and most strikingly clear, evidence for sterile oscillations, and is also very controversial because of that. It saw an anomalous excess of events of 3.8σ[65] (later revised to 2.3σ by HARP[66]). Its sister experiment **KARMEN**, with a shorter baseline of L=17.7 m and $E_\nu \in [16, 50] MeV$ constrained the $\Delta m^2 > 10 eV^2$ LSND oscillation region, but its more restricted results are compatible in the $< 2eV^2$ and $\sim 7eV^2$ regions[67].

Gallium experiments Based on two similar experiments: SAGE[68] and GALLEX[69] (see Section 1.2), they both probed the ν_e disappearance channel, by direct count-rate of the neutrino capture in ^{71}Ga to produce ^{71}Ge, with neutrino sources based on ^{37}Ar and ^{51}Cr ($E_\nu \sim 750, 430, 810$ keV). They both saw consistent deficits at the 2.7σ-level, constituting the so-called *gallium anomaly*.

MiniBooNE Pion decay $\nu_\mu \to \nu_e$ and $\overline{\nu_\mu} \to \overline{\nu_e}$ oscillation experiment with a L=541 m baseline and $E_\nu \in [200 - 1250] MeV$. It recognized the neutrinos by charged-current quasi-elastic (CCQE) events. It was actually designed to prove or disprove LSND, but produced a dataset that is highly disputed. It showed a low-energy excess that is considered anomalous in the neutrino channel, and an excess consistent with LSND in antineutrino data, but in tension with its own neutrino channel[70][71]. A near detector called SciBooNE was installed for a year 100 m away from the target source, and was used to study the ν_μ and $\overline{\nu_\mu}$ disappearance channel, but with little sensitivity to the allowed region.

MINOS Neutral-current ν_μ event rates over a long baseline of L=735 km would be affected by active-sterile oscillations and show as a deficit of NC reactions on the far detector, while no such thing would happen under an only-active scheme. It reported limits on the large mixing angle phase space[72], and more recently published[73], together with the Daya Bay reactor neutrino experiment, improved limits on ν_μ and $\overline{\nu}_\mu$ disappearance.

ICARUS Another $\nu_\mu/\overline{\nu_\mu} \rightarrow \nu_e/\overline{\nu_e}$ beam oscillation experiment with a L=731 km baseline and $E_\nu \in [10, 35] GeV$ range. It reported strong limits on the large mixing angle phase space[74].

IceCube An atmospheric neutrino observatory observing ν_μ and $\overline{\nu}_\mu$ disappearance, IceCube recently reported improved limits on this channel for the allowed phase space of light sterile neutrinos[75].

Reactor measurements Antineutrino oscillation studies are mainly performed through the use of nuclear reactors, which are a copious source of $\overline{\nu_e}$ ($2{\cdot}10^{20}$ $\overline{\nu}$/s in a 1 GW reactor). For that reason, electron-antineutrino disappearance studies can be performed at different baselines. In particular, there has been a recent re-evaluation of the short-baseline (L<100 m) reactor $\overline{\nu_e}$ fluxes[76][77] indicating an apparent widespread deficit in measured fluxes ($\phi_{predicted}/\phi_{measured}$=0.927±0.023,[78]) compared to the newly-calculated *ab initio* spectra combined with re-evaluated $\overline{\nu}$ cross-sections. Although several criticisms (see, for example [79]) have been raised and the weak magnetism dependency is so large it may account for the effect, the hint is compatible with the previous experimental hints and their ν_s modelling.

Cosmology constraints Cosmological constraints and hints towards non-active neutrinos come from the analysis of N_{eff}; that is, the effective number of neutrino families. Neutrino decoupling time is defined as the moment after the Big Bang (roughly at 1 MeV temperature for the primordial plasma) when neutrino interaction rates become lower than the Universe's expansion rate. Their ultra-relativistic Fermi-Dirac energy distribution is "frozen" at that moment. Further, the reheating of the photon population due to matter-antimatter annihilation happens shortly thereafter and therefore does not affect neutrinos, leaving primordial photons slightly warmer by $\sim 40\%$. There are some subleading corrections due to QED and non-instantaneous decoupling effects that raise slightly the neutrino energy density, and which are absorbed in the N_{eff} concept, which in the SM's 3-active neutral fermion scenario is $N_{eff} = 3.046$[80]. It is defined as:

$$N_{eff} = \frac{120}{7\pi^2}\frac{\rho_\nu}{T_\nu^4} \tag{1.48}$$

where ρ_ν is the total energy density deep in the radiation era, to which cosmological measurements are sensitive through the expansion rate $H(t) \simeq \frac{8\pi G}{3}(\rho_\nu + \rho_\gamma)$ $-\rho_\gamma$ is very well-determined by Cosmic Microwave Background (CMB) anisotropy measurements (acoustic peak analysis constrains the redshift z_{eq} at the matter-radiation equality era, which depends on N_{eff}; as does the anisotropic stress suppressing high harmonics $\ell > 200$) and Large Scale Structure (LSS) analysis. These parameters, measured by a number of different Earth- and space-based surveys over the years (most notably, WMAP, SPT, ACT and, recently, Planck) have shown a decreasing preference for non-standard N_{eff}, and in fact Planck's results are in tension with any simple sterile neutrino model[81]. However, these results rely on a number of poorly-constrained assumptions, even without taking into account unknown effects to the ΛCDM model such as a dark energy components. In any case, a process that affects the heating or cooling of the neutrinos prior to decoupling, or the presence of extra light, ultra-relativistic thermalized particles (including neutrinos), or even non-standard effects like time-dependent physical constants, will affect the expansion rate H(t). Further, Big-Bang Nucleosynthesis (BBN) would also enhance the Hubble expansion rate through N_{eff} in a light ν_s scenario, because they would enhance the light elemental abundance (particularly the mass fraction of ^{4}He, Y_p). Observational constraints, albeit with systematics that are not well constrained, currently faintly suggest an excess in N_{eff}[82]. Finally, light sterile neutrinos with active mixing would strongly affect supernova explosions, since their MSW non-adiabatic transitions (see Section 1.3) would result in a large fraction of ν_e being converted to ν_s, while the same would not be true in antineutrino mode, altering the conditions for elemental formation and r-process activation through neutrino-induced ejecta heating.

All these experiments and constraints have been incorporated into global fit models (most notably and recently, [83]), plus some less-critical datasets such as CDHSW[84], NOMAD[85], BNL-E776[86] and OPERA[87].

1.4.2 See-saw and other sterile mechanisms

Formally, a Dirac-Majorana framework for neutrino masses (both for active ν_L and sterile ν_R fields) is the basis for the see-saw mechanism that gives rise to the most popular sterile neutrino theories. It is important to note a Dirac-Majorana mass term implies a Majorana character for massive neutrinos, since it has that structure for the two chiral fields ν_L and $\nu_R^{\mathcal{C}}$, whose

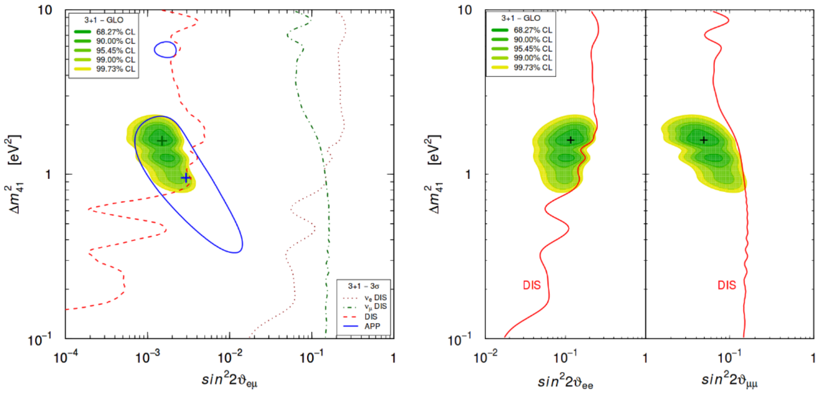

FIGURE 1.11: Global fits on the Δm^2_{14}-$sin^2 2\vartheta_{e\mu/ee/\mu\mu}$ channels considering a single sterile neutrino, from [83], with the appearance channel $\nu_\mu \to \nu_e$ on the left and ν_μ / ν_e disappearance on the right. This study disfavors at 6σ the no-sterile hypothesis, but only at 2σ if LSND data is not included in the fit, and cannot rule out the 3+1 as opposed to the 3+2 or 3+1+1 ($m_5 \ggg m_4$) models.

oscillations would depend (in a 2ν approximation) to their mass squared difference:

$$\Delta m^2 = \Big[(Re[m_L] + m_R)^2 \Big[(Re[m_L] - m_R)^2 + 4m_D^2 \Big] + (Im[m_L])^4 + \\ +2(Im[m_L])^2 \Big((Re[m_L])^2 - m_R^2 + 2m_D^2 \Big) \Big]^{1/2} \tag{1.49}$$

where the masses are determined by the Dirac-Majorana mass term:

$$\begin{aligned} \mathcal{L}^{D+M}_{mass} &= \mathcal{L}^{D}_{mass} + \mathcal{L}^{L}_{mass} + \mathcal{L}^{M}_{mass} \\ \mathcal{L}^{R/L}_{mass} &= \frac{1}{2} m_{R/L} \nu^T_{R/L} \mathcal{C}^\dagger \nu_{R/L} + h.c. \\ \mathcal{L}^{D}_{mass} &= -m_D \overline{\nu_R} \nu_L + h.c. \end{aligned} \tag{1.50}$$

This mechanism would imply new BSM physics to generate the m_R, with the field ν_R being part of a multiplet of the symmetries of a high-energy BSM theory, while the Dirac mass term m_D is "protected" by the SM symmetries and can only arise at the symmetry-breaking scale for electroweak theory (10^2 GeV). In fact, this is the reason for the name "see-saw": the smallness of one mass is implied *naturally* by the large energy scale of the symmetry breaking for the high-energy, BSM theory, which may be up to Grand Unification scales (10^{14-16} GeV).

See-saw theories which fit the mixing implied by the observed anomalies are generally classified into **type I** (or conventional): $\mid m_L \mid << m_D^2/m_R$ and **type II**: $\mid m_L \mid >> m_D^2/m_R$. The solar neutrino constraints show there is no significant mixing in those kind of neutrinos, offering a limit on the scale distribution for the different mass terms ($m_L, M_R \leq 10^{-9} eV$)[80]. There exist other see-saw-based "non-standard approaches" for light sterile neutrinos, such as the mirror models for axinos[88].

Active neutrinos are separatated by the so-called *solar* and *atmospheric* mass-squared differences, which as shown in Table 1.3, correspond to $\Delta m^2_{21} \sim 2 \cdot 10^{-3}$ and $\mid \Delta m^2_{31} \mid \sim 8 \cdot 10^{-5}$. Of course, since the sign of Δm^2_{31} is still undetermined, this leads to the *hierarchy problem* (is ν_3 heaviest or lightest; or even massless?), which is beyond the scope of this section. Suffice to say that the existence of (a) further, eV-scale neutrino would be removed enough from the mass scale of the active trio that for most situations we could consider a single splitting Δm^2_{14}, with the three active neutrinos being quasi-degenerate in this regime, as illustrated for a sample 3+3 phenomenological neutrino model[19].

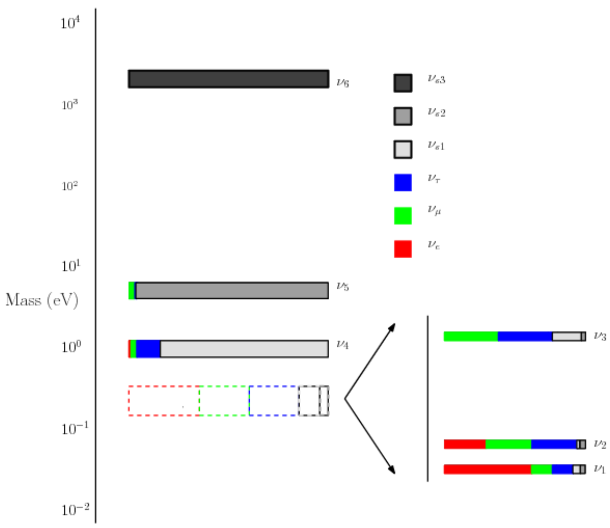

FIGURE 1.12: Sample mass spectrum for a 3+3 phenomenological sterile neutrino model, in which there is a null-to-small sterile mixing with the active neutrinos, and 3 sterile components, up to a heavy keV-scale 6th component with negligible mixing with the other 5 components (from [89]).

It is important here to distinguish between the *phenomenological* 3+N_s neutrino schemes, where N_s sterile mass eigenstates are added to the SM, and the *minimal* 3+n_R neutrino schemes, where n_R Weyl fermions are added to the theory to account for the extra degrees of freedom, and in general involve $n_R > N_s$. In fact, the simplest working minimal neutrino scheme is the 3+2, with one massless neutrino, four massive states, four mixing angles and 2 CP phases[90].

Borexino is specially well suited to study short-baseline oscillations in the disappearance channel at the $\sim$ 1% level, especially suited for 3+1 or 3+2 phenomenological models, although anomalous oscillation effects could be probed too.

The existence of anomalous neutrino oscillations needs not imply the existence of sterile neutrinos directly, however: there are other, more exotic effects that could provide the same observable results by considering additional "sectors", or undiscovered fields that have remained elusive so

[19]This model is especially well-regarded since, in principle, it could explain part or the whole Dark Matter problem with the lightest neutrino, and the leptogenesis-induced matter-antimatter asymmetry via the two heaviest ones, explaining at the same time why three families are present in the SM even if CP violation could be achieved with just two.

far because of their feeble interactions with the SM fields. In fact, the cosmological constraints that are in tension with the rest of the experimental hints, could get reconciled considering one light boson that couples to the sterile neutrinos through an unprobed interaction. This would also explain the origin of neutrino mass, either through a Dirac-like mechanism, a Majorana term with a mini-"see-saw" mechanism or even an *inverse see-saw* scheme[80]. Lorentz-invariance violation within the SM framework (SME, or Standard Model Extension) or CPT violation in the early Universe as a solution to the Baryon Asymmetry are also actively-researched plausible models that could explain these anomalous oscillations, should they be verified in the future.

Chapter 2

Borexino Neutrino Observatory

The Gran Sasso (*Great Boulder* in Italian) massif in the Appenines cordillera has been pierced from its Adriatic to its Thyrrenian side by a highway tunnel since 1984, and the Gran Sasso National Laboratories' underground facilities were built off this tunnel's midpoint. Borexino is one of the experiments installed in this privileged setting, whose carbonate rocks provide at least 1400 meters of shielding in any direction (or 3800 m.w.e.) from cosmic ray incident particles, allowing for a muonic flux of $\Phi_\mu \sim 1.2\ m^{-2}h^{-1}$. The Borexino detector is located in one of the three major experimental halls in the facilities, Hall C, between the LUCIFER technology demonstration setups and the DarkSide dark matter observatory.

Borexino is a liquid-scintillator calorimetric detector based on the principle of graded shielding[91], by which increasingly well-controlled (notably, in terms of radiopurity) volumes are located concentrically to one another, in an *onion-like* arrangement. The main goal of this strategy is to progressively reduce the background levels in the innermost sections, while allowing to constrain their limits with the outer volumes, because of the intrinsic indistinguishability of background events from neutrino events through Borexino's detection strategy based on ν-e elastic scattering. The detector has been in continuous data-taking, except for short maintenance and purification periods, since mid-2007 –and is expected to continue until beyond 2017.

2.1 Detection strategy

Neutrinos are detected in Borexino through their interaction with the liquid scintillator contained inside its Inner Vessel (more information about Borexino's structure in the next section 2.2), in particular through the scattering off its molecular constituents, according to the recoil formula:

$$E_k^{max} = \frac{2E_\nu}{mc^2 + 2E_\nu} E_\nu \tag{2.1}$$

FIGURE 2.1: A view of the Borexino detector from the North end of Hall C in September 2015.

Nucleon scattering (off neutrons or protons) is not used as a viable channel since nucleon scattering scintillation light is quenched by a factor of 5 with respect to electrons, and solar neutrinos have low energy: therefore, even the endpoint[1] from the most energetic of them (*hep* neutrinos, see Section 1.3) would provide a faint signal drowned under the dominant ^{14}C background and the *pp* neutrino signal from the other channel: **ν–e scattering**.

A neutrino scatters off electrons (see equation 2.2) thanks to its weak coupling with charged leptons, either through neutral or charged currents, with no threshold energy for the scattering[2]. Despite its massive nature needing an extension in the SM formalism, neutrino interactions are very well described by the bare SM predictions, based on the leptonic charged- and neutral-current interaction Lagrangians $\mathcal{L}_{I,L}^{(CC)}$ and $\mathcal{L}_{I,\nu}^{(NC)}$ in equation 1.3, with the addition of only very small kinematical corrections due to these masses.

$$\nu_\alpha + e^- \rightarrow \nu_\alpha + e^- \tag{2.2}$$

[1]In fact, most solar neutrinos (under 2MeV) would yield signals of ∼8 keV equivalent energy, far below the electronics' threshold.

[2]Although, for practical considerations, there needs to be a detector-dependent energy threshold to distinguish the electron recoil signature above the background.

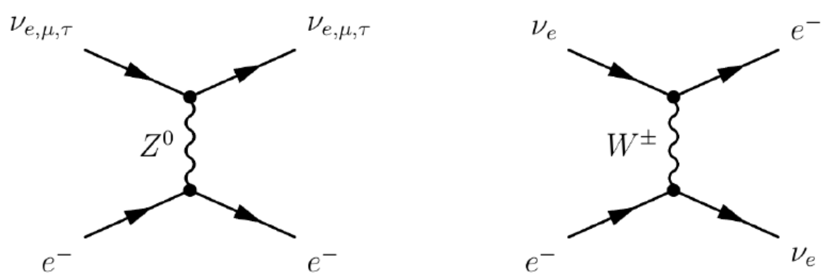

FIGURE 2.2: Feynman diagram for $\nu_e - e$ scattering

Both neutrinos and antineutrinos are susceptible to the elastic scattering reaction 2.2 off electrons, although in the case of $\overline{\nu}$, Borexino uses preferentially the IBD detection technique, which carries a threshold condition of $E_\nu \geq 1.8$ MeV.

All neutrino flavors are susceptible to the NC reaction on the left of figure 2.2, but only ν_es can exchange the charged mediator boson in the CC reaction on the right. The scattering process for the relevant neutrino energies in Borexino is codified in the Lagrangian:

$$\mathcal{L}_{eff}(\nu_\alpha e^- \to \nu_\alpha e^-) = -\frac{G_F}{\sqrt{2}}[\overline{\nu_\alpha}\gamma^\rho(1-\gamma^5)\nu_\alpha][\overline{e}\gamma_\rho(g_V^l - g_A^l\gamma^5)e] \tag{2.3}$$

for the NC, common interaction to all neutrino flavors. For just the ν_e, the Lagrangian gets modified with the CC interaction into:

$$\mathcal{L}_{eff}(\nu_e e^- \to \nu_e e^-) = -\frac{G_F}{\sqrt{2}}[\overline{\nu_e}\gamma^\rho(1-\gamma^5)\nu_e][\overline{e}\gamma_\rho((1+g_V^l) - (1+g_A^l)\gamma^5)e] \tag{2.4}$$

The interaction cross-section σ for each process is proportional to $G_F^2 s$, where s is the invariant Mandelstam variable: $s = (E_{\nu_i} + E_{e_i})^2 = (p_{\nu_{i/f}} + E_{e_{i/f}})^2$. Their energy-dependant values are listed in table 2.1[3], where the ν_e cross-section is the largest, at ~2.4 times the $\overline{\nu_e}$ cross-section, and at ~6.2-~7.1 times the other flavor neutrinos/antineutrinos respectively.

Applying energy-momentum conservation in the two-particle system, we get the recoil energy of the electron after scattering, dependent on its scattering angle θ from the neutrino's incoming trajectory:

$$T_e = \frac{2m_e E_\nu^2 \cos^2\theta}{(m_e + E_\nu)^2 - E_\nu^2\cos^2\theta} \tag{2.5}$$

[3] It is important to note that this cross-section is dependent on an eventual neutrino magnetic moment $\mu_\nu^2 \frac{\pi\alpha_{em}^2}{m_e^2}\left(\frac{1-T/E_\nu}{T}\right)$ (with T being the recoil energy) which would become dominant at low E_ν, as well as enable a hypothetical $\nu - \overline{\nu}$ transition in solar neutrinos, or even modulate the flux over the Sun's 11-year cycle[92]. Its upper limit has been constrained by several independent experiments[93] to $\sim 10^{10}\mu_B$.

Process	Total Cross-Section	Approximate value (x10^{-46}cm^{-2})
$\nu_e + e^-$	$\frac{G_F^2 s}{4\pi}\left[(1+2\sin^2\vartheta_W)^2 + \frac{4}{3}\sin^4\vartheta_W\right]$	93 s/MeV^2
$\overline{\nu_e} + e^-$	$\frac{G_F^2 s}{4\pi}\left[\frac{1}{3}(1+2\sin^2\vartheta_W)^2 + 4\sin^4\vartheta_W\right]$	39 s/MeV^2
$\nu_{\mu,\tau} + e^-$	$\frac{G_F^2 s}{4\pi}\left[(1-2\sin^2\vartheta_W)^2 + \frac{4}{3}\sin^4\vartheta_W\right]$	15 s/MeV^2
$\overline{\nu_{\mu,\tau}} + e^-$	$\frac{G_F^2 s}{4\pi}\left[\frac{1}{3}(1-2\sin^2\vartheta_W)^2 + 4\sin^4\vartheta_W\right]$	13 s/MeV^2

TABLE 2.1: Neutrino elastic scattering cross-sections for the different possible CC/NC channels, for usual energy regimes ($\sqrt{s} \ggg m_e$), taken from [14]. The Weinberg angle ϑ_W is given by the ratio of the SM coupling constants for the $SU(2)_L$ (g) and the $U(1)_Y$ (g') groups: $\tan\vartheta_W = g'/g$.

Obviously, the maxiumum recoil energy would be for forward/back-scatter, when $\theta = 0, \pi$, and $T_e^{max} = \frac{2E_\nu^2}{m_e+2E_\nu}$.

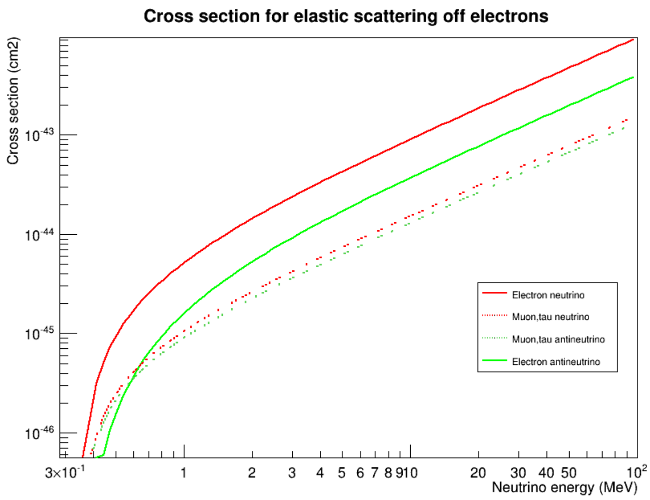

FIGURE 2.3: Scattering cross sections for different neutrino flavors and helicities in Borexino. The total cross section as a function of neutrino energy is $\sigma(E_\nu, T_e^{thr}) = \frac{\sigma_0}{m_e}\left[(g_1^2+g_2^2)(T_e^{max} - T_e^{thr}) - (g_2^2 + g_1 g_2 \frac{m_e}{2E_\nu}\left(\frac{T_e^{(max)2} - T_e^{(thr)2}}{E_\nu}\right) + \frac{g_2^2}{3}\left(\frac{T_e^{(max)3} - T_e^{(thr)3}}{E_\nu^2}\right)\right]$, for σ_0=88.06$\cdot 10^{-46}$ cm^2, T_e^{max} given by the maximum of expression 2.5, g_1 and g_2 being the V-A coupling constants for each flavor of (anti)neutrino, and T_e^{thr} being the detector-dependent neutrino energy threshold for the scattering detection above the background, which is 233 keV for Borexino.

These electrons will be scattered off the molecules in the detector to trigger ***scintillation***, with a small contribution ($\sim 0.75\%$) from Čerenkov light, when they surpass the group velocity of light in Borexino's medium (PC+PPO, see next section). This has been studied using the MonteCarlo simulation package for the detector ($g4bx$ and $g4bx2$) to be adequately modelled by inclusion in the energy scale[94].

2.2 Detector design

BOREX was proposed in 1986 by R. S. Raghavan[95] as a 1kT-fiducial mass detector with trimethylborate (TMB) scintillator to measure the high-energy ^{8}B solar neutrinos, which would rely on the charged and neutral current interactions on the ^{11}B in the material. However, both because of financial considerations and the fact that the high-energy solar neutrinos were being well-studied by other experiments (most notably the water Čerenkov ones), but the same wasn't true for the sub-MeV components, a smaller 0.1kT-fiducial mass version was devised[96] with the main goal of measuring the hugely-unconstrained ^{7}Be ν flux by relying on extreme scintillator purification: **BOREXino**.

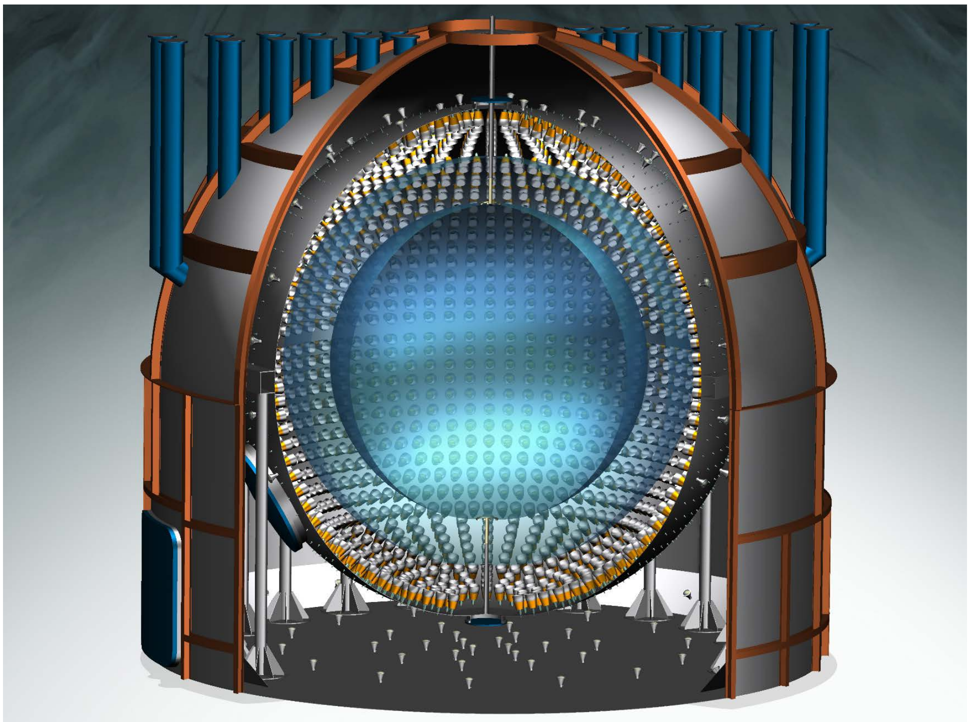

Figure 2.4: Cutaway diagram showing the internal structure of the Borexino detector, including its vessel system (inner and outer), the Stainless Steel Sphere serving as the boundary of the Inner Detector and the support for the internal PMTs, and the surrounding Water Tank Outer Detector which acts as a muon veto. On the tank's dome several pipes can be seen, nicknamed "organ pipes", through which most of the cabling goes inside. Not shown are auxiliary structures like the calibration cleanroom (CR4) located on the very top of the tank (although the insertion pipe that goes all the way to the inner volume can be seen protruding on the top), the connections to fluid handling equipment (both gases and liquids) and access structures (stairs, platforms, cranes) affixed to the exterior, as well as a grid platform connecting the equator of the SSS to the WT's internal walls.

The liquid scintillator technique has advantages over water Čerenkov and radiochemical detectors because of the superior ability to reduce backgrounds with respect to the former, and the inability to perform real-time and spectral measurements for the latter. Of course, this technique also presents its own set of challenges, like the aforementioned *need for extreme purity* *levels* to ensure a sufficient minimization of intrinsic backgrounds (see Section 2.4 for specifics on Borexino's), whose indistinguishability from the signal stems from the other main disadvantage: the *lack of directionality* in the (spatially-isotropic) light emission from the scintillation triggered by the elastic scattering, which means background β and γ events need to be well constrained and statistically substracted (α background can be discriminated thanks to its pulse shape).

After the experience with the very successful prototype Counting Test Facility[97] (CTF)[4], the (building and fluid-handling) techniques necessary for Borexino were in place. In particular, the choice to use pseudocumene (PC; 1,2,4-trimethylbenzene) as scintillator as opposed to the original choice of TMB for the BOREX concept, led to the definition of the purification strategy and the inclusion of the fluor PPO (2,5-diphenyloxazole), as well as the hardware, electronics and software for data acquisition and control for Borexino.

2.2.1 Inner Vessel and Fiducial Volume

Borexino's *sacrosanctorum* is its innermost volume, whose stability is ensured by the different spherically-symmetric layers around it, and is contained by the *Inner Vessel* (IV): a 125 μm-thick transparent[5] nylon membrane connected to the exterior by fluid loading and circulation steel/nylon pipes, and held in place by longitudinal Tensylon ropes and nylon/copper endcaps. It has a diameter of 8.5 m (320 m^3, 280 tonnes), although different fluidodynamical effects affect its shape and deviate it away from its nominal spherical shape; in fact, the control, mitigation and monitoring of temperature-induced changes is a major topic of this thesis.

The specific material used for this vessel (Sniamid) needed to have extreme radiopurity, since it would be in direct contact with the active scintillator, and the installation process from fabrication to deployment was done in a clean environment, leading to an estimated[99] <0.02 counts/day/100 tonnes.

Nevertheless, the background levels around the vessel are still larger than can be achieved some distance away. Therefore, only a "virtual" software-defined *Fiducial Volume* (FV) is considered for analysis. Its limits vary depending on the energy window of interest for each analysis, since some flux components may be insensitive to particular backgrounds that others aren't, but in general they contain a fiducial mass on the order of ~100 tonnes. Presently, there are 4 main "standard" fiducial volumes being used for analysis (see more about the rationale behind them in section 2.5):

[4]Construction started in 1993, with data-taking running in 3 main phases from 1995 to 2010. After this time, the CTF internal components and electronics were dismantled to adapt its cylindrical tank to house the DarkSide50 experiment, dedicated to dark matter WIMP searches[98]. Today, the internal armature for CTF's PMTs adorns the gardens on LNGS' external facilities.

[5]when immersed in PC

$\overline{\nu}$ FV A variable radial fiducial cut, usually set at 4 m.

^{7}Be FV This FV combines a radial cut of R<3.021 m with a flat cut on the Z component at ±1.67 m, truncating the upper and lower caps, in order to avoid more concentrated contamination around the IV's poles.

***pep* FV** Similar to the ^{7}Be FV, the radial cut is constrained to R<2.8 m and the flat Z cut is asymmetric: increased to 2.20 m on the upper volume, and to -2.40 m on the lower.

Seasonal FV The Z cut is no longer flat, but defined by the intersection of a parabola with the radial cut R<3.021 m. This parabola is defined by the exponent n in equation 2.6: $n = 1$ will generate a flat cut like the previously-mentioned ones, while even exponents ($n \in 2\mathbb{N} > 0$) will generate parabolas with increasingly steep slopes. The parabola's base level (θ=0,180°) is given by dr, which should be negative for the lower cut only when $n = 1$ (flat cut) because of its numerical implementation.

$$f(\theta) = \pm \frac{dr}{\cos^n \theta} \tag{2.6}$$

Each of these FVs was in principle "fixed" with respect to Borexino's absolute coordinate system. However, to reduce background contributions and increase statistics, a *dynamical fiducial volume* (DFV) was developed[100], by which the radial component of the FV is set from the reconstructed position of the vessel, as opposed to the fixed absolute coordinate system. This allows to keep a constant distant from the IV and avoid some background inhomogeneities present in the fixed FVs (see figure 2.5). Modifications to the parameters (radius, Z threshold, parabollic curvature...) of these shapes are done routinely, tailored to the needs of each analysis (for example, the FV used for the ^{7}Be day-night asymmetry study had the same shape as the standard ^{7}Be FV but with R<3.3 m and $z_{min/max} = \pm 3.3$ m).

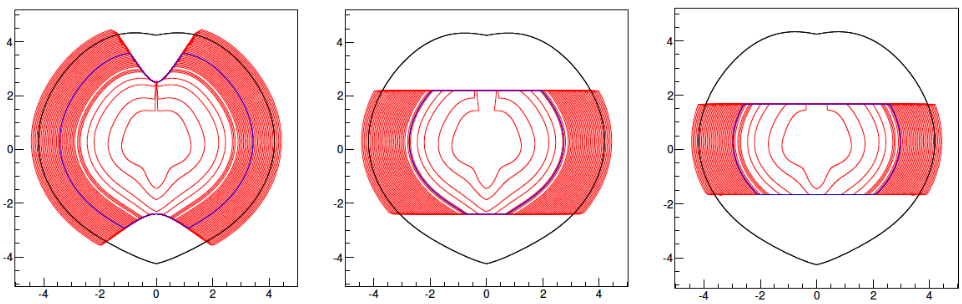

Seasonal Analysis: `seasbe7` *pep analysis:* `pepstd` *Be7 analysis:* `be7std`

FIGURE 2.5: Standard Dynamical Fiducial Volumes with varying radial cut thresholds, from [100].

2.2.2 Scintillation in Borexino

The active PC inside Borexino is doped with 1.5 g/L of PPO, since the scintillation light from pure PC is mainly ultraviolet (UV), and the efficiency of the photomultiplier tubes (PMTs) used to detect the signals inside Borexino falls inside the visible spectrum. In this subsection, an outline of the mechanisms at play from the signal to be produced by a neutrino or background interaction, until being detected by the PMTs is presented. More details about the theory of scintillation of aromatic molecules can be found in Birks' world-class reference work [101] and further discussion about the specific measurements done for Borexino's master solution can be found in reference [102].

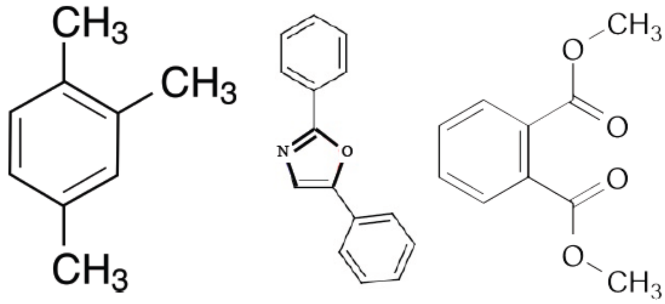

FIGURE 2.6: Formula diagrams for the organic liquid scintillator pseudocumene (PC; 1,2,4-trimethylbenzene), the fluor or wavelength shifter PPO (2,5-diphenyloxazole) and the quenching agent DMP (dimethylphthalate), from left to right respectively.

The scintillation event stems from the ionization of the benzene ring in the PC molecule, be it through the elastic scattering of an neutrino off a molecular electron, or caused by the products of the radioactive decay of a background element.

Benzene ring structures are enabled by the sp^2 hybridization, one of the three hybridizations (sp, sp^2 and sp^3) available to carbon electronic orbitals, where one of the $2s$ electrons is excited to a p orbital, and two of the $2p$ orbitals (typically named as p_x and p_y) hybridize with the s orbital into three equivalent sp^2 hybrid orbitals lying on the same plane. The remaining valence electron is perpendicular to this plane, and exists in a pure p orbital wavefunction (p_z). The sp^2 orbitals can form σ covalent bonding orbitals (for example, with the s orbitals in the methyl groups in PC, or more trivially being saturated with the $1s$ hydrogen orbital), while the p_z orbitals can form delocalized π bonding orbitals (therefore, the electrons occupying these orbitals are called π *electrons*) –but their most interesting property for us is the transitions and interactions they are capable of, since they will give rise to scintillation phenomena[6].

[6]Conversely, de-excitation or recombination of σ electrons dissipate energy thermally, through **radiationless transitions** between isoenergetic vibrational levels of different states (*internal conversion* for states of the same multiplicity; or *intersystem crossing* for states of different multiplicity), rather than through photon emission (**radiative de-excitation**), either *fluorescence* if the transition is between states of the same multiplicity, or *phosphorescence* if it happens between different-multiplicity states.

In the *Perimeter Free Electron Orbital* (PFEO), π electrons are considered free standing waves around the ring, with doubly-degenerate (for $q > 0$), quadratically-spaced energy levels given by the 1D Schrödinger equation:

$$E_q = \frac{q^2\hbar^2}{2ml^2} = 1.21 \cdot 10^6 q^2/l^2 \tag{2.7}$$

with $q \in \mathbb{N}$ being the *orbital ring quantum number* describing the number of nodes of this standing wave, and l being the radius of the ring; l=1.4Å (therefore, $E_q = 1.95q$ eV). The total ring quantum number Q is the sum of the individual electrons' q: $Q = \sum q$. Trivially, for all q=0, the ring system is in its ground state, denoted by A. The lettering B and C correspond to the first and second excited states, respectively. Further excited states are denoted K, L, M... (for Q=2n, 2n+1, 2n+2,... respectively), and all of them are again doubly-degenerate except the ground state A. However, this degeneracy predicted by the PFEO model is actually split because of spin-orbit interactions and the periodic potential ring caused by the proximity of the C nuclei in the ring, and their components are denoted X_a or X_b, where X=B,C,K,L... The A ground state is a singlet, with electron spins paired; while excited states can be either singlets (S_Q) or triplets (T_Q), depending on whether there is a spin reversal in the electronic transition or not, respectively, since the spin angular momentum $\mid s \mid$ can be 0 or 1 (in natural units).

The ionization electrons produced by signals and backgrounds in Borexino recombine in less than 0.1 ns[103] in the scintillator molecules, to yield very excited states with Q>2, which rapidly decay non-radiatively to Q=1 triplets and singlets. Molecules excited by vibrational excitation transfer generate only singlet excited states. These states will decay to the ground states through the radiative de-excitation transitions (see footnote in previous page for details):

$S_1 \to S_0$ **fluorescence** This is the prompt component of the scintillation signal, with a duration of several ns (this allows for precise position reconstruction in the detector). It competes with the non-radiative thermal internal conversion process: the ratio of fluorescent to total (radiative or radiationless) transitions $q_{FM} = \frac{N_{fluor}}{N_{IC}}$ is the quantum efficiency of the material, which in PC is 34-40%[101]. [7]

$T_1 \to S_0$ **phosphorescence** This process is spin-forbidden and occurs only in $\sim$ ms-s timescales, making it practically unobservable in our detector.

$2T_1 \to S_1 + S_0$+**vibrational energy fluorescence** *Bimolecular* processes (i.e. molecular collisions) can perturb the energy levels of the excited molecule(s), and the simplest, most likely such process is a homopolar interaction between two triplet-state molecules generating a long scintillation pulse of several μs.

[7] While the possibility of the singlet S_1 state to non-radiatively undergo an intersystem crossing exists, it is very suppressed (spin-forbidden) because of the spin flip it requires.

Apart from the aforementioned mismatch between PMT sensitivity and scintillation wavelength for pure PC, this scintillator's q_{FM} is so low (when already ∼95% of a particle's kinetic energy is converted into electronic excitation energy) and the position reconstruction that would result from the mean free scintillation photon path of 5.4 m would be so poor, that it is desirable to modify its scintillation properties to more favorable ones.

In particular, the addition of the chosen PPO fluor allows for the quantum efficiency to be raised to between 83-100%[101] and for the mean lifetime of its first excited state to be lowered close to the theoretical ∼1 ns limit, while allowing for transfer of energy from an excited PC molecule >95% of the times, allowing for a light yield of 11500 photons/MeV. Most ideally, the emission wavelength peak is shifted (see figure 2.7) from 290 to 360 nm, practically matching the peak quantum efficiency for the PMTs, but also falling completely within the largest 65% of their q.e. range. The light response of the scintillating mixture can be modelled by the function:

$$S(t) = \sum_{i=1}^{N} \frac{q_i}{\tau_i} e^{-t/\tau_i} \tag{2.8}$$

for N=3 in the case of β/γ excitations and N=4 for αs. The parameters τ_i and q_i are empirically-measured values given by the PPO's prompt and delayed fluorescence components, reported for example in [92]'s Table 2.6. A higher concentration of fluor would lead to higher self-absorption and a worsening of the light yield.

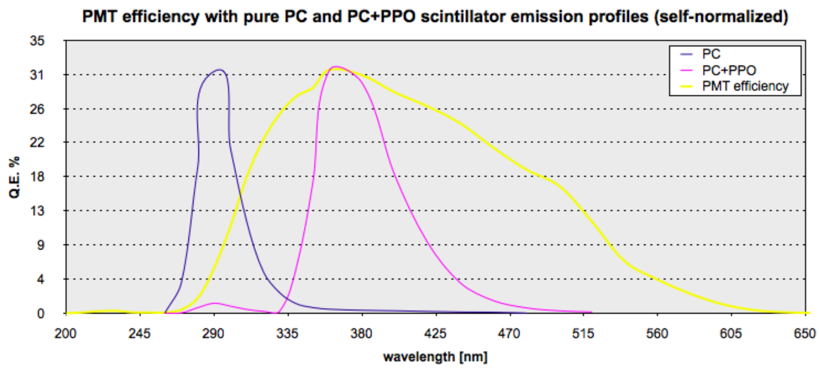

FIGURE 2.7: Quantum efficiency for the PMTs together with emission spectra for pure PC and PC+PPO

Finally, it should be noted α radiation will have an order-of-magnitude worse energy transfer to the scintillator's electrons than β/γ radiation: this is the so-called α *quenching*, and is due to the much greater stopping power of massive particles favoring Q>2 excitation states in the scintillator rings to interact non-radiatively with an ion produced through the dense energy deposition of the incident particle, instead of remaining in a first-excited state where radiative transitions are possible. The general expression governing the quenching phenomenon is given by Birks' formula 2.9:

$$\frac{dL}{dx} = \frac{S\frac{dE}{dx}}{1 + kB\frac{dE}{dx}} \tag{2.9}$$

where dE/dx is the stopping power for the incident radiation, and dL/dx the specific light emission of the scintillator. kB (not to be confused with the Boltzmann constant k_B) is the Birks parameter, and is treated as a single entity characteristic of the scintillator. BdE/dx conveys the density of ionized molecules along an incident particle's track. Integrating equation 2.9, we obtain the quenching factor $Q(E)$ (equation 2.10) which is the deviation of the light yield from a simple linear model, in practice always smaller than unity, although much more relevant for particles with great stopping power (such as αs or nuclear fragments), as well as for β/γs with energies of less than a few hundred keV:

$$Q(E) = \frac{1}{E}\int_0^E \frac{dE}{1 + kBdE/dx} \tag{2.10}$$

A very prominent example of this (see section 2.4) is ^{210}Po, whose 5.41 MeV α is actually seen as a ∼500 keV scattering signal, overlapping the "golden" neutrino window. Despite this complication, α backgrounds are relatively easy to discriminate, as mentioned earlier, by the shape of their scintillation pulse, caused precisely by the larger ion density created by the massive particle, which favors the triplet states in a proportion of 3:1. This means the T_1 population will be tripled with respect to other excitation mechanisms, leading to a preponderance of the slow scintillation component caused by bimolecular fluorescence processes. The prompt scintillation will remain largely unaffected. This allows for tail-to-total (*tailtot*) ratio[104] and *Gatti optimal filter* parameter[105] analyses to statistically discriminate these events (see section 2.5 and figure 2.8).

2.2.3 Outer Vessel and Buffers

To avoid leakage from the signals that comparatively higher concentrations of intrinsic background outside the IV would yield, the 1040 tonnes of PC outside the inner volume is doped with dimethylphthalate (DMP), which is a quencher that reduces the residual tails of pure PC scintillation which could fall inside the PMTs range of sensitivity, by a factor of 28±2[103]. It however does not influence negatively the PC's optical mean free path, index of refraction between the inner and outer volumes, or the Čerenkov emission, and obviously avoids the larger

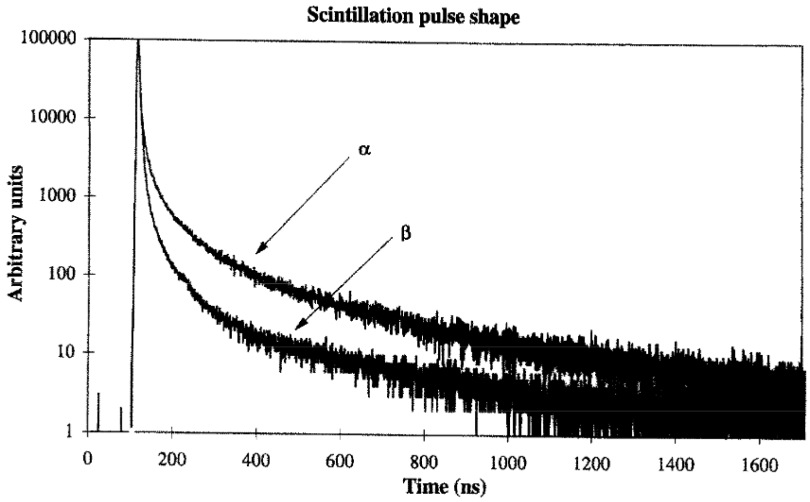

FIGURE 2.8: Difference in scintillation pulse shapes for $\alpha - \beta/\gamma$ radiation in Borexino's scintillator; measurement taken from [106].

buoyant forces that another liquid would induce on the vessels[8]. This *inner buffer* (IB) is separated from the larger sphere containing the sensitive PMTs by a second, larger (diameter of 12.6 m) nylon (Capron) ballon: the Outer Vessel (OV). It separates the two buffer volumes, otherwise identical, as an extra layer of protection from the much less radiopure liquid surrounding the PMTs: the *outer buffer* (OB). Further, its importance is paramount since radon does not readily diffuse through nylon, in contrast to most other materials. ^{222}Rn is a dangerous background (see section 2.4) whose decay signal falls squarely in the "golden" energy window of interest for Borexino (250-800 keV of recoil energy) and, most importantly, whose daughters are also radioactive and exhibit long lifetimes (particularly ^{210}Pb ($t_{1/2}$=22 yr) and its daughers ^{210}Bi/Po ($t_{1/2}$=5-138 days, respectively)).

The vessel system (IV together with the connecting structures and the OV) was tested for leak-tightness down to 5 mm^3 PC/s for the IV/OV interface, and 0.1 cm^3 PC/s for the OV/exterior buffer interface; and also for the withstanding of tensile stresses up to 20 MPa[99] (see figure 2.9).

Unfortunately, in spite of all the precautions a leak of ~1.33 m^3/month[108] in the inner volume developed around the 9th of April 2008[94], possibly stemming from a tear in the nylon, whence the active scintillator was found to be exiting to the Inner Buffer (IB) shell between the positions of $26° < \theta < 37\,°$ and $225\,° < \phi < 270\,°$, based on buffer sampling and an anomalously high event reconstruction rate outside the IV. The root cause for this has never been fully estabilished[94], although there is a strong suspicion that large, sudden temperature changes due to the raising of the scintillator temperature in December 2007 to get rid of a fogging "haze" in the scintillator

[8]The bouyant force is given by the difference in densities of PC+PPO ($\rho_{PC+PPO}(T)[g/cm^3] = (0.89179 \pm 3 \cdot 10^{-5}) - (8.015 \pm 0.009) \cdot 10^{-4}T(1 + (0.316 \pm 0.001)\eta_{PPO}$, where η_{PPO} is the PPO concentration) and PC+DMP ($\rho_{PC+DMP}(T)[g/cm^3] = (0.89179 \pm 3 \cdot 10^{-5}) - (8.015 \pm 0.009)x10^{-4}T(1 + (0.275 \pm 0.005)\eta_{DMP}$, where η_{DMP} is the DMP concentration)[107]. This produces ~250N of upward buoyant force for the present concentration of 2 g/L for DMP and 1.5 g/L for PPO.

FIGURE 2.9: Nylon vessel system inflation tests on the large covered space for the athletic and basketball courts at Princeton's Jadwin Gym, from [107].

(due to water condensing out when it cooled down) created very large stresses in the vessel through large buoyancy forces between the different densities of the outer and inner volumes. This effect that was visible as deformations in the vessel shape, and may have been exacerbated by operations in Hall C that raised the ambient temperature. Whichever the cause, the leak was controlled by means of purification and reduction of the quenching agent's concentration from 5 g/L to 3 g/L in a first phase, to then settle in to 2 g/L in a final phase. The leak rate was thus reduced by a factor of ∼300 to ∼1.5 m^3/year[94], and the vessel's volume has remained approximately constant ever since according to the latest estimates (see figure 2.10).

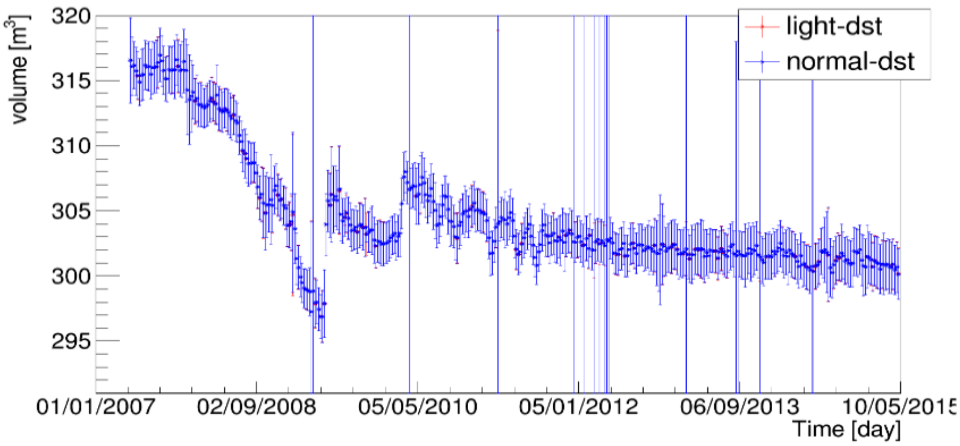

FIGURE 2.10: Evolution of the IV's volume through time, calculated through the ^{210}Bi "tomography" method for vessel shape reconstruction, from [109].

2.2.4 Stainless-Steel Sphere and Photo-Multiplier Tubes

Once scintillation has taken place, the emitted light should arrive in a very large proportion to the sensitive instruments that will record that interaction. A large fraction of the photons produced in PC+PPO radiative transitions will arrive in a straight line, undisturbed. However, the attenuation length ($\Lambda(\lambda)$ in equation 2.11, in the 5-10 m range in Borexino) has to be considered[102] for the intensity losses in such a large volume:

$$I(x, \lambda) = I_0(\lambda)e^{-\frac{x}{\Lambda(\lambda)}} \tag{2.11}$$

where x is the path travelled by the light, and I_0 is the light intensity when produced. This effect is due to the *inelastic scattering* (absorption and re-emission, with 80% probability and a gradual red-shift, within a few cm of the scintillation point) of the scintillation light in the PPO molecules, as well as *elastic (Rayleigh) scattering* off PC molecules, since absorption in PC is negligible due to its lowest transition energy being 320 nm. Rayleigh scattering limits the spatial resolution of the detector because it has an attenuation length of the order of 1 m, making some of the photon trajectories less linear.

Furthermore, since the position reconstruction accuracy relies on the accurate determination of the time-of-flight of the photons to different parts of the spherically-symmetric surrounding photodetectors, an extremely accurate index of refraction determination is mandatory, since $t = d(n/c)$, where c is the speed of light in vacuum and d is the distance travelled. There had always been differences in the index of refraction measured experimentally in samples in the laboratory (1.52 at 425 nm) and that used in practice to reconstruct events at a known position ($\sim$1.68). This was recently understood[110] to be a consequence of the difference between the phase velocity $v_p = c/n$ and the group velocity:

$$v_g = \frac{v_p}{1 - \frac{\lambda}{n}\frac{dn}{d\lambda}} \tag{2.12}$$

(λ being the wavelength in vacuum) for the ***non***-monochromatic spectrum of light emitted by scintillation, which causes a dispersion relation (n is dependent on the wavelength: $n_g = \frac{c}{v_g} = n - \lambda\frac{dn}{d\lambda}$).

The vessel system and scintillator/buffer volumes are surrounded by 2212 photomultiplier tubes (PMTs, of which $\sim$1500 remain in operation as of this writing, because of the age-related malfunction as well as the "infant" mortality rate suffered between installation and checkout and the finishing of fluid filling operations in the detector) where the surviving scintillation photons will arrive and produce an electrical signal. These tubes and other associated auxiliary hardware (CCD cameras, re-entrant tubes, fibers for PMT calibration during data-taking, etc.)

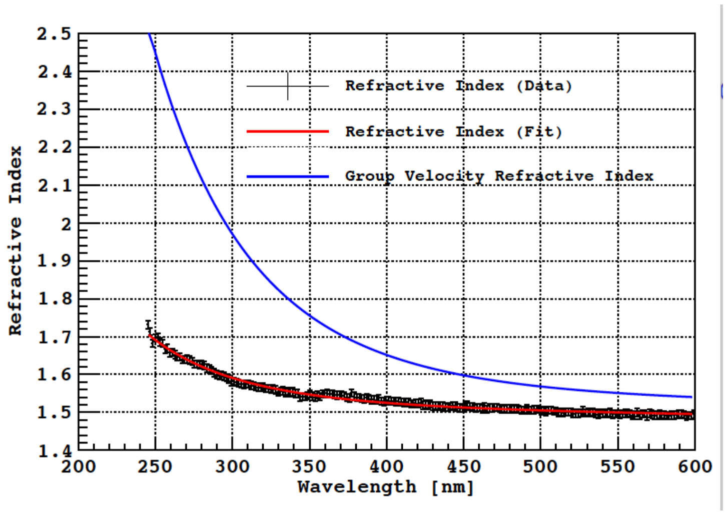

FIGURE 2.11: Difference between phase and group velocities for the scintillation light in PC+PPO, where one can appreciate the significant difference for a monochromatic pulse measured in the laboratory (black points and red fit) versus the group velocity in equation 2.12. Measurements courtesy of the Genova group[110], and adapted figure from [94].

are mounted on a 13.7-m diameter, 8-mm thick Stainless Steel Sphere (SSS) supported by 20 steel legs that withstand its weight, strong enough to avoid deformations under the large buoyant forces of the PC-based interior fluid immersed in the water around it, and covered by high-reflectivity white Tyvek both on the inside and outside (see figure 2.12).

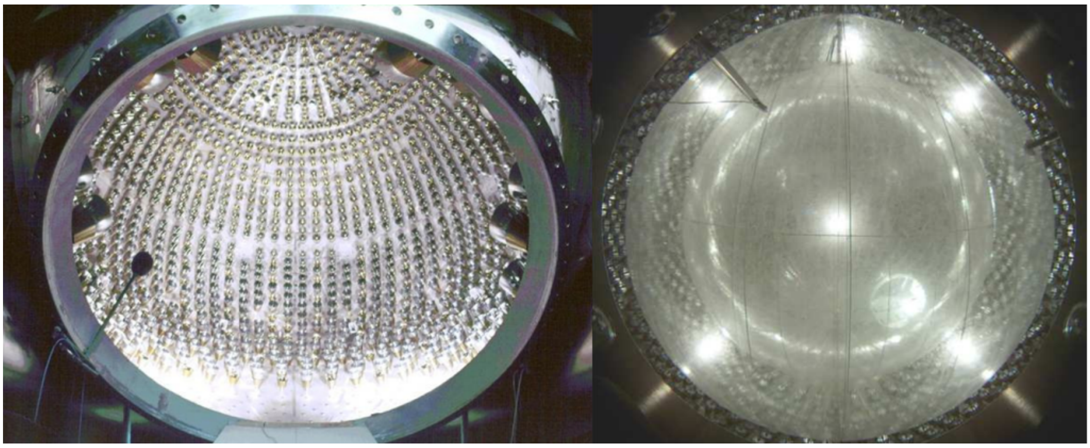

FIGURE 2.12: Interior views of an air-filled SSS during vessel and PMT installation, without (left) and with (right, taken by the VT CCD camera system) the vessel system installed.

The PMTs themselves[9] have a quantum efficiency at 420 nm of 26.5% (although tubes with >21% efficiency were accepted). When taking into account the nominal quantum efficiency at its peak at 360 nm (32%, see figure 2.7), the overall detection efficiency for each PMT is 19%. Furthermore, the effective aperture of 1839 of them[10] was increased to cover a fractional solid angle –for an event located at the center of the detector– of 30%, by means of truncated

[9]Hemispherical 8" ETL 9351 with projected photocathode area of 366 cm^2

[10]The remainder are used to distinguish point events in the IV from muon tracks.

paraboloid aluminium surfaces (90% reflective, 23 cm in height, with openings 16 and 9.5 cm wide) attached to the face of the PMT glass called *light concentrators*, which reflect light inwards when incident at less than a critical angle of 44°. When folding together the reflectivity with the overall detection efficiency and the effective coverage, the detector's photon-to-photoelectron (p.e.) conversion efficiency is found: ∼5.2%, which would give a photoelectron yield (from the scintillator's light yield) of ∼540 p.e./MeV (for a coverage of 2000 working PMTs), not taking into account the aforementioned PPO reabsorption effects or photon backscattering from the SSS or PMTs into the scintillator. The observed photoelectron yield has been measured to be 488±1.6 p.e./MeV, roughly consistent with this calculation.

2.2.5 Water Tank

Everything inside of the SSS is considered the Inner Detector (ID). Surrounding it, there is an 18-m diameter, 16.9-m high Water Tank (WT) which is 7.7 m high in its cylindrical lower section, and whose inner walls are also covered by high-reflectivity white Tyvek sheets (see image 2.13) to improve light collection through increased reflectivity (by more than 40%, up to ∼80%). As its name suggests, it is filled with 2100 tonnes of ultra-high purity water and it constitutes Borexino's last layer of defense against the external environment (predominantly the neutron and gamma backgrounds coming from the mountain walls) in Hall C. Its external walls are braced by I-beams, and it is in the "depression" between the I-beams profile and the WT walls that ∼20 cm of mineral wool insulation has been installed (although a thinner layer has also been used to cover the I-beams themselves) as part of the work of this dissertation, to provide an extra layer of thermal insulation.

On the external walls of the SSS, on the lower skirting ("slope") of the WT (at 45°) and in four concentric rings on its bottom floor, there is a collection of 208 PMTs (154, 20 and 34, respectively) without light concentrators, that utilize the water volume to obtain Čerenkov signatures of muons passing through and establish the proper inhibit safeguards to avoid misidentification of these surviving cosmic components as something other than background, in combination with the ID's 400 light-concentrator-free PMTs. Together, these two systems constitute Borexino's *muon veto*[92].

Apart from its role of further shielding for environmental background from the surrounding rocks, the muon veto is necessary to alert against the intrusion of the only main cosmic component (apart from neutrinos) to penetrate the mountain's overburden: cosmic muons. These are mostly considered a background; as mentioned, in Borexino's location the remaining flux is 1.2 $m^{-2}h^{-1}$ (a factor of $\sim 10^{-6}$ with respect to surface fluxes), with an average energy of 320±12 GeV[92]. They are produced by the interaction of primary cosmic rays (90% p^+, 9% α particles,

FIGURE 2.13: View of the final touches between the top of the SSS and the WT's dome. The OD's PMTs can be seen protruding, embedded in the reflective white film, as well as the PMT cables and other lines running from the "organ pipes", and the sampling/source insertion pipe running through the sphere's vertical axis.

and ~1% heavier ionized nuclei) with atmospheric molecules, giving rise to short-lived pions and kaons, which decay producing a hadronic shower consisting of (anti)muons and (anti)neutrinos:

$$\pi^{\pm}, K^{\pm} \rightarrow \mu^{\pm} + \nu_{\mu}/\overline{\nu_{\mu}} \tag{2.13}$$

It is estimated ~1-2% of the surviving muon flux in Hall C stops in some part of the detector[92]: the vast majority of the flux is through-going, ionizing the medium in their wake. The muon veto, with an efficiency of ~99.99%, recognizes these tracks in the WT, and provides context to avoid false events in the "golden" energy region. The main concern for physics are muons going through the buffers, where only Čerenkov light will be emitted.

Below the water tank there are two circular steel plates to provide additional shielding against the rock-emitted γs, separating the WT from the ground in the area where it provides the shortest water-filled volume between the SSS and the rock.

2.2.6 External facilities: fluid handling plants, cleanrooms and Icarus/SOX pit

Although not part of the detector itself, several adjoining facilities are integral part to the observatory:

Water purification plant Already used in CTF, the plant satisfies the demand of ultrapure, low-background (~ μBq/kg) water, through cascaded purification processes based on reverse osmosis, de-ionization, microfiltration, ion exchange and nitrogen stripping. It is

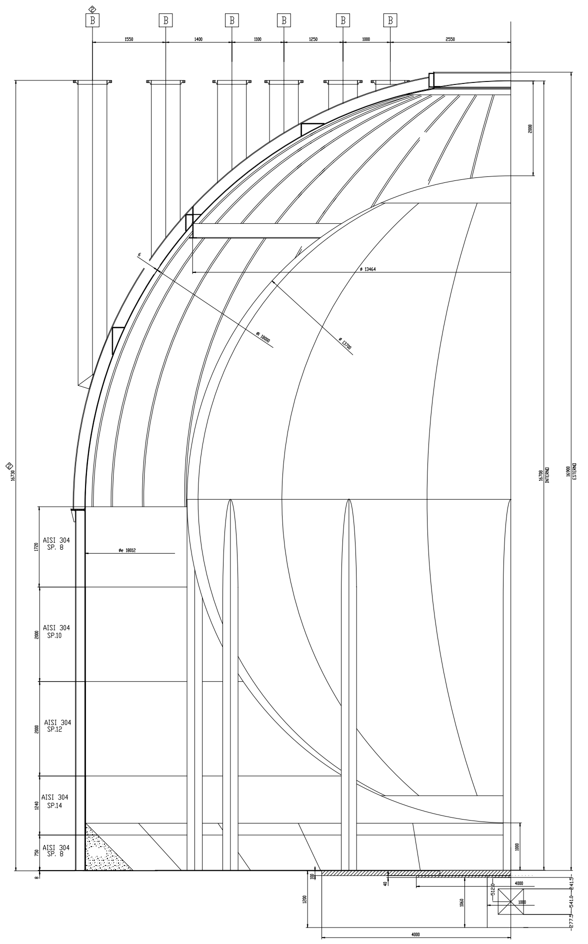

FIGURE 2.14: Technical drawing of the Water Tank structure and the Stainless Steel Sphere inside it.

used in production mode (aided by a 5m^3 storage tank) or in recirculation mode through the WT.

Scintillator storage and purification plants (skids) Four storage tanks on the side of the CTF/DarkSide50 tank, next to the ICARUS site, hold 100 tonnes of scintillator each, and are located in a concrete containment structure under fire extinguishing systems. One of the tanks is able to perform a first-stage purification through ultrapure nitrogen bubbling. No storage capability exists for the buffer fluid. The *skids* perform the distillation, water extraction, nitrogen stripping and micro-filtration for scintillator purification – reducing particulate and gaseous contaminants to extremely low levels.

Nitrogen distribution system The radon-free nitrogen needed for many routine and special operations in Borexino comes mainly from a distribution plant next to Hall C's entrance.

Control and electronics buildings Borexino's electronics are located in a multi-purpose structure separating the detector and DarkSide50, where office space, electronics and mechanical workshop areas and storage facilities are also found. The fluid handling facilities are mainly located on its side. The Borexino main control and data acquisition (DAq) room is located on the second floor of this structure, and gives access to the environmentally-controlled electronics room.

Clean rooms Clean Room 4 (CR4) is located on top of the water tank and contains the equipment needed for safe access to the inner volume (most notably, to insert calibration sources at different positions inside it, through the use of a tether or an articulated mechanical arm, more details in Chapter 4) as well as the fluid handling equipment to allow for sampling of the scintillator and buffer fluids. The CCD camera system feedthroughs and nitrogen purging is also located inside CR4, along with its control system. CR1 is located under the electronics/control/office structure, and was originally devoted to DarkSide50 construction. It is now shared with Borexino for the SOX program, since it gives access to the ICARUS/SOX pit, and provides valuable workspace for pre-insertion and calorimetry operations.

ICARUS/SOX pit This is a T-shaped tunnel (see figure 2.16) with a section of ∼1 m^2 (0.95x0.95 m in the tunnel and ∼1.05x1.05 m for the pit itself) located just under Borexino's WT/ground steel plates[11]. It now contains part of Borexino's Temperature Monitoring System (see Chapter 3) and rail supports for delivering the SOX sources from CR1 down under Borexino's center (see entrance mouth in Figure 2.15).

FIGURE 2.15: Pit entrance from CR1. Shown inside the pit are the last in-tunnel section of the SOX source railings and part of the calorimeter cart.

2.3 Electronics and software

Borexino's electronics must handle an event rate of $\sim 10^5$ events/hour, corresponding to a data stream of more than 200 kbps, which must be registered, digitized, filtered and tidily stored

[11] At the time of concrete setting, preliminary plans called for the LAr-based *Imaging Cosmic And Rare Underground Signals* (ICARUS) experiment to be located where Borexino stands now. As with Borexino, there was a desire to use artificial neutrino sources very close to the detector, and provisions were made to enable this through the construction of this pit. In time, Borexino has found good use for it.

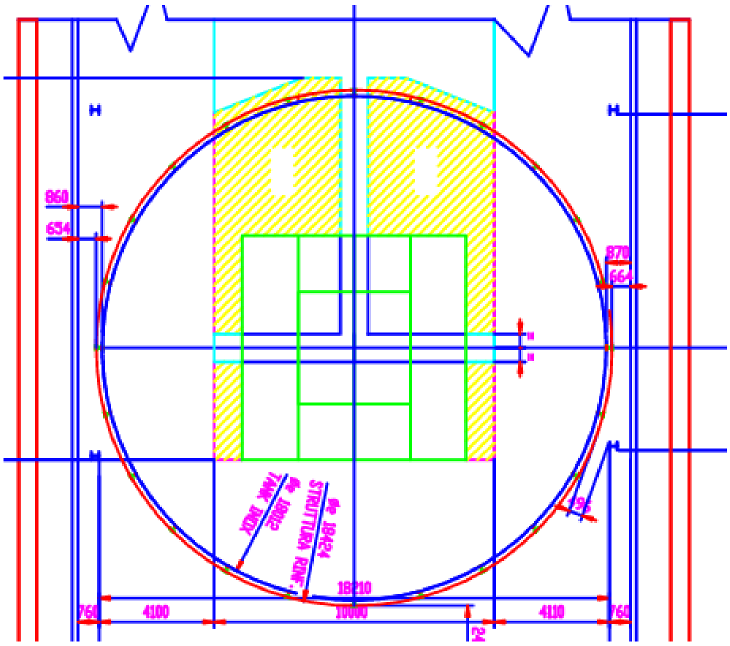

FIGURE 2.16: Technical drawing of the pit located under Borexino.

for further offline data processing. Although the topic of this thesis justifies not dwelling too much into their specifics, for completeness and the purpose of illustration of the full detector operation, they will be briefly enumerated and described below. For a much more exhaustive discussion, a particularly useful reference can be found in [92].

High voltage supply The PMTs, operating at a nominal gain of 10^7, have a nominal current draw of 100μA and must be kept at a tension of $\sim$1kV. This is supplied by the CAEN SY527 mainframes supporting 24-channel CAEN A932AP board units.

Racks, front end (FE) and laben boards Borexino's Inner Detector electronics sport 14 racks with capacity for 160 PMT signals and 8 spares. The PMTs are AC-coupled to the FE boards that decouple their signal from the HV's, and then duplicate it to generate reference signals: one for **timing** (fast linearly-amplified by $\sim$20x) and one for **charge** measurement (integrated through a gateless integrator strategy [111]). Each signal is afterwards digitized in the VME crate's digital electronics (*Laben* boards, named after the manufacturer company) and used for triggering. A typical PMT signal can be seen in figure 2.17.

The timing signal keeps the first photoelectron arrival time ($\sigma \sim 0.5$ ns) through the use of a dual-threshold discriminator, set at [min=0.1,max=0.25] single photoelectron signals (corresponding to [20,50] mV), which is then used through the *base-peak* sampling of the integrated input signal that digitizes the charge. Only PMTs crossing the maximum threshold are considered hit, in order to filter out dark noise. The effect of this threshold in single-p.e. hits is just important for a fraction of 0.13 of the photoelectron

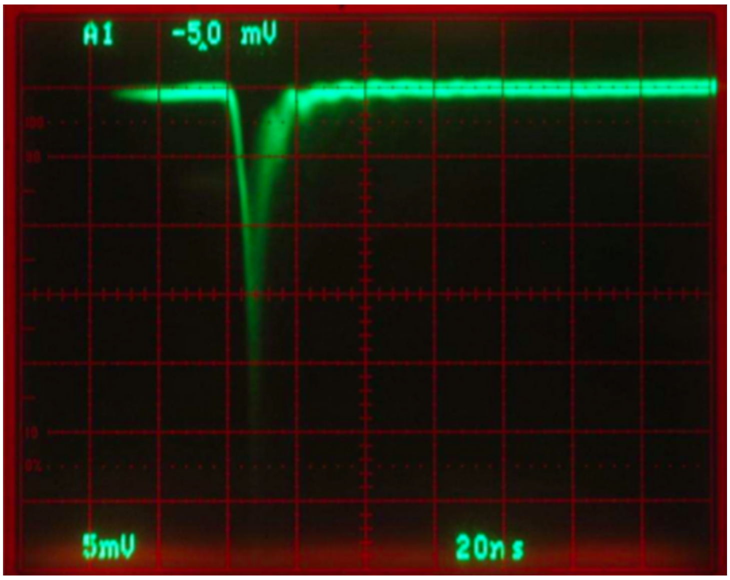

FIGURE 2.17: Typical signal from a Borexino PMT in an oscilloscope.

distribution[112], and negligible for multiple-p.e. hits. The integration of the charge keeps the full charge plateau for 80 ns and starts a τ=500 ns exponential decay thereafter. The discriminator is disabled for 140 ns after it fires, and any new photoelectrons arriving in the first 80 ns after the firing will be summed, generating **pile-up**. However, apart from the 140-80=60 ns of deadtime induced by the superposition of the discriminator deadtime with the charge integration window, there is an extra 40 ns software-imposed deadtime to avoid false retriggers because of signal taildown oscillation. Therefore, there is a period of 60+40=100 ns (between 80 and 180 ns from the hit time reference) in which no new hit is recorded in a given channel. The effect of this deadtime was studied[94] to be both energy- and position-dependent, and of a magnitude between <1% in the case of a 200 p.e. hit at the center of the detector, which can rise up to 2.5% for a 1000 p.e. hit. Physical events are between ~100-500 ns long. These processes are calibrated during special weekly *calibration* runs, thanks to the use of a fast (50 ps) diode reference laser (394 nm) 100-Hz signal that travels to the PMTs through optical fibers, with a precision of <1 ns. The intensity of the laser is adjusted to create between 0.1-0.5 p.e. (depending on the individual PMT response, studied beforehand) to reduce dark noise and reduce the possibility of multiple-p.e. hits, in order to measure the single-p.e. response more accurately. Finally, working channels are also monitored online, continuously during regular data-taking, thanks to dedicated 2-Hz triggers (classed as *electronic pulse*, *timing laser* and *random* triggers). Those exhibiting no timing information, or no information at all, are disabled for the rest of the ~6-hour run. Those exhibiting no charge information are still kept for its timing value, for position reconstruction purposes, but do not reconstruct events. The information recalled from the aforementioned processes is kept in memory awaiting a trigger signal for recording.

Differences between ID and OD electronics The Outer Detector PMTs are much like the ID's, but as mentioned none of them has light concentrators. Additionally, the electronics in the ID saturate at ~6.5 p.e., due to the sensitivity needed for the sub-MeV design specifications applicable to Borexino – so the signal from the muon veto (which can easily reach 100 p.e.) falls squarely out of its range. Therefore, a compromise is made with respect to resolution, which is not so important for these events, and custom-made Charge-to-Time Converters (QTCs), developed by the Princeton / TUM groups, are used for this task. The digital electronics, once commercial VME CAEN v673 units, have been upgraded for stability with new TDCs which are poll-read directly from the user space.

Triggers: MTB, BTB and GPS After data acquisition and storage in memory, the trigger establishes whether the signal is worthy to be recorded by establishing how many channels are hit in a given time window of 60 ns. Although this threshold has varied (and continues to vary) with time and depending on the studies performed, it is currently set at 20 (lowered from 25 because of the steadily increasing number of dead PMTs with time, see figure 2.18). It is worthwhile to note that events falling in the same gate are not subject to the trigger threshold, which is very important in case one wishes to select a sample of lower energies (and therefore lower number of hit channels). This was especially important to independently obtain the ^{14}C rate in the scintillator, in particular for the measurement of the ν_{pp} (see Section 2.5). In case the trigger fires, then detector-wide data falling within the trigger *gate* (16.5 μs) is recorded, after which there is a dead time of 2.5 μs. The system is ruled by the **Borexino Trigger Board** (BTB): a custom-made 6U VME device designed around a fully programmable Digital Signal Processor. It takes 3-4 μs to form the trigger signal, and fires at an average rate of ~26 Hz. Additionally, the *Muon Trigger Board* (MTB) is another custom-made 6U VME device developed by MIT that acts as a separate trigger to generate the OD's trigger signals and evaluate appropriately its coincidence with the general Borexino trigger. Clock electronics are implemented through the quartz oscillator of the *ClocK Generator* (CKG) board. Absolute time tagging is kept with a GPS receiver connected with the satellites through a precision fiber optic link, upgraded to ~100 ns precision during the *CERN to Gran Sasso* (CNGS) campaign to test the neutrino superluminal propagation claim from the OPERA experiment. This absolute time is needed for correlation with possible supernova events, gamma-ray bursts (GRBs), etc.

Each trigger contains six different fields with relevant information. All in all, there are 8 types of trigger, listed here by order of priority: neutrino (type 1), muon MTB (type 2), muonTotC (type 128), laser355 (type 4), laser266 (type 16), laser394 (type 8), calibration (type 32) and random (type 64). As mentioned in the *racks* description, there are periodic service trigger signals sent to the BTB by a NIM dual timer: types 32, 64 and 8. The other two laser triggers (16 and 4) are enabled and generated separately. The

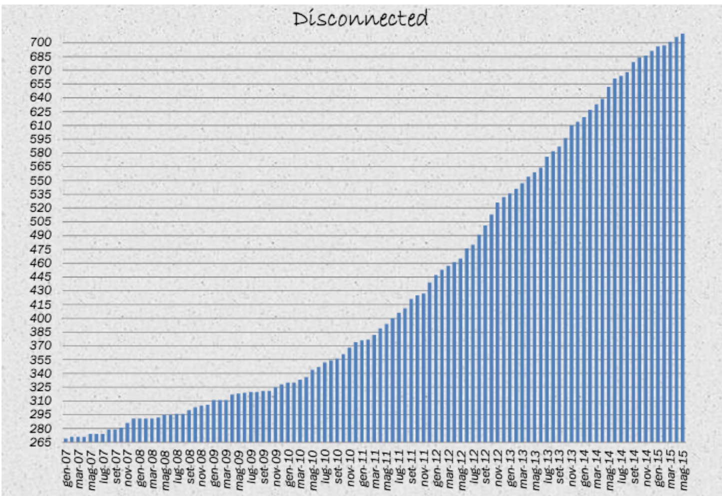

FIGURE 2.18: Progression of dead PMTs updated in May 2015. Taken from [113]

data inside each triggered window, in form of a "*raw*" data file, is then further processed to reconstruct the physical events falling in that timeframe by precalibrating the channels (i.e., synchronizing, calibrating and substracting the dark noise for each channel) and identifying the clusters inside each trigger window, which in first approximation will correspond to physical events. Position reconstruction and Pulse-Shape Discrimination (PSD) take place afterwards. All this sequence is performed through the *high-level software* codes based on CERN's ROOT platform: *Echidna* and *Mach4*, which were combined in mid-2010 into ***MOE*** (Mach4-on-top-of-Echidna). These will condition the data for analysis-specific treatment (see Chapter 3). An important note about the trigger is its –current– extreme old age. It was devised and built with 90s electronics, and has been in practically continuous operation for more than a decade. Several important signs of degradation started showing around 2013, and during 2014 and '15 it was decided it would be necessary to substitute it with a new one, especially considering the demanding regime it would be subject to during the second calibration campaign and the SOX phase. In fact, the so-called *start time problem* that plagued the BTB from the summer of 2015 to early 2016 (and one of whose recovery efforts are illustrated in 2.19) showed what was likely one of the final calls before complete failure, and illustrated the need to perform the trigger upgrade as soon as practicable, with a period of overlap to allow for troubleshooting and calibration, before the end of 2016. In practice, the most important actions would be to substitute one of the NIM modules (NIM-2) and the venerable BTB for an interface board and a CAEN v1495 6U module. This upgrade was performed over the summer of 2016, and a dedicated dual-trigger checkout period was performed over the next few months.

FADC High-energy 15-20 MeV events, although in principle covered up to ∼17.5 MeV by the *Laben* boards, are redundantly measured through *Fast Waveform Digitizers* (also known as *Flash Analog-to-Digital Converters* (FADC)) with the aim of performing PSD in high hit

FIGURE 2.19: G. Korga, G. Bonfini and M. Orsini in intense work following a trigger upset in mid-2015 that elevated the urgency of upgrading Borexino's trigger.

multiplicity events, for which the low-energy sensitive *Laben* boards were not designed. The system's nominal range of operation is 0.8-50 MeV and, apart from the high energy studies of ^{8}B and supernova neutrinos, are also very useful in antineutrino reconstruction[114], especially for the SOX ^{144}Ce-^{144}Pr source. Its usefulness for some analyses, such as for geoneutrinos, is hindered by low livetime with respect to *Laben* data (even if its duty cycle is generally better, it was installed 2 years after the beginning of data-taking), the lack of a calibration campaign (although self-calibration with neutron capture peaks, cosmogenic ^{12}B and Michel spectra is in progress) and its lower energy resolution.

Scalers Used to monitor dark noises and health state of the channels, the Marathon (Moscow)-developed scalers are modules for both the ID and OD that monitor the 12 channels in an FEB, or 64 channels with single-channel rate monitoring capability, respectively.

Workstations The majority of the sub-processes governing data acquisition (DAq) are controllable through a number of network-accessible workstations. Initial data processing takes place in *bxbuild*, the database is controlled and updated through *bxdb*, the server hosting the webpages needed for remote operation and documentation is *bxweb*, the power supplies are managed through *bxslow* and the system's firewall is *bxmon*.

Cooling Worth mentioning is the needed temperature stability to understand and nurse all the electronic equipment. The Laboratories provide a cooling loop that is used as the primary, with the old OPERA cooler (no longer in function since the beginning of this experiment's decommissioning in 2015) serving as backup.

2.4 Backgrounds

The scintillation photons produced by reaction 2.2 are indistinguishable from those generated by scintillation caused by radioactive decays whose visible energy, due to quenching, falls in the region of interest of the neutrino-scattered electron (see equation 2.5). α-decays can be discriminated with the Gatti technique, as mentioned in section 2.2.

Therefore, apart from the Compton distributions (further smeared by the detector's energy response) yielded by the solar neutrino signals fluxes in Figure 1.8, visible as ν_{xx} in Figure 2.20, we find several other components –in many cases overlapping and outweighing the neutrino signals by orders of magnitude– in Borexino's spectrum that have to be quantified, fitted and corrected for, in order to access the neutrino rates. Of course, several layers of signal conditioning need to take place to account for detector-specific behavior (energy and timing response, dark and electronics noise, muon filtering, gate clustering, energy and position reconstruction...) and analysis-dependent data selection (muon filtering, triggering, fiducial cuts, coincidences and uniformity...) before such a *reference spectrum* is attained. More details about the mid-level data processing that structures the raw data, as well as the physics-specific high level data analysis, based on data cuts on different variables, is presented in the signal overview Section 3.1.1.

The main backgrounds are hereby listed by their approximate relative rate in the plot. Actual rates are listed in Table 2.3. Needless to say, some of them may be more dangerous for certain analyses than others depending on where their distribution falls, even if their rates are comparatively small.

2.4.1 Carbon-14

Radiocarbon is produced from stable ^{14}N, majorly from the ^{14}N(n,p)^{14}C reaction of cascading neutrons coming from cosmic ray showers in the upper atmosphere (primarily between 9 and 15 km and high geomagnetic latitudes) with its ~78% nitrogen content[12]. This carbon, produced at a roughly steady rate of ~17000 m^{-2}s^{-1}, is mainly incorporated into CO_2 molecules, which are then respirated by the autotroph biosphere's living beings, and therefore replenished at a constant rate during the organism's lifetime (~10^{-12}g/g). Upon death and its implied cessation of respiration, ^{14}C is no longer incorporated and decays with its half-life of 5730 (±40) years[13] In the event the remains of this organism are geologically trapped in a fossil fuel repository instead of being re-incorporated to the biosphere, they are left to enrich in stable carbon for

[12] Other, mainly anthropogenic mechanisms exist for its production –like nuclear weapon atmospheric testing–, but are not important for the purposes of Borexino.

[13] As is well known, this makes the measurement of the concentration of this isotope very useful for dating of carbonaceous material up to ~60000 years, when its concentration becomes very low for current measurement techniques. It also means its contribution to Borexino's background throughout the experiment's operational life is, for all intents and purposes, constant.

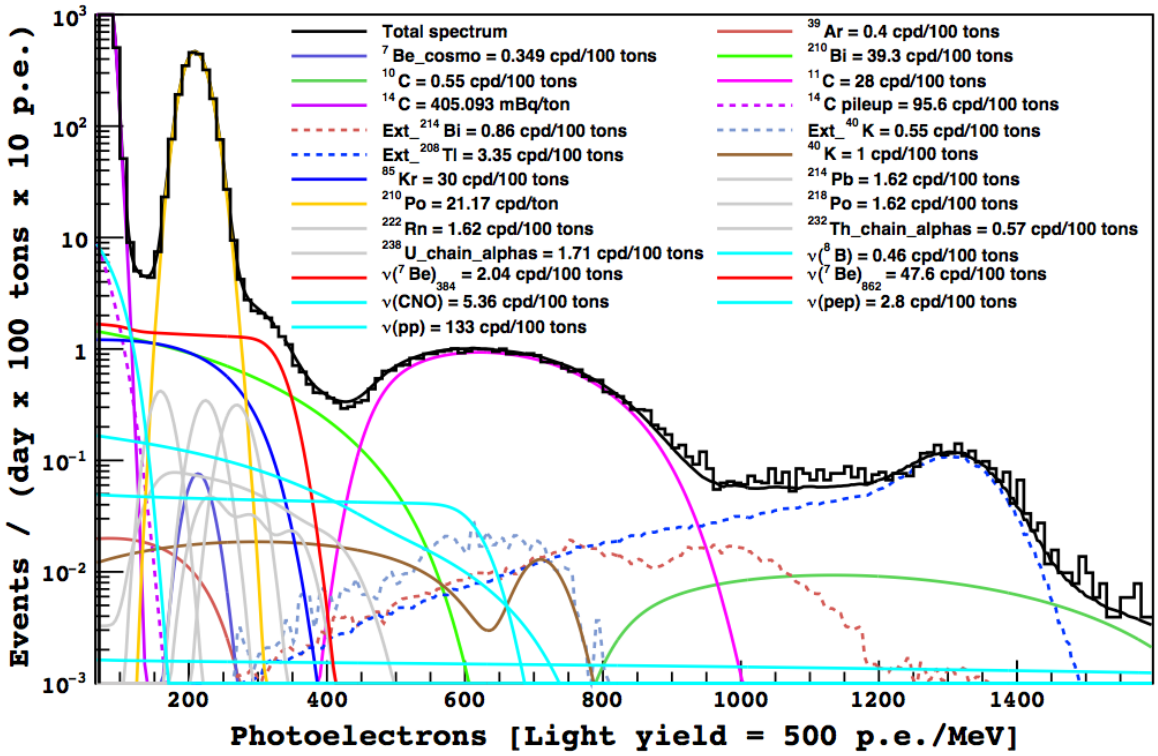

FIGURE 2.20: Spectrum simulation, after ^{7}Be analysis data selection cuts, superimposed with real data (black bins), with rates estimated by coupling theoretical calculations and data estimates, from [94]. The ^{7}Be spectrum is listed in the legend as two separate components for each monoenergetic line, which get merged in the same red curve in the plot. All other solar neutrinos are shown in light blue: the *pp* component has the lowest endpoint at ∼170 p.e., while *pep*'s is at ∼680 p.e. and CNO's at ∼740 p.e. ^{8}B neutrinos are the approximately constant component spanning all the spectrum at ∼1.5 ev/(day x 100 tonnes x 10 p.e.), and *hep* neutrinos are not pictured. Note some background components, such as ^{85}Kr, ^{222}Rn, ^{238}U, ^{232}Th or ^{210}Po have been greatly reduced in Phase 2 data, as explained in the text.

geological times (∼Myr), albeit with a small residual production of radiocarbon by the two-step (α,n) process on the ∼1-3%-abundant ^{13}C stable isotope initiated by the ^{238}U in the surrounding rocks. This carbon isotope becomes ^{14}N suitable to suffer an (n,p) reaction. Borexino's scintillator was distilled from several batches of deep petroleum sources, ensuring this very low concentration of ^{14}C (10^{-6}x the concentration in surface biomass![103]), and collected online under an inert nitrogen atmosphere in clean 1 m^{3} teflon containers in the ENIChem facilities in Sarroch, Sardinia. Swiftly thereafter, it was transported underground to the storage tank D201 (see Section 2.2.6) to minimize modern cosmic ray exposure.

In spite of all precautions taken, there is still an irreducible measured activity of 40±1 Bq/100 tonnes[42], inseparable chemically due to the organic nature of the scintillator fluid. Its mode of decay is β^{-}:

$$^{14}_{6}C \rightarrow^{14}_{7} N + e^{-} + \overline{\nu_e} \tag{2.14}$$

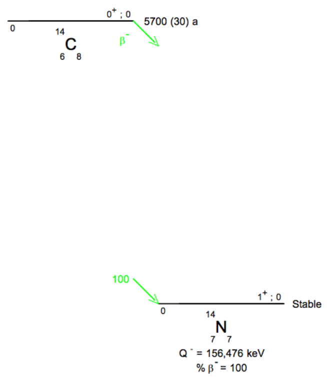

FIGURE 2.21: ^{14}C β^- decay. All decay schemes presented in this Section are reproduced from [115]

with an endpoint of 156 keV (average 49 keV). This is low enough that the ∼40 Hz/100 tonnes rate is reduced to ∼29 Hz in the IV through a hardware threshold at 50 keV. The *Golden window* for Borexino in the ^{7}Be energy range is mostly unaffected, but it presents a considerable challenge for low energy studies, most notably the *pp* neutrino flux determination, but also others such as the search for electron decay (see next Section 2.5).

2.4.2 Pile-up

Although not a "background" *per se*, pile-up is modeled as an independent background because of its nature: it is defined as the sum of two distinct physical events that occur within <250 ns of each other. The reason behind this number stems from the temporal distribution of the scintillation light in Borexino, coupled with the trigger window characteristics discussed before in Section 2.3. In particular, the 16.5μs trigger window length means there is a certain probability that, by probabilistic chance, two physical events (whose typical scintillation light emission is ∼100-500 ns, as mentioned) fall within the same window. The clustering identification software in Echidna/MOE will recognize them fine if they are separated by ∼>1 μs, since their scintillation profiles will be mostly separate in the time domain. Double clusters which partly overlap each other (when their Δt ϵ [0.25,1]μs) can be discriminated by their combined –distorted– pulse-shape, and rejected losing some livetime, or studied independently. The real problem becomes the fraction of events which overlap almost completely: in practice, which occur closer than the aforementioned 250 ns. All these may be counted as a single event, with peculiar and varied traits that make them very hard to model, stemming from the fact that they are really the sum of two independent events. For this reason, the ^{14}C-induced pile-up "endpoint" is 312 keV. Reconstructing the "event", because of its distorted shape, can lead to mis-identification as α-like (long tail) and artificial fiducialization.

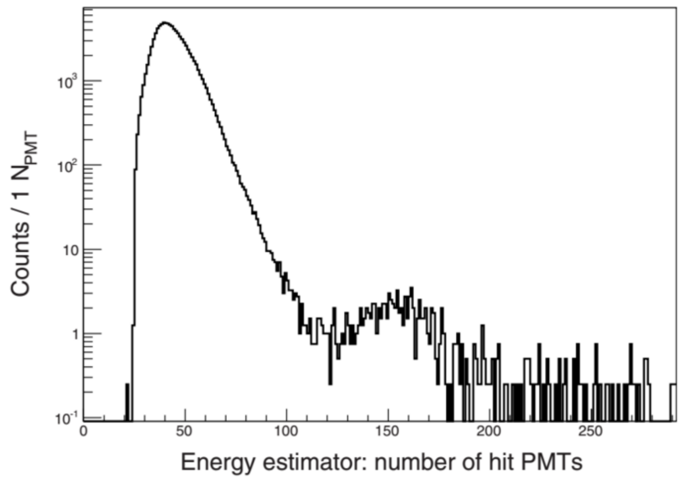

FIGURE 2.22: Pile-up spectrum derived from the synthetic data-driven reconstruction method[42], explained in Section 2.5

Because of its large rate, ^{14}C is the largest source of pile-up –and because of radiocarbon's β energy spectrum, pile-upped events partly overlap its event energy distribution, mixing with the tail of the *pp* neutrino spectrum at higher energies. An easily-calculable rate estimate[94] yields 125.9 ^{14}C pile-up events / day in the whole detector, assuming an average of 26.2 Hz trigger rate. The independent measurement developed for the *pp* neutrino flux determination measurement[42] yielded a rate of 154$\pm$10 cpd/100t in all the spectrum reconstructed by Borexino, with no energy threshold[42]. The second most important contributor to this rate would be ^{210}Po (see next subsection) pile-upping with ^{14}C, whose contribution would be $\sim$0.2% even when considering its historically maximum rate of $\sim$8000 cpd/100t[94]. Another relevant source is ^{14}C with dark noise.

2.4.3 Polonium-210

This α-decaying isotope (Q=5.31 MeV, see the decay 2.23) is part of the ^{238}U chain, but given its importance in Borexino and high rate (historically, especially in Phase I data, second only to ^{14}C), it is covered in more detail in this subsection. Its energy range, because of the quenching of the α particles' ionization in the scintillator (see Section 2.2.2), falls in the "golden window" of Borexino's energy spectrum, on top of the ^{7}Be plateau at around 210 p.e. (see Figure 2.20).

Another peculiarity of ^{210}Po is that it has been *out of equilibrium* with its progenitors in the decay chain because of wash-off from the detector's structures, and the success of the purification campaigns in reducing many other backgrounds (see, for example, next in Section 2.4.4) wasn't met in the case of this isotope, and its rate was furthermore brought up by scintillator refiling operations (see Figure 2.24).

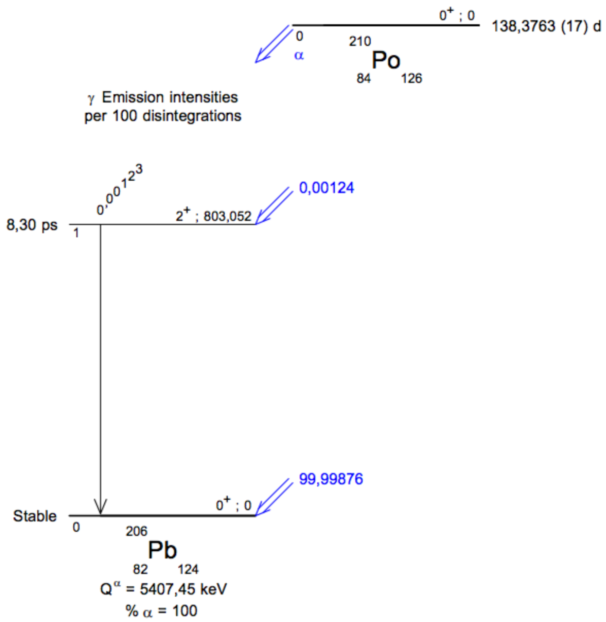

FIGURE 2.23: ^{210}Po α decay

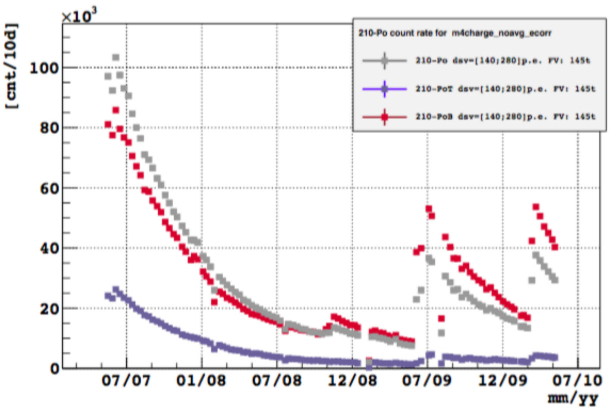

FIGURE 2.24: ^{210}Po concentration history in Borexino until mid-2010, showing the increases due to detector operations. More details about the Phase II concentrations will be discussed in the upcoming Chapter 3.

While the discussion of the polonium sources, diffusion and its correlation with temperature changes is one of the main topics of this thesis and many more details about its behavior will be given in the next Chapter 3, it is worthwhile to emphasize that –even if ^{210}Po itself isn't much of a problem since it can be tagged out with a proper $\alpha - \beta$ cut, as explained in Chapter 3 – this isotope provides a handle on the concentration of its much subtler ^{210}Bi isotope that precedes it in the decay chain, through the formula 2.15, where $\tau_{^{210}Po}$=138 days, $\tau_{^{210}Bi}$=5.012 days, and the S is a functional modelization of the source term:

$$\frac{dN_{^{210}Po}}{dt} = -\frac{N_{^{210}Po}(t)}{\tau_{^{210}Po}} + \frac{N_{^{210}Bi}(t)}{\tau_{^{210}Bi}} + S_{^{210}Po}(t) \tag{2.15}$$

2.4.4 Krypton-85

Although naturally occurring because of cosmic ray interactions with the stable ^{84}Kr in the atmosphere (57% of the $\sim$1 ppm krypton concentration in the atmosphere), this mode of production only accounts for a stable $\sim$90 TBq in atmospheric air, which is dwarfed when compared to the anthropogenic 5500 PBq (1.3 Bq/m^3) estimated in 2009[116], increasing at a rate of 0.03 Bq/m^3/year because of nuclear fuel reprocessing[94]. As the decay scheme in Figure 2.25 shows, it is a β^- emitter with a 687 keV Q-value ($\tau_{1/2}$=10.756 years), causing it to have a recoil spectrum very similar in shape and energy to ^{7}Be solar neutrinos. In spite of design specifications calling for ^{85}Kr levels of <1 cpd/100 tonnes, an air leak during filling meant that initial levels were in excess of 30.

Purifications before the start of Phase II data-taking brought this level down and, at present, is estimated at <4.7 cpd/100 tonnes (95% c.l.) since August 2010[117], accounting for 1.99 random coincidences of ^{14}C-^{210}Po pile-up. No new events have been seen since November 2013. They are reconstructed using the 0.43% branch that decays to metastable ^{85m}Rb, which emits a 514 keV γ (γ_4 in Figure 2.25), enabling for a $\beta - \gamma$ coincidence –complicated by the low statistics due to the small branching ratio, low beta energy of 173 keV that only allows $\sim$19% of events to be reconstructed, and the actual ultra-low background.

It should be noted that ^{85}Kr absence is key to the possibility to reliably measure ^{210}Bi and, consequently, CNO-ν because they are intimately correlated.

2.4.5 Bismuth-210

Arguably the most important background for this thesis, this Q=1.16 MeV β^- emitter's peculiarities, the data selection that yields its position distribution and rate determination, as well as its stabilization and abatement strategies will be explained thoroughly in the next Chapter 3.

For now, it should be noted it has been out of equilibrium as was the case with its daughter ^{210}Po, but being a β-decaying isotope its contribution to the spectrum, which spans most of the region of interest for solar neutrinos, cannot be filtered out with a pulse-shape discrimination technique. A precise determination of its concentration in the Fiducial Volume should be straightforward through the ^{210}Po's *if it was in secular equilibrium*. However, as mentioned before, the wash-off of polonium inside the scintillator and, more importantly, the influence even minute temperature fluctuations have on the mixing of the liquid inside the Inner Vessel, transporting higher background concentrations found in the external reaches of the volume towards the FV, complicate a rapid and reliable determination of its rate. This has profound implications for the measurement of low rate signals, such as *pep* and CNO neutrinos –whose latter spectral

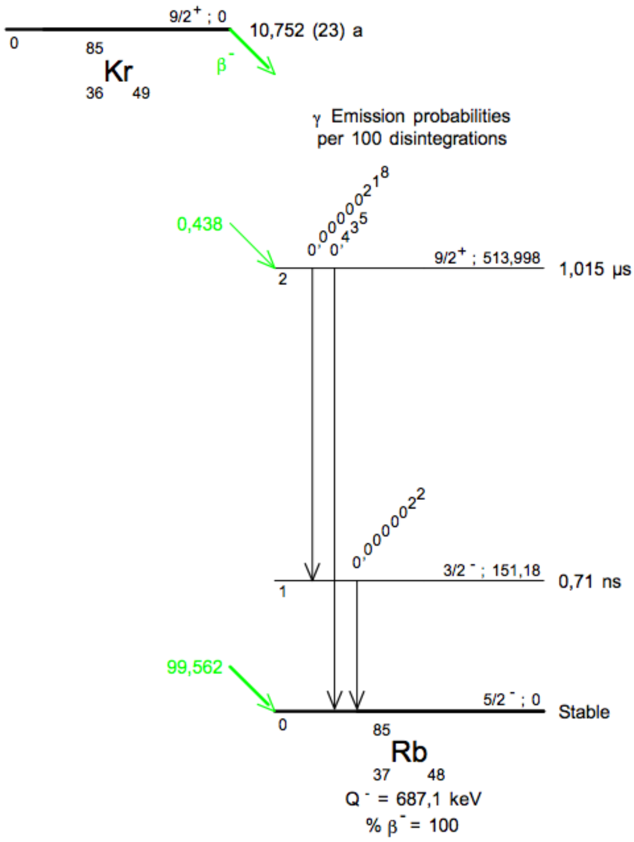

FIGURE 2.25: ^{85}Kr β^- decay

distribution and expected approximate flux make it extremely challenging to disentangle from the fluctuating ^{210}Bi.

Another further complication is the fact that ^{210}Bi undergoes a *forbidden* β decay that is far from Fermi's allowed shape, and whose spectral shape can only be precisely known from an experimental measure –and the most recent one was made in the sixties[118]. This further raises the uncertainty in the rate distribution in the Compton edge seen by Borexino.

2.4.6 Carbon-11

This radioisotope of carbon is not, like ^{14}C, intrinsic to the scintillator –but its production due to cosmic ray bombardment is, due to the organic nature of pseudocumene. It is the main cosmogenic background (see more in Section 2.4.15) and undergoes 99.75% of the times a β^+ decay with Q=960 keV and $\tau_{1/2}$=20.334 minutes, although it does experience electron capture through a 0.25% branching ratio, as evidenced in Figure 2.27. As can be expected, the fact that the decay expels a positron means that the measured energy deposition in the scintillator is the sum of the decay energy *plus* the annihilation photon's 2x511 keV. This increases the ^{11}C Compton curve in Borexino's spectrum to higher energies than the "golden window"'s, but still

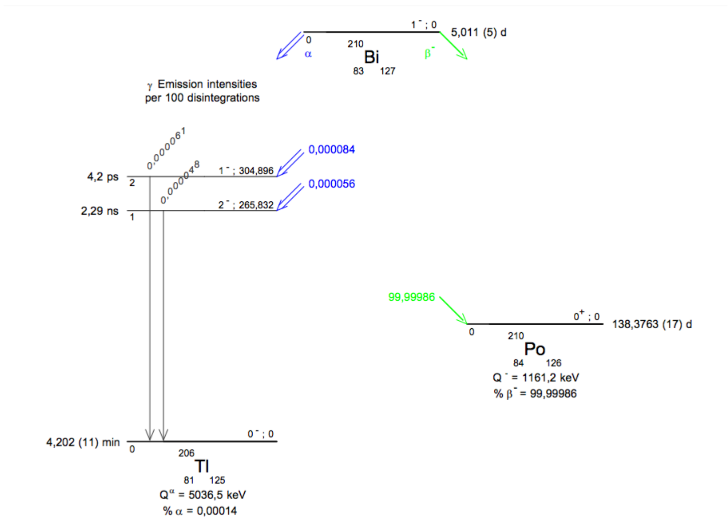

FIGURE 2.26: ^{210}Bi β^- decay

constitutes an important background for higher energy portions of the spectrum such as *pep* and ^{8}B neutrinos. The determination of its lower energy tail is also important for CNO νs.

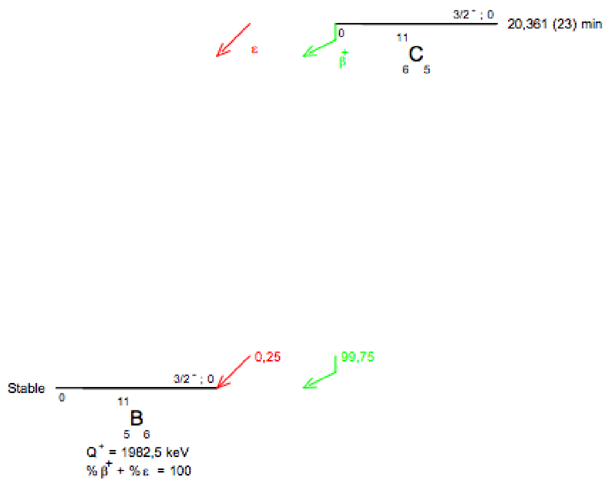

FIGURE 2.27: ^{11}C β^+ decay

Studied *ex-profeso* for Borexino[119] and confirmed by KamLAND[120], ^{11}C is mainly (95% of the times) produced through spallation of cosmic muons ($\sim$1650/day, see Section 2.4.14) in the organic molecules' carbon atoms, through the cascade 2.16, allowing for a higher-than-modeled rate in Borexino of 28.5 $\pm$ 0.2 $\pm$ 0.7 cpd/100t[121]:

$$\mu(+\text{ secondaries}) +^{12} C \rightarrow \mu(+\text{ secondaries}) +^{11} C + n^0 \tag{2.16}$$

This also liberates free neutrons, which are then thermalized and captured mainly in the hydrogen atoms available within the scintillator, within a τ of 0.26 ms and the corresponding emission of a 2.22 MeV γ-ray. This, in turn, yields for a prompt + delayed coincidence signal that, together with the high tracking efficiency of through-going μs thanks to the WT's OD, allows for the implementation of the so-called *Three-Fold Coincidence* (TFC) technique –which, in essence, follows an algorithm applying cylindrical (along the muon's reconstructed track) and spherical (around a neutron with a reliably-reconstructed capture position) cuts in combination with different blackout periods. This has been estimated[121] to successfully tag out ∼90% of ^{11}C events.

Furthermore, an independent validation technique to characterize the ^{11}C rate in Borexino was developed that makes use of the small probability of onium[14] formation between the e^+ emitted in the decay and a local electron in the form of ortho-positronium[15]. This is statistically observable through a ∼ns delay –consistent with o-Po's ∼142 ns half-life– between the deposition of the positron's kinetic energy and the emission of the annihilation γs, as a distortion in the signal's time profile and a slight deviation from a point-like position reconstruction for these events, as summarized in the study of the PS-BDT parameter in Figure 2.28.

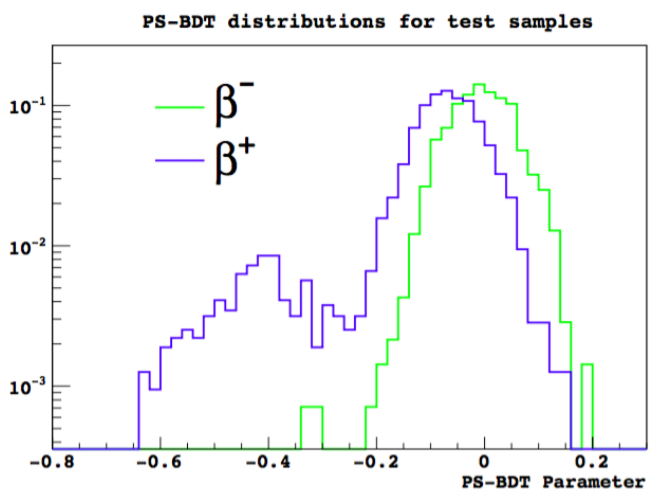

FIGURE 2.28: Distortion in the so-called *PS-BDT* (Positronium-Boosted Decision Tree) parameter interpreted as due to orthopositronium formation in β^+ events, where β^- events are ^{214}Bi decays selected through ^{214}BiPo coincidences and ^{11}C events selected through the TFC strategy, from [121].

More detailed information about the treatment of this radioisotope as a background over Borexino's signals can be found in [121].

[14] An *onium* is defined as a bound state of a particle and its antiparticle.

[15] Para-positronium, the singlet $^1S_0$ state of positronium (where both the e^+ and the e^-'s spins are anti-aligned, in contrast to the ortho- triplet $^3S_1$ case, where they are coaligned.) can also form, but its lifetime is ∼125 ps, much too small to be resolved with Borexino.

2.4.7 Radon-222

Another ^{238}U product, the α-decaying (Q=5.49 MeV for a $\tau_{1/2}$=3.8 days towards ^{218}Po, see Figure 2.29) ^{222}Rn isotope belongs to the same chain as the aforementioned ^{210}Pb, ^{210}Po and ^{210}Bi. Although fortunately the quality of the radiopurity control techniques and scintillator distillation and purification meant that its levels could be brought down to an extremely low level (see table 2.3) in Phase II data, the first calibration campaign and some refilling operations did introduce a slight amount in. Furthermore, its dangerousness lies on the fact that it, as a noble gas, can permeate easily most materials that are impenetrable to other substances. The Outer Vessel is actually in place to limit radon permeation to the innermost volumes through this material's 10^{-10} cm^2 s^{-1} wet diffusivity coefficient[122]. As a consequence, ^{222}Rn's ability to easily diffuse makes it become a background out of secular equilibrium with its progenitor isotopes.

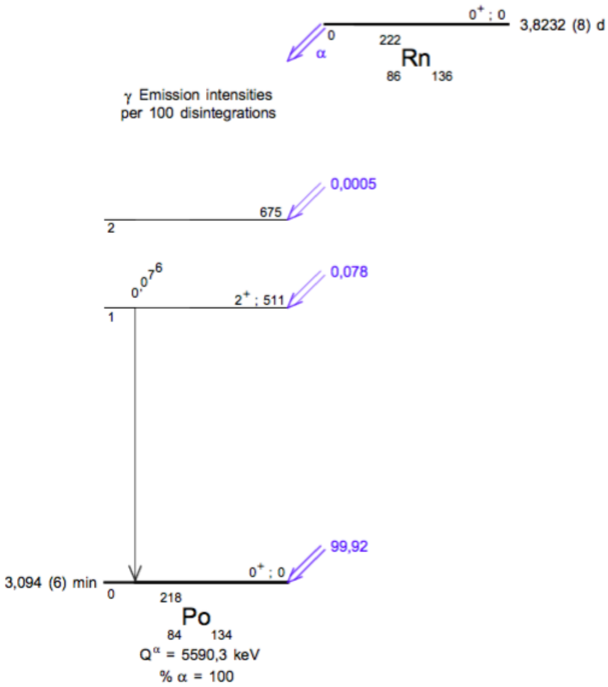

FIGURE 2.29: ^{222}Rn α decay scheme.

A double coincidence technique is employed to discern the concentration of radon background, which because of α quenching would be difficult to disentangle otherwise, in the busy but critical area between the ^{14}C and ^{210}Po peaks, through the rapid and –spatially and temporally– correlated decays of ^{214}Po and ^{214}Bi. As of early 2016, there were only 4 candidate events in the FV since the start of Phase II (July 2012)[117].

2.4.8 Polonium-214 and Bismuth-214

With a half-life of almost 20 minutes, ^{214}Bi β^--decays (Q=3.27 MeV with a huge excited state branching ratio, see 2.31) to its unstable, α-decaying ($\tau_{1/2}$=164.3 μs, Q=7.8 MeV, see Figure 2.30) daughter ^{214}Po. This pair of decays, as illustrated in the preceding subsection, allow for a precise tagging of their common progenitor ^{222}Rn, with which they share secular equilibrium, as illustrated in Figure 2.32.

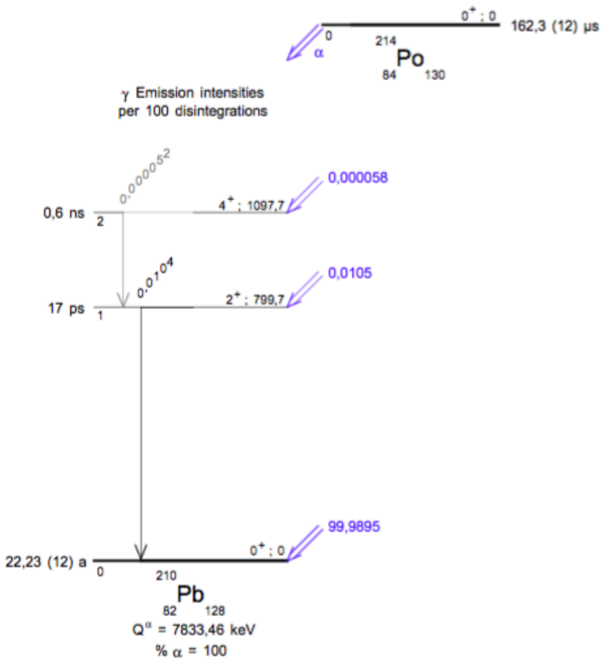

FIGURE 2.30: ^{214}Po α decay scheme.

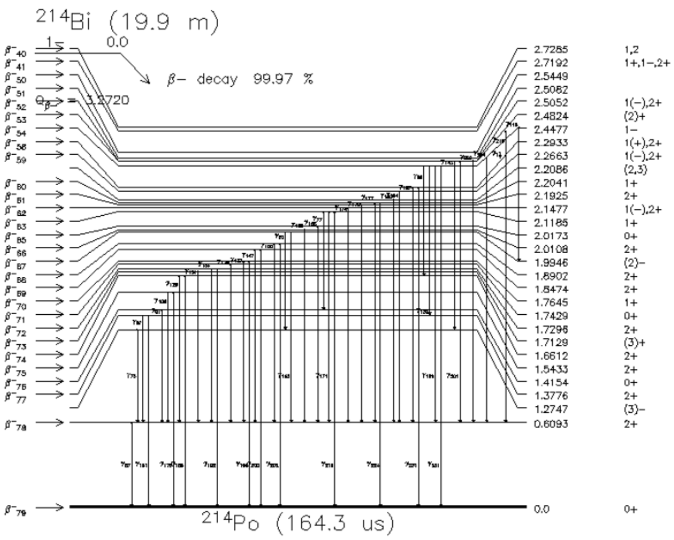

FIGURE 2.31: ^{214}Bi β decay scheme.

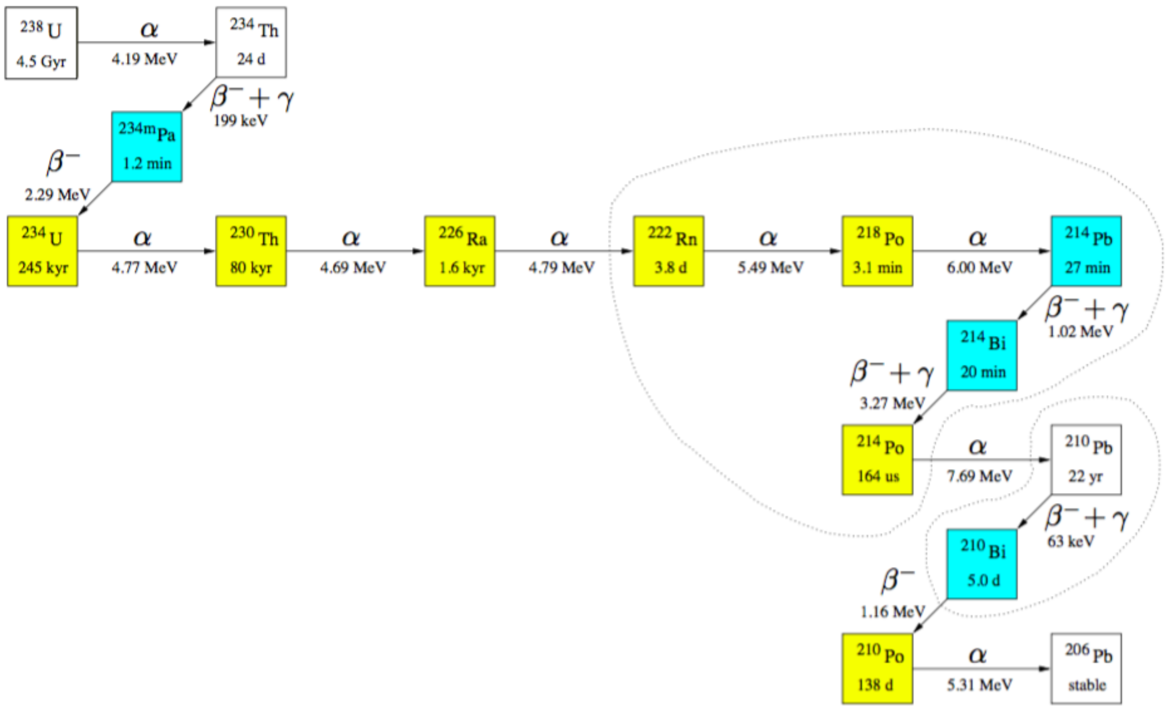

FIGURE 2.32: ^{238}U decay chain diagram, from [94]. Contained within a dashed line are the elements likely to remain in mutual secular equilibrium and, as indicated by the accompanying indexes, α and β decays *within Borexino's fitting region* are color coded in yellow and blue, respectively.

It is important to note the heterogeneous nature of the ^{214}Bi^{214}Po coincidences (see Figure 2.34 for the radial distribution, and Figure 2.33 for the α/β distinctive pulse shape discriminated by the Gatti parameter value), indicating a regional dependence of the ^{222}Rn contamination, as could be expected from its main sources in the SSS/PMTs (from radium salts) and air coming from refilling operations.

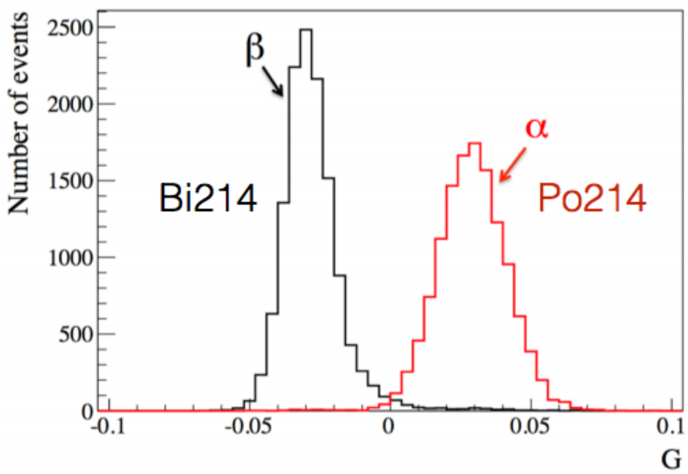

FIGURE 2.33: ^{214}Bi^{214}Po coincidence pulse shape structure evidence by their Gatti spectrum.

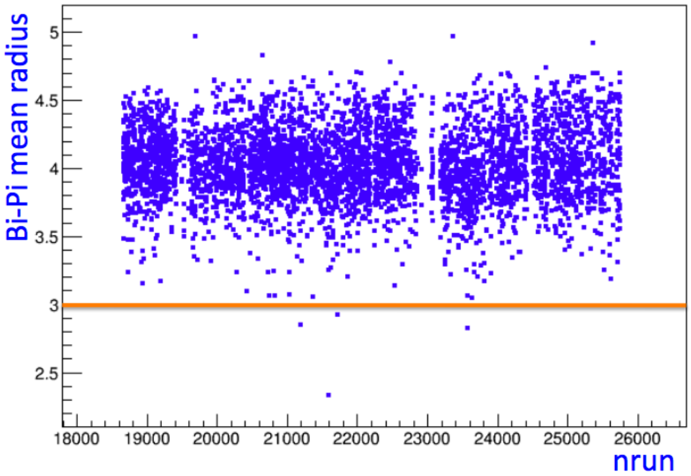

FIGURE 2.34: ^{214}Bi^{214}Po coincidences spatial distribution in the detector since July 2012, evidencing the lack of events inside the standard Fiducial Volume, while the concentration is much higher in the outskirts of the Inner Volume, and especially around the position of the vessel, which is obviously the major source of ^{222}Rn emanation despite all precautions.

Some γs coming from the ^{214}Po's excited states stemming from the progenitor bismuth decay also manage to leak inside the Inner Volume, producing a small but measurable signal referred to, together with other γs with a similar origin (mainly ^{208}Tl and ^{40}K, see dashed components in Figure 2.20), as **external background**.

2.4.9 Uranium-238 and daughters above ^{222}Rn

While secular equilibrium is held within the elements highlighted inside the dashed lines in Figure 2.32, progenitors of ^{222}Rn might not[16] necessarily be in secular equilibrium with their daughters. For the purposes of Borexino, it can be assumed –owing to all of these elements' long lifetimes– that their rates are similar. It is through these assumptions that the determination of an extremely radiopure $\sim<9\cdot10^{-20}$ g/g concentration is achieved through the Feld-Cousins method[117].

2.4.10 Thorium-232 and ^{212}Bi/Po

The only other heavy-element decay chain that has impacts on Borexino's energy region of interest, apart from the aforementioned ^{238}U, is ^{232}Th, since the contribution from the actinium chain (started with the (naturally abundant) 0.7% ^{232}U) is negligible considering the total uranium

[16] And, in fact, it has been estimated with an α fitter[94] that they are not, to within $\sim3\sigma$ compared to the ^{214}Bi^{214}Po coincidence rate.

contribution is ~1 cpd/100 tonnes; and the neptunium chain comprises elements with too short a half-life to occur naturally[17].

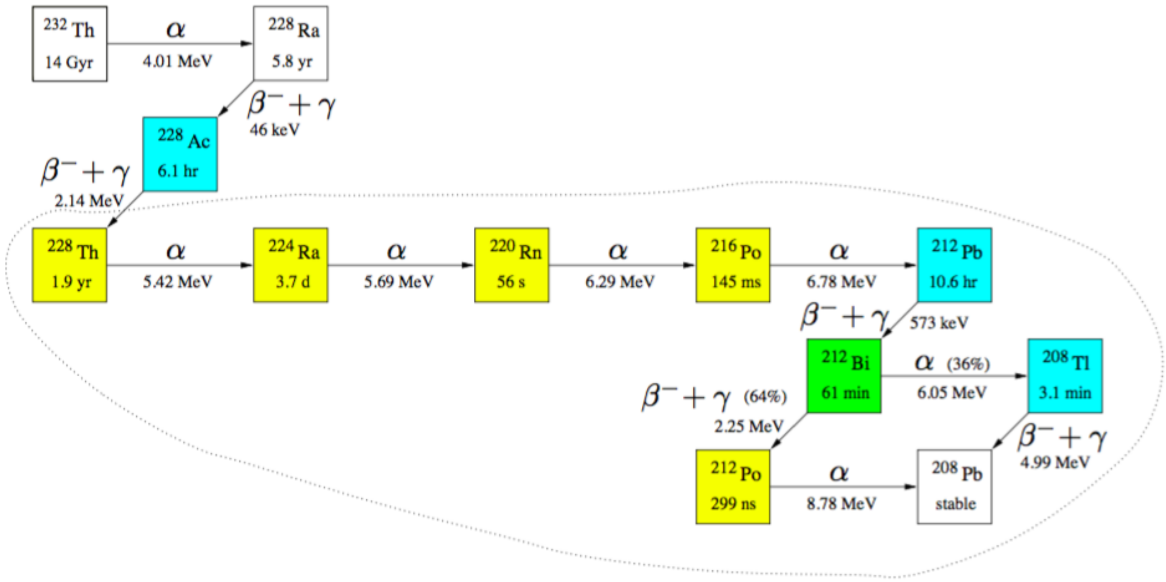

FIGURE 2.35: ^{232}Th decay chain diagram, from [94]. Contained within a dashed line are the elements likely to remain in mutual secular equilibrium and, as indicated by the accompanying indexes, α and β decays *within Borexino's fitting region* are color coded in yellow and blue, respectively (or green, when it's a mixture of both, as in ^{212}Bi).

This chain, that is started with the ~100%-naturally-abundant ^{232}Th, is quicker than ^{238}U's from ^{228}Th –ensuring all its daughters are in secular equilibrium with this isotope, unless some ^{220}Rn occurs. As with the uranium chain, another bismuth-polonium decay coincidence can be used to tag and estimate the thorium chain concentration: ^{212}Bi^{212}Po (^{212}Bi β: Q=2.25 MeV (b.r.=64%, see Figure 2.36); $\tau_{1/2}$=61min; ^{212}Po α: Q=8.78 MeV; $\tau_{1/2}$=300ms).

For both ^{238}U and ^{232}Th, only αs in their decay chains contribute in any significant way to the integrated rate in Borexino's spectrum –the β-decaying isotopes distribute their ionization energy over a wider swath of the spectrum and their low concentration makes the contribution negligible.

Since 2011, only 3 events were identified in the FV, thereby yielding a concentration of $<7.2{\cdot}10^{-19}$ g/g at 95% c.l. through the Feld-Cousins method [117].

[17] With the possible exception of ^{209}Bi, whose quenched Q=3.14 MeV α decay falls below threshold –and its importance is further reduced owing to its extremely long $\tau_{1/2}$=1.9$\cdot$10^{19}y, making it a *virtually stable* isotope.

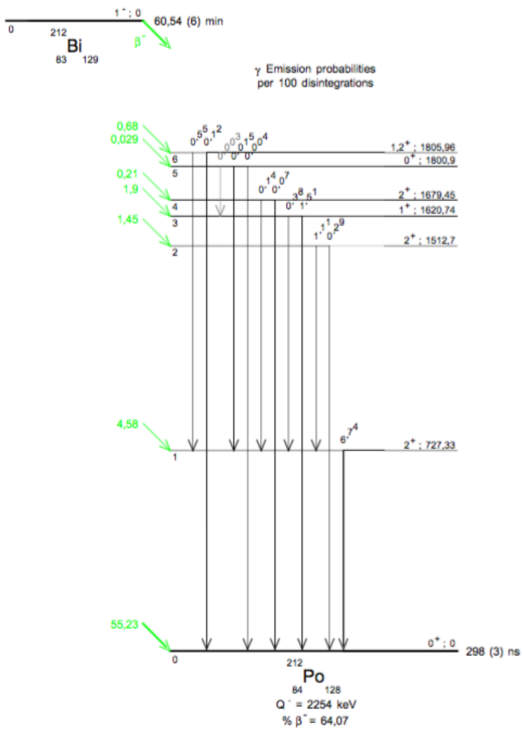

FIGURE 2.36: ^{212}Bi (64% b.r.) β decay scheme.

2.4.11 Thalium-208

Bismuth-212 also has an important branching ratio of 36% towards an α decay (Q=6.05 MeV, see Figure 2.37) that leads to the creation of ^{208}Tl, which has a short ($\sim$3 min) half-life ending in a β^- decay with many excited resulting states (see Figure 2.38). While the β Q value (5 MeV) leaves it beyond Borexino's sensitive range (and anyway the Tl concentration in the IV is very low being in secular equilibrium with the ^{212}Bi-^{212}Po-tagged elements in the ^{232}Th chain, see Figure 2.35), the long-travelling γs coming from the external volumes and leaking into the IV generate one of the greatest sources of external background –which is particularly important in the high-energy end of the spectrum, i.e. ^{8}B νs region[52].

2.4.12 Potassium-40

Relatively abundant (2.5%) in Earth's crust, potassium is a common element to find in small *dust* particulates. Although 99.998% of the natural abundance of potassium is its stable ^{39}K and ^{41}K, the remaining 0.012% is the long-lived ($\tau_{1/2}$=1.25$\cdot$10^9 y) but radioactive ^{40}K. It is a triply β-decaying isotope –meaning it undergoes both β^- (Q=1.33 MeV, b.r. $\sim$89.28%), β^+ (Q=1.5 MeV, b.r. $\sim$0.001%) and electron capture (Q=1.5 MeV, b.r. $\sim$10.72%) decays, the latter two toward ^{40}Ar and the first toward ^{40}Ca. The electron capture decay will leave the daughter ^{40}Ar in the excited state in 98% of the cases, which will relax in 1.6 ps emitting a 1.46 MeV γ.

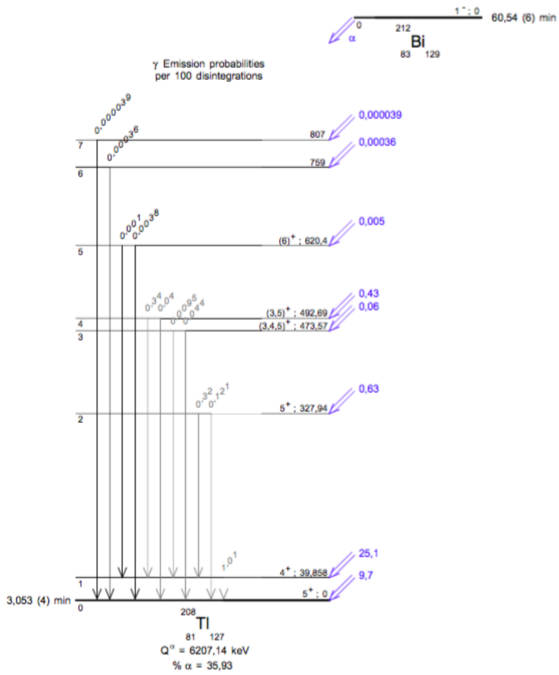

FIGURE 2.37: ^{212}Bi (36% b.r.) α decay scheme toward ^{208}Tl.

These decays fall squarely in the golden energy window for Borexino, and furthermore leaking γs from the SSS/PMTs (which are much more difficult to clean off from this isotope) can arrive in the IV as external background – therefore highlighting the dangerousness of this ubiquitous element. Extreme care was taken to filter it out through the distillation, purification and water extraction procedures. Furthermore, the flour PPO itself was found to have ppm levels of potassium, which would mean a level of background ∼6000x that of the expected ^{7}Be solar neutrinos[94]. This was reduced through water extraction of the scintillator solution, but no way exists to determine these efforts' actual effectiveness, except through the tagging of the ^{40}Ar*'s γ.

2.4.13 Argon-39

^{39}Ar is a pure β^{-}-decaying element (Q=565 keV, $\tau_{1/2}$=269 years), abundant in trace amounts naturally in the atmosphere due to cosmic ray interactions with the stable, 99.6%-abundant ^{40}Ar, causing it to lose a neutron and become radioactive. Although in principle very dangerous for the solar neutrino signal, since it offers a pure β signal indistinguishable from a neutrino scattering in the "golden window", with no delayed coincidences, accompanying γ rays or other discriminating characteristics –extreme measures were put in place to guarantee an extremely low concentration of this isotope. Primarily, Low Argon/Krypton Nitrogen (LAKN, 0.005 ppm by volume) stripping of the PC helped reduce the amount of these gases in the scintillator, and this was further ensured by the trace atmospheric concentration of ^{39}Ar. If these procedures were

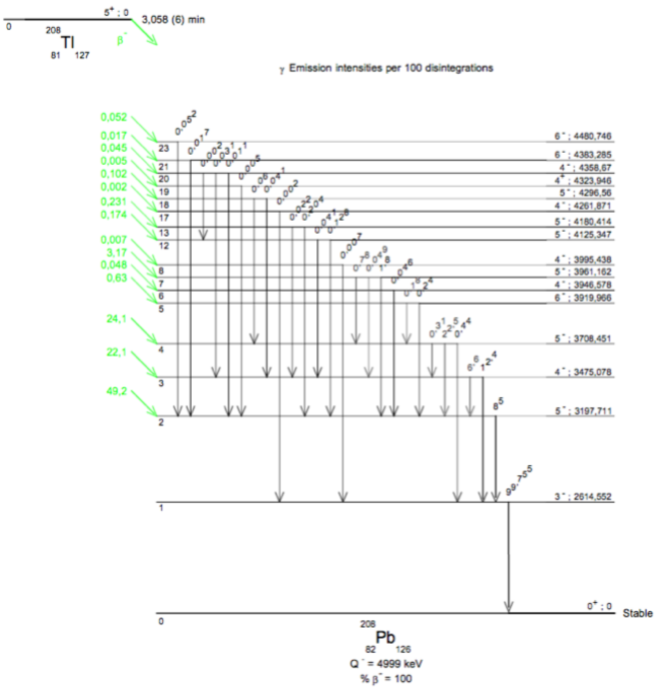

FIGURE 2.38: ^{208}Tl β decay scheme with de-excitation γ emission pattern.

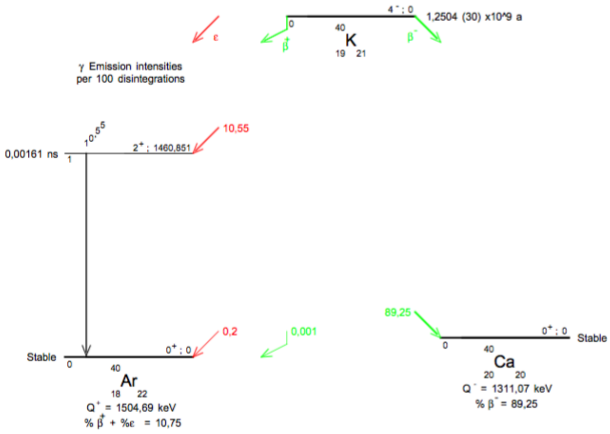

FIGURE 2.39: ^{40}K decay scheme.

perfectly efficient, a ∼0.02 cpd/100 tonnes rate due to it would be expected. Accidental air leaks, like the one presented in ^{85}Kr's Section 2.4.4, will have brought some amount of argon inside the detector. Using krypton as its "tracer", taking into account their respective atmospheric abundances, and considering all the ^{85}Kr background came from the same source through an air leak, ^{39}Ar would show a 20-fold increase from the ideal expectable concentration –which still leaves it at a negligible rate of ∼0.4 cpd/100 tonnes[94]. This, together with the MC modeling of the rate of external background (supposed to be larger than the internal) yields a method to expect a ^{40}K activity on the order of ∼1 cpd/100 tonnes, which still is kept as a free parameter in the relevant spectral fits.

2.4.14 Muons

Cosmic muons passing through Hall C (rest mass ∼105 MeV, $\overline{E}$ ∼320 GeV[92] with a surface spectrum determined by Equation 2.17 taking into account an idealized functional form of the primary cosmic ray spectrum), albeit with a much reduced flux with respect to the Earth's surface(∼1.2 $\mu/(\mathrm{m}^2{\cdot}\mathrm{h})$, around a million times smaller than at the surface) thanks to the Gran Sasso's overburden shielding the experiments within, they can still deposit hundreds of MeV of ionizing energy inside Borexino when entering it. In particular, they can cause a continuous ionization track along their path, or they can cause discrete radiative processes (i.e. pair production, bremsstrahlung and hadronization) from E∼>500 GeV.

$$\frac{dN_0}{dE_0}(E_0, \cos\theta) \sim 0.14 \cdot E_0^{-(\gamma+1)} \cdot [\frac{1}{1 + \frac{1.1 E_0 \cos\theta}{115\ GeV} + \frac{0.054}{1 + \frac{1.1 E_0 \cos\theta}{850\ GeV}}}] \tag{2.17}$$

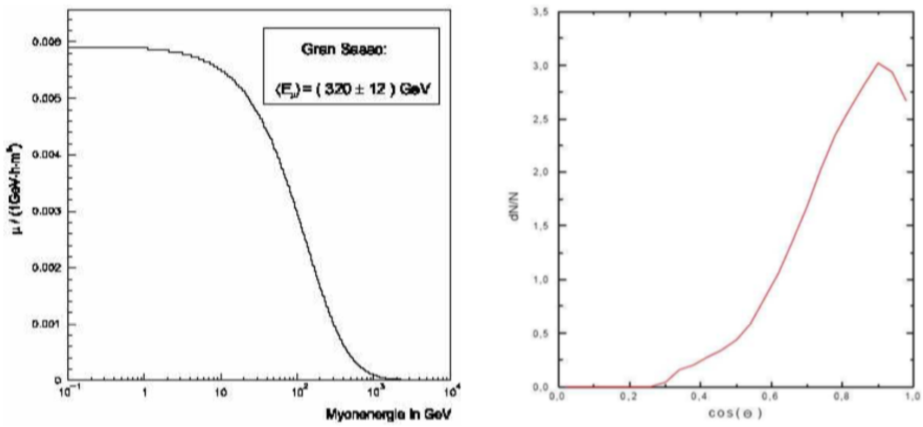

Figure 2.40: Muon energy spectrum (left) and angular distribution (right) of the flux passing through the LNGS facilities, as measured by the MACRO experiment[123].

Around 1-2%[92] of passing μs stop in Borexino. The ones that pass all the way through the IV saturate the PMT response and can be filtered out easily. On the other hand, the ones that *don't* pass through the scintillating volume but through the buffer volume alone, can only be distinguished by the Čerenkov signal, ∼50x weaker than a scintillation one and therefore potentially within the golden window.

Fortunately though, Borexino has a >99.99% efficiency in muon tagging thanks to its 3 independent muon tagging strategies with ∼95% efficiency each: concentrator-less PMTs with higher angle of acceptance mounted in the SSS, which have a higher chance of capturing the Čerenkov light in the buffer; larger photon arrival time spread due to the light being emitted along a track rather than at a point-like location (see Figure2.41 for an idealized muon pulse shape profile), as well as the larger ionization intensity they deposit in the upper (vs lower) regions of the detector since μs are mostly coming from above; and finally the Outer Detector that detects the muons that don't enter the Inner Detector as well as the external part of the track for those which do.

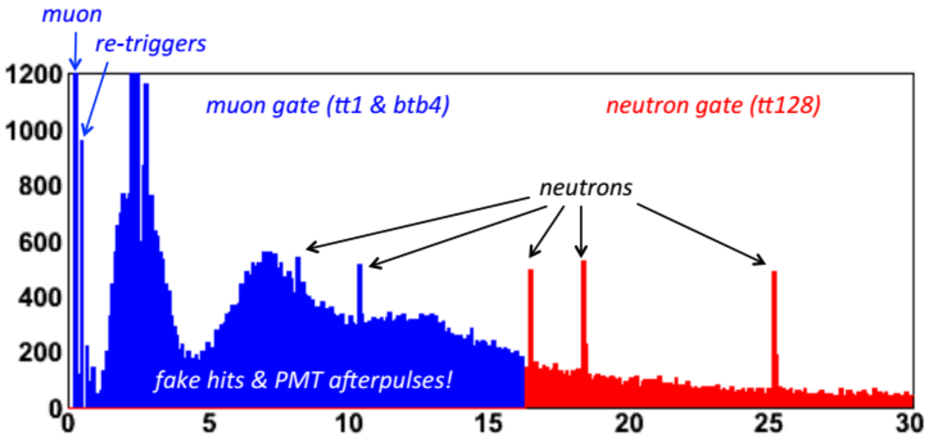

FIGURE 2.41: Muon idealized pulse shape profile, highlighting the characteristics of a muon pulse including triggering spallation neutrons that generate cosmogenics. Figure from [124].

Overall, it is estimated muons contribute to a background of ∼0.01 cpd/100 tonnes after these measures are taken and data selection cuts filter out some remaining rate.

2.4.15 Cosmogenics

Muons not only present a background source by themselves as explained in the preceding subsection, but also through their radiogenic effect: they may create radioactive elements through their passage, such as the aforementioned ^{11}C (see Subsection 2.4.6). However, many other elements may be created from the muonic spallation of carbon nuclei (see Table 2.2) –most of which have very short half-lives that enable their contribution to the background to be avoided by imposing a temporal (and sometimes spatio-temporal) veto around a muon track event. Only the longest lived ^{11}C, ^{10}C and ^{7}Be isotopes contribute a non-negligible rate to the background for solar neutrinos, although specific provisions need to be taken for other analysis-specific purposes (see, for example, the geoneutrino study in Section 2.5.2). Cosmogenic ^{7}Be levels can be reduced to some extent (at least a factor of 1000 from initial scintillator content[125]) by scintillator purifications through distillation, in spite of its very low concentration, since it forms organometallic compounds[125].

Isotope	τ (Mean)	**Energy [MeV]**	**Production rate [cpd/100 tonnes]**
^{12}N	15.9 ms	17.3 (β^+)	0.058±0.013
^{12}B	29.1 ms	13.4 (β^-)	1.41±0.04
^{8}He	171.7 ms	10.7 ($\beta^-\gamma n$)	0.026±0.012
^{9}C	182.5 ms	16.5 (β^+)	0.096±0.031
^{9}Li	257.2 ms	13.6 ($\beta^-\gamma n$)	0.071±0.005
^{8}B	1.11 s	18.0 ($\beta^+\alpha$)	0.273±0.062
^{6}He	1.16 s	3.51 (β^-)	0.395±0.027
^{8}Li	1.21 s	16.0 ($\beta^-\alpha$)	0.40±0.07
^{11}Be	19.9 s	11.5 (β^-)	0.035±0.006
^{10}C	27.8 s	3.65 ($\beta^+\gamma$)	0.54±0.04
^{11}C	29.4 min	1.98 (β^+)	27.65±4.45
^{7}Be	76.9 d	0.478 (EC γ)	3.35±0.22

Table 2.2: Cosmogenic isotopes produced in Borexino by muon passages, computed by a combination of FLUKA calculations and extrapolated measurements of the KamLAND Collaboration, adapted from [94].

2.4.16 Dark noise

Dark noise, though intrinsically linked to PMT operation and impossible to distinguish on an event-by-event basis, can be estimated statistically. It provides an positive offset on the energy spectrum scale, and some contribution to the pile-up as mentioned. It presents a rate of 550 kHz and accounts for an extra hit per event, which is substracted away.

2.5 Borexino results and current programs

Borexino has so far been able to fulfill its design requirement of a precision measurement of the ^{7}Be solar neutrino flux, as well as to observe most of the remaining solar neutrino fluxes with varying levels of ever-increasing precision, including the current best limit for CNO νs. Ongoing accumulation of high-quality statistics with improving background conditions (especially after the purifications before the start of the Phase II DAq period), in addition to the enhancement of analysis techniques and data selection, means a continuous improvement in the precision for the existing measurements, in some cases to very significant levels. An ongoing re-evaluation of the full statistics in order to enable a complete spectroscopy of the solar neutrino spectrum is also in the late stages of development as part of the *NuSol* project.

Additionally, the Collaboration has explored other applications apart from solar neutrino spectroscopy, especially capitalizing on the fact the detector is virtually background-free for $\overline{\nu}$ detection through the Inverse Beta Decay (IBD) coincidence signal. The geo-neutrino results are its prime result on this channel, and extra attention to the latest reanalysis will be devoted in

	Source	Typical	**Required reduction factor**	Limitation strategy (hardware)	Limitation strategy (software)	Phase I	**Phase II**
μs	Cosmic	$\sim$200 $s^{-1}m^{-2}$ (sea level surface)	$> 5{\cdot}10^{-13}$	Underground location and water veto	Veto, Čerenkov Pulse Shape analysis	$<10^{-10}$ (99.92% eff)	same
Ext. γs	rock, PMTs, SSS	-	-	Water veto and Buffers	Fiducialization	Negligible	Negligible
^{14}C	PC	$\sim 10^{-12}$ g/g	10^{-6}	Hydrocarbon selection	Energy threshold	$\sim 2{\cdot}10^{-18}$ g/g	same
^{238}U	Dust and metals	10^{-12} g/g of scintillator (10^{-6} g/g of dust)	$>10^{-4}$	Distillation, water extraction, filtration, material selection, cleanliness strategies	Tagging, α/β	$1.6{\pm}0.1{\cdot}10^{-17}$ g/g	$< 9{\cdot}10^{-20}$ g/g
^{232}Th	"	"	"	"	"	$5.1{\pm}1{\cdot}10^{-18}$ g/g	$< 7{\cdot}10^{-19}$ g/g
^{7}Be	Cosmogenic	$\sim 3{\cdot}10^{-2}$ Bq/-ton	$> 3{\cdot}10^{-5}$	Distillation	-	Not seen	Not seen
^{40}K	Dust and in PPO	$\sim 2{\cdot}10^{-6}$ g/g	$> 5{\cdot}10^{-13}$	Distillation and water extraction	-	Not seen	Not seen
^{210}Po	Surface contamination from ^{222}Rn	-	<1 cpd/-ton	Distillation, water extraction, purification, filtration, cleanliness, temperature control	Fit and α/β	**2007: 70 cpd/ton; 2010: $\sim$1 cpd/ton**	<1 cpd/-ton
^{210}Bi	"	$2{\cdot}10^{7}$ cpd/100t (unpurified scintillator)	$\sim 10^{-7}$	Water extraction, temperature control	Fit	**10-50 cpd/100 tonnes**	**$\sim$25 cpd/100 tonnes**
^{222}Rn	Emanation from materials and rock	$\sim$10 Bq/l in air and water; $\sim$100-1000 Bq/g rock	$>10^{-10}$	N_2 stripping and cleanliness	Tagging, α/β	<1 cpd/100 tonnes	<0.1 cpd/100 tonnes
^{39}Ar	Air, cosmogenic	17 mBq/m^3 in air	$> 5{\cdot}10^{-9}$	N_2 stripping	Fit	$<<^{85}$Kr	same
^{85}Kr	Air, technogenic	$\sim$1 Bq/m^3 in air	$> 10^{-7}$	N_2 stripping	Fit	**30±5 cpd/100 tonnes** ($\sim$30x too much)	<7 cpd/100 tonnes

Table 2.3: Concentration limits for the main backgrounds in Borexino, and achieved results summary table, adapted from [126]. Worrisome –past or present– concentrations are highlighted in boldface.

Subsection 2.5.2 since this author has collaborated in a significant way on this topic for part of this thesis' work. Other relevant results not involved with solar or geo-neutrinos are briefly summarized in Subsection 2.5.3.

The antineutrino signal will also be exploited extensively in the near future, to study possible anomalous oscillatory behaviors in an artificially-generated $\overline{\nu}$ signal coming from a high-activity ^{144}Ce-^{144}Pr source as part of the CeSOX project. If the achieved cerium results (and funding) warrant it, a ν ^{51}Cr source could also be used to generate a cleaner and easier-to-interpret signal –a significant contribution to this CrSOX project is discussed in Chapter 6.

2.5.1 Solar neutrino results

The main design goal for Borexino was the improvement of the precision (until then worse than $\sim$>20%) in the determination of the ^{7}Be solar neutrino flux. Of course, other objectives in solar neutrino spectroscopy around the same *golden* energy window were also hoped for –although the actual achieved results surpassed those initial expectations thanks to the unprecedented levels of radiopurity reached during construction, further improved after the outstanding results from the calibrations and purification campaigns in 2009-12. As of this writing, all solar neutrino components visible to Borexino have been observed –and the precision for these measurements has, or is in the process of being, improved from the first observation– except for the CNO signal, part of whose detection efforts are the main topic of this dissertation, for which the best current upper limit has nevertheless been determined. The extremely feeble *hep* signal is almost out of Borexino's sensitivity, but a recent analysis[127] has provided a reasonable upper limit on its flux, only to within a factor of two from the best available one. These measurements also contributed to the definitive backing of the MSW-LMA solution as the correct parameter space for the matter effect.

pp neutrinos In 2014, the Collaboration succeeded in disentangling the major component of the integrated solar neutrino flux from the irreducible and inherent ^{14}C background in Borexino's scintillator by measuring the rate of *pp* neutrinos with a $\sim$15% precision (9% statistical) as ϕ_{pp}=(6.37$\pm$0.46)$\cdot 10^{10}$ cm^{-2}s^{-1} (rate in Borexino: 144$\pm$13(stat)$\pm$10(sys) cpd/100 tonnes)[42][128]. This first-ever direct measurement required a lowering of the energy threshold to no longer avoid the high-rate low-energy area, as well as the development of several new techniques (no β-like selection criteria, ^{14}C rate determination through a threshold-less data selection approach after the trigger, and the two independent evaluations of pile-up effects –^{14}C with itself, ^{14}C-^{210}Po and ^{210}Po with itself– through the generation of *synthetic pile-up* from real data, and the use of a probability density function (PDF) to model the convolution of a randomly-sampled signal with a given spectral component) to enable the background to be subtracted in order to unveil the *pp* signal.

pep neutrinos In 2011, the first direct detection of *pep* neutrinos was achieved by the Collaboration with a $\sim$29% precision (20% statistical) as ϕ_{pep}=(1.6$\pm$0.3)$\cdot 10^8$ cm^{-2}s^{-1} (3.1$\pm$0.6(stat)$\pm$0.3(sys) cpd/100 tonnes rate in Borexino)[49]. In parallel, this measurement also set the strongest available limit on CNO neutrinos at $<$7.7$\cdot 10^8$ cm^{-2}s^{-1} at 95% c.l., since an integrated neutrino signal between 1.0 and 1.5 MeV was measured for this result. The ^{11}C background subtraction was the main challenge, that was tackled through the orthopositronium tagging (see Section 2.4.6) and Three-Fold Coincidence (TFC) techniques, in conjunction with a detailed external γ background MonteCarlo modelization.

^{7}Be neutrinos The flagship Borexino result, this was also the first direct detection of this particular solar neutrino spectral component. The most recent published result[51] has a $\sim$5% precision for an MSW-LMA flux of (3.10$\pm$0.15)$\cdot 10^9$ cm^{-2}s^{-1} (Borexino rate: 46.0$\pm$1.5(stat)$\pm$1.5(sys) cpd/100 tonnes). The 2009-10 calibration campaign was key in understanding the detector's response –especially with regard to the energy response– and enabling an accurate MonteCarlo fit of the background components. Pulse-shape discrimination for an $\alpha-\beta$ cut implementation and posterior statistical subtraction of the α-like ~1000 cpd/100 tonnes ^{210}Po background over the beryllium shoulder was also of paramount importance, through the use of a Gatti parameter-based technique.

^{8}B neutrinos Borexino's direct observation of the ^{8}B solar neutrino flux represents the lowest-threshold (3 MeV) measurement available for this spectral component, at a precision of ~20% in the Phase I-only latest published result ($\phi_{^8B}$=2.4±0.4(stat)±0.1(sys)$\cdot 10^6$ for a Borexino rate of 0.217±0.038(stat)±0.008(sys) cpd/100 tonnes[52]). This result also highlighted the downturn in rate due to the solar MSW effect in the transition region. Cosmogenic and external background modelization were the main challenges tackled during this analysis.

The ^{7}Be signal was also used for the seasonal modulation study[38] and the verification of the LMA prediction for the lack of diurnal/nocturnal asymmetry[44] in the solar neutrino flux reaching a detector on the surface of Earth ($A_{d-n} = 0.001 \pm 0.012$(stat) $\pm$ 0.007(sys) cm^{-2}s^{-1}).

2.5.2 Geoneutrino results

The Inverse Beta Decay (IBD) reaction $\overline{\nu_e} + p^+ \rightarrow n^0 + e^+$ is Borexino's main channel to detect antineutrino signals. It has a threshold of 1.806 MeV for the antineutrino energy, and therefore rules out very low energy measurements (mainly coming from ^{40}K). However, its coincidence signal in the detector's scintillator (**prompt** signal from the two back-to-back 511 keV γs resulting from the positron annihilation with an electron typically nearby the interaction point; and **delayed** signal from the 2.2 MeV γ resulting from the neutron capture on one of the abundant hydrogen atoms after thermalization within a mean lifetime of 259.7±1.3(stat)±2.0(sys) μs) is easily translatable to $\overline{\nu}$ energy ($E_{visible} = E_{\overline{\nu}_e} - 0.784MeV$) and affected by very few backgrounds. This visible energy range for Borexino allows for a small part of the ^{238}U (6.3%) and ^{232}Th (3.8%) antineutrinos to be detected, since they are the only geologically-abundant enough isotopes to yield a measurable fraction of $\overline{\nu}$ over the IBD threshold. The survival probability for antineutrinos is given by Equation 2.18, and for our purposes is averaged to ~0.54 for vacuum oscillations and ~0.55 for matter effects.

$$P_{ee} = \cos^4\theta_{13}\Big(1 - \sin^2 2\theta_{12}\sin^2\Big(\frac{\delta m^2 L}{4E}\Big)\Big) + \sin^4\theta_{13} \tag{2.18}$$

In particular, the main background identified is the reactor antineutrinos, which are nevertheless well-understood thanks to the International Atomic Energy Agency (IAEA)'s Power Reactor Information System (PRIS) that identifies the 435 known man-made reactor cores in operation.

These are fitted away according to the reported load factors, the method in [129] and a Monte-Carlo spectrum[130], with a $\sim$4% precision. In Figure 2.42, a Earth map projection shows the worldwide flux map for antineutrinos, combining results from PRIS, Borexino and KamLAND. Other secondary backgrounds for $\overline{\nu}$s in Borexino are shown in Table 2.4.

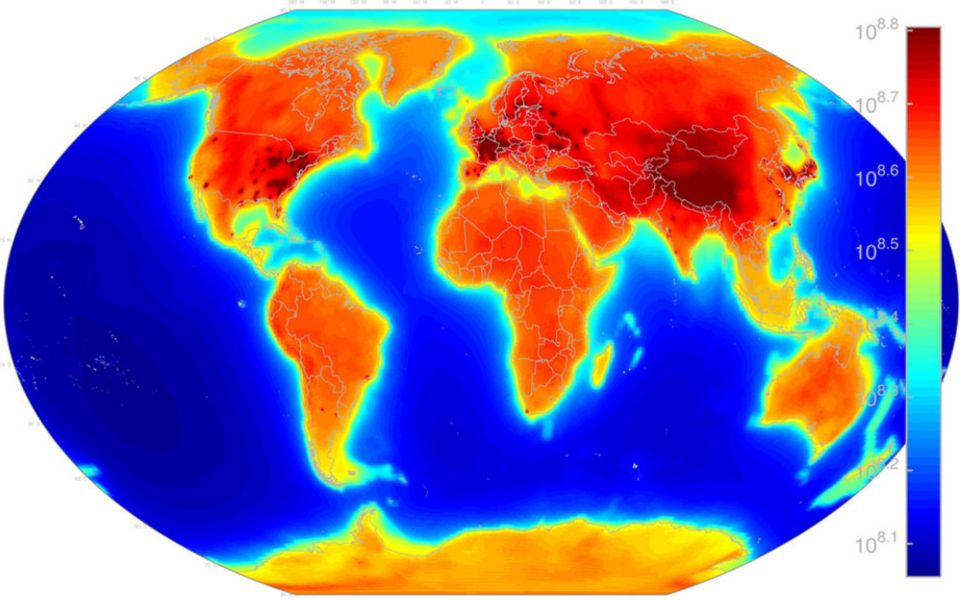

FIGURE 2.42: Global map of $\overline{\nu_e}$ fluxes from ^{238}U and ^{232}Th, as well as nuclear reactors, on the surface of the planet, in units of cm^{-2}s^{-1}, from [131].

Background	Rate (events)
^{8}Li-^{8}He	$0.194^{+0.125}_{-0.089}$
Accidental coincidences	0.221$\pm$0.004
Time correlated coincidences	$0.035^{+0.029}_{-0.028}$
(α,n) in scintillator	0.165$\pm$0.010
(α,n) in buffer	<0.51
Fast n^{0}s from μs in rock	<0.43
Fast n^{0}s from μs in WT	<0.01
Untagged μs	0.12$\pm$0.01
Fission in PMTs	0.032$\pm$0.003
^{214}Bi-^{214}Po	0.009$\pm$0.013
Total	$0.78^{+0.13}_{-0.10}$

TABLE 2.4: List of the identified $\overline{\nu}$ backgrounds in Borexino and their estimated rates (limits are 90% c.l.)[132].

Data were selected from a livetime of 2055.9 days (before any selection cuts) since December 15th, 2007 to March 8th, 2015. The PMT distribution for each run changed non-homogeneously with time, so energy is calibrated non-linearly as a function of detected photoelectrons. A scaling of 3.5% on the MC charge variable was used given the improved *g4bx2* MC code showing an overestimation of the charge compared to calibration data –this was introduced as a systematic uncertainty. The following selection cuts were applied. which were determined through a MonteCarlo study to have a (84.2±1.5)% efficiency:

1. Cosmogenic reduction (n^0s, long-lived cosmogenic isotopes) by discarding events occurring within 2 ms of every μ crossing the OD and within 2 s of every μ crossing the ID. Lifetime reduced to 1841.9 days.
2. Recorded charge (p.e.) lower limit for the prompt signal: Q_p >408 p.e. (equivalent to 1.022 MeV, that is, the integrated energy for the two annihilation γs).
3. Recorded charge (p.e.) lower and upper limits for the delayed signal: 860< Q_d <1300 p.e. (for the neutron capture peak).
4. Distance upper limit between the prompt and delayed signals of ΔR <1 m.
5. Time interval lower and upper limit between the prompt and delayed signals of 20< Δt <1280 μs.
6. Gatti parameter slight upper limit for $\alpha - \beta$ PSD: $g_{\alpha\beta}$ <0.015 for delayed signals.
7. Multiplicity cut to ensure a selected event is neither preceded nor followed by n^0-like events in a 2 ms window.
8. Dynamical fiducial volume[100] lower limit for a prompt event at least 30 cm inside of the reconstructed IV for that run's time period.
9. FADC independent analysis of candidate events.

Most of these items were automatically implemented in a user-friendly way –previous analysis[133][130] had used a more manual approach– in the `bx_antinu` filter tool, along with the option of varying these limits' values online to study their influence in the final result. The reported values are a stable tradeoff between maximizing statistics and minimizing background contributions. Points 7 and 9 represent new cuts compared to previous analyses, and the DFV cut was moved inward by 5 cm from the previous analysis to reduce backgrounds at the cost of a very small reduction in statistics (see Figure 2.43). An average of 4.8% uncertainty in exposure (based on vessel shape determination) is used, given the maximum possible deviation in the periods of greatest vessel deformation and possible greatest ϕ asymmetry. The efficiency-corrected exposure after all cuts is 907±44 tonnes·year (or (5.5±0.3)·10^{31} p·y). Seventy-seven candidate coincidences were found following this method, following three independent analysis tools –one of them, the aforementioned `bx_antinu`, implemented by the author.

Backgrounds in Table 2.4 were then evaluated using the same dataset and tools:

nrun	Dist_IV (cm)	FV Cut	31 cm	29 cm	27 cm	25 cm	23 cm	21 cm	19 cm
7248	0.301	EvNum	7248	7248	7248	7248	7248	7248	7248
8067	0.217			18924	18924	18924	9048	8067	8067
9048	0.247				21462	21462	18924	9048	9048
9761	0.203						21462	10256	9761
10256	0.214							11264	10256
11264	0.224							12390	11264
12390	0.226							18924	12390
18924	0.277							21462	18924
21462	0.257								21462
			1	2	3	3	4	8	9
		Total	77	78	79	79	80	84	85

FIGURE 2.43: Table showing the difference in candidate events considering different DFV distances.

1. ^{8}Li-^{8}He cosmogenics that decay via $\beta - n$ (wide visible energy spectrum with $\sim$5 MeV endpoint) were studied in the [2ms,2s] window after an ID-crossing μ, and 175 such coincidences remain in the whole time window after a muon. Their decay time was fitted to be τ=0.294$\pm$0.022 s (with no DFV cut for this fit, and with a 25-cm cut for consistency, see Figure 2.44) and therefore, 99.21% of all these cosmogenics are present in the selected [2ms, 2s] time interval. Considering that, in the [2s, inf) time interval lies $e^{-2/0.294}$=0.11% of the total background, the expected events in the golden $\overline{\nu_e}$ sample is the 0.194 events reported in Table 2.4.

2. Accidental coincidences were studied in the [2,20]s time window and were determined to be 3153 after all cuts were applied (3588 before the multiplicity cut) as shown in Figure 2.45 for a 25-cm DFV cut, which extrapolating to the time window of interest would yield 0.221$\pm$0.004 events.

3. Coincidences were also studied in a [2ms, 2s] time window to check for background excesses with respect to what would be expectable from an extrapolation of the aforementioned accidental background. A very marginally statistically-significant (26$\pm$20 events) excess was found with a fitted decay time of 1.124$\pm$0.239 s (see Figure 2.46) that would scale into the region of interest to the reported 0.035$\pm$0.028(stat)$^{+0.006}_{-0.004}$(sys) events.

4. The $(\alpha - n)$ background is determined by the ^{210}Po rate in the scintillator, which was monitored independently from this study (see Chapter 3). Extrapolating to the time window of interest we get the reported rate. The upper limit in the buffer is reconstructed from the `g4bx2` MonteCarlo.

5. The rest of the backgrounds were scaled from [130] for the new exposure, since their contributions are expected to be unchanged and/or very small.

After the backgrounds were constrained, an unbinned likelihood fit of the energy spectrum of the prompt $\overline{\nu}$ selected candidates was performed (see Figure 2.47). Two signal components (S_{geo} and S_{reac}) are left free and three background components (S_{LiHe}, $S_{\alpha n}$ and S_{acc}) are constrained

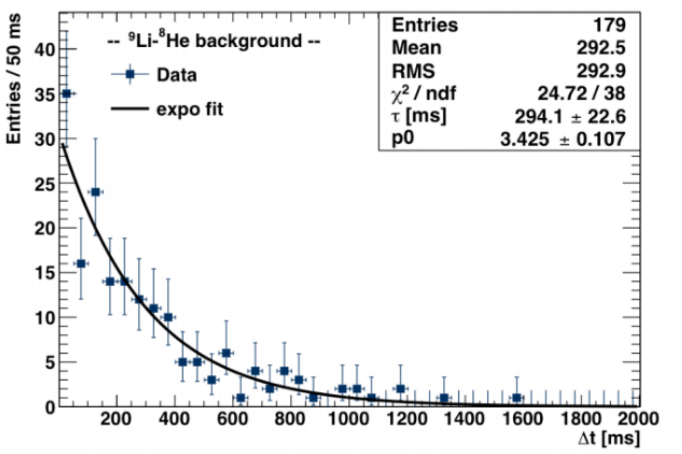

FIGURE 2.44: ^{8}Li-^{8}He fitted decay curve in event sample between 2ms and 2s with a 25-cm DFV cut.

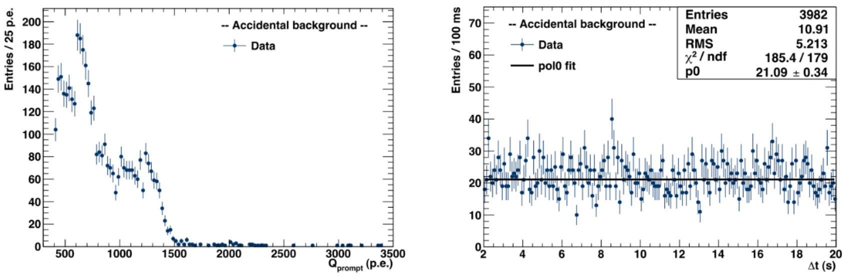

FIGURE 2.45: Accidental coincidences charge spectrum and delay time distribution for a 25-cm DFV cut.

to the reported values and 1σ deviations. The other components, owing to their small rate and uncertainty in energy spectrum, were left out as their uncertainty is absorbed in the systematics for the energy scale.

It is customary to express this type of results in Terrestrial Neutrino Units (TNU; 1 event/(year·10^{32} protons).). Thefore, the countrates for the best fit of the measured events are:

$$N_{geo} = 23.70^{+6.5}_{-5.7}(stat)^{+0.9}_{-0.6}(sys) \text{ ev} \leftrightarrow S_{geo} = 43.5^{+11.8}_{-10.4}(stat)^{+2.7}_{-2.4}(sys) \text{ TNU} \tag{2.19}$$

$$N_{reac} = 52.71^{+8.5}_{-7.7}(stat)^{+0.7}_{-0.9}(sys) \text{ ev} \leftrightarrow S_{reac} = 96.6^{+15.6}_{-14.2}(stat)^{+4.9}_{-5.0}(sys) \text{ TNU} \tag{2.20}$$

This corresponds to a uranium/thorium chain $\overline{\nu_e}$ fluxes at the detector of $\phi(^{238}U)$=(2.7±0.7)·10^6 cm^{-2}s^{-1} and $\phi(^{232}Th)$=(2.3±0.6)·10^6 cm^{-2}s^{-1}. The null hypothesis is discouraged with a probability of 3.6·10^{-9} (5.9σ) with this data. With a larger exposure, Borexino could disentangle the U/Th components (see Figure 2.48) and discriminate between different Earth models. The radiogenic heat production from Earth's uranium and thorium is then measured to be P_{rad}(U+Th)=28^{+23}_{-17} TW, for a global measured terrestrial output power of P_{tot}=47±2 TW. Of

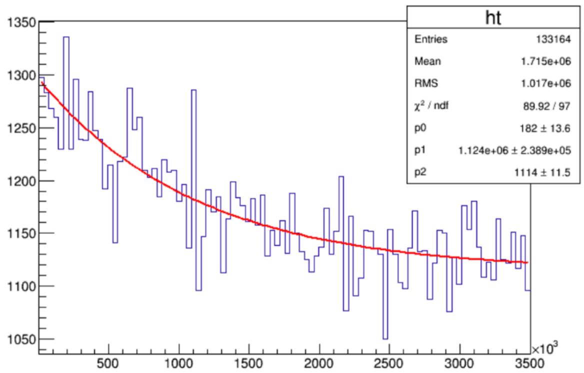

FIGURE 2.46: Fitted correlated background excess for a non-spatially-correlated (no ΔR cut and no DFV cut) sample of events in the correlated background window. X axis is Δt in μs and Y axis is the number of events.

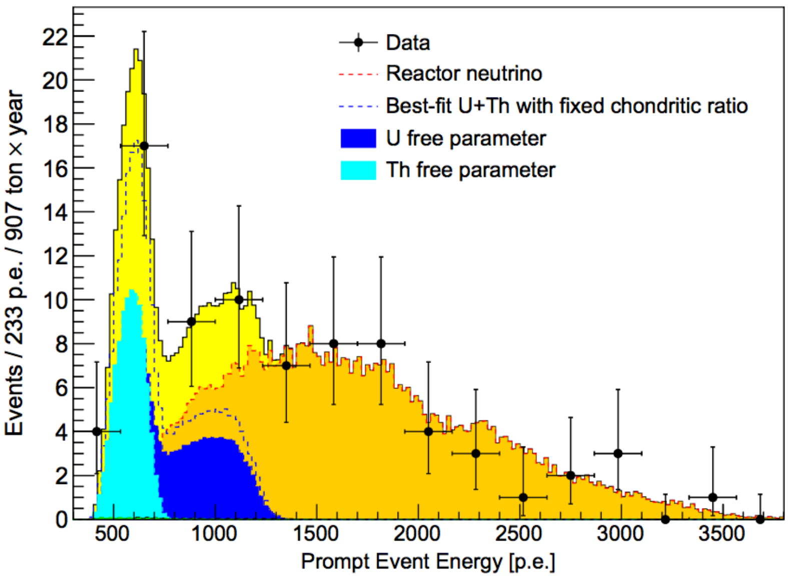

FIGURE 2.47: Observation (black points with error bars) of reactor and geoneutrinos at 5.9σ with 2056 days of data compared to a MonteCarlo-generated spectrum (color-filled histograms; blue hues = geoneutrinos and orange hues = reactor neutrinos). 77 total candidates were identified, with the cuts described further in the text, yielding a geoneutrino sample of $23.7^{+6.5}_{-5.7}$(stat)$^{+0.9}_{-0.6}$(sys) events (~27% precision).

fundamental importance to understand far-reaching geological questions such as plate tectonics dynamics, mantle convection and the geodynamo mechanics, the understanding of the Earth's energy budget is advanced with this measurement, by providing a slight disfavoring of the cosmo-chemical Bulk Silicate Earth models with P(K+Th+U)=11±2 TW (and a consistent agreement with the geochemical (P(K+Th+U)=20±4 TW) and geodynamical (P(K+Th+U)=33±3 TW) models, since the radiogenic heat released by decays from ^{40}K and Th/U chains are in a well-fixed ratio and each model presents a particular K/U ratio). Finally, a null mantle contribution to the signal is rejected at 98% c.l. and is estimated to be $S_{geo}(mantle) = 20.9^{+15.1}_{-10.3}$ TNU.

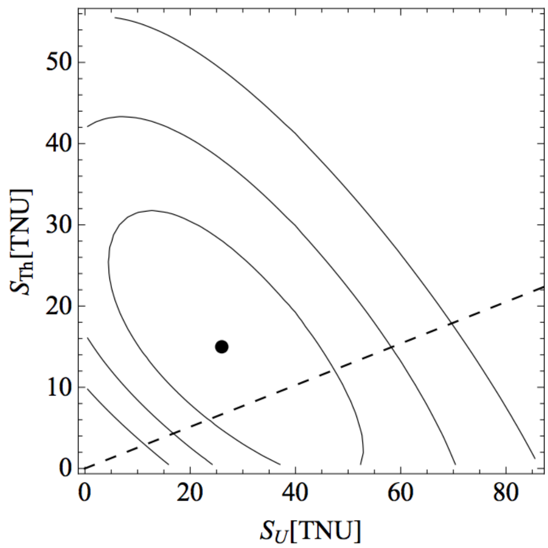

FIGURE 2.48: 1, 2 and 3σ best-fit contours for the reported statistics with the uranium and thorium contributions as free distinct parameters (dashed line is the chondritic assumption of Th/U = 3.9).

A full write-up of the latest update for this Borexino result can be found in [132] and previous, lower statistics results in [133] [130].

2.5.3 Miscellaneous results

Other significant results by the Collaboration include the study of **Gamma-Ray Burst (GRB)-correlated** neutrino bursts[134]; of **rare processes** such as Pauli-forbidden transitions in ^{12}C with data selection between 1-14 MeV[135]; of solar or other **unknown $\overline{\nu}$ fluxes**[136]; of the **seasonal modulation of the μ flux**[137]; for **5.5 MeV solar axions** yielding 2-4x better limits than previous searches through the analysis of a possible $p(d,^3He)A$ reaction in the high-energy end of the Borexino spectrum[138]; the test of the **conservation of electric charge** through a dedicated search for the hypothetical electron decay's ($e \rightarrow \nu_e + \gamma$) 256 keV γs in the low-energy region of the Borexino spectrum to yield a world-best limit of $\tau \geq 6.6 \cdot 10^{28}$ years[139]; the **search for heavy ν_s ($m_{\nu_s^H} > 2m_e$) produced in the Sun** decaying –pair-producing– in the 4.8-12.8 MeV area of the Borexino spectrum[140] yielding a ∼1000 times better limit than previous searches in the same energy range; and the measurement of the propagation speed of a ν_μ flux coming from the CNGS beam[141].

Part II

Calibrating and understanding Borexino's thermal behavior as a way toward a unified solar ν spectrum and CNO observations

Chapter 3

Background stability and the Borexino Thermal Monitoring and Management System

3.1 Data selection for ^{210}Po identification, concentration determination and tracking

Since the start of data-taking, the relatively low levels of ^{210}Bi present in the fiducial volume (FV) of Borexino rapidly increased until around 75 cpd/100 tons (current levels are ~25 cpd/100 tons), which was attributed to the turning on of the water loop in the water tank to remove the haze in the scintillator in late 2007[94]. It is hypothesized desorption of ^{210}Pb from the vessel's nylon into the Inner Volume's scintillator may have caused this increase, but several other explanations have been proposed.

Whatever the cause, ^{210}Po has been out of equilibrium since the start of data taking, with an initial rate $\sim$ 800 times higher than that of bismuth. While ^{210}Po is relatively straightforward to tag out using $\alpha - \beta$ Pulse-Shape Discrimination (PSD), it is a very useful handle for the ^{210}Bi levels, since it is this element's direct daughter, and its β decay make it indistinguishable from neutrino signals. Hence, once "legacy" polonium from construction and wash-off decays away, it will leave a plateau corresponding to the Inner Volume's intrinsic, equilibrium levels. This, in turn, would allow a much more precise measurement of the ^{210}Bi levels, necessary for further improvement of solar neutrino flux measurements in the so-called *bismuth valley* (see more about this isotope's role in Borexino in Chapter 2).

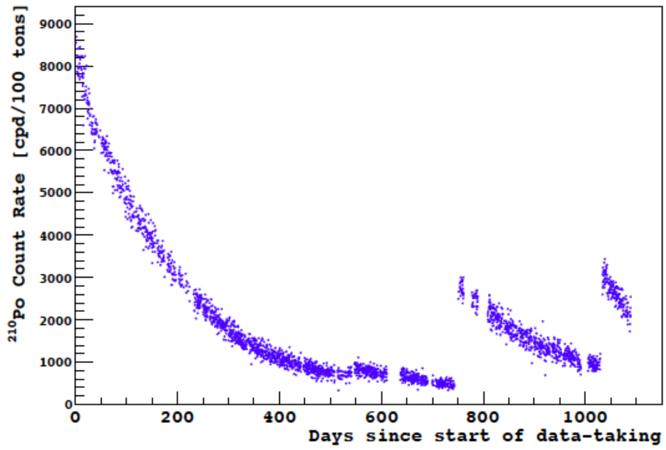

FIGURE 3.1: Historical ^{210}Po trend (May 2007 - April 2010) [94]

Of course, if these levels were to be stable, they could be subtracted from the constant CNO neutrino flux. Unfortunately, it has been determined that, even though the out-of-equilibrium ^{210}Po has all but decayed away, the combined bismuth+polonium levels have been oscillating in a non-predictable fashion (see Figure 3.3). Time-profiling this combined rate with simulated decay profiles has been attempted[142], as well as fitting the bismuth spectra during different periods, or accounting for ^{210}Po external sources[143] – but the low statistics and unpredictable fluctuations have hindered these efforts.

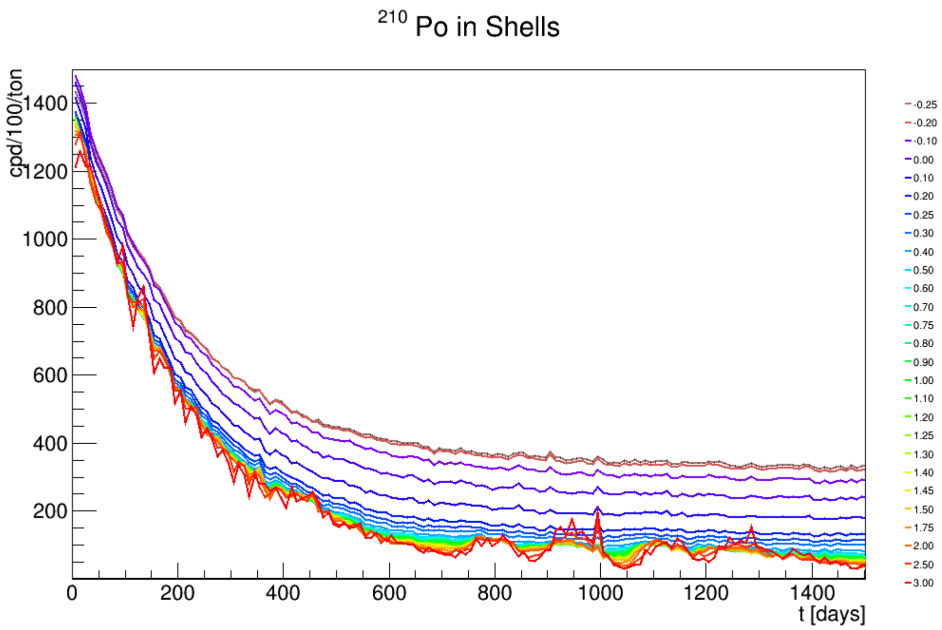

FIGURE 3.2: Evolution the ^{210}Po behavior in different concentric shells in the IV (distance from the Dynamical Vessel shape), from the 11th of December 2011 until mid-February 2016.

In conclusion, the identified problematic is two-fold: the precision required for a meaningful and rigorous ^{210}Bi statistical subtraction that would enable an improvement of the solar neutrino measurements in the bismuth valley, estimated to be of ∼<10% with Phase II data quality, is difficult to achieve because of, on the one hand, the uncertainty in ^{210}Po levels in the FV caused by scintillator mixing and, on the other hand, the lack of statistics in "clean enough" areas of the scintillator at the lowest purity levels after the multi-year ^{210}Po decay from its high, out-of-equilibrium Phase I levels. More information on the signal selection will be given hereafter.

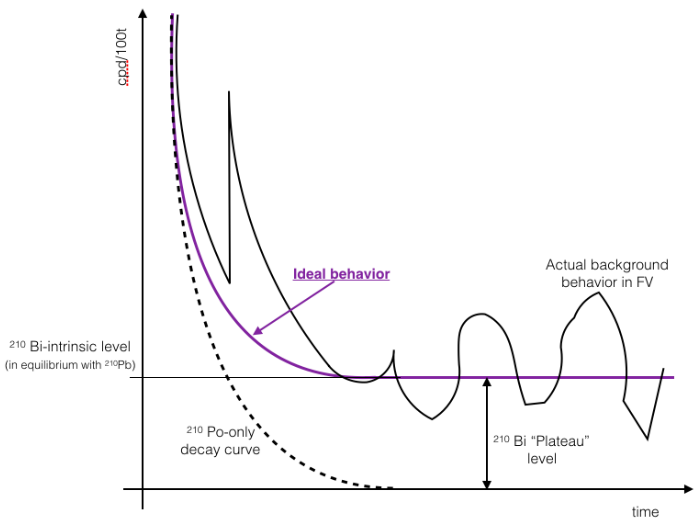

FIGURE 3.3: Idealized, conceptual representation of the ^{210}Bi-^{210}Po levels correlation and behavior, as seen in the last Figure 3.2.

3.1.1 Low- and mid-level data conditioning

Data conditioning for analysis-specific purposes takes over from the low-level data treatment explained in Sections 2.3 and 2.4. As mentioned there, data is first recorded in a *raw* datafile containing the information inside each triggered window (run and event number, trigger type, BTB input, GPS time of the trigger and the array of hit PMTs, consisting of the PMT logical channel (lg) and the hit time and charge (integrated in 80 ns)) –from here, a deliberate process starts to convert that data into physical events, assigning them position and energy characteristics, reconstructable from the hit timing at each PMT, the charge deposited in them, and which PMTs were triggered by the hit. This processing is considered the low-level part of the analysis, and as was mentioned before, is performed through the MOE package (for both ID and OD). However, some particular variables are still considered "better" when processed by Mach4 alone –this code's algorithms for these particular variables are being integrated into MOE, but this process hasn't been completed yet. This side note is important for ^{210}Po, since it is discriminated thanks to its location in the energy spectrum, more accurately determined through the charge variable `m4_charge_noavg`, a Mach4 variable.

The *precalibrations* are first to be performed, dealing with time and charge calibration, as well as dark noise subtraction and determination of the working channels for charge and timing information, or just timing (using instead, if available and the reconstruction code for the particular variable requires it, an average of recorded charge for each of the remaining hits in a 15-ns window around the one missing the charge information). Once these are completed, the aforementioned information about channel, charge and timing is assigned to each hit in the raw data's trigger window through the *event reconstruction* process. Once precalibrations and event reconstruction are complete, ~60% of hits have survived, on average: these are called *decoded hits*. These are the hits Mach4 processes on.

Mid-level data conditioning starts from there, saving trigger events (`BxEvents`, subdivided in *ntuples* representing the variables) into `ROOT` *tree* structures, or `bxtrees`. As part of this level of data processing, MOE performs the processes of:

Clustering Since several physical events can exist inside a trigger window (~1 μs long vs 16.5 μs long, respectively), individual hits have to be assigned to each single physical event. Clustering together hits falling under certain criteria takes care of this task: after estimating the dark noise level for that trigger and binning the trigger window in 16-ns bins, a moving window is used to determine the start of the hit (where it surpasses the noise by a certain threshold) and its end (where it falls down under that threshold again). Individual peaks inside that timeframe are considered clustered (see Figure 3.4), unless it is less than 20 bins long. An energy-dependent "tail" is assigned to each cluster[1], unless there is a *multi*cluster condition and the second cluster is immediately adjacent to the previous one; in that case, the last cluster starts where the previous finishes. Different trigger types have slightly different implementations of this general rule[94]. Hits not flagged as invalid under this algorithm are called *clustered hits*.

It should be noted this is the ideal logic for the clustering algorithm –nevertheless, real time profiles can offer difficult-to-interpret features that complicate clustering. Most of the problems occur with multicluster events in the same trigger window. This was of critical importance for some studies, most notably the *pp* analysis[42], since the pile-up in the lower-energy part of Borexino's spectrum was a feature of critical importance to the final result (see Section 2.4.2). Cluster length is of particular relevance to allow for α-like events to be included (because of its longer tail-to-total ratio, that is, their signal time profile, see Figure 3.5), as well as for background estimates dealing with coincidences and pile-up.

[1]This is a Mach4 feature that was retained for many of MOE's energy variables. However, the amount of non-coincident clusters with respect to Echidna's fixed-length clustering strategy is very low, and negligible for most studies –in fact, nowadays, the cut verifying events have at least one cluster in the window (see Section 3.1.2) includes also a rejection flag for non-coincident clusters between the two clustering strategies.

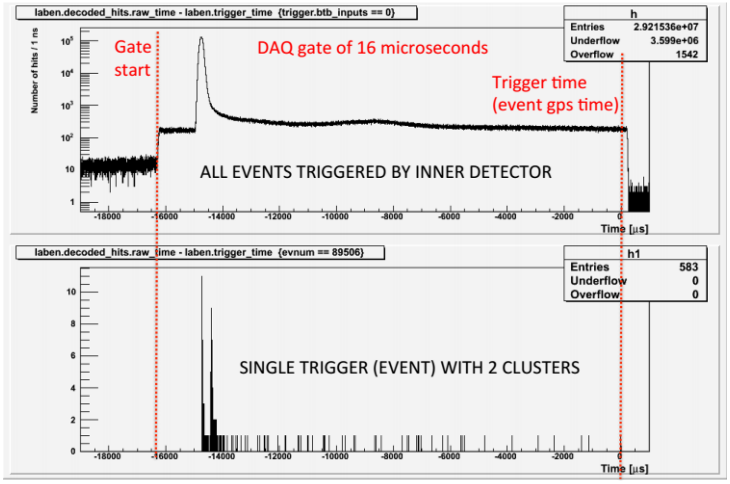

FIGURE 3.4: Real example of the time profile of a triggered window, with the sum of all ID signals, clearly marking the time profile of the trigger gate, its timing and the detected scintillation time profile, as well as the corresponding double-cluster event corresponding to a single PMT channel.

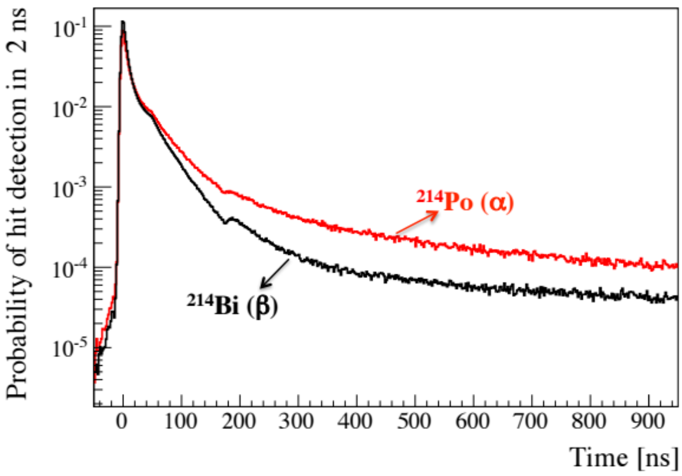

FIGURE 3.5: Time distribution of real events for α- and β-like signals, showing the importance of the cluster length determination for PSD. The deviations from a smooth curve at 75 and 180 ns are due to the photons reflecting off the SSS and the single-channel deadtime.

Position reconstruction Neglecting scattering and considering the time-of-flight (TOF) for a photon traveling in a straight line from the interaction point in the scintillator, characterized by an experimentally-determined index of refraction[2] n_r, we can assign a position in the scintillator volume relative to the PMT nominal position r_i through the following

[2]Its value was fixed at 1.68 from internal calibrations with inserted sources. This value significantly differs from the one determined from direct sampling, due to the difference existing between the group velocity of the scintillation light profile as compared to its phase velocity: due to dispersive effects, the former is smaller than the latter. This leaves as the second most important uncertainty the so-called *z-effect*, by which smaller values for the z coordinate of an event are measured through the position reconstruction to be lower than with the calibration system's CCD camera reconstruction algorithm (see more on this issue in Chapter 5). This bias (-3±1 cm) may also be due to the same effect, but a definitive answer to this long-standing shift has not yet been reached.

equation, also considering the interaction time in the PMT t_i:

$$|r_i - r| = \frac{c}{n_r}(t_i - t'_i - t_*) \tag{3.1}$$

Convolving the scintillator's probability density function (pdf), that is, the scintillation profile, the likelihood of an event at ($\mathbf{r}_*$, t$_*$) is determined, yielding its most likely position for a set of spatiotemporal coordinates, and assuming hits are statistically independent of one another. A charge-dependence of hit timing is implemented in the probability density function, to correct for the bias introduced by the electronics response, which record just the first photoelectron's production time in a given PMT[3].

Energy reconstruction Several different strategies exist, some better tuned for specific analyses than others, to estimate the energy of an event, but they are generally based on two methods. The exact relationship between this estimated charge and the actual physical charge is determined through the energy response functions (photon, photoelectron, single p.e., distributed source...) and energy scale for the scintillation profiles from different particles. These factors relate the energy estimator variable to the number of physical scintillation photons emitted on the event, as well as the energy deposited in the target.

The energy estimator variables are divided in:

`npmts` (and `nhits`) These variables proceed through the following logic:

1. Sum of the **number of** hits with valid timing in the cluster
2. Subtract estimated number of noise events, based on the estimated dark noise in the gate and the cluster length
3. Normalize to the number of live PMTs, multiplying by the normalization factor $2000/N_{live_{PMTs}}$.

While `npmts` may underestimate charge in multi-cluster high-energy ($\sim>$2.5 MeV) events, it can be useful for low-energy studies. `nhits` includes multiple hits in the same channel.

`npe` This variable follows the same general logic as the previous ones, but instead of summing the **number of** hits with valid timing in a cluster, it sums the **recorded charge of** each hit in the cluster that contains valid charge **and** timing information. Steps 2 and 3 are identical to `npmts/nhits`. A related variable, $\mathtt{npe}_{avg}$ (that is, an averaged `npe`) or its successor `npe_corrected` just requires valid timing information, regardless of its charge information validity, instead using the average charge of all other hits with valid charge in a 15-ns window around the hit in question.

Pulse-Shape Discrimination Although the *Gatti parameter* method for time profile separation is performed as part of MOE as a way to discriminate between α- and β-like events,

[3] This means that for N$_{p.e.}$ >1, the hit timing profiles are more skewed toward earlier times, on average.

the current analysis increasingly makes use of the *Multi-Layer Perceptron* (MLP) variable, further explained in the next Section 3.1.2. For more details about this, consult [94].

Muon tracking Especially useful to discriminate backgrounds (in particular ^{11}C), the muon track is reconstructed if a sufficiently bright event was noted in the ID or if the MTB was triggered, considering an isotropic light emission from said track, and using whole detector information if available (Echidna) or just the ID's (Mach4, MOE). Estimated accuracy is $\sim$30-40 cm in the impact parameter about Borexino's center, including an angular uncertainty of 2-3°[144].

Isotropy and rack noise Since scintillation events are expected to offer a spherically isotropic light emission profile, events with highly skewed hit distributions can be rejected. This geometrical uniformity parameter is implemented through a decomposition in Legendre polynomials (Mach4) or spherical harmonics (Echidna, MOE) of the triggered PMTs distribution for a given event. Related to this is the portion of events that are due to noise in a specific electronics rack, which follow an inhomogeneous distribution in one or several spherical lunes, given by the majority of the PMTs in a rack being cabled in these distributions. Both type of events show good position reconstruction, but are easily discriminated by the aforementioned homogeneity parameters.

Clustered hits after photon time-of-flight (TOF: PMT position minus reconstructed position) subtraction are then designated `rec_clusters`, and are used for the PSD and isotropy estimators. Once MOE processing is complete, a 1-week `ROOT` DST file is compiled, using the combined processed single-run `ROOT` files, where the different variable *trees* are contained. To qualify for a DST, events need to be of trigger type 1, 2 and 128 with clusters (or have triggered the MTB). Additionally, they have to pass either of these conditions: $\mathtt{N}_{hits}$>75 or >75 p.e. of recorded charge (to remove low-energy ^{14}C and pileup and make the dataset more manageable), two or more identified clusters, be a muon or occur 300 ms after a muon, or occur within 2 ms of another event. Additionally, so-called *light-DSTs* are produced to expedite data analysis: only certain most-useful variables are included in these, and the low-energy portion of the spectrum is left out, which saves processing time over 85% of events that otherwise would be checked, and is suitable for high-energy or "golden window" studies.

3.1.2 High-level analysis: how are ^{210}Po and ^{210}Bi estimated?

Within the light-DSTs, the `m4_charge_noavg` variable[4] is the one employed for most of the ^{210}Po determination studies, primarily developed by Nicola Rossi. It is characterized by the fact that it doesn't use the averaging procedure for channels with only valid timing information, and performs an integration of the total charge in all the channels showing short cluster windows, including retriggered channels, which is then dark-noise subtracted (from *tt64* counts) and normalized to the number of live PMTs:

$$m4\_charge\_noavg = \sum_{0}^{2218} \left[npe_i - (tt64_{avg} \cdot t_{cluster\_window})_i\right] \cdot \frac{2000}{N_{livePMTs}} \tag{3.2}$$

It should be noted efforts are currently underway to integrate this variable within the Echidna clustering algorithm to avoid signal consistency issues between the two scripts, that get worse as the signal-to-noise ratio is degraded by the gradual loss of PMTs and the aging of the electronics. For example, the dark noise estimate is taken as an *average* (tt64, last half of tt1, pulser tt4 and laser tt16) instead of just coming from the trigger type 64 rate. Also, a pile-up-corrected charge (`charge_mean`) is used instead of the raw Mach4 charge estimator. This is related to the work outlined further ahead on this Section, focused on the enhancement of the "subvolume analysis" by improving its resolution and better understanding its spatiotemporal variability.

The energy spectrum obtained through `m4_charge_noavg` is then subject to the ^{7}Be analysis cuts (codified in Echidna as the `cut>15` instruction), described in detail in Section 6.2 and Appendix A in [94]. In essence, noise and event-by-event-taggable backgrounds are removed by filtering muons, post-muon noise and muon-bred isotopes (cosmogenics), excluding trigger types 2 and 128, as well as events with no clusters which were kept in the DST creation for muon identification purposes, or those with a different number of reconstructed clusters in Mach4 and Echidna (mainly noise and higher-energy pile-up). Fast coincidences (<2 ms and <1.0 m separation) and multi-cluster events are then excluded (mainly to filter out ^{214}Bi-Po coincidences), together with clusters in an off-nominal position in the trigger window (usually mis-identified service triggers) and events with more than 75% of their hits in a single rack (f_{rack} >0.75, see the *Energy Reconstruction* summary in Section 3.1.1). Fiducialization is performed with the *standard* ^{7}Be fiducial cut (86.0084 m^3 / 75.7046 tonnes, see Section 2.2.1) and geometrical uniformity is imposed. Finally, a further step is taken toward pile-up by filtering out events with more than one visible peak in the cluster's hit time profile, as well as those noisy events which

[4] In fact, rather than a variable, the object corresponding to this name it is a *getter* function in the `bx_candidate` class of the `bx_filter` package dealing with DST creation. The actual variable the *getter* corresponds to is MOE's `m4s[].laben__cluster__npe_noavg_corrected`, meaning it is part of the clustered hits variables taken from the laben board signals (double underscores, in the MOE convention, correspond to dots, signaling advancing hierarchical subdivisions in the tree).

record too little integrated charge compared to the number of hit PMTs. The results of these cuts on the initial DST spectrum are visible in Figure 3.6.

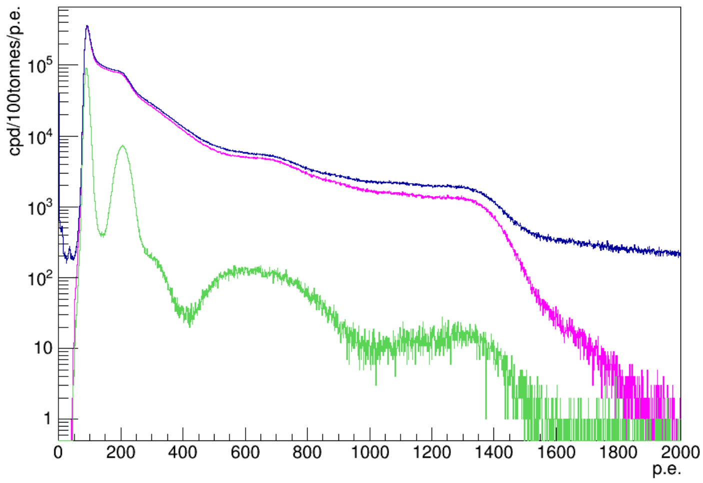

FIGURE 3.6: Borexino energy spectrum derived from the `m4_charge_noavg` in full (blue line), after ^{7}Be standard cuts (`cut>15`, purple line, showing a decrease in very low-threshold effects and high-energy background) and after a 3-m spherical fiducial cut (`lngs_r<3`, green line).

Later on, the window between 130 and 390 p.e. is selected (see Figure 3.8), and a PSD $\alpha - \beta$ segregation is performed. As anticipated in previous sections, the Multi-Layer Perceptron (MLP, currently v.6, whose inefficiency is estimated at ~0.6%) is used for this purpose. The MLP is a neural network based on an algorithm for supervised learning of binary classifiers (functions that can decide which class an input belongs to), that can select events through non-linear discrimination techniques. This translates to our case of interest by the possibility of training the network with variables that were previously not employed (multi-variate analysis) such as those in non-reconstructed clusters (`rec_hits`), as well as the use of quantiles instead of tail-to-total (tailtot) ratios for shape identification, which is problematic at low energies because of distribution quantization effects[145]. In addition, the pdf for reconstructed clusters can be fit very efficiently with the neural network. Selection criteria for particle identification with respect to their MLP PSD parameter value is:

- α-like events: <0.05
- β-like events: >0.95

The inefficiency is practically negligible in ^{210}Po determination, especially since Phase II levels are so low. For ^{210}Bi, it is taken into account in the reconstruction formula. ^{85}Kr and the ^{222}Rn chains are considered 0.

For bismuth analysis, the p.e. upper range is extended a bit to include the valley between ^{7}Be and ^{11}C, where both are constant and can be neglected away. Its rate is estimated from the β-like estimation parameter:

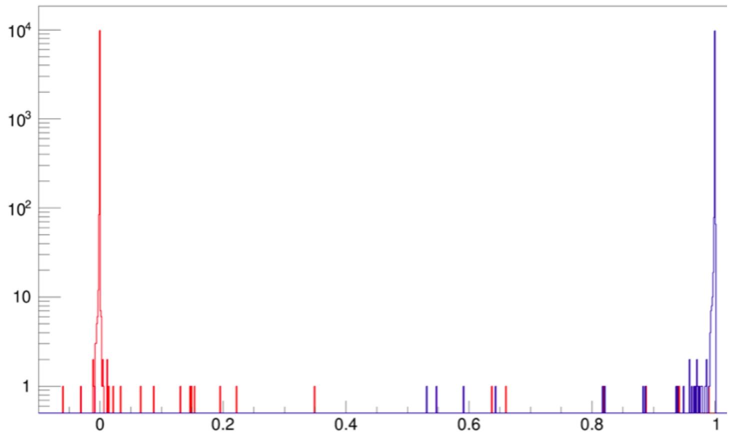

FIGURE 3.7: MLP tailtot variable distribution for a sample of 10^4 ^{214}Bi and 10^4 ^{214}Po events, as part of the neural network training for its v6. The recent introduction of quantiles replacing tailtots improved the rejection efficiency.

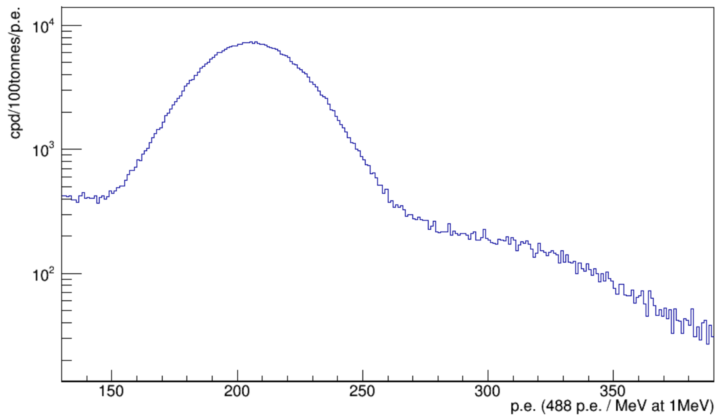

FIGURE 3.8: P2B-C spectrum after ^{7}Be and spherical fiducial cuts are applied in the window of interest [130,390]p.e. for ^{210}Po-^{210}Bi analysis.

$$\beta_{corr} = \beta_{0.95} - (1-\epsilon)\alpha_{0.05} \tag{3.3}$$

where ϵ is the MLP's efficiency (0.9995±0.0001). The final ^{210}Bi rate for each of the 10-day time periods where it is tracked (as is ^{210}Po) is determined by:

$$R_{^{210}Bi} = \beta_{corr} - (R_{solar} \cdot seas) \tag{3.4}$$

where *seas* is the seasonal modulation geometric parameter which varies to within ±3.5% according to $1 + 2\epsilon_{orbit} cos\left(\frac{2\pi t}{T} - \phi\right)$, where ϵ_{orbit} is the eccentricity in Earth's orbit and T=1 year. The solar neutrino rate R_{solar} is fixed to the Borexino-measured Phase II values in the energy window considered (most recently, 27.9 cpd/100 tonnes). This, of course, is the rate in the region of interest, which has to be scaled to the full rate in Borexino by dividing by the fraction that is measured in this ROI (43% in the nominal 130-390 p.e. range).

Since the spatiotemporal inhomogeneity of these rates are our focus of interest, they are calculated in 59 spherical[5] sub-volumes contained in a 3m-radius spherical Fiducial Volume and 1-m-tall slices of the same FV, as well as 10cm-thick shells in the DFV. The goal of these different subdivisions would be to understand the B (supported, or equilibrium rate for bismuth and polonium) term in the ^{210}Po decay rate:

$$R_{^{210}Po} = (A - B)e^{-t/\tau_{Po}} + B \tag{3.5}$$

where A would be the unsupported, or out-of-equilibrium, term only affecting polonium coming from regions external to the FV. A 300-day moving window fit (with high χ^2 agreement) is implemented on the different sub-volumes' polonium decay curves to estimate these parameters.

Several different strategies were, and are being, tried in order to understand where the cleanest –and dirtiest– sections of the scintillator are, in terms of ^{210}Po, in order to understand as precisely as possible the ^{210}Bi levels. In that sense, the "standard" analysis has become to follow the vertical movements of the polonium background through its $cos(\theta)$ distribution. For the most part and in almost all temporal periods, the angular and radial (r^3) distributions show no deviations from an ideal case (azimuthal symmetry, approximately linear gradient in ^{210}Po concentration with respect to radial distance). In this sense, just choosing the cleanest sub-volume to set a "mini-FV" around would introduce a statistical bias, so different averaging techniques have been employed so far, with mixed levels of success:

- Mean average around the immediately co-located sub-volumes to the one under analysis, on the same horizontal plane, following a numerical ordering.
- "`ROOT` average": mean average with assignment of weights to the value of the adjacent sub-volumes whose center is closer to the one under analysis, following the same ordering as with the mean average.
- "Smart average": using the *spatially* adjoining cubes instead of the numerically-ordered ones.

A large analysis effort is ongoing in this direction, with the sub-volume rate estimators approaching maturity, but a lot of work is still in progress toward the overall strategy for selecting

[5]As a curiosity, the first iterations of this type of analysis that relied on dividing a fiducialized volume of the active target into several regional sub-volumes were implemented with *cubes* instead of spheres: hence the jargon of referring to the ^{210}Po-^{210}Bi analysis informally as the "*cubes analysis*". Concerns about the biases that the vertexes and edges of such subdivisions would introduce led to the "spherization of the cube", while keeping the same initial volume for each sub-volume.

the radiocleanest sub-FVs without incurring in statistical or systematic biases or losing too many good statistics in the selection process. The MLP is also in a continuous process of improvement, with v.12 being the latest internal release –although it is used for many other analysis applications and for the present matter of discussion its inefficiency is already extremely low and not a cause for concern.

A MonteCarlo of the effect of the inhomogeneous live PMT distribution is the most critical source of uncertainty at the moment, which will lead to time- and spatially-dependent resolution correction factors, whose implementation is still pending.

The position of the polonium peak in the p.e. spectrum is being currently used as an anchor to estimate the energy estimation correction for each sub-volume. Clearly however, this position will not be the same for central or peripheral sub-volumes because of different effects dependent on time and spatial location of the sub-volume in the detector. Until recently, an average of this position for all sub-volumes in a given time stretch was taken as "true" and used to correct the energy scale. A more correct approach would be to replicate with MonteCarlo the position of the peak for the known PMT distribution for a short time period (on the order of weeks at most). The position of the peak would then be studied for each sub-volume at each time step, and the resulting correction applied to the corresponding background rate estimate. This improvement is close to full implementation. Other possible approaches in work are to study smaller DFV-defined shells that only span a certain angular region, in order to discriminate directional effects in a radially-symmetric sub-volume.

Another intriguing open question is the homogeneity of ^{210}Bi distribution, whose decay rate should match that of its progenitor ^{210}Pb ($\tau_{1/2}$ ~22 y; bismuth is much more short-lived at ~5 days), unless there were other sources of ^{210}Po than fluid mixing: however, estimates for its regional (FV top vs bottom) decay rate show much lower values of ~1/3 the expected value for a transient equilibrium condition.

The spatial distribution of the cleanest / most contaminated areas in the Inner Vessel has also been ongoing, considering azimuthal symmetry, through the use of Voronoi diagrams (implemented by Z. Nieckarz). These diagrams assign cells whose center is a point (in our case, a ^{210}Po event) and whose limits span the same distance to that central point than to the nearest neighboring point. This means areas with low contamination will have larger Voronoi cells than areas with lots of polonium events. This can be seen in Figure 3.9, where the different cells are color coded from dark red (smallest, most contaminated) to white (cleanest areas, larger Voronoi cell in the diagram). This technique has only been implemented starting in late 2013, since ^{210}Po levels before that were too high to allow meaningful cells to be drawn.

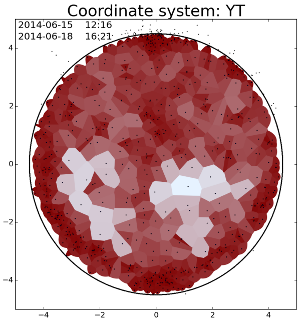

FIGURE 3.9: Sample of Voronoi cells representing increasing levels of ^{210}Po (red=higher; white=lower) throughout the Inner Vessel.

3.1.3 Summary of ^{210}Po dynamics through data analysis and perspectives

Data (both Phase I and II) used for ^{210}Po-^{210}Bi analysis is divided in the following periods, determined by variations in detector and background conditions:

P1 Before first calibration campaign, since the beginning of data-taking (Phase I): 17th of June, 2007 until 28th of September, 2008.

P1B Before water extraction purification campaign (Phase I): 5th of October, 2008, until 6th of June, 2010.

PWE Water extraction purification, characterized by spiking levels of ^{210}Po because of the mixing of scintillator: 13th of June 2010 until 7th of August 2011.

P2A After water extraction purification campaign and before external calibration campaign (Phase II): 14th of August 2011 until 3rd of November, 2013.

P2B-C After external calibration (Phase II): 11th of December, 2013 until present date, dominated by seasonal evolution of temperatures inside Hall C.

A possible P2D (or P3) will likely be added in the future as a way to mark the stabilization introduced by the installation of the thermal insulation system and the subsequent change in background behavior.

While important features and interpretative anchors are available through P1-P2A analysis[146], we will center our discussion in the recent, most stable and cleanest periods P2B-C, where the situation described at the beginning of this chapter can more clearly be observed.

The main remarkable feature that is present in the $\cos(\theta)$ diagram highlighting concentration changes along the Z direction is that oscillations in ^{210}Po backgrounds have a $\sim$1 year period (at least until the TIS installation, see Figure 3.10), which could point towards a seasonal effect.

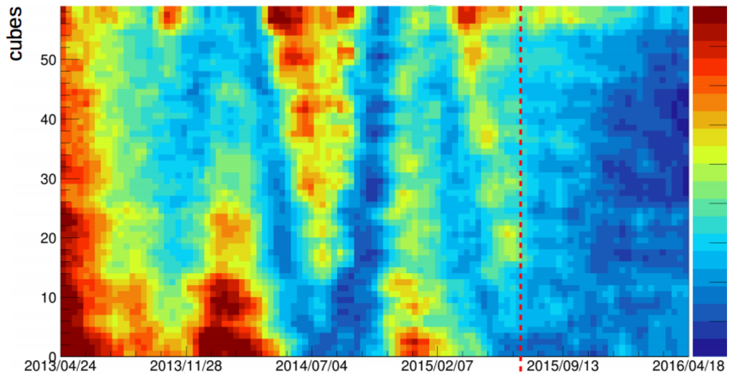

FIGURE 3.10: Results from N. Rossi's "cubes" analysis [147] with the aim to understand the movement of the "low background" volumes inside the FV. An oscillation of the purest areas of the scintillator, with a $\sim$ one year period, is evident. The dashed red line represents the summer of 2015, when the TIS stabilizing effect started to become really noticeable in the ID, suppressing the previously strong seasonal effect.

A key feature that gave more credence to the (convective) fluid movement as being the main cause for fluctuating backgrounds was a low-^{210}Po volume that appears to develop around August 2014 in the bottom of the Inner Vessel, and rises slowly to the top until mid-November 2014, most visible through the Voronoi diagram or the YZ plane sub-volume plot approaches. This can be understood complementarily as polonium falling along the vessel's periphery to the bottom, and then upsurging through the middle of the IV. The "clean" volume is then observed to disperse (or rather, rising polonium mixes into the trapped clean area in the top) during December 2014 until mid-February 2015. This coincides with the decrease in countrate, arguably showing scintillator mixing with no external polonium input. Since then, until April 2015, an unstable clean area appears to have been in development in the central part of the IV, tending to fall towards the bottom.

Furthermore, since the extremely clean scintillator period during a few weeks in autumn 2014, mixing events brought up the levels again because of this seasonal effect, but even the areas with the most ^{210}Po showed a decrease consistent with its out-of-equilibrium decay. Except for some mixing on the top that endured until early 2016 (and can be argued to still be active), however, since late summer 2015 the thermal stabilization showed its worth by providing a much more low and homogeneous background concentration in the FV. Recently, a slight but noticeable increase in the bottom has been seen.

The ϕ distributions in time show the approximate azimuthal symmetry in ^{210}Po distribution shown in Figure 3.11, although it does not convey as readily the mixing information shown in the Voronoi diagram approach. Radial (r^3) plots do highlight the mixing events, as in Figure 3.12.

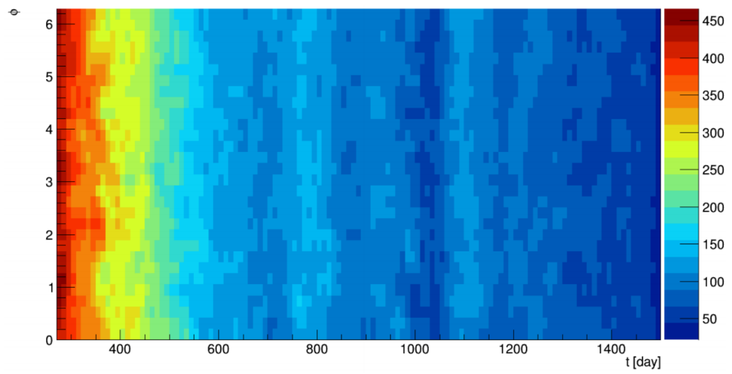

FIGURE 3.11: ϕ vs time plot for ^{210}Po distribution in a 3m-radius FV. Time starts on 2011/12/11, when Period 2B begins.

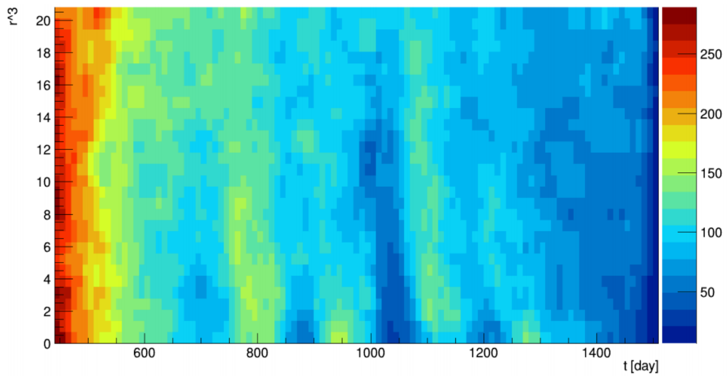

FIGURE 3.12: r^3 vs time plot for ^{210}Po distribution in a 3m-radius FV. Time starts on 2011/12/11, when Period 2B begins.

3.2 Latitudinal Temperature Probes System (LTPS)

The situation concerning the fluctuations in Borexino's ^{210}Bi background, as described in [148], have long prompted ideas throughout the Collaboration on how to actively minimize their impact. Along with a purification campaign to tackle the problem from the root –that is, minimizing the background levels–, it was decided to:

1. finely measure the temperature profiles inside (and outside) the detector, as well as
2. thermally insulate it from the Hall C's ambient temperature excursions.

Both items were subject to a multi-year effort that first saw the deployment of the **Latitudinal Temperature Probes System** (LTPS) since late 2014 in several phases, from an experimental setup to a full-fledged 65+ probe ensemble. At the equinox of this system's deployment, the **Thermal Insulation System** (TIS) started installation, after its conceptual and technical designs were completed in early 2015. Both systems were fully deployed by the end of 2015, and the Active Gradient Stabilization System (AGSS) was brought to an operational status by early 2016 as a last step to complement both the monitoring and the insulation systems.

3.2.1 Design and hardware for the LTPS

The primary objective for which the LTPS was designed is the measurement of the temperature profile inside Borexino's Stainless Steel Sphere (SSS), at different latitudes and with unprecedented precision. This will allow for a clearer understanding of the temperature-driven background fluctuations at play in the FV, and hopefully point the way towards a long-term stabilization.

A pathfinder system was developed during the summer of 2014 by the VT group, and was initially just considered an experimental system whose expected performance was not well constrained. However, the excellent performance shown meant that, with some touch-ups, the original probes were used as the foundation of the full-fledged LTPS: the rest of the system would be built following the same principles and using roughly the same hardware elements.

The exterior thermal insulation of the WT (TIS) was expected to lead to a profound change in the boundary conditions with the Hall C environment, potentially negatively disrupting –even if just through a transient condition– the natural stability attained after the OPERA magnet shutdown. The installation of external sensors between the insulation and the external walls (Phase II.a) was proposed in order to provide high-resolution measurements of these conditions, complementing the LTPS' thermal transport study potential, and serving as a "failsafe" system to guide executive actions during the TIS installation.

The existence of a positive gradient (warmer temperatures on top, cooler temperatures on the bottom) in Borexino's fluids is paramount to keep good stability conditions and minimize internal currents. For this reason, although the bottom of the detector is in contact with the rock foundations and should be stable, it is desirable to monitor the bottom boundary condition, which was done through the insertion of more sensors inside the SOX / Icarus pit (Phase II.b).

The probes used for the LTPS (Vernier Extra-Long Temperature Probe system, order code TPL-BTA, see Table 3.1 for details) output a voltage differential that is routed through the Signal Conditioning Box (SCB). This is sent to the LabQuest Mini 12-bit digitizer, which outputs the raw data for each of the probes connected to it (up to 3) converted to a digital format (integer number, scaled to 16 bits). This is then sent to the computer they are connected to through a USB port. Once sent to the computer, a C++ program converts the raw data back to voltages and temperatures, according to some empirically-determined calibration functions. The probes are not "smart" probes; therefore, they do not store calibration data internally and use default values for the probe type to covert from the raw ADC value to a temperature. The probes are qualified for usage in water environments (one of their advertised uses from the vendor is measurement of temperature gradients in lakes and rivers). However, this is understood to be a transient usage, not long-term – hence the need for the purging system.

Specification	**Value**
Order Code	TPL-BTA
Temperature transducer model	AD590JH
Cable length	30 m
Maximum diameter	7 mm
Range	-50°C – 150°C
Advertised (absolute) Accuracy	±0.2°C
Resolution	0.07°C
Power	7.4 mA at 5 VDC
Response time	8-10 s (still water)
	45 s (stirred water)
	100 s (moving air)
Factory calibration values (°C)	Intercept (k_0) = -53.073
	Slope (k_1) = 58.341

TABLE 3.1: Vernier Extra-Long Temperature Probes specifications

A primary level of on-axis scintillator temperature monitoring is already present through the 8 legacy sensors located in the vessels' hold-down structures at the poles (4 top + 4 bottom, 2 in the outer buffer and 2 in the inner buffer, respectively) installed before the filling of the detector, as well as 32 Water Tank sensors (28 reliable, 3 failed and 1 suspect). The most stable probes achieve an instantaneous precision no better than ∼0.05°C (see Figure 3.13 and 3.14).

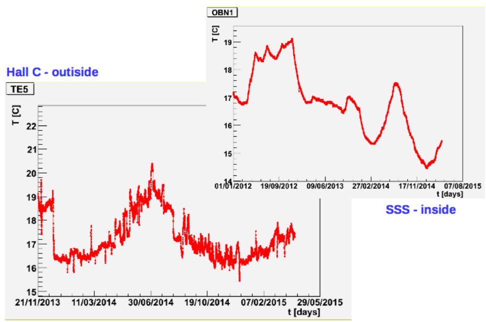

FIGURE 3.13: Example of historical profile of legacy temperature probes

The full LTPS system, as of this writing, was installed in steps between the aforementioned summer of 2014 experimental deployment and early 2016. It consists of:

Phase I. The original experimental system that later became operational (Phase I.a) is located in the so-called *re-entrant tubes*, which were envisioned in principle for the external calibration of the PMTs and OD, and were used during the external thorium calibration campaign[64]. These ports, whose entraces (or "organ pipes") are located next to the PMT cable ports, on the top platform of Borexino next to CleanRoom-4, were sealed with SwageLock plugs after the aforementioned calibration and rested unused ever since. Their only future expected use would be the second external calibration campaign. Therefore,

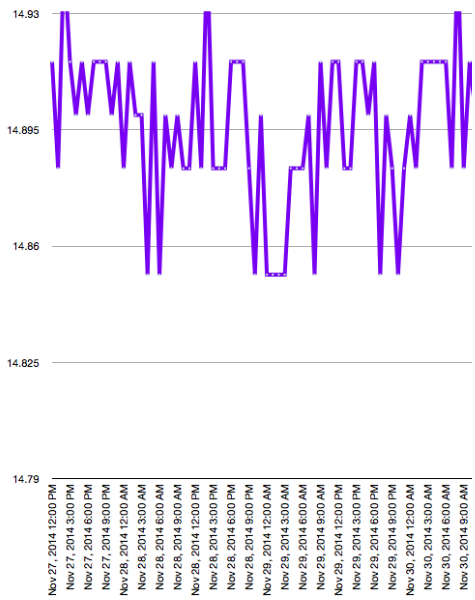

FIGURE 3.14: Detail of historical profile of legacy temperature probes

the LTPS design accommodates easy removal, also to allow for easy replacement of faulty probes or upgrades, such as the installation of the Phase I.b WT probes.

The chosen design for the Phase I.a internal probes was then to insert them sheathed inside a low-friction PVC tube (10 mm OD, 8 mm ID), terminated with a small section of smaller (8 mm OD) diameter polyethylene tube through which the probe just fit, to provide support for its tip and avoid disconnection or slippages between the probe and the PVC sheath. The ends of these tubes were smoothed with the sophisticated use of a pencil-sharpener to avoid having the straight cuts seizing on the entrances to the re-entrant tubes. Additionally, in the lowermost sensors (which are more difficult to insert anything into, given they look upwards), a very small section of flexible PVC tubing was also inserted on the tip of the probe to "lead" the sensor in (see Figure 3.17). Additionally, two small slits were cut a few cm before the sensor on the PVC sheath, to allow for nitrogen purging and drying of the ports. All of the gas system junctions were 10-mm RapidGas fittings – the openings where the probes cables go in were sealed with silicone to prevent nitrogen from escaping, forcing it to go through until the end of the sheath for purging. Phase I.a (outer buffer sensors alone) started data acquition on the 29th of October, 2014, at the locations indicated in Table 3.2.

The raw data integer, the voltages and the temperatures are all written to output files through code provided by Vernier and custom-modified. This code also allows for setting of the sampling rate and measurement time.

The re-entrant tubes (see Figure 3.16) consist of a 1.27 cm ID endcap-welded stainless steel tube which protrudes ∼50 cm into the Inner Detector's Outer Buffer and connected

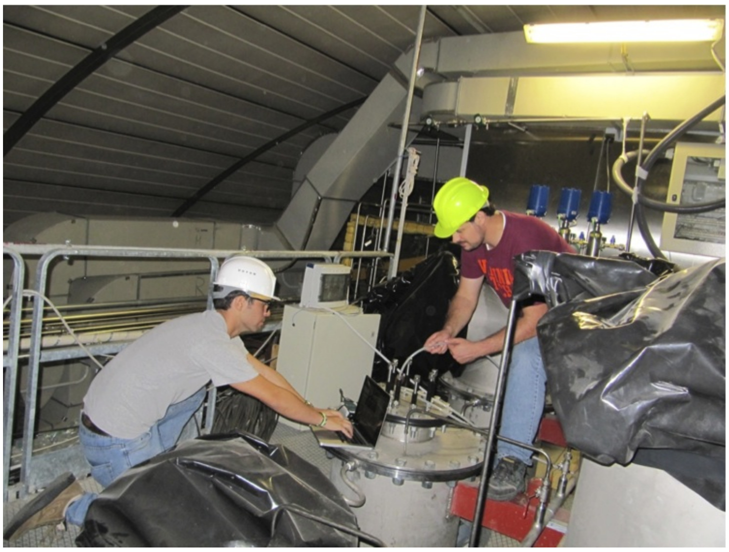

FIGURE 3.15: Phase I.a insertion work in the South "organ pipe" re-entrant tubes

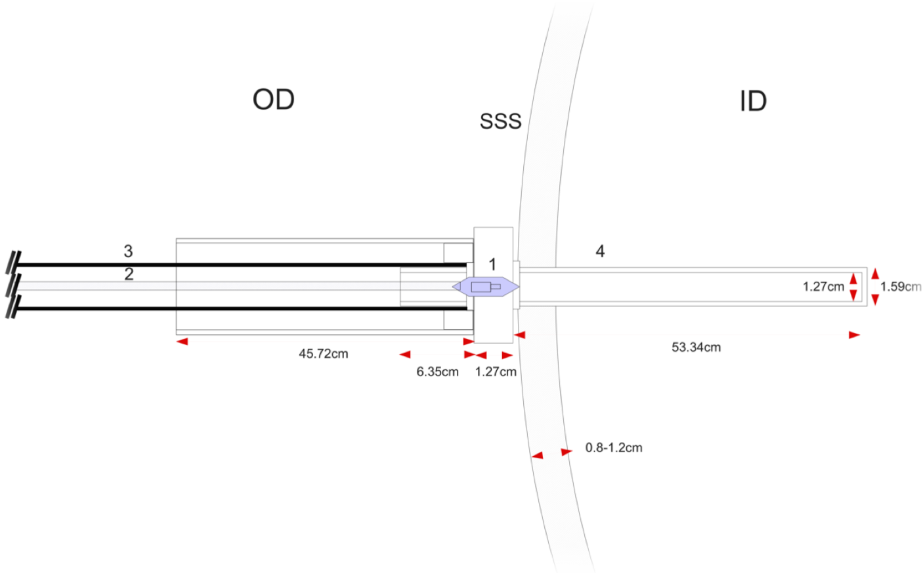

FIGURE 3.16: Technical diagram of a re-entrant tube in the SSS interface

via polyethylene tubes going through the WT, ending on the platform above the WT of Borexino (see Figure 3.15). One organ pipe is located north of the clean room of the internal calibration system, one south of it. The tubes are thick enough to relieve the buoyant forces that they have been exposed from the water in the OD. A wider-diameter metallic tube is connected to the flange joining them to the SSS, to avoid kinking of the polyethylene tube at the flange interface. Some of the deepest tubes, however, have been shown to have an amount of water inside. For this reason, another requirement for the LTPS is to have a purge capability, which was implemented through a nitrogen flow.

Phase I.b (sensors located 50 cm just inside the SSS into the outer buffer at the tip of the re-entrant tubes, as well as 50 cm just outside the SSS in the WT), whose installation

FIGURE 3.17: Phase I.a LTPS outer buffer sensor termination

finished on the 10th of April, 2015, includes an extra opening ∼1 m from the Phase I.a buffer sensors, where the second sensor was inserted in each port. (see Figure 3.18 for a diagram of the Phase I system, and Figure 3.19 for the Phase I.b internal sensors design)

Phase II. Contemporarily to the installation of the TIS, it was deemed necessary to expand the LTPS to cover not only the fluid temperatures inside the detector, but also the boundary conditions that determine it, and how the thermal transport took place. This was the last occasion to install such a system in a simple fashion, since once the thermal insulation was put in place, the several layers it consists of would have to be sliced and removed otherwise. Furthermore, the installation of the scaffolding around the detector, or the operators rappelling down Borexino's sides, would provide a unique opportunity to access mostly anywhere on the WT's surface. A suite of 20 sensors, located at roughly the same N/S plane as where the Phase I sensors approximately lie, were set up over a period of months, while the TIS was covering the WT. They were inserted in flexible polyethylene tubing (in a much less convoluted fashion than the Phase I probes, since the tube only has to offer a bypass through the insulation and position the sensor accurately against the wall) sandwiched between insulation sections, as can be seen in Figure 3.20. For this reason, it is possible to access, remove or replace them as needed. Additionally, as mentioned above, 4 probes were also inserted in different points on the ICARUS/SOX pit's ceiling (at the T-shaped junction and ∼2 m from the T's junction in each of the three possible directions, with its cables passing through a small utility passage tunnel on the side of the pit, see Figure 3.21) to monitor the stability and regional dependence of the heat sink in contact with Borexino's bottom. In autumn 2016, Phase II.b was extended by two sensors at the

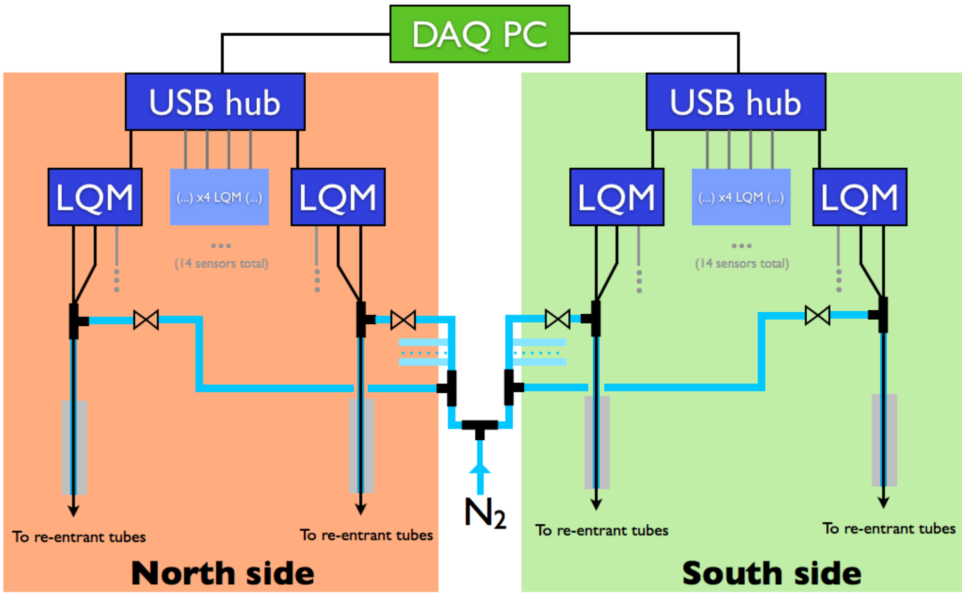

FIGURE 3.18: LTPS Phase I.b cable and gas diagram

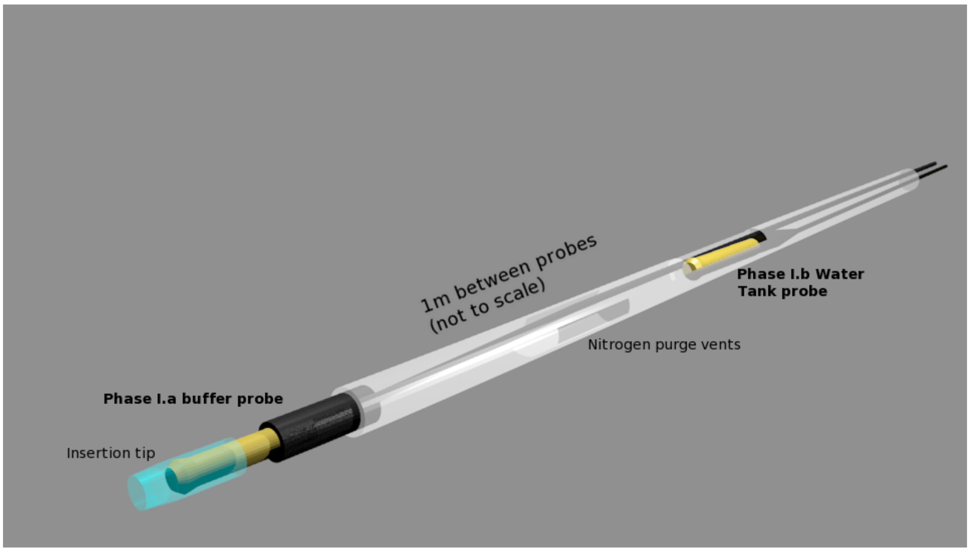

FIGURE 3.19: LTPS Phase I.a and I.b design conceptual rendering.

far ends of the tunnel, placed inside drilled holes in the rock on the tunnel floor. These are expected to give a good indication of the heat sink temperature, represented by the aquifer temperature at that location (∼6.5°C). Another sensor was also inserted in the runoff water in CR1 –however, this water temperature was seen to be affected by exterior fluctuations and warmed up to a certain degree, so it is not considered part of the main LTPS sensor suite.

Phase III. In order to document, with the same level of precision, the whole range of the

Cable length inside	Port	Angle	x	y	z	LQM#
4.86 m	S1	67.12°	0	244.9	580.4	3
4.63 m	S2	50.67°	0	399.3	487.3	4
7.6 m	S3	27.4±0.8°	0	564.2	280.1	1
12 m	S4	7°	0	625.3	76.78	1
14.65 m	S5	-26.3±0.7°	0	564.2	-280.1	2
19 m	S6	-50.67°	0	399.3	-487.3	3
20 m	S7	-71.0±0.7°	0	244.9	-580.4	2
4.85 m	N1	66.7±0.3°	0	-244.9	580.4	5
4.7 m	N2	51.8±1.0°	0	-399.3	487.3	5
7.6 m	N3	27.0±0.1°	0	-564.2	280.1	1
10.24 m	N4	10.5±0.2°	0	-625.3	76.78	4
14.3 m	N5	-25.9±0.4°	0	-564.2	-280.1	4
17.85 m	N6	-49.6±0.2°	0	-399.3	-487.3	3
19.9 m	N7	-67.8±1.1°	0	-244.9	-580.4	2

TABLE 3.2: Details and locations of the Phase I.a LTPS sensors. Angle is measured from the equatorial plane. Positions were reconstructed through the use of the ^{228}Th external calibration source from the campaign, and errors are quoted from the results of that study (excepting S1, S2, S4 and S6, where no source was inserted –here nominal positions are quoted)[149]. The X coordinate points through the geographical North Pole (long axis of Hall C) and Y towards the East, in cm. Phase I.b sensors are just ∼1 m shorter in length, approximately perpendicular to the local SSS surface.

temperature gradient inside Borexino, the top "ring" on the Water Tank dome had to be instrumented. The water level on the Tank does not reach the very top of the dome, and a blanket of a few centimeters of LAKN is kept flowing on that area. Therefore, the temperatures on that area will not be quite the same as if they were just extrapolated from the topmost Phase II.a sensors. To this end, the Phase III.a and III.b sensors were installed. Phase III.a consists of six sensors located under the insulation, next to the AGSS but not in contact with this system, in alternating sectors of Borexino's uppermost "ring" (see Figure 3.22). Additionally, 4 outlet and 2 inlet sensors are installed as part of the AGSS fluid handling system (one inlet and two outlet sensors for each half of the AGSS), but are not considered as part of the LTPS. Phase III.b consists of a single sensor inside CleanRoom-4 (CR4), under its recently-installed insulation layer and walking floor. Finally, Phase III.c is a set of several sensors located in contact with the exterior air, to provide a counterpart to the legacy (less precise and stable) thermometers in use before LTPS was in place.

3.2.2 Calibration

The calibration method for the probes went through several iteration cycles, as more information was gleaned with each subsequent installation phase. Their overarching objectives were, in this order:

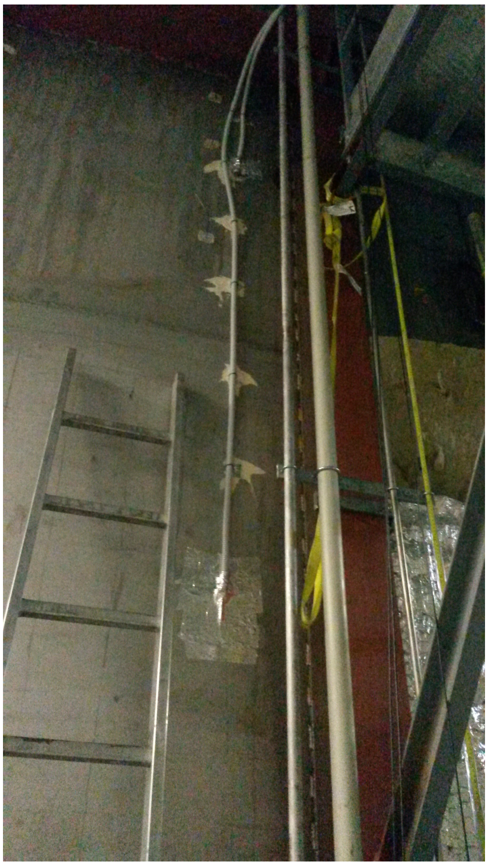

FIGURE 3.20: Phase II.a WT sensor final configuration after installation inside the bellowed guide PVC sheath, and affixed to the proper position on the wall by aluminized heat conductive tape. The 2 layers of the main TIS were installed on top of it shortly afterward.

1. Characterize the probes' behavior and detect eventual individual anomalous outputs.
2. Check the probes' short-term and long-term stability.
3. Converge on their relative precision through the addition of extra (individually-tailored) calibration correction coefficients: an offset term and –if necessary– a linear term.
4. Improve their advertised absolute precision, if possible, through the tuning of the correction factors to a reference temperature.

To sum up, we can divide the calibration of the Phase I (a+b) probes to fulfill these objectives, as follows:

1. *Characterization runs in air.* To familiarize ourselves with the probes' behavior, as well as to perform initial work in the DAQ software, we started by running them in air. Currents and low thermal inertia masked their full potential though, so this approach was soon abandoned.

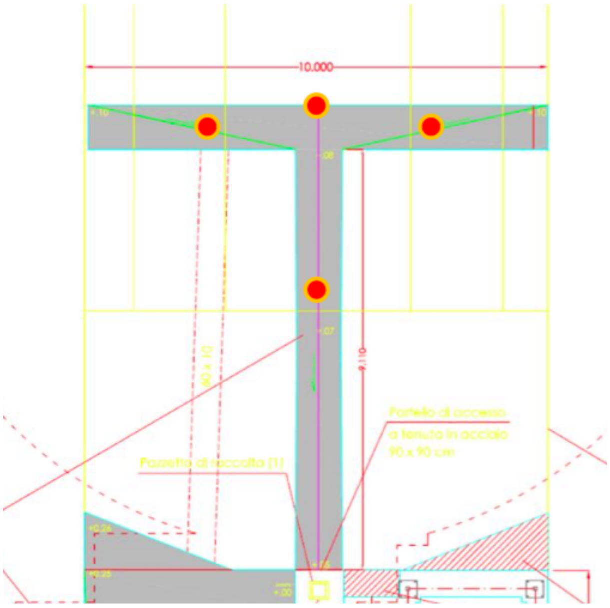

FIGURE 3.21: Schematic view of the ICARUS/SOX pit under Borexino and its interface with CR1 (lower side of the image), with the locations of the Phase II.b pit sensors marked. Also shown is the layout of the utility passage tunnel through where the probes' cables run (dashed red parallel straight lines on the left side of the drawing).

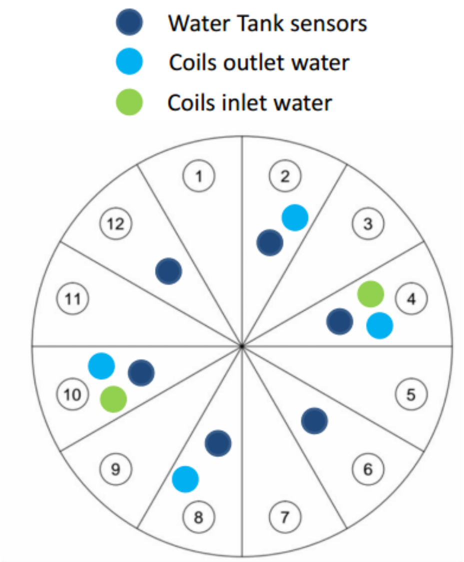

FIGURE 3.22: Schematic of the Phase III.a sensors in conjunction with the AGSS operation sensors.

2. *Absolute temperature bath calibration trials.* We tried to perform absolute calibration with fixed reference baths to check for absolute and relative stability. Fine-tuning for our range of temperatures in the detector (∼10-20°C) was challenging with this method, and we lacked high-precision equipment large enough to accommodate all of our probes and simultaneously mantain the reference temperatures (0°C and ambient temperature) stable enough. This method was only pursued with the first 4 probes, which nevertheless gave

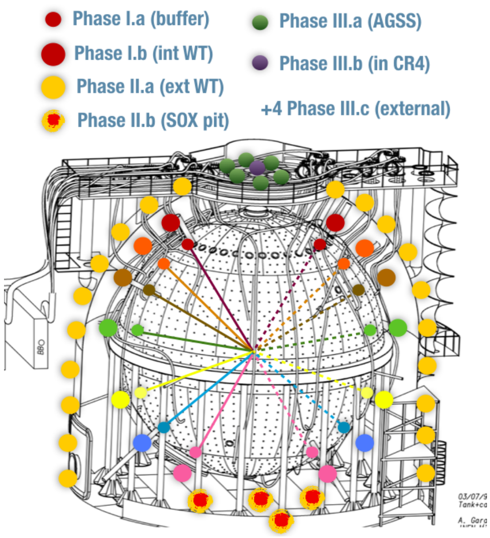

FIGURE 3.23: Conceptual design of LTPS sensor positions within Borexino. Although shown to lie on the same plane, Phase I and II sensors actually show some scatter around the ϕ=0 plane because of the re-entrant ports' actual positions and/or structures to be avoided, as for example the doors on the SSS or WT.

us a good handle on their behavior, and we verified a ~0.01°C short-term jitter (less than 1/5th of the legacy probes, see Figure 3.24), as well as ~0.05°C long-term stability or better.

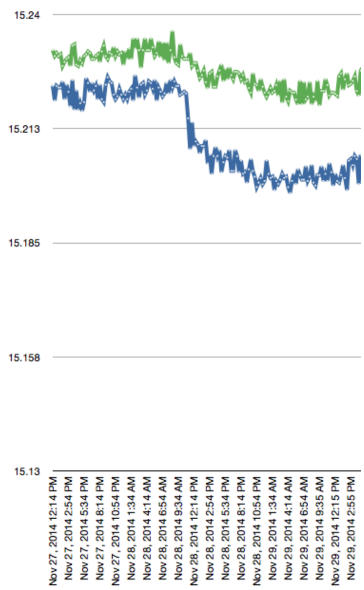

FIGURE 3.24: Jitter in LTPS probes - around 5x less than in legacy probes

3. *Absolute benchmarking + relative tweaking.* Using the recorded absolute temperature in the thermal bath all probes shared, as measured by an alcohol thermometer (assumed precision $\pm$0.1°C, although some drift was unavoidable when taking it out for reading) and

substracting it from the measured temperature in each probe, preliminary correction factors were calculated. Then, these corrections were applied on the measured temperatures inside each re-entrant port in Borexino.

Other analytical methods, such as finding the average temperature for a short acquisition run for each probe, and using the difference between this value and the "absolute" temperature from the alcohol thermometer as the correction factor, gave poorer results: it was observed that the top-bottom gradient in temperatures was the most-linear (as expected) and the difference between the North/South sides the smallest, when the former method was used (see Figure 3.26).

This result was not taken at face value, however. It was determined the benefits of performing a relative calibration between all sensors in a single point with an extremely stable temperature would be two-fold: on the one hand, it would validate the simple approach used in the absolute "benchmarking" strategy described above. Additionally, it could allow for better "tweaking" of the correction factors down to better accuracy. Regardless of the actual absolute temperature value (unknown to us), all sensors would read the same temperature when inserted in the same points of the same re-entrant port (chosen to be 2 m inside the water tank and in the bottom of the tube) within a few minutes of each other. Therefore, the correction factors determined in the thermal baths would show their convergence if they were indeed applicable to all conditions, and better precision could be achieved by slightly altering their value so that all probes converged towards a single point in a scatter plot showing "*Corrected bottom temperature* vs *Corrected WT temperature*".

The results of such a strategy can be seen in Figure 3.25, where the relative dispersion between sensors never surpasses $\sim\leq 0.04°C$, and is typically much less than that.

4. *Absolute water bath cross-checking.* Using a much more precise water bath, run at temperatures within the expected range inside Borexino, we were able to independently cross-check the correction factors to which we had arrived with the previous technique. Furthermore, a linear correction term was also added, which albeit small, provided improved precision in the measurements. This method was primarily employed for the Phase I.b sensors (WT probes), in conjunction with the relative "tweaking" described in the previous point. It was also performed for the Phase I.a sensors, but the results were equivalent or slightly worse, so the previous method's corrections were kept [150].

These calibrations yielded the result of a $\leq 0.04°C$ relative accuracy and a similar level of absolute precision. Slight (~ 0.01°C) harmonizing differences were introduced in the Phase I.a (outer buffer) probes after the Phase I.b (WT) sensors were installed, owing to the different calibration techniques employed.

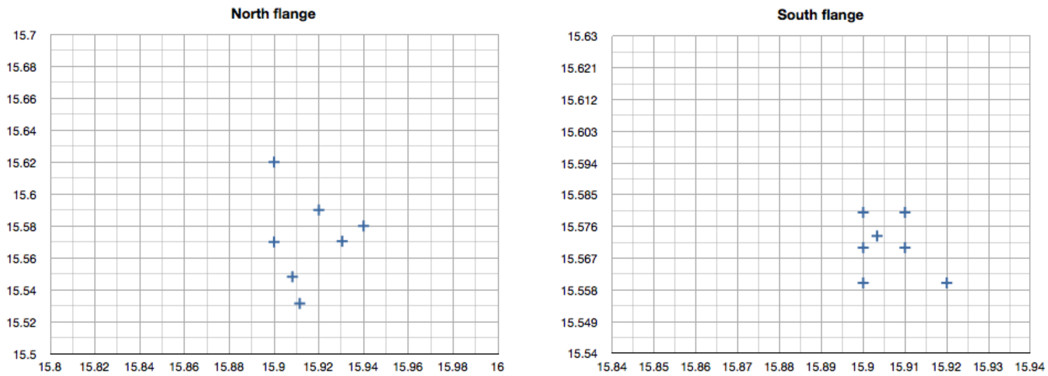

FIGURE 3.25: Scatter plot (corrected temperature 2m inside the WT vs corrected temperature at the bottom of a single re-entrant tube) used to "tweak" the offset corrections between probes in each side of the detector.

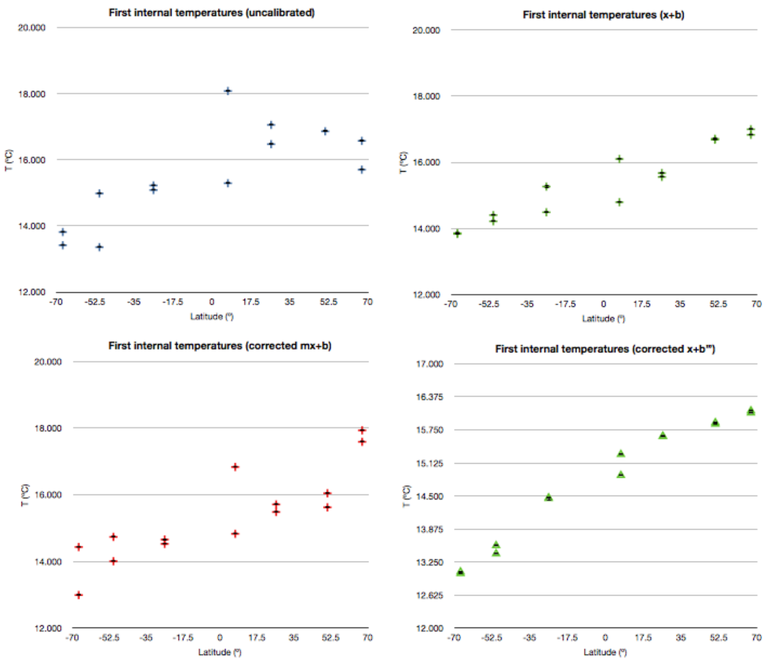

FIGURE 3.26: Effect of different correction analytical procedures in the measured gradient in Borexino: uncorrected (top left, blue); offset term from averaging (top right, dark green); linear and offset term from averaging and using 0°C and ambient temperatures (bottom left, red); offset term resulting from "true" vs measured temperature difference (bottom right, light green). There are two points per latitude (North/South). Notice the change in scale in the last plot, showing a much better convergence between sides, and an overall cleaner trend

The second Phase I.a calibration campaign meant a downtime of around 2 weeks (November 6th to November 19th) after start of data acquistion on the 29th of October 2014. Phase I.b insertion and calibration, coupled with two blackouts in January and March lost other combined 2 weeks of data. No major upset events ocurred during that time, according to the legacy thermometers, so the trend can be easily reconstructed.

After the deployment of Phase I, the remaining sensors for Phases II and III were understood to be well-characterized and their installation could be exempted from new calibration techniques –also because a new approach would have meant a recalibration of all probes following this updated strategy, which would introduce downtime in Phase I for little gain. Therefore, it was decided to use the correction factors mentioned above, together with a cross-calibration of a few old sensors with the new ones intended for Phase II. These would then be used to propagate the cross-calibration for later sensors, in conjunction with the absolute-temperature water bath technique. Although it is expected the precision to which these sensors' behavior is known would be worse, their peripheral position, subject to many more environmental perturbations from the surrounding air –even if shielded by the TIS in the case of Phase II.a– wouldn't make this issue so critical as for the internal ones.

Phase II.a sensor deployment occurred during the summer of 2015, when all the TIS was completed except for the final few meters of the dome (in fact, 9 out of 10 sensors were installed quite some time (a few months) before Phase II.a was deemed as complete with the final installation of its topmost sensor S0). Phase II.b went online, because of the need of a different cable routing than for the sensors on top of Borexino, a bit later than the sensors were physically installed in the pit.

Phase III sensors went online contemporarily to the AGSS installation, by the end of 2015/early 2016, depending on their exact position.

3.3 Data Acquisition (DAQ) software

Data readout coming from each of the probes, as explained in the preceding section 3.2.1, once converted by the SCB and the LQM from a raw voltage differential to a digital 16-bit integer raw signal, is sent to the low-level C++ DAQ software in charge of data handling.

This code is based on Vernier's `NGIO_DeviceCheck` simple acquisition program, already supplied with the probes when purchased. This code was modified in order to facilitate the readout from a USB hub instead of a single USB port, given the layout needed for the LTPS. It also allows for the addition of the correction factors empirically obtained from the calibrations, as well as the selection of the sampling rate and measurement time (typically set to a measurement every 30 minutes, and continuous measurement, respectively).

The acquisition system is built upon two *node* computers belonging to a subnetwork within Borexino's main underground network system. In particular, there are two main control machines: the main one for Phase I (a+b), Phase II.a and Phase III sensors, whose cable exit ports all arrive in the same general area around CR4 on top of Borexino. In addition, there is another machine in the support building's technical control room on the second floor, used for the Phase II.b sensors which, being inside the pit through CR1 on the ground floor, do not offer appropriate cable length to reach the main computer. When the system was being devised, it was favored to add a long-range USB extender to deliver the data to the main hub and computer on Borexino's top. However, for the distances involved, a powered extender would be needed, which presented its own set of problems, both in data quality and connectivity as well as cost considerations. For this reason, and to give a desired level of redundancy to the system, the option to install a second computer was finally implemented.

Once the signal is read out from the LQM through the USB hub with this code, data is stored in the *BxSlow* machine in the `bx_db` node, through a PSQL database (`temperatures`). This database can be queried for the desired sensors, for the desired amount of time, through the appropriate instruction – its output is typically transferred to a text file from where other analysis codes can read it. Currently, these queries are performed in *BxMaster*, and the resulting data is transferred to CNAF for analysis (typically ∼once a month), typically in monthly files containing all sensor input from the 29th of October, 2014 (start of data taking) to the end of the specified month –although data formatting is completely flexible. There are currently 5 sub-databases, roughly but not necessarily corresponding to the chronological LTPS "Phases" described in Section 3.2.1:

1. BxDetectorTemp (14 probes, Phase I.a)
2. BxDetectorWaterTemp (14 probes, Phase I.b)
3. BxWaterTankTemp (20 probes, Phase II.a)
4. BxIcarusPitTemp (6 probes, Phase II.b)
5. BxDetectorACTemp (15 probes, Phase III + AGSS inlet/outlet probes)

An online LabView visualization tool was also created for day-to-day monitoring, which queries the database directly through a machine located directly connected to *BxSlow*. This provides a one-stop view of the selected period of time for all probes (see Figure 3.27). A remote connection must be established with this server if the visualization tool cannot be accessed on-site.

Another visualization tool that also provides high-level analysis capability is the `TempViewer ROOT` macro. Located in the CNAF Borexino cluster, it reads the PSQL query text files when a specific "*monthYEAR*" combination is provided as input. It outputs a `ROOT`file consisting of –currently– three main tree structures, one for each LTPS Phase, where the history for each sensor is stored for the selected period, since the start of data taking (or whichever period the input file contains).

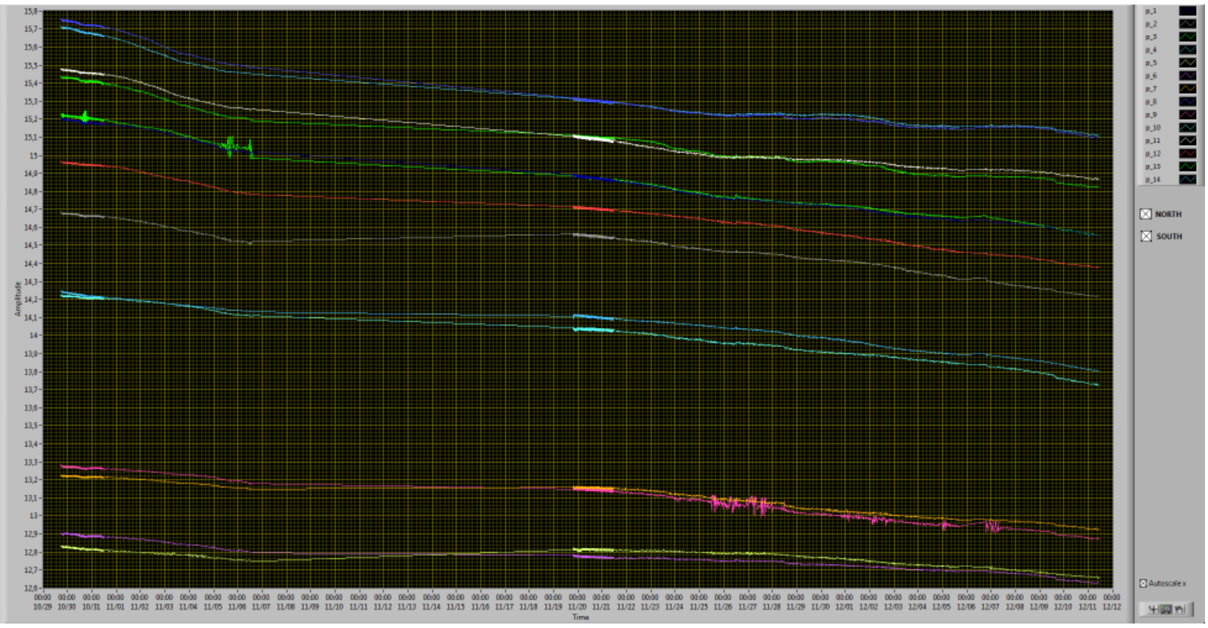

FIGURE 3.27: Screenshot of the LabView interactive visualization tool in the control room computer connected to *BxSlow*

There are 4 branches in the Phase I.a tree, but three of them (`Previous`, `Differences` and `SensorsS`) are used for internal calculations. The main branch containing the probes' temperatures –corrected for spurious (out of range) data– is `Sensors`, representing the Phase I.a sensors. The Phase II.b tree structure (`watertree`) contains the branch representing the Phase I.b sensors: `SensorsW`, and another one (`WTtree`) that represents the external WT sensors of Phase II.a: `SensorsWT`. In each of these branches, there are two leaves: *North* and *South*, which are 7-member vectors storing each latitudinal sensor in order (for example, *Sensors.North[0]* is Phase I.a probe at -67° on the Northern side of Borexino; *SensorsW.SouthW[6]* is Phase I.b probe at +67° on the Southern side of Borexino, etc). Finally, the time is stored in another leave stemming directly from each of the main trees. A folder diagram of the described structure can be seen in Figure 3.28.

In interactive mode, the macro also provides a few default visualization options:

- **Single-sensor history plotting** (Figure 3.29), when specifying the side (North/South) and latitude (7, $\pm$26, $\pm$ 50, $\pm$67), for the Phase I.a probes.
- **Side-by-side**: Phase I.a measurements on each side (North/South) separately, or all together (Figure 3.30).
- **"Slope check" mode** (Figure 3.31): all sensors are normalized to the same value at the start of data taking, and then color-coded plotted together to check their relative evolution.
- Phase I.a measurements together with the corresponding Phase I.b sensor measurements (when available), for **thermal transport** studies (Figure 3.32).

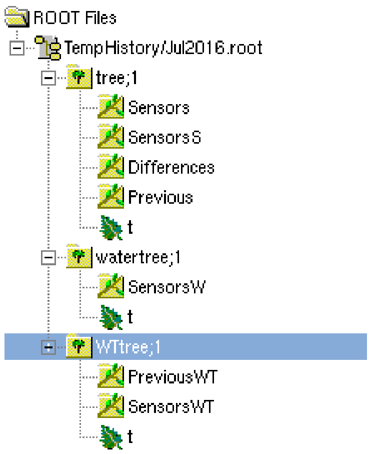

FIGURE 3.28: Structure in the ROOT file generated by the ***TempViewer*** macro.

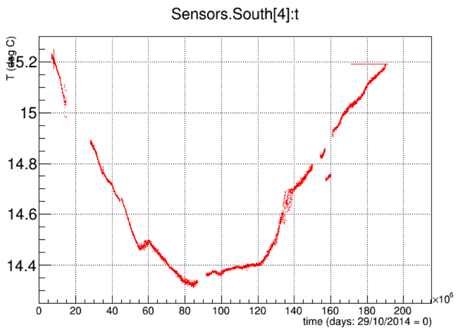

FIGURE 3.29: Visualization of single-sensor history (*Sensors.South[4]* = Probe from Phase I.a on southern side of Borexino at +50° latitude)

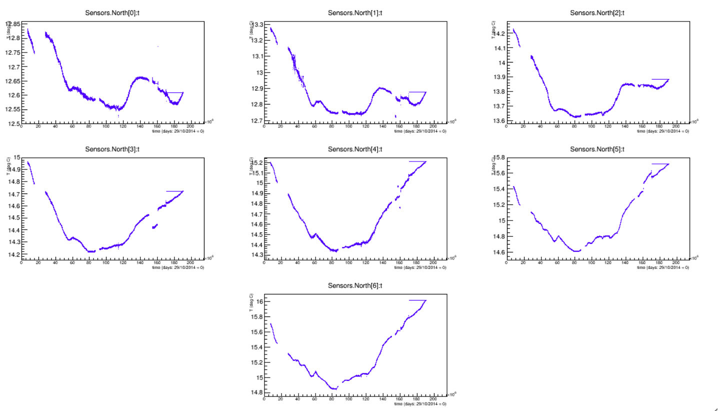

FIGURE 3.30: Visualization of multiple-sensor history (all Phase I.a probes on the Northern side of Borexino)

- Phase II.a WT wall sensor data.

Of course, since all data is stored in the ROOT tree described above, many other types of custom visualizations and analyses can be performed as desired.

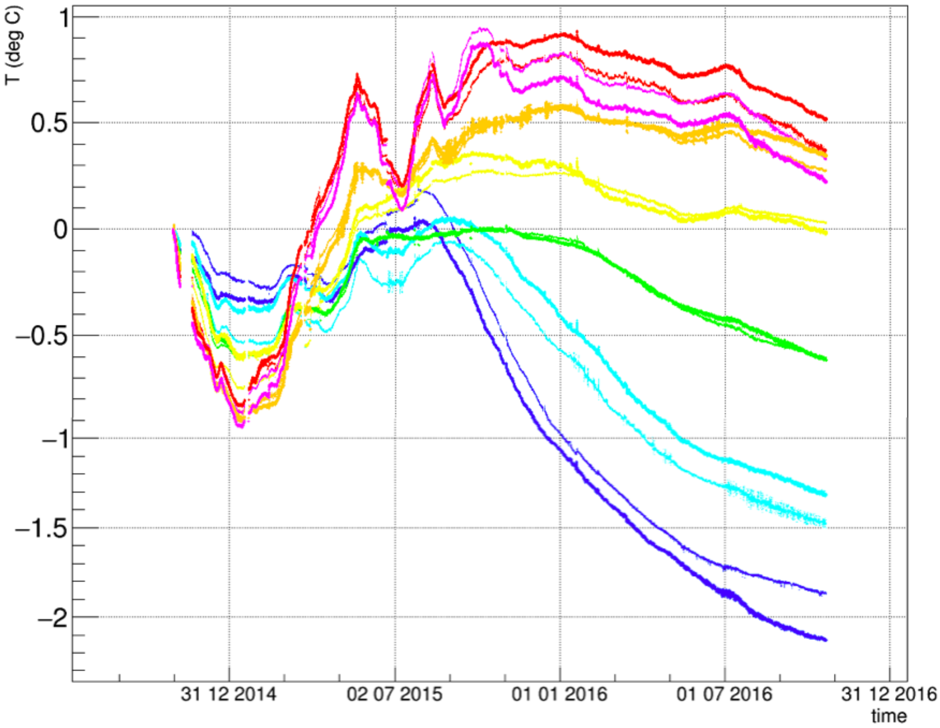

FIGURE 3.31: Visualization of relative temperature evolution for Phase I.a Outer Buffer sensors. Note the obvious stabilization effect of the water loop shutdown and TIS installation in late 2015-early 2016, and the start of global cooling by the summer 2016.

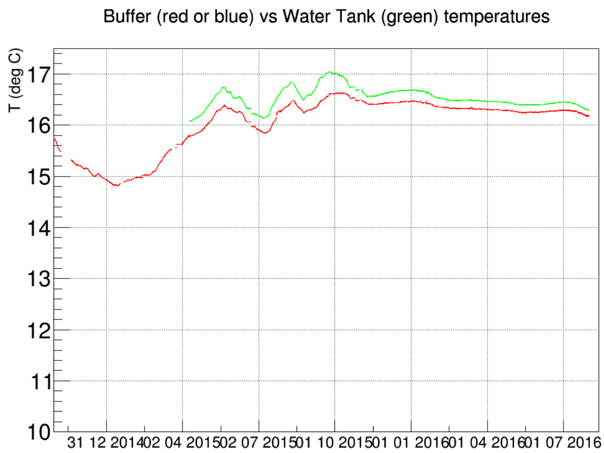

FIGURE 3.32: Visualization of paired Phase I.a and I.b single-latitude sensors

3.4 Dataset prior to thermal insulation and interpretation

3.4.1 Data breakout in periods and most relevant features

Data obtained so far can be divided into three main periods (see figure 3.34), with some sub-period features :

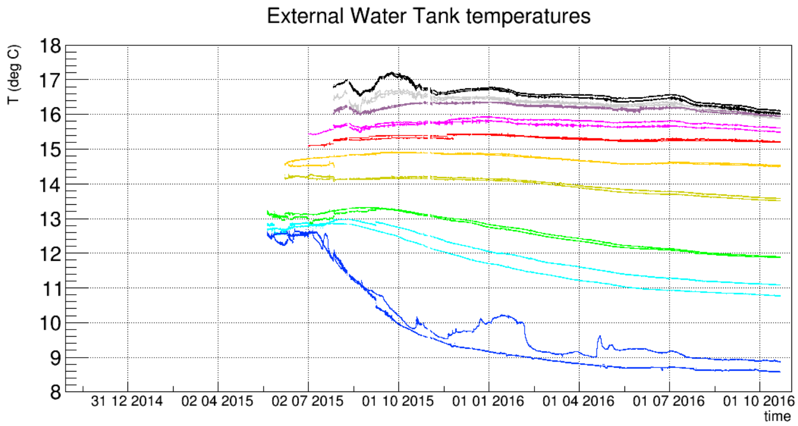

FIGURE 3.33: Visualization of Phase II.a WT wall sensors

- **Uninsulated period**, red hue. From the start of LTPS data taking on the 29th of October, 2014; until mid-January, 2015, a large (up to ∼ 1°C for the bottom of the sphere) **decrease in overall temperature**, but **also in top-bottom gradient** can be noted. About two-thirds into that period (centered around ∼New Year's 2015), a "spike" upset of ∼ 0.07°C, most noticeable in the bottom of the detector, but visible throughout, constitutes a relevant feature that breaks the trend during around 2 weeks. The overall temperature and gradient fall continues thereafter. Historical data from the legacy thermometers show us the minimum reached in overall temperature and gradient was probably the *lowest ever reached since the start of Borexino data taking* (∼ 2.2°C between the extreme instrumented latitudes: +67° and -67°).

  Starting in mid-January 2015, **temperatures stabilize** for a period of around a month (middle/end of February 2015). The bottom sees a moderate increase (∼ 0.15°C) while some areas of the top had already started to stabilize around the time of the "spike" event in the previous subperiod.

  Finally, since the beginning of March 2015 until late May 2015, a rapid increase in gradient is evident: the bottom sees a slight temperature increase (∼ 0.15°C), but the top sees almost half a degree of upwards change in less than 3 weeks.

- **Transient period**, yellow hue. This period covers the timeframe between the start of TIS installation (May 2015), including the water loop shutdown, until the achievement of complete TIS surface coverage (November 2015). It starts with a short (∼1-2 weeks) inertia period with the same behavior as in the precedent subperiod. Rapidly though, a noticeable decrease in overall temperature **and** gradient starts taking over. The TIS only covered a few portions (1-2 m) of the lowermost WT wall levels, and is not expected to have played a significant role on this behavior, except maybe for a slight contribution toward the cooldown of the lower half of the water in the OD, mixed through the still-operational water loop. Much more important was the drastic cooling of the topmost detector temperatures, with all probability due to environmental changes in the Hall.

This effect continued until early July 2015, when top temperatures started climbing again (possibly due to a seasonal effect and the stopping of Hall C air conditioning, combined) and the *water loop was shut down* (11:45 am CET on the 10th of July, 2015), allowing for the lower half of the WT to more stably stratify and transmit that condition to the PC. Water thermal inertia was overcome by this natural tendency about a month later as seen in the Inner Buffer Phase I.a sensors. Stratification and cooling from the bottom heatsink was immediately seen for the -67° Phase I.b and lower Phase II.a probes.

At about that time, when TIS coverage was around 50-60% during the technical stop, the top temperatures reached their new local maximum, and started declining with the start of the autumn. This lead to a small (0.2°C), ∼3 week reduction in the gradient, which would then dramatically rise to all-time heights until mid-summer 2016. During this subperiod, the TIS' influence was obvious in the lower half of Borexino, and a strong cooling effect on the bottom started appearing in the lowermost Phase I.a sensors.

To finish this second period, a time of newly-increasing top temperatures started in late August 2015, while the bottom cooling became established thanks to the die-down of the residual water loop currents. Progressively more stable conditions started showing, with approximately flat mid-detector temperatures, strong bottom cooling and predominantly increasing top temperatures, which tended to flatline with the finalization of TIS deployment.

- **Insulated period**, green hue, see Figure 3.36. As late autumn and winter settled in, Hall temperatures would be reaching their annual minima. TIS coverage ensured that this effect's amplitude got reduced, but an overall decrease in the slope the gradient was increasing with was evident (see Figure 3.35). In spite of this, the first ∼half-year of the fully-insulated period showed remarkable stability in all areas of the detector, except for the foreseen –and stabilizing in the long run– cooling of the detector's bottom with an approximately constant descending slope, whose magnitude was proportional to the latitude in the lower hemisphere.

  This situation lasted until early summer 2016, when new changes in the Laboratories' air conditioning system meant a cooler global air environment around the detector, which inevitably seeped under the TIS with time. This led to the rapid stabilization of the local gradient maximum around ∼5.2°C, and a subsequent dip downwards –more evident on the North side of Borexino, since the air conditioning ducts exhaust on that side. This was the first such decrease in gradient since the second subperiod in the Transient phase, and marked the end of a ∼1-year-long monotonically-increasing trend in gradient. The shutdown of the Lab's extra air conditioning units showed a tiny rebound in the gradient, which nevertheless would need AGSS operation to keep its upward trend, since the bottom temperatures were starting to level off.

Indeed, we can subdivide this *Insulated* period into a *Stable* subperiod, when the stratification increased or kept constant by the increase/level-off of the top temperatures and the consistent decrease in bottom temperatures; and a *Cooldown* subperiod, when the gradient started to decrease due to the combined effect of the continued decrease in bottom temperatures (although starting to level off) and the marked decrease in top temperatures due to seasonal environmental effects and the lack of AGSS operation.

It is expected this period will transition to a new *Stratified* period, where the AGSS will keep the top temperatures near the seasonal maximum (∼16.5-17°C) and the leveling-off of the SSS' bottom temperatures will reach the plateau, as the lower water in the WT is showing as of this writing. This should create a stable stratification with maximized gradient and minimal vertical fluid movement.

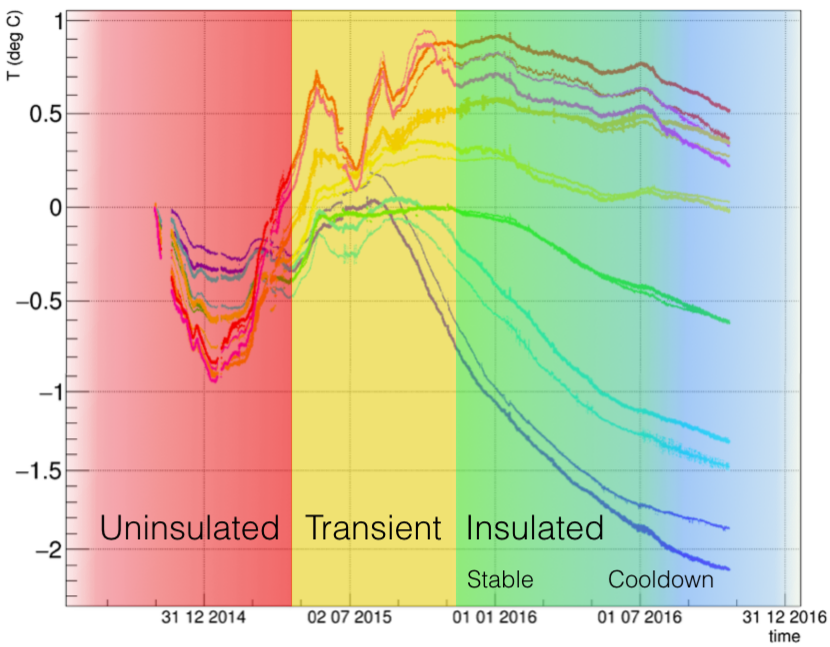

FIGURE 3.34: Main periods in the October 29th, 2014 to October 21st, 2016 LTPS data-taking.

3.4.2 Interpretations: gradient, North/South asymmetry and thermal inertia between outside/inside of the SSS

The most intriguing feature, and that with the most interest for the thermal stability of the detector, is the **top-bottom gradient** obtained from the difference between the topmost and bottom-most probes (see figure 3.35). The gradient's historical decrease to about 2.2°C, coupled with the sudden increase of ~ 1°C in 2 months can easily be observed.

Interestingly, in most of the LTPS's instrumented period, there appears to be a consistent $+\sim 0.05$°C difference between the South and North sides, respectively – which would mean the gradient is slightly stronger in the South side, closer to the Hall C's doors and the electronics rooms. However, the middle third of the *uninsulated* period (around 50 days before the "spike" event and bottoming out of the gradient) shows an inversion in that trend. The effect is within the sensors' jitter and just inside their relative accuracy, so it is believed to be significant.

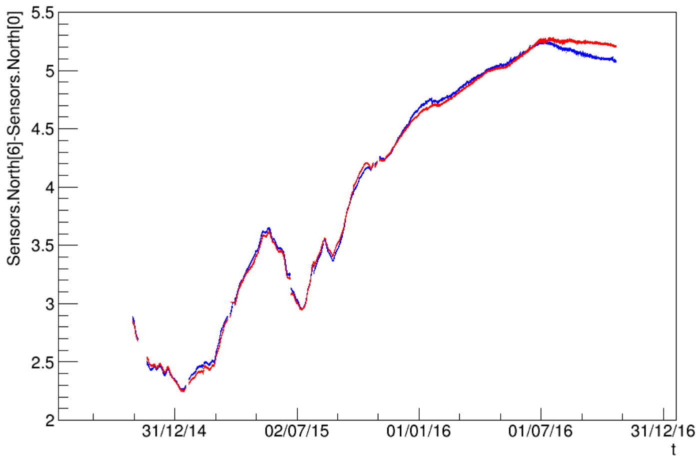

FIGURE 3.35: Gradient evolution ($T_{+67°}$–$T_{-67°}$) in Borexino. The blue curve indicates the North side, while the red curve indicates the South side. Note the largest asymmetry occurs beginning in the summer 2016, due mostly to diverging cooling profiles on the bottom of the WT.

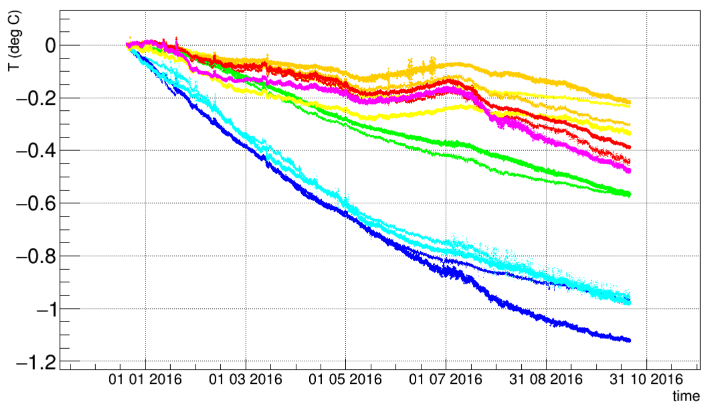

FIGURE 3.36: Differential temperature change in the various Phase I.a sensors since the end of TIS installation in November 2015 until mid-October 2016. Notice the divergent trends in the bottom sensors (-67°) mentioned in the previous figure.

Since the LTPS is a symmetrical system organized in the two main meridians of Borexino's SSS, a direct comparison between the temperatures shown by the North and South sensors at the same latitude should indicate whether temperature transients are directional within Hall C (with a 180° resolution). As seen in figure 3.37, **there doesn't appear to be directionality involved**, within the error associated with the calibration of the probes ($\pm$0.04°C, as quoted in the calibration section 3.2.2).

A constant positive shift of $\sim 0.15 - 0.2$**°C** appears to exist, however, between the North and South sides around the equatorial plane (+7° latitude, dark green in figure 3.37), although the general trend is similar to the rest of the sensors. After months of puzzlement, since this did not appear to correlate with exterior conditions, a re-evaluation of the re-entrant port positions with external source calibration data was performed[149], which showed their nominal positions in engineering drawings were not precise. In fact, as can be noticed in Table 3.2, the difference in latitude between the Northern and Southern nearly-equatorial sensors reach >3°. Being the N4 sensor the one located more upward, it is now clear the reason why it would show a higher temperature. Incidentally, this gave a blind verification that the Phase I.a cross-calibration campaign was extremely precise, being able to showcase this ~0.2°C effect.

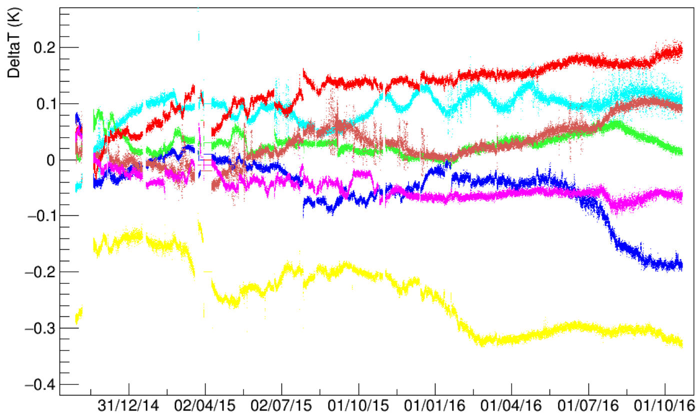

FIGURE 3.37: Historical temperature differences between North and South Phase I.a sensors (red=-67°, yellow=-50°, light green=-26°, dark green=7°, light blue=26°, dark blue=50°, purple=67°)

Evidence for **low thermal inertia** has been pervasive throughout all the temperature data available. The Phase I.b probes bring an even more accurate picture thanks to the several upset events visible in the bottom probes. Already apparent by eye, a "Higgs potential-like" fit (see Equation 3.6) shows a robust delay between the similar features seen in the Outer Buffer probes and those a meter distant, in the Water Tank:

$$\Phi = \alpha(x - x_0)^4 + \beta(x - x_0)^2 + ax + \Phi_0 \tag{3.6}$$

(where the effect of the formula's coefficients within our range of interest are: α "closes" or "opens" the main parabola, β increments the central "bump", a skews one relative minimum over the other and x_0 determines the position of the central local maximum).

Fits were performed fixing the 5 parameters to empirically-determined bounds, and allowing for dithering around these "reasonable" values. Once MINUIT found the best minimization, the parameters were left free one by one, which generally improved the fit both in χ^2 and visual agreement.

While the feature is not sharp enough to allow an extremely well-defined fit, results ranging from 0.3 to 0.6 days in delay from the external to the internal sensors are consistent in all cases (see, for example, Figures 3.38, 3.39 and 3.40). Study from other, more difficult to fit features, such as the sharp peak in the top sensors in July 2015, support this result, with perhaps slightly larger results (on the order of ∼1 day).

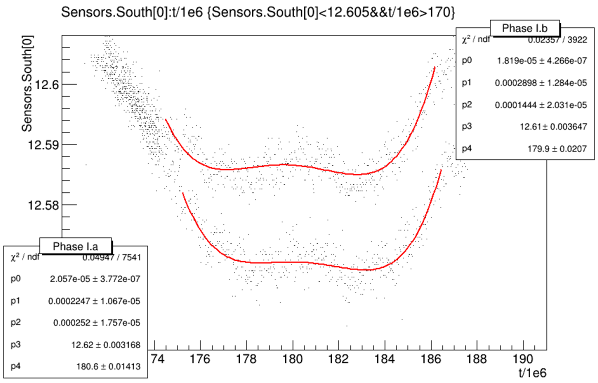

FIGURE 3.38: Phase I.a and I.b -67° South probes showing the slight upset event in April 2015, fitted to a quartic function. p_4 shows the position of the central local maximum, which yields a displacement of ∼0.7 days between probes

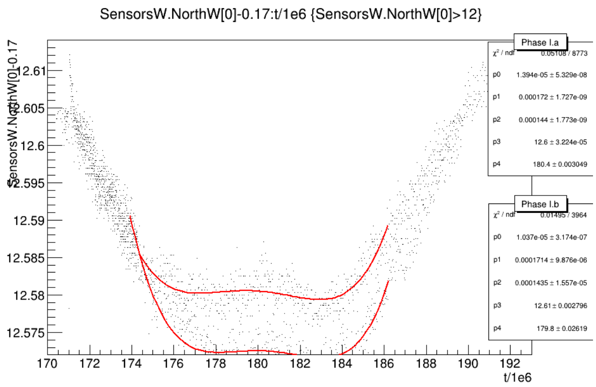

FIGURE 3.39: Same situation but with Northern probes, which yield a displacement of ∼0.6 days between probes

We can then establish an upper limit of ∼18-24 h/m for the transmission of thermal perturbations through the SSS, from the water into the scintillator, consistent with previous estimates[151], but setting a much tighter limit.

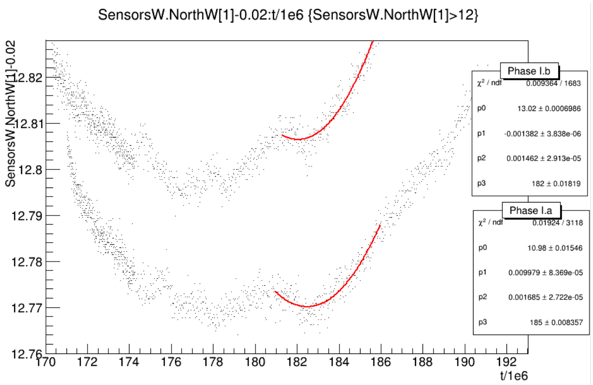

FIGURE 3.40: Same situation but with Northern -50° probes, which yield a displacement of ∼0.5 days between probes when the local minimum is fitted with a quadratic equation $p_2(x-p_3)^2 + p_1 x + p_0$ (note in this situation p_3 does not show the local minimum's position by itself)

3.4.3 Interplay with background levels analyses

No temperature inversions in the buffer (temperature on a lower latitude being higher than that in a higher latitude) are noted throughout the data taking period, as can be seen in Figure 3.41, where temperature differences between consecutive (in latitude) probes are shown). Therefore, we can disfavor a mechanism by which PC located higher up somehow becomes cooler than PC located further down (not necessarily inverting the whole IV's gradient, just causing a local temperature imbalance) and forces a mixing movement between two close-lying latitudes.

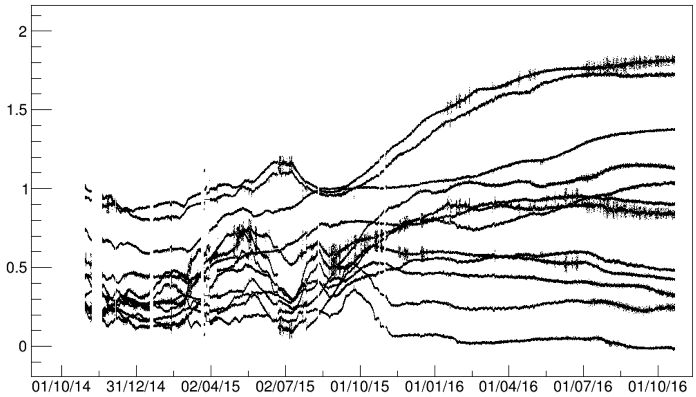

FIGURE 3.41: Temperature differences between couples of probes with neighboring latitudes. No local inversions which could potentially lead to local convective areas are noted, although a worrying very reduced difference between the topmost sensors (at 67° and 50°) started to appear in recently.

From the historical on-axis temperature probes, we know the temperature started to fall around July 2014 until, as noted, mid-January 2015, when it reached the all-time low in absolute and gradient terms. It is then reasonable to consider this decrease in temperature as the cause for the migration of the clean scintillator vertically across the FV. Since we have seen thermal inertia is low, we cannot consider the central scintillator to retain warmer temperatures for longer.

However, the weakening of the gradient seen during this time can invigorate small currents that were already present (the magnitude of the ones transporting the "clean blob" would be $\sim\leq 10$ cm/day).

Another clear feature is the coincidence between the end of the uninsulated period (stabilization of all temperatures and small gradient upturn) with the fall in overall ^{210}Po countrate, coincident with the disappearance of the "clean blob" by mixing with underlying polonium.

Finally, the sharp upturn in the countrate on the top roughly coincides with the sharp increase in gradient marked by the onset of the *Transient* period, while the overall ^{210}Po levels are falling, as expected from the more stable situation caused by the 1°C increase in gradient.

Finally, increasing gradient levels and stabilization of stratified temperatures due to the aforementioned effects of the large-scale bottom cooling and upper regions roughly maintaining their elevated temperatures achieved during the Transient period, showed a very positive effect in the overall background mixing situation, vindicating the decision to install the TIS (see next Section). A small "recirculation" (more rigorously, elevated ^{210}Po levels) on the bottom of the IV is believed to be caused by the cooling down of the liquids in that area, motivating some kind of fluid movement from the periphery of the IV toward the FV. The top two thirds of the volume see a gradual, radially-symmetric decrease in polonium, getting close to the constant bismuth pedestal of ∼20 cpd/100tonnes.

3.5 Thermal Insulation System (TIS)

The thermal insulation system consists of a double layer of mineral wool material (Ultimate Tech Roll 2.0 - *Isover*) that covers the full surface of the Water Tank, to a depth of 20 cm. It has an extremely low thermal conductivity value of ∼0.03-0.04 W/m·K in our thermal region of interest (7-20°C), as can be seen in Table 3.3. The exterior layer features a reflective aluminized film reinforced with an internal fiber glass grid, as well as a metallic wire mesh netting on the outside face (Ultimate Protect Wired Mat 4.0 Aluminized Isover, see Table 3.4 and Figure 3.42). 20-cm long metallic anchors were epoxyed (Foster 85-75, see Figure 3.43) on the WT walls in order to support this insulating material, with a surface density of $\sim 5/\mathrm{m}^2$. The full surface that was insulated is 1000 m^2, including the major "organ pipes" through which the PMT cables enter the tank towards Borexino's interior. Additionally, ∼430 m^2 of I-beam were also insulated on their external face, albeit with just the 10-cm thick Aluminized Isover rolls.

Two distinct insulation installation phases were performed, for budgetary and bureaucratic reasons. The first phase saw the insulation of most of the cylindrical section of the tank from the bottom up, with some parts of the dome. Most of the I-beams were left uninsulated, with

FIGURE 3.42: Mineral wool Ultimate Protect Wired Mat 4.0 Aluminized Isover, used as the outermost 20-cm layer of Borexino's TIS. A similar 20-cm layer, without the aluminized finish, was employed between this material and Borexino's external surfaces.

FIGURE 3.43: TIS layers anchors epoxyed to the WT walls.

their red external faces protruding in between wall insulation sections (see Figure 3.44). By summer 2015, most of this work was completed except for some areas with difficult access. All work on this first phase was finished by September 11th, 2015 (see a view of the TIS reach at that point in Figure 3.45).

FIGURE 3.44: Installation operations during the first period of TIS installation: work was focused on the cylindrical part of the WT walls, and most of the I-beams surfaces were left exposed.

FIGURE 3.45: View of Borexino's top at the end of the first phase of TIS installation: some insulation was applied on the dome, but more easily-accessible areas were prioritized until a new batch of material needed to be ordered for continuing.

Attainment of thermal stability in the detector was apparent since the very first lower layers were installed, but nevertheless the TIS installation was closely monitored, with the option of stopping it at any time, in order to avoid transient instabilities that may have compromised the metastable stratification already achieved, as well as other possible subtler effects. No such upsets were noted, as can be seen in Figure 3.34, and the second part of the insulation progressed much quicker: from November 4th to December 9th, 2015. This second phase saw the complete insulation of the remaining bulk WT walls, all the I-beams and the 3 first organ pipes (see Figures 3.46 and Figure 3.47). As will be noted in the next Section 3.6, the Active Gradient Stabilization System's water coils and temperature sensors was also implemented under the insulating layers on the uppermost "ring" in parallel with TIS installation. Of course, in parallel to the TIS installation, LTPS Phase II.a and III.a (see Section 3.2) probes deployment was performed. Finally, in September-October 2016, the floor of CR4 and the remaining (upper) sections of the organ pipes which still remained exposed were insulated as well, completely covering the surfaces of Borexino's WT in contact with the exterior air of Hall C.

It should be noted the insulation of the topmost part of the tank was quite technically challenging, requiring rappelling workers to perform the work. Furthermore, at the time of TIS conceptual definition, the fear of a global runaway detector cooling was deemed as a very distinct possibility which could shrink the natural thermal gradient between top and bottom of the detector by several degrees. If this were to happen, because of an extremely efficient insulation and a larger-than-expected thermal sink effect from the contact with the foundations on the rock at the bottom, **larger** instabilities could occur as a consequence of the TIS installation, rather than the sought stabilization effect. For this reason, a maxed-out AGSS concept was put forward, whereupon a large "tent" structure around the top of the detector would contain

FIGURE 3.46: Detail of an insulated I-beam. Only a 20-cm layer of the aluminized insulation was used for these, as the heat transfer area is much smaller..

FIGURE 3.47: Borexino's top fully insulated, including I-beams, organ pipes and other structural elements deemed of importance to heat transfer.

recirculating heating air that would forcibly keep the top water/scintillator volumes at higher temperatures than the cold, insulated lower volumes. The outcome of this design was evidently more dynamical and subject to more uncertainties than a simple "imperfect" (understood as possessing a certain degree of thermal leaks over long periods of time) TIS, in combination with an AGSS to be used only as a safeguard rather than a necessity. Fortunately, further analysis and simulations (see Chapter 4), as well as the empirical proof attained every time the TIS gained in height, showed that these concerns were exaggerated and the system would keep a good stratification with a very long global cooling time constant.

Indeed, for illustrative purposes, a naïve calculation can show the cooling time constant of an ideally-insulated detector (i.e., with adiabatic walls that let no external air influence seep in, and is therefore only constrained by the heat losses through the bottom). Although simplified, this calculation represents a worst-case scenario of global, irreversible cooling, since convection will not play an important role when the lowermost fluids are stratified – therefore, a conduction-only scenario is a very good approximation to this case, where only along-structure faster heat transport (through walls, legs...) may induce some small deviations by causing small, localized convection. However, this should only cause localized "cold finger" structures, that also have been shown to be of no or little concern (see Chapter 4).

Taking the nominal ρ_{H_2O}=1000 kg/m^3; C$_{H_2O}$=4186 J/(kg·K) and ρ_{scint}=870 kg/m^3; C$_{scint}$=1723 J/(kg·K), and considering we get a mass of 280 tonnes (IV) + 1040 tonnes (OV) = 1320 tonnes of scintillator, as well as 2100 tonnes of water in the WT, we can estimate the total detector's heat capacity as:

$$1.32 \cdot 10^6 kg \cdot 1723 \frac{J}{kg \cdot K} = 2.27 \cdot 10^9 J/K \tag{3.7}$$

$$2.1 \cdot 10^6 kg \cdot 4186 \frac{J}{kg \cdot K} = 8.8 \cdot 10^9 J/K \tag{3.8}$$

$$C_{BX}^{total} = 11.1 \cdot 10^9 J/K \tag{3.9}$$

From empirical analysis[152] using the lowermost Phase II.a (and -67° I.a) sensors showing an approximately-linear temperature drop, and extrapolating these trends to isothermal volumes at the same corresponding heights, the worst-case heat loss (since the data points were chosen at the beginning of the fully-insulated phase, when the inner fluids are still warm, and furthermore at the start of winter) through the bottom heat sink can be estimated at ∼<250 W = 250 J/s = 7.9·10^9 J/year. More realistic estimates are to be shown in Chapter 4, but this provides a useful upper limit.

According to this simple study, we can conclude that the very conservative maximum global cooling rate in the detector is 7.9·10^9 J/year / 11.1·10^9 J/K, that is τ_{cool} <0.7 K/year. This cooling would, in any case, be regionally-concentrated in the lowermost areas of the WT, increasing stratification and stability in the beginning. Only slowly would this front start moving up into the areas of interest around the FV, after several years. This scenario, as disclaimed above, is neglecting any thermal drive coming through the thermal insulation around the WT walls which, as we shall see later, is actually not negligible –and indeed may globally overwhelm bottom cooling.

Characteristics	**Value**	**Units**	**Standard Norm**
Fire class	A1	-	EN 13501-1
Maximum service temperature (under 500 Pa)	300	°C	EN 14706
Maximum service temperature (under 250 Pa)	360	°C	EN 14706
Air flow resistivity	10	kPa·s/m^2	EN 29053
Acoustic absorption	0.81	α_w	EN ISO 11654
Thermal conductivity λ_D (at 10°C)	0.033	W/m·K	EN 12667
Thermal conductivity λ_D (at 50°C)	0.040	W/m·K	EN 12667
Thermal conductivity λ_D (at 100°C)	0.050	W/m·K	EN 12667
Thermal conductivity λ_D (at 300°C)	0.121	W/m·K	EN 12667

Table 3.3: Technical specifications for the TIS thermal insulation material Ultimate Tech Roll 2.0 (Isover), adapted from [153].

Characteristics	**Value**	**Units**	**Standard Norm**
Fire class	A1	-	EN 13501-1
Maximum service temperature (under 500 Pa)	600	°C	EN 14706
Air flow resistivity	48	kPa·s/m^2	EN 29053
Acoustic absorption	1	α_w	EN ISO 11654
Thermal conductivity λ_D (at 10°C)	0.030	W/m·K	EN 12667
Thermal conductivity λ_D (at 50°C)	0.035	W/m·K	EN 12667
Thermal conductivity λ_D (at 100°C)	0.040	W/m·K	EN 12667
Thermal conductivity λ_D (at 600°C)	0.170	W/m·K	EN 12667

Table 3.4: Technical specifications for the TIS thermal insulation material Ultimate Protect Wired Mat 4.0 Aluminized Isover, adapted from [153].

3.6 Active Gradient Stabilization System (AGSS)

The Active Gradient Stabilization System (AGSS) was conceptualized in order to avoid possible transient or long-term effects that could negatively affect fluid stability through the maximization of a positive thermal gradient between the top and the bottom, as well as the minimization of external disturbances coming into the ID's fluid. In that sense, as explained in Section 3.5, different-scale concepts were put forward, until a final design was chosen for final installation (but its activation was set as contingent on a necessity, rather than by default, stemming from a decreasing thermal gradient).

This design (see Figure 3.48) consists of two independent sectors of a ∼18m-long, 14mm-OD copper serpentine water loop, connected to a 3 m^3/h centrifugally-pumped, 3 kW water heater thanks to a multilayered transfer pipe and a 12 input/output manifold. The system also includes an expansion tank, a temperature controller for the heater and a mass flowmeter to manually adjust the flow (see Figure 3.52). Furthermore, the serpentine coils are maximally-bonded to the subjacent WT dome thanks to copper anchors and a layer of aluminized tape (see Figures 3.50 and 3.51) to ensure directional heat transfer toward the bottom of the heat exchanger assembly.

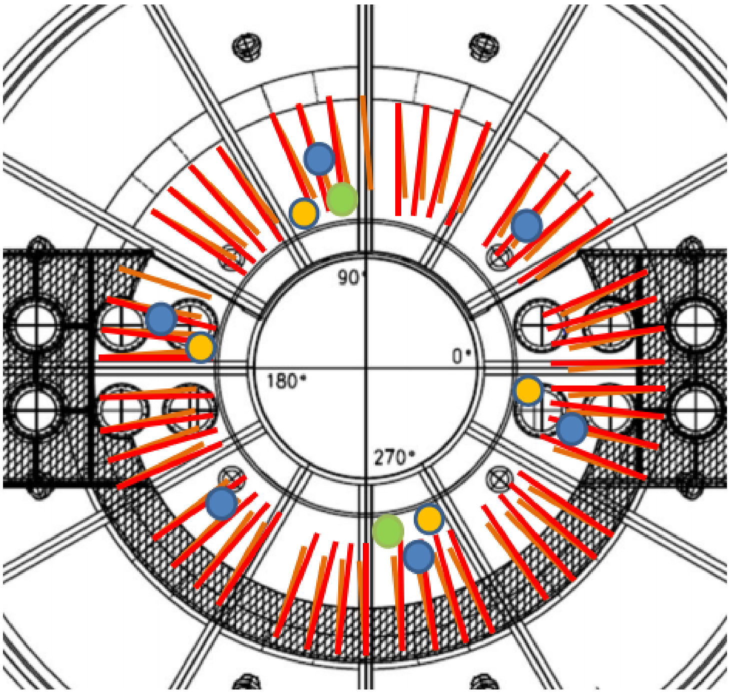

FIGURE 3.48: AGSS schematic view, looking down on the top of Borexino's dome. Marked as blue dots are the Phase III.a dome "crown" sensors (see Figure 3.49), to monitor the top water temperature. Yellow and green dots mark the AGSS-specific temperature sensors located in the circuit's reading ports, to monitor outlet (4 probes) and inlet (2 probes) temperatures, respectively. Inlet sensors are less since the initial water temperature is coming from a single source and precisely controlled from the heater/pump assembly.

As is apparent, the serpentine's inlet is located on each sector's serpentine, and the coolest serpentine water is drained through the outlet located at the lowermost positions. This, as is evident, ensures the heat transfer is kept maximal at the top of the WT, and is kept constant or reduced toward the bottom –thus avoiding temperature inversions in the water and the appearance of potentially harmful currents. Nevertheless, even a constant-temperature water throughout the whole serpentine is expected to provide detector stabilization, since the surface covered by the AGSS is quite small compared to the WT's dome, and it would provide an "anchor" effect on the topmost fluid.

A *Slow Control* system with National Instruments' LabView software was implemented with the data readout from 12 thermocouple precision temperature probes, in conjunction with the mass flowmeter, pressure and flow switches readouts.

As of this writing, the start-up of the AGSS is foreseen for the beginning of November 2016, since the overall gradient has started to visibly decrease (see Figure 3.35), potentially inducing a less stable fluidodynamical situation.

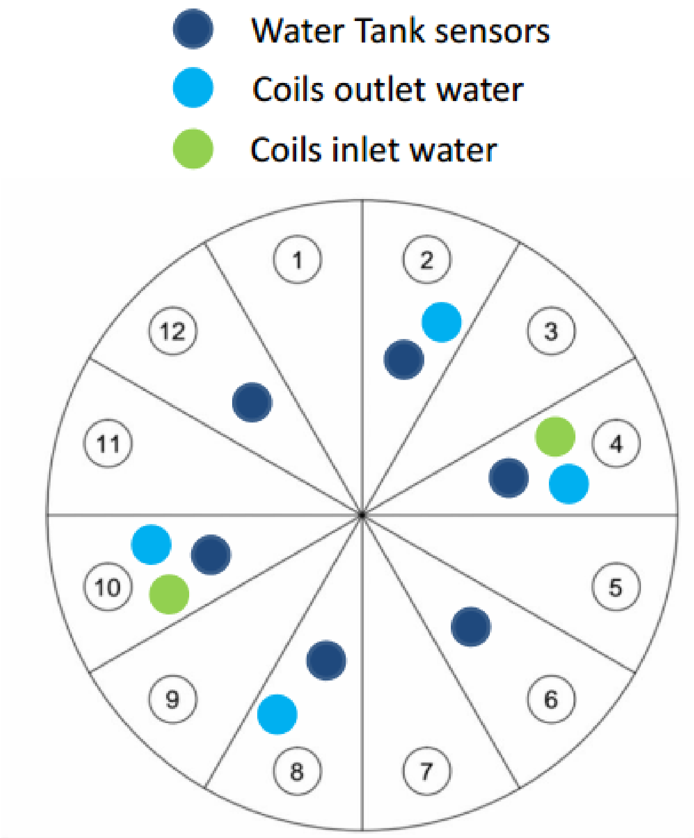

FIGURE 3.49: Detail of one of the six Phase III.a dome crown LTPS sensors affixed to the exterior of the WT wall with aluminized thermally conductive tape, and guided to its position by a semirigid bellowed PVC tube.

FIGURE 3.50: A sector of the AGSS water loop serpentine just after installation on the WT dome wall.

FIGURE 3.51: A sector of the AGSS serpentines after bonding to the WT wall and being taped over with aluminized tape for heat transfer directionality optimization. This was the final configuration before being covered by the TIS.

FIGURE 3.52: AGSS core equipment. Except for the two serpentine loops on Borexino's upper WT walls around CR4 and the computers controlling the flow, the system is fully contained in this picture. Visible are the expansion tank (top, red), the manifold with the flowmeters leading to the loops (left), the water heater (lower center silver/red cylinder), the centrifugal pump (between the manifold and the heater), the electrical panel (right) and the pressure gauge (under expansion tank).

Chapter 4

Fluidodynamical simulations for Borexino

4.1 CFD for Borexino's background stability

While the strategy to install Borexino's Temperature Monitoring and Management System (BTMMS) was seemingly successful, a proper understanding of the fluidodynamical environment stemming from foreseeable thermal developments in the regions of interest inside Borexino (namely the IV, especially in its centermost areas constituting the nominal FV) was deemed mandatory. Furthermore, it would enable to elucidate the future directives for the operation of the AGSS and provide an important reference for ensuring the highest stability achievable in background shifting.

For these reasons, the *ANSYS*® `FLUENT`^{TM} (v. 16 and 17)[154] Computational Fluid Dynamics (CFD) simulation package was employed, as well as the computing resources from Milan Polytechnical University's CFDLab in the Energy Engineering Department in Bovisa. The simulation strategy would not be rooted on just principles, but would attempt to use the real, high-fidelity data gathered during more than a year (at the start of the simulation effort) through the LTPS.

As a first step, the simulations only employed **conduction** inside the detector, to rapidly establish general information and lower limits on the heat transmission throughout the detector –since convection will only increase it, while imposing a prohibitive computational time cost for the purposes of faithfully simulating the whole detector at the required regimes and faster-than-reality timeframes.

Benchmarking **convective** simulations were then implemented to try to gain an understanding on the limitations and performance of the analysis package with well-referenced, scholastic cases.

These were implemented in a qualitative fashion at first, to establish general operating principles that would apply to Borexino's case, to then go on to more quantitative results that fully addressed the reproducibility of experimental results, near the regime of Borexino's operation, in FLUENT^{TM}.

Detector-specific convective models were then used to ascertain the behavior of the detector model itself, since the regimes FLUENT^{TM} is optimized for are not necessarily ours, and certainly a multi-month simulation with minute changes in the temperature/velocity fields in an isolated system, even if simplified, is not within the tried-and-true expertise of either the package itself or its technical experts. In this sense, several scenarios were devised to progressively gain confidence and anchor points on the best parameters for the operation of the simulation, to then move on to cases more founded in reality. Gradually, these provided positive results on the understanding of the **thermal transport behavior** of the simulation and its correspondence with reality.

Finally, a restricted case of an ideally-shaped spherical Inner Volume with a realistically-imposed temperature field, set on its outer boundary, was developed. This temperature field was propagated to the IV through simulation from the LPTS Phase I sensor positions, taking their recorded historical data as reference, to then minimize the complexity of a model focusing on the fluid movement in the area we are interested in (FV) and its immediate environment.

4.2 Bi-dimensional conduction models

The 2D model used in these simulations includes the following structural elements:

- Water Tank (steel, 1 cm thick, 16.9 m high, 18 m OD)
- SSS (steel, 8 mm thick, 13.7 m OD)
- North / South leg (steel, 14.3 mm thick, 32.4 cm OD, water-filled)
- Equatorial platform (steel, 1 mm[1])
- Inner and Outer Vessels (nylon, 150 μm thick)
- Bottom steel plates (steel, 10+4 cm)
- Concrete under base, on the sides of the plates (14 cm)

[1]This unrealistic thickness was chosen because of the grilled nature of the platform: even though the actual thickness is ~2 cm, the porosity is estimated at ~90%

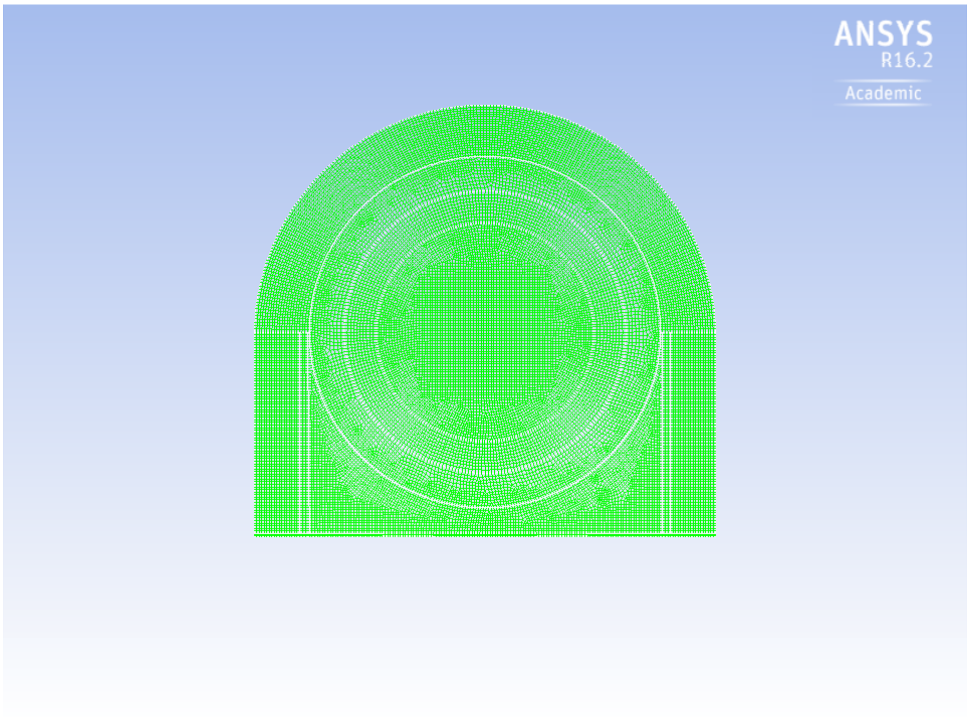

FIGURE 4.1: Mesh used for the bi-dimensional simulations.

The Water Tank is filled with water and the SSS with pseudocumene (PC). The model only extends until 14 cm under the base of the water tank, where the steel plates end. An imposed temperature boundary condition is implemented on that base (at -14 cm). We made no further assumptions on the rock temperature or influence of the Icarus/SOX pit because the LTPS Phase II.b sensors are installed on the pit's ceiling, and it was difficult to determine how to accurately model a cylindrically-asymmetric pit on a 2D model. We considered the AGSS to be a fixed-temperature section 2.1 m long at the appropriate height around the 6th ring, without modeling the actual system's tubes.

The mesh is based on 10-cm side square cells on the bottom half of the water tank, transitioning to radial on the spherical dome and interior of the SSS. To avoid inaccuracies and instabilities in the center of the detector, we established a rectangular cell pattern again in the detector center, causing a transition around 3 m (see Figure 4.1 for a graphical depiction).

Another caveat worth noting is that the structural elements are *just barriers* that have zero physical thickness. That is, they are not modeled with cells, as doing so would generate an asymmetry between the structure's cell size (∼mm) and the bulk's cell size (10 cm). Therefore, the listed "thickness" only provides a measure of the *resistance* of that barrier to thermal transport, but not a medium through which to transport heat. In 3D, there is the possibility of using the "shell-conductive" tool, which allows for thermal transport along these boundary elements without actually creating cells for them. It is emphasized that, in these 2D models, *there is no heat transport along the structural elements.*

Next, the model was subdivided in a series of 15 different "domains", according to the height separations established by the positions of the LTPS's Phase I.a (OB), Phase I.b (WT) and Phase II.a (WT wall) sensors. Furthermore, these domains were divided between *North* and *South* sides (and, if applicable, *Center* for the volume inside the SSS). A list of the domains' limits is shown in Table 4.1.

Domain	R_1(m)	R_0(m)	h_0(m)
D1	5.60	0.00	14.6
D2	7.10	3.58	13.6
D3	7.80	4.00	12.7
D4	8.45	6.60	11.2
D5	9.10	5.60	10.7
D6	8.80	6.80	8.7
D7	9.22	6.80	6.6
D8	9.22	5.60	5.05
D9	9.22	6.60	4.6
D10	9.22	4.00	3
D11	9.22	2.94	2.1
D12	9.22	2.45	1.1
D13	9.22	2.45	0.55
D14	9.22	0.00	0.1
D15	9.22	0.00	0

TABLE 4.1: Domain limits: h_0 is the bottom height of one domain, and consequently the top height of the next one. D1's top height is Borexino's height of 16.9 m. R_0's and R_1's sign is positive as shown for the North domains, and negative for the South domains.

The reason for using the position of the sensors for establishing these domains is simple: we only know the temperatures in some discrete points. We can interpolate linearly between them to get the temperature in any point in between, assuming a smooth behavior. The discontinuity between domains is left to happen at roughly the position of the SSS to avoid unphysical rough areas in the center of the detector, whose behavior is more important for us. When possible, the domains vertices were made to coincide with the position of a sensor, so as to impose its initialization temperature directly. In cases when a sensor wasn't available at that position, or there were two sensors in close proximity to a single vertex, an average of the two closest sensors was assigned to that domain vertex.

Later, the interpolation functions 4.1 and 4.2 were used in each domain to give an initialization temperature for each point in the model. T_i, with i=1,2,3,4, are the sensor-derived temperatures imposed at each domain's vertices, as shown in figure 4.2, and A is the rectangle's area (height x width). The temperatures were taken from the recorded data on the 20th of December 2015,

FIGURE 4.2: Arrangement of temperature point naming convention for South and Center domains. North domains show a mirror image arrangement, with T_1 and T_2 on the right, and conversely T_3 and T_4 on the left. If the domain was a "Center" one, R_1=-R_0

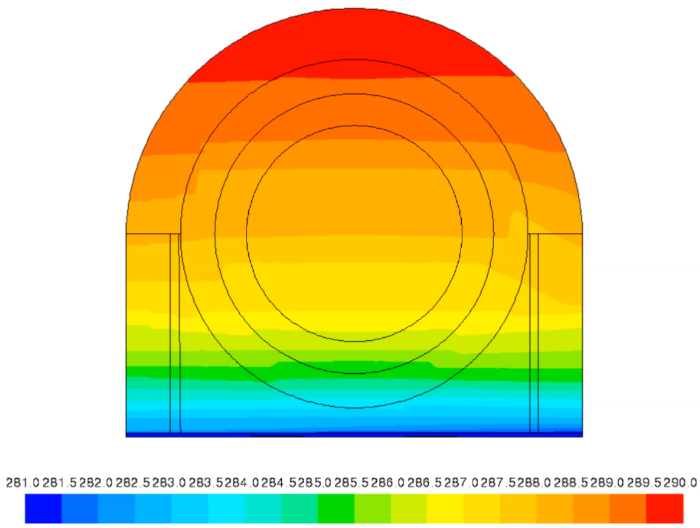

FIGURE 4.3: Initialized temperature profile in the Borexino 2D conduction model with the 2015/12/20 temperatures and the interpolation method described above.

since that period offers at least ∼1 month of both prior and subsequent thermal stability, and is wholly within the fully insulated phase of Borexino's lifetime.

$$T^{N/S}(x,y) = \frac{1}{A}\big[(\Delta T(R_1)|x-|x_0|| + \Delta T(R_0)|x-|x_1||)y + \\ +|x-|x_0||(T_1y_1 - T_2y_0) + |x-|x_1||(T_4y_1 - T_3y_0)\big] \tag{4.1}$$

$$T^C(x,y) = \frac{||x|-R_0|}{A}\left[(\Delta T^S(R_0) + \Delta T^N(R_0))y + (T_4^S + T_1^N)y_1 - (T_3^S + T_2^N)y_0\right] \tag{4.2}$$

The result of the initialization is shown in Figure 4.3.

It is evident that the biggest gradation in temperature occurs at the bottom half of the detector, changing from the ∼8°C at the bottom to ∼14.5°C around the equator. The stratification is, generally, much less defined in the top half, although ever present. Also we accurately modeled the North/South asymmetry of the water temperatures, where the North side has a much sharper gradient around the equator than the South side, which keeps the discontinuity between the temperature distribution inside and outside the SSS at the Sphere itself, avoiding unphysical jumps in the scintillator Inner Volume. It is worth noting that, for the most part, these carefully-modeled irregularities disappear after a few days of our idealized simulation, so they are not of critical importance for this stage. With this setup, we imposed several different boundary conditions for the system's evolution:

4.2.1 Adiabatic walls

Setup

The simplest scenario we considered was that of an **adiabatic outer detector wall**, with a set "rock" temperature of 8°C on the bottom. Although physically impossible, it provides us with a zeroth-order scenario where the **exterior air provides negligible power transmission to the WT**, either because the insulation is perfect or because the air near the tank closely matches the temperature distribution in the water inside.

Being the simplest, we also took advantage of this model to check the influence of the mesh size on the results, making a variant with ∼cm-size cells. **No differences** were observed in the simulated timeframe of 120 days.

Results

As expected, the major phenomenon is a **global cooling** of the detector through its bottom. More interestingly, although not unexpected, is the fact that the cooling "creeps up" from the center of the detector (see Figure 4.4), creating a lenticular-shaped feature in the gradient and transferring progressively colder areas towards the bottom of the Sphere, while keeping a practically-horizontal stratification on the outside edges of the WT. Inversely, the cooling is faster on the edges of the WT on the top part, leaving the top of the sphere at roughly the same temperature as the top of the WT, while a difference of ∼1°C exists between that topmost area of scintillator and the water at the same height.

A simple calculation was performed already in December 2015 showing an approximate upper limit for the cooling constant[152] of 0.3°C/year through the bottom, supposing a year-round constant 8°C heat sink, which would imply 110 W of lost power in a steady-state condition. Our result showcases a large power loss of ∼630 W over the bottom, that follows an exponentially

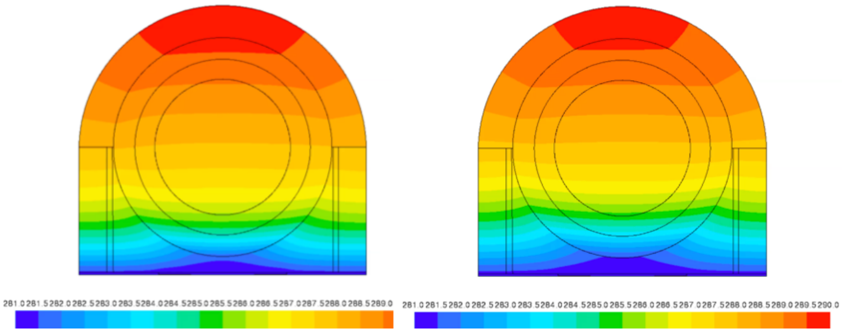

FIGURE 4.4: Temperature evolution of the adiabatic-wall scenario after 365 (right) and 120 days (left). As explained in the text, a noticeable "lenticular" bottom/top stratification is evident.

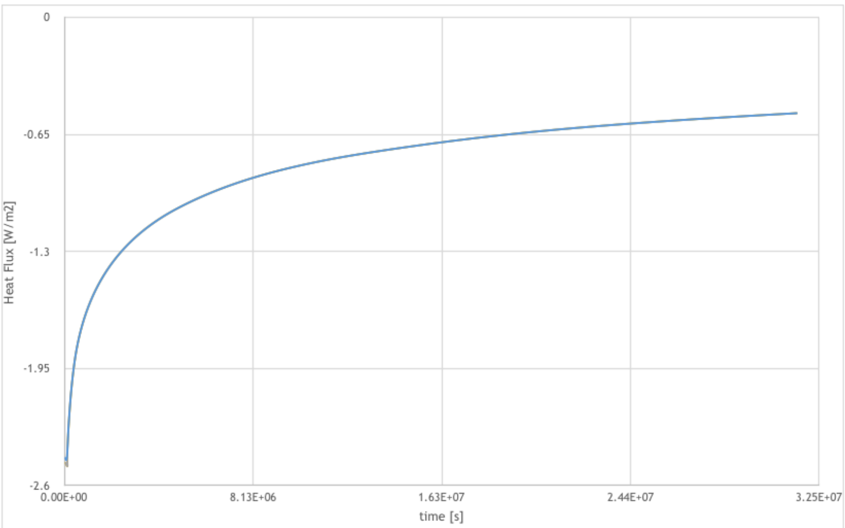

FIGURE 4.5: Behavior of the power loss through the bottom (and therefore for the full detector) for the fully adiabatic walls case. X-axis is read in seconds and Y-axis in W/m^2. After ~3 months, the power loss stabilizes at less than 1 W/m^2, and reaches an approximately constant 0.5-0.6 W/m^2 after around half a year, with an approximately linear decrease in the absolute value of the lost power of ~0.05 W/m^2/month.

decreasing power loss with a slight linear component. It decreases to ~300 W after a month and stabilizes around **140-200 W** after 100 days (see Figure 4.5).

4.2.2 Adiabatic walls, AGSS on

Setup

As a modification of the previous scenario, we applied a very conservative activation of the AGSS, keeping the temperature on the 6th ring as it was at the initialization instant (17°C). The adiabatic condition holds for the rest of the non-heated walls. From the previous result, it is clear this won't create a large change in the overall behavior, since the top didn't see a large

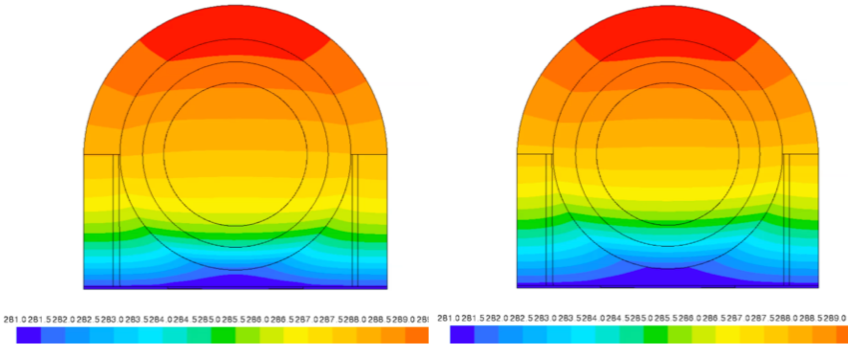

FIGURE 4.6: Temperature evolution of the adiabatic-wall scenario after 365 (right) and 120 days (left) with AGSS on at 17°C. No significant difference in the bottom half of the detector is evident, although a clear effect on the top temperature distribution is visible.

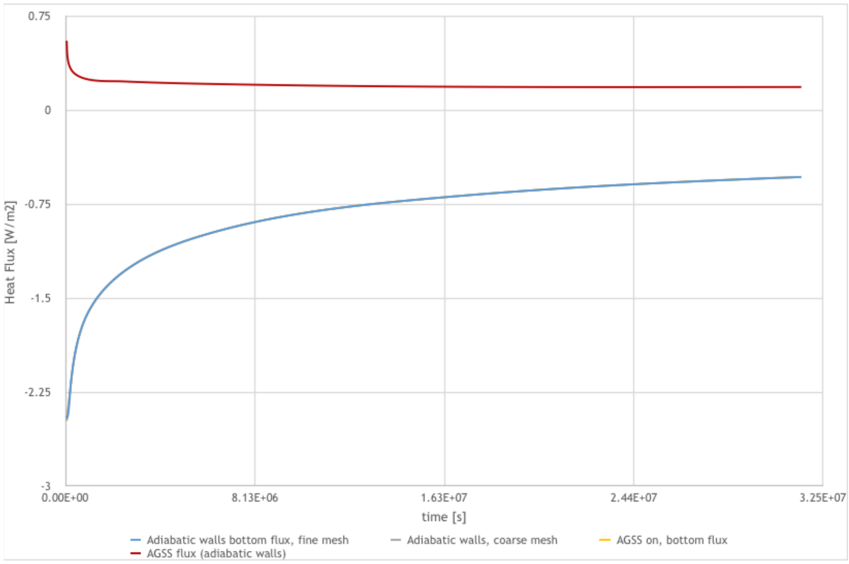

FIGURE 4.7: Power loss evolution for the partially adiabatic walls case with AGSS on at 17°C. X-axis is read in seconds and Y-axis in W/m^2. Power loss through the bottom is superimposed with the fully-adiabatic case (light blue and grey, with the coarser and finer meshes respectively). Power gain though the AGSS is the green curve on the top.

change in temperature. The overall temperature structure remains roughly the same as in the above case, but the higher-temperature areas occupy a larger volume than in the preceding case.

Results

The overall effect in the power loss through the bottom is negligible, and the actual heat input through the top is an extremely small $\sim$0.2 W/m^2 (with just a few days of a $\sim$>0.5 W/m^2 transient), as seen in Figure 4.7. Of course, the actual 3D effect will be multiplied by a different factor than the bottom (smaller by $\sim$15% for the AGSS power), since the surface area of the bottom is $\sim$250 m^2 and the AGSS occupies an area of $\sim$60 m^2. This is seen clearly in Figure 4.13, where each specific power transmission is multiplied by Borexino's real surface for each particular area (*walls*: 1000 m^2, *AGSS*: $\sim$60 m^2 and *base*: 250 m^2) to show the total estimated power.

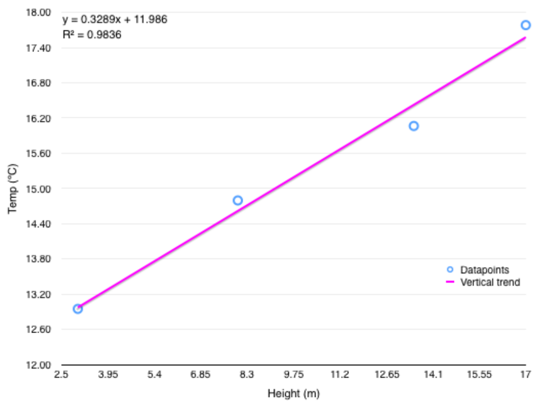

FIGURE 4.8: External air gradient modelization for the realistically-insulated WT walls.

4.2.3 Non-adiabatic walls, constant external air gradient

Setup

Next, we implemented a more realistic condition for the wall insulation which would be closer to the implemented TIS. We neglected the effect of the steel wall, since its contribution to the insulation is very small and in this conductive-only scenario we can't simulate the effect of the heat flow along the steel, and considered the WT wall to be made exclusively of the 20-cm-thick rock wool (κ=0.034 W/m/K and h=7.5). Outside, we established a linear gradient (see Figure 4.8), constrained by 4 values taken by the LTPS Phase III.c external temperature sensors and the TE-3 to TE-8 legacy external sensors. AGSS was kept off.

Results

The effect of the external temperature was to **"anchor" the gradient** along the walls, impeding the rise of the "cold front" seen in the bottom part of the fully-adiabatic case (see Figure 4.9). The hottest volume around the top also was stabilized and its effect grew in a similar way to the effect of the AGSS with adiabatic walls. Of course, this modelization does not include convection, which would increase the thermal flux in this case. For that reason, this is just a **lower limit** on the power transmission along the walls, as opposed to the bottom transmission, which is expected to be mainly dominated by conduction.

The power loss through the bottom was affected this time, although only by a small amount. The exponential behavior with a small linear component was seen again, and coincided with the adiabatic case in the steepest part, up to $\sim$3 months. Later, the lost power was slightly larger by $\sim$1 W/m^2 (see Figure 4.10). The power gained through the walls was approximately linear with a slight positive slope in time, although the contribution remained at the few-watt level.

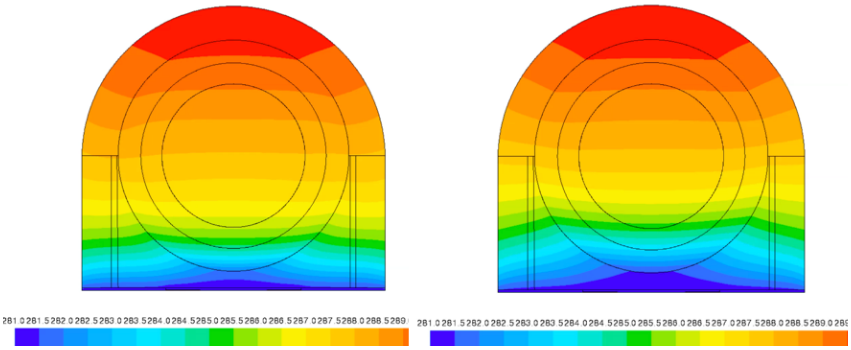

FIGURE 4.9: Modelization for the realistically-insulated WT walls and a constant linear external air gradient.

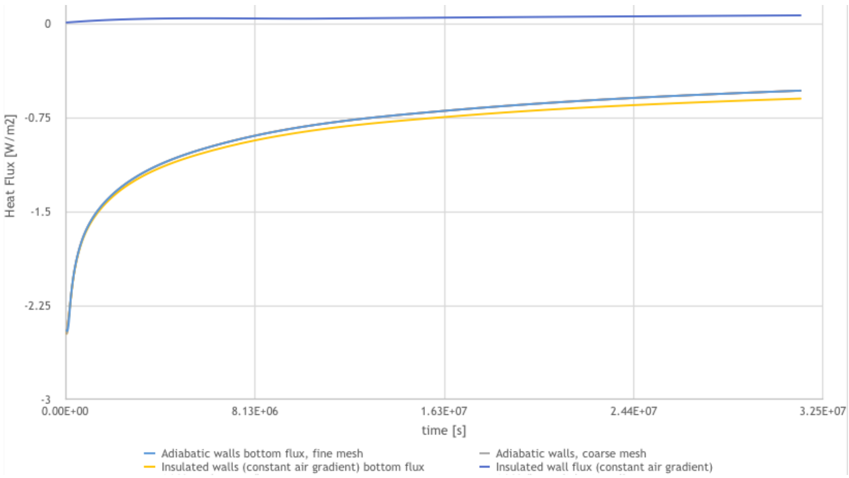

FIGURE 4.10: Power exchange through walls (>0) and base (<0) for a realistically-insulated scenario, compared to the adiabatic (with or without heating) case.

4.2.4 Non-adiabatic walls, seasonally-varying external air gradient

Setup

Finally, we modeled a very simplified simulation of an external air gradient that changed seasonally following a sinusoidal, as an idealized approximation to the actual temperature changes in Hall C. The chosen oscillation had an **amplitude of ± 2.5°C** and a period of, obviously, one year (see equation 4.3). We did not include at first a gradation of the sinusoidal effect with height, meaning that the **seasonal variation in temperatures was as strong in the bottom as in the top**. This is clearly not the case, and the bottom air temperature is much more stable than the top's. Therefore, even though the heat transmission through the walls only takes into account conduction and is consequently a lower limit estimate, the actual temperature variation along the walls is a *very conservative* scenario.

$$T_{\text{inf}}(t) = 273 + \left[11.986 + 0.32789y - 2.5 \cos \left(\frac{2\pi t[s]}{31536000} \right) \right] [K] \tag{4.3}$$

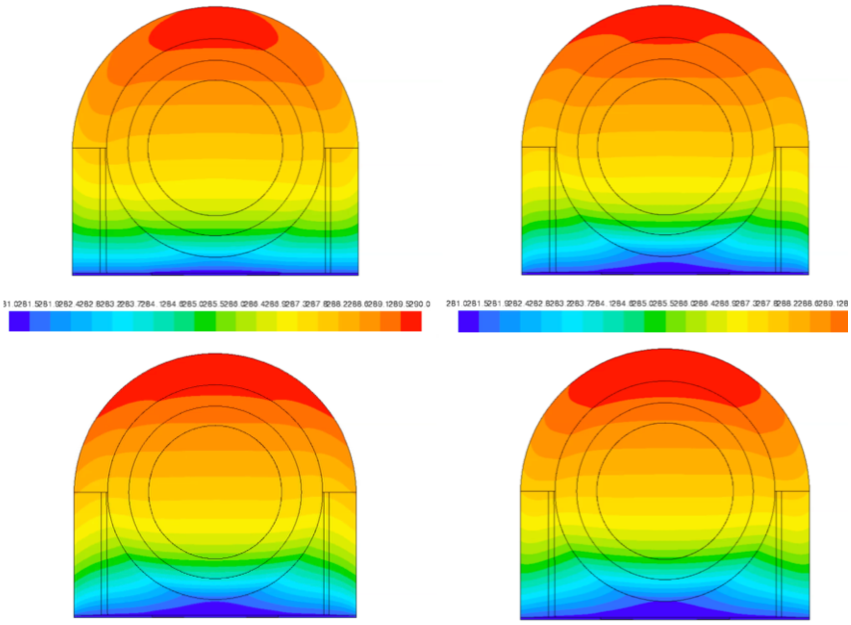

FIGURE 4.11: Modelization for the realistically-insulated WT walls and a sinusoidally-varying linear external air gradient (equation 4.3). Upper left inset is 3 months after the start of the simulation (∼May), upper right is after 6 months (∼August), lower left is after 9 months (∼November) and lower right is after a year (February).

Results

The model's behavior is illustrated in Figure 4.11's series of screenshots after 3, 6, 9 and 12 months.

The transmitted power (see Figure 4.12) dwarfs that obtained through the previous model, although at least half of that amount is expected to be a very conservative simplification.

However, even halving the effect shows a very large influence of the external air *variations* (rather than the air gradient itself) in the detector's temperature. Furthermore, based on the Phase I.a vs Phase I.b LTPS sensor data, we see that the temperature transmission across the sphere happens quite fast (∼0.5-1 day)(see [155]'s Figure 21 and 22, in agreement with empirical LTPS Phase I.a-to-b transmission studies), which presumably means that convection likely plays an important role on the redistribution of these changing temperatures in the ID, since we cannot see large changes inside the Sphere in this simplified conduction-only model.

4.2.5 Non-adiabatic walls, realistic seasonally-varying external air gradient

Setup

As a means of checking the influence of the gradient on the above result, we added a **height dependence on the sinusoidal variation** (multiplying the last summing term in equation 4.3

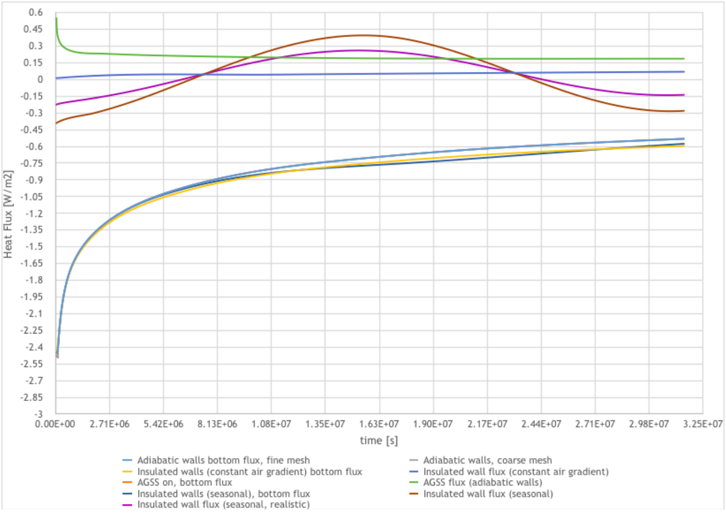

FIGURE 4.12: Specific power (W/m^2) transmission modelization for the realistically-insulated WT walls and a sinusoidally-varying linear external air gradient (equation 4.3), with and without a linear weight in height for the oscillation. The difference in the bottom flux is small compared to the static air gradient case (see yellow and dark blue curves) while the power variation through the walls is very important.

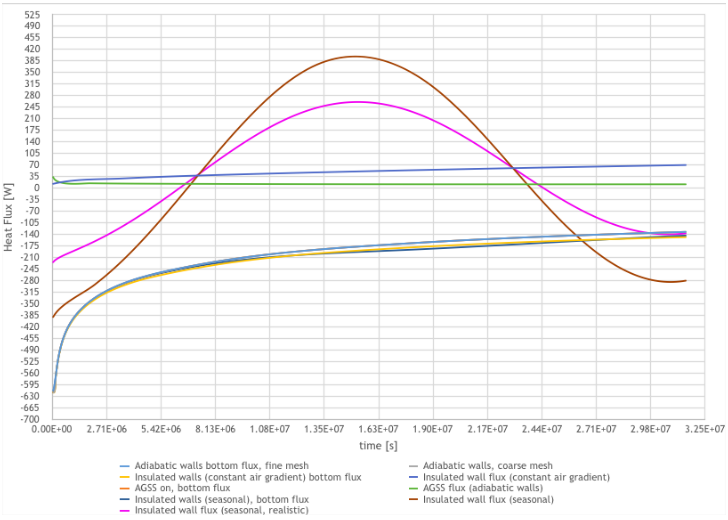

FIGURE 4.13: Total power transfers in a year, obtained by multiplying the specific powers in Figure 4.12 by the corresponding surface areas of each of Borexino's components (walls: 1000 m^2, AGSS: ~60 m^2 and base: 250 m^2).

by a (normalized) y factor). To that effect, we modified Equation 4.3 in the following manner (H_{BX} is Borexino's height in meters):

$$T_{\text{inf}}(t) = 273 + \left[11.986 + 0.32789y - 2.5\frac{y}{H_{BX}}\cos\left(\frac{2\pi t[s]}{31536000}\right)\right][K] \tag{4.4}$$

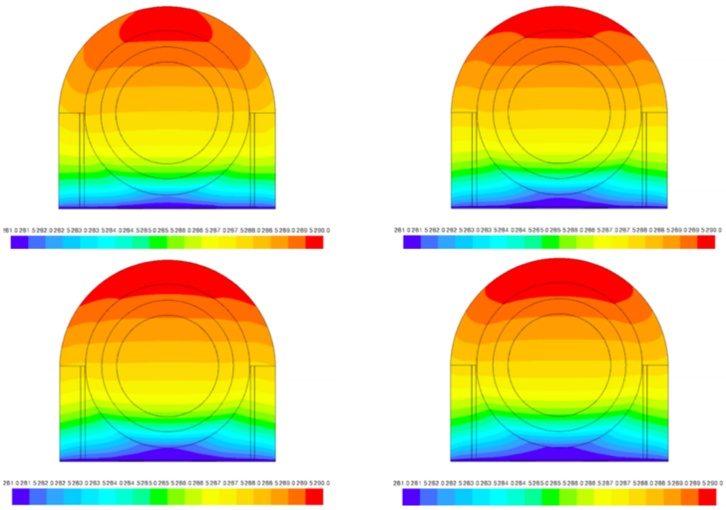

FIGURE 4.14: Modelization for the realistically-insulated WT walls and a sinusoidally-varying linear external air gradient weighted with height (equation 4.4). Timing of the insets is as in Figure 4.11.

Results

As expected, the transmitted power was approximately halved (see Figures 4.12, 4.13 and 4.14) with the greatest effect occurring in the top, but still has a great influence in the overall thermal flux budget, and as mentioned in the previous subsection, it should be noted convection can only increase this effect.

Even though there are large qualitative differences among the different models presented here, and the average temperatures on the exterior wall vary significantly (see Figure 4.19), the behavior within the Sphere is quite similar –to within hundredths of a degree– in all previously discussed cases (see Figure 4.17).

4.2.6 Uninsulated walls, realistic seasonally-varying external air gradient

Setup

We considered an **un-insulated** Water Tank scenario which, in spite of being historically inaccurate –since the water loop was inducing turbulence in the bottom half of the water in the WT during its life before the Thermal Insulation System (TIS) installation–, is useful to establish an **upper-limit bound** for heat transfer. It also provides an important reference point to **quantify the TIS effect on the idealized seasonal effect** we previously modeled. To that end, we used exactly the same scenario as in Section 2.5 in [156], but with a 10-cm thick WT steel wall with *no insulation* applied.

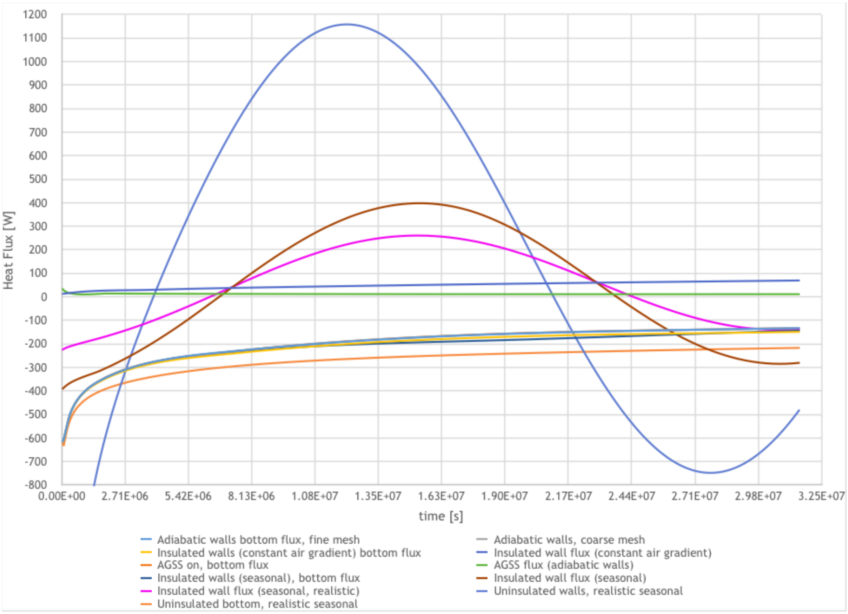

FIGURE 4.15: Comparison of the conductive-only uninsulated model with a realistically-varying, idealized seasonal variation of the air gradient outside the WT. The total wall heat flux is shown in dark blue, with an amplitude ∼3x larger than the insulated seasonal case, and the heat flux through the heat sink in the bottom is shown in the orange curve –showing a similar starting period and then stabilizing at ∼50W more than in previous cases.

Results

The resulting heat flux is shown in Figure 4.15, compared to the previous[156] cases. As expected, we get a much larger seasonal heat transfer (∼3x) oscillation that gets dampened as the overall detector temperature gets closer to the air gradient's mean. Also somewhat expected is the temporal **phase shift of ∼1 month** given by the thermal resistance of the 20-cm thick rock wool layer. The heat flux through the bottom is also increased in absolute value by ∼50W. The specific heat flux is also shown in Figure 4.16.

The difference in the IV temperatures is now more pronounced (see Figures 4.17, 4.18), although the general stratification and stability is maintained in this conductive case. Most of the conductive seasonal effect is confined in the water (see Figure 4.19), even without insulation, because of the system's thermal inertia. An interesting effect seen on the top water volume is a temperature inversion, that nevertheless doesn't get propagated inside into the SSS. This inversion probably wouldn't be present in the real system, because of convection.

4.3 Three-dimensional conduction model

A 3D approximation to the conductive case offered the following broader scope, which couldn't be implemented in the bi-dimensional cases:

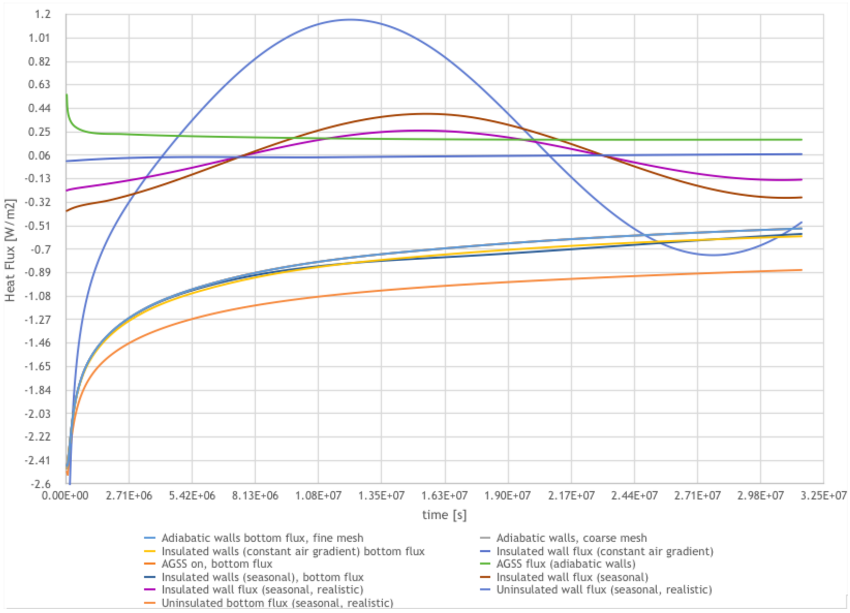

FIGURE 4.16: Specific heat flux rates for the previous models compared to the uninsulated reference.

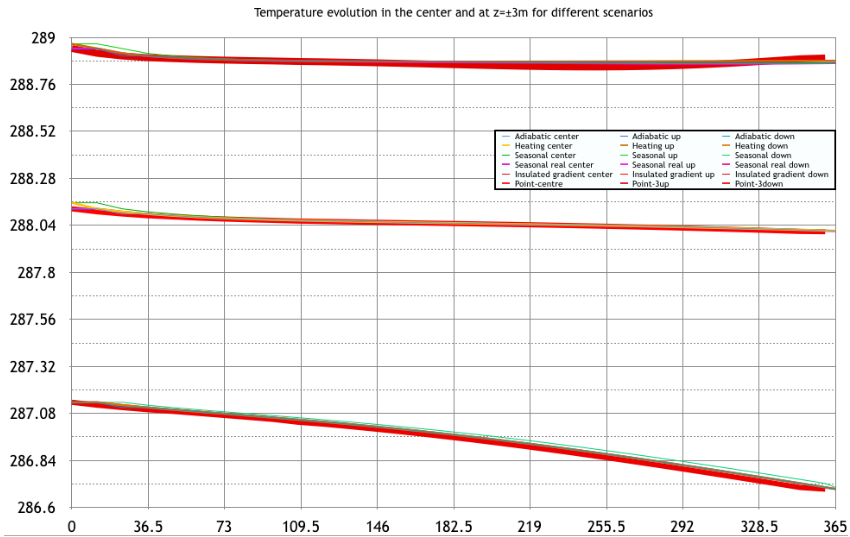

FIGURE 4.17: Temperature evolution of 3 points in the IV (center, 3m up and 3m down) for all conductive cases. As explained in the text, even in the most extreme case of no insulation and a height-weighted 5°C seasonal variation, the overall effect due to conduction is small.

Conduction along structures Determine the along-structure heat conduction from the major identified heat sinks and sources (bottom of the detector, Active Gradient Stabilization System (AGSS) and equatorial platform) and their influence in overall detector heat dynamics. This will enable us to discriminate which structures are indispensable in the simulations (and quantify their influence in the case where they cannot be simulated, i.e. 2D models) and which have negligible influence. Since no convection will occur inside these elements, if conduction is found to have a small or negligible effect in the overall heat transmission, their presence can be neglected without a penalty in the realism of the

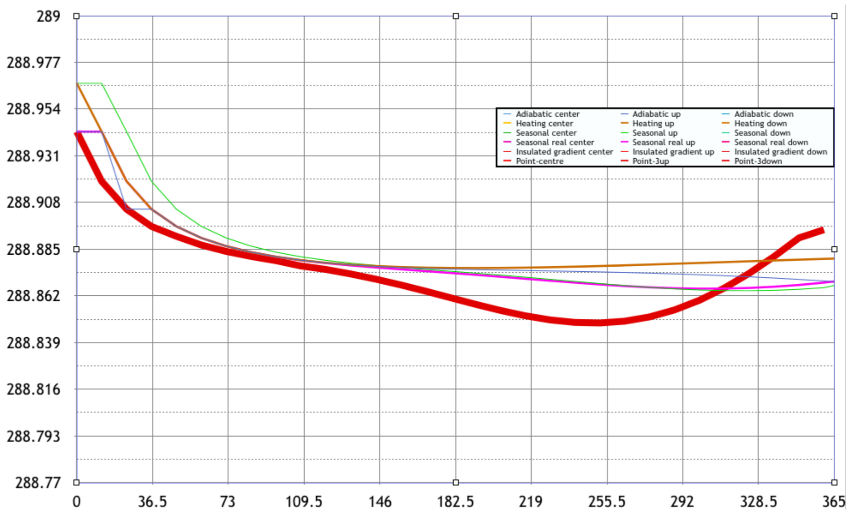

FIGURE 4.18: Temperature evolution of the point located 3m upward with respect to the center of the IV for all conductive cases, highlighting the differences not appreciable in Figure 4.17.

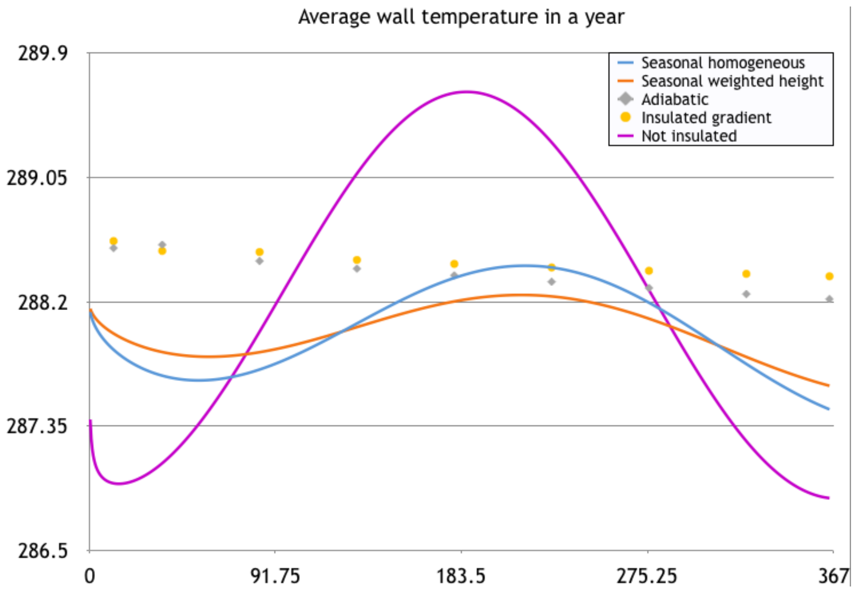

FIGURE 4.19: Evolution of the average WT wall temperature for all conductive cases. The scenario with the AGSS activated at 17°C (Section 4.2.2) is not shown because of the imposed temperature bias.

simulation, and the model can be lightened in order to achieve better computational efficiency. Furthermore, it will set the "safe use" operating envelope for the AGSS, verifying its heat transfer is mainly *through* the walls toward the inside of the WT and **not** *along* the tank's walls. Although the AGSS was engineered trying to maximize thermal contact of the water tubes with the walls, it is paramount to verify heat is not carried through the walls a significant distance downwards, where it could induce potentially dangerous vertical convective motion within the water in the top of the WT.

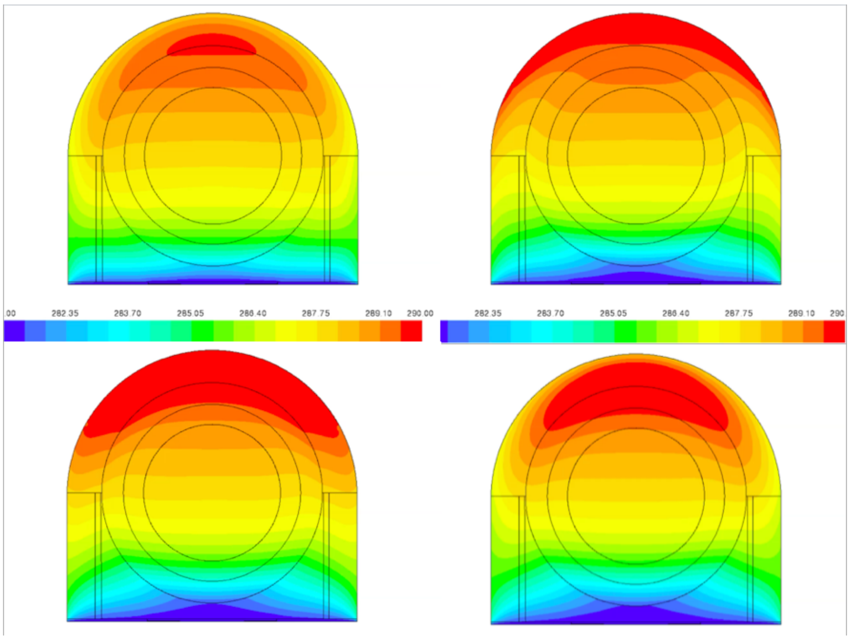

Figure 4.20: Contours showing temperature evolution for the uninsulated conductive case, every ∼3 months.

Pit modelization In the 2D simulations run so far, the pit was *not* modeled since its non-cylindrically symmetric shape made it difficult to estimate an "effective" 2D profile and, in any case, we only have the ceiling temperature data from the Phase II.b LTPS sensors. However, the existence of vastly different materials with respect to heat capacity (cement vs air) might produce some observable differences depending on whether certain Borexino base areas are immediately on top of the pit volume or not.

2D vs 3D differences For internal consistency, we should check the results obtained so far for the 2D conductive-only models match reasonably well those obtained with the 3D one, once corrected for the two points above.

4.3.1 Model setup

The model considered remains azimuthally-symmetric on its major components: the WT, AGSS, Sphere and base plates are just revolution surfaces of the bi-dimensional model surfaces. Additionally, however, the equatorial platform was modeled connecting the WT exterior walls with the SSS, as a solid ring with an effective density and heat conductivity representative of the real perforated steel. Realistically-distributed (water-filled) legs were also added connecting the equatorial platform with the base surface – although, since they were not expected to play an important role in heat conduction, only 14 of them were modeled: if they were seen to provide a heat conduction path, the whole set would be modeled. As will be seen, this was not necessary. The pit was added with the actual dimensions, although the base temperatures are still imposed

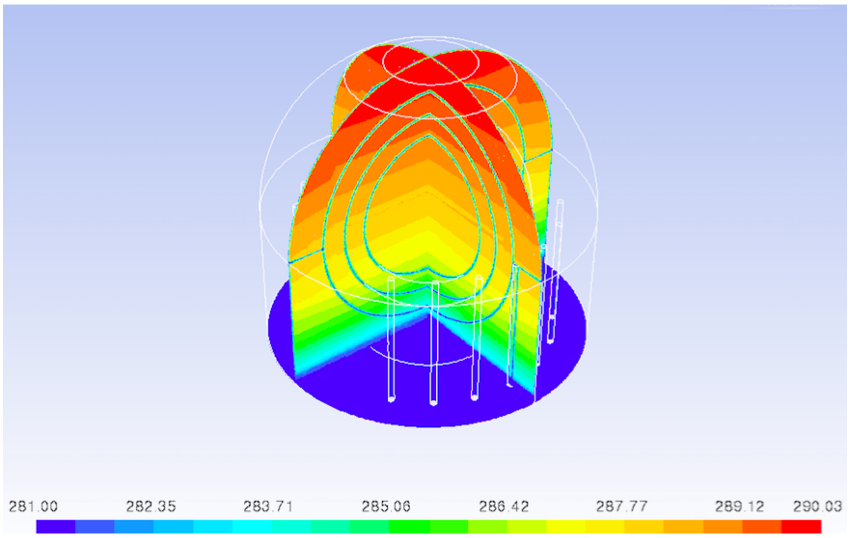

Figure 4.21: Initialized tri-dimensional mesh outline and orthogonal temperature contours for the conductive case. Note only 14 legs are modeled and the pit is not rendered in this image.

on the top of the pit, since it is the only place actual temperature measurements take place for now. Therefore, this shouldn't affect much the simulation's outcome. A view of the mesh can be seen in Figure 4.21.

Temperature initialization was extended for a 3D case, to achieve 3D validity for the linear interpolation between the North and South LTPS-measured temperatures as revolution isothermal surfaces. This model was then let evolve with the conductive conditions without fluid movement. A single case with AGSS heating at 20°C and adiabatic walls was considered, and several factors were checked for:

4.3.2 Effect of major structures in heat conduction

From first principles, the heat paths through structures should not be an issue since they carry so little heat capacity compared to the surrounding mass of water. Therefore, they should be kept at thermal equilibrium with the surrounding water in any reasonable operating regime. However, this was an important thing to check for certain with the simulation package. Convective processes would actually *decrease* heat conduction since more *local* mixing with the surrounding fluid would occur, resulting in an overall decrease of the heat transmission front through the structure. Therefore, this fully-conductive case would actually be a worst-case scenario.

No noticeable along-structure heat transfer was detected (see Figure 4.22), and the modifications in temperature profile were fully compatible with the surrounding fluid's general trend. No *cold front* could be seen climbing the legs that was not in line with the regional cooling of the bottom WT water (see Figure 4.23).

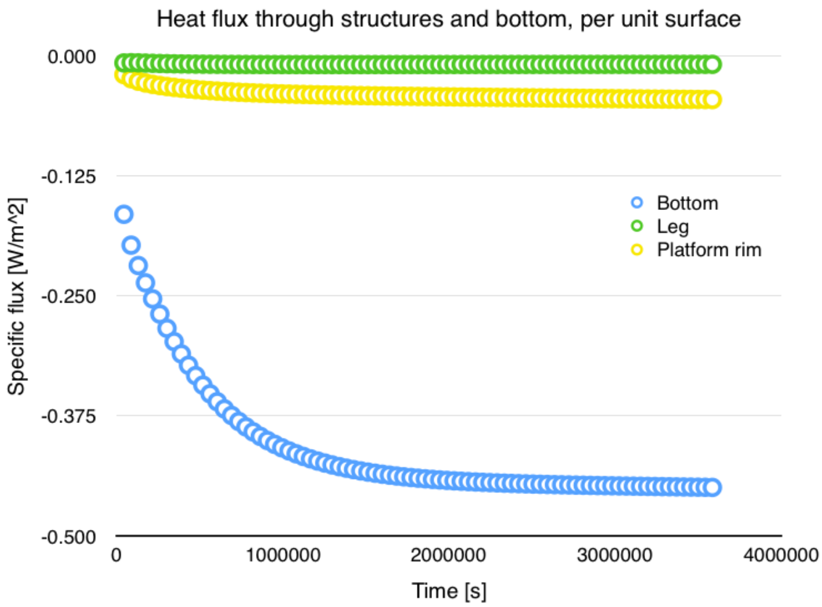

FIGURE 4.22: Along-structure heat fluxes compared to the bottom cooling heat flux for the major structural elements (legs and equatorial platform), normalized per unit surface.

4.3.3 AGSS heat transmission through the WT's skin

Another important aspect that potentially showed more uncertainty was the along-structure heat transport from the AGSS beyond its nominal spatial range of operation in the WT's 5^{th}

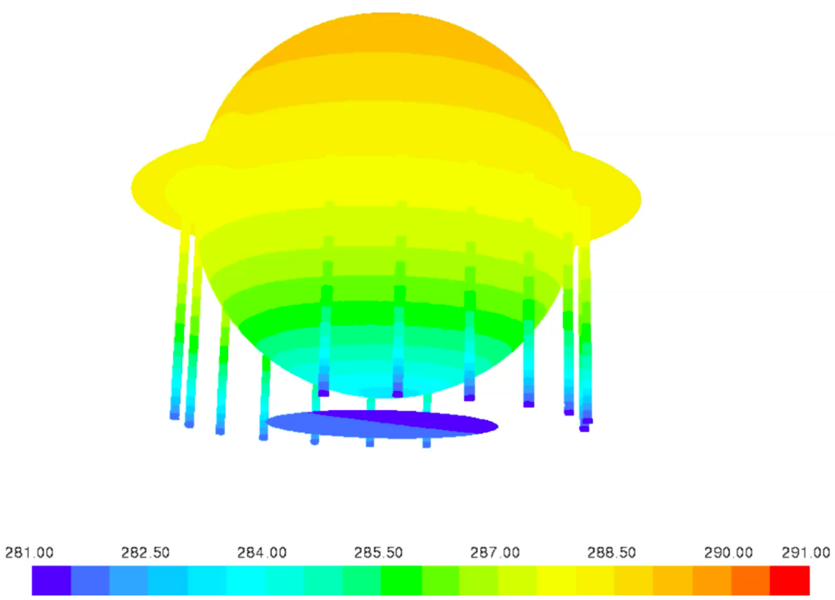

FIGURE 4.23: Temperature distribution during the running of the 3D conductive case, where it can be seen no significant "cold front" advance is present through the legs upward, or through the equatorial ring outward/inward, because of the metal's higher heat conductivity. The isotherms are horizontally aligned with the surrounding water temperature to within <0.01°C.

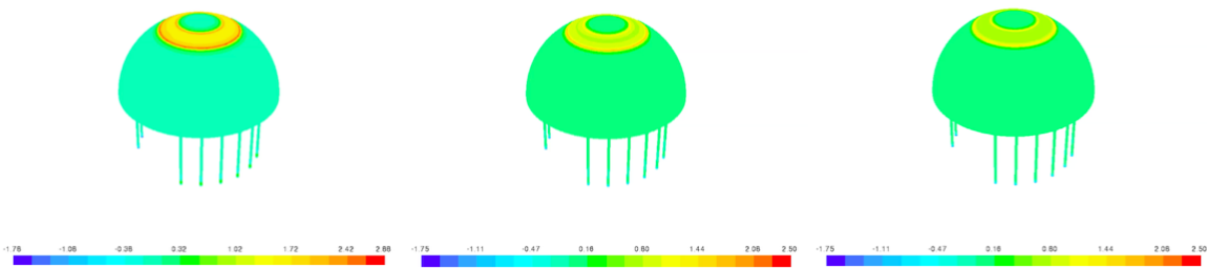

FIGURE 4.24: Along-structure heat fluxes compared to the bottom cooling heat flux for the major structural elements (legs and equatorial platform), normalized per unit surface. The color scale shows temperature difference with respect to the interior side of the wall (i.e., the temperature of the water in contact with the WT's skin). It is clearly visible the "heat front" does not arrive beyond a few centimeters past the AGSS's nominal heated band.

ring. In particular, the concern was the heat from the heating serpentines would be reaching lower latitudes in the WT than desired because the steel plates would more readily accept and conduct heat downward than the water directly in contact with the steel could transport to more inner volumes at the same height. The severity of this potential effect could range from creating too large convective cells that reach the SSS' height, to even reaching the equatorial platform and conducting heat to the SSS equator and disrupting the stable stratification therein. This last extreme is very unlikely due to the distances and temperature differences required, as well as the disproval of major along-structure heat conduction through the platform (accentuated by its low effective density surrounded by water).

For this reason, the AGSS was modeled as a revolution surface of the AGSS segments described in Section 4.2.2, with a constant temperature of 20°C. This constitutes a very conservative scenario, because the AGSS is never expected to be set at such a high temperature, and certainly not several degrees above the adjacent water's temperature. Moreover, the serpentines' structure, even if located under the TIS layers, will not provide such a wide area of constant high temperature –and its heat transfer will be maximal at the top, where the heated water arrives directly, and then cools down progressively as it reaches the lower part of the serpentines toward the outlet. Finally, convection in the water directly affected by the AGSS will only diminish the along-structure heat transport, since better mixing in the upper part will restrict the localized heating that may favor vertical transport.

As can be seen in Figure 4.24, no along-structure adverse heat effects were seen. Likewise, the internal behavior in 3D is practically identical to that in the 2D configuration, vindicating the previous bi-dimensional results as applicable to the real system, when only considering conductive contributions.

4.4 Benchmarking convective examples

In order to characterize FLUENT's fidelity in reproducing physical results obtained from literature on well-studied cases (both in physical experiments and in well-understood simulation works) and gain an understanding of the main basic phenomena at play in a system "topologically-similar" to Borexino (closed system with a $\sim$10°C temperature difference and a liquid of moderate fluidity and viscosity), several benchmarking cases were implemented. The convective behavior of a cylindrical system with completely stable stratification to which destabilizing perturbations are applied was studied first, to then move on to several similar geometries with different fluid movement conditions that were well-referenced in literature. All these models were implemented in two dimensions.

The choice of dimensions and ΔT for the following benchmarking models needed to be motivated to at least lie close to, or ideally overlap, Borexino's regime of interest. The determination of the Rayleigh number for Borexino offers the simplest, most rigorous way of relating seemingly dissimilar geometries to the detector case. The definition of the Rayleigh number is very dependent on the model geometry, and in non-standard ones (such as Borexino's spheric geometry with distributed, gradual temperature differences) may be somewhat arbitrary if not keeping a close watch on the phenomenon under study. The Rayleigh number (Ra) is a dimensionless parameter defined, in general, as:

$$Ra = \frac{\beta[K^{-1}]\Delta T[K]g[m/s^2]L^3[m^3]}{\nu^2[m^4/s^2]}Pr \tag{4.5}$$

where β is the thermal expansion coefficient of the fluid, ΔT is the temperature difference in the characteristic lengthscale of the system, g is the gravitational field acting on the system, L is the characteristic lengthscale for natural convection in the system, ν is the kinematic viscosity of the fluid and Pr is the Prandtl number, which is itself defined as the quotient between the momentum diffusivity and the thermal diffusivity. In practice, the Prandtl number is only dependent on the fluid's nature and state. The quotient multiplying Pr is referred to as the *Grashof number* Gr, which is a measure between the buoyancy and viscosity forces on a fluid.

As can be inferred from this definition, the Rayleigh number is most dependent on the characteristic lengthscale L for convection in the considered system. Ra is therefore a way of relating buoyancy-driven fluid flows coming from different fluid natures, conditions and system geometries –and therefore, contains information about the convective/conductive dynamics of a fluid flow, irrespective of the fluid. This is in contrast to the Grashof number, which depends upon the fluid under consideration.

Rayleigh numbers are usually calculated in idealized geometries with well-defined temperature differences. In the case of Borexino, since we are mostly concerned about Inner Volume dynamics, we might be tempted to calculate it simply using PC's β, Pr and ν, with ΔT being the temperature difference between the upper and lower poles at a given time, and therefore L being the distance between these two extreme points: 8.5 m for the IV. This would yield a $Ra \sim 10^{11}$.

However, while this may hold some truth in the case of global convective motions triggered by large temperature upsets happening **just** at the top and/or bottom of the vessel, keeping the lateral surfaces at around the same temperature, this is not the general condition under study for Borexino's nominal operations –instead, the temperature differences are small and distributed approximately evenly across the whole IV surface. For the sake of clarity, we shall point out here that the ΔTs whose effects may presumably be driving convection in the IV are clearly **not** the same as the overall temperature gradient between top and bottom of the IV. Indeed, in a perfectly stable configuration, a horizontally-symmetric stratified condition would take place, where relatively weak currents would only take place horizontally. Neglecting vessel deformation, this configuration would be most stable with increasing gradient, and Ra would have no incidence in this case. From this remark, it is clear the ΔT under study in our Rayleigh number determination shall not be the overall gradient, but rather the temperature upsets that cause local isotherm displacement, at times with an added left/right asymmetry. Furthermore, this imposes a change in choice of L, because the dimensions of the overall volume are no longer important –even if local upsets, when happening all over the geometry, may trigger volume-wide currents, this would happen irrespective of the vessel being smaller or larger.

This motivation brings us to consider the $\mathcal{O}(0.1)$°C temperature differences routinely happening in short timescales in Borexino, which may be causing the internal stirring concerning us. The L in this case would be the characteristic lengthscale over which this ΔT would cause isotherm displacement. In other words, if the overall gradient was very large, the isotherms would be very close together, and a given ΔT seeping in from the outside would show up at a smaller lengthscale than if the overall gradient was smaller, and the isotherms were farther apart from each other –in which case the isotherm displacement to match the boundary condition would occur over larger lengthscales. If we consider the typical overall gradient of Borexino's IV to be $\sim$5°C, over the 8.5 m between the top and bottom poles of the vessel, we get $\sim$1.7 m/°C: that is, $\sim$17 cm separating each 0.1°C isotherm. Considering this is our L, $Ra \sim \mathcal{O}(10^7 - 10^8)$ (with Pr=7.78 for PC, $\beta_{PC}^{10C} \sim 10^{-3}$ K^{-1}, and $\nu_{PC}^{10C} \sim 7 \cdot 10^{-7}$ m^2/s).

We are of course assuming a linearly-stratified fluid, which is not the real case in Borexino (which exhibits a laxer stratification on the top than on the bottom). Therefore, we should keep in mind the order-of-magnitude Rayleigh number estimate above would be approximately 1-2 order(s) of magnitude larger, locally, on the top, and smaller on the bottom. Consequently, we can estimate *Borexino's Rayleigh range* as $Ra \epsilon [\mathcal{O}(10^6), \mathcal{O}(10^9)]$.

4.4.1 Simple cylinders

In order to better understand the phenomena underlying convective-like currents in a spherical closed container such as the IV/SSS of Borexino, a simpler geometry was devised as a first benchmarking effort that would more clearly show characteristics such as:

- Influence of **top and/or bottom sudden temperature perturbations** in driving convective processes, including, but not limited to, the threshold ΔT at which convective cells clearly form, the difference in number/size of convective cells with temperature upset, the differences between a lowering temperature on the top wall and an increasing temperature in the bottom wall, if any; and the different convective modes triggered for different "reasonable" (for Borexino purposes) ΔTs.
- Global temperature increase/decrease along both the top/bottom walls and the lateral surfaces, with a certain gradation –which would give insights into the way convective processes are transmitted into the central fluid, or indeed whether this transmission ever takes place under a certain ΔT or $\partial T/\partial t$ threshold –or conversely, conduction dominates at these certain thresholds and no convection is triggered.
- Convective modes in the case of a global boundary condition change as above.

The models employed would be two-dimensional, since three-dimensionality in a realistic Borexino case would not be feasible in the timescales pertinent to this research. The interior fluid (modeled as pseudocumene) would be kept at a linearly-stratified temperature profile, with maximum/minimum at the initial top/bottom surface setpoint temperature:

$$T(h) = T_2 + (T_1 - T_2)\frac{h - h_0}{H} \tag{4.6}$$

where H is the cyclinder's height (13.7 m) and T_1 (T_2) is the top (bottom) temperature. The cylinder is 11.2 m wide and has a mesh cell size of ∼3 cm (11 cm^2). The mesh grid is chosen as rectangular to conform with the model's bi-dimensional symmetry.

Adiabatic lateral walls

The lateral cylinder walls in this case would be kept at a perfectly insulated, adiabatic condition, while the top and bottom surfaces would remain at a fixed temperature, with a step function changing this setpoint at a given instant, triggering the model's instability, by a given ΔT. Therefore, temperature changes would initially only be seen at the top and/or bottom of the cylinder. The initial temperature range was chosen to be [10,18]°C –that is, a gradient of 10°C.

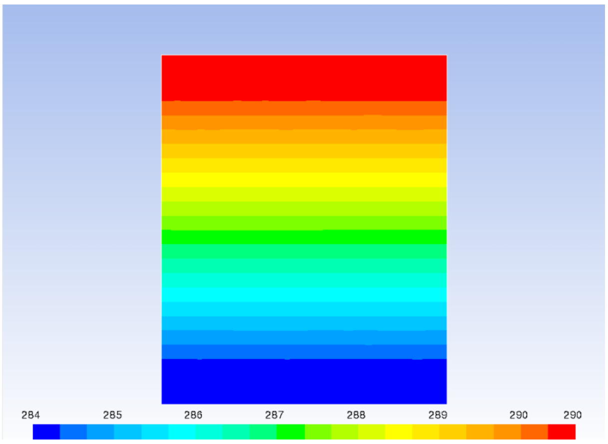

FIGURE 4.25: Expected final thermal state of the benchmark cylinder with adiabatic lateral walls, once the change in temperature from the top/bottom surfaces has propagated to equilibrium.

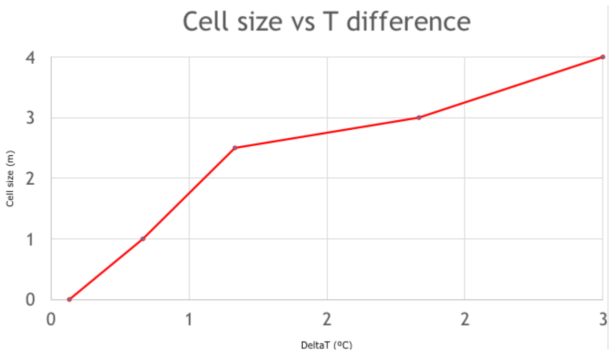

FIGURE 4.26: Indicative convective cell size (m) with ΔT (K) on top/bottom surfaces with adiabatic lateral walls. There is a threshold for convection (cell size = 0) at $\sim$0.2°C.

The final state expected is shown in Figure 4.25, where the isotherms have risen in the bottom and gone down in the top, while the overall gradient temperature difference has decreased by $2\Delta T$ (top temperature has decreased and bottom temperature has increased by the same amount). The height of this rise/descent is consequently dependent on the ΔT, and the chosen ones were: 0.1, 0.5, 1, 2, 3 and 4°C.

It was observed the threshold for convection triggering was $\Delta T >$0.1°C, since there was none for the model with the smallest temperature jumps. Further, the convection cell size was measured and found to be approximately linearly dependent (with the aforementioned threshold) with increasing ΔT (see Figure 4.26). Despite clearly exhibiting fascinating dynamics, this study was not continued further, since these simple benchmarks were just intended as enablers to establish general behaviors.

Further, examples of the observed convective motions are shown in Figure 4.27. No major differences between the top and bottom behaviors were seen, indicating they present equivalent dynamics. An example of velocity magnitude maps is seen in Figure 4.28.

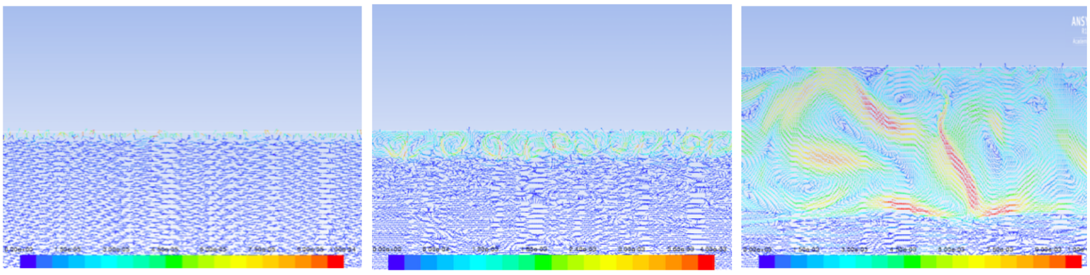

FIGURE 4.27: Velocity magnitude maps indicating fluid movement for ΔT=0.1, 0.5, 1°C. As indicated above, no structured convection is seen for ΔT=0.1°C, while 0.5°C already show organized convective cells.

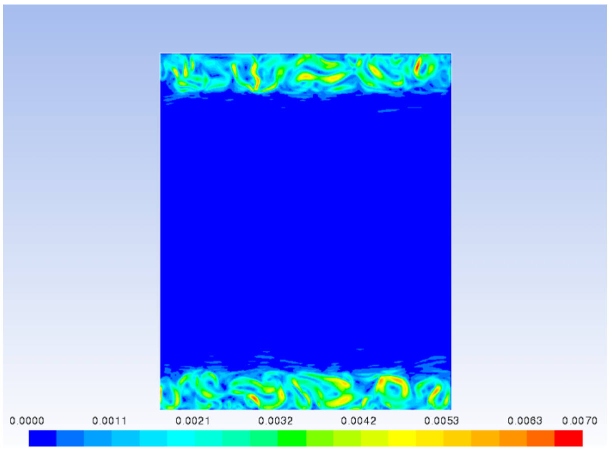

FIGURE 4.28: Top/bottom convective cells in the ΔT=1°C case. No substantial asymmetry is observed, as was the case with the other cases.

Another important observation is that the convective effects are constrained to the height where isotherms rise/descend. This result is especially important for the purposes of the AGSS safety: this verifies that the conductive result, with increased AGSS operational temperature beyond the maximum "naturally" achievable temperature for Borexino's top, would result in only localized convection around the heated area, not transferrable to the ID or, ultimately, to the FV. On the contrary, the "lobes" concentrated around the area of operation of the AGSS in the conductive case would be distributed horizontally through convection until homogenizing the temperature to an approximately-constant equilibrium stratified distribution without inducing fluid movement further below.

The largest currents observed were on the order of $\sim$**dm/s**.

Changing-temperature lateral walls

The ΔT in this case would be applied as in the previous case, but this time also on the lateral walls. Further, instead of reducing the gradient by $2\Delta T$, this time it would be kept constant by just increasing or decreasing the overall baseline level. That means the 8°C temperature

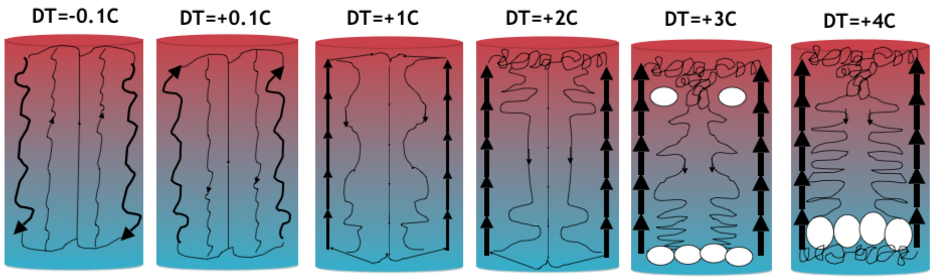

FIGURE 4.29: Convective motions in the lateral walls with changing temperature scenarios, for different ΔTs. Thicker lines with more arrows indicate stronger currents, white circles are structured convective cells and the "wiggly" lines are unsteady circulation currents.

difference between top and bottom will be kept, but the top/bottom temperature would be raised by ΔT, as would be any given lateral wall temperature.

Several cases were run, with ΔTs of: -0.1, 0.1, 1, 2, 3 and 4°C. While very varied and structured phenomena were visible at every different ΔT (see Figure 4.29), the most remarkable result was the observation of a well-structured **global convective mode** spanning the whole cylinder geometry. Increasing ΔT would increase the velocities, motion complexity, local convective motion and number/strength of convective cells present (only appearing for ΔT >3°C), but well-defined global currents appeared in the fluid for any of the studied changes in temperature, in contrast with the threshold for cell formation in the case of adiabatic walls. Furthermore, this global convective mode did not appear constrained to a two-lobed simple motion, but rather exhibited a weak return current along the cylinder's central axis –with stronger, albeit more unstable (with instability increasing with ΔT), returns skirting along the sides of this central current.

This introduces a critical condition for IV fluidodynamic stability in Borexino: there is no allowable threshold on the amount of temperature difference if this takes place in a short timespan, if global convective currents are to be avoided.

Other important features are the development of a progressively more sinuous path for the fluid recirculation with increasing ΔT, causing an unsteadiness that eventually results in the production of turbulent-like structures (ΔT > 2°C). Well-formed local convective cells only appear for large temperature differences (ΔT > 3°C), as mentioned before –starting with isolated vortices near the upper turbulent-like flow and in the bottom of the cylinder, to then progress to larger ones on the bottom of the cylinder, fed by downward flows feeding them, and separated from the bottom by a turbulent-like layer. Vertical circulation along the lateral wall increases visibly, and becomes more laminar, with increasing ΔT.

Another working hypothesis when designing and installing the TIS in Borexino was the concept of a threshold $\partial T/\partial t$ over which conduction would either dominate over convection or, at least,

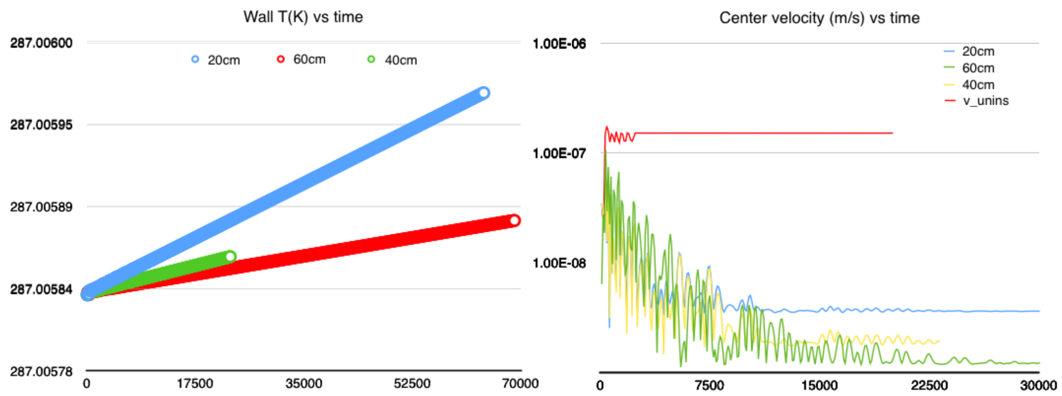

FIGURE 4.30: Wall temperature increase (left) and velocity magnitude measured at the center of the cylinder (right) for the uninsulated and differently-insulated cylindrical cases. The temperature change in the uninsulated case is not shown to better appreciate the small ΔT that seeps through the insulation in the other cases (the uninsulated case would show a Heaviside-like step jumping to +0.1°C).

cause global convective currents to be slower than the lifetime of ^{210}Po (i.e., >0.38 years for a vertical displacement from the IV poles to the FV, which means $\sim<10^{-6}$-10^{-7}m/s). This effect was implemented through the addition of TIS insulation-like resistance to the one-dimensional cylinder wall, similar to the method employed in Section 4.2. Four "thicknesses" were considered: 20, 40 and 60 and 100 cm. The external step-like ΔT was 0.1°C. Boundary condition (at the center of the inner side of the lateral wall) temperature and central velocity magnitude evolution plots can be seen in Figure 4.30.

It was observed that, although some currents enter the realm of the resolution limit for the model ($\mathcal{O}(10^{-9} - 10^{-8}$ m/s), **there is no threshold** for the organization of the current vectors into the same type of structure found for the uninsulated, step-like ΔT case. Therefore, in spite of the actual currents being of too small a magnitude to be called such, at least for the purposes of our project, we can expect the general convective structure to remain in place even for minute temperature differences. This is in contrast to a static model with no ΔT, where the numerically-induced structures show a pseudo-random pattern in the interior of the cylinder, as seen in Figure 4.31–showing the structure has a physical base.

A further refinement of this model saw the temperature change being dependent with height (that is, no temperature change on the bottom while the top temperature would be reduced to trigger instability, with lateral wall temperature change being larger with height). A single case with no time delay was run with this setting to understand differences in behavior, with ΔT=-0.5°C, and following the aforementioned height-dependent linear gradation:

$$\Delta T(h) = \Delta T \cdot (H - h)/H \tag{4.7}$$

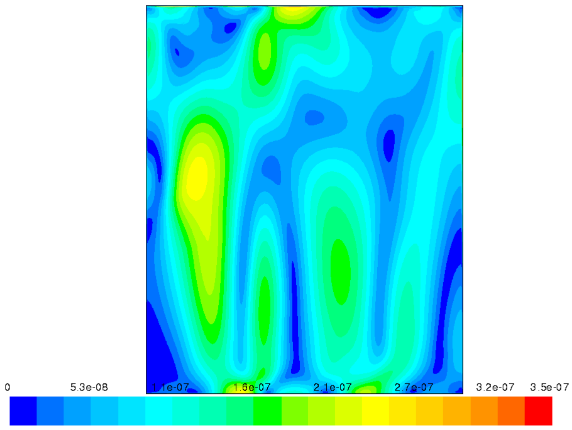

FIGURE 4.31: Numerical noise pattern for a static temperature cylinder case with the same stratification as before.

with H being the usual cylinder height of 13.7 m. This configuration showed the same global convective mode with the development of instability regions in the middle part of the cylinder, separating a weak recirculation area in the bottom third of the cylinder, from a stronger one in the upper third. A thin weak vertical circulation column was also present as in the previous small ΔT cases.

4.4.2 Concentric annuli

Once some relevant insights about FLUENT-simulated convective motion in a simplified geometry were acquired with the aforementioned cylindrical models, as a way to extend our confidence in and knowledge of the simulation method employed, it was advisable to attempt to re-create –or understand the model's limitations if differences arose– well-studied academical examples from the literature. In particular, we selected the two-dimensional cases of a circular cylindrical (or spherical) section with a concentric/eccentric annulus fully contained inside. The inner annulus' outer surface would be heated to a higher temperature than the exterior's inner one, and the fluid behavior would be studied in the space between them. This fluid would be initially at a constant volume-weighted mean temperature defined by:

$$T_m = \frac{(r_{av}^3 - r_i^3)T_i + (r_o^3 - r_{av}^3)T_o}{r_o^3 - r_i^3} \tag{4.8}$$

where r_{av} is the average radius $(r_o + r_i)/2$ and r_i (T_i), r_o (T_o) are the inner and outer radii (temperatures), respectively[157].

For the first cases, taken from[157], the Grashof numbers given in the reference were converted to the dimensionless Rayleigh number and this was taken as reference to calculate the inner/outer

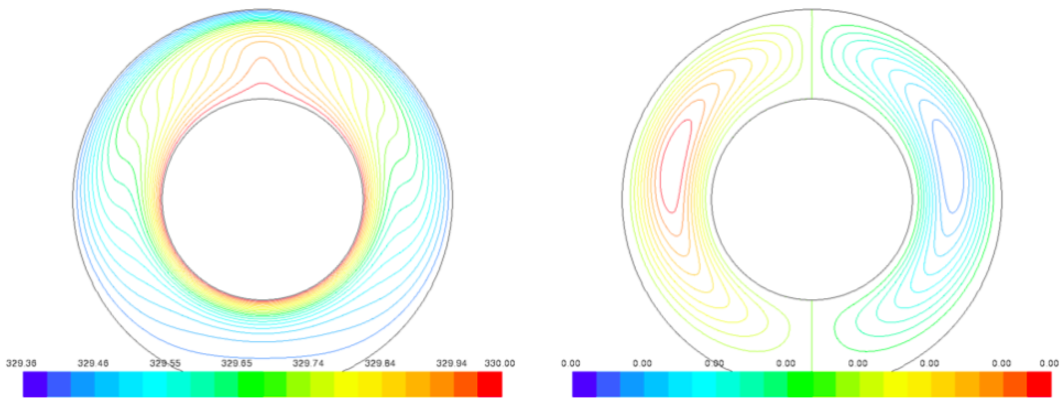

FIGURE 4.32: Rayleigh=5880; D_o/D_i=1.78 with air showing basic recirculation pattern through isotherms (left) and stream function of velocities (right).

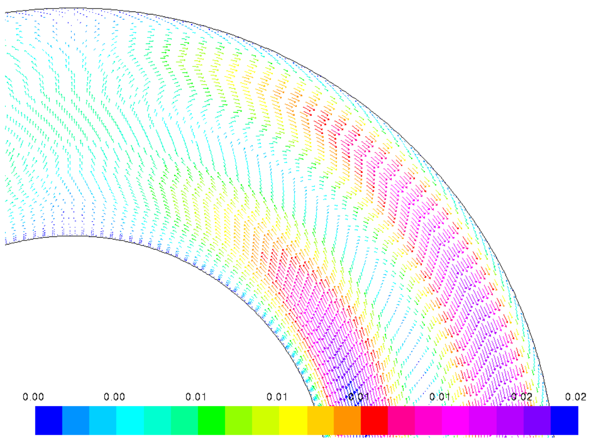

FIGURE 4.33: Rayleigh=5880; D_o/D_i=1.78 with air showing detail in the pattern.

surface temperatures, as well as the fluid's parameters according to Equation 4.5. This involved an amount of (informed) arbitrariness, since the literature reference did not indicate the absolute temperatures they worked with. For that reason, ranges around Borexino's 10-20°C were chosen when possible. The fluid employed was water, since the reference parameters are much better constrained than for PC/benzene at the small ΔTs involved. Sometimes, owing to the low Ra used, the temperature difference for a high-viscosity fluid such as water would be too small ($< \mathcal{O}(10^{-3}$ °C)), and air was chosen instead. The dimensions were kept as in the reference. Several representative cases were chosen to cover all non-turbulent regimes:

1. **Steady flow conditions at Ra=5880 with D_o/D_i=1.78.** The basic recirculation cell pattern seen in the physical examples is well-replicated in this model, as can be seen in Figures 4.32 and 4.33, with a well-developed upper-central "chimney". This model employed air as working fluid, due to the small ΔT needed for water under any reasonable temperature range.

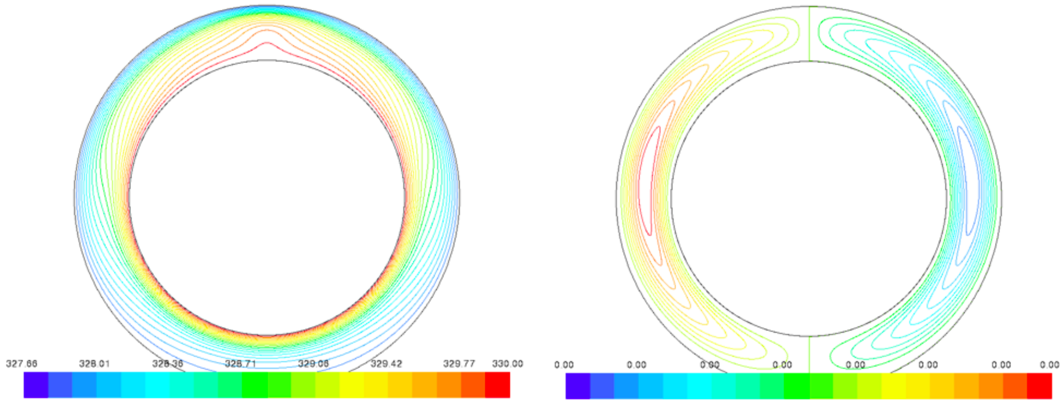

FIGURE 4.34: Rayleigh=5880; D_o/D_i=1.4 with air showing recirculation pattern through isotherms (left) and stream function of velocities (right).

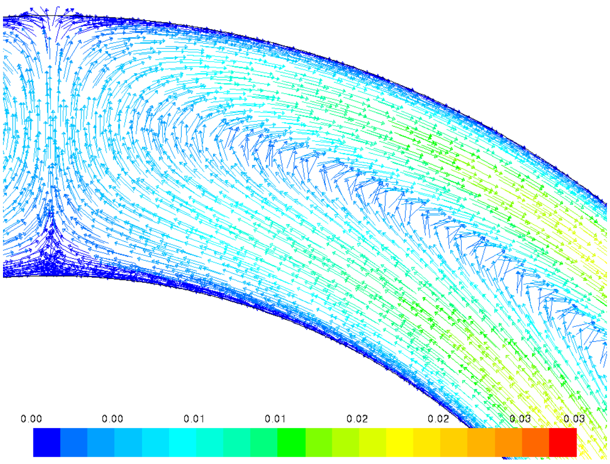

FIGURE 4.35: Rayleigh=5880; D_o/D_i=1.78 with air showing absence of upper recirculation cells seen in the Figure 4 of [157].

2. **Steady flow conditions with secondary vortices at** Ra=**5880 with** D_o/D_i=**1.4**. The basic stream pattern is well-replicated again as seen in Figure 4.34, but the two very prominent but small-scale upper circulation cells expected to appear flanking the "chimney" are not seen or even hinted at (see Figure 4.35). This is a two-dimensional model that has cylindrical symmetry, while the experimental setup uses a spherical arrangement, which could provide a source of differentiation. Moreover, the temperatures on the inner sphere, at this low Rayleigh regime, might not be as well-controlled as in the ideal CFD case, and a source for vorticity may be present in the physical setup generating these secondary vortices. Two mesh adaptation rounds were performed on this model, as well as a timestep decrease to 2s per iteration, with no change in flow conditions. This case was also performed with air as working fluid.

3. **Unsteady flow conditions with kidney-shaped circulation cells at** Ra=**739200 and** D_o/D_i=**2.17**. This case was tried with water as working fluid, as the ΔT required was marginally larger than in the previous cases. However, unsatisfactory agreement was

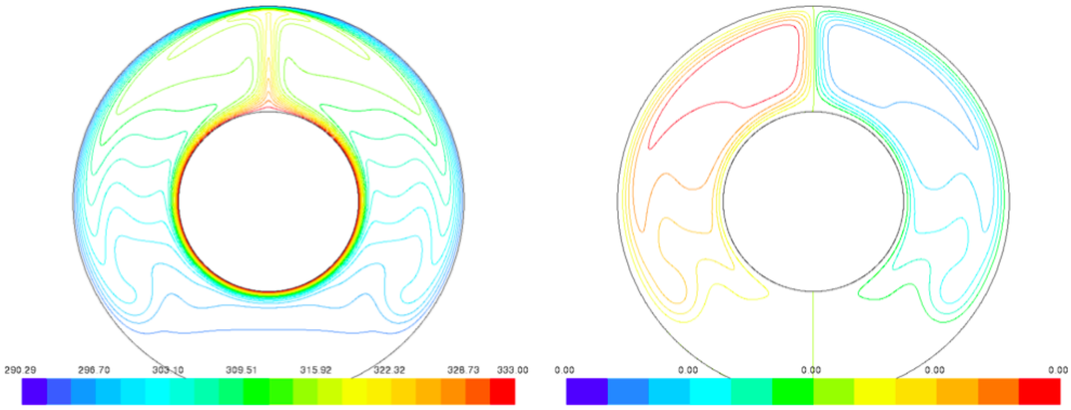

FIGURE 4.36: Rayleigh=739200; D_o/D_i=2.17 with air showing kidney-shaped recirculation patterns through isotherms (left) and stream function of velocities (right).

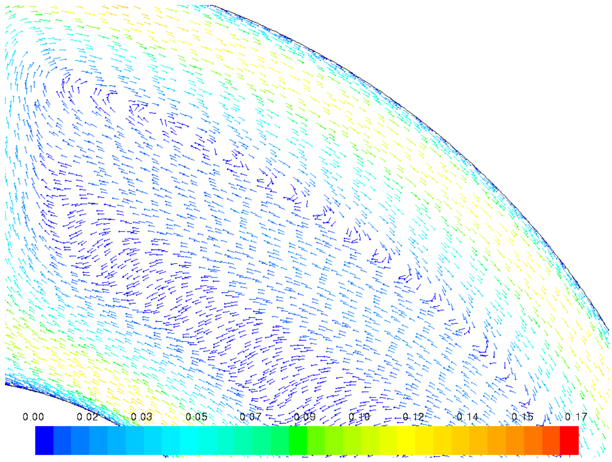

FIGURE 4.37: Rayleigh=739200; D_o/D_i=2.17 with air showing the presence of an elongated vortex as in the physical reference case.

reached and it was decided to switch to air as working fluid as a check –which showed much better agreement, pointing to an insufficiently-detailed determination of water properties at that small temperature difference as the likely culprit. In any case, the air case showed good agreement of the large-scale features (see Figure 4.36), although it can be argued their modeled position is slightly higher than in the literature. The elongated vortex located in the upper right portion of the cell is seen in Figure 4.37 too.

4. **Basic steady flow pattern at Ra=1492800 and D_o/D_i=2.17**. This model showed good accuracy with water, although small-scale vortex formation was stronger than in the literature case (see Figure 4.38).

5. **Steady flow pattern threshold (Gr=1184000) toward unsteady case (see next) at Ra=7104000 and D_o/D_i=1.78**. This case showed the transition between the steady flow pattern in the previous case and the unsteady vorticity in the next one. As such, it

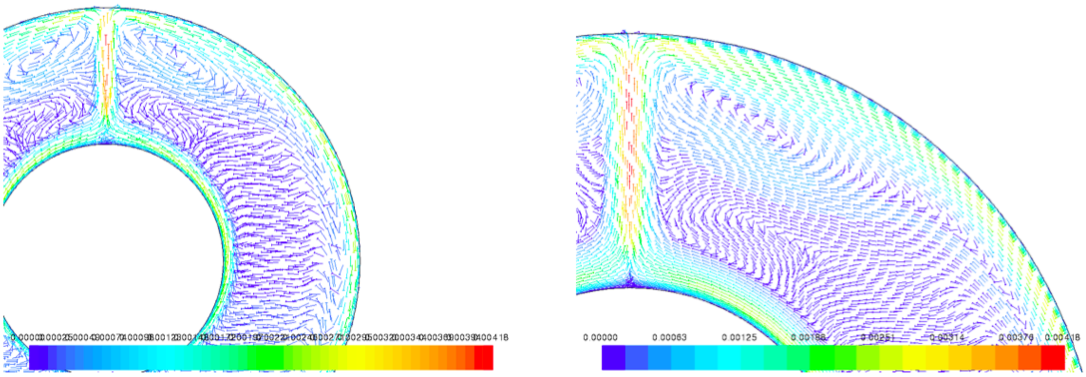

FIGURE 4.38: Rayleigh=1492800; D_o/D_i=2.17 with water showing the basic steady flow recirculation pattern in general (left) and in detail (right), featuring a stronger vorticity than in the reference case, but a good agreement with the general circulation pattern, especially at the angle between the upper circulation layer on the inner sphere and the "chimney" feature.

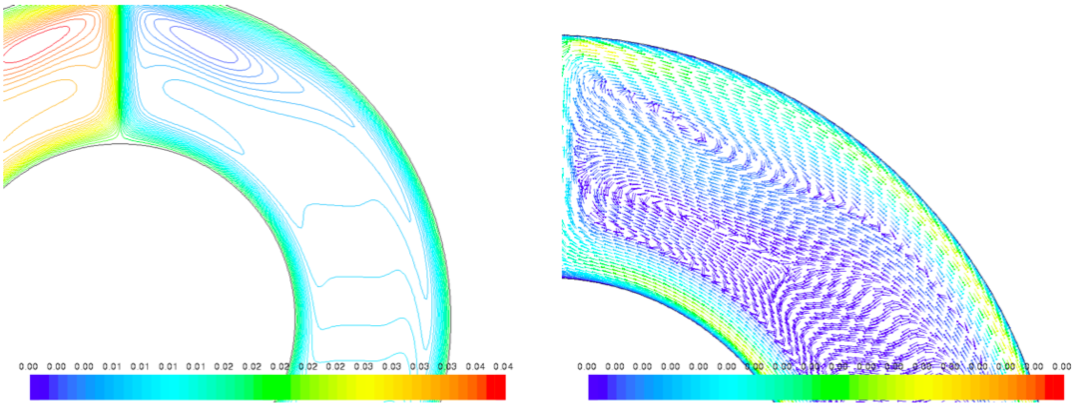

FIGURE 4.39: Rayleigh=7104000; D_o/D_i=1.78 with water showing the basic steady flow recirculation pattern at the threshold ΔT, where a transition, distorted state between the previous steady condition and the next case's unsteady complex case is expected, as observed.

is expected no large unsteady features will be seen, but just a distortion of the previous pattern, which is indeed the case as can be appreciated in Figure 4.39.

6. **Unsteady flow after threshold, with unsteady circulation cells, at Ra=10128000 and D_o/D_i=1.78**. This case was the most delicate one, since it shows a series of small-scale circulation features that nevertheless are arranged into a medium-scale pattern. The ΔT was therefore slightly increased from the nominal Rayleigh, without affecting it too much, to enhance the apparition of these features without changing the regime. The double-vortex structure on the upper sides of the "chimney" appears (see Figure 4.40), along with the shear structure separating these counter-rotating vortices –although their precise position and shape is changed from the one appreciated in the reference picture. However, it can be appreciated the fluid flow is largely the same, and the unsteadiness and instabilities of the upper fluid portion adjacent to the "chimney" is largely mimicked

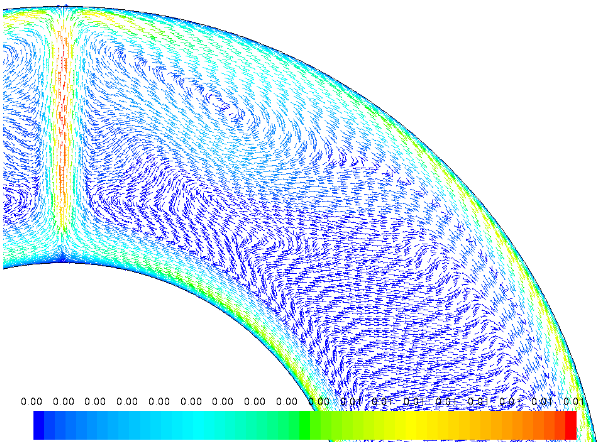

FIGURE 4.40: Rayleigh=10128000; D_o/D_i=1.78 with water showing the complex unsteady flow recirculation pattern beyond the critical threshold and a slightly increased Ra from the reference, to better show the double-vortex structure and other details shown in the next figure.

in the model: the large velocity L-shaped region to the right of the upper vortex; the high-speed feature located at ∼45° next to the high speed flow coming from the inner sphere, but separated from this boundary layer by a relatively-stagnant layer; the diagonal detached current at ∼60° coming inward from the outer sphere (see Figure 4.41)... which indicates the high degree of reproducibility inherent in the model even for complex features at Borexino-like Rayleighs.

7. **Unsteady flow pattern with largest Ra=21600000 and D_o/D_i=2.17**. In this case, the features are simpler, mostly showing an upper recirculation cell and a detachment of the outer downward current at ∼60° in a manner similar to the previous case, as seen in Figure 4.42. The rest of the fluid is relatively stagnant.

A further example based on a physical model, but this time with real cylindrical symmetry instead of spherical (and, consequently, more akin to our 2D model's geometry) was taken from [158], and a study of its concentric cylinder case was performed for Ra=2510000 and D_o/D_i=2.6 (9.25 and 3.56 cm, respectively). This case offered a much more detailed and quantitative comparison with the reference data than the previous cases, because of the charts showing the heat transfer coefficients and Nusselt numbers.

As a first step, we can confront the average Nusselt number $\overline{Nu}$ from the inner cylinder's exchanged power (59.654 W). From the reference, we know that:

$$\overline{Nu}_{conv} = \frac{\overline{h}_i D_i}{\kappa} \tag{4.9}$$

where $\overline{h}_i$ is the local heat transfer coefficient in the inner cylinder, D_i is its diameter and κ is the thermal conductivity. We also know that $Nu = \overline{\kappa}_{eq} \cdot Nu_{cond}$, and since $Nu_{cond} =$

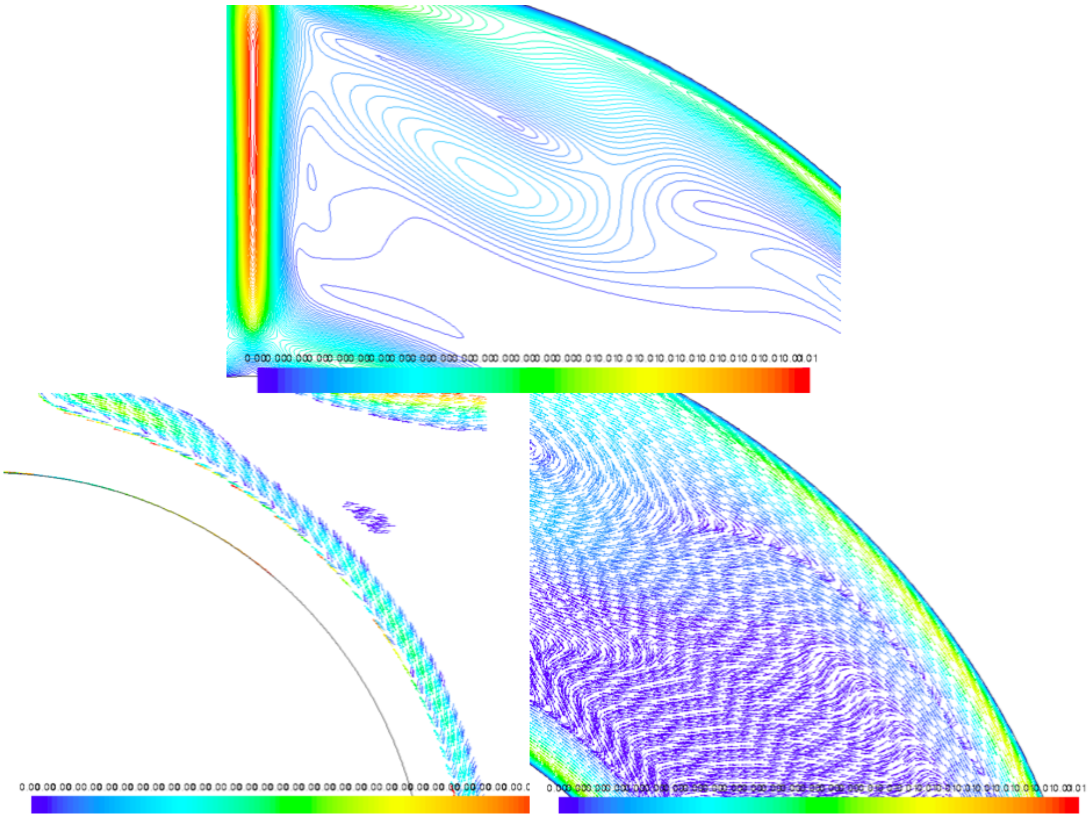

FIGURE 4.41: Rayleigh=10128000; D_o/D_i=1.78 with water showing details of the L-shaped region to the right of the upper vortex (upper inset); the high-speed feature (lower right inset) and the diagonal detachment (lower right inset) visible in the complex structures seen in this case.

$2/ln(D_o/D_i)$=2.09, we can calculate the Nu from the $\overline{\kappa}_{eq}$=7.88 provided in the reference's Table 1 (for our Ra=2.51·10^6). Indeed, the total average Nu is then Nu=7.88·2.09=**16.47**.

We shall compare this adimensional number to the one obtained through the data from the simulation, because the Nusselt number offers a way to find a correspondence between very different cases, from the point of view of geometry and fluids, with regard to heat exchange. It is noted the heat transfer coefficient cannot be the same as in the reference case because we use water instead of air for reference fluid, among other model considerations. However, the fact that the model is not precisely equal to that in the paper increases confidence in the validity of the modelization. The Rayleigh number is the adimensional number to compare natural convection in different cases, the Reynolds number is the one used for forced, or turbulent, convection in different cases, and the Nusselt number compares the heat exchange behavior of different cases.

In any case, from the numerical point of view, we have a different $\overline{\kappa}_{eq}$, and we want to obtain the $\overline{Nu}$ shown in Equation 4.9. For that, we need $\overline{h}_i$, defined as:

$$\overline{h}_i = \frac{Q}{\pi D_i Z (T_i - T_o)} \tag{4.10}$$

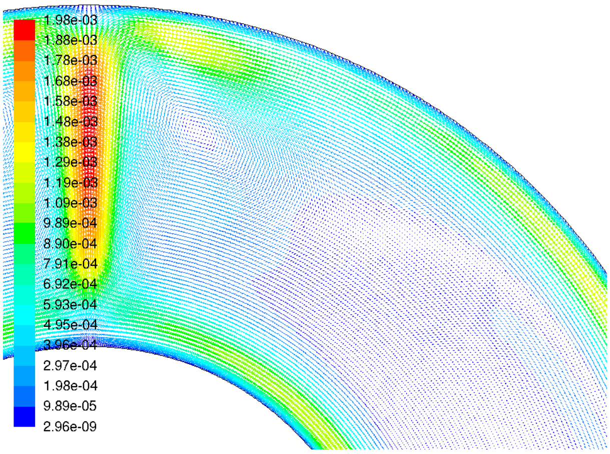

FIGURE 4.42: Rayleigh=21600000; D_o/D_i=2.17 with water showing the simpler unsteady flow recirculation pattern showing the upper weak recirculation vortex and the relatively stagnant inner fluid condition, accompanied by the high speed flows on the spheres and enlarged "chimney" structure.

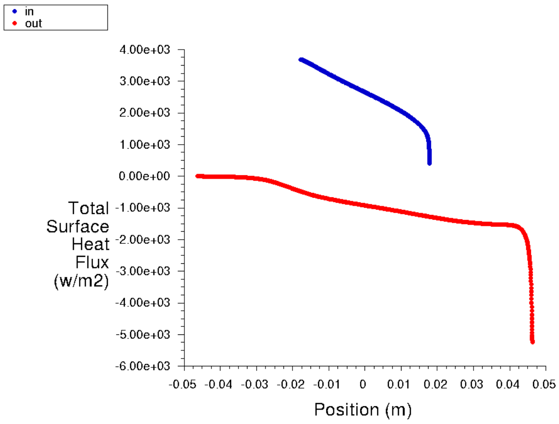

FIGURE 4.43: Total surface heat flux for the inner (blue) and outer (red) cylinders vs height position of its surface points.

where Q is the total power exchanged and Z is the depth of the cylinder (20.8 cm). The ΔT is 9.26°C. With this data, we have $\overline{h}_i$=2.76. This yields a $\overline{Nu}$=**16.431** (with a thermal conductivity κ=0.6 W/(m·K)), which is in very good agreement with the Nu found with the reference data.

We can also compare the h_i for different points along the inner/outer cylinder's surface to establish a comparison with Figure 8 in the reference, which shows the local heat transfer coefficient versus the angular position considered, from the total surface heat flux (W/m^2) shown in Figure 4.43.

From the values reported, we can readily see the extremal point for the inner cylinder at 0° (top) tends to zero, as is the case for the simulated model. This is expectable since it will be in this region where the "chimney" structure will rise, at a very similar temperature to the imposed

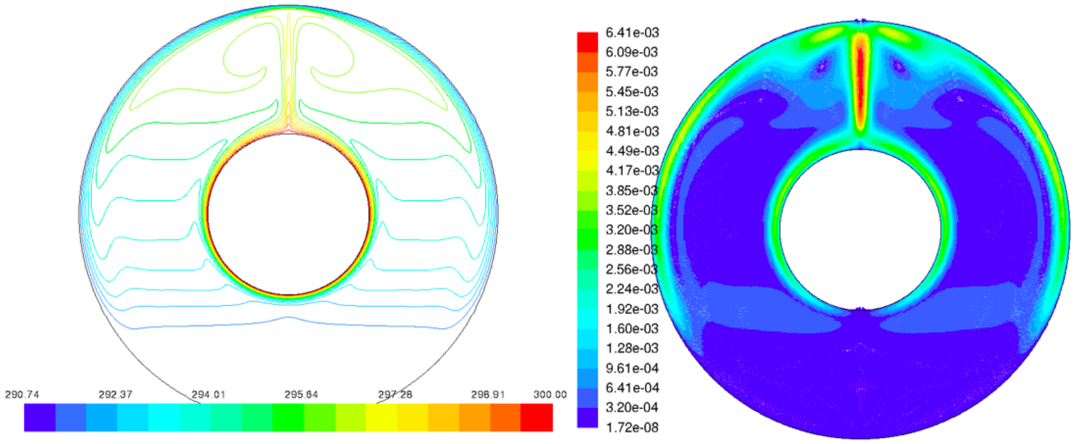

FIGURE 4.44: Rayleigh=2510000; D_o/D_i=2.6 with water showing the isotherms agreeing well with the general features seen in the interferogram for this case in [158] (left), as well as the circulation pattern (right).

inner cylinder one. This tendency starts at a steep decline ∼4 on the κ_{eq} (i.e. 4·2.09=8.36) on the reference plot, which is in reasonable agreement with the value we get from the ∼1000 W/m^2 from the FLUENT plot, from the formula $h_i = q_{w_i}/\Delta T$ and converting that to a Nusselt number by dividing by the thermal conductivity κ=0.6 W/(m·K), into Nu=6.4. On the other extremal point at 180°, which in the reference Figure 8 lies at κ_{eq} ∼11 for the inner cylinder, here we find a value of ∼3.7·10^{3}W/m^2. This translates to a Nusselt of Nu=23.7, in even better agreement with the plot-provided value of Nu=11·2.09≈23.

For the outer cylinder, we can do similar calculations to compare the extremal point at 0° between the κ_{eq} ∼31 in the reference plot (Nu ≈64.8) and the 4500 W/m^2 from the surface heat flux plot (Nu=74.9), or the plateau value at ∼60° of around 11 in the reference plot (Nu ≈23) and the ∼1500 W/m^2 in the surface heat flux plot (Nu=24.97). The curves also follow similar trends, as can be appreciated in spite of the polar vs cartesian coordinates employed for the reference and FLUENT plots, respectively.

Also, the interferograms shown in Figure 2 in [158] provided a good comparison with the isotherm contours offered by the postprocessing tools in FLUENT (see Figure 4.44).

Finally, a comparison with a CFD-based study[159] was employed to cover all ranges of interest for the purpuse of these benchmarking academic examples. In particular, this reference provided a good semi-quantitative handle to directly compare the results given by our model with those obtained by their simulation strategy (which nevertheless is expected to show a more computationally-influenced behavior than ours, owing to the more advanced stage of CFD modeling that FLUENT represents, as compared with the 1992 code utilized in the reference).

Three cases were modeled and their isotherms/streamlines compared to the reference (Ra=90000 (Figure 4.45), 250000 (Figure 4.46) and 1000000 (Figures 4.47 and 4.48), showing very good

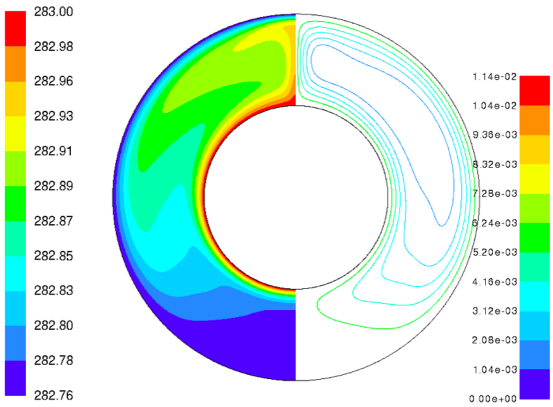

FIGURE 4.45: Rayleigh=90000; D_o/D_i=2 with water showing the isotherms (left) as well as the circulation pattern streamlines (right). The agreement is good although the recirculation pattern in the streamlines shows a higher-than-expected center, compatible with the same phenomenon being seen in the previous benchmarks. The general circulation pattern and shape is nevertheless quite good.

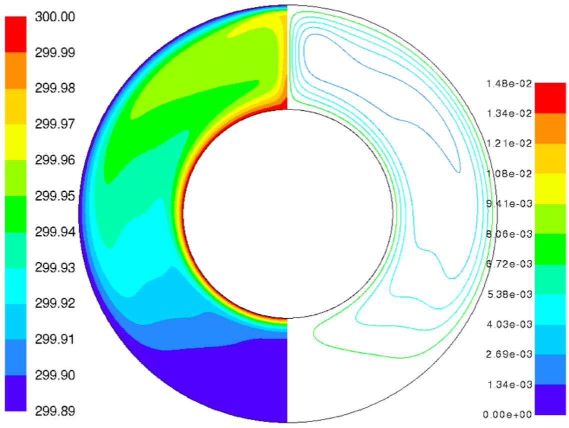

FIGURE 4.46: Rayleigh=250000; D_o/D_i=2 with water showing the isotherms (left) as well as the circulation pattern streamlines (right). Note this reference case in [159] was run with air instead of water as working fluid, but nevertheless the agreement is reasonable in the large scale. Some deviation from the "kidney shape" circulation pattern center position is seen, but both the isotherms and streamlines follow the expected general pattern.

large-scale agreement in all cases, although particular features, especially at low Ra, show some deviations.

In Table 4.2, a summary of the large-, medium- and small-scale reproducibility of physical and computational steady-state features by our FLUENT benchmark models is presented.

In conclusion, the benchmarking initiative showed good reproducibility of the thermal environment (when available to compare in the references) as well as the large- and medium-scale features present in each of the cases. Furthermore, the general fluid flow pattern was faithfully reproduced in practically all regions of all cases, which is the most important aspect to be looking for in the fluidodynamical simulations for applications in fluid current-induced background

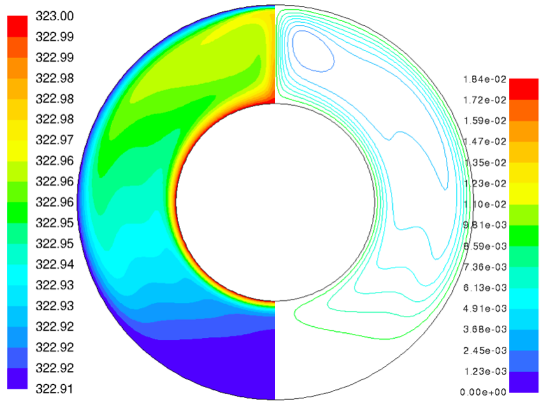

FIGURE 4.47: Rayleigh=1000000; D_o/D_i=2.6 with water showing the isotherms agreeing well with the general features seen in the interferogram for this case in [158] (left), as well as the circulation pattern (right). The upper vortex is clearly seen, as is the "squared kidney" shape of the main recirculation pattern. Again, the center of the main pattern is a shifted upward with respect to the reference, and the lower weak vortex at 180° is not visible, although a flow separation occurs. However, as can be seen in Figure 4.48, the circulation pattern is actually a better fit than what the streamline plot shows, and the detailed view with vectors brings that up.

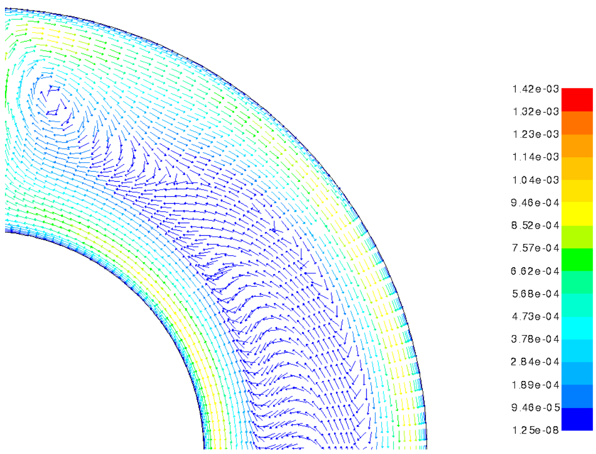

FIGURE 4.48: Rayleigh=1000000; D_o/D_i=2 with water showing the circulation vectors that agree to a high degree with the "square kindey" shape of the main circulation pattern, which was not adequately visible in the streamlines in Figure 4.47.

shifts in Borexino.

Medium			Features		
Ref	**Sim**	**Ra**	**Small**	**Medium**	**Large**
Air	Air	5880	-	Chimney	Crescent
Air	Air	5880	Upper vortices	Flow direction	Crescent
Water	Water	90000	-	Cell center	Crescent, isotherms
Air	Water	250000	-	Cell center	Kidney, isotherms
Air	Air	739200	Vortex structure	Cell center	Kidney, isotherms
Water	Water	10^6	Vortices	Streamlines	Isotherms, fluid flow
Water	Water	$1.493{\cdot}10^6$	Stronger vortices	Upper flow	Fluid flow
Water	Air	$2.51{\cdot}10^6$	Heat transfer Nusselt	Isotherms	Nusselt
Water	Water	$7.1{\cdot}10^6$	Stronger vortices	Transition threshold	Fluid flow
Water	Water	$10.128{\cdot}10^6$	Double vortex and shear	L-shape detached features	Fluid flow and structure
Water	Water	$21.6{\cdot}10^6$	Vortex position	Vortex detached features	Flow stagnant region

Table 4.2: Summary of results for the CFD literature benchmarking cases. Well-reproduced features, features present with small deviations from literature and absent features or features present with large deviations from literature are marked in green, yellow and red, respectively.

4.5 SSS convective bi-dimensional models

A convective model (even bi-dimensional) of the full detector would either take up too much computing time (*i.e.* the simulated time would approach the real time, negating its usefulness as a predictive tool and delaying too much the availability of the results) or be too coarse for the expected convective speeds to surface under the numerical noise. Furthermore, the detailed behavior of the water inside the WT is not important to us, beyond its role of distributing the temperature towards the scintillator volumes. Additionally, it is expectable from the results in Section 4.2 and [156] (especially the seasonal studies) that, given the large power transmission from the air column to the water, the fluid's behavior in its most external layers would present the system's most complex –and consequently, computation-intensive– dynamics.

In consequence, and capitalizing on the precise data offered by the internal Phase I sensors, a simplified model of the Stainless Steel Sphere (SSS) was chosen as the next steps in the simulations, and the first model to characterize the Inner Detector's convective behavior.

4.5.1 Model setup

The "Simple Sphere" model is, as its name suggests, much simpler in structure than the conductive-only models. However, its *closed* system condition as well as the presence of fluid movement means that it is much more delicate with respect to iterative timing, mesh geometry and iteration divergence probability.

For these reasons, a "barebones" sphere *without* vessels was set up. This would enable us to iron out the most important technical aspects:

- **Time-dependent boundary condition** setting and its influence on model divergence.
- **Mesh geometry** and its effect on spurious effects or numerical noise.
- **Δt for iterations** (simulated time per iteration) and its effect on simulation accuracy.

For the first item, we followed a similar approach to the conductive models and set a series of 8 domains, bounded by the temperatures of the Phase I.a OB sensors (and the topmost/lowermost Phase II.b water sensors, which are approximately at the same height as the top/bottom of the SSS) at their corresponding heights –extrapolated horizontally to the Sphere's boundary–, and set the interior temperature through the linear interpolation in x and y used for the initialization of the conductive cases[156] (see Figure 4.49).

Then, as the simulation progressed, a custom-made software tool developed by us (`time_evo`) took care of checking, at each iteration, at which point the simulated time was, comparing it

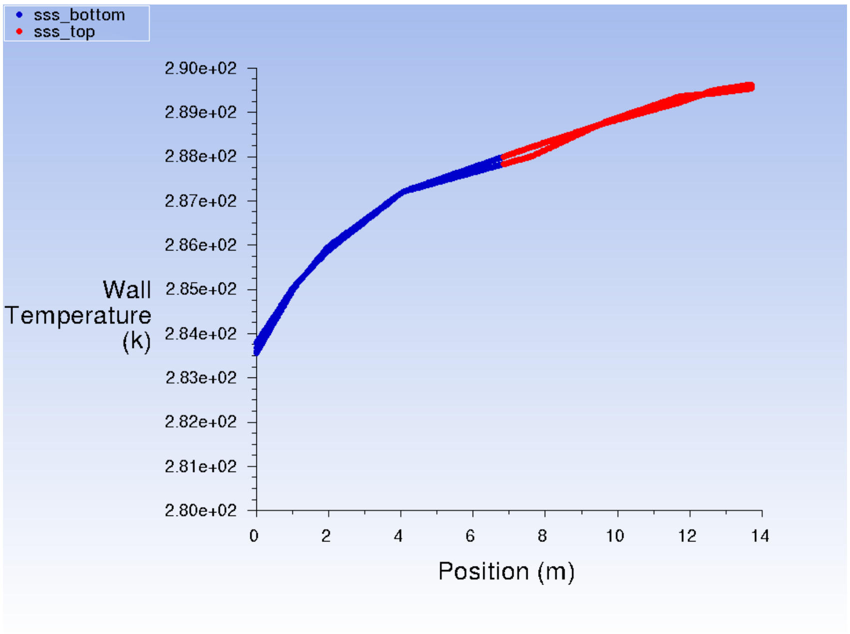

FIGURE 4.49: Typical temperature profile in the *Simple Sphere* SSS boundary.

with the listed times in the recorded data from the LTPS probes. Once this simulated time reached or exceeded a given time limit (set at **1800 s**, since that is the standard time delay between data acquisitions by the LTPS sensors), the appropriate historical temperatures were updated as the imposed boundary condition. Provisions were implemented to ensure good data for the boundary conditions would always be available: in case dropouts in data acquisition were present, as sometimes is the case, the imposed temperature would be kept at the last available value. This can cause a slight upset once new data is available, but the need to select relatively small periods for computation efficiency meant the dropout periods were short and few. Also, these "jumps" are small enough in magnitude that the modeled fluid's thermal inertia will moderate and smooth out the excursion.

A linear interpolation (see Equation 4.11, where i$\epsilon[1,8]$ is the corresponding domain, N/S is the side of the SSS under consideration and h_0, h_1 are the heights bounding the different domains) was also used here for the boundary points between the different probes' heights.

$$T_{N/S}(t,y) = \frac{1}{h_1^i - h_0^i}\left(T_{N/S}^{i+1}(t)(y-h_0^i) + T_{N/S}^i(t)(h_1^i - y)\right) \tag{4.11}$$

This tool was verified to not cause large enough "upsets" on the boundary conditions with respect to the simulated medium to motivate divergences in the numerical solver, at least with the refreshing rates we are interested in, and will be used in all time-dependent models from now on.

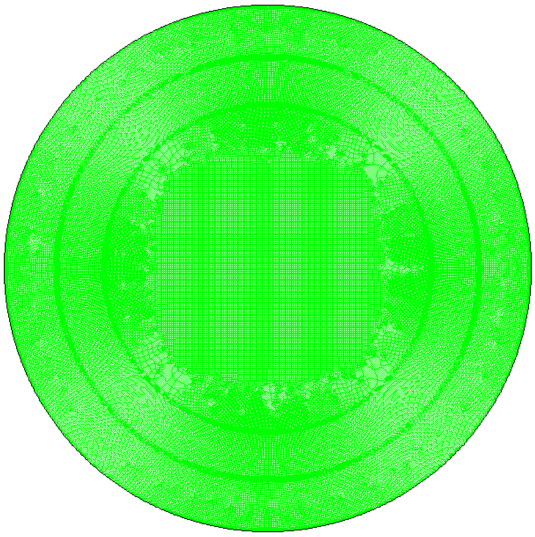

FIGURE 4.50: Rectangular strategy for mesh vertex convergence, following the pattern developed for the conductive cases.

Secondly, we developed several different mesh designs for the Sphere (seen in Figures 4.50 and 4.52), with the vessel shapes in place but not assigning them a physical substance initially, and "turning them on" later on. The outermost sections of the model are practically identical to the corresponding ones in the full detector, conductive-only model: they present a radial mesh with an average cell size on the order of 10 cm^2. However, as was noted before, the number of vertices on the Sphere's boundary **must** match the number of vertices in more interior areas, or be reduced through convergence of several vertices into one. There are different ways of doing this, and their effect on the result must be checked carefully.

We tried the same approach as in the conductive models, and established a rectangular grid area with a side of $\sim$3 m in the Inner Volume, as seen in Figure 4.50. This had a very obvious numerical noise effect, in the form of currents, concentrated around the transition between one mesh disposition and the other (see Figure 4.51).

Another approach we tried was the *pave*-creating algorithm for cell creation (see Figure 4.52), which resulted in an irregular structure in the central areas where vertex convergence is necessary, offering a cell setup with no definite preferential direction. This, even if it has the potential of creating locally stronger numerical effects, should allow for an overall reduction of regionally-large artifacts that may mask real trends.

This approach showed a tendency to reduce discretization in the currents observed in the buffers of the rectangular-based mesh as well as eliminating the along-boundary instabilities seen in the rectangular-to-spherical transition in the previous model. On the other hand, as

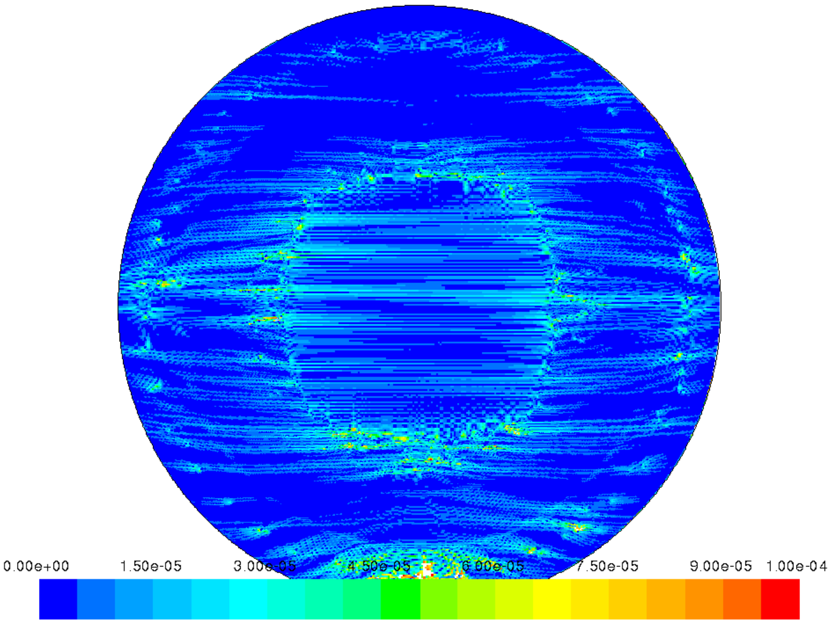

FIGURE 4.51: Velocity magnitude plot following the patterns of (ir)regularity in the rectangular mesh, evidencing a probable numerical noise origin for them.

can be seen in Figure 4.53, distributed features along the whole Inner Volume were seen, which could or could not be the result of numerical instabilities, due to their small magnitude –which nevertheless could be compatible with the observed polonium fluctuations if indeed caused by fluid movement carrying it. Of course, further investigation is needed to ascertain to what level these initial features can be trusted, especially since the vessels are "off" in this configuration and there shouldn't be *a priori* any justification for stronger IV activity not translating to the buffer areas.

4.5.2 "Simple Sphere" results

A characterization of the simulation performance can be estimated through its velocity convergence times. In particular, choice of the mesh size and simulation timestep is conditioned by the required fidelity on the one hand, but also on the compromises that can be made for computational efficiency. As can be seen in Figure 4.54, some mesh sizes cause unacceptably large equilibrium velocities (coarse (∼50cm), medium(∼20cm)), and the preferred timestep of 9 seconds of simulated time per iteration (already suggested by experience in other CFD cases) showed similar performance to a shorter 5-second timestep that would nevertheless increase simulation time. Mesh distribution did not show important changes to convergence time or residuals.

A way to determine the level of numerical noise inherent in the model is to establish a presumably stable configuration, such as a N/S-symmetrical, top-bottom positive linear thermal

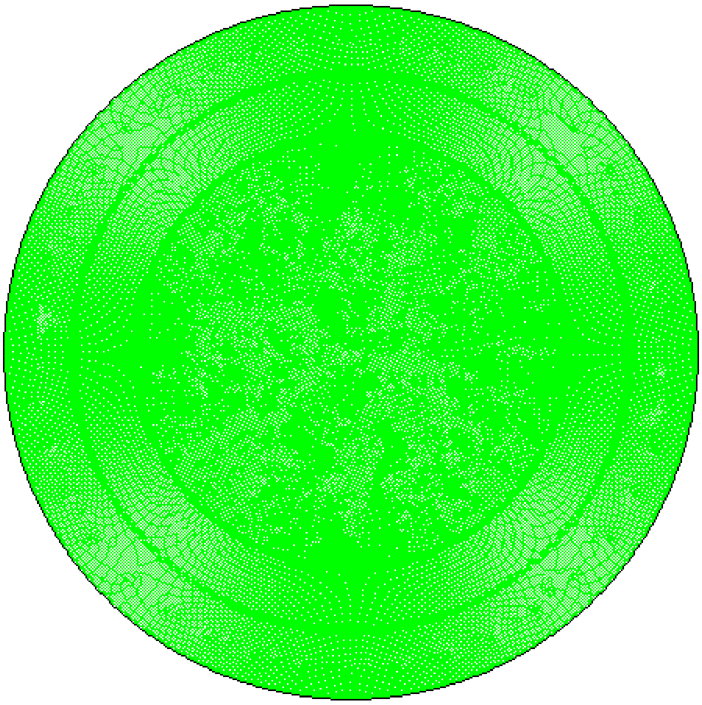

FIGURE 4.52: "Paved" strategy for mesh vertex convergence in the IV's center, avoiding preferential directions in numerical noise that may mask underlying physical effects.

stratification in the Simple Sphere, and impose that same temperature profile as a constant boundary condition (see Figure 4.55). This is an ideal configuration under which Borexino's ID is presumed to be stable (although based on observation this stratification wouldn't be linear, having a steeper gradient in the top than in the bottom –however, we ignore this operational difference to avoid complications in this baseline model).

Through this *Stratified* Simple Sphere without vessels, a handle on the current velocities inherent to the numerical CFD method on the paved mesh was obtained: $\mathcal{O}(10^{-6})$ for absolute magnitudes spanning large scales (see Figure 4.58). It can also be seen the majority of the velocities lie in the horizontal direction, with very localized numerically-induced larger velocity regions ($\sim \mathcal{O}(10^{-5})$ m/s) in the Y direction. However, overall Y velocities are compatible with zero ($<10^{-7}$ m/s). A detailed view of the largest inhomogeneities in the lower right side of the IV can be seen in Figure 4.57.

4.5.3 Vessel-separated SSS results in different periods

Next, the vessel structures already present in the previous Simple Sphere model were "activated", meaning they no longer were infinitely permeable to the fluid and presented a different composition (nylon) that the surrounding fluid. This represents a realistic approximation to the ID's real geometry, neglecting local disturbances such as the PMTs, hold-down structures,

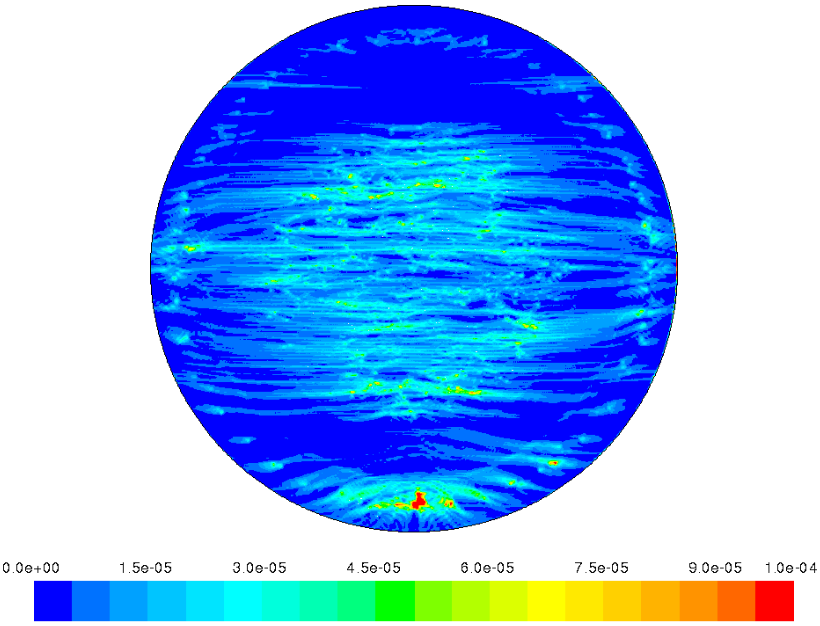

FIGURE 4.53: Currents obtained for the "paved" Simple Sphere geometry with no vessels. Although the trend to assign local currents around the irregular mesh areas (mainly around the vessels limits, where the mesh size is tightened), the overall trend is now more uniform. It should be noted the strong recirculation feature in the OB's bottom is present in both this and the previous model, suggesting a physical origin.

etc. Being bi-dimensional, the inclusion of these features would result in a less realistic model than without them, also adding unnecessary complexity –since the phenomena under study are constrained to the IV.

A *Stratified* scenario was first implemented, identical to the one in the previous Section but with the vessels in place, both for the rectangular and the paved meshes. As could be expected, the horizontal currents spanning the length of the SSS are now cut to just within the IV, with a somewhat radial distribution of small currents also in the OB. The IB appears remarkably free of currents, as can be seen in Figure 4.59. However, a further rationale toward dropping the rectangular mesh in favor of the paved one emerges here again: the horizontal currents are much better distributed than in the clearly mesh-influenced rectangular case, showing a more convincing unbiased pattern. In both cases, vertical currents remain at a very low level ($<10^{-7}$) as in the case with no vessels, but again these vertical currents linger in inhomogeneous mesh areas in a more structured way in the rectangular model (see Figures 4.59 and 4.60).

The different periods in Borexino were considered according to Section 3.4.1. The uninsulated period was less considered in the following simulations, since it didn't exhibit such a rapidly changing behavior as the transient one, and at the same time was less important to Borexino's future thermal environment, with the TIS now in place. For that reason, the start of the *Insulated* period was simulated ($\sim$1 month), as well as the first 15 days of the *Transient* period. The insulated period provided a benign environment for troubleshooting and stable conditions

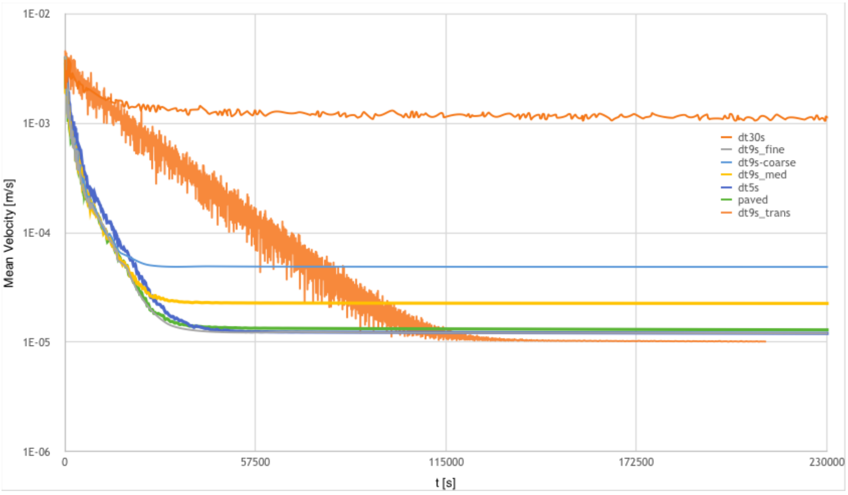

FIGURE 4.54: Mean velocities convergence for different vessel-less "Simple Sphere" models. More rapid convergence to lower equilibrium values is generally a good indicator for model fidelity. Mesh size is seen to be a major influence for the latter, while simulation timestep tends to delay convergence. The noisy dt_9s_trans case represents a different, more dynamic period of recorded temperatures.

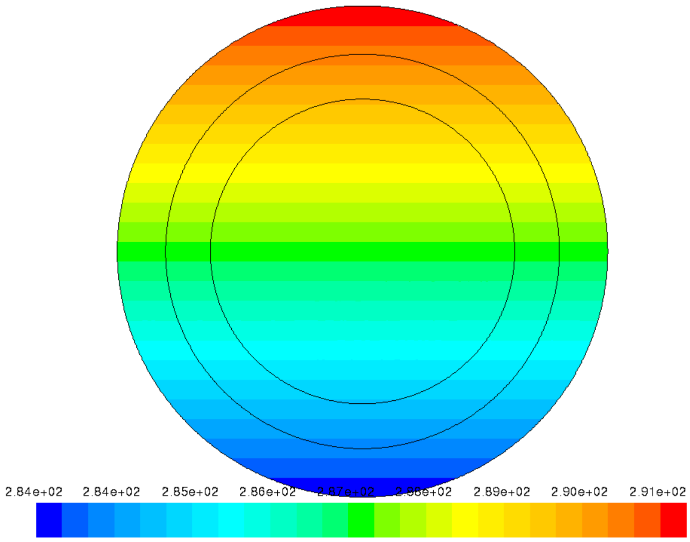

FIGURE 4.55: Initial temperature distribution for the stratified Simple Spheres. Contrary to Borexino's, this stratification is homogeneously linear in nature, and horizontally symmetric –thus inherently stable apart from possible small horizontal instabilities. This distribution was mimicked as constant boundary condition on the model's edges.

on the order of weeks-months, while the transient period offered marked temperature changes happening on the order of days-weeks, therefore enabling less subtle driving forces for convection to occur.

As can be appreciated from Figure 4.61, showing a snapshot of the state of the system after being let evolve for ∼one month in the beginning of the *insulated* period, the currents are still quite low in magnitude, only surpassing $\mathcal{O}(10^{-5})$ in particular regions of the bottom and top of the OB, possibly triggered by the imposition of the approximated interpolated boundary

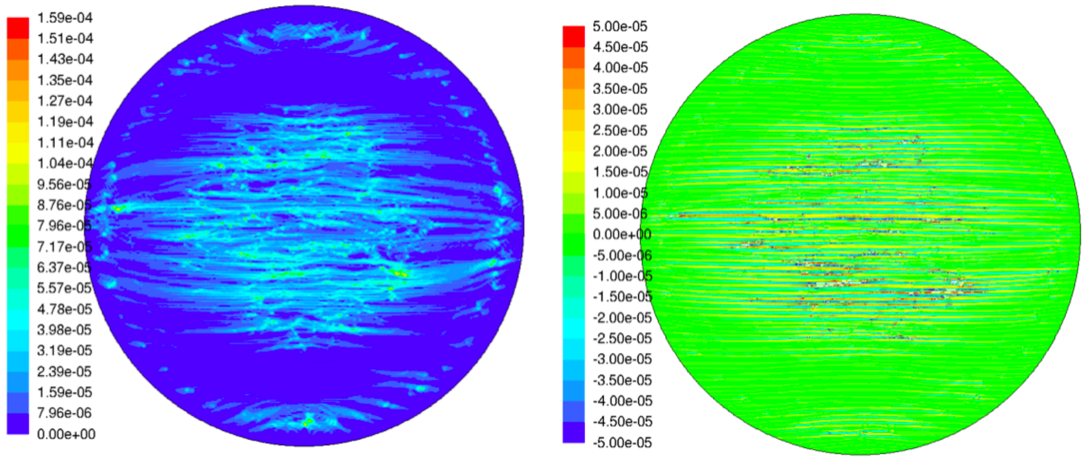

FIGURE 4.56: Velocity distribution in the stratified, no-vessel geometry. The overall structure is clearly the same as in Figure 4.53, albeit with slightly smaller magnitude. While this clearly points to the mesh geometry as a source of instabilities, not all the currents are just numerical noise, since it is physically reasonable that a horizontally-stratified distribution should offer minimal resistance to horizontal currents. Indeed, the right-hand side image shows the X-velocities, exhibiting SSS-wide paths.

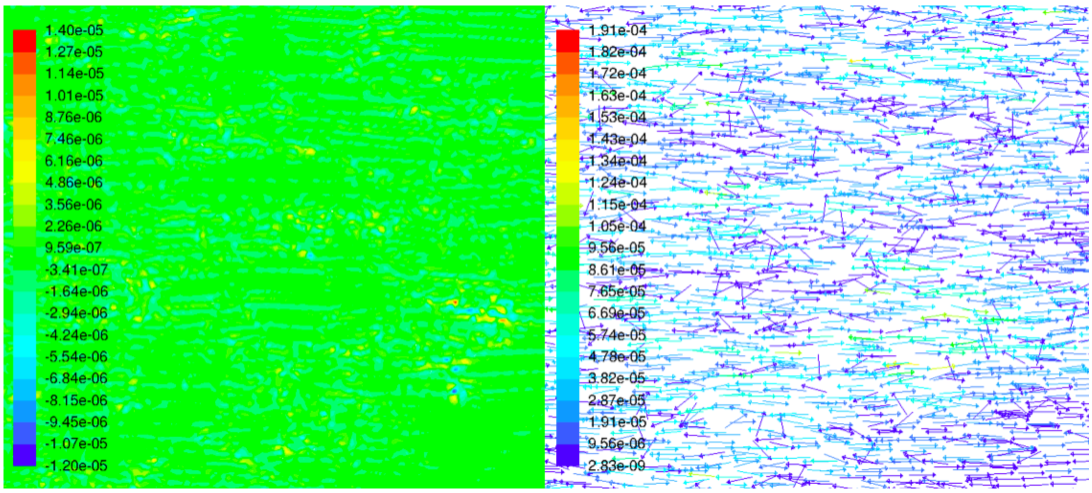

FIGURE 4.57: Details of largest Y velocity distributions in the no-vessel scheme. Both on the left-hand side (contours of Y velocity) and right-hand side (velocity vector distribution) images, the numerically-induced vertical velocity are very low ($<10^{-7}$ m/s), and even compatible with 0, except for very localized areas ($\mathcal{O}(10cm)$).

conditions. The bottom feature appears to be consistent with previous cases however, and although possibly triggered by mesh irregularities, does still show larger currents and more structured appearance than the upper one (which is mostly horizontal in nature in this case). The IB shows Inner Vessel-grazing horizontal features that are not present in the stratified control case. The IV shows a similar pattern to the stratified case, although with larger magnitudes and some small differences, mainly enlarged horizontal currents. The largest-magnitude currents are shown to occur along the outer boundary, with peaks $\sim 10^{-3}$ (see Figure 4.62). Vertical currents remain very low and unstructured, with peaks of $\sim 10^{-5}$ m/s.

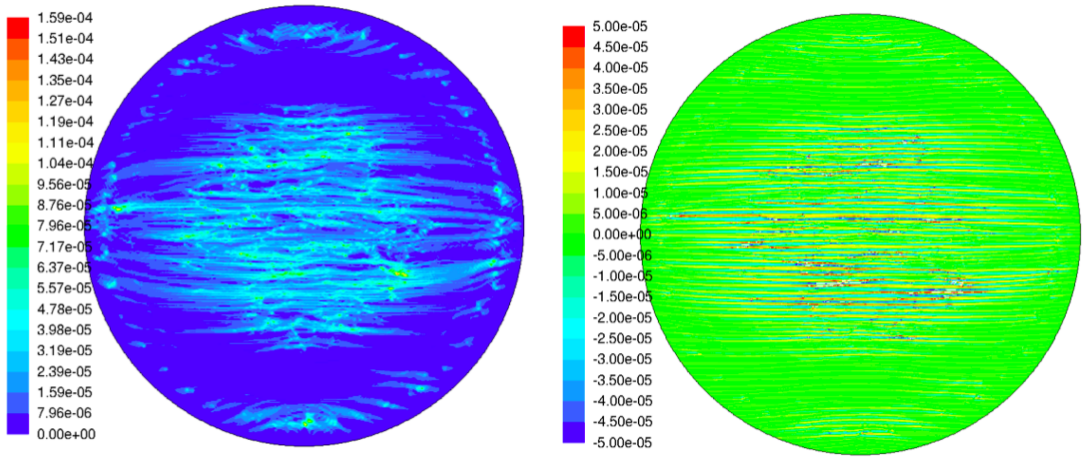

FIGURE 4.58: Velocity distribution in the rectangular and paved stratified geometries with vessels. Similar orders of magnitude are visible, albeit slightly lower in the paved case. The mesh-induced preferential direction in the rectangular mesh case is clearly visible though, promoting IV-wide horizontal currents while seemingly cancelling out vertical ones, even locally. Also, the irregular transition from the radial to the rectangular section of the mesh causes strong local currents ($>10^5$ m/s), avoided in the paved case.

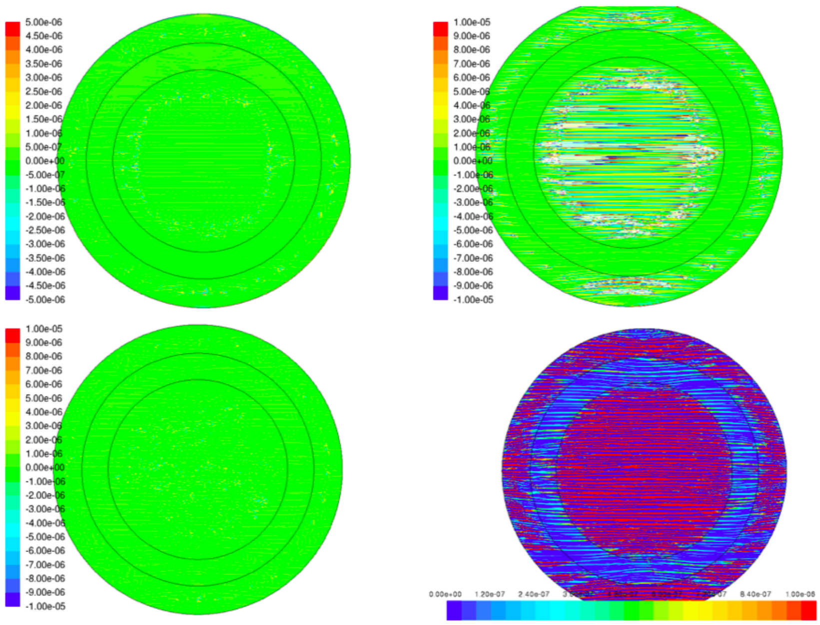

FIGURE 4.59: Y and X velocities (left and right, respectively) of the rectangular and paved meshes (top and bottom, respectively) for the stratified model with vessels.

For the transient period, a much more dynamic situation presents itself, as could be expected. The "rising" recirculation pattern seen at the bottom of the OB in the insulated case is, in this case, exchanged for a large approximately horizontal pattern that spans this volume's length (see Figure 4.63). Vertical velocities are much stronger, compared to the insulated case, in particular in the top of the buffers. A stronger downward component in the velocities also appears that was not present in the previous case. Nevertheless, apart from a slight increase in magnitude, the features visible in the IV remain largely unaffected, showing that they are

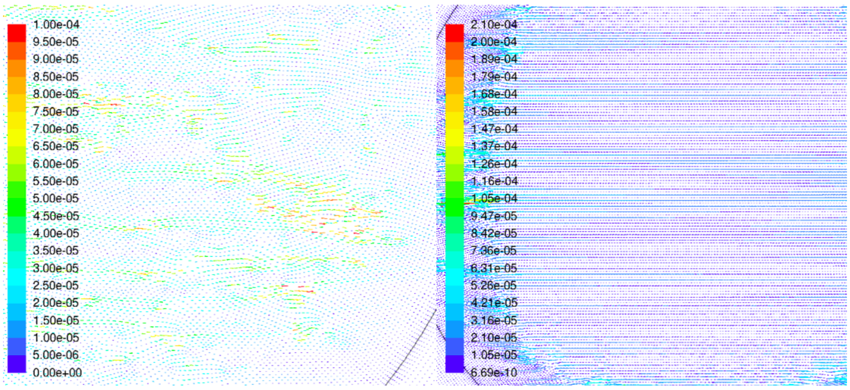

FIGURE 4.60: Detail of the (un)structured nature of the rectangular, on the left, (paved, on the right) mesh for the largest velocity areas in the stratified model with vessels.

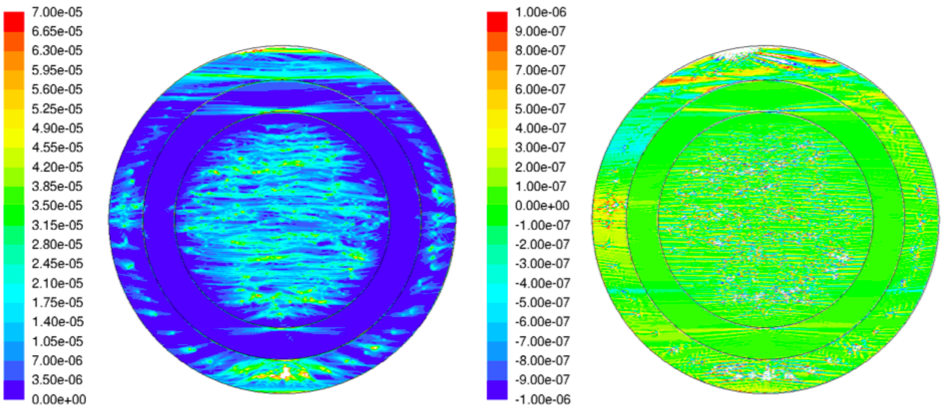

FIGURE 4.61: Velocity magnitudes and Y velocity component for the insulated scenario with the *Simple Sphere* after 2518000 s of simulation.

mesh-enhanced. A comparison between the stream functions ([kg/s]) shows their asymmetrical nature in the transient case, while they are much more horizontal in the insulated one. Moreover, the magnitude of the ones affecting the center of the FV reaches ~50% more in the transient case, as could be expected.

4.6 *Water Ring* convective bi-dimensional models

The *Simple Spheres* offered very valuable insight into the behavior of the model for both a presumably-stable system (the stratified condition) as well as real temperatures being imposed as boundary condition on the SSS surface. However, even if clear differences could be observed between the stratified and the real temperature cases, the level of presumed numerically-induced currents was still high. Although physical meaning can be assigned to some features seen in the *insulated* and *transient* cases, there remains the question of how much of them would still be present if the numerical noise was reduced –and, in general, how certain we can be that the reproduced results somehow match the real situation taking place inside Borexino. The currents

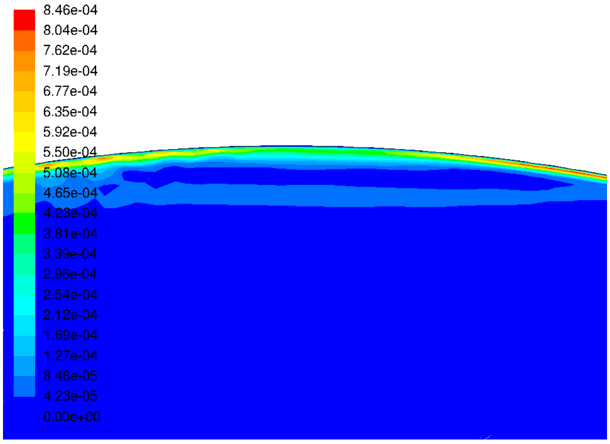

FIGURE 4.62: Detail of the peak velocities along the SSS boundary, at least in part caused by the interpolation jumps, for the insulated case with vessels of the *Simple Sphere* model.

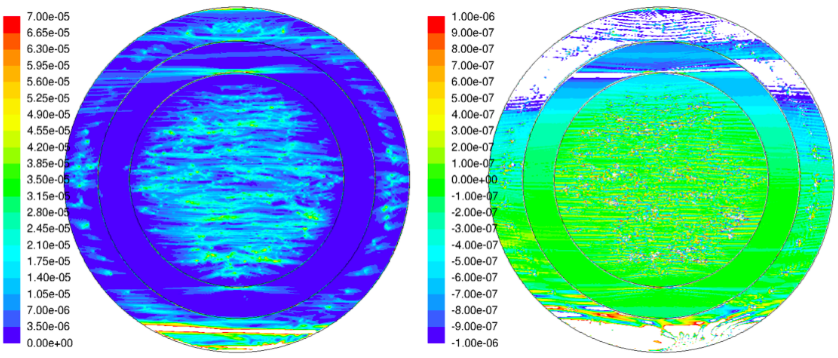

FIGURE 4.63: Velocity magnitudes and Y velocity component for the insulated scenario with the *Simple Sphere* after 1382000 s of simulation.

observed are of the approximate order of magnitude that we believe is correlated with the ^{210}Po movements inside the FV, but there are many complicating factors that may be masking stronger effects, or even subtler ones that get masked under the CFD-induced noise. Furthermore, we would need a good handle on $\mathcal{O}(10^{-8})$-level currents to be certain we understand the model to the required level –that is, where the currents would be too slow compared to the lifetime of ^{210}Po to no longer present an operational problem for Borexino's ^{210}Bi precision level determination.

Due to the aforementioned factors, it is advisable to benchmark not only the general reproducibility of results seen in Section 4.4 but also the model behavior in our particular cases of interest. Although we have no way of directly measuring fluidoynamic effects inside the SSS, apart from the limited inference obtained from the background movement analyses, we do have a good thermal transport probing system: the Phase I LTPS sensors. Indeed, as seen in Section 3.4.2, we were able to empirically measure the time constant for the thermal inertia between inside and outside of the SSS from the Phase I.a and I.b sensors. We can now employ the temperatures registered on the outside (water, Phase I.b) and see their transmission toward the inside of the Sphere. Moreover, these temperatures can be interpolated with greater precision

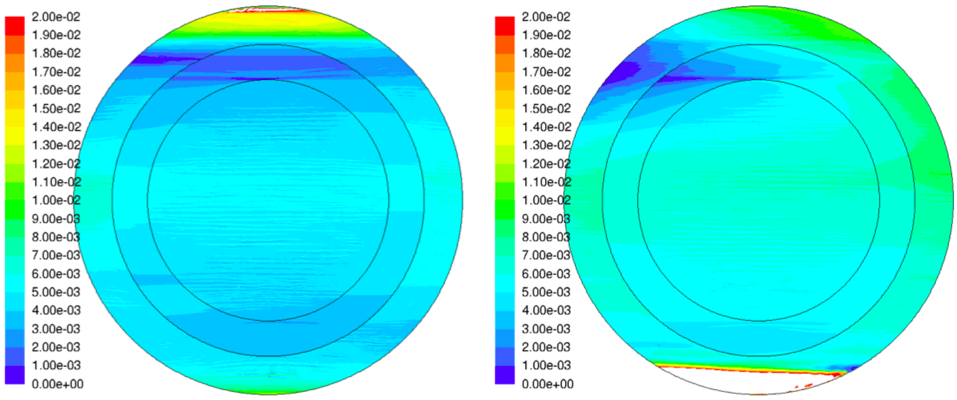

FIGURE 4.64: Comparison of the stream functions [kg/s] of the insulated (left) and transient-selected (right) cases after 1382000 s of simulated time. A clear asymmetric and more dynamic situation is evidenced in the latter case.

than for the *Simple Sphere* case. However, the most interesting feature is that the simulated transmitted temperatures for the inside can be confronted with the internal (buffer, Phase I.a) recorded temperatures, and therefore establish the level of fidelity on thermal transport that our CFD strategy can offer.

4.6.1 Model setup

The *Water Ring* geometry is based on the *Simple Sphere* cases with vessels "activated", just adding a water volume around the SSS reaching until the nominal positions of the LTPS Phase I.b sensors in the OD: 0.5 m outside the sphere in its radial direction. Therefore, the water volume around the sphere is a 0.5m-thick ring, truncated at the poles (see Figure 4.65) to avoid complications with interpolating higher/lower than the measuring heights of the temperature probes.

A separate initialization was used for the water and SSS' interior, using the same interpolation strategy as in Equation 4.11, adjusting it for the number and positions of the Phase I.b sensors in the case of the water, and imposing each temperature map on its domain of influence (Phase I.b data on water ring, Phase I.a data on the interior of the SSS). Once the simulation started to run, a `time_evo` file would act as in the *Simple Sphere* cases, only this time imposing the boundary conditions on the model's boundaries: the edge of the water ring, following historical data from the Phase I.b sensors. The conditions inside the SSS were left free to evolve.

The benchmarking power of this model was realized by placing "tallying spots" in the nominal positions of the Phase I.a sensors, as seen in Figure 4.66. Although some error is to be expected in the beginning of the simulation, since the extrapolation routine for initialization is assuming the "true" temperatures from the Phase I.a probes are located on each domain's vertices as

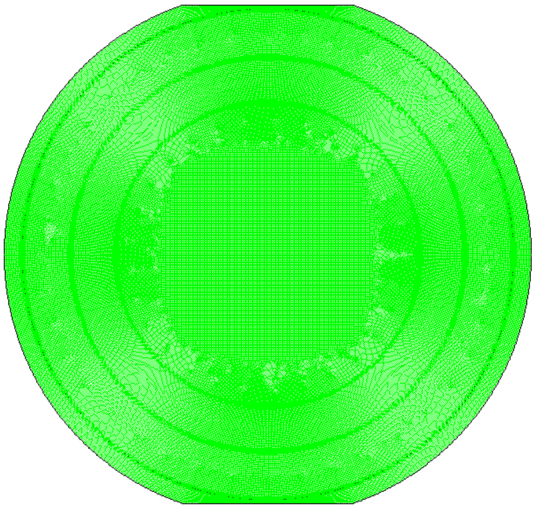

Figure 4.65: Addition of a 0.5m-thick water ring (with truncated poles) around the SSS in order to impose Phase I.b sensor boundary conditions, instead of projected Phase I.a data on the SSS' surface.

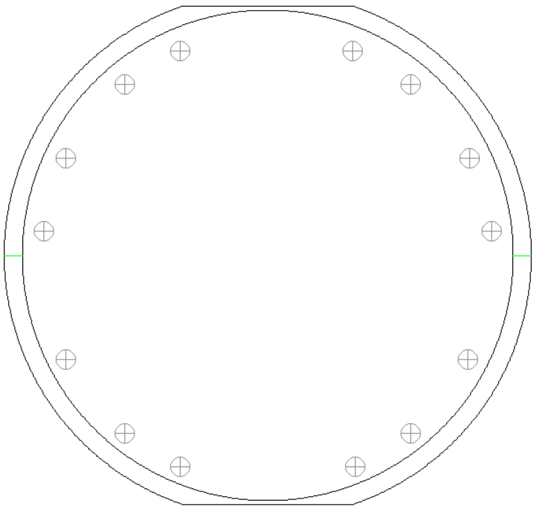

Figure 4.66: Monitoring points on the corresponding Phase I.a LTPS sensor positions.

explained in Section 4.5, it was observed the time evolution of the system with the water's boundary conditions tended to naturally correct the discrepancies away.

These cases, as with the previously mentioned *Simple Spheres*, focused on the *Transient* and *Insulated* periods, with simulated times on the order of ∼1 month. Moreover, the *Water Ring* setup needed good temperature data from the Phase I.b sensors to be available, in order to

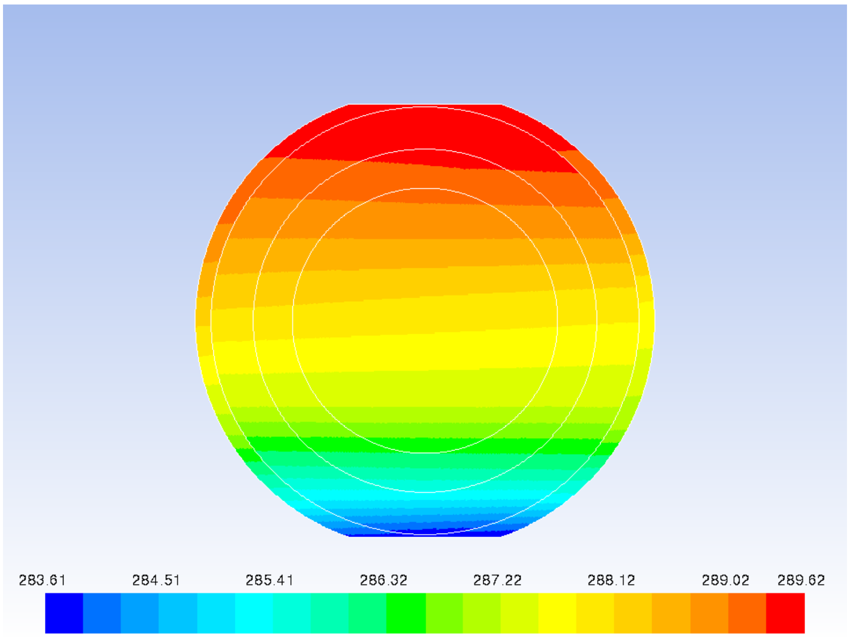

FIGURE 4.67: Initialization profile of the *Water Ring* model. As explained in the text, the ID and WR are considered different domains, hence the –physically reasonable– discontinuity at the SSS.

properly impose the time-changing boundary conditions on the periphery of the model, as well as to properly initialize the water ring temperature profile. Therefore, the earliest possible date for this model to be applied was April 10th, 2015 –which roughly coincides with the end of the transient period.

4.6.2 Insulated period

The WR insulated period considered the recorded temperatures from November 15th, 2015, during ∼16 days with the paved model. Although the rectangular model was also used for a longer period of ∼23 days, its results showed more divergence with respect to the recorded data and are therefore not reported further here.

Figure 4.68 shows the residuals ("true" historical temperature minus simulated temperature at the same time and position) for the 14 positions of the LTPS Phase I.a probes. Good agreement can be seen, with a smooth exponential trend toward stable errors, up to ∼<2.25°C –although equilibrium errors are no bigger than ∼0.15°C. The overall trend shows a remarkable agreement between recorded and simulated data, as shown in Figure 4.69. Even more remarkably, the simulation shows an "automatic" correction behavior, whereupon the temperature initialization profile that sent temperatures to slightly incorrect values, due to the interpolation strategy followed, is corrected by the time evolution profile and allows the behavior to follow the recorded

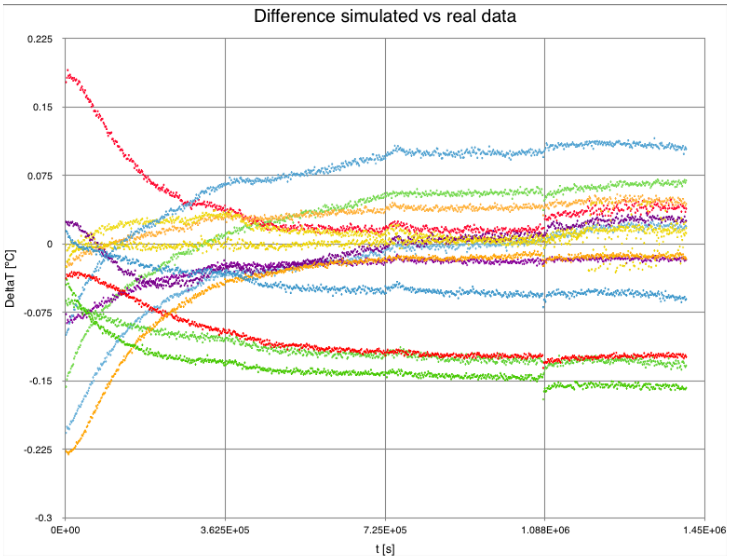

FIGURE 4.68: Residuals between real recorded temperatures and simulated ones for the same locations in the same timeframe (insulated period).

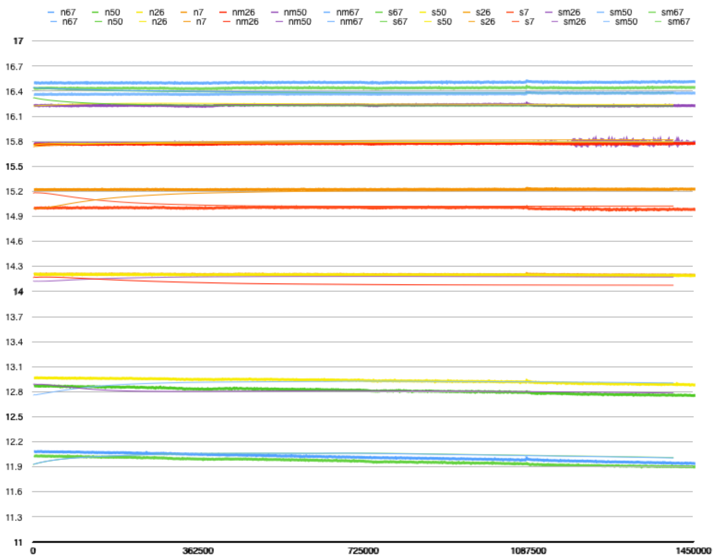

FIGURE 4.69: Time evolution for the real (thick lines) and simulated (thin lines) temperature profiles for the insulated time period considered. Note the simulation's "automatic" correction behavior at the beginning of the run, where due to interpolation errors the initial temperature field did not correspond with the one imposed by the changing boundary conditions. After ∼48 h of simulated time, the temperatures converge to their true values, within the errors in Figure 4.68.

data profile within 2 days of simulated time. This highlights the robustness and benchmarking potential for the *Water Ring* approach.

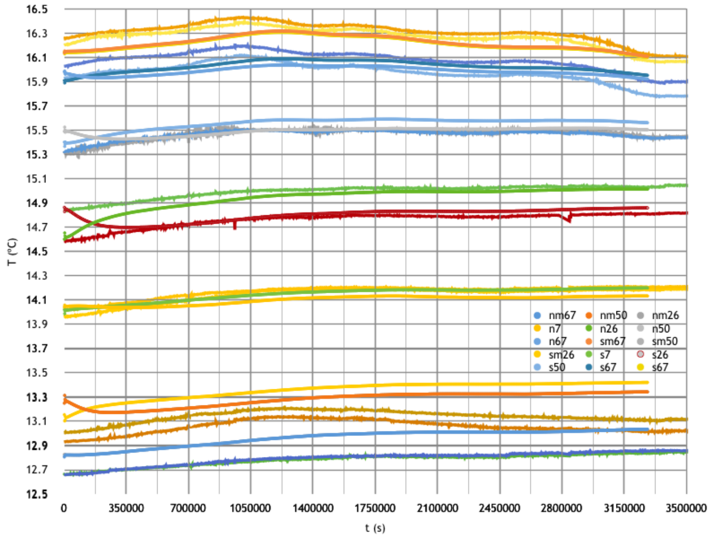

FIGURE 4.70: Time evolution for the real (thick lines) and simulated (thin lines) temperature profiles for the transient time period considered. The automatic "correcting" behavior is still visible, and matching of the simulated vs recorded temperatures is very good, with ∼<0.2°C maximal deltas.

4.6.3 Transient periods

Two transient periods were considered: one from the start of this period (May 10th, 2015), and one overlapping the end of this period and the beginning of the insulated one (October 20th, 2015). The first one, also called *Transient Selected*, offers very dynamic events in the upper part of the ID, and therefore permits a straightforward comparison of the temperature features in the recorded data, to be confronted with the simulated ones. On the other hand, the second one, also called *Bridge* Period, allows for overlap between the more dynamic phase of the transient period with the calmer, and already simulated phase of the insulated period, as a way to check the model dependency of the residuals.

Transient Select

The *Transient Select* simulation period was ∼37 days, covering the peaking features visible in detector's top sensors at the start of the Transient period (see Figure 3.34). In this case, the existence of these features represented a more challenging set of rapidly-varying conditions that needed to be reproduced accurately in the simulation. As shown in Figure 4.70, this was achieved with high fidelity, and the maximum residual differences between the absolute simulated and recorded temperatures are still kept to the ∼0.2°C level as in the more stable *Insulated* regime.

A temporal phase shift is evident due to the sharper features characterizing this time period. Although one would be tempted to blame that on a more-sluggish-than-real thermal transmission in the model compared to the real case, this effect can actually be determined not to be caused by that upon closer inspection: indeed, a slower thermal transport would be causing a broadening

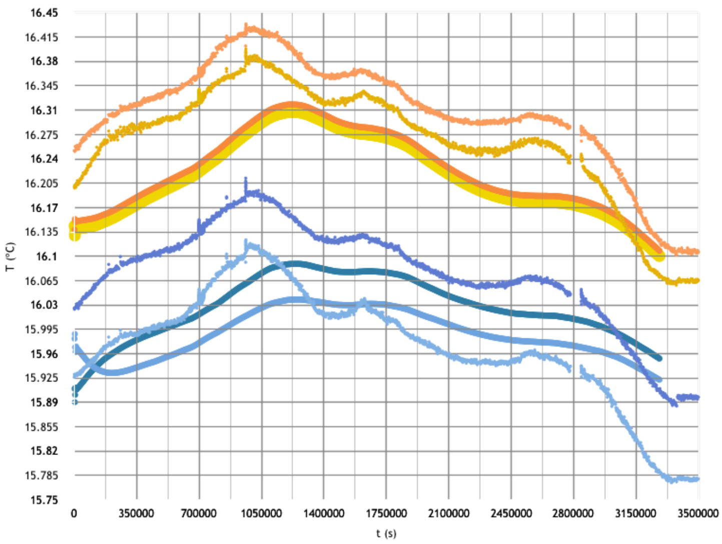

FIGURE 4.71: Detail of the real (thick lines) and simulated (thinner lines) temperature profiles for the transient time period considered, for the two top sensors (67° and 50°). A phase shift of ∼1-2 days is visible, apart from the obvious slight offset (maximal for these four sensors) in the abscises axis (see discussion in text).

of the features, with increasing lag between the simulated and the real feature. On the contrary, the shift is constant and the features (if the phase shift is cancelled out manually) are seen to line up almost perfectly, albeit with a certain –small– decrease in slope change. The cause for this effect, first thought to be a simple mistake in choosing the time period to compare (which was later disproven), is still under investigation, but is considered not to negatively impact the overall reliability of the thermal transport benchmarking power of this model, given it represents a small and constant shift.

"Bridge" Period

In order to fully ascertain the reproducibility of the temperature offsets (and phase shift) in a different, intermediate period between the very dynamic *transient* and the much calmer *insulated* periods, a *"bridge"* period was simulated. This period also featured several ∼day-long data dropouts in the Phase I data, due to detector operations and blackouts. We could use those to verify the stability of our simulation. As can be seen in Figure 4.72, the matching is even better than in the *transient* case, with maximum residuals on the order of ∼<0.1°C.

4.6.4 Water Ring model as a thermal transport benchmark

From the previous results, the *Water Ring* models are seen to provide a powerful benchmark for thermal transport, quite faithfully (< ±0.2°C, and much better in some cases) replicating the temperature evolution in the OB's LTPS Phase I.a probes positions when the boundary condition represented by the Phase I.b sensors is imposed ∼1 m away, in a different medium (water) and

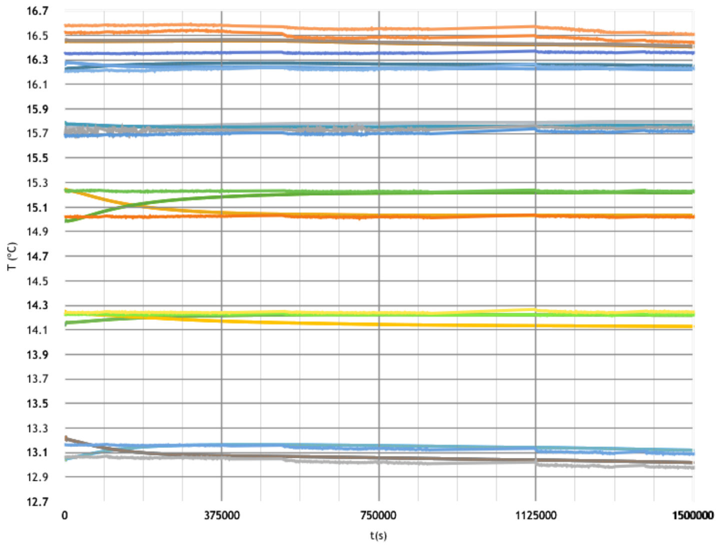

FIGURE 4.72: Time evolution for the real (thick lines) and simulated (thin lines) temperature profiles for the "bridge" time period considered. The automatic "correcting" behavior is still visible, and matching of the simulated vs recorded temperatures is very good, with $\sim$<0.1°C maximal deltas.

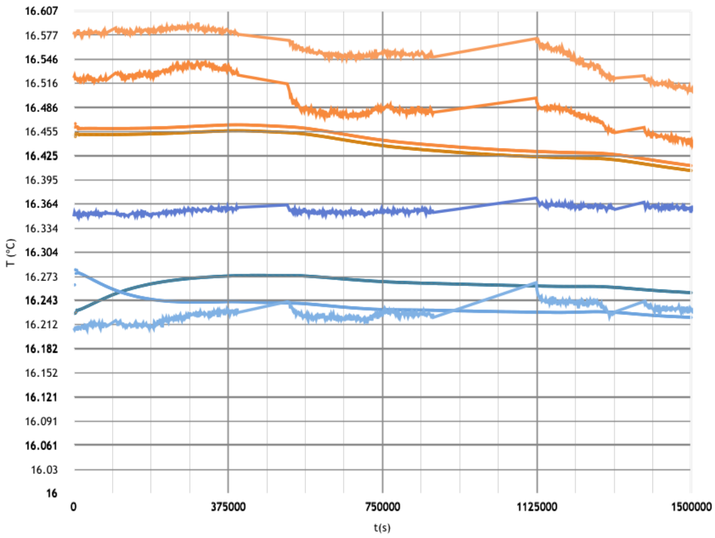

FIGURE 4.73: Detail of the real (thick lines) and simulated (thinner lines) temperature profiles for the "bridge" time period considered, for the two top sensors (67° and 50°). The phase shift of $\sim$1-2 days is visible, apart from the obvious slight offset (maximal for these four sensors) in the abscissas axis. Note the dropout periods in data as straight lines standing out from the jagged profile of continuous DAq.

having to pass through the SSS structural element. Therefore, at least as far as thermal transport capabilities, the implemented FLUENT models are a useful tool to understand, replicate and foresee the thermal environment in the detector. Further, it is reasonable to believe that this extrapolation will hold, for the same geometry (and possibly for similar ones), at other points in the model.

It is not, however, a benchmark for *fluid* transport: in principle, the model could be replicating well the temperature fields while generating unrealistic currents or flow patters that would not match reality. This is a complicated issue to test, since the regimes modeled are not the main ones FLUENT is optimized for, and the *Simple Sphere* stratified models showed at least some of the observed currents to be inconclusive or fully numerical in nature. Moreover, there is no "ground truth" data from Borexino, since no "tracer" is available –other than the same backgrounds we are trying to study through this research.

4.7 IV convective bi-dimensional model

A simplified geometry can be devised to attempt to filter out model complexity where it is not needed (buffers) and focus more intently on the area of interest (IV/FV). In other words, a model of the IV alone can be developed, while using the *Water Ring* thermal transport benchmark beyond its confidence-building role to an operational one: time-dependent *Water Ring* simulated temperatures on the IV would be used as "true" temperatures to be imposed as boundary conditions. Then, only a spherical (circular) model would be needed, with no internal barriers, and reduced dimensions, reducing complexity to the minimum –and allowing to minimize systematic model-dependent errors in order to more accurately understand not only thermal transport, but also fluidodynamics in the FV. An "adaptation" (more precisely, a reduction in mesh cell size) was performed on the old IV model to increase performance and simulation reliability. Also, a smaller timestep (half of the previous one, i.e. 4.5 s of simulated time per iteration) was employed.

4.7.1 Model setup

Still using the same initialization and time-evolving boundary condition as the previous models, this case arguably employs the simplest geometry of all –as mentioned, with the aim of reducing superfluous complexity that may limit faithful detailed reproduction of physical effects that may be so subtle as to fall within the numerical noise levels found in the *Simple Sphere* and *Water Ring* schemes. The IV is modeled as a perfect circle of nominal Inner Vessel radius of 4.25 m. The paved mesh approach is used, with a cell size of $\sim$5 cm^2 ($\mathcal{O}(10^5)$ cells, see Figure 4.74). No internal structures or localized mesh tightening is employed away from the model's boundary. Initialization (see Figure 4.74's right panel for an illustration of the initialized model) is performed picking the simulated temperatures a few centimeters outside the vessel in the *Water Ring* models. This small distance away from the vessel is chosen so as to avoid boundary layer effects that may locally shift the isotherms in a way that would falsify the most realistic temperature mapping in the bulk of the IV. As such, these temperatures were also used

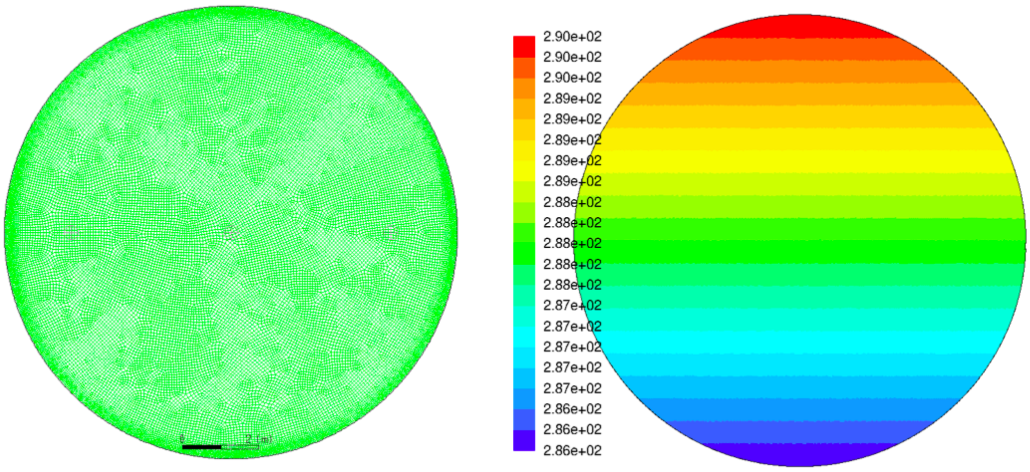

FIGURE 4.74: IV-only model with paved mesh and adapted cell size. On the right, initialized (and constant) stratified temperature profile for numerical noise determination.

as input for a `time_evo` script, in order to impose time-varying boundary conditions on the model's outer wall.

4.7.2 Results

A perfectly-stratified model was also run in order to characterize the level of unphysical currents induced by the numerical iterative process, yielding a background level of $\sim \mathcal{O}(10^{-5})$ m/s, with a distribution similar to that of the *Simple Sphere* IV when it had the buffers around (see Figure 4.76). It is noted part of these currents, despite having a physical origin (especially in the horizontal direction), are mesh-enhanced. The absence of boundary currents along the vessel is notable (see Figure 4.75), in sharp contrast with the model with time-changing realistic temperatures imposed as boundary conditions, as we shall see in the next paragraphs. The model's intrinsic numerical noise level, if the mesh can be regularized, can be much higher ($\mathcal{O}(10^{-8} - 10^{-9})$ m/s), although the circular geometry of this model prevents a mesh that is completely regular all over the geometry. Trial runs with a so-called "quad" mesh, with four approximately-checkerboard patterns that converge in a central rectangular mesh, akin but not equal to the very first meshes employed in these simulations, yielded these order-of-magnitude currents, but induced localized unphysical instabilities in the transition areas that would be unassumable in a realistic case. A three-dimensional model may be able to sidestep these geometrical instabilities, but the large computational time required left this potential for numerical noise reduction as a future perspective to be developed.

The extrapolated temperatures from the *Transient* period harvested from the *Water Ring* model during a month of simulated time were employed as boundary condition for the IV-only

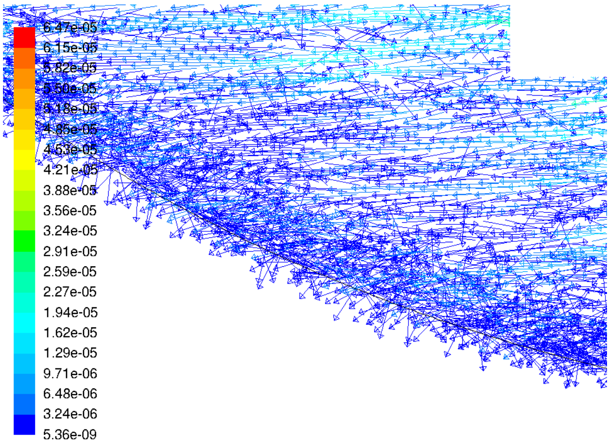

FIGURE 4.75: IV-only model with stratified, constant temperature distribution showing the lack of along-wall currents.

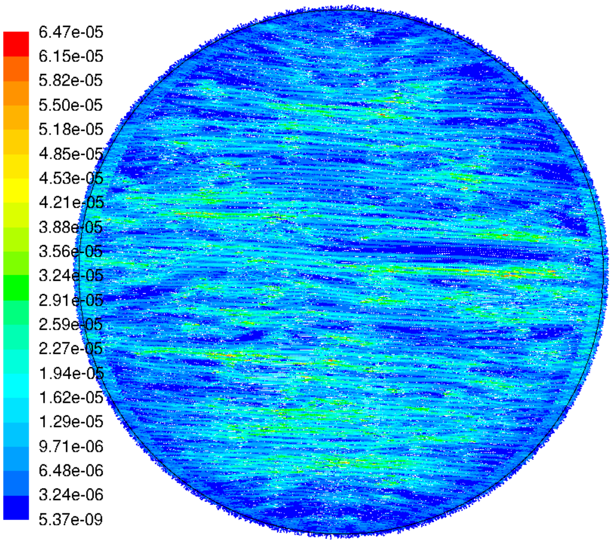

FIGURE 4.76: IIV-only model with stratified, constant temperature distribution induced currents. Note some of these currents, apart from the regional "hotspots", are expected to be of much less magnitude, as explained in the text, judging from results from a more regular mesh that nevertheless caused middle-scale large instabilities that gave a worse overall quality to the model and is therefore not discussed further. However, their presence is believed to be physical.

sphere and the observed behavior was analyzed, taking into account the features observed for the stable stratified model above.

As can be seen in Figure 4.78's left panel and the detailed view of Figure 4.77, important streaming currents were seen to appear at the lower $\sim 1/4$ of the IV, which showed an interesting possible explanation of the recirculation pattern seen in the lower part of the FV in the polonium analysis. However, in this particular period, the bottom recirculation was not seen to be very important, and indeed the streaming function appears to be more restricted in latitude than the top one, which albeit slower, shows a much more widespread distribution on the top third of the IV. This would already come inside the FV, which is in agreement with the increased ^{210}Po levels

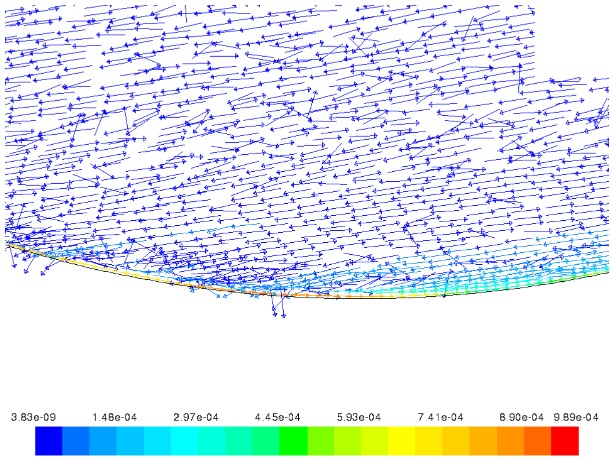

FIGURE 4.77: IV-only model with realistic temperature distribution evolving in time, showing strong along-wall currents, especially at the bottom of the volume. This shows a similar behavior to the observed recirculation at the bottom of the FV through the ^{210}Po analyses.

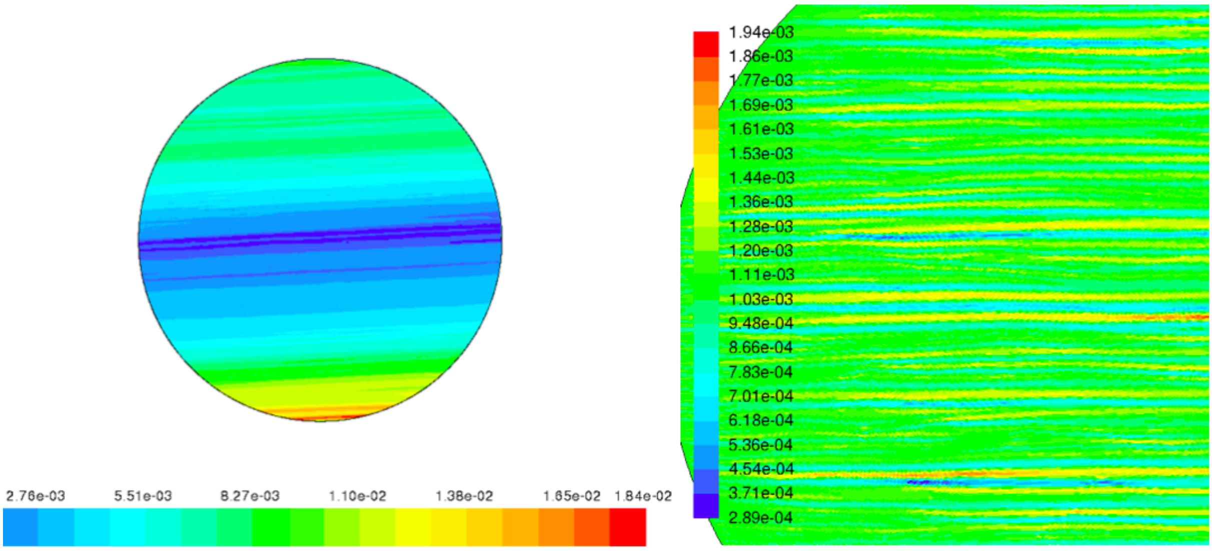

FIGURE 4.78: Stream function [kg/s] contours for the IV-only model with realistic temperature distribution evolving over time (left), showing the strong horizontal currents and along-wall current-induced bottom recirculation, as well as a moderately-increased streaming function at the top third, which is coincident with the simulated *transient* time period. These are compared to the stream functions for the stratified model (right), which are seen to be of much different nature and magnitude.

in that time period. The velocities are $\sim 10^{-5}$, consistent with the apparition of not-yet-decayed ^{210}Po and, therefore, problematic for background stability. However, we shall remind the reader of the results of the stratified model, where horizontal currents were seen to be mesh-enhanced to a certain level, even if based on physical effects. Nevertheless, the distribution and nature of these currents is much different in each of the cases, which clearly points toward the validity of these results in an approximately quantitative way.

4.8 Fluidodynamics and background correlations

The conductive models yielded an important characterization of the *general features* of the detector's ideal, insulated and uninsulated thermal regimes. In particular, they established an upper limit on the expectable *cooling constant* for the system, which is consistent with recorded data-based analytical extrapolations, of ~150-200 W in the long term, or ~0.4°C/year. Furthermore, they clearly showed the topology of such cooling phenomenon, through a lenticular-shaped feature that is accentuated in the middle of the detector, presumably because of a combination of the higher heat conductivity of the bottom steel plates and the cylindrical symmetry, and "crawls" up to the bottom of the SSS. The insulation induces a phase shift of ~1 month between the arrival of a temperature upset event from the exterior environment in an uninsulated condition and that in the fully-insulated system. Furthermore, there is a reduction factor of ~3.5 in the amplitude of such changes, when measured on the interior WT wall. Nevertheless, the largest observed difference in the IV only accounts for ~<0.25°C as the largest seasonal variation –although this would be a lower limit not affected by convection and possibly could trigger large fluid movements, as suspected in the past uninsulated history of Borexino. Therefore, the TIS is shown to have a critical positive influence in the detector's stability through thermal conditioning. Additionally, major structural elements linking the SSS with heat sinks/-sources affected by the external environment are shown to play a negligible, if any, role in the ID's thermal environment.

Moreover, the Active Gradient Stabilization System is shown to have a small effect if operated within reasonable boundaries (17-20°C): the along-structure heat transfer is minimal, while the only noticeable effect in the case of the conductive models is a tendency to anchor the top temperature to a stable value instead of letting it fluctuate with the external environment (or its quieted down version that seeps through the insulation). Convective simulations were not run due to their complexity and computational price, added to the relatively small importance of the water's dynamics –however, it is clear that the heated "lobes" attached to the surroundings of the AGSS contact area in the interior of the WT would be redistributed to generate a layer at that mean temperature, spanning the height of the AGSS serpentines, and not moving down beyond that. For that reason, an active AGSS is strongly suggested and its influence is believed to be beneficial to the overall stable stratification environment and ID's fluidodynamical stability. Finally, it should be noted *all* conductive models, except perhaps for the uninsulated model in some locations, show a remarkably similar behavior, no matter what WT walls boundary conditions are imposed, highlighting the large insulating effect the water and buffer regions have on the IV/FV, only disrupted if the external perturbations are strong while the TIS was still not installed. Therefore, it is expected only small changes will affect the thermal environment of the FV regardless of any fine-tuning operations. Fluid movement and, with it, background stability, still needs the input from the convective simulations to link its behavior with the thermal's.

The benchmark examples, apart from establishing specific reproducible cases from which to interpret the range of validity and fidelity of the simulation package, also showed the existence of global circulation modes when changes in temperature occur along the whole boundary condition, even if those changes are small (∼1% of the stable stratified temperature gradient). Furthermore, temporal delay –modeled with the addition of a variable-thickness insulation layer between the boundary condition instantaneous ΔT imposed and the interior fluid– showed no threshold for the appearance of a structured flow, similar to the uninsulated case, although obviously with much smaller velocity magnitudes. Even if the currents in this structure can be considered negligible for our purposes, it is worthwhile to note no threshold appears to exist for perturbations to cause fluidodynamic effects, where conduction would be the only force at play and the fluid could be considered stationary.

Furthermore, the benchmarking examples with behavior anchored by well-studied previous literature were shown to provide a very good predictive capability for the range of Rayleigh numbers of interest for Borexino for practically all important features. While there was a larger discrepancy in relation to smaller, local features at much lower Rayleigh numbers ($\sim \mathcal{O}(10^3 - 10^5)$), the overall system behavior was still well-reproduced.

In order to more fully understand the predictive capability the developed CFD strategy has for the particular case of the Borexino temperature ranges and geometry, the best available thermal benchmarking data was employed to develop a model that could compare simulated to recorded temperatures: the *Water Ring* model. It showed very good matching in all considered regimes, with ∼<0.2-0.1°C (and, with certain sensors, sub-hundredth-°C accuracy) agreement and feature reproducibility. A slight ∼1-2 day constant temporal phase shift was also seen, which is not fully explained yet, but should not affect the reliability of this thermal transport benchmark.

With this in mind, the *Simple Sphere* models can be trusted in their thermal transport capabilities –but the question remains on how accurately thermal transport translates into good reproduction of internal currents, which in the end is what we aim to correlate with background movement. These models showed insights into the general lack of vertical fluid flow at large scales in the IV (and, in general, all over the SSS), as well as intriguing features showing approximately-horizontal currents spanning the length of the Inner Volume, along with larger current levels on the bottom pole of the vessel. Large scale currents were observed to be on the order of 10^{-5}m/s on the horizontal plane, with small-scale currents reaching no more than $\sim 10^{-6}$ m/s in the vertical direction. Nevertheless, at least ∼half of the model is quite superfluous, since we are not interested in the behavior of the buffers –just of the IV and, in particular, its relation to the FV and immediately neighboring areas. Since model reliability and precision is directly dependent on mesh size and iterative timestep, reducing the model size, cell dimensions and simulated time between iterations, should offer us less numerical noise, artifacts and uncertainty in the model's fluidodynamical results.

The IV-only case set out to achieve just that, by utilizing the reliability of the thermal transport behavior to impose boundary conditions (considered "true") where no temperature probes are available to provide real-world data: the surface of the IV. Doing away with the buffers, the model can be much refined mesh- and timestep-wise, while allowing for similar computing times –thus offering what in principle should be a much higher fidelity. A stratified case was also developed to constrain numerical noise, showing similar, but much more detailed, features than in the *Simple Sphere* case, which proved good consistency.

The appearance of features consistent with first-principles phenomena (see Chapter 7 for more detailed overview discussion) attributable to the time periods simulated when imposing the time-evolving realistic temperatures on the IV model boundary, showed the large potentiality of this type of approach in understanding, or predicting in the case of simulated forecasted temperature profiles, the fluid motion in the FV which should carry the background along. A topic of future research would be to find the optimal configuration, if possible, to limit those streaming currents to a level that would not pose problems with respect to increased or fluctuating ^{210}Po concentrations that would mask the pedestal ^{210}Bi levels ($> \tau_{^{210}Po} \approx 0.39$ years $\rightarrow < \mathcal{O}(10^{-7})$ m/s). The modelization of the past major mixing events that prompted the hypothesization of $\mathcal{O}(10^{-5})$ m/s currents bringing clean scintillator areas up and down in the IV until their dissaggregation, although in principle extremely interesting in order to fully understand the maximal changes correlated with background movement we have data for, cannot be modeled reliably due to the lack of LTPS data for that period.

Further developments in the predictive capability of the CFD models will include a better understanding of the currents for both historical periods with available recorded data on the Phase I sensors. This will enable temperatures to be propagated with either the *Simple Sphere* and/or the *Water Ring* models to give the boundary conditions for the IV-only case. Also, forecasts for approximate detector temperature distributions, including with AGSS operation will also be developed in the future. In particular, emphasis will be placed on utilizing FLUENT's *particle tracking* tool, which would enable to better visualize the paths followed by ideal "weightless particulates" (assumed to be carrying the ^{210}Po) migrating from the less radiopure areas in the periphery of the IV.

The convective behavior of Borexino's topmost area directly affected by the AGSS will be modeled, also possibly including the actual serpentine structure instead of a simple heated "band". This will clear any doubts as to what dynamics are at play for even large set temperatures in the heater. Optionally, a full 3D model could be developed for this, since it is expected such effects in this case will not be negligible, although they are expected not to reach the ID. Likewise, it is important to ascertain if the flexible vessels would see any further deformation from increased gradients, or from rapid gradient variations. At the moment, the IV deformation is close to the historical maximum at the time of the leak (although still smaller), and it is unclear if the increasing gradient during the insulated period has contributed to that condition.

Chapter 5

Calibration system upgrade and preparations for a second calibration campaign

The first calibration campaign[160][161][64] provided a superb opportunity to test all the critical aspects of detector response, through the extensive use of carefully-prepared, well-characterized radioactive sources across a broad spectrum of energies and emitted particle types, thanks to the different isotopes and containment techniques employed.

Moreover, the relevant long-lasting background levels that were left in the IV after the internal calibration campaign was finished and its source insertion hardware taken out, were extremely low compared to the record-low levels achieved by the end of Phase I and, especially, to the spikes seen during scintillator re-filling campaigns (see [161]'s Section 8.2 for a detailed assessment of ^{238}U, ^{238}Th, ^{85}Kr and ^{210}BiPo levels before and after the calibrations).

Data collected during these campaigns in 2009/10 (internal) and 2013 (external) represents a precious benchmark that is still in very active use during analysis development as of this writing. The main rationale behind the calibrations at the time of their inception was, as is evident, to reduce systematic errors (in particular, in the detector's energy response and the Fiducial Volume mass and extent):

- Energy and position reconstruction bias response functions with respect to source position, emitted particle type and particle energy.
- Quenching coefficient through γs.
- PSD efficiency function with respect to position and particle energy.

- FV cut efficiency function for close-lying events.
- Trigger efficiency and trigger threshold effects.
- Effects of PMT inhomogeneous distribution on SSS (as-designed and aging-related).

Despite their effectiveness in constraining and reducing these errors, Borexino's PMT layout has changed very appreciably over the intervening years, some electronics have been replaced (most notably, the trigger board in 2015-16) and its background levels have fallen so far below those of Phase I as a result of the purification campaigns in 2011, that a renewed calibration campaign is very well justified on the same grounds as the first one. Moreover, several techniques were not tried in the past because of different factors including lack of time and the need to prioritize the most result-effective sources over more risky or complicated ideas. This was especially critical considering that by the end of those calibration campaigns, Borexino was still very much in its primary data-taking phase, and many results were pending their on-time conclusion with minimal accidental internal radiocontamination –whose potential risk was inevitably higher with every operation involving hardware insertion operations in the IV.

Furthermore, the upcoming SOX program (see Chapter 6) will exploit the detector in a different way than what it was envisioned for: instead of a homogeneous flux of neutrinos of natural origin, this new program will involve an external, intense neutrino source whose signal in the active volume will be inhomogeneous by its intrinsic geometric properties due to the close range it will be located at. With the source located under the detector, the neutrino signal will be much stronger on the bottom areas of Borexino, precisely those more afflicted by PMT loss and inhomogeneity in their distribution, as well as increased uncertainty in Inner Vessel shape due to missing CCD cameras and structure interference directly dependent on the vessel's deformation. Being an anti-neutrino generator (ANG), the CeSOX source will employ the IBD $\overline{\nu}$ detection channel (see Section 2.5.2), whose efficiency and position-dependent characterization can be further improved with a dedicated high-intensity neutron source calibration campaign.

In short, the new calibration campaign's objectives are, apart from the updating of those listed above:

- PMT distribution and electronics upgrade (especially trigger system, see Section 2.3) impact on energy and position reconstruction bias response functions.
- New, customized locations and energies for MLP, TFC and other new analysis techniques developed after the first calibration campaign was over.

- Deployment of high-intensity sources with the largest achievable activity for dataset statistics optimization (up to hardware saturation threshold of ∼100 Hz[1]), while maintaining or improving low quenching levels in those which are scintillator-based[2].
- Precision fine mapping of FV edge response, especially on the lower half of the IV.
- Improvement of position reconstruction accuracy through an upgraded source location system to confront data-reconstructed source positions with optical position reconstruction with CCD camera system, as well as further study of the Z-axis reconstruction bias (the so-called *Z effect*; see for instance Section 8.3.3 in [161] or Section 4.3.1 in [94])
- High-intensity, low-background neutron calibration for SOX signal calibration.
- New source isotopes to offer β^+ and high-energy γ signals.
- FADC system high-energy in-situ calibration through UV-triggered scintillation.
- Possibility of multi-source insertion (different simultaneous positions in the arm) for hard-reference, hardware-based lengthscale checks.

The foreseen implementation for these objectives will be further detailed in the rest of this Chapter.

5.1 Calibration system overview and upgrades

While an extremely detailed overview of the calibration system already exists in [162] and [161], a summary of its main parts will be offered here, for the sake of completeness when introducing the upgraded infrared (IR) source location system to be used in the next campaign, as well as the modifications to the source positioning arm for the inclusion of the direct scintillation trigger UV system.

5.1.1 CCD Camera system

A series of seven 4-Mpx Kodak DC-290 CCD consumer-grade cameras are installed in custom-built, dry nitrogen-purged containers around the SSS, which also hold a Nikon FC-E8 fisheye lens

[1]While this limit was significantly exceeded during the last radon source deployment in 2010 (which had an activity at deployment inside Borexino of ∼300 Bq, see ***Second Off-Axis Calibration*** in [161]'s Section 7.3.3), the trigger board threshold has been lowered since then owing to the lower amount of PMTs available: this limit is not a *hard* one, but it was chosen for the new campaign as a safe target that can accommodate unavoidable deviations in the fabrication process.

[2]Quenching of the scintillator-based sources in the first calibration were not as good as the loading station hardware allowed due to the imperfect condition the scintillator mixture was in, among other complications (see [161]'s Section 7.3.3).

for wide-angle imaging beyond the camera's field of view. The container lets light in through a glass dome rated for underwater photography. Three are located at 55.1°, other three at 124.9°, and a final one at 34.35°, considering 0° the top of the SSS and 180° its bottom, in accordance with Borexino's coordinate system. Their azimuthal positions are detailed in Table 5.1.

Camera#	Θ (°)	Φ (°)
1	55.1	65
2	55.1	185
3	55.1	305
4	124.9	125
5	**124.9**	**245**
6	124.9	5
7	34.35	240

TABLE 5.1: CCD camera system positions with respect to Borexino's SSS coordinate system frame of reference. Camera 5 (in boldface) failed since 2009 and is no longer usable, rendering the camera distribution in the bottom hemisphere a bit sparse as compared to the top hemisphere.

The cameras are remotely controlled through custom software and Kodak-based DigiScript start-up scripts, also taking care of their calibration and image tweaking (with the aid of precisely-positioned reference LEDs on the housing) to correct for spurious deviations in image geometry which are inherent to the camera's operation and impossible to predict beforehand. Their original objectives were diverse, playing crucial roles even before the detector was commissioned –especially concerning the fluid-filling operations– as well as their critical role as part of the Source Location System during calibration source deploy, and vessel shape monitoring during the detector's life, as described at length in [161]'s Chapter 5. They provide an estimated uncertainty of ~1 px/cm at 6.6 m (detector center).

5.1.2 Clean Room 4

Located on the top of Borexino's WT, the Class-100 Clean Room 4 contains all the critical hardware for source insertion, location and positioning, as well as the entry ports for the CCD cameras' cables and gas purging, the head tanks for fluid pressure equalization and sampling; and the control computers for the glovebox and cameras. As mentioned in Chapter 3, it also contains the Phase III.b temperature probe.

5.1.3 Source insertion system hardware

Inside CR4, the majority of the space is occupied by the glovebox located on the very top of the WT, over a port that gives access to the interior of the detector through the polar hold-down structures and piping. Access through this port is controlled by a dedicated pneumatic gate valve, remotely controlled from the computer that also takes care of gas management for conduit purging (to evacuate any atmosphere with quenching oxygen and radioactive trace isotopes) and pressure control (since the pressure level maintained inside the detector would bring the scintillator up into the source insertion hardware if not kept in check). The gate valve lies just below the so-called *six-way cross*. This structure connects to the underside of the glovebox, which itself contains the different rods making up the source insertion mechanical arm.

The last rod section (the first one to enter the detector) is usually kept in glovebox-to-cross access port, where the tube sliding seals are located, to limit air ingress into the glovebox when the cross is opened for access operations. Additionally, the glovebox has been kept under positive LAKN pressure at all times since the last calibrations, except for a few short downtime periods, to avoid radioisotopes building on the equipment. It features 6 *North* butyl drybox 15 mil gloves (size 9-3/4"), recently replaced from the old ones which started to develop leaks, and contains the necessary tooling and supplies for Source Insertion System operation and deployment, including cleaning and lubrication PC, as well as the manual mechanism to move a sweep arm that verifies the source has been retracted above the gate valve at the end of a deployment campaign, to avoid inadvertent detector misclosure or valve collision with the source. One of the rods has a hinge mechanism at its midpoint that allows for off-axis source location.

The lowermost rod features the *source coupler*, which mechanically holds the Source Location System's light source as well as the calibration source itself. Furthermore, it serves as the mechanical coupling for the 30m-long, 1/4" OD, 3/16" ID UltraClear PFA Teflon *tether*, which runs alongside the mechanical arm and serves as both the mechanical tensor that hinges the arm to the desired angle (up to $<90°$, and operationally $\sim<70$-$80°$) and the conduit through which the light is fed, or electricity cables run, to provide energy to the Source Location System's light source. This tether, when the arm is retracted, is wound and stored in the *tether drum* located on one of the glovebox's side walls. The tether exits the drum to CR4 through a hermetic SwageLock fitting to finish in a differential length correction box. Since the tether tube extends and contracts depending on the mechanical tension and temperature, and fiber optic exhibits exhibits a shorter length than the tube when wound (since it is free to make a slightly tighter curve close to the tube's inner walls), this box holds the extra length of the fiber that would be shortened if the tether was fully deployed. In the next subsection, an explanation of the stripe system used to quantify this effect and have a reliable mechanical estimate of the amount of tether introduced in the detector is provided. Additionally, this box holds the red laser for the visible Source Location System light source, coupled to the end of the fiber once it exits the inside of the box. The tether and box are both connected to a LAKN purge system for safety.

All the components in contact with the IV scintillator are held to the Class-30 cleanliness standard (as defined by Military Standard 1246C[163]).

5.1.4 Source location systems

The Source Location System's "wet" segment (the part that goes inside the IV at a small and precisely-measured distance from the source vial) is comprised of a light source which is visible to the CCD cameras described in the previous Section 5.1.1. In its original design with the CTF on-axis source holder (which didn't feature the arm described above, instead relying just on the tether to lower and raise the source), it consisted of a diffuser coupled to a green laser located on the platform outside CR4 and fed through a fiber optic (see characteristics in Table 6.1 in [161]). Cameras are very sensitive to green light since the pixels under the green color of the Bayer array used by the camera sensors are duplicated to account for higher sensitivity of the human retina to those wavelengths. Unfortunately, Borexino's PMTs are also very sensitive to the range of frequencies around green, so simultaneous operation of both the internal Source Location System (even if limited to just the few seconds when the light needs to be on during picture-taking) and PMT HV was impossible –further, the HV cycling carried its risks to the electronics and the dinodes, and this effect would be aggravated as time passed and the systems aged.

When the mechanical arm Source Insertion System was introduced, so was a new light source: in this case, a 3/16" OD, ∼2" long Pyrex test tube with a stainless-steel transition neck was employed. Inside it, a small cylindrical Teflon diffuser was fed light from a red (∼650 nm) laser located in CR4 through the fiber optic. The camera control computer was in charge of the laser switch-on in conjunction with picture-taking operations. Alongside the fiber, a suitably long vinyl stripe 1/8" masking tape, marked by hand every centimeter, was placed, as well as a kevlar fiber which was epoxy-glued at its exterior end in CR4's expansion box as well as to the vial's SS neck. This tape provided a reliable measurement reference, readable through the transparent Teflon tube wall, which accounts for the differential extension of the fiber optic and tether tube, in order to provide an independent, reliable mechanical estimate of the amount of tether inserted in Borexino. This is important for source location purposes, providing a mechanical comparison to the CCD- and DAq-derived source positions, but also operationally to understand how much off-axis angle is being provided to the arm by pulling on the tether.

While this red laser optical system is still kept as a spare, its impact on PMT operation was still substantial, increasing the dark noise currents to levels not compatible with DAq stability, even if HV could be in principle kept on. Furthermore, the CCD camera system sometimes showed poor resolving power when finding the Source Location System light spot, with no apparent blockage coming from the identified inner structures. Reflections in the nylon vessels, small unfocused condensation spots in the lenses or container dome, blind spots in the presumably isotropic distribution of light from the diffuser, or some other subtle effects could be at play there, but this inconvenience directly increased the uncertainty in source location, directly influencing systematics in Borexino-wide analyses.

For this reason, a new Source Location System source was devised: one which used Infra-Red Emitting Devices (IRED), or long-wavelength LEDs emitting at near-infrared wavelengths. Charged Coupled Devices such as the ones in commercial-grade cameras are quite sensitive to these wavelengths, and are even used professionally for land-use and vegetation cover monitoring. Most recent camera designs use coatings in the optics or even on the CCD sensors themselves, in order to block off these –to the human eye– "invisible colors" that perturb brightness balances in pictures intended to replicate what a human would see, but this blocking technique is less frequent in simpler (such as cell phone cameras) or older camera models. Indeed, a testing campaign was performed in Virginia Tech, with a simple purpose-built setup mimicking the optical configuration found inside the camera canisters, and facilitating an LED/IRED at different positions, ~30 cm from the fisheye lens' surface. After checking positions off the optical axis did not show any unexpected dimming effect, subsequent trials were made on-axis, employing both visible (VIS) and infrared (IR) wavelengths (see Table 5.2). Off-axis losses were minimized through visual adjustment of the LED on its frame, to ensure it would be facing the camera at its maximum emissivity angle (typically, directly facing it). A laboratory breadboard with DC power supplies was employed to drive the IREDs through a simple resistive circuit.

Peak λ (nm)	Make & model	Max Power (mW)	Viewing angle (FWHM, °)
400	Jameco LDUV3333	120	20
468	LiteOn LTL-2P3TBK5	120	15
505	MCD MCDL-5013BGC-T	-	18
565	Jameco LG3330	100	36
585	Jameco LY3330	60	36
635	Jameco LE3330	100	36
660	Jameco LUR3833	120	12
697	Jameco LH3330	40	36
730	Everlight ELSH-Q61F1-0LPNM-JF3F8	150	120
770	Marktech MTE1077M3A-R	60	160
810	Marktech MTE1081C	120	50
850	Vishay TSHG6400	180	44
880	Jameco UT1883-81-880-R	75	10
890	Optek OP290A	1110	50
940	Ligitek LVIR3333	100	20

Table 5.2: List of LEDs/IREDs used during the wavelength-dependent camera response characterization studies.

Before the images could be used for a wavelength-dependent sensitivity determination, the linear response from both the cameras and the IREDs needed to be verified. In the case of the camera, this is needed to verify the number of illuminated pixels (or rather, their integrated RGB value) increases linearly with the delivered current until a saturation value (RGB=255),

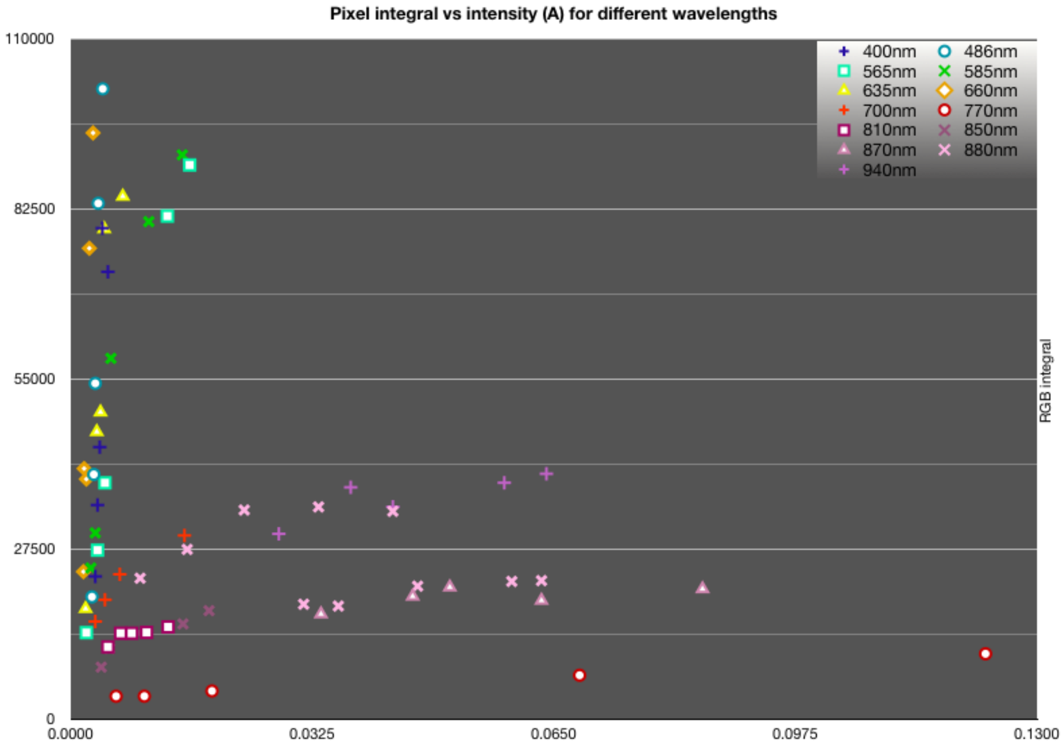

FIGURE 5.1: CCD linear saturation curve measurements for VIS and IR wavelengths. No CCD saturation plateau was achieved for the red (660 nm) and blue (486 nm) curves although brightness in the image was remarkable: this is due to the camera sensitivity to these particular wavelengths, which seeped into adjacent pixels and kept the linear trend. This effect, although much smaller, is still visible in most of the other curves, which show a positive-slope plateau.

where it plateaus off. This curve, of course, will vary with changing wavelength, depending on the CCD sensitivity to each particular wavelength and its resistance to saturation.

After pictures in this setup were taken, RGB integration ($L_v = 0.2126R+0.71526G+0.0722B$) of the illuminated pixels (including subtraction of white noise from a blank (dark) reference photograph) led to the desired saturation curves shown in Figures 5.1 and 5.2.

This is enough to check the camera's linearity, but a correction for each particular LED is needed to account for the relative brightness at a given current. This was implemented as a multiplicative factor f:

$$f = L_v \cdot I/20 \tag{5.1}$$

where L_v is the luminance value quoted in the technical documentation of each LED/IRED at 20 mA (in units of mW/sr) and I is the current in mA. Currents were always kept in the linear response range quoted by the technical datasheets.

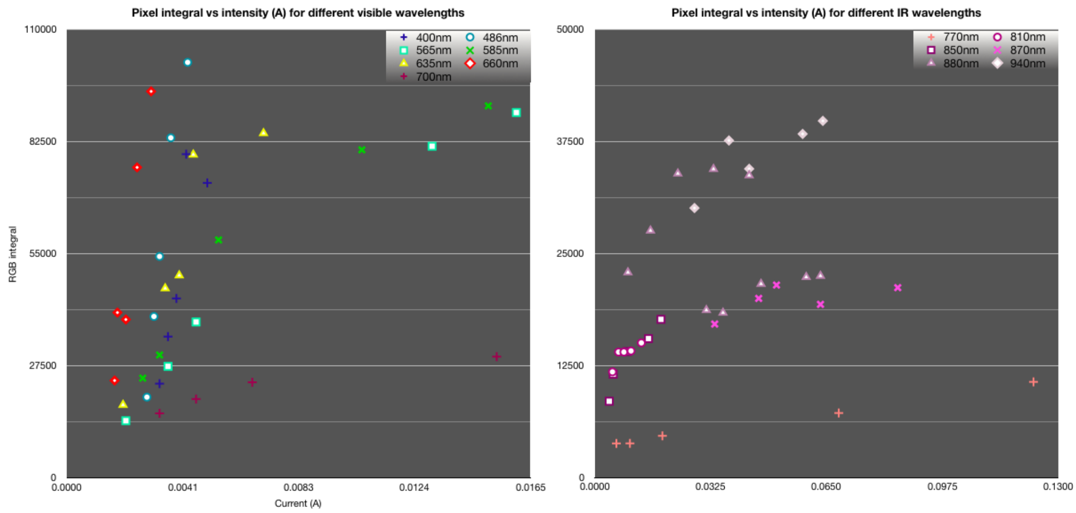

FIGURE 5.2: Separate detail of VIS and IR CCD saturation curve linearity measurements, separately.

The whole objective of this system is to provide a wavelength which could provide similar or better visibility for the CCD cameras than the red laser emitter, improving the reliability of the Source Location System, **while** keeping or improving a benign environment for the PMTs, avoiding their HV being switched off when the light source is turned on, while limiting the rise of dark currents. For this reason, the above normalizations are not enough, since they only verify and account for the IRED and camera linear responses, but do not consider the PMT's response.

The PMT's quantum efficiency has been repeatably and precisely determined for most wavelengths of interest, from ∼250 nm to ∼650 nm (see Figure 2.7), but their response for longer wavelengths was poorly understood, except for the fact that it was "low". How low was "low" and how it compared to long visible wavelengths such as red was mostly unknown. At first, an analytical strategy was implemented for the purposes of the system presently discussed. In particular, two approaches were followed. The trivial one, and most conservative, would be to consider the quantum efficiency to be minimal at the long wavelength tail (0.008), and extrapolate that to infrared frequencies. This had the obvious drawback of being unrealistically pessimistic, but it could be a reasonable start. Another option would be to fit the quantum efficiency decay curve tail to an analytical function and propagate that to the wavelengths of interest. Although no *a priori* assumption regarding the analyticity of the decay curve could be made, reasonable trends could be explored. A Gaussian, exponential and power function were tried, achieving the best overall fit with the first one, but likely underestimating the q.e. at the tail. The exponential and power functions, on the other hand, had a worse fit in medium-range wavelengths (500-600 nm) but seemed to better approach the end bins of the curve.

When using these q.e. projections shown in combination to camera response alone in Figures 5.3 and 5.4, and normalizing the relative efficiency of the camera (weighted by the inverse

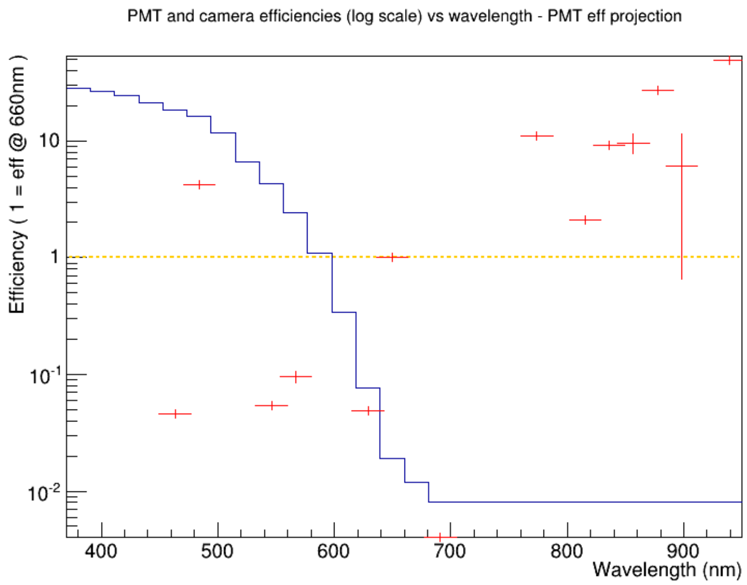

FIGURE 5.3: Projected (constant 0.008) PMT quantum efficiency at long wavelengths (blue curve) and camera efficiency (red datapoints). Vertical error bars are standard deviation between different pictures with the same setting and analysis technique; horizontal error bars take into account the reported LED bandwidth. The yellow dashed line indicates the "unity" relative efficiency, normalized to the response with the red (660 nm) LED.

of PMT response) to unity at 660 nm (red), to consider that the baseline against which to compare response to other wavelengths, the results in Figure 5.5 were found.

This analytical approach, however illustrative, still contained many uncertainties in it, and could not be rigorously defended beyond a feasibility study. Nevertheless, it provided an important encouragement toward further exploring the use of IR wavelengths for camera detection and PMT safeguard, since combined efficiencies were consistently shown to be larger than the red baseline (except perhaps for a dip around 900 nm), while providing the potential of orders of magnitude of improvement.

For this reason, it was decided to move ahead with the next step in this study, namely to study the camera and PMT response side by side, in the same setup, and with a precision measurement of the dark noise at different wavelenghts. For this reason, the dark room in *Hall di Montaggio* in the external laboratory facilities of LNGS was employed, along with the expert help of Giorgi Korga. A PMT coming from the same batches as the operational ones in Borexino was employed, in particular one coming from OD tests. The mineral oil contained in a thin film in front of its dome glass had been purged away, and its transmissivity characteristics were identical to those in the ID. A scaler/counter, amplifier, discriminator and multivibrator system was set up (see diagram in Figure 5.8) to have a finely-tuned response from the PMT. Careful control of the camera settings was ensured by the loading of start-up scripts with the same settings as Borexino's CCD system (5 m manual focus, 7 s exposure, medium/better Kodak image quality,

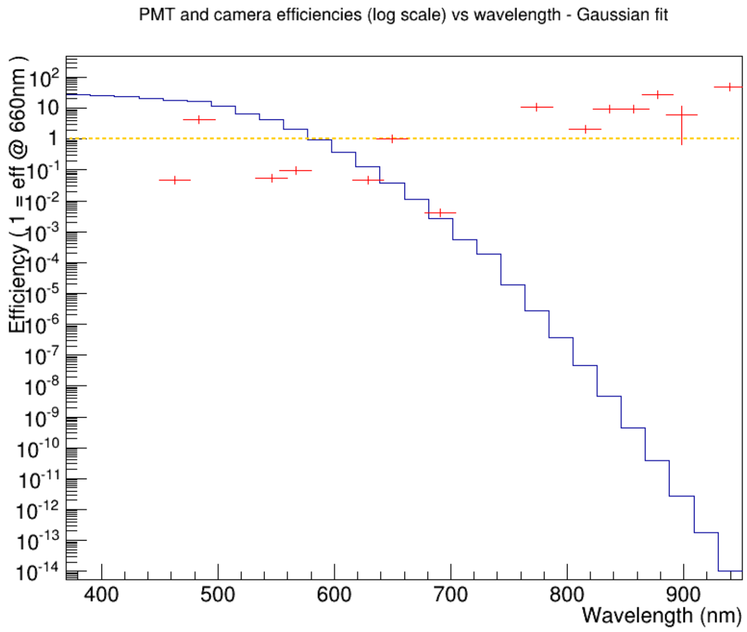

FIGURE 5.4: Projected Gaussian PMT quantum efficiency at long wavelengths (blue curve) and camera efficiency (red datapoints). Vertical error bars are standard deviation between different pictures with the same setting and analysis technique; horizontal error bars take into account the reported LED bandwidth. The yellow dashed line indicates the "unity" relative efficiency, normalized to the response with the red (660 nm) LED.

same white balance and zoom (76mm) as in Borexino), and remote operation of the camera was ensured through a scavenging of historical importance: the old camera control box in CTF was re-used for this purpose (as was the camera itself, salvaged from one of the containers extracted from the detector at decommissioning). A breadboard with different LED/IREDs (660, 850, 870, 880, 890 and 940 nm, each connected to a 47Ω resistor) was fixed to the ceiling with cable ties, to ensure uniform distance (∼1.8 m) to both the camera and the PMT. The LED/IREDs were driven by carefully-controlled currents, normalized to the power output of each emitter, through a power supply. Photographs of the "dark" (PMT and LED/IREDs) and "lighted" (camera controls and electronics) systems can be seen in Figures 5.6 and 5.7.

New saturation curve measurements were taken to ensure the previous linearity data taken at VT was applicable to the new setup. Measurements of the PMT dark rates, together with picture taking of the emitter, were performed at three different regimes: low discriminator threshold (30 mV, yielding dark rates similar to Borexino's), high discriminator threshold (190 mV) and low discriminator threshold at camera saturation values. A blank comparison picture and PMT dark rate measurement was also performed with all emitters off, to subtract intrinsic dark noise in both CCD and dinode: 0.0078 RGB integral for the camera, and 1750±107 Hz (109.42±12.81) for the PMT high (low) threshold, respectively.

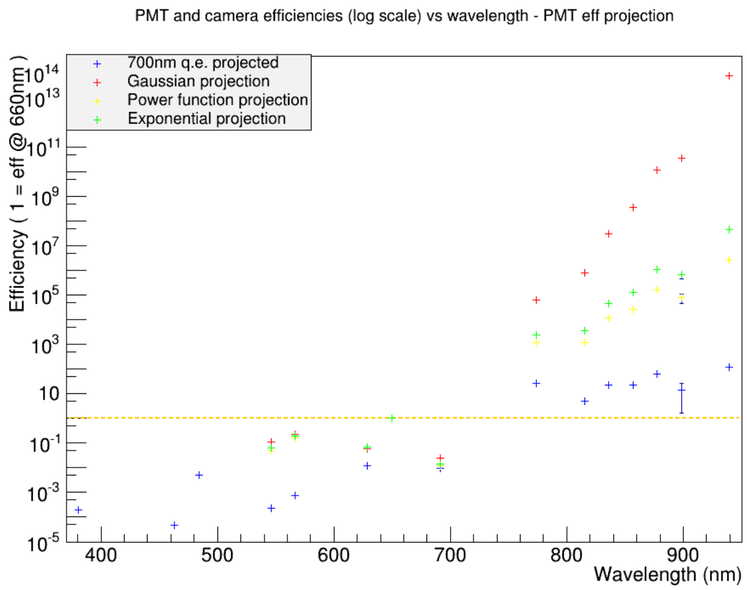

FIGURE 5.5: Camera/PMT relative efficiency according to several PMT quantum efficiency projections.

FIGURE 5.6: Dark room camera/PMT setup. Inset shows breadboard with LED/IREDs.

The combined relative "efficiency" resulting from the convolution of all the aforementioned factors can be expressed as:

$$\epsilon_{rel} = \frac{DN}{W_{px}} = \frac{\sum_i \frac{DN_i}{n}}{\sum_i RGB_{avg}^{(i)} \cdot N_{px}^{(i)} \cdot \frac{L_v(20mA) \cdot I[mA]}{20[mA]}} \tag{5.2}$$

where DN is the average dark noise rate, which comes from the average from all measurements at a certain threshold and for a certain wavelength; W_{px} is the weighted pixel value, which comes from the pixel value for a wavelength (average of the RGB average value for a picture, summed over the number of pixels, for every picture in a wavelength) weighted by the multiplicative

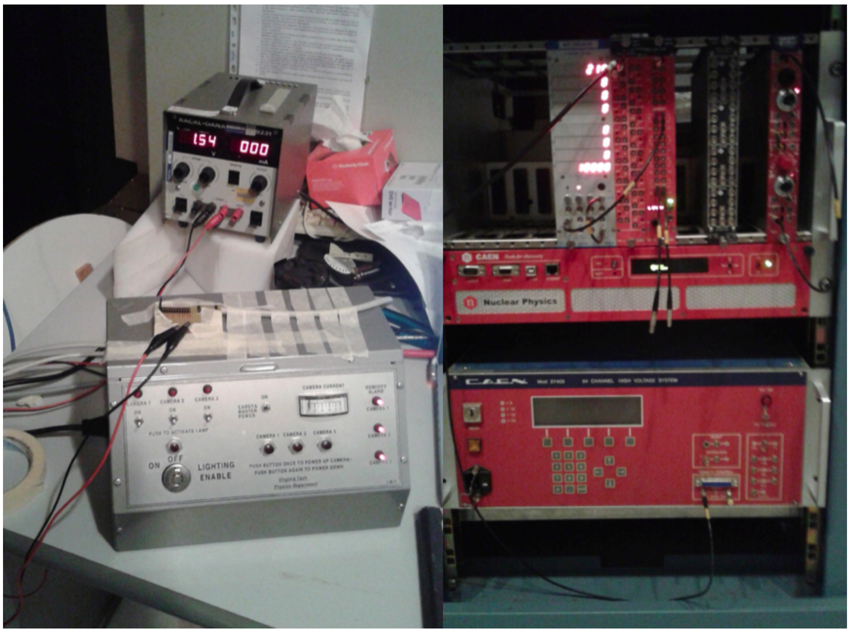

FIGURE 5.7: Camera control box from CTF and power supply (left) and PMT electronics (right) for the dark room tests. A detailed schematic of the electronics is available in Figure 5.8.

factor f described above: the luminance value normalized for the specific current the IRED was driven by for each wavelength.

Errors were added in quadrature according to this formula:

$$\sigma_{W_{px}} = \sqrt{\left(\frac{\partial W_{px}}{\partial px}\right)^2 \sigma^2(px) + \left(\frac{\partial W_{px}}{\partial f}\right)^2 \sigma^2(f)} \tag{5.3}$$

$$\sigma_{DN/W_{px}} = \sqrt{\left(\frac{1}{W_{px}}\right)^2 \sigma^2(DR) + \left(\frac{DN}{W_{px}^2}\right)^2 \sigma^2(W_{px})} \tag{5.4}$$

There is still another factor that needs to be taken into account after convoluting the LED, camera and PMT responses –but which, as opposed to the previous factors, cannot be tested conclusively in an indirect fashion, without testing it in the detector itself: the scintillator and buffer absorption to these particular wavelengths.

Nevertheless, a reasonable estimate can be provided through absorption spectrometry: samples of scintillator and buffer mixtures with the same recipe as in Borexino's (1.45 g/L PPO in pure PC for the scintillator, and 2 g/L of DMP in pure PC for the buffer) were prepared and their absorption response recorded through Virginia Tech's Thermo Scientific spectrometer Evolution 600 (UV-VIS). The resulting curves contained the information of the compound's relative absorbency at different wavelengths, in the [380-900] nm range. These readings were converted to mean free path length by considering a reasonable maximum mean free path length

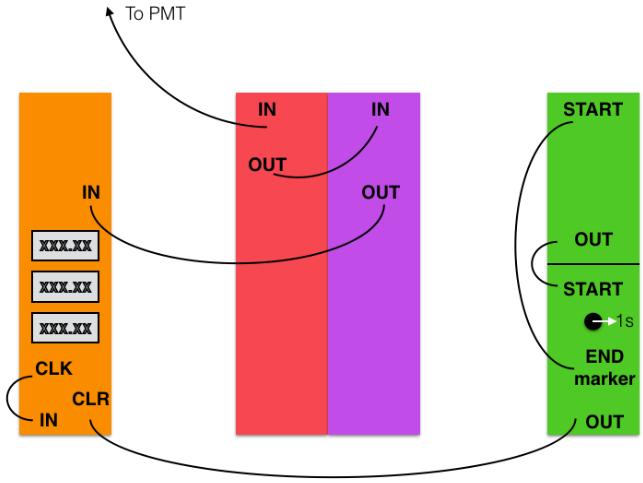

FIGURE 5.8: PMT control setup schematic: the scaler (left box) is connected to the amplifier, discriminator and multivibrator, while the discriminator is also connected to the amplifier. The setup provides 10x amplification, which the discriminator uses to select over a certain (low, high) threshold in mV. The multivibrator prepares a precise 1 s window during which to count the number of triggers. This window timing is not provided by the scaler counter, hence the need for the multivibrator. The scaler has counter screens to record the reading every second, and provides an "inhibit" signal that ensures the reading is displayed for manual recording until the RESET button is pressed to take another reading.

of 20 m (although the relative proportions wouldn't change with this choice, and the absolute values obtained would be merely scaled), and taking into account the test cell with the specimen for the spectrometer was 10 cm in length. This resulted in Figure 5.9's curves for mean free path length.

Although this provides a reasonable estimate of how much absorption is to be expected at the different wavelengths, the fluids involved are obviously not the same as the ones inside Borexino, and more importantly, the tested lengthscale is so different from the real one (cm vs m) that subleading effects lost in the spectrogram's uncertainty may be of importance in the actual detector. Also, the relative radiance of the red laser and diffuser system could not be tested in the same conditions as the LED system, since operational constraints limited the transportation of the original CR4 system to a test setup, and replicating it separately turned out not to be feasible. For that reason, and the limitations imposed by the thermal/currents operational envelope for the IREDs, it may turn out the emission radiance from the old system cannot be replicated by the new one, even if the latter is better than the former on a per-Watt basis. As will be seen shortly though, these uncertainties should be overwhelmed by the much better response expected from the IR system, and at minimum provide a comparable source location accuracy while spectacularly diminishing the impact to the PMT response. If, on the other hand, absorption-related effects turn out not to be so significant, major improvements to the position reconstruction and FV determination systematic errors may be realized during the upcoming calibrations.

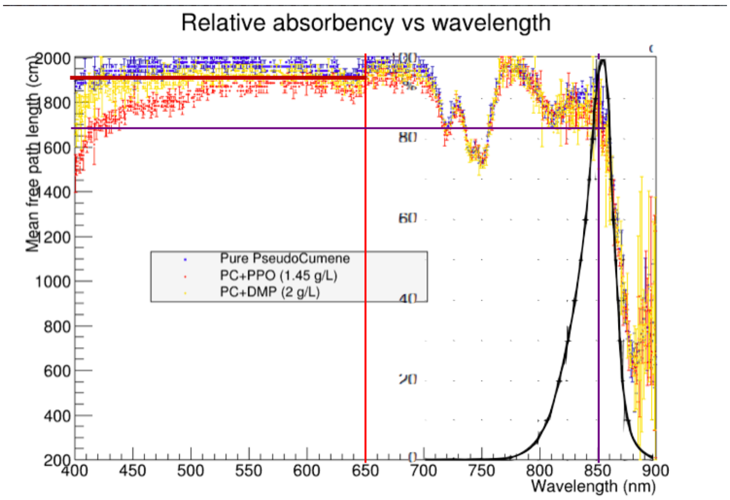

FIGURE 5.9: Mean free path lengths for pure PC (blue), PC+1.45 g/L PPO (scintillator, red) and PC+2 g/L DMP (buffer, yellow), considering a maximum mean free path of 20 m. The blue curve shows the wavelength distribution for the SFH 4716S IRED chosen for the IR Source Location System, with the centroid emission wavelength of 850 nm shown in the purple vertical line. The mean free path is shown to drop precipitously to 30% of its maximum value at wavelengths between 870-900 nm (albeit with large error bars). Fortunately, for ∼75% of the IRED's emission bandwidth, the mean free path is only ∼10% shorter than for red light.

Adding an extra absorbency factor to Equation 5.2 accounting for the loss of mean free path for each of the tested wavelengths, taken from Figure 5.9's data, the "efficiency" plot seen in Figure 5.10 can be generated, convoluting PMT, camera, LED and fluid response:

As can be seen, a factor of 10^3 (or at least 10^2 to within 1σ) of better relative dark rate over visibility ratio is available for any wavelength. Also, 850 and 870 nm are the wavelengths showing the best efficiency ratio. Considering the mean free path drops strongly with wavelengths over 855 nm, also introducing potentially higher uncertainties, and the fact an IRED with a large (150°) viewing angle and high available radiant flux ($\sim$ 1W) was found for a relatively reasonable price, the 850 nm wavelength was chosen for the job. The selected IRED (SFH 4716S, see specifications in Table 5.3) was also available on demand, showing it has a fairly good degree of reliability, and has a *centroid* wavelength of 850 nm, peaking instead (∼5% more relative emissivity) at 860 nm –which would still give us the benefit of increased emission in longer wavelengths if absorbency was found to be in the lower end of the error bars.

With the feasibility of the system proven, the new system could be designed. It was decided the source coupler would not be modified, and the mechanical functions of the tether should remain unchanged. For this reason, it was decided to just change the interior of the Source Location System, substituting the fiber optic used with the red laser for electrical cables carrying the direct current to drive the IREDs, and changing out the contents of the Pyrex ampoule located next to the source at the end of the arm.

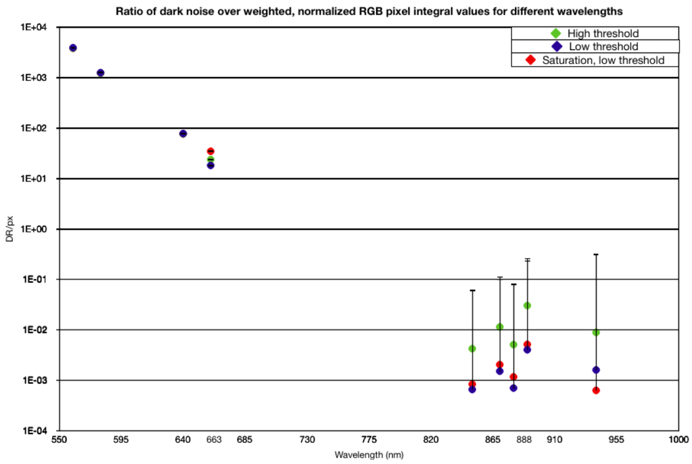

FIGURE 5.10: Ratio of PMT dark rates over weighted pixels with absorbency data for different wavelengths under different PMT and IRED regimes (low/high threshold in linear IRED/camera regime, and low threshold at camera saturation). Visible wavelength data is shown for comparison, using the PMT quantum efficiency in place of the dark noise, by anchoring it to the dark rates through a scaling factor of $3.56 \cdot 10^6$ taken from the ratio between the dark rate and quantum efficiency data for the red (660 nm) wavelength. The uncertainty would be practically invisible for any wavelength not taking into account the contribution from the absorbency measurement. When adding that in quadrature, the error bars shown are obtained. Lower error bar limits are not shown to reduce clutter, but they would obviously extend to the bottom of the graph.

The chosen design[3] utilized a "tower" of three planes, separated by 60°, each composed of two IREDs organized back-to-back, plus a single one perpendicularly looking down from the bottom of the "tower". This is conceptualized in Figure 5.11. This design ensured there would be emission isotropy within the 50% variability inside the guaranteed viewing angle to any point around the device, except an extremely small region which would be mechanically interfering with the arm anyway. To double-check, an isotropy measurement was performed with the cameras and a single IRED oriented at several different angles, whose results can be seen in Figure 5.12, where it was found the visibility at operational power draws, expressed as RGB integral, exceeded in any geometry (even those unfeasible ones) the borderline visibility condition of the red laser diffuser system.

The IREDs would be linked in series among themselves with non-insulated single-strand silver-coated copper wire to save space. This design would be inserted in a Pyrex test tube similar to the one in the old design, only with an enlarged diameter of 4mm ID to fit the IRED dimensions. The 7 serialized IREDs would be difficult to keep in place given the "handmade" nature of the

[3]Several designs were considered, owing to the fact the small IRED could be positioned in many ways, but a key driver was to maximize light emission isotropy, a major problem with the previous design that was partially solved with the use of a diffuser that, nevertheless, still showed signs of anisotropy in its emission. For this reason, on top of the large 150° half-intensity viewing angle of the SFH 4716S, it was decided to space them by no more than 90° in all directions, except perhaps on the side facing the coupler, which would in any case be mostly obscured by physical interference with this component. Distributing IREDs on the shape of a sphere, or utilizing reflecting prisms similar to the diffusers in Christmas lights, were examples considered.

Make and model	OSRAM Semiconductors OSLON Black Series SFH 4716S
Radiant intensity [mW/sr] at 1A and 10 ms pulse	225 (>160)
Maximum reverse voltage [V]	1
Maximum forward current [mA]	1000
Surge current ($\leq$ **500** μ**s)** [A]	5
Maximum power consumption (W)	3.4
Peak wavelength [nm] at 1A and 10 ms pulse	860
Centroid wavelength [nm] at 1A and 10 ms pulse	850
50% I_{max} **spectral bandwidth [nm] at 1A and 10 ms pulse**	30
Half-intensity angle [°]	±75°
Active chip area dimensions [mm x mm]	1x1
Forward voltage [V] at 1A and 0.1 ms pulse	2.9 ($\leq$3.4)
Forward voltage [V] at 5A and 0.1 ms pulse	3.5 ($\leq$4.5)
Total radiant flux [mW] at 1A and 0.1 ms pulse	1030
Radiant flux temperature coefficient [%/K]	-0.3
Forward voltage temperature coefficient [mV/K]	-2
Wavelength temperature coefficient [nm/K]	0.3

TABLE 5.3: Technical specifications of the IRED model chosen for the new IR Source Location System emitter. All parameters are measured in a 0.1 sr pinhole and at 25°C. Further details, diagrams and relationship plots (such as relative spectral emission, radiant flux with I_F, I/V curves...) can be found in [164].

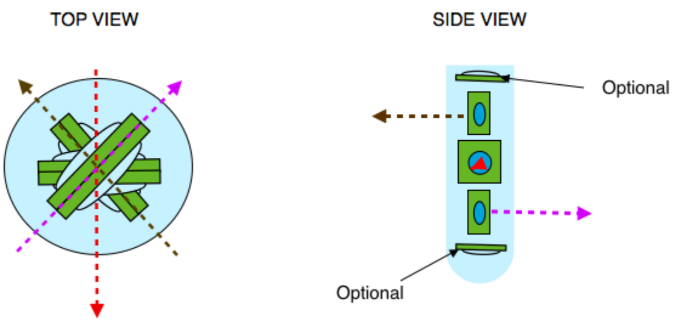

FIGURE 5.11: Conceptual illustration of the IRED "tower" source location emitter design. The arrows are shown perpendicular to the chip's long axis. The *optional* label was kept in the design in case of the bottom IRED, but the top one was eliminated to leave room for the cabling.

integrated system, and inadvertent shorts between the exposed IRED leads would be inevitable. Therefore, it was decided to add a "backbone" structure machined down from a black nylon rod, composed of three "planes" linked through their vertical axes, where the back of each IRED would be pressed against each of the 6 faces –with the 7th, bottom IRED (the 4th in the series chain) pressed against the bottom edge of the lower plane. Thus arranged, the "tower" was carefully inserted in the Pyrex test tube, and the power leads were shrink-wrap insulated to avoid shorts inside the neck. The resulting device can be seen in Figure 5.13. Once tested, the

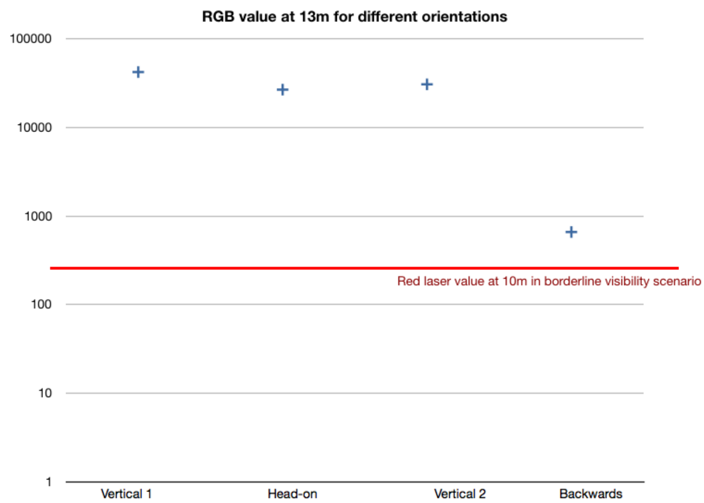

FIGURE 5.12: Emissivity isotropy measurements for the SFH 4716S IRED "tower" design. "Head-on" refers to the bottom IRED pointing toward the camera, while "backwards" refers to the vial's opening pointing toward the camera (no direct vision of any IRED), which represents the worst-case scenario which wouldn't be possible to have in Borexino, since the arm would interfere with this geometry. Note these datapoints do not include convolution with the wavelength-dependent absorbency, which would bring them down by $\sim$10%. The red baseline corresponds to a "barely" visible photograph of the actual Source Location System in Borexino during a calibration run.

lead cables were temporarily coiled and stored inside the vial, some distance away from the open top of the vial. This was a necessary step to add a stainless steel transition neck to the vial, whose OD matched the ID (3/16") of the tether tube. The glasswork was completed at VT's Chemistry Glass shop, who provided also the Pyrex vials and the calibration source ampoules. Once this operation was accomplished, the coiled leads were carefully "fished out" with a hook, paying attention not to displace the IRED tower or, worse, break off one of the top leads. Once extracted, the leads were straightened and the device was ready for soldering with the power wire.

The small physical dimensions of the IRED (3.85x3.85 mm, see Figure 5.14) meant its leads would be soldered to an extremely small surface. As evidenced during testing, this meant that care must be exercised when driving the emitter, since too much power density will physically *melt* the soldering and cause the connection to weaken or even detach. This factor limits the radiant power we can provide, but it was very well characterized for long times to be acceptably close to the 1W nominal power draw, and in Borexino we would have the added bonus of being submerged in a thermal bath at $\sim$15°C where the system would only need to remain lighted while the cameras took their pictures, that is, on the order of 10 s, at maximum –providing a more benign cooling environment than in long tests in an ambient-temperature air bath. It was determined that for a current of 0.3 A at 3.4 V, it was acceptable for a single IRED to remain on for periods on the order of tens of seconds or even minutes without getting too hot. This limit

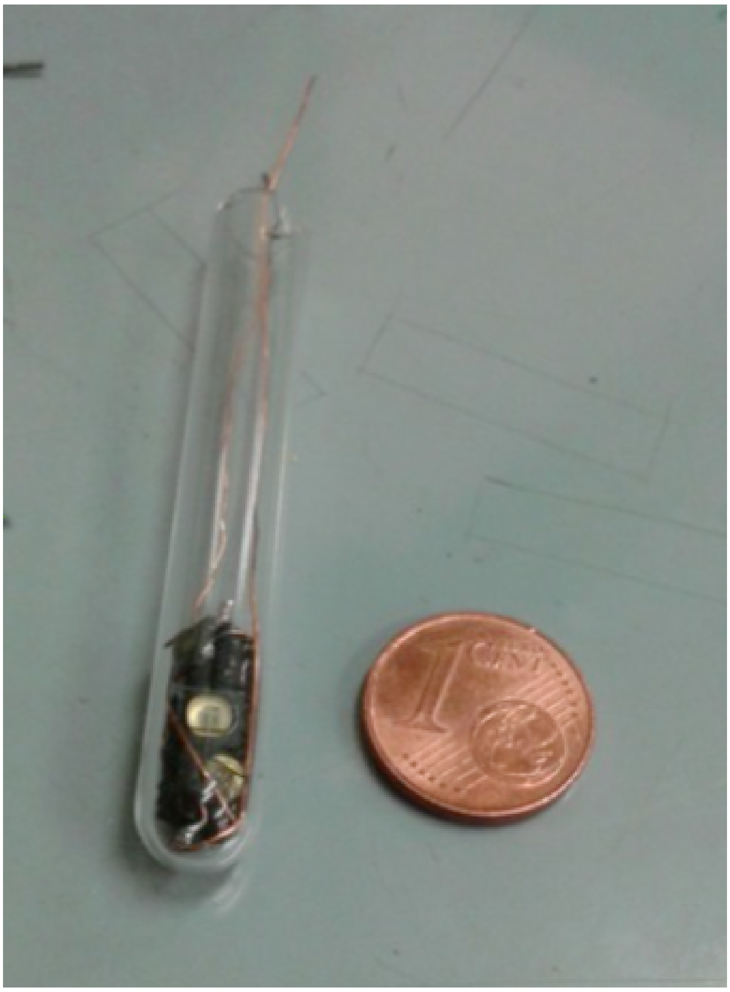

FIGURE 5.13: Working prototype of the SFH 4716S "tower" design for the source location emitter. Still missing was the transition to the stainless steel transition neck for coupling with the Teflon tether tube.

was found to be quite precise though: 400 mA at the same potential would invariably make a solder joint fail within ∼5 s, and raising the current to 600 mA only left ∼1 s until failure.

An LM2596 (see Figure 5.15) current regulator scheme was adopted after some consideration as to what type of regulation should be provided for the IRED system[4], drawing power from a DIN rail-mounted, 39.8W power supply connected to the 220V regular power supply in the Laboratory. An extra LM2596 is connected in series, unregulated in voltage but safeguarding the 300 mA current limit in case of failure of the downstream LM2596.

It was thus determined the operating potential would be ∼2.8V for each IRED at 300 mA (output LM2596: 3.64 V to account for the voltage drops in the cable), yielding a total voltage

[4]A simple resistor would not suffice, since maximum permissible forward current would decrease with temperature, rapidly falling over ∼100°C of internal temperature, risking to damage the emitter devices; and other alternatives such as a DC-DC adjustable switching power supply (such as XL4015) carried high electronics noise levels with them that might affect PMT operations, or the LM317 in current-regulating mode could dissipate too much heat.

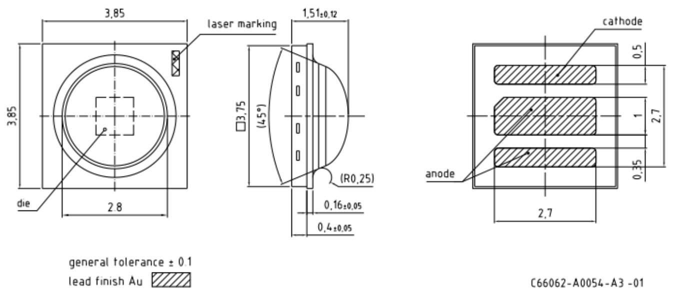

FIGURE 5.14: Technical diagram of the OSRAM SFH 4716S IRED 850nm emitter. Dimensions are shown in mm.

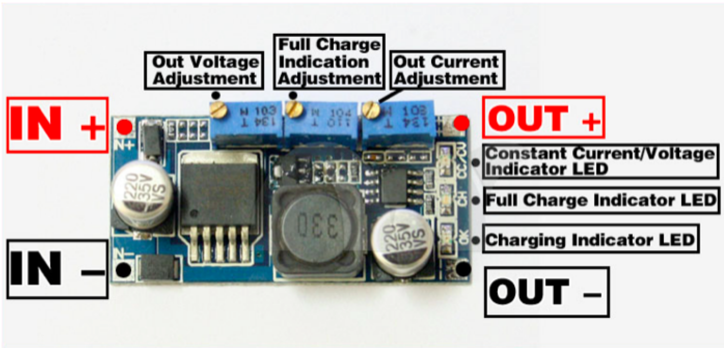

FIGURE 5.15: LM2596 constant current/voltage regulator.

drop in the actual IRED tower of 19.6 V. If used for long (>1 min) operations, the current should be decreased to ∼200 mA and 2.7 V/IRED (output LM2596: 3.3V). These circuits would all be kept outside CR4, because of safety rules against potential flammability/explosion dangers they are not certified against, and would operate from the electronics cabinet where the control computers are located. An opening through which the power cable can be routed to the inside of the tether tube is already in place.

The electric cable itself was chosen for its good conductivity, low background, small diameter and flexibility. It is the 24 AWG, Kapton-insulated coaxial cable TYP5-15', whose specifications can be found in Table 5.4.

The integrated system was put together in the spring/summer of 2016 in the *Hall de Montaggio* of the external LNGS, over the upper level's railing (see Figure 5.16), since an easily-accessible, ∼30m-long surface was needed to fix both the tether tube and the cable and assemble them together with the IRED vial. The stripe marked every cm that was stuck to the fiber optic's outer cladding in the old system could no longer be used, since the Katpon plastic proved to be resistant to adhering anything on its surface, and this operation was further complicated by the cable's small diameter. It was then decided to mark the cable surface itself (see Figure 5.17)

Make and model	AccuGlass Products Inc TYP5-15'
Materials	Kapton, Ag-plt Cu
Max. Bake Temperature [°C]	250
Max. Operating Temperature [°C]	250
Max. Vacuum level [torr]	10^{-10}
Wire gauge (AWG)	24
Voltage rating [kV]	0.6 AC, 2 DC
Current rating [A]	4.5
Resistance at 20°C [Ω/km]	88.3
Capacitance [pF/m]	300
Minimum bend radius (long-term) [inch]	0.5

TABLE 5.4: Technical specifications of the cable model chosen for the new IR Source Location System. Further details can be found in [164]. The model comes in 15' "units" but the actual length purchased was 105'. ∼25 m were actually used in the tether.

with white acrylic paint[5] every centimeter, and add a small "label" made of the aforementioned masking tape every 10 cm, where the actual length from the middle of the IRED tower was written.

Once complete, a leader line was vacuum-sucked through the Teflon tether tube, and this was used to pull the now-marked cable through it, along with a nylon rope that would serve the same purpose as the Kevlar strength member from the fiber optic in the previous system. Finally, the IRED tower leads were pulled out by a few millimeters and carefully soldered to the cable ends, making sure the resulting length matched that recorded in the labels (which were now inaccessible being inside the tube). Prior to inserting the metal transition neck in the open end of the Teflon tube, heat-conductive Epoxy was inserted in the neck, together with the nylon safety string. This way, once hardened, the cable and string would be mechanically bonded to the vial, ensuring an accidental slippage of the Teflon tube on the neck would not release the vial or allow scintillator flow inside it. With the Epoxy cured and the vial neck inserted in the Teflon tube, several turns of steel wire were used to tighten the tube around the stainless steel neck, in a manner similar to the old tether system, as shown in Figure 5.19. After leak checks and cleaning, the new tether and Source Location System is ready to be integrated with the glovebox, arm and coupler for operational use inside Borexino.

The tether drum on the glovebox was initially conceptualized to be easily interchangeable with other spools. However, the final mechanical conception impeded this initial objective, which in the end was seen as not so crucial since the full calibration campaign could be completed with a

[5]Some parts were marked with ink corrector, but that was observed to become slightly more brittle as it dried than the paint

FIGURE 5.16: Final assembly process of the new Source Location System tether and emitter, on the *Hall de Montaggio*'s upper level railing.

single tether, provided it suffered no major damage[6]. The flange passing through the glovebox lower panel for tether deploy is too narrow for the Pyrex vial containing the diffuser, and since its stainless steel transition neck is epoxyed to the fiber and Kevlar strand, it is impossible to remove once installed unless this vial is is cut off or the fiber is disconnected from the laser. Furthermore, the silicone coupling of the drum to the glovebox's side wall cannot be defined as "plug-and-play", meaning it would be quite involved to re-attach it back again and would possibly mean a major ambient air infiltration inside the glovebox. However, the re-design of the new tether for the IR Source Location System provided an opportunity to revisit that original easy tether changeout objective.

[6] In fact, an incident occurred during the extremely delicate source deployment campaigns, which left the teflon tube deformed and kinked the fiber optic, limiting its light transmission capability. Fortunately though, the entire assembly didn't need to be changed out since the accident happened close to full arm retraction into the glovebox, which meant the damaged section of the tether and fiber could be cut off while still leaving enough extra length for unimpeded operational deployments anywhere in the IV. Had it happened when the tether was more extended though, full tether changeout would have been necessary.

FIGURE 5.17: Marking the Source Location System power cable every centimeter, in place of the old solution of sticking making tape to the fiber optic's cladding. After the correcting fluid was seen to be sensitive to fracture after drying if the cable was spooled and there had been too much fluid applied, the offending marks were re-painted with acrylic paint.

To this end, a new feedthrough was drilled in the exterior side of the drum, which now features two such ports. The IR tether is inserted, with the IRED vial already attached, though the six-way cross, passing the underside of the glovebox and exiting the drum from the inside, to be linked with its expansion box and hooked to its electronics and power supply on the electronics cabinet outside CR4. The UV FADC calibration system tether (see next paragraph), if needed, can be seamlessly exchanged with this main tether performing the same operation in reverse. Furthermore, the option to revert back to the old red laser optical source without a major system refurbishment is still available, although this would require a bit more of extra work considering the diffuser vial needed to be cut off from the tether to remove it, and would need to be re-fabricated and re-attached. An extra fiber optic was purchased, in case it was preferred to use a new tether or the old one suffered further damage, which is very similar to the CeramOptec Optran UV[161] fiber which is no longer in production. Its technical details are listed below in Table 5.5.

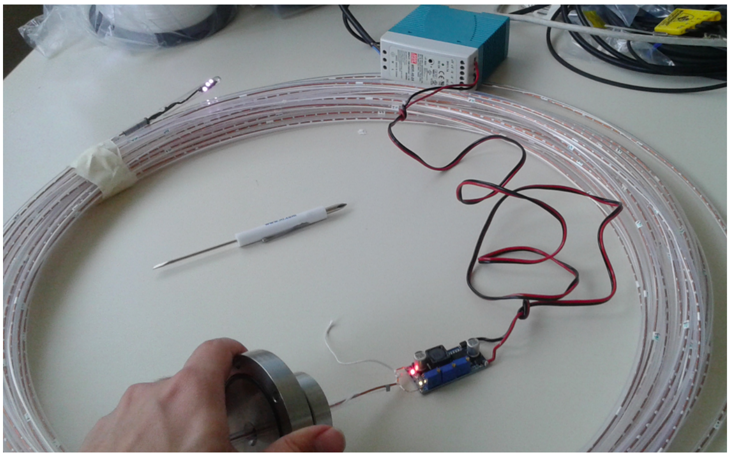

FIGURE 5.18: Finished, powered Source Location System, together with its power supply and current regulator, to operational power. Also visible are the labels where the actual length from the middle part of the IRED tower is written, to complement the relative centimeter markings with absolute values. Held in the author's hand is the new feedthrough for the tether drum, to be used with the UV FADC calibration system detailed in Section 5.1.5.

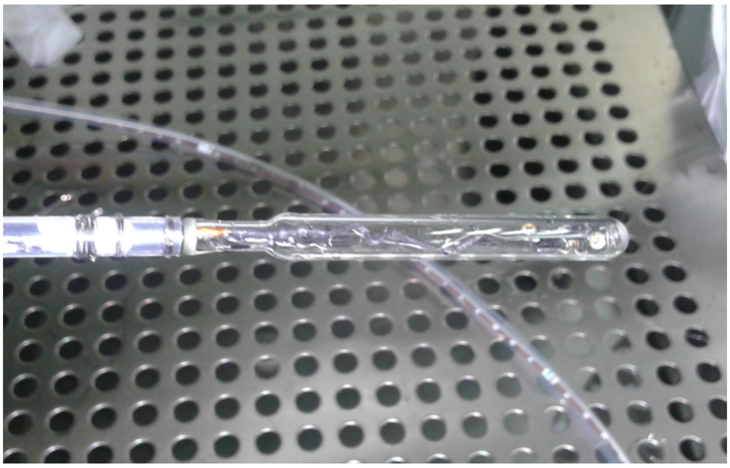

FIGURE 5.19: Finished Source Location System emitter in CR1, after stainless-steel-wire adjustment of the Teflon tube to the vial's transition neck, prior to final cleaning, bagging, and transportation to CR4 for integrated assembly.

5.1.5 UV FADC calibration system

As explained in the preceding section, the option exists to replace the Source Location System tether with another if so desired. The reason this option was exercised, apart from preserving the flexibility to revert back to the old light source and providing the option of future simpler upgrades to the calibration system, was the design of a system providing optical scintillation stimulation through short-wave UV (UVC at 265 nm). This system is being developed by the Kurchatov Institute and Moscow State University collaborators, but a brief discussion of its design and objectives are provided here for completeness.

A system capable of directly producing scintillation events in the IV through optical stimulation

Manufacturer and model	Bay Fiber Optics Optran UV
Part Number	SMA1P/UV400/424/450P/BPVC-3.8mm/30.0M/VT
Numerical Aperture	0.22±0.02
Length	30 m
Optimal transmission range	[200,1200] nm
Pure fused silica core	400 μm ± 2%
Fluorine-doped silica clad	424 μm ± 2%
Polyimide coating	450 μm ± 3%
Jacket	Black PVC simplex with Kevlar members (sheathing OD ∼3.8mm)
Connectors	Amphenol metallic SMA-905; knurl round nut, fine flat-polished to 0.3μm spec. Other end bare.

TABLE 5.5: Characteristics of the newly-purchased (2015) fiber optic for spare role in the internal calibration system.

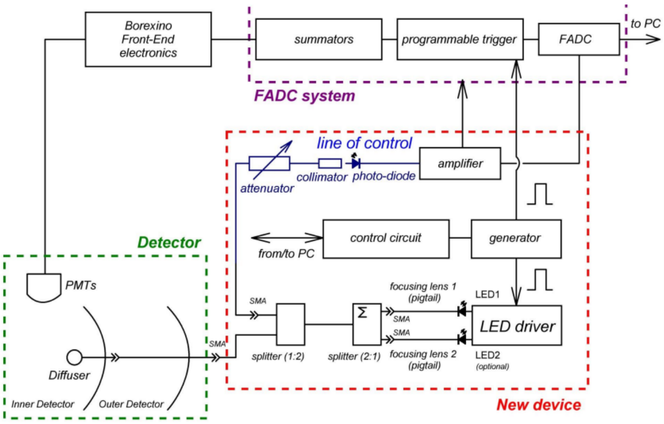

FIGURE 5.20: UV FADC online calibration system diagram, from [165].

is considered essential for a proper FADC system (see Section 2.3) online calibration, needed for its full commissioning and full data exploitation following the merging of DST Laben board data with FADC events, which has already been done, and its offline calibration through the reconstruction of the energy scale by several reference points[165] (2.22 MeV neutron capture peak, 4.95 MeV neutron capture on ^{12}C and cosmogenic ^{12}B β^- decay). This system would produce direct scintillation through the emission and diffusion of the mentioned 265 nm UVC signal, directed from a fast LED pulser through a fiber optic down to a diffuser (or even the bare fiber) at the tip of the arm, taking the place of the Source Location System emitter. Positioning accuracy will not be as crucial as for the main calibration sources, only requiring ∼10 cm positioning accuracy, which allows for the system to be used independently of the other tether. A diagram of the envisioned system is shown in Figure 5.20.

The UV system's tether would be inserted from the outside of the drum, all the way into the cross, to be outfitted with its diffuser. The same fiber could be used if its transmissivity capabilities were deemed acceptable, or a new tether with better short-wavelength transmissivity fiber could be fabricated. If the same tether were to be used, the corresponding fiber expansion box could be retained, and the fiber itself could be spliced into two light feeders: on one side, the existing red laser and, on the other, the UV LED pulser located on the exterior electronics cabinet.

5.1.6 External calibration hardware

In addition to the main facilities in CR4 envisioned for internal calibrations, the re-entrant ports mentioned in Chapter 3 (see Figure 3.16) in the context of their utilization for the LTPS Phase I system were originally conceived as a way of easily inserting calibration sources to the neighborhood of the SSS, in the Outer Buffer, with the aim of characterizing external background activity[64] coming from the surrounding mountain rock and the less radiopure components of Borexino itself, mainly in the SSS and PMTs (see Sections 2.4.11, 2.4.12 and 2.4.8; neutron thermalization γs are also considered external background, although their flux is 3-4 orders of magnitude smaller). The main component coming from within Borexino is the 2.615 MeV ^{208}Tl γ line –therefore, a ^{228}Th source with a 35.6% probability of emitting the ^{208}Tl decay daughter line, was employed (see Figure 5.21) and deployed in the external calibration re-entrant tubes, using a "switch" relying on the non-conductive nature of the polyethylene tube and the fact the end of the re-entrant port is made of metal, to reproducibly position the source. The remaining α, β and low-energy γs are absorbed either in the source container, the re-entrant tube material or the buffer. The source material was thorium oxide (^{208}ThO$_2$) in a metallic gold (Au) foil matrix to minimize ~1.5 MeV neutron production, which would not be problematic for Borexino itself, but would present inconvenients when used in the underground LNGS, because of possible interactions with dark matter WIMP search experiments. The ^{228}Th activity was 5.77 MBq ($\pm$15% at 1σ), with some trace activity from the thorium-229, 230 and 232 isotopes. An estimate of the activity of the external components and their contribution to the external background was achieved through the analysis of the external calibration data taken in summer of 2010. It was useful too for scintillating volume monitoring, energy scale determination and MonteCarlo tuning.

For the new calibration campaign, a revamped approach to the external calibrations phase is foreseen. MonteCarlo tuning for the newly-developed (after the calibration campaigns were over) `g4bx2` code is one of its most important objectives, but also to further refine the (position-dependent) energy reconstruction and energy scale variables, especially at large radii in enlarged fiducial volumes previously not considered. Finally, a check of plausible effects due to scintillator aging, or purification-related light yield changes after 2012, will also be possible. For this, the old source (now 1 MBq in activity –more precisely, 0.89$\pm$0.13 MBq in March 2015) would be used. Furthermore, a specially-designed ^{241}Am^{9}Be source lent by the *XENON* experiment could also

FIGURE 5.21: Thorium source stainless steel outer container photograph (left) and thorium source with insertion hardware ready to be deployed (right), from [64].

be deployed in the same positions to study neutron and external γ effects on very large FVs, by characterizing the buffer-to-scintillator boundary light yield and energy scale. The AmBe source would be accompanied by a "leader" containing three 10-12 cm long metallic nickel cylinders, to provide high-energy neutron capture γs (in a manner similar to the new internal neutron source, see Section 5.3.3).

5.2 Unquenched high-activity ^{222}Rn source fabrication

5.2.1 Motivation in Borexino

The choice of ^{222}Rn as a radioisotope for calibration in Borexino owes to the fact that it (and its short-halflife daughters in its decay chain, see diagram in Figure 2.32 and ^{222}Rn's decay in Figure 2.29) offers the three main types of decay radiation (α, β and γ) within the energy ranges of interest to the detector, allowing to cover the full energy spectrum up to $\sim$3 MeV with the same source. Since most of the αs and βs would not travel outside the container used to confine the gas to deposit their energy in the scintillator around it, it has to be dissolved in scintillator to profit from those decay particles –requirement which the pure γ sources do not share, and therefore can be carried in another medium such as water, see Section 5.3.1.

It should be noted that β^- capture in the vial walls will lead to spectral distortions, similar in effect to scintillator quenching in that spectral area, that nevertheless have been accurately modeled in the past[161][160]. A scheme to generate an undistorted pure β signal, involving plastic-implanted β^--emitting isotopes or containing those in an extremely thin micropipette have been considered for years[162], but were not deemed crucial for Borexino's objectives at the present time, considering their potential release risks, the need to deploy them separately, incurring in important time constraints, and the fact their potential for improvement lies mostly in the lower part of the spectrum. The intentional release of ^{32}P in the scintillator as a way of tracing fluid movement in the context of Chapters 3 and 4 was also proposed but never implemented.

In the previous calibration campaign, radon sources were used extensively in all of its phases (see [161]'s Appendixes C, D, E and F) and, even if the quenching introduced by the raw PC was noticeable (∼30%, see pages 280-282 in [161]), the calibration results obtained thanks to them were among the most important in the whole campaign, especially for position reconstruction studies –since the confinement of α and β events to within the vial[162] gives an extremely good handle on this behavior, provided the source is very well located thanks to the source location system hardware (Sections 5.1.1 and 5.1.2). It is of course expected new α data will greatly benefit further refinements and tweaking of the MLP tool (see Section 3.1.2), should any unexpected changes to the detector have remained uncorrected during the development of the method. Energy reconstruction analyses will also be benefited, in conjunction with the water-solved γ sources.

5.2.2 Technique basis and development

The basic principle at work for the development of the new high-intensity, unquenched ^{222}Rn sources dissolved in the PC+PPO scintillator mixture withdrawn from Borexino's IV is explained in detail in [161]'s Sections 7.2.1 and 7.2.3, as well as in [160]. This procedure was developed after poor results with the then-standard methods employed before in Borexino and CTF, based on radon trapping in a charcoal filter.

There are significant differences in the current method since it had to be re-designed from scratch, considering nobody from the previous workforce dealing with the creation of the scintillator-solved sources was available for direct knowledge transfer, nor was any legacy hardware available. As a consequence, a degree of flexibility was possible while keeping true to the essence of the technique that had yielded best results, while being able to apply lessons learned in the first source loading campaigns.

The vial design employed for the current technique was kept identical to the previous one[161], although the option exists to enlarge the ampoule containing the radon-loaded scintillator. The Pyrex neck of the vial would be kept the same, having a constricted area where fire-sealing was performed, separating the source from the sacrificial neck length that served as attachment to the loading station, as well as the immediately-adjacent glass ring used as an attachment point for the source holder in the mechanical arm. The dimensions for the quartz ampoule containing the ^{222}Rn-loaded scintillator could be changed from the standard ∼1" OD (which would yield ∼7-7.5 mL capacity, taking into account the typical wall thickness) to ∼1.5" OD (or ∼23.5 mL). Vials are thoroughly cleaned in its interior with several baths of acetone, isopropanol, critical-cleaning detergent and de-ionized water. Maximum source activity at deploy should be kept ∼70 Bq, for the aforementioned electronics saturation threshold of ∼100 Hz, taking into account the ∼30 Hz of intrinsic detector signal (mainly ^{14}C), yielding a specific activity range of ∼[10,3]

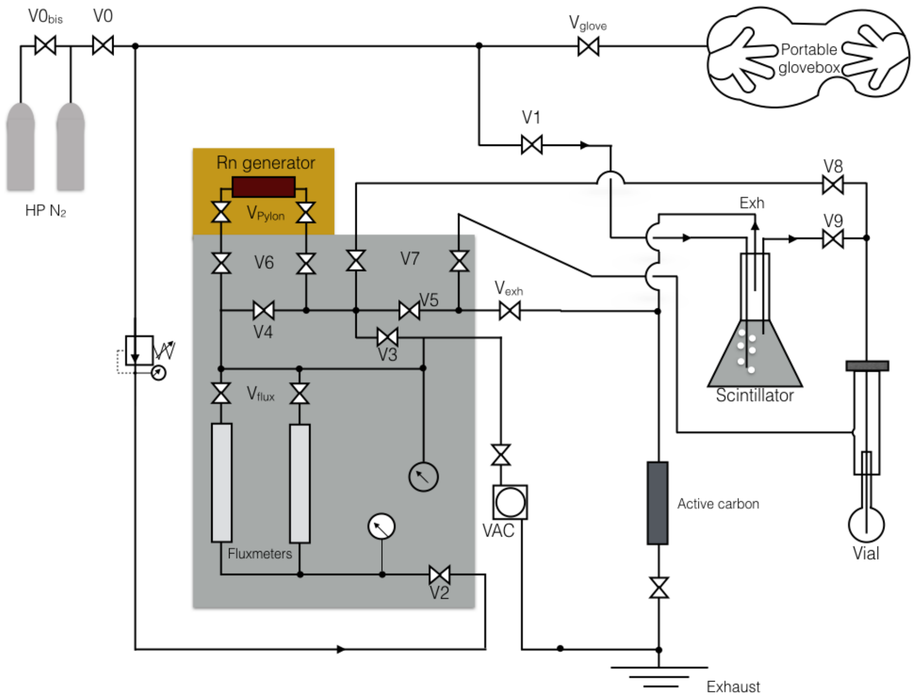

FIGURE 5.22: Radon loading setup diagram for the unquenched, high-activity ^{222}Rn sources developed in the Federico II University of Naples. The upper left cylinders represent the High Purity Nitrogen supply. The portable glovebox was used for (dis)assembly of pieces, such as the vial or scintillator flask, when exposure to atmospheric oxygen is not desired. The grey box represents the monolithic panel employed for pressure determination and core valve control, scavenged from CTF's source production campaigns. The activated carbon filter is employed to avoid indirect transport of PC vapors to the rotary vacuum pump when the upstream panel lines are evacuated, even if V_{exh} is nominally closed.

Bq/mL. This means, considering the transportation time from Naples to LNGS, in addition to the source cleaning, preparation and insertion steps, estimated at no less than 2 days, that the source's minimum activity at production cannot be less than $70{\cdot}e^{2/\tau_{222Rn}} \approx$120 Bq.

The loading station was completely re-designed, and the few similarities shared with the previous setup were due to convergent designs aiming for similar objectives. However, the current aim was to lower the quenching to the minimum, which was not reliably achieved in an operational manner during the first calibration campaign. Furthermore, the source loading had to be demonstrated to be scalable with reliability to achieve the activity required. A diagram of the system is shown in Figure 5.22, and a photograph of it located in the fume hood in Naples University Federico II is shown in Figure 5.23.

The system consists of a heritage panel from CTF loading experiments, containing the core fittings and instrumentation for gas distribution. It was kept unmodified, except for a thorough interior cleaning, since the Swagelock fittings and welds had already been proven and leak-checked. This panel includes two parallel flux-meters (coarse and fine) for flow control, a manometer in series with those for pressure monitoring, and the radon generator in/out ports,

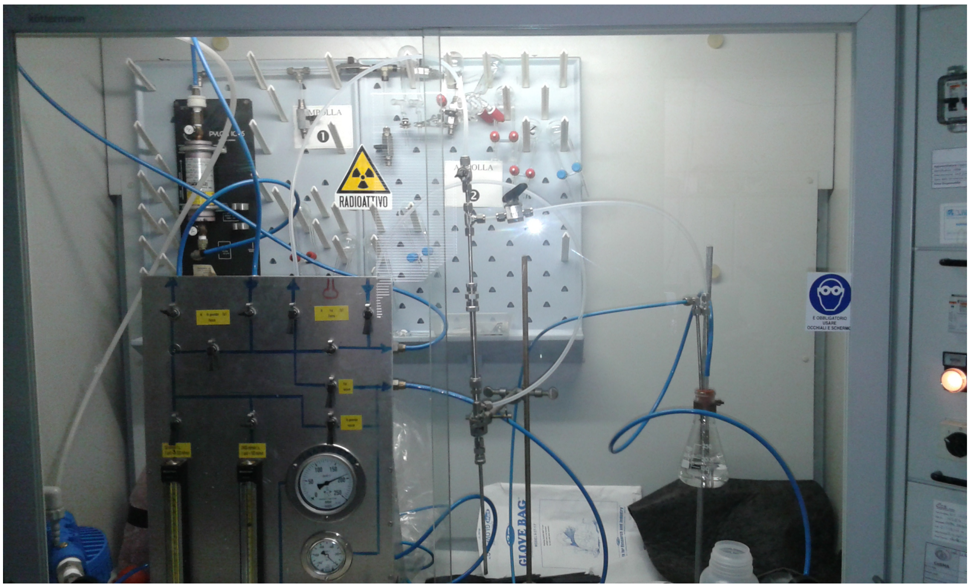

FIGURE 5.23: Actual picture of the final version of the radon loading station.

as well as those for the source loading. Finally, an exhaust port for the source was also provided, as well as a vacuum port for fluid drawing, also useful for line evacuation, purging and cleaning.

The vacuum pump employed was a low-power membrane pump capable of bringing line pressure down to a few millibar, more than enough for source creation purposes, and adequate after a few iterations for line evacuation and pumping to avoid oxygen presence.

An ultra-high-purity nitrogen ($UHPN_2$) supply was connected to three different points in the system:

1. The flow intake ($V2$) in the panel for the drawing of gas from the radon generator, as well as for the flow supply to the source vial.
2. The scintillator flask containing the liquid used for source filling, that was kept under constant, low-intensity sparging as a precaution against inadvertent exposure to oxygen or other gaseous quenching agents[7].
3. A portable glovebox that served as an oxygen-free environment for flask filling operations, vial adjustment when filled with scintillator, and other quenching-critical operations.

The flask containing the scintillator (drawn directly from Borexino's IV under LAKN atmosphere in CR4's facilities) was connected to the system through a triply-perforated rubber cap

[7]Exhaust for this flask was directed through an activated carbon filter to the fume hood ventilation system. While the fume hood wouldn't necessitate this precaution, the connection to the panel through the V_{exh}-to-$V5$ line meant that, in the absence of the filter, PC condensation would have the chance to reach the vacuum pump. This, in fact, happened in the first test design for the loading station, and meant a –fortunately– temporary inability of the pump to provide low enough pressures in the vacuum line

FIGURE 5.24: Picture showing our Pylon RN-1025 flowthrough gas source.

that ensured a reasonably hermetic closure. The overpressure inside the flask caused by the UHPN_2 bubbling was kept in a safe range to avoid it forcing the cap out or damaging the flask, as well as to prevent too much scintillator sloshing and bubble ingestion during scintillator drawing to the vial. The two connecting tubes going inside the flask and in contact with the scintillator (sparging line and drawing line) are Pyrex glass, while the exhaust tube is Teflon.

All the lines not contained within the panel are Teflon tubes with steel or plastic (depending on the criticality of their position within the system) Rapid Fittings, except for gas-only lines which are polyethylene tubing.

The source vial is seamlessly held in a sleeve-needle leak-tight holder since the beginning of the procedure until sealing. It is composed of a thin steel tube through which the radon-loaded nitrogen flux and drawn scintillator is directed into the vial; and a concentric, larger diameter sleeve that serves as an exhaust container for the nitrogen flux. This sleeve features two viton O-ring fixtures at its top and bottom that serve as the needle height regulator and vial holder, respectively: the top fixture can be loosened enough to permit the needle to be retracted before or inserted beyond the fire-sealing neck constriction, while keeping the overpressure inside it to make sure no quenching agents get into the system.

The radon generator is a commercially-available Pylon RN-1025 flowthrough source[166] owned by the Federico II University in Naples, as part of their radon specialist group led by Dr Vincenzo Roca. This source is an aluminium cylinder with two attach fittings (see Figure 5.24), with a capsule containing ^{226}Ra salts (see decay scheme in Figure 5.25), sandwiched between particulate filters to avoid release of non-gaseous substances. It has an equilibrium activity of 106^{+25}_{-10}kBq, with a rated stable emanation of 13.4 Bq/min under continuous gas flux (maximum flow rate: 10 L/min).

After assembly, the system was air- and vacuum-cleaned, and several sacrificial PC drawings were performed through the tubing areas where scintillator was expected to flow through. In

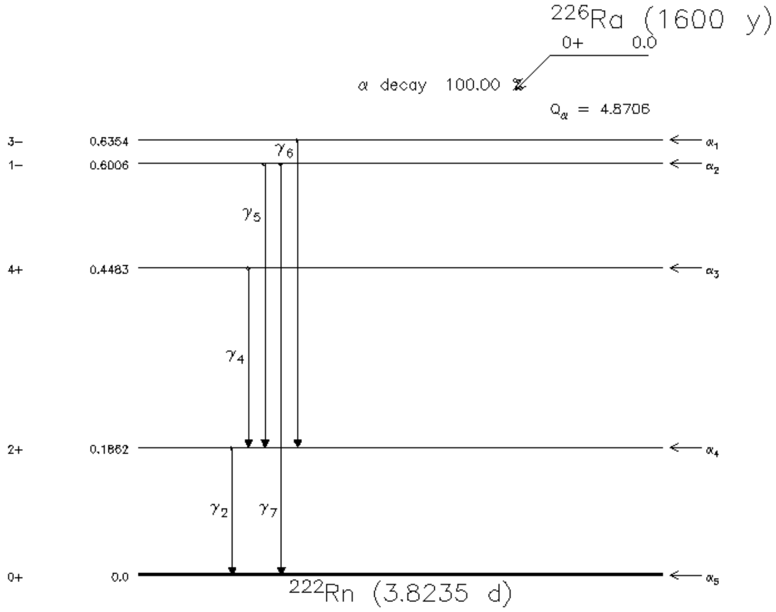

FIGURE 5.25: Radium-226 decay scheme, yielding the ^{222}Rn needed for the calibration sources through the 100% b.r. α decay, as well as the possible de-excitation γs. The $\sim$1600 year half-life means that the radon generator emanation activity will be constant for any Borexino-related program.

spite of those precautions, particulate contamination was still present in the first few test runs. For that reason, and since a system improvement was made after high-activity loading feasibility runs were completed, in order to reduce oxygen levels to <ppm levels, the system was thoroughly re-cleaned again, including flushing a hot Cytranox detergent mixture through the piping that would see liquid flow. This was repeatedly rinsed with water flows and airflow-vacuum cycles afterward. However, the first few subsequent test drawings showed foaming and a degree of white particulates that, while not impeding the successful demonstration of unquenched, high-activity sources, showed a potentially undesirable feature for future operational sources. Later isopropanol and PC flushings showed their effectiveness through the absence of noticeable contamination when performing the last trial source creation runs.

5.2.3 Results and comparison with previous sources

Several test runs to verify the integrity of the core system and the feasibility of high-intensity radon loading were performed with the simplified system, which didn't guarantee ppm oxygen removal, prior to the final assembly of the system described in the previous section. The objectives for these dry and wet dress rehearsals were:

- Verify leak tightness and proper operation of the core panel.

- Test new needle/sleeve vial holder.
- Design and test scintillator withdrawal and sparging system.
- Demonstrate large amounts of radon could be deposited with the LN2 bath with the current system, and adjust flushing durations to achieve the desired activity levels: dry runs (no scintillator; 164±8 Bq deposited).
- Develop, test and refine scintillator withdrawal and vial filling procedures.
- Demonstrate reliable line clearing techniques to avoid vial overfill after the initial filling operation was completed.
- Test acceptable limit for vial ampoule filling.
- Practice integrated (loading + filling + freezing) operations: wet runs.
- Develop and practice source fire-sealing. Previous sources had relied on professional glass-makers who were not available on this occasion.
- Practice legacy procedures.

Several test vials were employed, some of which could be re-used since no loading or fire-sealing had taken place. By the end of this phase, all objectives were achieved except the 6th point above: reliable line clearing techniques after the primary filling operation was complete. Reproducibility of the fill level was poor and accidental overfilling was very likely, although its amount was very difficult to predict, so it could not be reliably estimated and corrected for during the primary filling. Additionally, as was expected, scintillator quenching was severe.

Regarding activity levels, the radon laboratory in the Federico II University of Naples provided a very sensitive and well-calibrated Ortec hyperpure germanium crystal spectrometer (gamma-X type), allowing to very well characterize the fabricated test (and operational) sources in-situ, mere seconds after their sealing. This detector features a beryllium entrance window for the emitted radiation, allowing to bring the observed spectra's lower limit to ∼20 keV, with a 2 keV energy resolution (at 1.33 MeV) and a relative efficiency of around 48%. Furthermore, the interpretative expertise of Dr Vincenzo Roca and the Ortec Gammavision v.6.0 software provided a quick and precise assessment for the equilibrium activity measurements. This activity is determined from the γ-emitting daughters from the ^{222}Rn decay, in particular ^{214}Pb and ^{214}Bi, which is then assumed to come from the radon α decay. This condition is verified after 3 hours of measurement, following sealing of the measurement chamber. The γ lines are Gaussian-fitted by the software to yield the activity and uncertainty.

A test source was left loading for 36 minutes at a measured UHPN$_2$ flux of 21 mL/min. However, after a few minutes of this operation, it was discovered the RN-1025 input port was not well secured to the flush line, and therefore the pre-loading radon generator flush to stabilize its emanation had not been performed, and the loading hadn't been taking place until the line was tightened. Therefore, the source didn't get the full 36 minutes of loading, but conversely it got a "hit" of the ^{222}Rn that had accumulated in the RN-1025 generator. Final activity was 363±16 Bq. Considering as a measure of the efficiency of the loading procedure the specific activity per unit of time and flux, it would yield ∼0.48±0.02 Bq/(min·mL).

It is emphasized the deposition of the accumulated radon would have provided an initial boost in activity, artificially raising this efficiency, although on the other hand radon deposition on the vial walls has an unknown freezing efficiency, which very probably doesn't scale linearly with radon concentration in the flux: some of it will be exhausted away, and the areas most impinged by the flux might get "saturated" more rapidly than more peripheral ones. The discussion of these phenomena was not further researched and is beyond the scope of the present discussion.

Subsequently, the fluid-handling part of the system was completely renewed, except for the scintillator flask and the needle/sleeve holder, by using the new high-quality metal Rapid Fittings and relying on more extensive use of thoroughly cleaned Teflon tubing. Procedurally, routine high-fluence UHPN$_2$ flushing and vacuum pumping cycles were put in place to evacuate the system of oxygen to the ∼ppm level. A more detailed overview of the procedure can be found in Appendix A.

The new system provided excellent quenching results compatible with unquenched, pure scintillator, as shown in Figure 5.27. These results were provided by Milan's University time decay profile measurement setup for scintillator mixtures[167] (see Figure 5.26), based on a previous heritage design[168], featuring two photomultiplier tubes: a strongly-coupled one (high-level PMT) and a loosely-coupled one (low-level or fluorescence PMT, for single-p.e. sampling) providing the stop and start signals, respectively. The loose coupling between the specimen and the fluorescence PMT is achieved with a set of neutral filters. An electronic DAq system consisting of a counter, constant fraction discriminators connected to the anode, timer and coincidence units and a digitizer (10 bit, 2 Gb/s Agilent Technology) was integrated through a LabView software architecture. Particular attention was devoted to the long scintillation decay time profile tail, since it is extremely sensitive to quenching, both by shortening of the long scintillation response in time as well as reducing its yield.

While during the previous calibration campaign light yield measurements were of utmost importance, considering the scintillator was made separately from the mixture used in Borexino itself, in this new setup they are less crucial, since the differences should be minimal if no quenching is detected through the analyses quoted in the previous paragraph.

The first loaded source spent about an hour (62 minutes) in loading mode, with a UHPN$_2$ flux of 40 mL/min, and was measured to have ∼650 Bq just after sealing. An overnight measurement

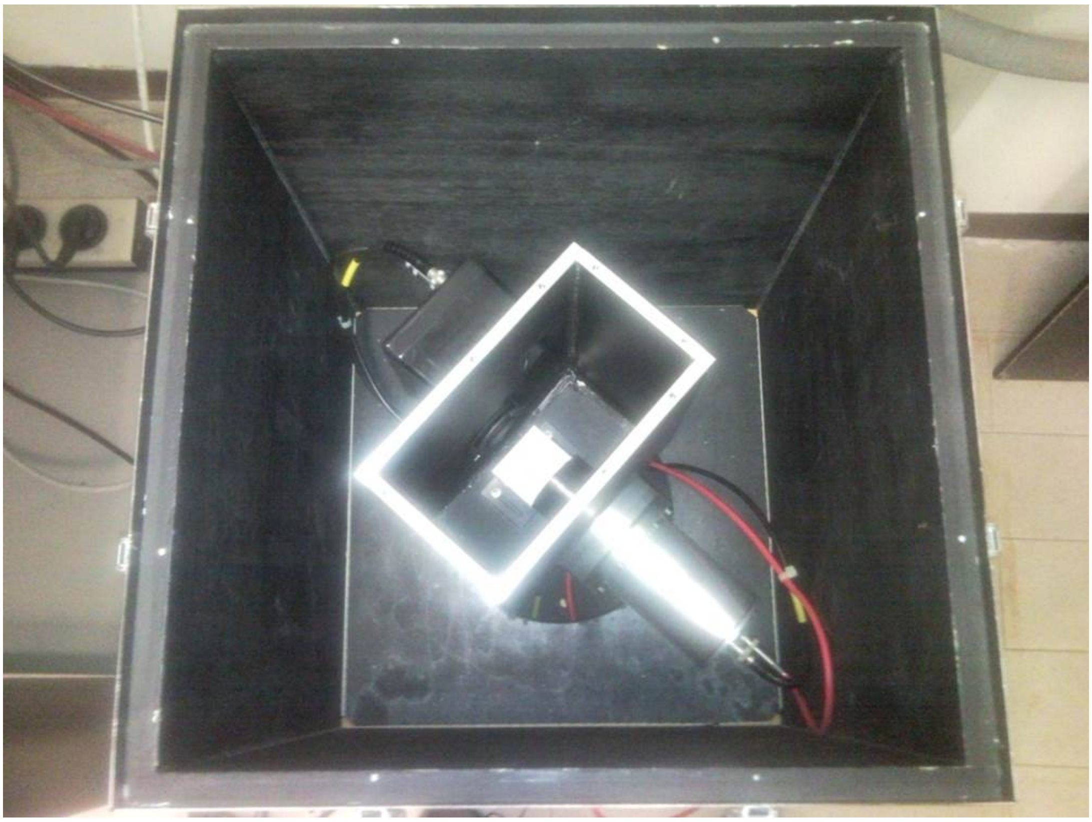

FIGURE 5.26: Actual photograph of the single-photon setup used for the source's scintillation decay time measurements shown in Figure 5.27.

(12 h of integration time) led to the more precise determination of 665±28 Bq. This would yield a loading efficiency of 0.269±0.012 Bq/(min·mL).

A second test source with 20 minutes of loading time and the same flux yielded 105±5 Bq, or 0.131±0.001 Bq/(min·mL).

In light of the preparation of these sources, as well as the dry runs performed with the old system, it is apparent a high level of ^{222}Rn deposition is achievable and repeatable while providing an environment for the scintillator compatible with negligible amounts of quenching agents. Actual demonstrated initial source activities are far beyond the requirement of ∼120 Bq at production, up to more than 5 times. Loading flow time can be extended if necessary, and is in principle not constrained by any factor other than fluid (UHPN$_2$ and LN2) availability. It is then expected larger activities can easily be achieved with the same setup, raising the initial activity ceiling to no less than 1 kBq, which could potentially allow for more flexibility in the calibration campaign, either by increasing the available wait time to ∼10 days between production and deployment in Borexino, or by shortening data-taking time during the calibration runs if the trigger threshold was raised to avoid radiocarbon's ∼30 Hz of irreducible signal, to permit a ∼100+ Bq source to be inserted without saturating the electronics.

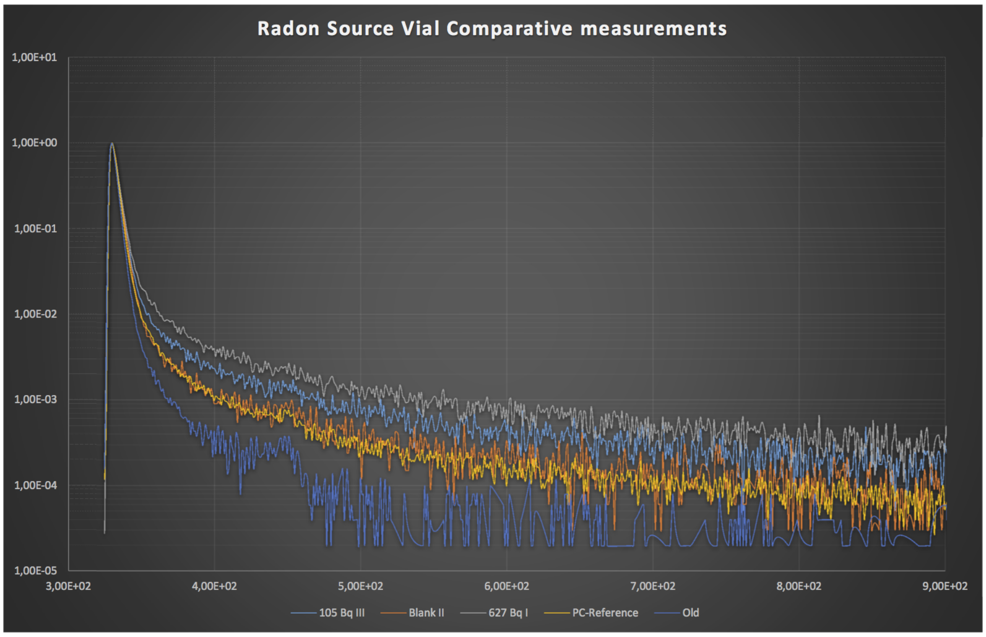

FIGURE 5.27: Newly-fabricated, unquenched radon sources comparison to blanks, pure PC and quenched sources: the dark blue curve ("old") shows one of the first sources created with the test system. The yellow curve ("PC reference") shows a reference spectrum of unquenched Borexino scintillator. The orange curve ("Blank II") shows blank vial filled and sealed as per the developed procedure, but with no radon loading. The light blue and grey curves show the actual unquenched sources. The slow component of their scintillation profile is, as could be expected, the scintillation response to the higher α activity (grey=627 Bq and light blue=105 Bq, both as measured just after sealing) of ^{222}Rn solved in the liquid.

Further, an approximate estimate of $\sim$0.2 Bq/(min$\cdot$mL$_{UHPN_2}$) of average deposition efficiency is expectable from the produced sources, and can conceivably be brought up to twice as much by not performing a pre-flush of the radon generator, thereby profiting from the amount accumulated during its previous dormant phase. This option, however, is understood to not be without risks, since air leakage into the RN-1025 might introduce quenching agents that could negatively affect the source's light yield and hence its usefulness as a calibration tool.

These numbers show that the method employed in [161] can be reproduced in a completely new setting, comfortably allowing for ^{222}Rn deposition activities on the order of the ones produced for the first calibration campaign. However, the renewed technique shows excellent non-quenching results, which had been a problem for the last production campaign, even if part of the culprit could be attributed to the scintillator batch employed as solvent.

5.3 Other new sources

As in the 2009/10 calibration campaign, this new opportunity to insert calibration sources in Borexino means that several isotopes, covering a wide range of energies and particle types, will be employed. Some of the sources have already been used previously (most of the γ sources, as well as the AmBe neutron source), albeit with lower activities than envisioned for this new campaign – while it is expected there will be some new additions to further expand the calibration's objectives and capabilities.

5.3.1 γ sources

The γ-emitting isotopes to be employed, apart from the ^{218}Bi-Po coming from the aforementioned ^{222}Rn source, are listed below in Table 5.6.

Isotope	**Energy** (keV)	$\tau_{1/2}$ (days)
^{139}Ce	166	285
^{203}Hg	279	47
^{85}Sr	514	51
^{54}Mn	835	313
^{65}Zn	1116	245
^{40}K	1461	$3{\cdot}10^{1}1$
^{58}**Co**	811 (+2γ)	71
^{22}**Na**	1274 (+2γ)	949

Table 5.6: γ-emitting isotopes to be employed in the next calibration campaign. ^{57}Co is not expected to be employed anew, while it was used in the previous campaign for low-energy trigger threshold effects, that are considered to be well-understood now. ^{40}K is to be taken from natural KCl in solution, since the natural abundance of radiopotassium is ~0.012%.

All isotopes will be mixed in a standard or enlarged quartz-Pyrex vial as described in the previous Section 5.2, for faster and more convenient deploy, and are purchased as a salt solution in acid (HCl) water. It is desired to reach a much higher activity than previously, to allow for faster data-acquisition and therefore have access to more different positions while shortening data-taking time. Amounts of each isotope will be weighted according to their half-lives to ensure a balanced emission from each energy region. Furthermore, the isotope mix will include the β^+ emitter (see next section) so the specific activity will be further increased. Special procedures will be put in place to perform this mixing safely on-site, since the provider company will only supply a master solution of each separate source: as a consequence, loading in Borexino's custom vials will take place after the purchase.

5.3.2 β^+ source

The motivation to create signals which mimic as faithfully as possible the β^+ prompt event in an IBD signal exists for any analysis based on this channel (geo-ν, reactor neutrinos...) but has been boosted by the needs of the upcoming CeSOX program (see Chapter 6). Due to the large number of IBD signals stemming from the ^{144}Ce-^{144}Pr source happening at the same time, the detector's response to triple-γ (3γ) events (two back-to-back from the positron annihilation (511 keV x 2 = 1022 keV) plus the one coming from the neutron capture (1.2 MeV)), especially at large radii, is desired to be studied. Furthermore, the whole ^{144}Pr energy range ($Q_\beta \approx 3$ MeV) will need to be covered as much as possible ([1,2.2] MeV). For this reason, two β^+-emitting isotopes are expected to be used in combination with a ^{65}Zn to provide a high-energy pure γ side-by-side comparison, see following Table 5.7:

Isotope	**Energy** (keV)	$\tau_{1/2}$ (days)
^{58}**Co**	811 ($+2\gamma_{annh}$)	71
^{22}**Na**	1274 ($+2\gamma_{annh}$)	949

TABLE 5.7: β^+-emitting isotopes to be employed in the next calibration campaign. The extra two γs in parenthesis indicate the positron annihilation, while the quoted *energy* corresponds to its γ emission. Only high-order branching ratios are quoted. Cobalt will cover the mid-energy range while sodium reaches until close to the spectral end-point expected for CeSOX signals.

Positrons, as opposed to electrons, are mostly immune to the quenching-like effect due to interaction with the vial walls mentioned in Section 5.2.1, especially when their source isotope is solved in water, since β scintillation effects will be mostly lost.

The possibility to introduce the β^+ source in a microcapillary as suggested before, while keeping that microcapillary confined inside a sealed vial with unquenched scintillator mixture following the procedure developed for the ^{222}Rn source (see Section 5.2), to mitigate the danger of breakage and emitter spillage in the IV, is also a considered possibility.

5.3.3 Neutron sources

The aforementioned sources provide a wide range of radiation types and energies, but one important radiation particle remains for which the detector response must be precisely characterized: neutrons. As explained in Chapter 2 and Section 5.1.6, the main expected neutron signals in Borexino are the neutron background from cosmic-generated spallation neutrons, those coming off the minerals in the surrounding rocks, and more importantly for the future, those liberated during IBD reactions (such as those derived from $\overline{\nu}$ interactions, mainly geo-neutrinos, reactor neutrinos and those emitted by CeSOX's source). For this reason, neutron calibrations were an important part in the first campaign in 2009-10 and will be even more in the upcoming one, especially driven by SOX considerations. Two neutron sources will be employed, driven by the

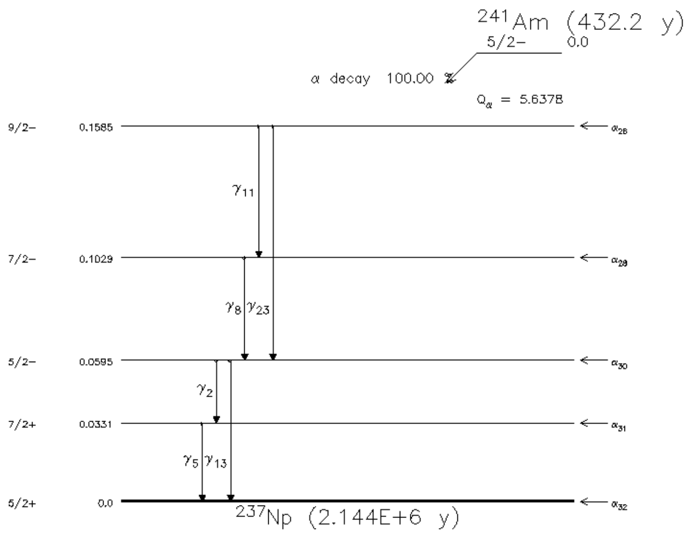

FIGURE 5.28: ^{241}Am decay scheme.

α decay of the ^{241}Am isotope (see Figure 5.28): these particles can drive nuclear captures in the elements of other nearby materials and, under the right circumstances, emit neutrons (accompanied by relaxation γs which need to be properly shielded against). The surrounding elements selected for use in Borexino's internal calibrations are:

^{241}Am^{9}Be high-intensity source The central "pill" of the source consists of an "active element" disk of ^{241}Am(NO$_3$)$_3$ (americium nitrate) sandwiched between two ^{9}Be windows, to ensure efficient α absorption by the latter, as well as an outer cladding of radiation-resistant plastic. The (α,n) reaction takes place as:

$$^{9}Be + \alpha \rightarrow n^0 +^{12} C; Q = 5.70 \text{ MeV} \tag{5.5}$$

The (γ,n) reaction below does not take place in ^{241}Am^{9}Be sources, since it requires γs over a 1.63 MeV threshold:

$$^{9}Be + \gamma \rightarrow n^0 +^{8} Be; Q = \ 1.63 \text{ MeV} \tag{5.6}$$

The expected neutron spectrum, according to the international standard ISO 8529-1, can be seen in Figure 5.29.

The relaxation γs in Figure 5.28 will need to be shielded, and the design choice in Borexino's standard AmBe source holder is to keep the source capsule in a 3mm-thick lead enclosure[161], to ensure proper background reduction. Additionally, for neutron moderation, the holder is made out of Delrin, a hydrocarbon-rich material. Metallic bolts are used to hold the cap in place once the source is encapsulated; this cap also has a protuberance

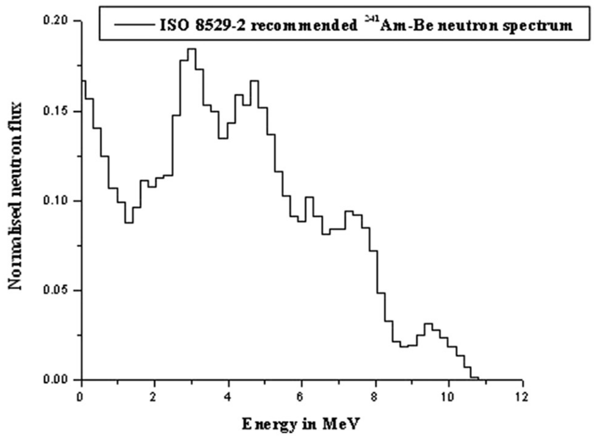

FIGURE 5.29: Expected neutron spectrum according to standard ISO-8529-1 for an AmBe source[169].

to facilitate tying with the source coupler. A picture of this holder is shown in Figure 5.30 and its configuration when ready for insertion during calibrations in Figure 5.31.

Since the source utilized during the last calibrations was less powerful than could be supported, a new one with a higher neutron fluence would expedite measurement time and potentially allow to be deployed to more positions while obtaining the same statistics for each point. Given the desire to more carefully map the IV, especially around its edges for FV enlargement, as well as to establish a precise map of the neutron response in the bottom part of the IV to optimize data collection during the CeSOX program, a new source was purchased, whose technical specifications can be found in Table 5.8.

Provider and model	Eckert&Ziegler AMNB20698
Activity (uncertainty) [kBq]	850 ($\pm$10%)
Diameter (active diameter) [mm]	18 (11)
Height (active height) [mm]	5 (1)
Estimated neutron activity [n^0/s]	$\sim$50

TABLE 5.8: Specifications for the newly-purchased ^{241}Am^{9}Be source for the new calibration campaign.

High-energy γ source In combination with the new, higher activity source, a potentially complementary use was devised for the ^{241}Am^{9}Be source, apart from internal neutron calibrations. In a manner similar to the external calibration source (see Section 5.1.6), nickel metal could be used to capture neutrons and create a high-energy γ source, predominantly via the (n,γ) reactions:

$$^{58}Ni(n^0,\gamma)^{59}Ni \tag{5.7}$$

and

FIGURE 5.30: Open AmBe source holder.

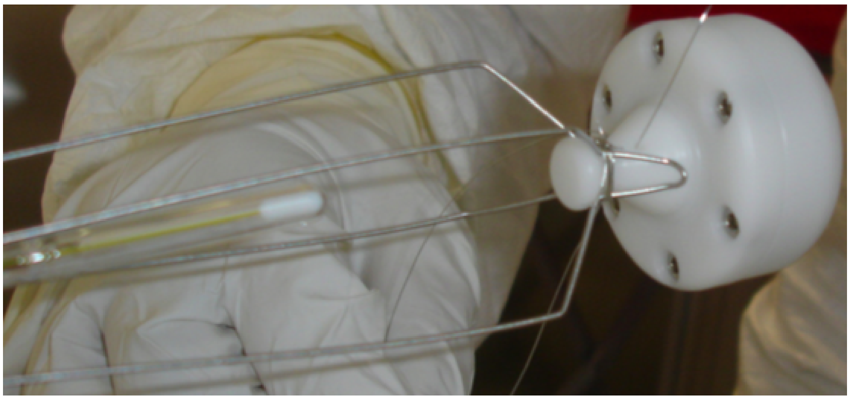

FIGURE 5.31: Neutron source installed atop the source coupler, ready for insertion in Borexino, in 2010[161].

$$^{60}Ni(n^0,\gamma)^{61}Ni \tag{5.8}$$

The most interesting γ peak for the purposes of high-energy calibration is the 8.99 MeV one, although a wide array of peaks of [5,9] MeV will be available.

For this reason, a design that would allow a certain amount of moderation (with a hydrocarbon-rich material such as Delrin) for the neutrons prior to their arrival at the nickel material (of a 5 mm thickness) was devised. Furthermore, in an exercise of extra caution, in order to avoid unexpected interactions of the nickel with the scintillator (either chemical or radiological), as well as to avoid the need to create a smooth, unique outer mold surface for the nickel material to be able to clean it appropriately prior to insertion in the detector, it was decided an outer Delrin casing would be added, also ensuring no sharp edges existed on the bottom of the holder, to reduce risk of damage to the vessel if the source got too close to it during deployment.

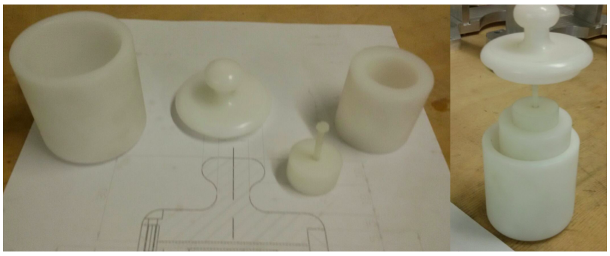

FIGURE 5.32: Delrin components of the new neutron source holder with the option of employing nickel foils for high-energy γ production. On the left picture, from left to right: outer mold, top cap with protuberance for coupling with the Source Deployment arm, top cap to close inner cylinder, inner cylinder to hold the source and its lead casing. The 6 nylon bolts closing the external container, as well as the o-ring for leak-tightness, are still not machined in this picture. On the right, *matrëshka*-like arrangement of the components. The nickel foils will surround the inner container, together with the nickel disks on top/bottom. The removable "handle" rod is seen here holding the top cap: this threaded rod is auxiliary and just used to open the inner container to access the source.

The chosen design utilized 4 concentric cylindrical natural nickel sheets surrounding a Delrin core where the source and lead shield (identical from the previous holder) would be held. A top Delrin cylinder serves as a cap to ensure similar amounts of Delrin surround the source on every direction. This cap has a threaded orifice on top to facilitate removal, employing an auxiliary threaded rod as removable handle. Eight additional natural nickel foil circles would be located on top and under the Delrin source-holding cylinder, four on each side. This nickel thickness would enable a $\sim$1.6% capture rate (in other words, 0.8 captures/s in our nominal 50 n^0/s source, which would give an accuracy of 0.04% in the 9 MeV peak determination after $\sim$3.5 h, or 10^4 captures). This way, the neutrons emitted by the source would have a similar or greater amount of Delrin to moderate into as in the old holder. Finally, this ensemble would be positioned inside an enclosing Delrin container, with a top cap holding a Viton o-ring to ensure leak-tightness, and a protuberance for coupling to the arm. The metal bolts employed in the old source were replaced by nylon ones, to avoid unwanted captures in their alloy's iron, polluting the clean nickel γ spectrum. The holder can also be used without the nickel foils, providing a backup to the old system or volumetric flexibility for possible future uses. Depictions of the holder can be seen in Figure 5.32.

Technical specifications of this new holder can be found in Appendix B.

^{241}Am^{13}C source As part of DarkSide-50's Liquid Scintillator Veto (LSV) calibration campaign in late 2015-early 2016, a ^{241}Am source was employed but featuring ^{13}C as the α-capturing isotope. This source is based on a 100μCi (3.7 MBq) type AFR (A-2 disk) ^{241}Am Eckert&Ziegler source. The active element is mixed with a metal matrix, and a gold cover is placed on top. This source is based on a stainless steel 12.7 mm OD container capsule which holds the active matrix and gold cover, with a $\sim$4.2 mm ID depression that serves as the source's active α area. It is in this recess that a solid ^{13}C (99% purity, 3%

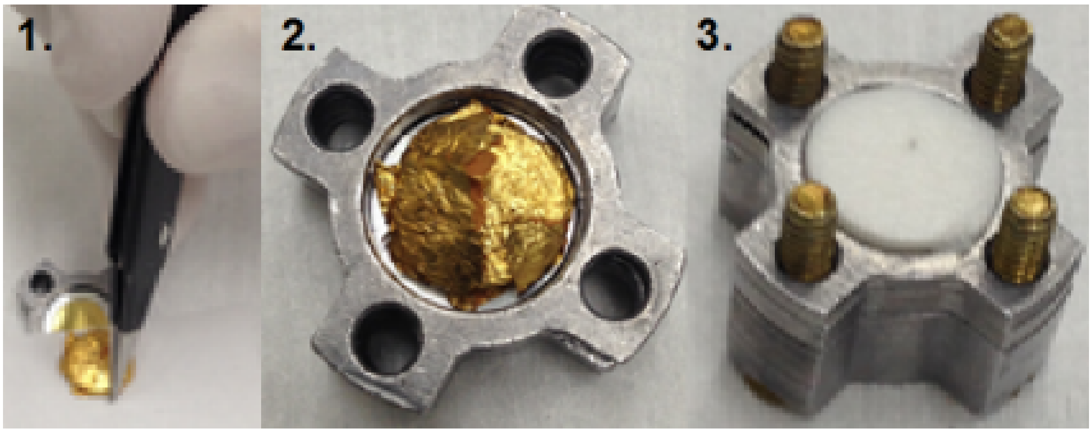

FIGURE 5.33: AmC source assembly in the DS-50 calibration source holder. The ^{13}C pellet is covered in the gold foil (1) and located atop the active gold window of the ^{241}Am α source already placed in the star-shaped DS-50 source holder (2), to then be held in place by a polyethylene plug (3). Images from [170]

by weight $^{nat}C_4H_6O_2$ binder) is placed, surrounded by a 1μm-thick gold leaf. The carbon pellet is infinitely thick to αs coming from the source. A polyethylene spacer is mounted on top of the Au-wrapped carbon pellet to keep it securely in place (see Figure 5.33), and the ensemble is enclosed in a lead casing attenuating the 60 keV γ from ^{241}Am by a factor of $>3.7{\cdot}10^{-5}$ ($<9{\cdot}10^{-9}$ Sv/h dose rate at 2.5 cm distance). This configuration provides $\sim$few n^0/s: the source's activity has not been entirely characterized as of this writing, but estimated activity lies around 2 n^0/s[170].

The advantage in this design is that the ^{13}C(α,n)^{16}O reaction (Q=2.2 MeV) provides a large energetic gap to the first ^{16}O excited state at 6.05 MeV: in particular, 5.05 MeV (due to the center-of-mass energy). Therefore, if the α spectrum from ^{241}Am can be attenuated to below 5.05 MeV, this ^{16}O* state will never be populated, and there will not be correlated γs emitted during neutron production –instead, just ground-state ^{16}O will be produced. The Au serves as attenuator for ^{241}Am's α spectrum, which otherwise would initially be over the aforementioned 5.05 MeV threshold. This yields a very low-background neutron source, which could be used in the new holder with or without the nickel foils, with minimal modifications from the AmBe.

It should also be noted that the source design introduces a zenith-angle correlation with the emitted neutrons' kinetic energy (see Figure 5.34).

5.3.4 Elbow-implanted ^{51}Cr secondary γ source

A check of the lengthscale reconstruction in Borexino has never been performed, since calibrations have always consisted of a single inserted source, and its position was determined using intrinsic means such as the CCD camera system and the PMT data acquisition. Although its

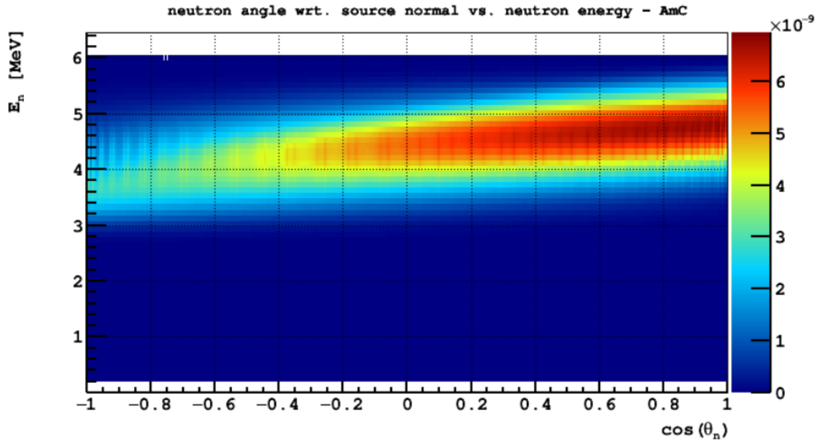

FIGURE 5.34: MonteCarlo simulation of the source geometry-induced zenith dependence of the neutron energy spectrum for the AmC source, from [170]

absolute position could be determined mechanically by the length of the inserted tether and the number and position of the arm's rods, this method carries a considerable uncertainty because of flexing and stretching effects and is not considered accurate enough to test lengthscale effects. Even though there is no reason to believe such effects may exist, or at least impact the current analyses techniques, the as-of-yet unexplained existence of the *Z effect* makes it more desirable to conduct such a check.

For a lengthscale calibration to be feasible, two sources should be inserted *at the same time* while separated by a reasonable distance on the order of a few tens of centimeters, or up to 1-2 meters, without of course saturating the detector's DAq. Moreover, since we want to check how closely the position reconstruction finds the sources and their relative distance, we need to have an extremely well-understood distance between them, one that does not change with relative position in the detector and is rigid with θ angle rotations. Since the source coupler's design does not easily allow to safely insert another source at a large enough distance to the main one, and there is no other attach point along the arm, this objective does not seem achievable without a major redesign of the Source Insertion System.

However, a strategy that employed the structural elements of the arms as sources could fulfill these requirements. In particular, the bolts connecting the rods among themselves offer a particularly appealing possibility: to use them to "implant" a source while retaining their shape and function. Among these, the elbow hinge bolt (see specifications in Table 5.9) is the best candidate, since it is the biggest and offers the most volume for this idea. An illustration can be found in Figure 5.35.

As part of the development of CrSOX (see Chapter 6), the chipped chromium metal that served as the ^{51}Cr source for GALLEX/GNO was procured and taken to LNGS from its storage

Provider and model	McMaster-Carr 94035A308
Shoulder diameter (tolerance) ["]	3/8 ($^{+0.001}_{-0.000}$)
Shoulder length (tolerance) ["]	3/8 ($^{+0.000}_{-0.002}$)
Shoulder fit	Precise
Thread size (type) ["]	1/4 (UNC)
Thread length ["]	7/16
Head length (diameter) ["]	1/2 (7/32)
Material	18-8 Stainless steel
Hardness	Rockwell B55
Tensile strength	70,000 psi
Head type	Socket

TABLE 5.9: Specifications for the 94035A308 elbow hinge bolt.

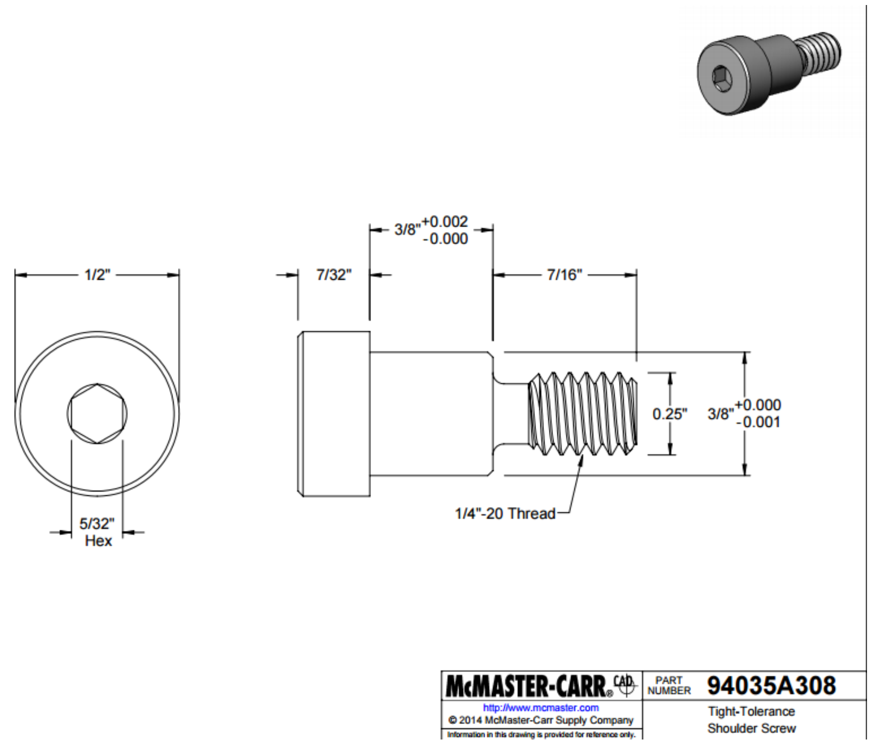

FIGURE 5.35: 94035A308 elbow hinge bolt

facility in France, in 2014. Due to the postponement of this SOX-A campaign owing to the start of CeSOX, the material is available for use, and contains low levels of background radioactivity, most of which have decayed away since its last irradiation in 1995. In particular, the remaining levels of activity are coming from impurities, mainly ^{60}Co and ^{108m}Ag (see Figure 5.36) at $\sim$40 Bq/g and $\sim$190 Bq/g, respectively. Considering a steel density of 7.8 g/cm^3 and the γ lines mainly emitted by these isotopes, we can calculate the positions in the bolt where the screening would be less strong and would allow for their transmission into the scintillator. At the same time, the position to implant the source in the bolt should be strong enough to withstand the carving out of the receptacle and its sealing by welding. Estimates of the expected rates can be found in Table 5.10.

N	Campione	Peso [g]	Rivelatore	Radionuclidi		Concentrazione di attività [Bq/g]	Incertezza [Bq/g]	MDA [Bq/g]
1	Cromo in scaglie	1,32	4	^{60}Co		1.89E+02	1.15E+01	1.96E-01
				^{94}Nb	<	MDA		2.38E-01
				^{108m}Ag		4.16E+01	2.63E+00	3.48E-01
				^{137}Cs	<	MDA		2.39E-01

FIGURE 5.36: Remaining background from radioisotopes in the chromium chips irradiated for GALLEX's ^{51}Cr campaigns in 1995.

Isotope	E_γ **[keV]**	**Most exposed (∼0.2 cm) rate (%)**	**Least exposed (∼1 cm) rate (%)**
^{108m}Ag	433	86.4	48
	614	88.7	55
	711	89.5	57
^{60}Co	1200	93	65
	1300	92	67

TABLE 5.10: Rate percentage (100%=unshielded) coming from the chromium chips according to γ line, isotope, and bolt thickness shielding it from the environment.

Because of handling safety rules, the chromium chip cannot be inserted as-is in the bolt and welded shut. It should be inserted in a double container, consisting notionally of a cylindrical can, electron-beam-welded (EBW'd) on its top side once the chip is in place, turned upside-down and inserted in a slightly bigger cylindrical container, to be EBW'd again on its top side. This cylindrical ensemble could then be inserted in the bolt and arc-welded in position, to be used as the regular hinge bolt. The whole process is conceptually depicted in Figure 5.38.

Chips were estimated to consist, for modeling purposes, of three populations with an average weight: large (0.4494 g), middle-sized (∼1/2 the large ones, 0.2247 g) and small (∼1/4 the large ones, 1/2 the middle-sized ones, 0.1123 g). From this, and considering a ∼50 Bq γ activity, we can convolute the attenuation factors in Table 5.10 with the required weight, to understand how much material we should select, and the volume limitations it would impose: ∼0.25-0.5 g, depending on where exactly on the bolt it would be located (and therefore shielded). Combinations of chip sizes could be arranged depending on the actual final design of the container, which would be driven by the portion of the bolt that can be drilled safely without compromising its strength characteristics: a middle-sized and a small chip could be joined to better profit the space in the inner container, or a suitably-sized large chip could suffice. Of course, detailed measurements of the actual candidate individual chips still need to be performed to account for chip-to-chip impurity content variability, as well as a final technical approval from the EBW companies contacted to ensure the encapsulation process is feasible and safe along all of its steps.

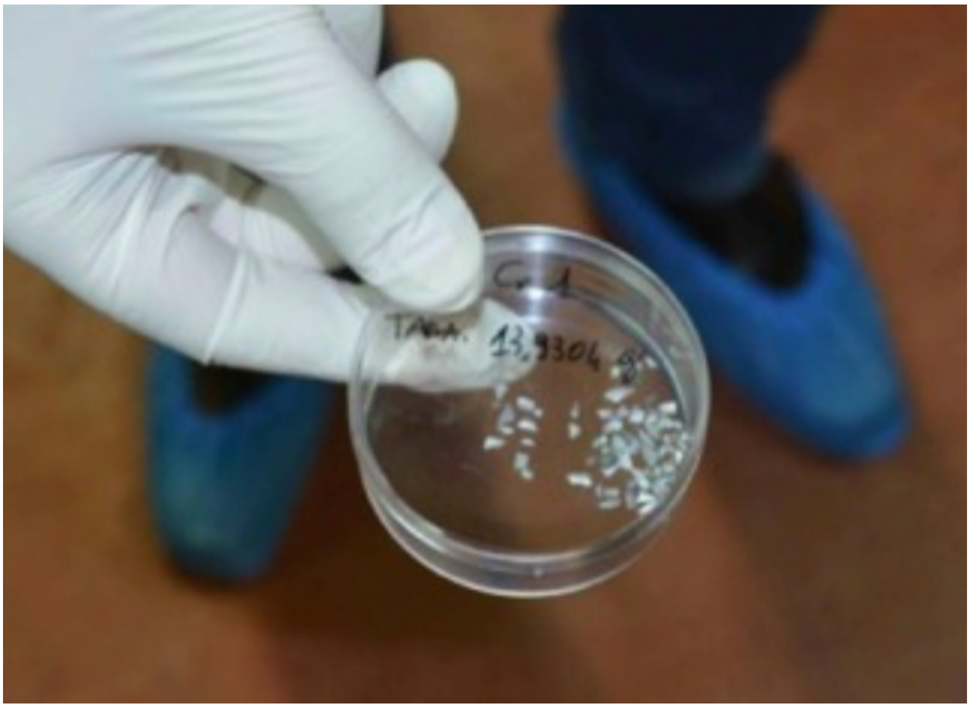

FIGURE 5.37: Depiction of chips samples taken in 2014.

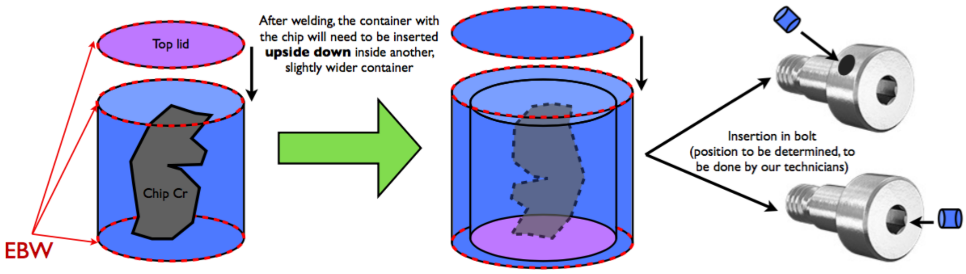

FIGURE 5.38: EBW and source implantation in hinge bolt concept.

5.4 Foreseen outline for the calibrations

Final choreography definition for the new calibration campaign is still ongoing as of this writing, and no precise schedules have been redacted yet. However, the wealth of calibration sources to be deployed and the new objectives the aging of the detector and its new applications require, showcase several constraints that can already be assumed as necessary.

In particular, it is expected the internal calibration campaign should take no more than 3 months, although that schedule was driven by programmatic needs from SOX that have since been somewhat relaxed. However, any internal calibration is both invasive (therefore holding the potential of long-lifetime radiobackground release in the scintillator, especially with the newly attained ultra-low levels after purifications and the effort toward fluid stability through thermal control) and incompatible with regular data-taking, shortening the time available to gather good quality statistics for solar analyses.

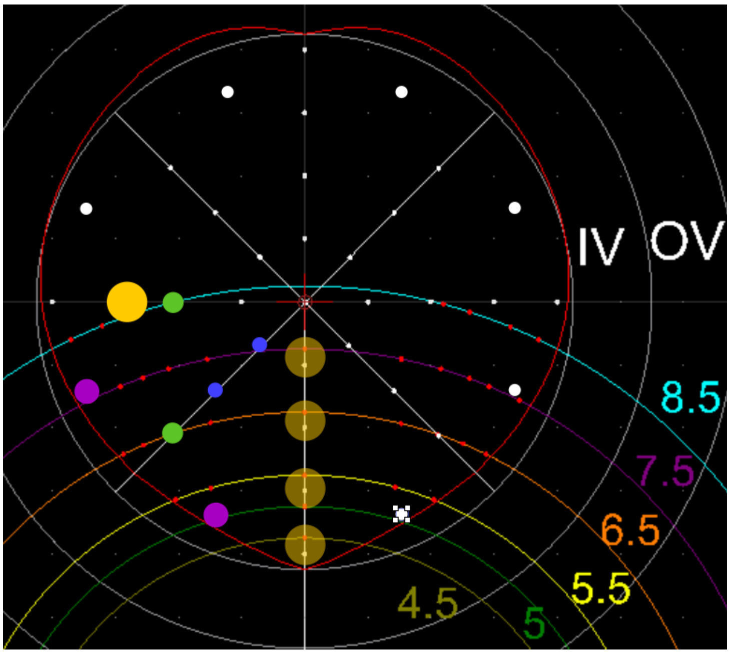

Figure 5.39: Preliminary positions studied for the neutron source calibration campaign. Actual Inner Vessel shape is shown in red, with nominal IV/OV/SSS positions in white lines. The circumference sections labeled with numbers show the areas of the detector at the same labeled distance from the CeSOX source, weighted to be more dense toward the exterior of the IV. Red points show proposed source deployment positions in these areas (which would be repeated in every octant in ϕ). White points show "orthogonal" points intended to provide a uniform mapping of the detector, focusing on the FV. Larger white points are proposed orthogonal peripheric positions to complement poorer mapping on the external reaches of the IV. The green dots indicate points from the orthogonal/SOX requirements that almost (<3 cm) overlap, highlighting the possibility to combine both into one. The violet dots highlight the same possibility, but combining with the large white points. Yellow circles indicate less tight overlap (25-40 cm), making them less interesting candidates for combining. In blue, points from the orthogonal scheme which are trivially accessible following SOX's arm movement routine. ^{222}Rn and γ/β^+ sources are expected to follow just the orthogonal scheme, with perhaps a few extra positions added.

The neutron calibration section is the best-defined, since CeSOX requirements for a thorough understanding of the IV's bottom region, as close as possible to the vessel and therefore to the highest source-induced event region, are well-described. The need for volume-scaled tight mapping of this volume to optimize future physics results should be married with the technical constraints of the Source Insertion System to ensure the best utilization of time and manpower possible. In this sense, refinement is ongoing for the proposed deployment positions (see Figure 5.39), while an assessment of the positioning uncertainty is paramount in this new phase of the calibrations: whereas in the first campaign it was not necessary to approach the source as much as possible to the periphery of the IV, since the main objective was to characterize the nominal FV, this is no longer the case for the neutron sources.

Vessel reconstruction is accomplished with a custom code contained in the CCD camera system control software[161]. This technique employs a manual selection to fit the vessel shape and,

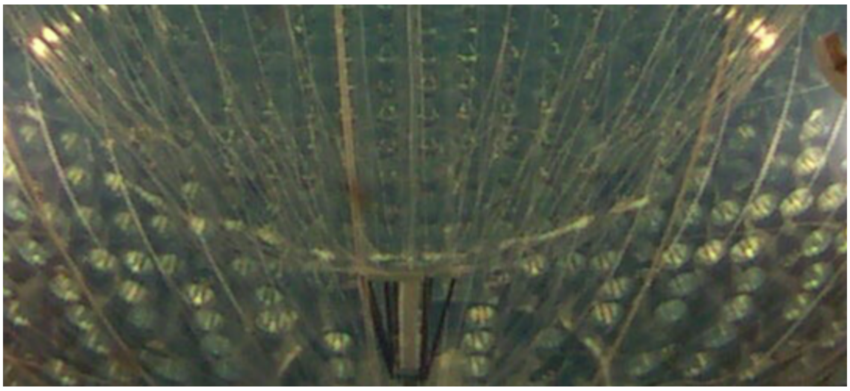

FIGURE 5.40: Crop from a 2008 picture showing the under-inflation of the bottom hemisphere after the IV leak developed, and the difficulty in following the vessel shape in that area due to resolution, structure obstructions and lightning conditions.

even though subjective effects due to the individual operator's choice of points were deemed to be negligible for an overall vessel reconstruction, poorly-defined sections of the image can signify large errors in some vessel areas, unfortunately in particular around the lower endcap. This is due to both image interference from surrounding structures such as the tensioning ropes, under-inflation of the vessel in that area, and only having two perspectives available since the failure of camera 5 (see example picture in Figure 5.40 and a screenshot of the reconstruction software highlighting the lack of points for interpolation in the bottom half of the vessel in Figure 5.41). At best, vessel position can be determined to $\sim \pm 1$ cm, but re-analysis of the camera pictures during a renewed effort to improve the "tomography" technique for vessel shape reconstruction[38] showed the aforementioned difficulties can bring the uncertainty up to $\sim$7 cm. These studies are ongoing and are expected to reduce the uncertainty somewhat more if new pictures of the fully-lit detector can be taken before the next calibrations, providing new images to work with (the last ones were taken on May 27th, 2010).

The arm mechanical position accuracy is estimated at ± 2 cm, and the possible extent of the ϕ asymmetry of the vessel shape (not considered in current vessel reconstruction analysis, either optical or from PMT data) is estimated to reach an upper limit of ± 3 cm. Therefore, typical vessel-to-source uncertainty can be estimated at $\sim$4.5 cm, and can reach a maximum of $\sim$9 cm in particular areas which are more deformed and/or have worse fit, especially around $\theta \sim$140-170°.

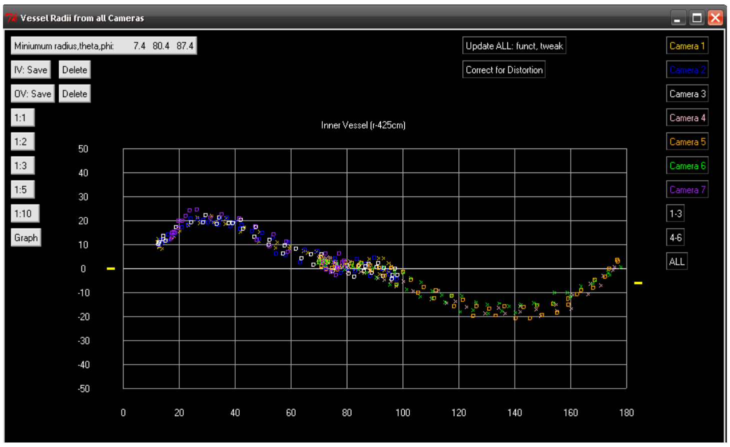

FIGURE 5.41: Screenshot of the reconstruction software after vessel shape manual selection in pictures. Considering azimuthal symmetry, the points selected with the different camera views are projected in a $\Delta r - \theta$ plot showcasing the deviation from a perfectly spherical shape. These points are then interpolated as explained in [161]. It is clear the bottom hemisphere has a chronic lack of points that make the interpolation less reliable –but their relative "quality" should also be taken to be lower because of the impediments illustrated in Figure 5.40. The region between 140-170° is especially troublesome.

Part III

Anomalous neutrino oscillations and sterile neutrinos in Borexino: Short-distance Oscillations with Borexino (SOX) program

Chapter 6

SOX program and SOX-A(Cr) simulations

Man-made artificial neutrino sources (also known with its euphemistic form, neutrino generators, NG) have been a technical option entertained for Borexino's physics program since its inception, as the existence of the ICARUS/SOX pit can testify (see Section 2.2.6). The main scientific objectives of Borexino did not urgently call for such a device though, all of them dealing with naturally-occurring (anti)neutrino sources (the Sun, supernovas, Earth's radioactive elements...) or from large artificial facilities located at long baselines (reactors, accelerators), except when considering a non-LMA solution to the matter effect[171].

Nevertheless, several experimental anomalies (see Section 1.4), some of them arguably more precise than its preceding estimates, showed controversial tensions in data which are theoretically reconcilable, however barely, with sterile neutrino scenarios or other, more exotic models involving "anomalous" (more precisely, BSM) oscillations. Despite an ever-shrinking allowed phase space for most of these models, as of this writing, the motivation for a strong experimental dataset that conclusively disproves (or confirms) the main anomalies is sound. Furthermore, many of the proposed experimental tests, utilizing unique equipment and facilities, have in common that they would provide equally unique insight into many other (B)SM phenomena.

In particular, Borexino proposed its ***S**hort-distance **O**scillations with Bore**X**ino* program[172] in 2013, roughly coinciding with the publication of the White Paper[80] detailing the worldwide initiatives toward resolving the issue of these neutrino anomalies. In essence, the detector is well-suited to short-baseline (low L/E) oscillation studies facilitated by high-intensity (anti)neutrino sources, being able to observe directly (through rate and oscillometry) the "ripples" in the source-induced neutrino signal provided they lie between the detector's size ($\sim$ meters) and the detector resolution (~10 cm) –which is expectable if the most favored models that explain the anomalies are correct.

SOX would be conceptually divided in three distinct phases:

SOX-A Also known as SOX-pit, it would utilize the existing external facilities without important modifications (CRs, pit) and leave the detector untouched, deploying the source on its exterior –namely, at the pit under it, at ~8.25 m from the detector center. For this reason, at a constant source activity, this phase would be in principle the least sensitive to possible signals just from the geometrical acceptance factor, although source-induced backgrounds and the actual technical implementation (source activity measurement, heat output...) may lessen this disadvantage.

SOX-B Also known as SOX-WT, would be an intermediate step in detector invasivity. The source would be deployed without, in principle, interfering with the Inner Detector (thereby maintaining its intrinsic radiopurity levels, although a possible filling of the IB with scintillator would be performed), despite probable major OD interventions being needed. The source would be located inside the WT, at ~7.15 m, which would reduce the distance to the center, while keeping source-induced backgrounds low and lessening volumetric constraints. On the other hand, the source would be inaccessible once the detector returned to operations.

SOX-C Also known as SOX-internal, would be the most sensitive, and most invasive, phase in the search for anomalous oscillations. It would involve a detector-wide update, and the loss of the current radiopurity level owing to the need for fluid withdrawal and structural operations inside the ID. On the other hand, it would cover at least the whole allowed phase space for the 3+1 sterile neutrino models.

SOX-A could utilize both ^{51}Cr and ^{144}Ce-^{144}Pr sources, while both SOX-B and SOX-C would utilize just the latter. Preliminary sensitivities for the three phases and sources are shown in Figure 6.1. Other isotopes, such as ^{37}Ar, ^{90}Sr, ^{75}Se or ^{152}Eu, were considered[173][174][175] given prior experience in their use in other experiments and similarly adequate spectra, but were downselected because of their inferior overall characteristics for the program.

As hinted at the beginning of the section, SOX is expected to yield additional SM physics[172]. The electroweak Weinberg angle θ_W can be directly measured at the ~MeV scale from the $\nu_e - e^-$ cross section with an expected precision of 2.6%: this value is better that any other obtained at this energy scale. Furthermore, SOX-A will provide significant information about the neutrino magnetic moment μ_ν and improve the current best limits on it. Additionally, the combination of electron-neutrino to electron scattering data from the ^{51}Cr source with the $\overline{\nu}_e$-to-proton data

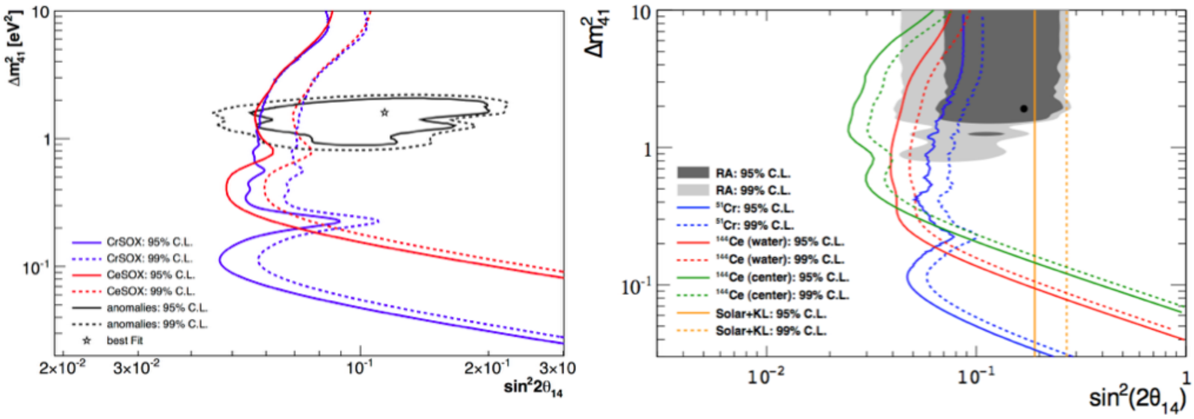

FIGURE 6.1: Illustrative preliminary sensitivities for the three SOX phases. The source utilized for these results is a ~100 kCi ^{144}Ce^{144}Pr source, considering a 1% uncertainty in FV determination, 1% SOX-A uncertainty in source activity determination, and 2% bin-to-bin uncorrelated systematic uncertainty, combined with 1.5% source activity determination uncertainty, for SOX-B and -C. On the right plot, the estimate for SOX-A (10 MCi ^{51}Cr) is also shown. Detailed modeling of backgrounds and minor intrinsic detector uncertainties is not included.

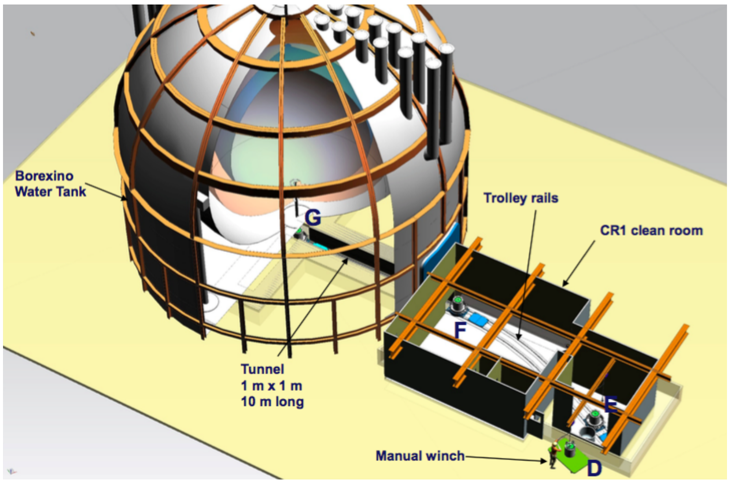

FIGURE 6.2: Schematic cutaway view of the foreseen source deployment facilities for SOX-A in the ICARUS/SOX pit, as well as the rails and deployable calorimeter assembly in CR1.

from the ^{144}Ce-Pr source will give information about the g_A and g_V axial and vector current coefficients of the low-energy Fermi CC interaction. Apart from improving their precision level within the SM, they can be checked for BSM effects: the best measurement at low energies (relatively, 10 GeV) is held by CHARM II[176] –and its sensitivity is matchable by SOX, but using a much lower energy range of ~MeV, where BSM non-standard interactions (NSI) effects are more easily probed, since the Fermi cross-section grows with energy and the SM interaction in Borexino will be ~10^{-3} times smaller.

This Section will be mostly dedicated to the SOX-A phase of the program, reason why the -*A* designator will be dropped henceforth. An detailed illustration of its foreseen deployment facilities can be found in Figure 6.2.

It should be noted due to a combination of managerial, political and, to some extent, financial reasons meant that, even though the SOX program was due to start in earnest with the chromium source in ∼2015-16, this plan was indefinitely delayed due to the apparent faster availability of the CeSOX source with a higher-than-expected activity level (150 kCi), making it preferable to start with this source instead. As will be explained in Section 6.4, problems with the procurement of the active $^{144}CeO_2$ material caused renewed delays to the overall SOX schedule to be inevitable anyway.

6.1 CrSOX: a high-activity chromium source for Borexino

6.1.1 Source characteristics

One of the isotopes with the cleanest neutrino spectral signature, while offering a reasonable raw material extraction and irradiation cost and half-life, as well as low correlated radiation, is ^{51}Cr. It is obtained through ^{50}Cr neutron bombardment, with a cross-section of 15.9 and 7.8 b for thermal and epithermal neutrons, respectively. Since the natural occurrence of ^{50}Cr is quite low (^{nat}Cr = 0.838 ^{52}Cr + 0.095 ^{53}Cr + 0.024 ^{54}Cr + 0.043 ^{50}Cr), and furthermore ^{53}Cr would be a competitor with its large ∼18 b thermal neutron capture cross-section (see Figure 6.3) and its larger concentration of ∼10%, enrichment of the selected chromium material in ^{50}Cr is desirable.

^{50}Cr itself is a quasistable $\beta(+/-)$-decayer with a half-life of >∼$1.3{\cdot}10^{18}$ years (to ^{50}Ti). The synthetic ^{51}Cr electron-capture-decays according to Equations 6.1 and 6.2:

$$^{51}Cr \rightarrow ^{51}V + \nu_e \text{ (E}_\nu\text{=751(9\%) and 746 (81\%) keV; b.r.}\sim\text{90.08\%)} \tag{6.1}$$

$$^{51}Cr \rightarrow ^{51}V + \nu_e + \gamma \text{ (E}_\gamma\text{=320 keV, E}_\nu\text{=426 (9\%) and 431 (1\%) keV; b.r.}\sim\text{9.92\%)} \tag{6.2}$$

The two different neutrino energies E_ν per branching ratio shown above are due to internal rearrangement processes after the electron capture from the nucleus, either by electronic shell re-arrangement with X-ray emission or by Auger emission (5 keV for K capture and negligible for L capture, with L/K=0.1)[178]. The emitted γ in the ∼10% branching ratio reaction is both easy to shield with a few centimeters of a high-Z material (i.e. Pb, W...) and useful to determine the source material's activity through γ assay.

As extensively reported in literature, the highest-activity ^{51}Cr sources were employed in the GALLEX[178][174][179] and SAGE[68] detectors in the 90s. Abundant information about their techniques and results can be found in their references, but the GALLEX 35-kg source material (see Figures 6.4 and 6.5 for recent pictures) is especially interesting for the case of CrSOX,

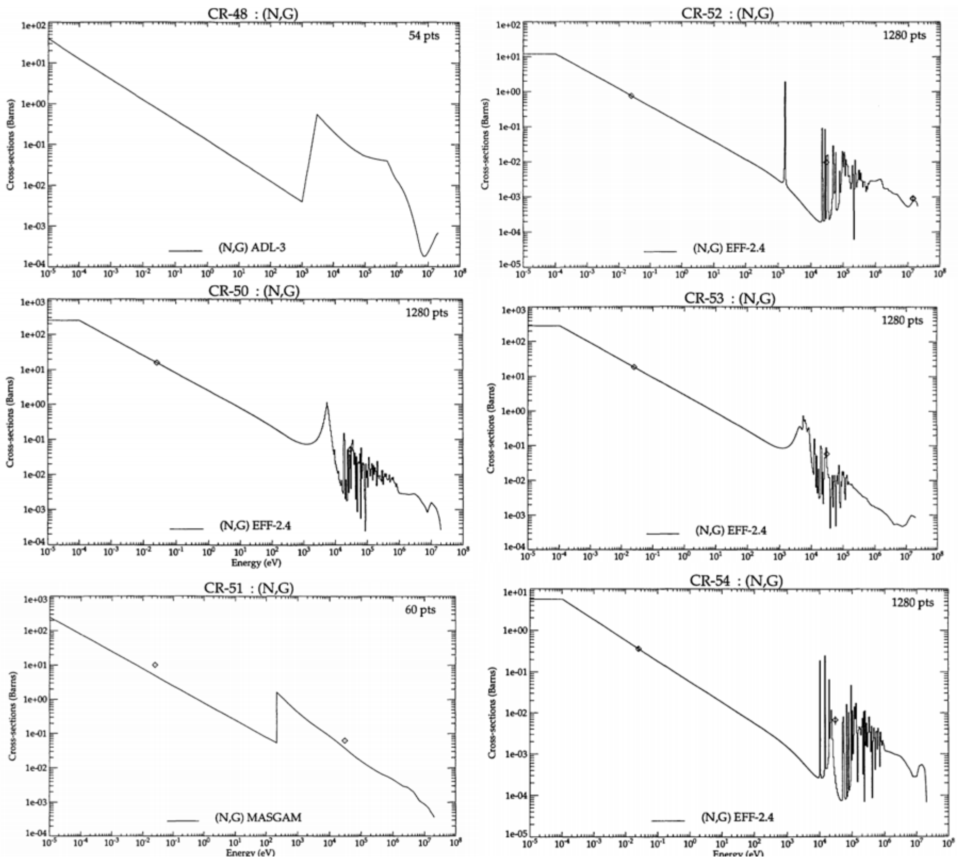

FIGURE 6.3: Neutron capture cross sections for chromium isotopes with ∼>1 day half-lives, from [177].

since the same 38.6%-51Cr enriched (^{SOX}Cr $= 0.378^{50}$Cr $+ 0.615^{52}$Cr $+ 0.71^{53}$Cr $+ 0.02^{54}$Cr), chipped chromium material was baselined to be re-used for this project, given the inadequacy of natural chromium to achieve the required levels of activity in any current irradiation facility, and the technical, environmental and financial complications[180] associated with newly-enriched chromium (up to ∼100% ^{51}Cr) –although this option was kept in case technical complications with the irradiation facility were greatly alleviated when using it. Also, a smaller physical source size will reduce smearing of the possible signal modulation to the lower bounds of detector resolution (and increase it to ∼twice as much in the case of keeping the baseline 38% enrichment), which would slightly increase the experiment's sensitivity.

Owing to ^{51}Cr's short lifetime, the baseline for CrSOX was ∼100 days of data-taking, or about 4 half-lives, for an event sample size of ∼10^3. Using this information, the needed activity for a good coverage of the $\Delta m^2/\theta_{14}$ phase space was determined to be **5-10 MCi** (185-370 PBq), or two separate campaigns of 5-6 MCi (∼200-250 PBq), considering post-purification backgrounds and ∼10 cpd/100tonnes of remaining ^{210}Po in the energy window of interest [0.25-0.7] MeV[172]. An illustration of the source's signal over the combined intrinsic Borexino background plus solar neutrinos is shown in Figure 6.6, the spatial distribution on the IV in Figure 6.7, and a simulated positive sterile neutrino-induced oscillation signal in Figure 6.8. Of course, the number

FIGURE 6.4: GALLEX source in stainless steel container, photographed on the occasion of its acquisition and transport from France to Italy in 2014. Right-hand side picture shows a few illuminated chips through the open container's top port, before sampling.

of collected events at each point in the detector, illustrated by the last figure, will be dictated not just by the source activity, but also by a geometric and spatiotemporal variation factors:

$$N_0(L,E,T_1,T_2) = n_e \frac{I_0}{4\pi L^2} \tau e^{-\frac{\Delta t}{\tau}} \left(1 - e^{-\frac{\Delta t}{\tau}}\right)$$
$$2\pi L^2 \Big(1 - \frac{d^2 - R^2 + L^2}{2dL}\Big) P_{ee}(L,E) \int_{T_1}^{T_2} \frac{d\sigma_e(E,T)}{dT} dT \tag{6.3}$$

In other words, for the k^{th} L/E bin, the number of events would be given, in general, by:

$$N^k = N_{decays}(T) \cdot \rho_d \cdot \int_{(L/E)_k}^{(L/E)_{k+1}} d(L/E) \cdot \int_0^{\inf} dEES_{\overline{\nu}}(E) \cdot \mathcal{H}^{ext}(L,d,R_d,\theta,\Delta m^2, L/E) \tag{6.4}$$

where $S_{\overline{\nu}}$ encompasses the ^{144}Pr spectrum and uncertainties, R_d is the active volume's radius, d is the distance to the source and θ and l are the angle and distance to a given detector point, respectively, considering the source to be at the coordinates' origin. The $\mathcal{H}^{ext}$ factor is the *Antineutrino Path Length Distribution*, which acquires an analytical form for a point-like source, as in Equation6.3, or can be modeled through MonteCarlo in the case of a realistic, extended-size source[181].

6.1.2 Source-related backgrounds

On the other hand, a very important issue to address would be the source-induced backgrounds. If the material was pure chromium, the 320-keV γs would not constitute a problem, as explained

FIGURE 6.5: Chromium material samples retrieved from the stainless steel container in Figure 6.4.

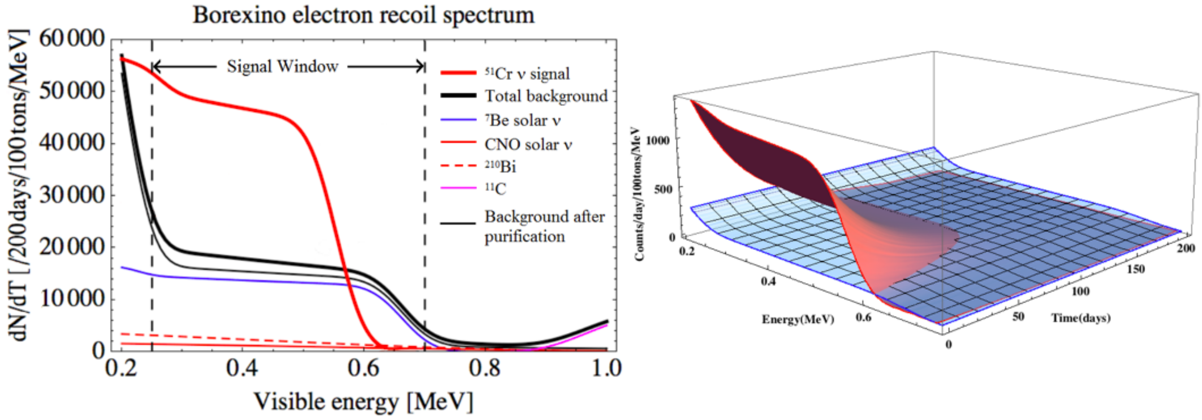

FIGURE 6.6: Simulation scenario for the CrSOX signal with a possible sterile neutrino positive result ($\Delta m^2_{14} = 2eV^2$ and $sin^2(2\theta_{14})$=0.3).

above, and could easily be shielded against. However, even high-purity metals contain impurities, and the enriched chromium used in GALLEX has been precisely sampled and γ-assayed to determine its impurity contents (see Tables 6.1 and 6.2). The activity from these impurities is much more important than anything coming from the chromium itself, and need to be carefully accounted for, both for biological protection and signal analysis reasons. Additionally, as shown in Section 5.3.4's Figure 5.36, recent assays have shown the remaining levels of radioactivity, mostly coming from ^{60}Co and ^{108m}Ag, to be consistent with the above.

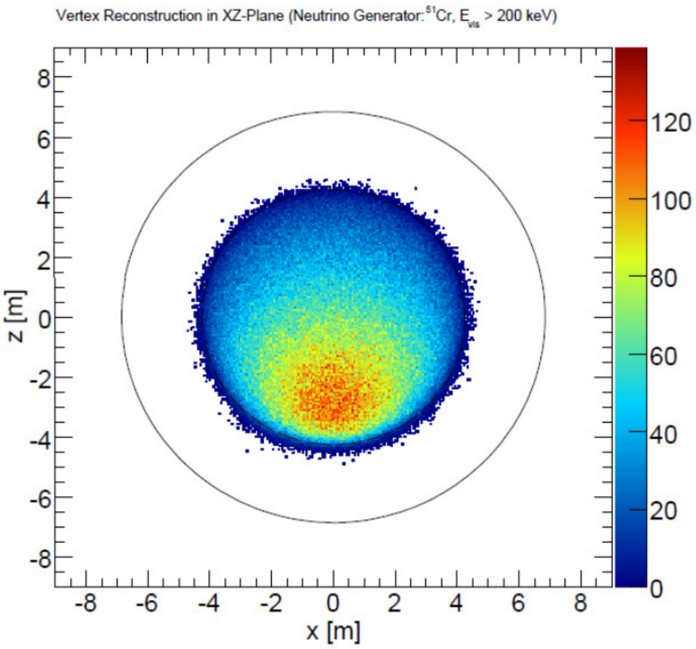

FIGURE 6.7: Simulation scenario for the CrSOX signal within Borexino's IV, from [182].

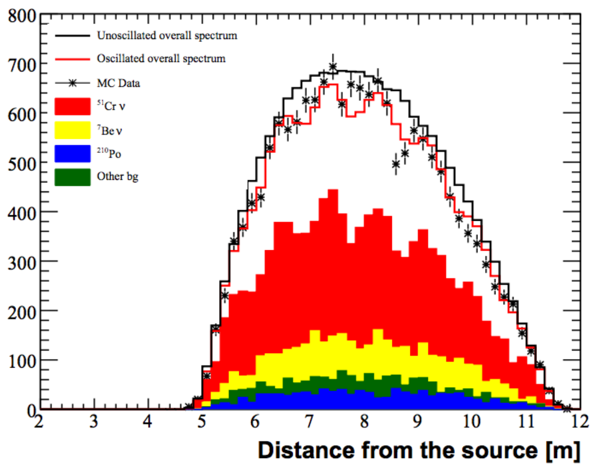

FIGURE 6.8: Integrated and instantaneous spectra for a 10 MCi CrSOX source. On the right-hand side plot, the blue component is the constant solar neutrino signal, and backgrounds are not shown for clarity.

Atom	**Contamination** (ppb)			
	Meas (HiRes,'14)	Meas (MedRes,'14)	Meas. ('95)	Allowed
Na	6000	9000	38±5	600
Sc	<80	-	6±1	1000
Fe	-	<500	<2000	5000000
Co	<8	-	16±1	8000
Cu	1500	-	70000±10%	-
Zn	<80	-	<500	1000000
Ge	<80	-	110000±40000	-
Ga	-	-	<3	100000
As	-	-	93±7	10000
Se	-	-	< 4000	-
Br	<20000	-	<500000	2000000
Rb	<700	-	<8000	-
Zr	<50	-	200000±70000	-
Mo	-	-	<20000	-
Ru	-	-	<20000	-
Pd	<80	<60	<2000000	-
Ag	400	-	6100±400	600000
Cd	-	-	<10000	-
In	<1.6	-	<400000	-
Sn	<400	<300	<800	-
Sb	<16	<20	120±12	-
Te	<800	<1600	<200000	4000000
La	<50	-	<50	500
Ce	<200	-	< 10	-
Pr	-	-	<5	-
Nd	<30	-	<80	-
Sm	<30	-	<1000000	-
Eu	<2	<160	<5	-
Tb	-	-	<1	8000
Ho	<100	-	<7	-
Gd	<16	-	-	-
Lu	<0.2	-	-	-
Er	-	-	<5000	-
Ta	-	-	<5	-
W	<200	-	<500	-
Re	<3	<2	<70	-
Os	1.6	-	<800000	-
Ir	<0.3	-	<600	-
Au	-	-	<100	-
Pt	240	-	-	-
Pb	3	-	-	-
Th	<500	<0.2	-	-
U	<5	<0.2	-	-

TABLE 6.1: Elemental impurities in the GALLEX enriched chromium material, as measured in 1995 in [179] and in 2014 in [183]. All values are 95% c.l., and the "allowed" values are GALLEX's, so SOX's should be taken to be slightly lower due to the ~3-6x higher activation levels required. In **boldface** are the elements with surprisingly low concentrations in the new, 2014 measurements –which were performed dissolving a 0.1238 g sample in ultrapure HCl, and diluting it to ~600 ppb of Cr. However, sodium showed increased levels, which are suspect to be caused by sea salt contamination. More information about the sodium problem and relative thermal neutron capture cross-sections in [180].

Isotope	**Meanlife**	Energy (keV)	Activity (GBq)	
			After extraction	After removal
^{24}Na	14.8h	1368.5	0.10±0.02	-
		2753.9	0.07±0.01	-
^{46}Sc	83.9d	1121	0.13±0.02	0.025±0.003
^{48}Sc	43.7h	983.5	0.05±0.03	-
		1037.5	0.07±0.03	-
		1312.1	0.10±0.01	-
		1332.5	0.04±0.01	0.04±0.005
^{60}Co	2770d	1173.2	0.02±0.01	0.028±0.003
^{64}Cu	12.7h	1345.8	210±20	-
^{77}Ge	11.3h	2342.3	0.5±0.2	-
^{76}As	43.7h	1212.7	6±3	-
		1216.0	3±1	-
		2096.3	1.5±0.2	-
^{97}Zr	17.0h	1749.9	0.40±0.15	-
^{110m}Ag	249.8d	657.7	4±2	-
		763.9	10±3	4.0±1
		818	-	2.7±0.5
		884.7	4.3±0.5	4.2±0.4
		937.5	4.2±0.5	4.2±0.5
		1384.3	5.0±0.5	4.5±0.4
		1475.7	5.1±0.5	4.0±0.4
		1505.0	4.3±0.5	4.2±0.4
		1562.3	4.0±0.5	2.9±0.5
^{124}Sn	60.2d	1368	-	0.18±0.06
		1437	0.4±0.15	0.21±0.06
		1691	0.36±0.05	0.12±0.02
		1919	-	0.09±0.03
		2039.6	0.4±0.03	0.10±0.03
		2091	0.51±0.08	0.12±0.01
		2185	-	0.07±0.03
		2294	-	0.09±0.03

TABLE 6.2: Isotopic impurity activity levels in the GALLEX enriched chromium material.

6.1.3 Sensitivity estimates

SOX will sieve through the source neutrino events through a two-fold strategy: a rate analysis, aiming to observe any deviation from the expected neutrino interaction rate derived from the independently-determined source activity; and a combined analysis using rate and oscillometry techniques (*rate+shape*). The oscillometry study intends to detect the short-baseline (low L/E) geometric deviations from the nominal scheme (SM, only 3 active neutrinos with no additional components they can oscillate into), therefore providing data into both Δm^2 and θ_{14}. The rate analysis, being a counting strategy, is much more sensitive to the mixing angle than to the mass square difference, since it provides no spatial information. Clearly, both studies rely critically on the achievable precision in determining the number of neutrinos emitted by the source, and therefore the expectable number of events in the active volume. The use of several independent techniques for this determination was baselined, including:

- High-precision, continuous calorimetry of the full source before, during and after the Cr-SOX DAq period (see Section 6.1.5).
- Detaled sampling of source material to look for the elemental composition through ionization chamber and High-Purity Germanium (HPGe) counters.
- Gamma sampling of selected source material to look for the 320-keV de-excitation γ from $^{50}V^{*}$.
- Vanadium content assay, since pre-irradiation content is very precisely determined at the ppb level, and the only element decaying into V isotopes is ^{51}Cr.
- Neutronics studies based on the neutron flux in the different sections of the irradiation reactor and the irradiation geometry, employing analytical and MonteCarlo (MCNP, Scale, TRIFON...) techniques.

Sampling strategies, while being very precise, have the obvious problem of strong dependence on the representability of the selected samples: local differences in irradiation due to geometry and neutron shadowing may create large differences between the activity levels. Good characterization of the sample provenance and interplay with the "global" techniques is crucial. The last strategy (neutronics) would be employed with actual data after the irradiation, but constituted the main handle on source creation feasibility and optimization studies before that. Upcoming Section 6.3 will detail the VT-led effort dedicated to such objectives. More information about this and the other techniques as characterization tools for the GALLEX sources (62.5±0.4 and $69.1^{+3.3}_{-2.1}$ PBq) can be found in [180], [184] and [179], and a feasibility study using the Lyudmila-2 (L-2) reactor in Mayak's (Russia) heavy-water high-flux reactor in [185].

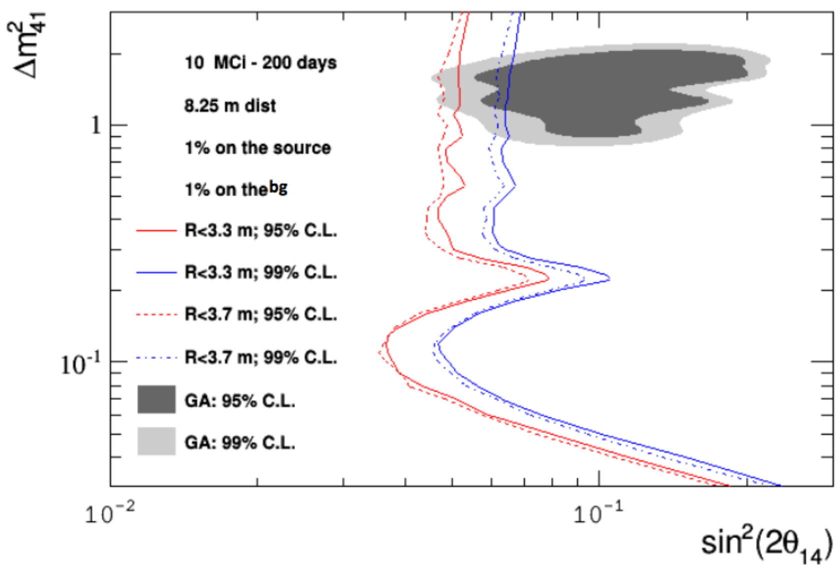

FIGURE 6.9: Latest sensitivity study for CrSOX at 10 MCi and 1% FV, activity and background levels determination, with a 3.3 and 3.7-meter FV, from [186].

The function measuring the likelihood of entries per bin is the Poisson probability of observing N_{exp} counts compared to the prediction of N_ν of signal and N_{bkg} background events, and takes the form:

$$\begin{aligned} P(\theta, \Delta m^2, f_\nu, f_{bkg}) = P(N_{exp}, N_\nu(\theta, \Delta m^2, f_\nu) + N_{bkg}(f_{bkg}))+ \\ +P(f_\nu - 1, \sigma_\nu) + P(f_{bkg} - 1, \sigma_{bkg}) \end{aligned} \tag{6.5}$$

where there are two *pull terms*; one for neutrino normalization (f_ν): $\sigma_\nu^2 = (1\%)^2_{FV} + (1\%)^2_{act}$ (uncertainties for FV and source activity); and another one for background normalization, taken to be 1% based on pre-source statistics. The sensitivity analysis is then performed on a profile of log(likelihood) minimization with the aforementioned nuisance parameters f_ν and f_{bkg}.

Then, the sensitivity in Figure 6.9 is calculated as:

$$\Delta\chi^2 = -2 \cdot log(P(0,0)) + 2 \cdot log\big(P(\theta_{true}, \Delta m^2_{true})\big) \tag{6.6}$$

where $P(0,0)$ is the no-(sterile)-oscillation scenario.

More advanced techniques taking into account a wide array of detector (and source) subtleties, such as near-vessel sensitivity and reconstruction accuracy, vessel shape uncertainty, calorimetry uncertainty... are available for CeSOX, but these were not applied on CrSOX sensitivity analyses from mid-2014 due to the shifting focus of the program.

6.1.4 Shielding and other source auxiliary components

Impurities in the source material, even at the ppm level, sensitive to (n,γ) through cross sections in the barn range, can cause a serious $\sim\geq$1 MeV γ emission issue, as introduced in the previous Section 6.1.2. The optimal compromise material to attenuate the emission coming from the isotopes in Table 6.2 was tungsten/wolfram (W), offering ~65% more stopping power than lead, in order to reduce said backgrounds to a biologically-imposed safety level of 200 μSv/h at contact with the shielding's surface. In particular, it was determined the material would be in an alloy form to simplify metallurgy, with a density of at least 18 g/cm^3 (Densimet 185 alloy).

The chromium material would be inserted in one or several containers, depending on the final form the chromium would be formed into: by the end of the present feasibility studies, the optimum form was still not determined (solid rods, solid material in other shapes, chips, sinterized chips...). The main driver on these considerations was the handling in the irradiation facilities (and the potential for impurity contamination) and, to a lesser extent, the thermal characteristics once sealed in the source assembly. Therefore, the option existed for having **(i)** the chipped material in a few (~5) disk-shaped copper or tungsten containers, sealed in a hot cell just after irradiation; **(ii)** the chipped material in several (~220) small cylindrical containers welded shut in a hot cell just after irradiation; **(iii)** the chipped material pressed and sintered into semi-solid form, with inert gas in the voids, and in a variety of different forms; **(iv)** the material re-formed into solid cylindrical bars, of different possible lengths, either in a single cylindrical assembly or in "wedges" transporting ~1/3 of the rods each (see Figure 6.10); and **(v)** the material re-formed into solid crescent/semi-cylindrical shapes. Technical designs for the most studied of these concepts can be found in Appendix C.

Depending on the chosen material form and geometry, the tungsten shield could exhibit slight variations in dimensions, but the source assembly's diameter always stayed at ~540-580 mm, with ~>120 mm of W thickness in the axial direction. Height would vary between having an approximately square cross section (~560 mm) and somewhat taller designs (up to ~668 mm), depending on the source's core design. Dimensions do not consider auxiliary structures such as the crane pintles or finned heat radiators. Also important for the core design, depending on the shape and form of the material, would be thermal considerations to stay under the 750°C chromium sinterization temperature (in the case of chips).

Copper heat exchangers would envelop the tungsten shield for optimal heat rejection and coupling to the copper/aluminium heat rejection fins added to the source assembly's exterior side perimeter. A lid with radiation-resistant O-rings (possibly copper compression) would be fixed in place with 12 bolts to cover the core assembly, and a spring system (Helicoflex or custom-made) would assure its stability in place.

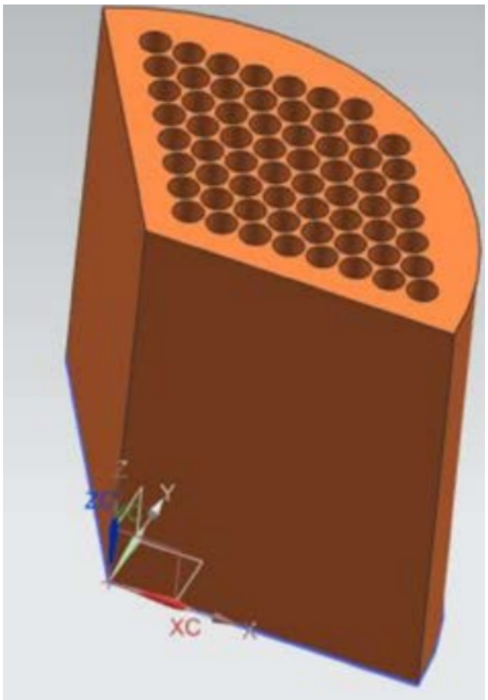

FIGURE 6.10: "Wedge" design of the core source assembly with the chromium material re-formed into rods, containing ∼1/3 of them. The full source core would consist of 3 of these assemblies, plus a possible central high-activity central core.

Finally, a CROFT SK172/SK173 shock-absorbing package would be used for transportation inside a Class B certified transport container, to achieve safe and reliable transfer between the irradiation facilities' hot cells to the NUCLECO/INFN facilities and, ultimately, LNGS. Such container arrangement would also be used for disposal, once the CrSOX campaign was finished but the source still retained a moderate amount of radioactivity.

6.1.5 Thermal issues and calorimetry

^{51}Cr's radioactive decay will produce ∼0.19 kW/MCi. Although this amount of output is not a severe problem, and a purely passive system with just the dissipation fins has been shown to be able to keep external source temperatures within very reasonable limits (<90°C on the exterior of the shielding), such thermal environment might not be desirable for Borexino operations. Furthermore, special attention has to be devoted to the internal temperatures of the chromium. Of course, this condition will be much less severe in case of re-formed solid material (either rods or other geometrical shapes), as long as they are well-coupled to the core holder. In the case of chipped material however, the design has to allow for efficient heat transport to avoid sinterization problems. ANSYS heat transport studies have shown the "five can" design to be able to keep internal temperatures below ∼370°C (see Figure 6.11), while rod-based source cores would keep the maximum temperatures, located on the periphery of the holders, within ∼320°C.

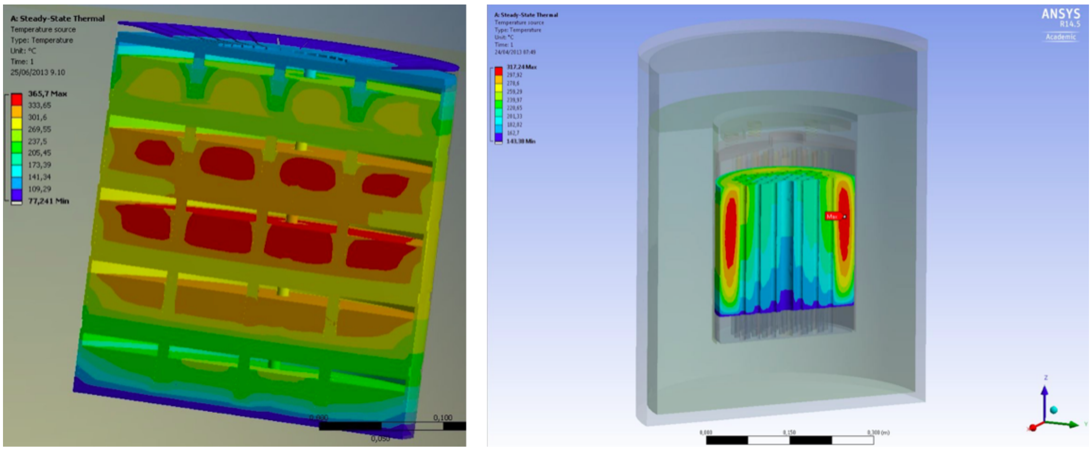

FIGURE 6.11: Thermal profiles of the source's "core" in the 5-can –left– and the 76 rods (single assembly) –right– scenarios.

This energy release can be further controlled while performing the high-precision calorimetry determination of the source activity. Furthermore, it was baselined that, owing to the short half-life of ^{51}Cr and the ∼3 month duration of the CrSOX campaign, it would be advisable to perform a continuous calorimetric measurement of the integrated source heat output, to be able to more accurately fit the heat decay curve. Additionally, this would bring the welcome benefit of controlling the temperature of the assembly in contact with the thermal environment in the pit, reducing or eliminating possible unwanted fluidodynamical effects on Borexino's interior.

This objective meant a very compact calorimeter, capable of holding the entire source inside while deployed at the pit and while keeping it completely thermally decoupled from the exterior, needed to be designed. Moreover, its accuracy for this large heat output had to reach, as estimated previously, $\sim<1\%$.

The chosen calorimeter design, to be completed by the combined efforts of the Genova and TUM teams, would be a closed-loop water calorimeter, consisting of a vacuum vessel jacket containing the source, which would be suspended on a platform inside a load-bearing ring structure, surrounded by super-insulating Mylar material (see Figure 6.13), by thermally insulating Kevlar ropes (which nevertheless showed a slight thermal link behavior that was discovered during characterization runs –but quickly modeled away to maintain accuracy). Strain gauge, pressure and thermal sensors are installed on the platform, suspension pulleys and interior of the vacuum vessel for monitoring, and fed through appropriate ports on the base of the main structure. Nominal operational pressure inside the vacuum vessel is $\sim 10^{-4}$ mbar, sustained by a turbopump attached to the calorimeter vessel. The main water coils are embedded in a copper heat-exchanging structure that would surround the tungsten shield, in parallel or separately from the radiator fins mentioned before. Secondary water coils would surround the jacket structure and are *heated* to minimize the gradient between the equilibrium temperature inside the pressure vessel and that outside, thus minimizing radiation heat losses. A Savitzky-Golay filter is applied

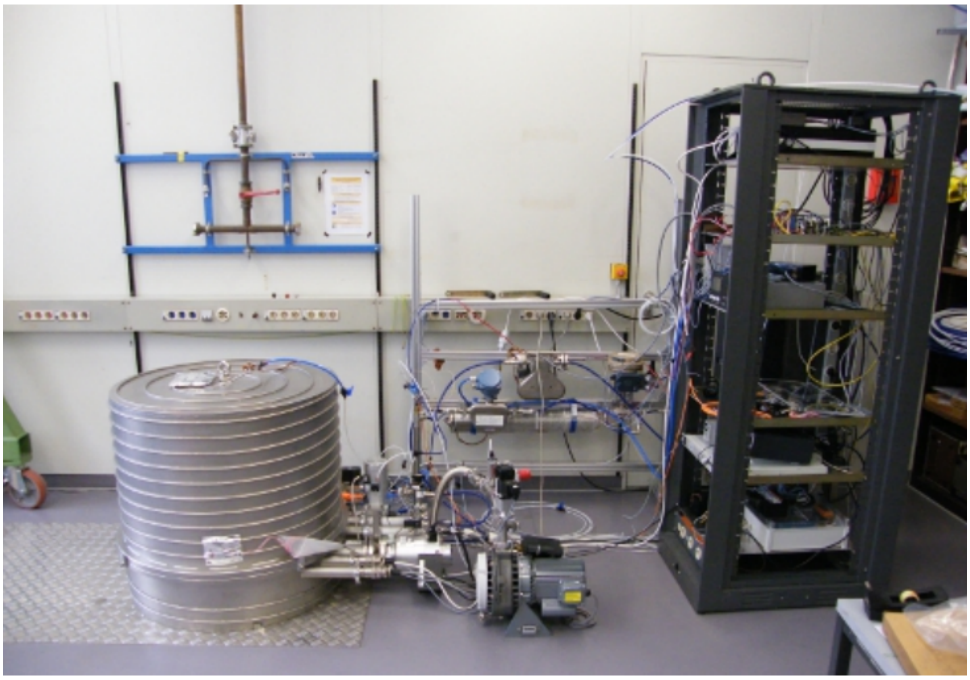

FIGURE 6.12: Complete calorimeter assembly during its mock-up electric source test runs in TUM in 2016.

FIGURE 6.13: Super-insulator material covering the mock-up source inside the calorimeter vessel, before encapsulation.

to raw output data to minimize fluctuations and obtain stable equilibrium measurements. A picture of the whole calorimeter test setup at TUM is shown in Figure 6.12.

Three approaches are used to extract the source's power output from the temperature difference between the water circuit's input and output channels, taking into account the mass flow rate $\dot{m}$:

- Integral of the change in water temperature, considering water's heat capacity c_P at constant pressure. There *is* a slight pressure drop of ~100 mbar in the calorimeter, but that is neglected as a systematic.

$$P = \int c_P dT \tag{6.7}$$

where $c_P = \left(\frac{dh}{dT}\right)_P$ is the specific isobaric heat capacity of water at a constant p.

- Change in specific enthalpy at a known flow rate, with continuously variable temperatures. An analytical function of the water's specific enthalpy per mass unit $h(p,T)$, from [187], is used:

$$h(p,T) = (U + pV)/m \approx (288.1 + 87.76 \cdot p[bar] + 4181 \cdot T[°C])J/kg \tag{6.8}$$

from there, the error can be estimated as $\sigma_{\Delta h,tot} = 274J/kg \rightarrow \sigma_P \approx 274 \cdot \dot{m}[W]$.

- Change in specific enthalpy at a fixed temperature, with adjustment through the mass flow rate $\dot{m}$. Measured values of $h(p,T)$ are used, which brings a smaller $\sigma_{\Delta h,tot}$ than the previous technique. This is the preferred power determination strategy.

In general, the systematic uncertainty in the measured power will be:

$$\begin{aligned} \sigma^2_{P_{meas}} = \sigma^2_{\Delta T} \cdot [\frac{\partial P_m}{\partial \Delta T}]^2 + \sigma^2_c \cdot [\frac{\partial P_m}{\partial c}]^2 + \sigma^2_\Phi \cdot [\frac{\partial P_m}{\partial \Phi}]^2 \approx \\ \approx 3502[J^2/kg^2] \cdot \Phi^2 + 200[J^2/kg^2] \cdot \Phi^2 \cdot \Delta T^2 \end{aligned} \tag{6.9}$$

Since this calorimeter would effectively be the "container" for the source during deployment, and would have to be operational, a rail design was implemented from CR1 to the deploy position at the center of the pit. The calorimeter would be mounted on a cart riding these rails (see Figures 6.14 and 6.15), while a second cart would be attached carrying the associated equipment: pumps, sensor systems and water loop circuit.

The calorimeter design was chosen since the beginning to be compatible with both the chromium and the cerium sources. With the schedule re-arrangement and the prioritization of CeSOX, the same basic calorimeter design was used, and this part of the program was brought onward from the CrSOX era. As of this writing, the calorimeter was delivered to LNGS after its initial round of checkouts and calibrations with a mock-up electrical resistor "source" (see Figure 6.16) after final assembly was completed in Münich, and has joined the tungsten shield for load and fit checks, as well as for further calibrations.

The latest blind analysis results[188] yield power reconstruction accuracies of at least ~5 times the baseline 1%, at operating conditions of $\dot{m}$=5 g/s; T_{input}=17°C and $T_{chamber}$=31-41°C. The

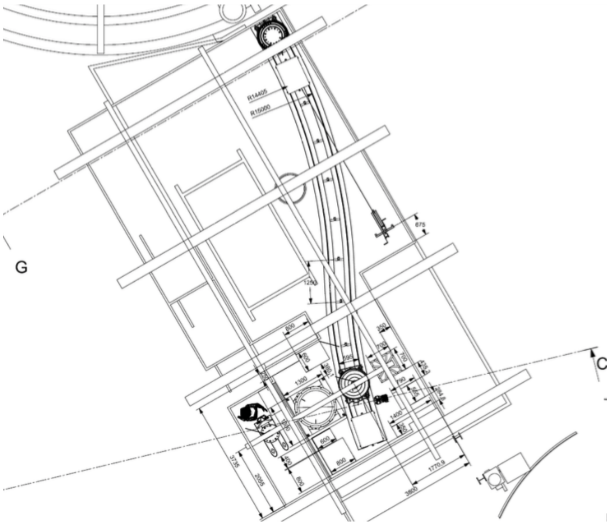

FIGURE 6.14: Technical drawing of the rail deployment system for SOX-A, along with the double calorimeter scheme foreseen for CeSOX (the *Genova/TUM* calorimeter with its auxiliary cart on the rails, the *CEA* calorimeter on its permanent position in CR1 next to it).

FIGURE 6.15: Photographs of deployment tests with the rail system in CR1.

third technique for power determination above was used, and power at equilibrium was taken to be the average of each power determination through specific enthalpy at every point. Statistical uncertainty was taken as the standard deviation of the averaged power, and systematics were taken to be 0.05% for $\dot{m}$; 0.2 kg/m^3 for the density, 3 mK for the temperature and 100 J/kg for the enthalpy. The mock-up run errors were thus between: 0.02%-0.21% –as advertised, at least a factor of $\sim$5 better than required at high (840 W) power, and up to 50x at 720 W.

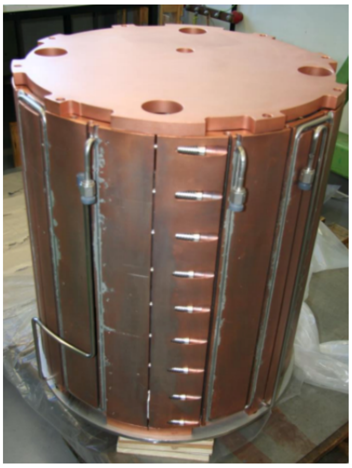
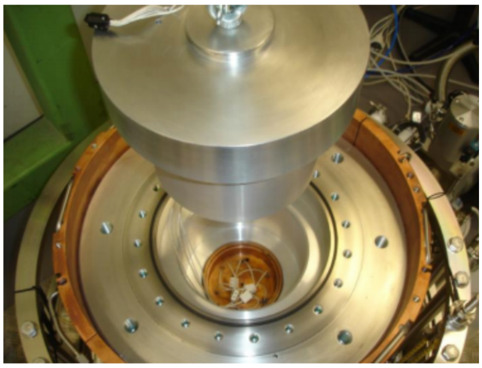

FIGURE 6.16: Mock-up electrical "source" with primary water loop embedded in the copper heat exchanger surrounding it. On the right, a detail of the inside of the mock-up with the lid removed.

6.2 Chromium irradiation facilities: ORNL's HFIR

From the 5-10 MCi requirement, the CrSOX source would need a specific activity of **∼140-280 Ci/g** (∼5-10 TBq/g), if the whole 38.6%-enriched material available from the GALLEX source was to be employed. Prior experiences in several different high neutron flux reactors around the world show achievable specific activities close (order of magnitude) to that, making the project feasible in similar facilities, with optimizations, in principle: Siloè[184] (∼0.5-2.5·10^{14} $n^0 \cdot cm^{-2} \cdot s^{-1}$, ∼10% of required activity, but with a 21 day cycle and large containers); L-2[185] (∼1-2·10^{14} $n^0 \cdot cm^{-2} \cdot s^{-1}$; 330-140 Ci/g depending on material density, position and irradiation cycle duration, with an average of ∼230 Ci/g); SM-3[189] (∼0.1-5·10^{15} $n^0 \cdot cm^{-2} \cdot s^{-1}$, advertised as ∼280 Ci/g in 43 days); BN-600[189] (∼2-3·10^{15} $n^0 \cdot cm^{-2} \cdot s^{-1}$, ∼484 Ci/g in 160 days, power plant); HFR (∼5·10^{14} $n^0 \cdot cm^{-2} \cdot s^{-1}$); BR-2 (∼2-10·$10^{14}$ $n^0 \cdot cm^{-2} \cdot s^{-1}$); and finally HFIR[190] (∼1-2·10^{15} $n^0 \cdot cm^{-2} \cdot s^{-1}$, ∼20-40 Ci/g with *natural* chromium).

It is important to note the equilibrium between production of new ^{51}Cr and its decay will be reached after ∼60 days of continuous irradiation, from Equation 6.10. Furthermore, expedited transportation after irradiation is mandatory, given ∼2.5% of the resulting ^{51}Cr activity is being lost each day after the end of irradiation[178].

$$N_{^{51}Cr}(t) = N_{^{50}Cr}(t=0)\frac{\tau_{51}}{\tau_{50}-\tau_{51}}\left(e^{-t/\tau_{50}} - e^{-t/\tau_{51}}\right) \tag{6.10}$$

While both experimental and simulated precedents exist for the production of high specific activity amounts of ^{51}Cr, the range of total activity needed for CrSOX is on the upper range of the estimates, and furthermore no detailed study on the use of enriched chromium material was available in Oak Ridge National Laboratory (ORNL)'s High Flux Isotope Reactor (HFIR) facilities, which were desirable because of their geographical proximity to the Virginia Tech campus ($\sim$400 km) and because of its extremely high neutron flux, on the order of $\sim 10^{15}\ n^0 \cdot cm^{-2} \cdot s^{-1}$, one of the largest in the world. Preliminary estimates from ORNL personnel[191] showed encouraging results but considering 100%-enriched ^{50}Cr targets in geometrically-averaged, non-optimized cases.

Analytical efforts[192] were pursued to more rigorously establish parallelisms between the GALLEX irradiation and HFIR's possible results. In particular, the effects explored are the increased flux of HFIR as compared to Siloè (8-25x, depending on the considered positions), the core temperature difference (affecting the spectrum of the emitted neutrons, and therefore also the effective, flux-averaged neutron capture cross sections), an estimate on the effects of flux depression due to self-shielding, and the amount of ^{51}Cr that disappears because it manages to capture a further thermal neutron during irradiation. The concept of double-cycle irradiations, considered before for other facilities[185], was briefly discussed too as a way to increase final total ^{51}Cr production. While cross-comparison with the results in [190] and the preliminary studies by ORNL's technical staff showed discrepancies that meant a lowering of these estimates, the results kept being nevertheless encouraging, and the need for more detailed, simulation-based feasibility studies was highlighted.

ORNL's HFIR is a light water-moderated and -cooled, 85 MW thermal nuclear reactor with beryllium reflector elements. It follows a "blade"-like (involute) arrangement of the 540 highly-enriched, inhomogeneously-distributed $^{235}U_3O_8$-Al fuel elements (inner+outer), with europium oxide (EuO) cylindrical removable control elements (*control cylinder* and *plate quadrants*) in a 94" (ID) pressure vessel made of carbon steel with stainless steel cladding, surrounded by a concentric removable and a permanent beryllium reflector featuring several cavities (see a photograph in Figure 6.17 and annotated diagrams in Figures 6.18 and 6.19). In order to flatten the radial flux peak (and thus increase fuel cycle efficiency), a burnable poison (^{10}B) is embedded in the inner 171 fuel elements. The mean radius of the fuel elements (from the reactor's central axis) is 14.2875 cm, marked by the water gap between the IFEs and OFEs. The central axis of the cylindric reactor contains the so-called *Flux Trap*, where irradiation spaces are also provided. The reactor core is $\sim$2 ft high.

Being a research reactor, HFIR was designed with plenty of positions that could be accessible for material insertion and neutron flux extraction. In particular, CrSOX's source material would be interested in the following in-vessel irradiation target regions:

Vertical eXperimental Facilities (VXFs) The VXFs constitute the highest volume facilities. They are subdivided into Large (LVXFs, 6, 3.59918 cm ID, 46.27626 cm from the reactor's main axis), Small Outer (SOVXFs, 6, 2.01168 cm ID, 44.05376 cm from the reactor's main axis) and Small Inner (SIVXFs, 10, 2.01168 cm ID, 39.2115 cm from the

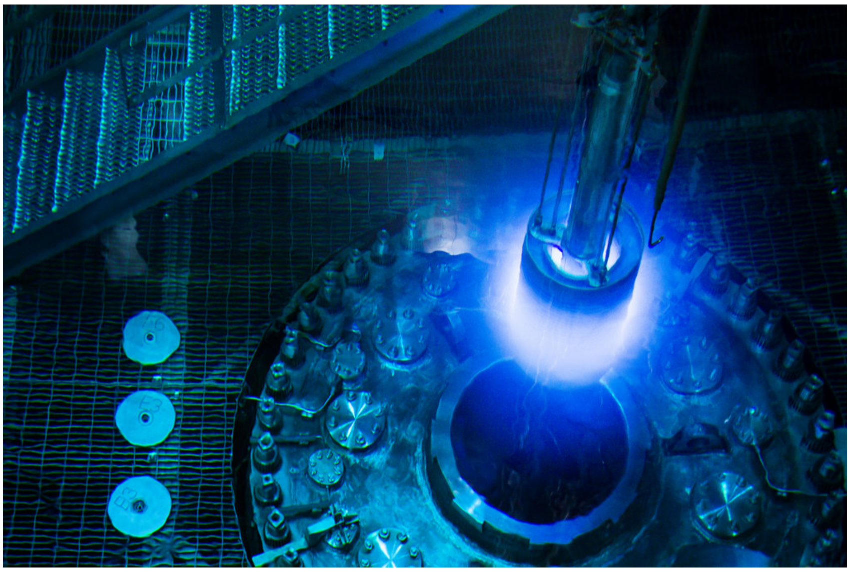

FIGURE 6.17: Refueling of HFIR with a fresh fuel element assembly, courtesy of ORNL's Flickr page (Genevieve Martin/ORNL).

reactor's main axis), at progressively larger distance from the core. All of them are vertical cylinders with permanent aluminium liners, located in the Permanent Beryllium reflector and span its whole height.

Pneumatic Tube Facility (PTF) Technically a SIVXF (#7), this facility allows for remote insertions and withdrawals of samples, but not bulk material insertion.

Flux Trap (FT) A diagram of this centralmost region with the highest neutron flux can be seen in Figure 6.20. It contains 31 target positions, all of them arranged so that 0.83058 cm OD uncooled (0.31623 cm OD cooled) target rods can be inserted, except for one: the Hydraulic Tube (HT), which permits rapid remote deployment and withdrawal of small samples. On the periphery of the FT there are 6 Peripheral Target Positions (PTPs), which show steep neutron flux gradients, with a ~1 cm OD uncooled (0.889-0.5486 cm OD cooled) target.

Removable Beryllium Facilities (RBFs) As their name suggests, these facilities are located in the Removable Beryllium reflector, and offer large and small diameter irradiation spaces. The LRBFs were not considered for CrSOX since the removal of so much beryllium reflectors would negatively impact the reactor cycle's life. The SRBFs, 2.32918 cm ID, while not the primary facilities considered, would complement the FT positions, where not too much material could be loaded due to reactor cycle shortening issues.

Control Rod Access Plugs Facilities (CRAPFs) These imaginatively-named irradiation positions are located in the semi-permanent berylium reflector, consisting of eight separate, removable Be pieces 0.635 cm OD whose positions can accommodate capsules similar to

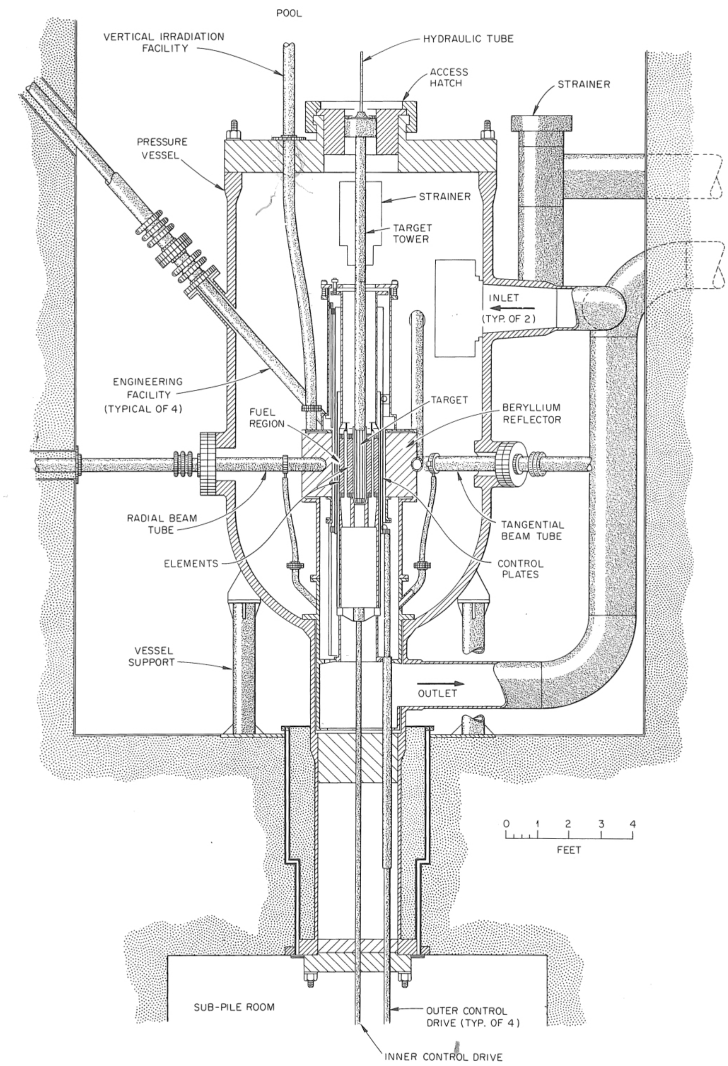

FIGURE 6.18: HFIR's pressure vessel cut-out diagram (annotated), including the reactor's basement, from [193].

the ones used in the SRBFs when not covered. Their positions were taken as back-up complements to the SRBFs.

Since the VXFs offer the largest volumes with the least influence over neutron flux depression on the cycle lifetime, they would be the determining factor in the final activity of the CrSOX source, and therefore the primary focus of our study. FT positions, while offering temptingly high neutron fluxes, could not be used at will due to fuel cycle life, shielding and scheduling conflicts. PTPs would preferably not be used for chromium irradiation, since not much vertical space would be offered. SRBFs could be used although they would provide a comparatively small neutron flux and small volume, while shielding some of the larger VXFs behind. As mentioned, LRBFs could not be used due to fuel cycle life shortening issues. The PTF and CRAPFs were considered as back-up positions.

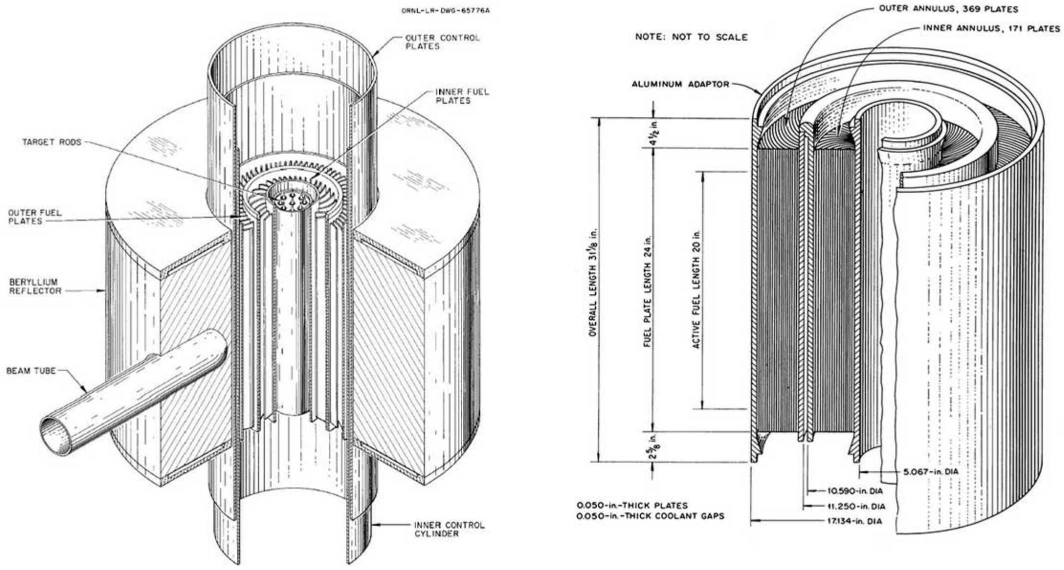

FIGURE 6.19: HFIR's core cut-out technical drawing (annotated), and detail of the fuel assembly on the right.

An annotated horizontal cross-section diagram with the relevant irradiation regions is shown in Figure 6.22, while representative radial fluxes can be seen in Figure 6.21.

The chromium material, depending on its form during irradiation, would be inserted in containers, sheathed within a liner, or bare. Once the irradiation cycle(s) were completed, they would be extracted remotely, and manipulated to a hot cell, where their containers would be opened or their holding components removed, so that they could be inserted in the basic source core assembly components. These operations would be delicate because of the potential of contamination of the material with radioactive impurities –which would be aggravated by the large amounts of material to go through processing– and only preliminary concepts were developed during the feasibility studies in the scope of this thesis. Once hot cell operations were complete, the insertion into the tungsten shield (and later transport container) would be performed, in principle in a nearby facility within the reactor property.

Preliminary transportation and logistics concepts devised showed an important limitation: a 2.4 MCi limit in air transport of radioactive material. Therefore, the source would have to be divided into several pieces, since freight ship transportation would be inadequate for this type of material, given its short half-life. Once across the Atlantic, the source would land in Fiumicino International Airport near Rome, from where it would be transported to ENEA's Casaccia facilities for characterization, final permits and transportation to LNGS.

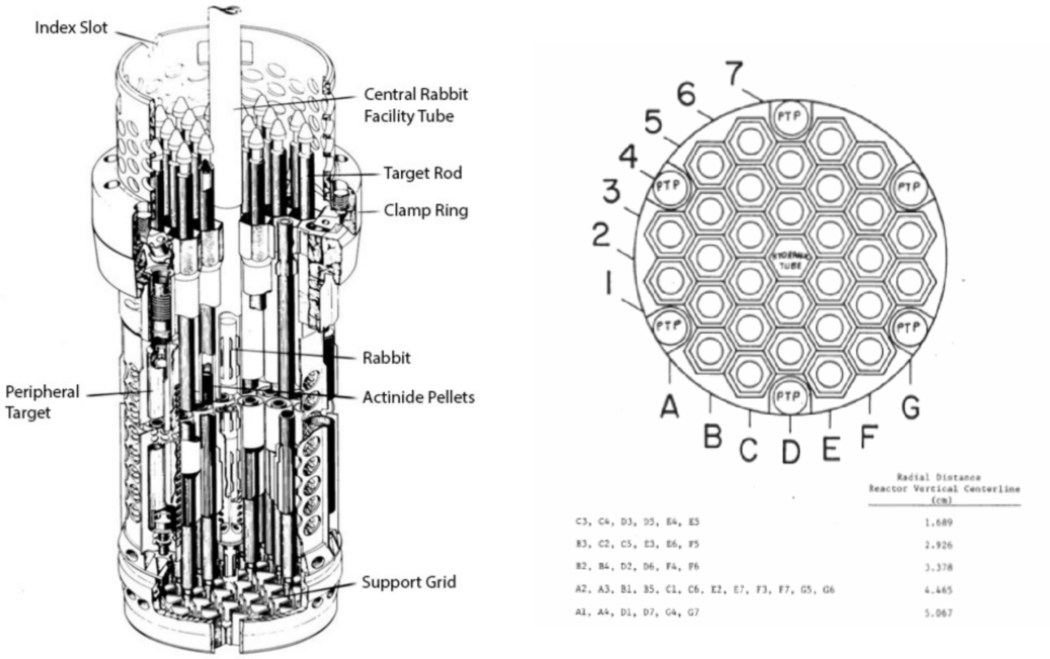

FIGURE 6.20: HFIR's Flux Trap (FT) cutaway conceptual drawing (left, annotated[193]) and position designations (right[194]). The position with the protruding upper tube is called the Hydraulic Tube (HT, also known as Central Rabbit Facility Tube (CRFT)) and permits rapid remote deployment and withdrawal of small samples. The facilities labeled PT are the Peripheral Tubes. The rest of the positions are arranged in target rods.

6.3 Estimates of irradiation strategies on ^{51}Cr activity

MonteCarlo N-Particle (MCNP) is a general-purpose code intended for modelization of continuous-energy, generalized-geometry, time-dependent, coupled neutron/photon/electron transport, either separately for each type of radiation or combinations thereof (neutron/photon with γs generated by neutron interactions; neutron/photon/electron, photon/electron or electron/photon), with $E_{n^0}\epsilon[10^{-11}, 20]$ MeV (up to 150 MeV for selected isotopes); $E_{\gamma}\epsilon[10^{-6}, 100]$ GeV and $E_{e^-}\epsilon[10^{-6}, 1]$ GeV. Furthermore, it is optimized for k_{eff} calculation in fissile systems. Because of its versatility, proven reliability in nuclear and particle engineering, and experienced ORNL technical staff available for support on its operation and interpretation, this code was used to further the feasibility studies for CrSOX's source. **MCNP5** was used[195] for the following simulation studies –although MCNPX was an option for follow-on refinements, given it allows tracking of light and heavy ions, as well as taking into account brehmmsstralung or other charged particle effects that could prove important, its use was never deemed crucial for the level of accuracy required.

Broadly speaking, the simulation package was used according to the following premises:

Geometry definition Using an ORNL-provided operational MCNP model of HFIR (v4.0), the main task here was to optimize the chromium material geometry, location and shape in

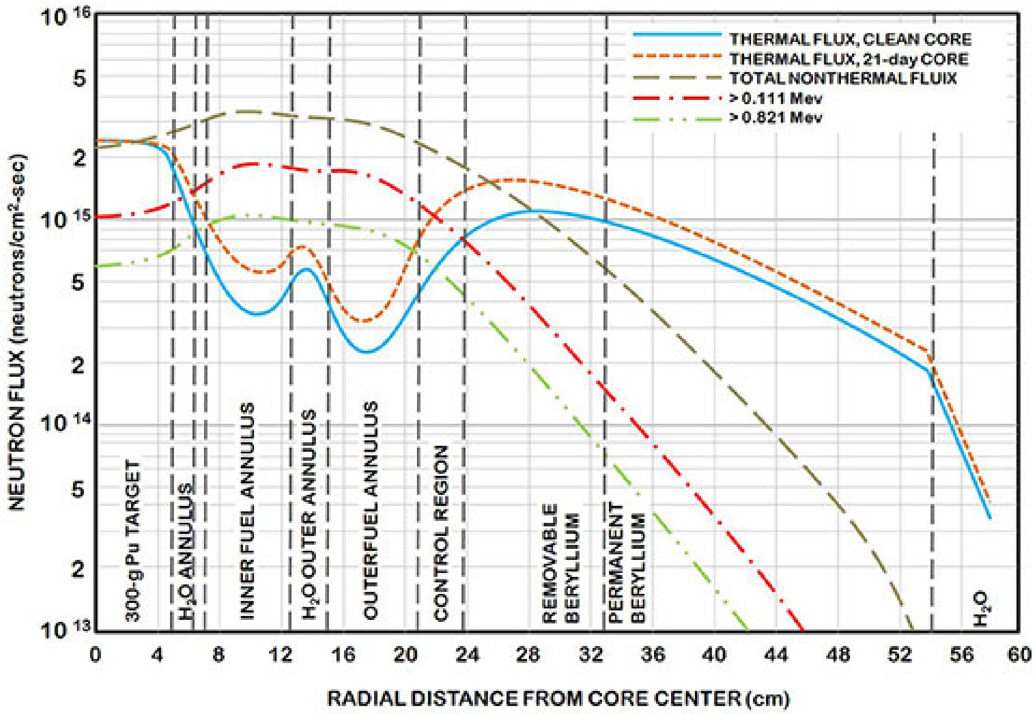

FIGURE 6.21: Thermal and non-thermal neutron fluxes in HFIR. Actual fluxes will vary with core life, control element positions and possible non-standard operations (≠85 MW), from [193].

the reactor to maximize resultant activity. The technical word *cell* here refers to a volume area of homogeneous properties.

Cell material definition Allowing different densities (thereby simulating chips, sintered/pressed and solid material) and isotopic compositions (for ^{50}Cr enrichment scenarios).

Tally definition The large amount of options in MCNP output called for a focused approach into the parameters of interest for our purposes.

Variance reduction Even though it will not reduce other sources of error, variance-reducing techniques can be effective in minimizing computing time to obtain higher *precision* results. Since the estimated relative statistical error is proportional to the number of run histories ($R = 1/\sqrt{N}$), and $N \propto T$ (T being the simulation time), we can express $R = C/\sqrt{T}$, being C a proportionality constant. If we want to decrease R without ballooning computing time, the proportionality constant can be reduced –variance reduction strategies achieve that. Efficient tally selection is already an important variance reduction technique, but MCNP5 incorporates others, some of them used in these simulations (model truncation, population control such as particle splitting and Russian roulette upon energy or location thresholds, energy/time/weight cutoffs) while others are not, either because they may bias the simulation too much or because they are not readily applicable (modified sampling

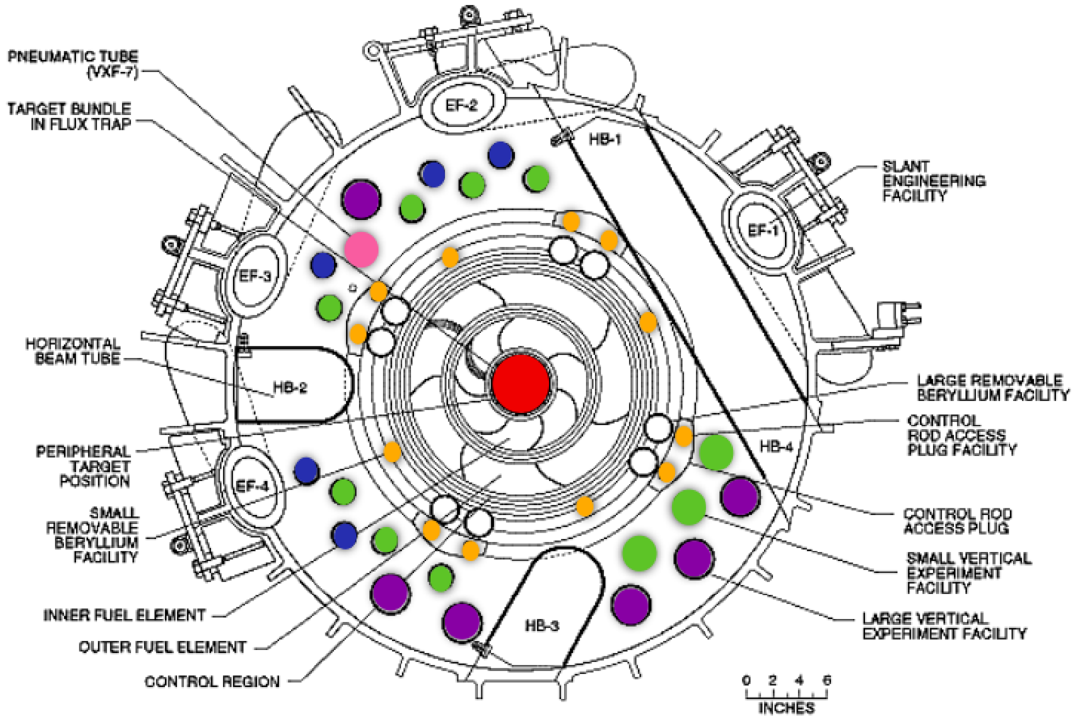

Figure 6.22: HFIR target irradiation facilities annotated in a mid-plane horizontal cross-section diagram. Marked in red is the Flux Trap (FT), a detailed view of which can be found in Figure 6.20; green are the SIVXFs, blue the SOVXFs, purple the LVXFs, yellow the SRBFs and CRAPs, and pink the PTF (also known as VXF#7). The 8 LRBFs are non-colored since it was not likely they could be used.

though exponential transforms, implicit captures, forced collisions, source biasing... or partially deterministic methods such as DXTRAN and correlated sampling).

Simulation run Performed in the `TBird` cluster of Virginia Tech's Physics Department.

Output analysis Statistics tables and run parameters, tallies and tally fluctuations and KCODE calculations for statistics (for non-predefined neutron sources such as ours). Tallies employed in these simulations include:

Fluxes More correctly, the ones we are interested in tally the track length estimate of the flux:

$$\overline{\phi}_V = \frac{1}{V}\int dE \int dt \int dV vN(r,E,t) \tag{6.11}$$

where $N(r,E,t)$ is the density of particles at a point, regardless of trajectory. This quantity, multiplied by the infinitesimal unit of track length ds ($ds = vdt$), can be interpreted as the track length density –and therefore, the average flux can be estimated by summing track lengths together, for all particle tracks in a cell. This estimates the average flux in the volume $\overline{\phi}_V$ quite reliably: especially when tracks are more frequent than collisions in a given cell, increasing statistics to this tally.

Additionally, MCNP needs the S_n factor accounting for the number of fission neutrons generated each second, given by:

$$S_n = \frac{P\nu}{Q\epsilon k_{eff}} \tag{6.12}$$

where P is the reactor power ($8.5{\cdot}10^7$ W in nominal operation), ν is the number of neutrons per fission (given by MCNP), Q is the recoverable energy per fission, ϵ=$1.602{\cdot}10^{13}$ J/MeV and the criticality factor k_{eff} is also given by MCNP and should oscillate between 0.99-1.01 for stable reactor operation. For first estimates of non-fissionable targets, Middle-of-Cycle (MoC) conditions are a good approximation, although more fine temporal binning was made for refinement considering Beginning-of-Cycle (BoC) and End-of-Cycle (EoC) conditions –these are implemented in geometry positions (mainly control element withdrawals/insertions) and in the Q (Q_{MoC}=201 MeV/fission; Q_{BoC}=200.2 MeV/fission; Q_{EoC}=200.75 MeV/fission). These tallies are subdivided into 1, 3, 44 or 238 groups (i.e. *energy bins*, in the physics jargon), depending on the complexity of the modeled element. For our purposes, we are mostly using 44-group fluxes (F4 and F2, but mostly the latter unless important deviations occur) in the measured irradiation positions. More detailed information about tally calculation can be found in Section 2.V.B and .C in [195]

Reaction rates They are 1-bin averaged to the whole energy range, and can be more properly considered reaction rate density (pre-multiplied with the S_n factor in $[n^0/s]$), where the given quantity is equal to the macroscopic cross section for a given energy bin multiplied by the flux. They are applicable to all neutrons, not just thermal. Therefore, they have units of $[n^0/(b \cdot s)]$.

Calculation of ^{51}Cr(t) is then approximated by the simple formula:

$$^{51}Cr(t) = RR_c(1 - e^{-\lambda t}) \tag{6.13}$$

with t being the cycle duration. In the actual calculations, RR_c (the "reaction rate") has to be multiplied by the number of target atoms N, in units of $[atoms/(b \cdot cm)]$, because of the technical considerations described above, in order to get the actual number of atoms of ^{51}Cr produced. This formula, although overlooking isotopic depletion, has been demonstrated to reproduce to within ~3% full depletion calculations (mainly performed with the `ORIGEN` package, but more computationally-intensive), and thus was deemed appropriate for the optimization studies, where much greater operational uncertainties were at play.

The input file therefore consists of three major sections: (i) **Cell cards**, defining cell material properties and geometry; (ii) **Surface cards**, defining boundaries, generally according to pre-determined shapes; and (iii) **Data cards**, defining tallies, material compositions and sources.

More than 30 different scenarios were studied, varying the relative loading of each irradiation facility, the material's shape and form, and other factors such as single/double irradiation schemes, B/M/EoC regime influence in final activity, enhanced reactor operation or k_{eff} management. The main focus of these simulations was to study the effect of self-shielding and optimize geometrical distribution (both in material shape, location within the irradiation facilities and physical form/density). The most relevant results are listed in the following Subsections 6.3.1-6.3.5.

6.3.1 Baseline full-cylinder cases

The most trivial case at hand would be to fill all VXFs to the same level around the mid-plane of the reactor, where the flux is greatest, regardless of actual position from the fuel elements. This would allow for a first approximation of the level of activity achievable. Chipped material was used.

At this point it is useful to say a few words about chromium's self-shielding. It is obvious that, apart from the geometrical decrease factor, the neutron flux getting to the target chromium would be affected by the material it had to traverse. Most reactor materials will attenuate the neutron flux, but those containing atoms with large cross sections will obviously impact it more (like water). On the other hand, HFIR's operation heavily relies on neutron reflectors that bounce back part of the outgoing flux from the fuel elements, backscattering those neutrons to increase k_{eff}, and, in the process, increasing the neutron flux in the areas located within these reflectors –primarily made of beryllium metal[1].

While it would be a trivial analytical problem to calculate the attenuation coefficient of a chromium "cylindrical shell" surrounding the reactor, and therefore the expectable levels of specific/total activity derived of such a geometry, HFIR's geometry provides irradiation facilities totally (VXFs) or partially (RBFs, CRAPFs) surrounded by the reflectors, which will increase the induced activity in the chromium areas not directly facing the reactor, as well as those that would be significantly shielded by the thickness of the chromium separating it and the incoming flux. Indeed, chromium self-shielding has been shown to influence as much as 50% the activation profile for 20" thin wafers[190], and the 38.6%-enriched material at hand can be calculated to have a ~ 3.5 cm attenuation length ($\phi(3cm) = \phi_0/e$) for chipped, 3 g/cm^3 material. The attenuation length is inversely proportional to density (see Equation 6.14), so re-cast solid material with ~6.9 g/cm^3 would have just ~1.5 cm of attenuation length. While the SVXFs

[1] Additionally, beryllium is also a very good neutron moderator, enabling faster-than-thermal fission-emitted neutrons to be more efficiently utilized for sustaining the chain reaction once reflected. Graphite is slightly less neutron-absorbing, but also more difficult to work with in high-temperature environments.

are only about 2/3rds of the attenuation length for the chips, this will still reduce by ∼50% the material activation.

$$\lambda[cm] = \left[N_{av}\rho \sum_{i=50}^{54} \sigma_i \epsilon_i\right]^{-1} \cdot 10^{24} \tag{6.14}$$

This clearly explains why this scenario is just a basic approach that does not take into account important optimization factors. Furthermore, the actual location of some VXFs within the permanent beryllium reflector (see Figure 6.22) mean that some of the inner positions actually "shadow" the more externally-lying ones, especially the LVXFs, locally depressing the neutron flux (and thus reducing the available number of neutrons available for reflection) and shielding positions behind them.

These concerns will be addressed in the next sections, as the model gets refined.

Homogeneous filling

Be as it may, this "simple" model would fill the VXFs to a uniform height of 13.5 cm above and below the midplane, modeling 36 kg of chromium at a 3 g/cm^3 density. The rest of the VXF is filled with water above and below, and the rest of the reactor is unmodified from the basic cycle 400 configuration. The obtained value is:

$$A(^{51}Cr) = 2.651 \pm 0.001 \; MCi \tag{6.15}$$

for a specific activity of 198.1±0.8 Ci/g. A slightly less conservative example with a realistic estimate of the density (ρ=3.6 g/cm^3) yields a compatible activity of 2.652±0.002 MCi, well within statistical error.

Both configurations were analytically projected for the case of a double-cycle irradiation, where two 24-day irradiation cycles would be separated by an 8-day downtime. This would increase activity by ∼44%, although errors are larger here since we are essentially duplicating the statistical uncertainties, and the depletion effects will become more pronounced. Bearing that in mind, a ∼5% uncertainty can be conservatively assigned to these estimates, yielding 3.82±0.17 MCi.

Enrichment effects

The next step was to get a handle on how much enrichment affected total yields. Although greater concentrations of ^{50}Cr will in principle result in greater ^{51}Cr production simply from the larger amount of transmutable atoms, scaling is not obvious when not considering an infinitely-dilute target, where self-shielding and geometrical effects are of great importance. In fact, a

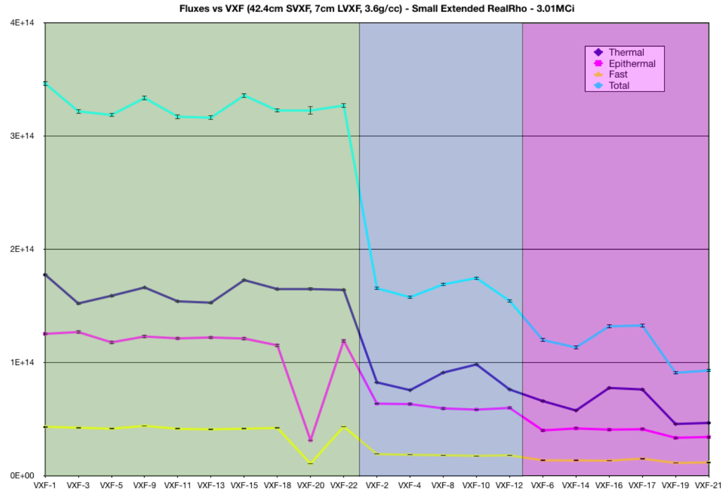

FIGURE 6.23: Neutron flux vs VXF position in a full-VXF, chip material scenario.

scenario with identical geometry to the previous one, but with 100% ^{50}Cr-enriched material (that is, ~35.22 kg of ^{50}Cr at a lower-than-nominal density of 3 g/cm^3) yielded an activity of:

$$A(^{51}Cr) = 3.30 \pm 0.05\ MCi \tag{6.16}$$

for a specific activity of 93.7±1.3 Ci/g.

Density effects

A higher and lower density scenario of 4 and 2 g/cm^3 with the same previous geometry and realistic enrichment were also used to gauge the influence of density in total activity: $A^{\rho=4}(^{51}Cr)$=2.81±0.02 MCi (although this used more material than available at ~47 kg); and $A^{\rho=2}(^{51}Cr)$=2.39±0.02 MCi – thus highlighting the crucial effect of density on the achieved activity, by the comparison of their specific activities: 157.3±1.2 Ci/g and 267.8±2.2 Ci/g, for the high and lower density scenarios, respectively.

Finally, a somewhat more realistic case of newly-enriched chromium at 60% ^{50}Cr was also run at high (4 g/cm^3) and low (2 g/cm^3) densities, yielding 3.12±2.5 MCi (110.0±0.9 Ci/g) and 2.77±0.02 MCi/g (196.5±1.6 Ci/g) respectively.

Effect of relative bulk distribution in VXFs

LVXFs, despite offering the largest irradiation target, also feature a considerably smaller neutron fluence and may be somewhat shielded by SVXF chromium targets lying closer to the fuel (see Figure 6.23 and Figure 6.24).

For this reason, a scenario was created by filling just the SVXFs with the chips (to a greater height of 21.2 cm above and below the midplane; or 15.4 cm more material in the SVXFs

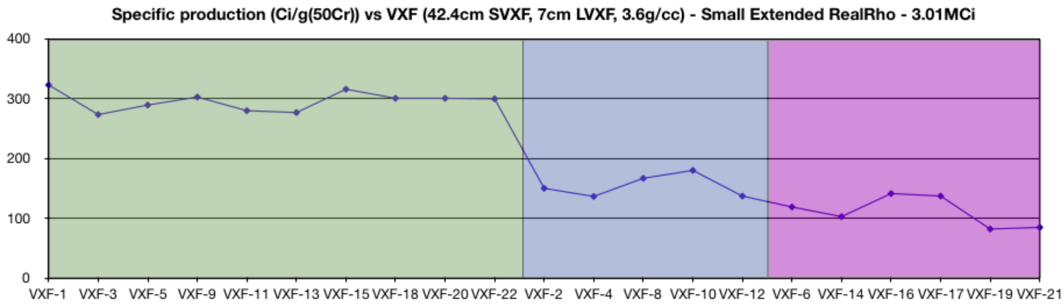

FIGURE 6.24: Specific activity production vs VXF position in a full-VXF, chip material scenario.

than in the previous scenarios) and leaving the LVXFs empty, in order to evaluate their relative importance. In one variant, the LVXFs were just filled with water; in another, beryllium reflectors were installed in those positions to attempt to increase the backscattered neutron flux. Both were filled with 3 g/cm^3, slightly less dense than nominal, chromium material. The achieved activities were:

$$A(^{51}Cr)_{H2O} = 2.61 \pm 0.03\ MCi \tag{6.17}$$

$$A(^{51}Cr)_{Be} = 2.60 \pm 0.03\ MCi \tag{6.18}$$

for average specific activity values of 282.4±4 Ci/g in both cases.

Because of size limitations, these models with chromium in just the SVXFs did not include all the available material. For that reason, *extended* versions of these models were devised in which the remaining chromium was used to fill equally all LVXFs, to a height of 7.5 cm above and below the midplane. Resulting activity in this case was $A(^{51}Cr)_{H2O}$=3.06±0.03 MCi (228±3 Ci/g). A check with realistically modeled 3.6 g/cm^3 material (21.2 cm height in SVXFs, 4 cm in LVXFs) yielded $A(^{51}Cr)$=3.01±0.03 MCi (224±3 Ci/g).

6.3.2 Flux Trap role

The Flux Trap features the highest neutron fluxes in the whole reactor, as its name suggests and can be seen in Figure 6.21. Also, the target positions cannot be too thick, alleviating the self-shielding effects –also minimized thanks to the target being *inside* the fuel elements, and therefore receiving the neutron flux from all around. However, ^{50}Cr is a large neutron sink, and too much of it in such a central location with the highest neutron fluence in the whole reactor can lead to a too large reduction in k_{eff} and cycle lifetime. This is impractical for financial and

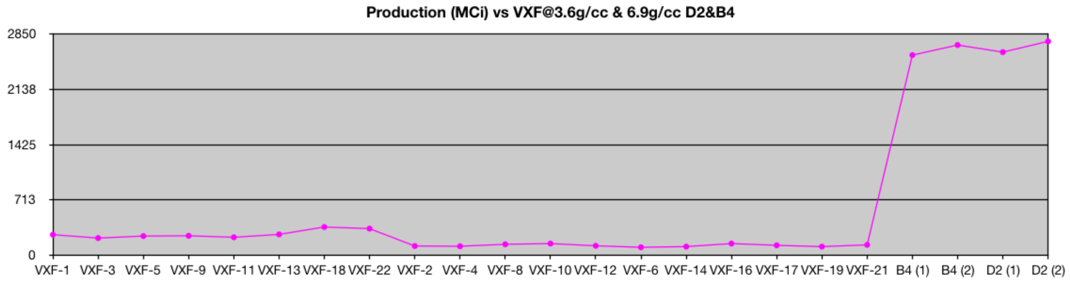

FIGURE 6.25: Specific activity production vs VXF and FT position, in a typical chip/solid FT rod scenario. As explained in the text, the presence or absence of 2-3 FT rods affects very little the external achievable activity in the VXFs, and their specific activity is practically constant for a small number (2-3) of target rods.

reactor operations reasons, and would also be detrimental to overall specific activity since the inner targets would see shielding from the outer ones, if the full flux trap was to be utilized. VXF fluxes would be similarly reduced.

Nevertheless, a moderate amount of chromium inside the FT may provide a small amount of activated material with extremely high specific activity, while having a small overall effect on the rest of the reactor dynamics. This compromise was tested in different geometries with both chipped and solid material in the VXFs, and was verified to be greatly stable regardless of the exterior target distribution, and providing a negligible impact, within statistical error, for VXF activity.

For the FT, it is desirable to have solid chromium, since the targets are thin: it is desirable to increase density as much as possible, because self-shielding within the target rod will be small. This approach led to the optimization of space in the VXFs that will be mentioned in the next Section 6.3.3. With a 6.9 g/cm^3 density, solid chromium can be inserted in FT positions which are far away from each other (usually, two target rods of ∼110 g in the B-4 and D-2 positions) yield ∼2700 Ci/g, or ∼>0.1 MCi/rod (see Figure 6.25 for a specific activity profile for the VXFs compared to the FT targets). This would provide a boost in activity of 0.2-0.3 MCi at "no cost" (with respect to the achievable activity levels in the VXFs), or ∼0.5 MCi in a double-cycle irradiation with 8 days downtime. Furthermore, the high specific activity means these rods could be included in the source core without significantly affecting overall dimensions.

Prior scenarios did not make use of the FT, but some of the ones detailed henceforth will. Unless otherwise noted, activities reported will be for the overall material in the VXF positions, not taking into account this *FT boost*, which remains a constant addition.

6.3.3 Self-shielding management through material geometry

Tallies in the scenarios above are not discretized within the VXF, i.e. the results consider the whole *cell* as the interior of the VXF and do not offer insight into the regional dependence within it. However, from the previous discussion earlier in this Section, it is evident there will be an important amount of self-shielding even when factoring the reduced density of chips into the problem. An obvious way to avoid this phenomenon is to reduce the thickness of target material visible to the incoming neutron flux, and to have the remaining chromium have as unobstructed a (neutron) view toward the reactor core as possible.

Basic geometrical optimization: *No Shadow* scenarios

The simplest way to start tackling the cross-shielding problem is to avoid loading the VXFs that would most affect nearby irradiation positions with large amounts of material through their regional neutron flux depression: VXFs 15, 18 and 20. These would be left filled with water, and the rest of the 3.6 g/cm^3 material would be filled to 21.2 cm above and below the midplane in the remaining SVXFs and to 5.5 cm in the LVXFs. This scenario yields:

$$A(^{51}Cr) = 2.63 \pm 0.03\ MCi \tag{6.19}$$

for an average specific activity of 210±2 Ci/g. This showed that, even though specific activity was higher in the LVXFs closest to #15, 18 and 20, the tradeoff to leave these empty was not positive toward obtaining an overall higher activity. A refined version with just SVXFs 15 and 20 (not 18) left without chromium and filled with water, yielded $A(^{51}Cr)$=2.99±0.03 MCi (225±2 Ci/g).

In order to lower the chips density to 3 g/cm^3, like unrealistically imposed before in order to be conservative about material amounts in the irradiation facilities, would be to *mix them with beryllium*. This would in principle boost neutron flux inside the chips by the reduced density and the neutron reflectiveness of the mixer. For this, 33.3 kg of chromium were mixed with 11.1 kg of ^{9}Be in the previous configuration:

$$A(^{51}Cr) = 2.77 \pm 0.04\ MCi \tag{6.20}$$

for an average specific activity of 219±2 Ci/g.

Another attempt based on not using LVXFs, reducing the number of employed OSVXFs and re-using ISVXFs 15 and 20, all with 30 cm of chips above and below the midplane, yielded a worse result of 2.33±0.04 MCi (233±3 Ci/g). This clearly evidenced the optimization process

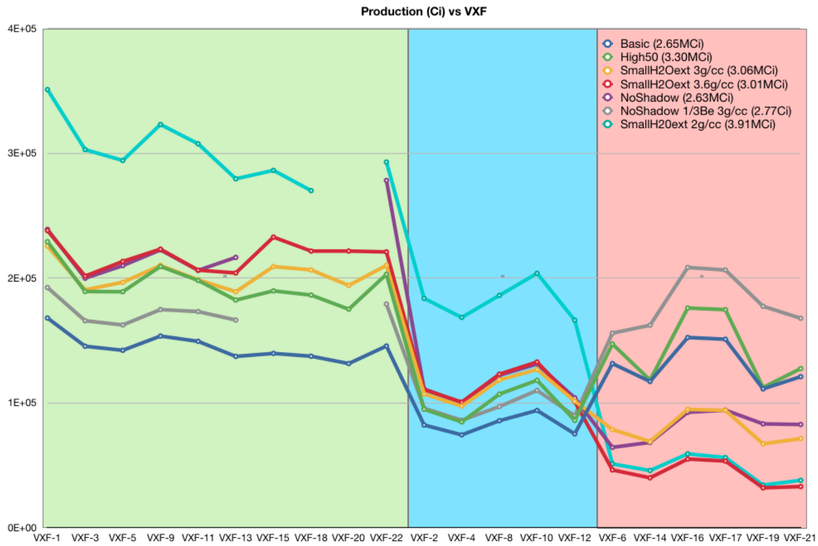

FIGURE 6.26: Total ^{51}Cr activity yield comparison for the most notable full-VXF chip scenarios simulated.

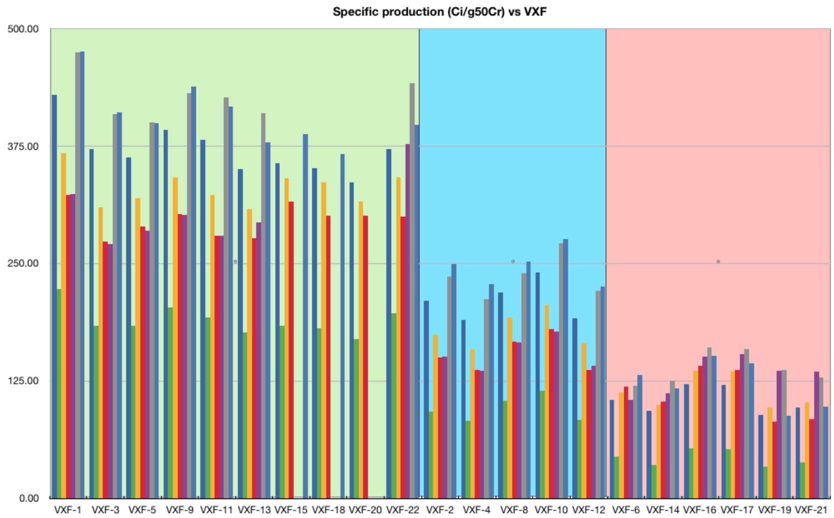

FIGURE 6.27: Specific ^{51}Cr activity yield comparison for the most notable full-VXF chip scenarios simulated.

reaching the limit with the VXFs fully filled, even when trying to optimize geometrically just by discriminating between them based on their positions.

A plotted comparison of the most remarkable full-VXF chip scenarios in terms of total and specific activity per VXF is shown in Figures 6.26 and 6.27

Other ideas, such as leaving half the VXFs filled with a semicylindrical beryllium reflector and only loading its fuel-facing side, were also considered and baselined, but not simulated due to increased interest toward pursuing a high-density approach with solid chromium elements which would more efficiently occupy the highest neutron flux areas.

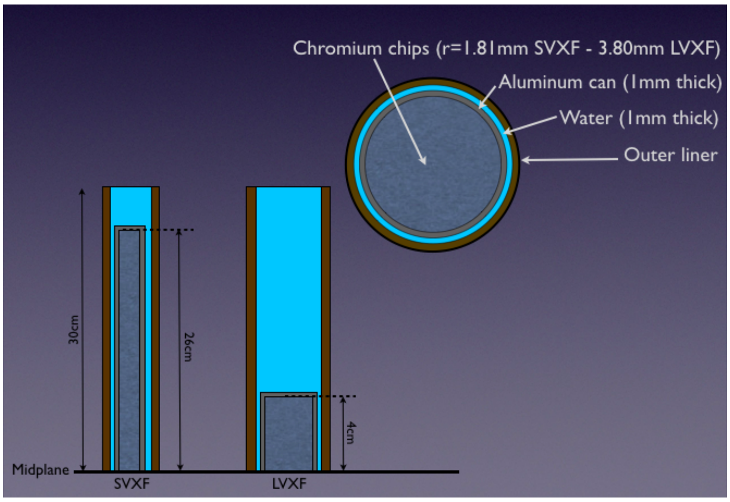

FIGURE 6.28: Illustration of a realistic container design for non-reformed chromium chips irradiation. On the left, vertical sections of the VXFs to the midplane. On the upper right, a cross-sectional view.

Chips realistic, baseline case: containers

Before moving on to more complex scenarios, a baseline optimization case was created for the case in which re-forming the chromium material would not be possible and the chips would have to be utilized as-is. This would constitute the maximal activity achievable for a technically-realistic irradiation campaign. The chips would be held in 1mm-thick aluminium cans, with 1 mm of water around them for cooling purposes, as illustrated in Figure 6.28. The cans could be engineered so to be made of a fine mesh, in order for the water to flow through the chips; however this level of detail was not modeled as it would not affect much the activation simulation. All VXFs would be utilized in this case, filling them with 3.6 g/cm^3 material to 26 cm above and below the midplane in the case of the SVXFs, and to $\pm$4 cm for the LVXFs, for an activity of:

$$A(^{51}Cr) = 3.02 \pm 0.03 \ MCi \tag{6.21}$$

or, in other words, an average specific activity of 228$\pm$3 Ci/g. Other configurations in the *"No Shadow"* arrangements or with other attempted simple optimizations yielded lower activities, establishing this value as the expectable one for a single irradiation campaign with non-reformed material in technically-feasible containers. A double-cycle irradiation with an 8-day downtime would, as always, provide a $\sim$44% activity increase to $\sim$4.34 MCi. Flux Trap 2-rod boosts were simulated specifically for this scenario and yielded a 0.22 MCi increase (single cycle; 0.32 MCi for double cycle) with average specific activity between 2600-2800 Ci/g, for a total of 3.24$\pm$0.04 MCi (4.66$\pm$0.05 MCi) for a single-(double-)cycle irradiation campaign.

Reformed material: rods

The Flux Trap experience showed the convenience of using the chromium in high-density form, shaped with a small enough thickness to avoid large self-shielding effects within it. Furthermore, operationally these shapes would be much easier to handle, in principle not necessitating containers, and offering much better heat conductivity and thermal dissipation properties both in the reactor and once assembled in the source. Techniques explored to enable this material reforming will be detailed in Section 6.3.5.

For this reason, a test run was modeled to come up with an optimal way to arrange the rods inside the VXFs, as well as their dimensions. It was determined a 0.66 cm radius would provide a maximum of around an attenuation length through the rod, thereby keeping at least 40% of the thermal neutron flux at any given location in the rod. Furthermore, the rest of the VXF not occupied by the chromium rods could be filled with beryllium reflectors, which were modeled as identical rods for simplicity in model modification. Water would be modeled in the interstitial spaces between the rods, although it is conceivable that "beryllium enclosures" could be used for insertion in the actual VXFs, if thermal considerations didn't impede it, thus slightly boosting the activity levels simulated here.

A 7-rod hexagonal close-packed (HCP) arrangement for the SVXFs was selected, with a "side" of the hexagon perpendicular to the radial direction of the reactor, and a central rod surrounded by the other 6. This configuration was tested in VXF#1 to optimize rod positions, since an orthogonal arrangement was facing almost directly (to within 4.5°) the reactor center. Specific activity results for each rod are shown in Figure 6.29.

It was clear a large regional dependence in irradiation exists between rods, with a factor of more than 2 between the highest- and lowest-activity rods. As expected, achieved activity decreases with distance to the reactor, except for the #4 rod, which has the lowest activity of all due to shielding from all other directions. This very clearly demonstrates how a full-VXF filling would be wasteful, and strategically-localized, high-density material placement is preferable. Since $\sim$>300 Ci/g are sought for the non-FT, largest-activity material in VXFs, it was decided to sacrifice rods #1, 2 and 4 because of their relative lower activity, and instead insert the aforementioned beryllium reflector "blanks". Achieved activities are shown in Figure 6.30. Depending on VXF position (i.e., for the OSVXFs), it might be preferable to also avoid using the locations closest to the neutron sink of a nearby, shadowing VXF.

LVXFs distributions would be based on a heptagonal "core" of 8 rods surrounded by 13 peripheral rods. Of course, following the previous relative specific activity distribution, it would never be wise to fill those central positions, and only selected frontal rod positions in the LVXFs would be used with chromium material; the rest being filled with beryllium blanks as before.

Vertical optimization

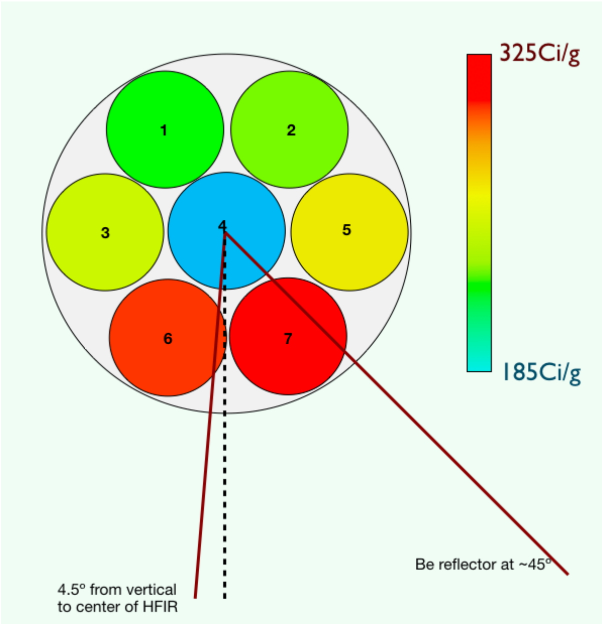

FIGURE 6.29: Illustration the VXF#1 hexagonal rod arrangement test scenario. The direction of the reactor center is shown on the left line, and the approximate location of a Large Removable Beryllium Reflector is shown on the right line –which explains the slightly specific activity levels in the seventh rod.

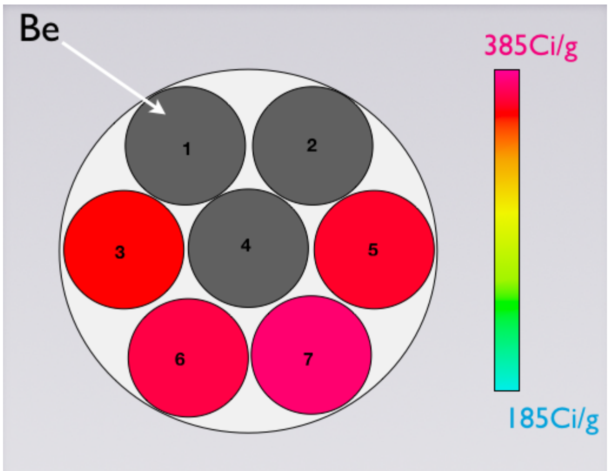

FIGURE 6.30: Illustration the VXF#1 hexagonal rod arrangement test scenario with optimized positioning and Be rod "blanks", clearly showing the resulting activity boost from replacing rods 1,2 and 4 with beryllium.

HFIR's VXF targets can be as much as 60 cm tall. After checking better optimization strategies, trying to relocate lower-activity material located on the axial upper bounds to more exposed locations in the midplane of other VXFs, it was determined (see Figure 6.31 and 6.32 for example analyses) that having as long rods as possible was preferable; for this reason, the optimized rod distribution will employ this maximum length of ± 30 cm above and below the midplane.

Optimized rod distribution model

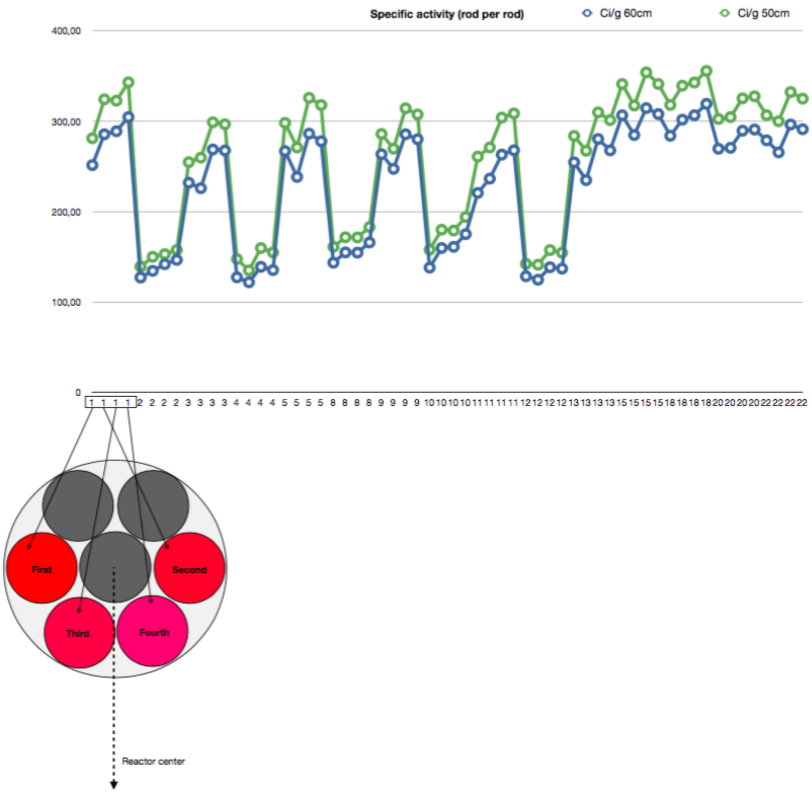

FIGURE 6.31: Specific activity yields for different rod height. This plot also highlights the large regional dependence in rod position. Largest specific activities correspond to ISVXFs, with the rod arrangement shown in the lower diagram, and lower to OSVXFs. No LVXF rod yield is shown.

A large number of rod positioning scenarios were run, to understand which locations were most regionally favorable for irradiation purposes with this type of targets. For the sake of brevity and conciseness, here we report the latest optimization achieved in 2014 before the project shifted focus. Although further activity maximization through positioning could potentially still be possible, the major effects have been worked out and optimized, and the latest simulations performed *a posteriori* by engineering personnel in ORNL yielded extremely good agreement with the above, further boosting confidence in these feasibility studies.

Positioning optimization was aided by custom-developed `Mathematica` and `Excel` geometry tools that returned the positions needed for each rod in each VXF for maximum thermal neutron flux exposure. The diagram of the VXF rod positions for this optimized scenario can be seen in Figure 6.33, containing 34.7 kg of material ($\sim$1 kg less than available for a conservative estimate; full material utilization would bring $\sim$0.5 MCi more if used in a VXF).

Single-cycle ^{51}Cr activity yields for this scenario were:

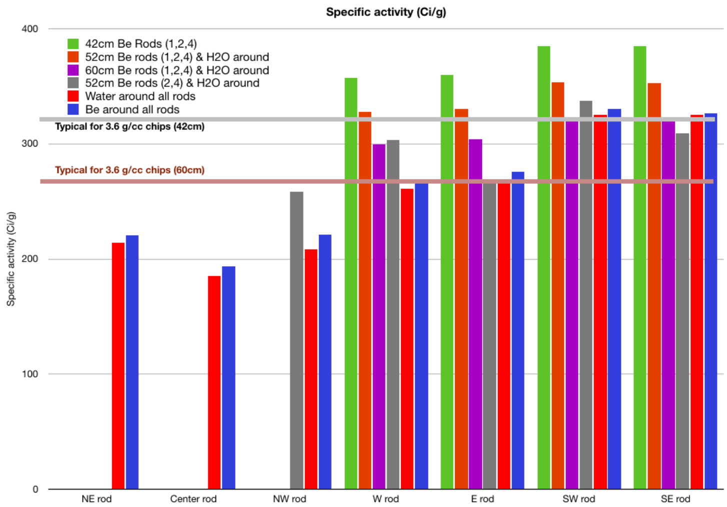

FIGURE 6.32: Specific activity yields for different rod height and material around rod positions (H_2O or ^{9}Be). Reference levels for chips at different fill levels are also shown.

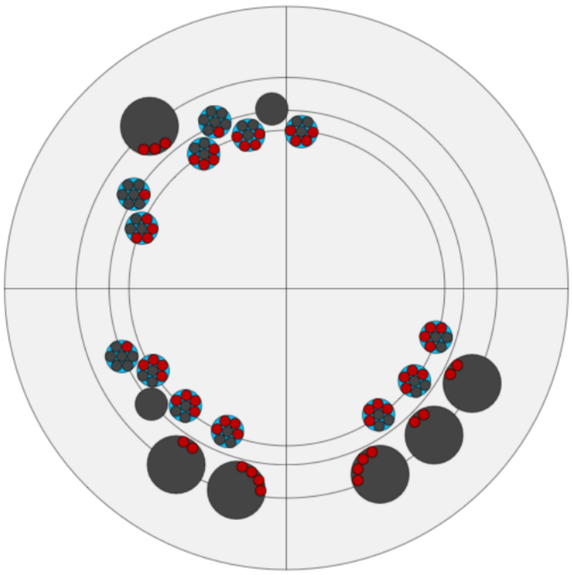

FIGURE 6.33: Geometry of the latest optimized version of the rods scheme for maximum ^{51}Cr activity yield. In red, chromium material. In grey, beryllium reflector elements in VXFs. In blue, light water. Not shown is loading in the FT.

$$\begin{aligned} A(^{51}Cr)_{VXFs} &= 3.26 \pm 0.05\ MCi \\ A(^{51}Cr)_{VXF+FT} &= 3.48 \pm 0.05\ MCi \end{aligned} \tag{6.22}$$

for the rods-alone and rods+FT boost, for a VXF-averaged specific activity of 246±5 Ci/g. An comparison graph with non-optimized, optimized and chips reference case can be seen in Figure 6.34.

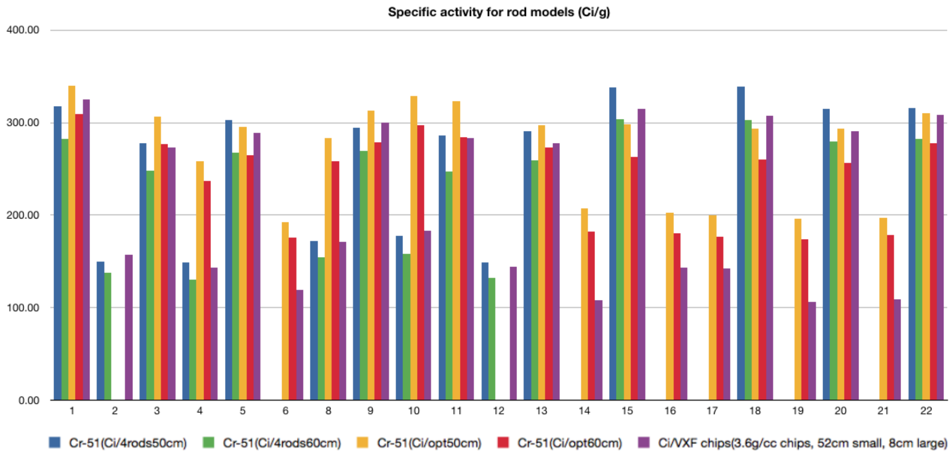

FIGURE 6.34: Tally comparison of specific activity result per VXF for long/medium-sized rods in a non-optimized (4 rods) and optimized (opt) scenario, compared to a chips full-VXF fill baseline case. Some tallies are not present for some cases (for example, no rods in VXF#12 in the optimized scenarios).

6.3.4 Temporal optimization

An important caveat toward rigorously estimating activation potential is the temporal evolution of the reactor during the irradiation cycle(s). As was specified at the beginning of Section 6.3, all the previously calculated simulations consider Middle-of-Cycle (MoC) conditions. This is fine for a rough representation of what that cycle would look like, but as can be seen in Figure 6.35, neutron fluences change by large amounts (up to 35%) with the reactor fuel burnup and control plate movement. While this change in fluence is mostly averaged out in the midplane (BoC decrease with respect to MoC is mostly cancelled out by EoC increase), VXF axial ends may see an important EoC flux increase of ∼20%. Just how critical this is for final activity can be estimated, but is better simulated in an actual scenario.

Before discussing the simulation, a few words on the control plates: as specified in Section 6.2, HFIR has control plate elements that rise or descend on the core's periphery. Each plate, additionally, has areas with larger or lower thermal neutron absorbing power. The overall effect during reactor cycle operation is a small "window" through which the majority of the flux can pass through, which increases in size until its maximum "opening angle" is reached by the end of the cycle (see Figure 6.36). While this is adjusted to account for k_{eff} management, it also provides a so-called *lighthouse* effect where the opening angle of the majority of the (thermal) neutron flux increases with cycle time –therefore increasing axial end irradiation in the VXFs, with a larger effect in the LVXFs, being the most outlying ones.

Taking into account this aspect of HFIR operation, a pseudo-time-dependent simulation was developed by dividing in 3 parts the nominal reactor cycle time of 24 days (that is, 8-day simulated runs) and implementing the control plates positions and average fuel composition for

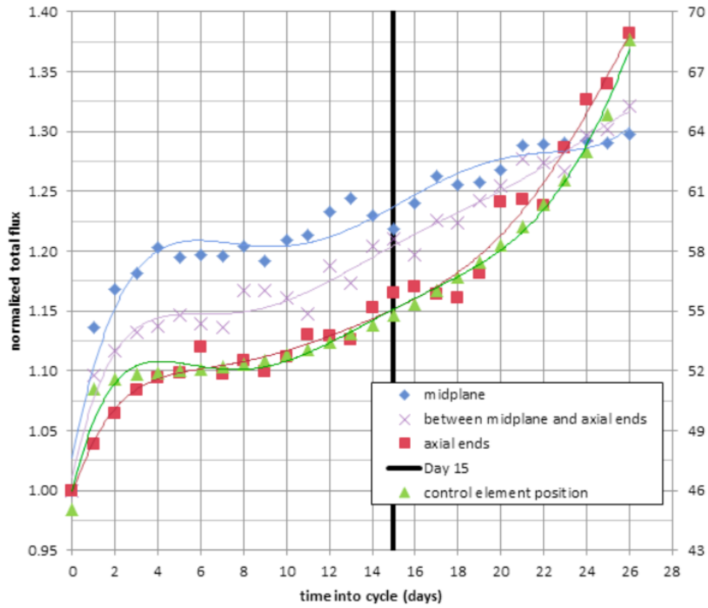

FIGURE 6.35: Typical (normalized total) fluxes evolution in different reactor position with time. Right-hand side abscissa axis shows control plate position in cm for the green triangle data series.

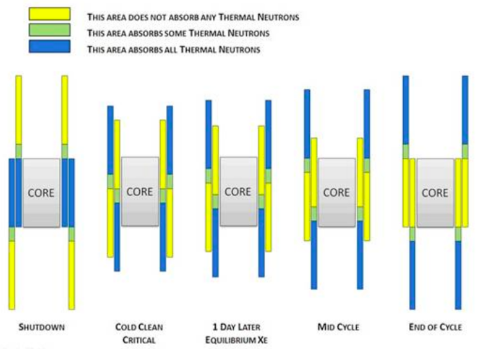

FIGURE 6.36: Illustration of control plate movement during a typical HFIR reactor cycle.

each of the three cycle conditions. The optimized 60cm-long rod scenario detailed above was used with a two-target FT loading. Achieved activities in time and location can be seen in Figure 6.37, with total activities representing a ~5% increase with respect to MoC-only conditions. Taking into account Beginning and Middle-of-Cycle ^{51}Cr decay until the end of the EoC condition for the VXFs, overall time-averaged specific activities of 55.0±1.1 Ci$_{BoC}$/g, 91±2 Ci$_{MoC}$/g, 105±2 Ci$_{EoC}$/g for the rods (251±7 Ci/g overall), and the usual 2653±27 Ci/g for the FT targets, are arrived at. Although the statistical uncertainty is higher in this case because of the shorter simulating time, and the total activity sums up all these, incurring in a larger overall uncertainty of ~6% than a single-run result, a similar order-of-magnitude effect was expected to exist in the first place from simple operational reasons, so there is some confidence this increase would be approximately the one seen here –and further exploration of these pseudo-time-dependent scenarios could be used to further reduce statistical uncertainties if needed.

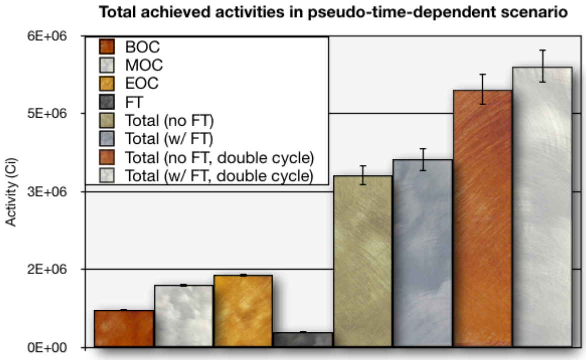

FIGURE 6.37: Tallies of total activity in different reactor temporal conditions and locations, as well as total single- and double-cycle total ^{51}Cr activity yields.

It should also be noted the option for a reduced *back-to-back* double-cycle irradiation with just 3 days downtime (as compared to the nominal 8 days) was also considered a possibility.

6.3.5 Other geometries and variants

The nominal reforming concept of turning the chipped material into cylindrical ∼30cm-long rods, or some other shapes to be discussed in what follows, requires a high-throughput, reasonably-fast process that minimizes the potential for impurity introduction in the material –which in its chipped form is within specifications of secondary radiation emission due to ppm/b contamination in the chromium.

In particular, a collaboration with the South Dakota School of Mines (SDSM) and Pacific-Northwest National Laboratory (PNNL) pursued during 2014 the definition and initial development of the reforming techniques. Although it is beyond the scope of this thesis to go into the different alternatives, compromises and options in much depth, the latest status of this project as of early 2015, when CrSOX was superseded by CeSOX in the SOX-A program (see Section 6.4) and the reforming studies were stopped, will be provided for the sake of completeness.

The chips would be melted and recast into 70 or 35 mm long rods, 12.5 mm in diameter, numbering 650 (or 1300 in the case of shorter rods). After verifying impurity content, they would be sent to Virginia Tech for inspection and finally to HFIR for irradiation. The most favorable recast method was identified as being *induction melt*: an induction field would be driven by a 465 kHz AC current, which would heat the sample by eddy current resistance. This process is well-suited for vacuum, to minimize gas mixture, and could be done in a 10^{-7} torr environment inside a vacuum bell evacuated by a clean diffusion pump. The induction coil would be water-cooled.

The chromium chips would be held in a high-temperature crucible surrounded by graphite and a heat shield, while the induction coils would surround this contraption on the outside. This crucible could serve as the mold for the recast (*cast in place* strategy) or feature a mechanical slide gate or passive plug to communicate the inside of the crucible with the casting mold once the material was melted. The passive plug strategy, by which the crucible would be sealed by a material that would melt together with the chromium, allowing the liquid to fall to the cast mold, was deemed highly preferable compared to the other two.

Although this was the latest method employed, electroforming the material in a manner similar to what was done to create the GALLEX chips, was also considered. This method could potentially bring down impurity introduction risks, but also would make it more complicated to create cylindrical rods unless a large number of "mandrels" (or rather chromium "strings" that served as cathodes) were used. For practical reasons, large (20-30 cm radius, ~60 cm high) cylindrical mandrels were expected to be used as cathodes, where electrodeposition of the chromium would take place. Machining the resulting cylindrical shell into cylindrical rods (assuming the required deposited thickness of ~12.5 mm could be reached) would be time-consuming, expensive, waste material and possibly introduce impurities. For this reason, if electroforming was employed, as the reforming strategy, it was expected other shapes could be used.

In particular, approximately-square rods (cut radially from the cylindrical shell coming from the mandrel) could be used in a similar way to cylindrical ones, with minimal volume and VXF distribution change –even allowing for more efficient packing in the most irradiated areas.

Another seriously-considered idea was to cut *lune* shapes form this mandrel form, which incidentally would allow for a near-optimal filling of the most-irradiated VXF areas while keeping a low self-shielding impact. Each lune would offer ~2.8 times the volume of a rod, with a cross-sectional area given by:

$$A_{lune} = 2\Delta + a^2 \sec^{-1}\left(\frac{2ac}{b^2 - a^2 - c^2}\right) - b^2 \sec^{-1}\left(\frac{2bc}{b^2 + c^2 - a^2}\right) \tag{6.23}$$

where $\Delta = 1/4\sqrt{(a+b+c)(b+c-a)(c+a-b)(a+b-c)}$, and a, b and c are the smallest radius, the largest radius and the center thickness, respectively. A special case of this would be a *crescent*, which is a lune where the inner curve intersects the outer at its semicircumferential point.

$$A_{crescent} = \frac{\pi R_{VXF}^2}{2} + R_{inner}\sqrt{R_{inner}^2 - R_{VXF}^2} - R_{inner}^2 \arcsin\left(\frac{R_{VXF}}{R_{inner}}\right) \tag{6.24}$$

where R_{VXF} refers to the VXF's ID, which would match the outer lune's radius (largest one), and R_{inner} refers to the inner curvature of the lune (smallest radius), which would correspond to the mandrel radius in the electroforming method (or a smaller one to increase mass performance).

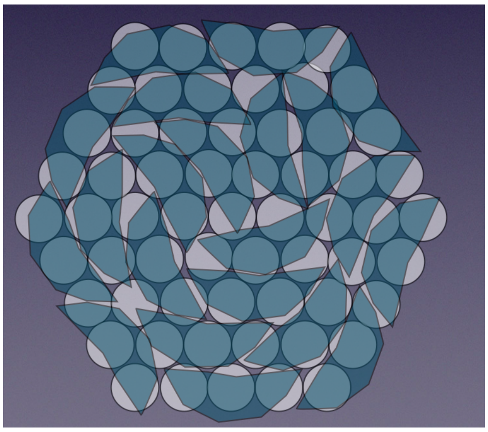

FIGURE 6.38: Illustration of a possible packing arrangement for reformed lune-shaped rods for the chromium that would contain the same material as the rods in approximately the same volume.

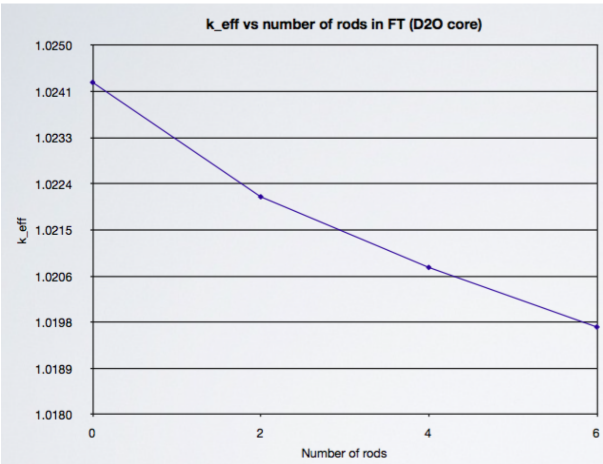

FIGURE 6.39: Variation of k_{eff} with the number of rods in the FT for a D2O core, to be compared with k_{eff}=0.99904 for an equal core geometry with no FT chromium, just in VXFs.

Packing strategies to fit the whole chromium mass in the same volume as the equivalent packing for rods were studied, an example of which can be appreciated in Figure 6.38 with generalized lunes.

If machining were to be a problem, these lunes could be straight cut from the cylindrical mandrel shell to form triangular pieces that would fill approximately the same volume as the lunes.

Another possibility that presented itself in the last stages of the currently reported feasibility studies was to run the reactor with heavy water (D_2O) instead of regular light water (H_2O), which would enhance k_{eff} (see Figure 6.39 for a quantitative study of k_{eff} vs FT loading in a D2O core) and offset the neutron flux depletion and subsequent reactor cycle lifetime diminishment that too much chromium in the FT would entail. This way, higher activities could presumably be attained.

It was found a ∼10% increase in achieved activity (up to 6 MCi in a double-cycle irradiation) could be expected from such a change, not counting the enhancement of the FT loading, which could bring activities up by an extra ∼>0.2 MCi/rod in this scenario. If D_2O loading was possible, even if only locally, it was shown it could open the door to >6.5-7 MCi CrSOX sources.

A summary of all estimated activities reported above can be found in Appendix D.

6.4 CeSOX and perspectives

The re-arrangement of the SOX program schedules due to the presumed faster availability of the ^{144}Ce-^{144}Pr source with high enough activity to allow for a similar sensitivity in the region of interest than that possible with the ^{51}Cr source, combined with the aforementioned stall in CrSOX source fabrication after the feasibility studies in the preceding section, meant that from early 2015 the organizational and regulatory efforts were directed to start this program first instead. Lack of complex backgrounds in the antineutrino channel also offered an advantage, and in principle the signal would not disrupt solar observations, which was desired given the *NuSol* perspectives on wideband, precision spectroscopy. The longer campaign also allowed for more calorimetry techniques to be implemented.

While the calorimeter and CR1-pit rail insertion facilities were largely common to both sources, the radiation and thermal environment of the source is quite different. Additionally, the Centre d'Études Atomiques (CEA) team in Saclay (France), being the most involved with the source procurement, decided to perform an additional, complementary calorimeter for redundancy (see Figure 6.40), to reduce systematics –this second calorimeter would not be deployable in the pit, and therefore not be subject to tight clearance requirements. It would be kept in CR1, and the source would be inserted at least 3 times (at arrival, mid-campaign and at the end of CeSOX). Continuous precision calorimetry with the CrSOX-style deployable calorimeter was no longer possible due to the slightly larger source shielding. However, it is expected a coarse continuous calorimetry (with no vacuum pumped in the vessel) will still be possible. Full-up calorimetry will be possible with both calorimeters, but just during the times the source will be out in CR1.

CeSOX's active material will be in the form of cerium-144 oxide ($^{144}CeO_2$) compressed powder (ρ=[2.5,5] g/cm^3), obtained from reprocessing of spent nuclear fuel (SNF). This SNF, containing 5.5% (3.7%) ^{144}Ce as U (Pu) fission products, will be provided, handled and processed by the Mayak Corporation in Chelyabinsk Oblast, Russia, following a complex separation and purification multi-step process[196][189] based on separation columns, unique to the RT-1 radiochemical plant there. Impurities will be controlled at the $\sim 10^{-5}$ Bq/Bq(^{144}Ce+Pr), or to the $\sim \mu$g/g(CeO_2) level, for a total contracted source activity at delivery of 3.7-5.5 PBq, engineered so that the total duration of the CeSOX program remains unaltered: that is, a later delivery

FIGURE 6.40: *CEA/Saclay* calorimeter in 2016.

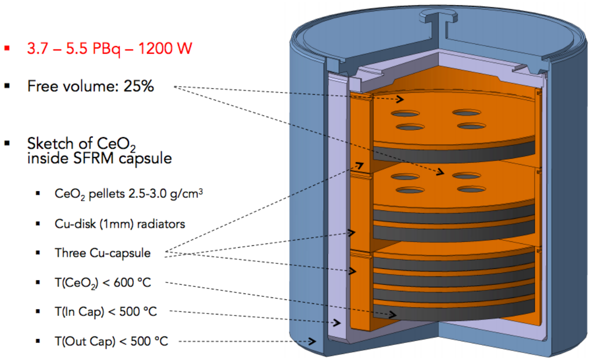

FIGURE 6.41: Schematic view of the preliminary design concept for the CeSOX antineutrino generator (CeANG), or source "core", in mid-2016.

would imply a higher source activity. The source preliminary design as of this writing is shown in Figure 6.41.

The radioactive β decay of ^{144}Ce ($\tau_{1/2}$=284 days, Q=318 keV see Figure 6.42), apart from causing a greater amount of γ emission, has the added complication that its decay daughter ^{144}Pr has a very short half-life ($\tau_{1/2}$=17 min, Q=2.996 MeV), β-decaying to pseudo-stable ($\tau_{1/2} \approx 2.4{\cdot}10^{15}$ years) ^{144}Nd, emitting harder-to-shield γs of up to 2.86 MeV. This double decay causes an overlap of the $\overline{\nu}_e$ β spectrum, producing antineutrinos over a broad spectrum until its Q-value of almost 3 MeV (the actual cutoff energy for Borexino is 1.8 MeV due to the IBD reaction threshold; therefore, only ^{144}Pr-emitted $\overline{\nu}_e$ will be observed). The ^{144}Pr decay is a $0^- \to 0^+$ first non-unique forbidden transition, and the shape factor is poorly defined. This is critical to CeSOX's sensitivity, and could very negatively impact it –therefore, an effort to produce the most sensitive spectral determination of the β decay shape is ongoing as part of the program both within the German TUM and French CEA teams.

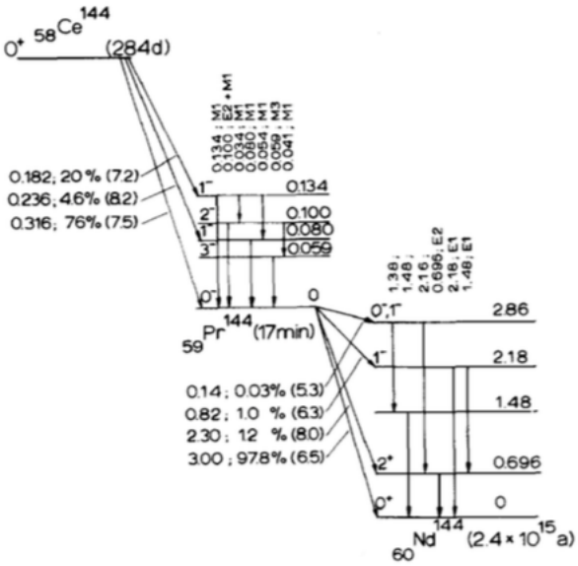

FIGURE 6.42: ^{144}Ce-^{144}Pr decay scheme.

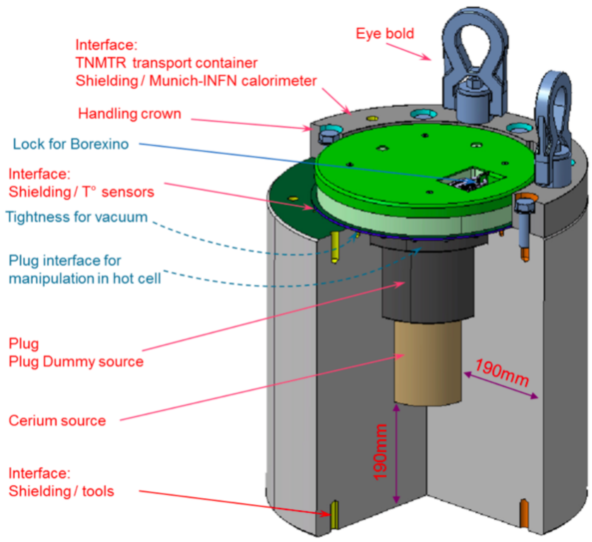

FIGURE 6.43: CeSOX W shield design (annotated).

The shielding will take a similar shape to CrSOX's, but adapted to the smaller physical size of the CeANG and the requirement for more attenuation power from the source's emission: 190 mm of W separate the exterior of the source container from the outside of the shield (see Figure 6.43). A TN-MTR transportation container will be used to move the source between its production site in Mayak to St Petersburg Harbor, where it will board a freight ship to Le Havre (France), to be transported by road first to Saclay (for preliminary measurements) and Cadarache –to then proceed to Italy, making several stops along the way until its final delivery to LNGS.

The latest analysis for CeSOX's sensitivity to the updated remaining phase space (95% c.l., from[83]) incorporates show the different coverage potentials for each analysis and confidence

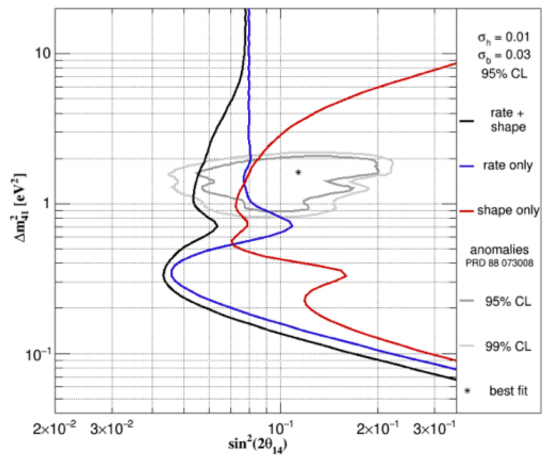

FIGURE 6.44: Sensitivity plots for the rate analysis, the oscillometry alone, and the combined rate+shape analyses (left), as well as the confidence levels for R+S (right)[197].

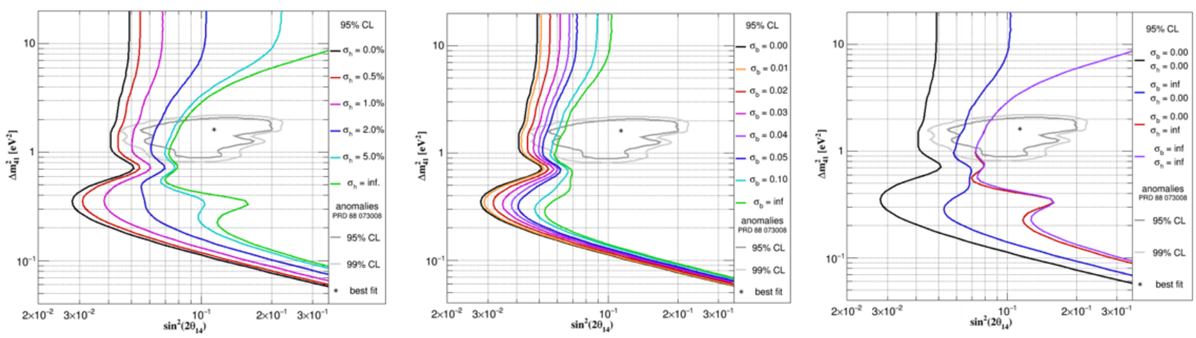

FIGURE 6.45: Sensitivity plots for the main sources of uncertainty: the activity determination accuracy (left), the $\overline{\nu}$ spectral shape (center), and their combined effect (right)[197].

level (Figure 6.44) and the effects of spectral shape and activity determination (and both, see Figure 6.45).

As of this writing, it is expected the source would be made available NET December 2017, and more possibly toward March 2018, to be deployed in Borexino's pit between 1Q and 2Q'18, for a ∼1.5 year measurement campaign.

Chapter 7

Conclusions and perspectives

The following chapter intends to amalgamate the four main parts of this dissertation into the overarching aspects and perspectives that unify them, with the intent of bringing together its core topics that are inscribed in the overall strategy to perform a precision, wideband spectroscopic measurement of the solar neutrino components. This would be achieved both by reducing the uncertainty in those whose direct measurement has been performed in the past, as well as by tightening the allowed values of those for which only upper limits exist: in particular, the CNO component. Having a Compton-scattered spectrum in Borexino, the detection of this component's signal is hindered by the intrinsic backgrounds in the detector's scintillator: in particular, ^{210}Bi, whose levels (intrinsically convolved with ^{210}Po, which is out of equilibrium in the IV, albeit with ever-reducing concentration) have shown to be erratic and difficult to precisely constrain.

In that sense, this work concentrates on **i)** the thermal stabilization of Borexino as a critical component for precisely determining ^{210}Po's concentration in the Inner Volume of the detector –in particular, in its Fiducial Volume– and, consequently, the ^{210}Bi levels in the aforementioned regions, which is a *si ne qua non* condition for the precision determination of the solar neutrino components lying in the energy region of its decay ($\sim$[250,450] p.e.). This was achieved through the deployment, calibration and operation of Borexino's Thermal Monitoring and Management System (BTMMS, Chapter 3). Next, **ii)** Computational Fluid Dynamics (CFD) thermo- and fluidodynamical simulations were developed in order to glean insight into the behavior of Borexino's ID fluid environment, hypothesized to directly influence the aforementioned background levels, driven by subtle, yet measurable, thermal excursions and fluctuations in the fluid stratification present inside Borexino (Chapter 4).

Additionally, **iii)** improved and novel calibration techniques were developed and upgraded, aiming for a new calibration campaign foreseen for 2017 (Chapter 5), which would involve the deployment of several low-activity radioactive sources inside Borexino's ID, capitalizing on the first (and only, for now) such campaign which took place early in the data-taking life of the detector (2009-10). This renewed campaign would greatly benefit both the upcoming short-baseline source-driven study of anomalous oscillations (SOX), as well as the wideband solar neutrino spectroscopy analysis. Finally, **iv)** the feasibility of the creation of a ~6 MCi ν_e ^{51}Cr source which could be inserted in the SOX/Icarus pit under Borexino as part of the SOX-A program (CrSOX) was explored, as an alternative to the CeSOX $\overline{\nu}_e$ program –itself under the final stages of development at the moment, and expected to begin data-taking operations NET March 2018– as an optimal low-background compact source intended for low-baseline oscillometry studies of the allowed phase space for neutrino anomalies that has so far resisted conclusive investigation.

These topics seamlessly concatenate with each other in Borexino's short- and mid-term future life and constitute the best part of its scientific program for the coming years.

7.1 Borexino's thermal environment management, control and modelization

The deployment of the LTPS sensor suite has provided a $\mathcal{O}(0.01°C)$-level precision in the latitudinal determination of the thermal environment in the main accessible areas of the detector (i.e. the WT's exterior water layer, the water immediately surrounding the ID around the SSS and the OB) and has proven to constitute a critical tool in executive decisions aiming to stabilize it for background stability purposes. Its three *Phases* have organically built upon the first, prototypical system, to constitute the complex monitoring reference asset it is today. Its data during the deployment of the TIS insulation layers throughout 2015 unequivocally showed the increase in top-bottom gradient and the smoothing-out of environmental thermal upsets transmitting inside the detector to have a direct and positive impact toward the stabilization and reduction of the ^{210}Po background levels that motivated its installation.

The data provided by the LTPS served as the basis for the development of the benchmarking CFD model that demonstrated the accuracy of the technique for, at least, $\mathcal{O}(0.1°\mathrm{C})$ thermal transport modeling in a fully convective bi-dimensional case, which set the stage for more focused studies on the fluidodynamics induced by said environment, always founded in realistic data.

With the completion of the TIS in mid-2016, the upcoming startup of the AGSS top heating system and the asymptotic behavior of the lowermost WT temperatures (see Figure 3.33), it is expected the stratification of the fluids inside Borexino will be the most stable ever, separated by one of the largest gradients achieved since it was filled. The actual effect of this stratification stability on fluidodynamical (and hence, background) stability on the FV is an open question, given the horizontal currents observed in the CFD simulations of the SSS and/or IV or, on the other hand, the bottom recirculation pattern observed in those same simulations, possibly caused by the cooldown of that part of the detector. This feature has been a constant in the ^{210}Po monitoring plots since approximately the time the TIS was fully deployed (see Figure 7.1).

Indeed, that cooling is the differentiating factor that is probably driving the recirculation observed at the bottom, and *not* at the topologically-equivalent top, given heating there has been neither as pervasive nor as large in magnitude during the insulated phase. Conversely, as can be seen in Figure 7.1, the rapid heating of the top between the uninsulated and transient phases will create the same recirculation effect as seen for the cooling at the bottom: the rising fluid will be given a horizontal component due to the spherical geometry of the IV boundary, and the horizontal currents that need minimal driving energy will be enhanced, bringing down fluid from the top. For this reason, AGSS activation was encouraged to happen at the warmest period of the year, so that the top heating would be minimal, and would just be kept constant while the rest of the detector cooled with the advent of winter. Conversely, the cooling of the bottom part of the IV generates a mirror image of the phenomenon just described: a horizontal component is imparted by the spherical geometry of the vessel as the peripheral cooler liquid sinks, which enhances the minimal-energy horizontal currents already in place.

This recirculation has been reliably shown to be fed from relatively large ($\mathcal{O}(10^{-4})$ m/s) surface currents that are then given a horizontal component. The spherical geometry of the IV, paired with the cooling, is expected to be the driver of this behavior, that exacerbates the migration of less-radiopure scintillator from the peripheral areas of the IV toward the bottom of the FV. A large-scale convective motion, similar to that seen for a cylindrical geometry, is expected to be of secondary importance for these reasons.

A more precise determination of the role of the horizontal currents observed in the models in the real physical system will warrant further study in the near future as enhanced models are developed to study that particular phenomenon. Indeed, with the advent of the stably-stratified condition in Borexino (foreseeably in early 2017), horizontal currents spanning the length of the IV triggered by small asymmetrical (North vs South) temperature upsets on the exterior air, rapidly transmitting toward the interior of the detector (as demonstrated both through CFD and empirically with LTPS Phase I.a+b data), could be the main fluidodynamical effect impacting background level stability throughout the FV. In this sense, after the applicability and stability of the CFD strategy has been proven and shown to provide important insights into the ^{210}Po movements in past conditions, short-term priorities dictate the preferential need to utilize tools –such as the particle tracking utility available in FLUENT– which may allow forecasting future behaviors, or the influence future directives impacting temperature evolution will have on background stability.

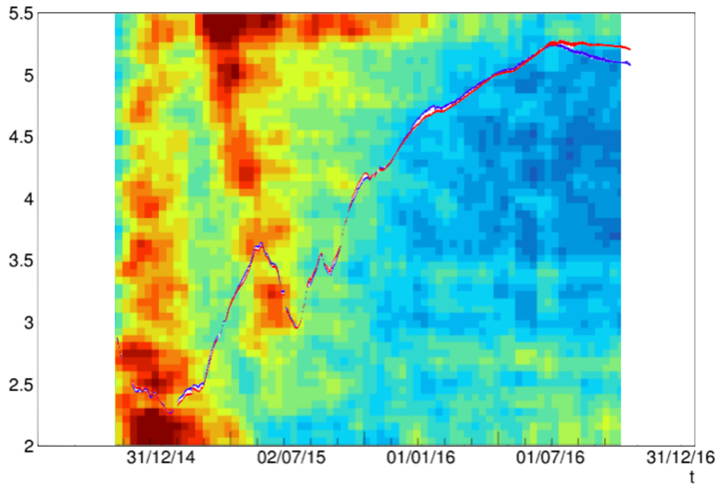

FIGURE 7.1: Composite figure of the ^{210}Po levels evolution with time as measured with the "cubes" analysis and the corresponding top-bottom gradient in the OB as measured by the Phase I.a probes. A correlation between increasing gradient and decreasing backgrounds cannot be established, although a clear upward-surging peak appears at the lowest gradient due to the phenomenon explained in the text. The falling plume of background coincident with the increase in gradient is seen in Figure 3.34 to coincide with a rapid increase in top temperature, with rising or stable bottom temperatures. The bottom recirculation present since late 2015 is expected to be caused by the bottom cooling paired with the stable stratification favoring horizontal currents, as explained in the text.

Despite offering a clear correlation between stable stratification with historically-maximized top-bottom gradient and background stability, based on the empirical data seen above and the results of the CFD analysis, establishing a precise, quantitative correlation between the level and nature of gradient and thermal upset stability in Borexino's ID with ^{210}Po-^{210}Bi levels is not possible, at least at this stage of the studies. It is however possible to perform a simple prediction on the amount of data that would need to be accumulated with approximately the current background fluctuation behavior and levels, in order to reach a certain uncertainty threshold in the ^{210}Bi level measurement. Moreover, given the "recirculation" at the bottom of the FV during the insulated phase would unnecessarily worsen the precision on determining this background level's uncertainty, it would conceivably be advisable to tailor a "restricted" FV which avoids that area, at least for the extremely sensitive CNO analysis, in spite of the associated loss of statistics that would entail. In that sense, a sensitivity study was recently performed (see Figure7.2) in which the amount of data-taking under the present conditions ($\sim A$=60 cpd/100 tonnes and B=20 cpd/100 tonnes), assuming no large deviations from those levels, is judged –for different target masses– with respect to its potential to enable reaching lower ^{210}Bi rate uncertainties.

Considering the full FV of $\sim$86 m^3, $\sim$200 days of data at the current levels would bring the uncertainty down under 10%. It is interesting to note that, unless severely reducing the FV to less than $\sim$30 m^3, the amount of further data required to reach that uncertainty level

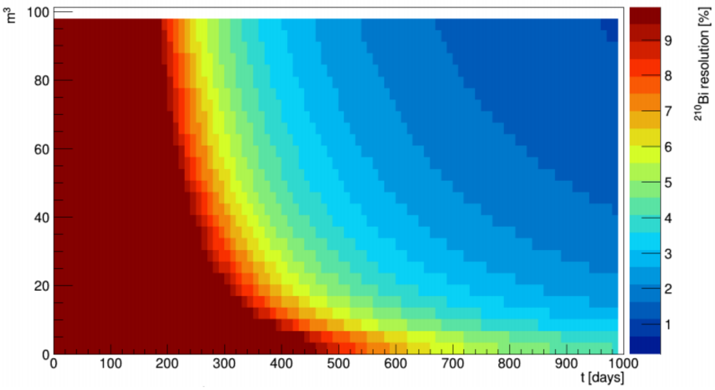

FIGURE 7.2: Toy-MC sensitivity analysis of fiducial exposure (left axis, m^3) and consequent expected ^{210}Bi term resolution (right colormap (%)) according to the number of days of accumulated statistics. An out-of-equilibrium source term A of 60 cpd/100 tonnes and a "pedestal" term of ^{210}Bi of 20 cpd/100 tonnes were used as input, as a conservative estimate of the realistic levels as of this writing. Figure courtesy of Nicola Rossi.

does not greatly vary. It can be then expected, if temperature stability is maintained and the strongest large-scale streaming horizontal currents spanning the length of the vessel can be kept restricted to the polar areas, enough data to reach these reduced levels of ^{210}Bi uncertainty can be accumulated in the near future, and certainly before the start of the CeSOX program. It should be noted that part of this dataset has already been acquired in the last few months. The 10%-level is often quoted as the "magic" number because, as we shall see in the coming paragraphs, it determines the threshold under which sensitivity to CNO is not greatly improved upon further reductions.

Correlation studies have been performed through the MonteCarlo package `g4bx2` by M. Agostini, S. Marcocci and others, in order to understand the role that the determination of each global fit component has on that of others, as well as the statistics-imposed sensitivity limits. Spectral fits from 140-1400 p.e. are performed with multiple realizations of Borexino's foreseen data products by sampling the MC's pdfs. Best fit values are determined through the likelihood ratio approach and a binning of 5, with all parameters free by default. For illustrative purposes, a 75.5 tonne FV was selected, with 1000 days of data. No multivariate fit is employed and the luminosity constraint imposed from ^{7}Be on *pp* and, consequently, *pep* rates is not taken into account –all these factors would improve the fit's sensitivity. On the other hand, only TFC ^{11}C discrimination is employed, but no other systematics or cuts efficiencies are taken into account, which will inevitably imply a complementary worsening of the sensitivity. Therefore, roughly speaking, the sensitivity and discovery potential of these studies should be similar to reality's, if no systematics are left unaccounted for.

Considering a high-metallicity countrate of 5 cpd/100 tonnes for CNO, and a bismuth uncertainty constrained to 10%, the plot in Figure 7.3 is obtained. These types of plot show, in the red/black panels, the different components of the fit. The black-dotted curve shows the countrate introduced in the MC run for that component, while the red curve shows the reconstructed value for that countrate. Some components (see external background at 2 or CNO/^{85}Kr at 0, for example) are restricted to a threshold level under/over which the fit is forbidden to go, which usually results in the deviation of the reconstructed countrate curve's shape from a Gaussian profile. If the black-dotted curve (injected value) is not centered over the red curve (fit-reconstructed values), the fit is showing a bias –conversely, if it is, the fit is working well. If the distribution is multiple-peaked or flat, the fit shows poor/no sensitivity to that component, respectively (see Figure 7.4).

The matrix of blue-to-red plots shows the correlation between each component of the fit and the others. A diagonal contour with positive slope indicates a direct correlation, while one with negative slope indicates an anticorrelation. A uniform circular contour indicates no correlation between those particular two fit components. Other shapes, such as the double-contour structure seen in Figure 7.4's ^{85}Kr-^{210}Bi insert, shows a weak anticorrelation with no central preferred value, for instance. It is clear from such plots that a properly-constrained ^{210}Bi level avoids the anticorrelation with CNO. The large anticorrelation between CNO and *pep* fluxes would be alleviated by the aforementioned solar luminosity constraint.

These correlation values then impose the "discovery power", or sensitivity, to a signal measurement (specific signal hypothesis, H_1) or to a null-hypothesis refusal (H_0, shown in Figure 7.5).

7.2 Borexino's second calibration campaign, SOX perspectives and future steps

The Borexino calibration system has seen a major improvement and refurbishment effort as described in the present work, which intends to reduce the largest overall systematic uncertainty present in the detector at the present time: the FV determination (and, relatedly, the determination of the vessel shape). The new IRED Source Location System aims to better localize the inserted calibration sources in order to mitigate this uncertainty, and the foreseen deployment of relatively large activity sources of every kind of interest to Borexino's sensitivity will map out in more detail than ever before the detector's response –including those with stringent quenching requirements, such as the ^{222}Rn sources whose quenching-free fabrication has reliably been demonstrated.

Moreover, the new requirements imposed by SOX-A of more-finely mapping peripheral areas close to the vessel will also bring a more thorough understanding of the detector response at large radii, with good regional sensitivity. This will also be crucial for regional correction factors such as the ones in development for the ^{210}Po "cubes" analysis, where the position of the polonium peak for each of the regional subvolumes is of utmost importance to achieve a precision

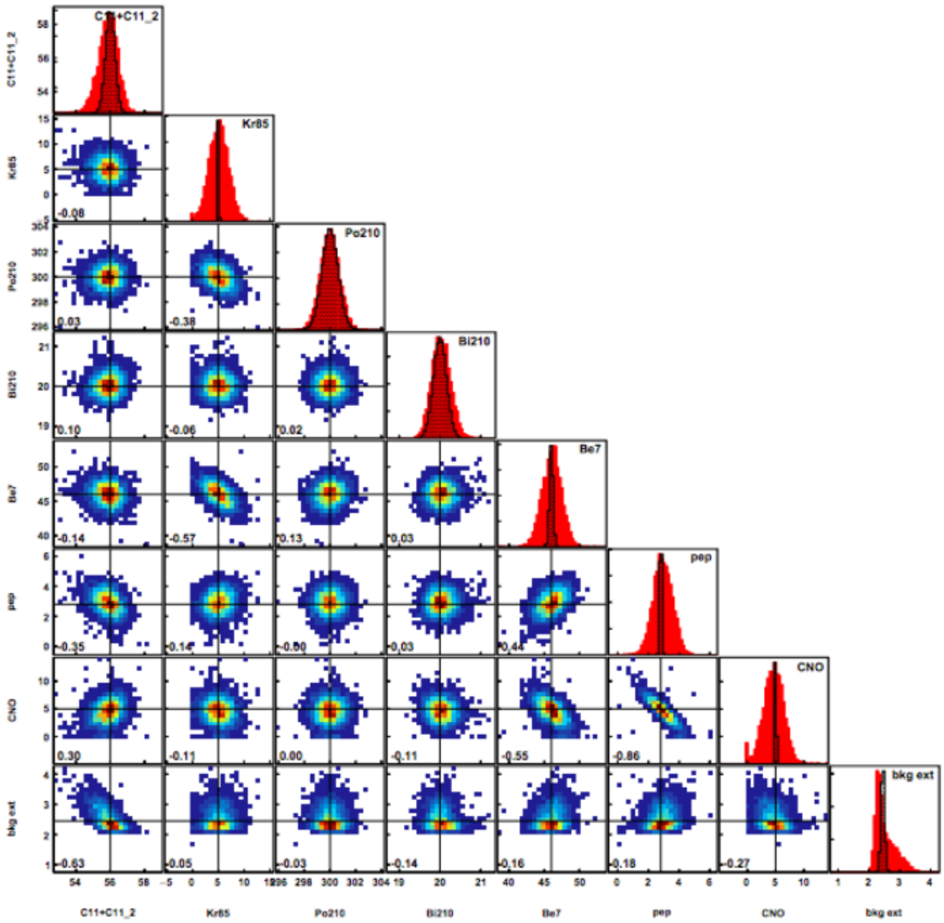

FIGURE 7.3: Correlation plot for 1000 days of Phase 2-level statistics at a "true" MC 20 cpd/100 tons ^{210}Bi rate and high-metallicity 5 cpd/100 tonnes CNO rate, with a 10% uncertainty in the constraint of the "true" MC bismuth level. Note there is a slight tendency of the fit to undershoot the "true" MC value for CNO, then railing against the lowest threshold limit (0 cpd/100 tonnes) imposed on the fit parameter.

determination of very low background countrates with minimized uncertainty. It is obvious the ramifications such studies would have for the CNO sensitivity in particular, and for the solar programs in general. Moreover, a more detailed high-statistics neutron response and the possible first deployment of β^+ sources will greatly improve the antineutrino analysis beyond CeSOX's needs.

Although the new calibration campaign's hardware is basically ready for operations, the unprecedented and extremely delicate background levels achieved during this latter part of Phase 2 data, together with its improvement by the BTMMS's recent deployment finalization, have repeatedly delayed their start in an effort to acquire ever-improving statistics during this unique data-taking period. Indeed, changes worsening by a lot the detector condition could have prompted a decision to calibrate as swiftly as possible, with the possibility to improve the detector's knowledge in the aspects described above, as well as accounting for the many changes (including trigger changeout, electronics aging and PMT deathrate) that, while believed to

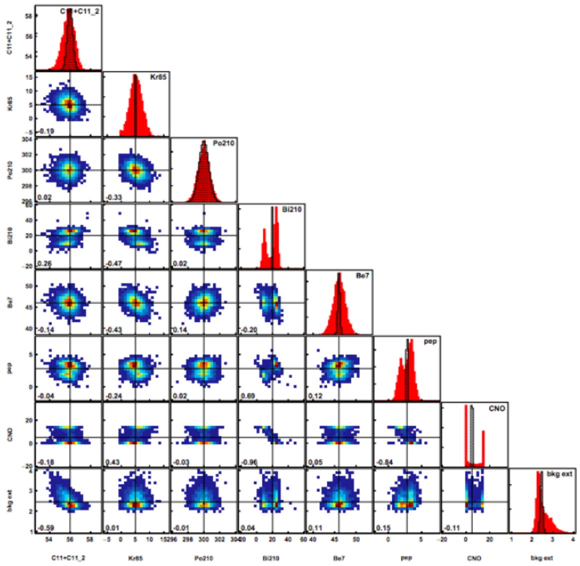

FIGURE 7.4: Correlation plot for 1000 days of Phase 2-level statistics at a "true" MC 20 cpd/100 tons ^{210}Bi rate and high-metallicity 5 cpd/100 tonnes CNO rate, with an unconstrained uncertainty on the "true" MC bismuth level. Note there is absolutely no sensitivity to CNO levels that way (the double peak structure is the fit railing against the upper and lower threshold values imposed in the parameter: 0 and 15 cpd/100 tonnes) and a large spread in the *pep* rate. ^{210}Bi reconstructs at two most-frequent values significantly differing from the "true" injected value.

be sufficiently well-modeled by the `g4bx2` MC, would benefit from the clear, empirically-based "ground truth" provided by the new calibrations. However, this condition never presented itself, and a decision to calibrate would entail the inevitable possibility to irreversibly introduce minute quantities of long-lived contaminants –and this possibility could be larger than for the 2009-10 campaign, given the background levels now are so much lower than then.

The immediate needs of the solar program for wideband, global precision neutrino spectroscopy are adequately covered by good detector knowledge accumulated during its almost 10 years of operation (to be celebrated in mid-2017) as well as the advanced status of the MC package –but at least a neutron calibration at large radii in the bottom of the IV is needed for SOX, in order to avoid losing most of the statistics from the source. In that sense, every centimeter gained for FV toward the IV surface represents a large increase in available data from the ^{144}Ce-^{144}Pr source that would enable to more reliably chart the anomalies' phase space. For that reason, and having the expected start of the CeSOX program in March 2018 in sight, the calibration system will foreseeably be in operation during 2017.

CeSOX will be in principle compatible with solar neutrino studies, given its signal will be purely composed of $\overline{\nu}$s –as opposed to CrSOX, which nevertheless would offer a cleaner signal with a much easier-to-interpret spectrum and less backgrounds. For this reason, and based on the feasibility studies to generate a $\sim$>6 MCi ^{51}Cr source in a high-thermal-neutron-flux reactor such as ORNL's HFIR that were developed as part of the present dissertation, the possibility

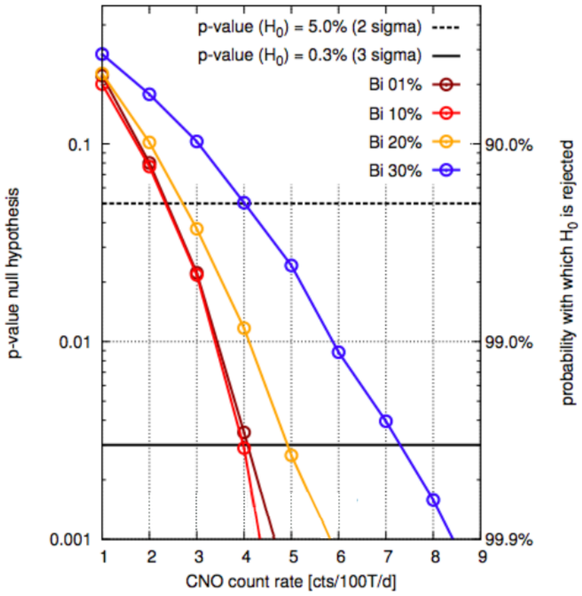

FIGURE 7.5: Discovery potential plot for the 1000 days of the MC-simulated Phase 2-level statistics toward CNO null hypothesis rejection, for different constraints in the ^{210}Bi rate, depending on the actual (as-of-yet unknown) CNO rate in Borexino, from 1 to 9 cpd/100 tonnes. As indicatd, 2σ level is evidenced by the dashed horizontal line, while 3σ is the solid one. Preliminary plot courtesy of M. Agostini.

exists, if results from the cerium source warrant it, to proceed to the fullest with the SOX-A program utilizing the existing infrastructure and calorimeter devices already in place for CeSOX, which would require minimal adaptations.

With Borexino acquiring its best dataset yet, and a record-setting stabilized detector condition, its continued operations have been confirmed until at least after the completion of the nominal CeSOX DAq period (~2020), also taking into account foreseen PMT coverage degradation –but only time will tell the true extent of its physics program in the years to come.

Appendix A

^{222}Rn source loading procedure

1. **Operational sparging and line cleaning**

   a) Open UHPN$_2$ and UPHN$_2$ sparging valve $V1$ slightly (with $V0$ (and $V0_{bis}$ if appropriate) open and bottles set) to initiate scintillator bubbling. Verify bubbling present without liquid splashing in the flask.

   b) Open valves for lines to be cleaned at the same time: V_{flux} (coarse), $V2$, $V4$, $V7$ and $V8$, $V9$[1].

   c) Verify RN-1025 needle valves are fully open.

   d) Close $V7$, $V8$ and $V9$. Open $V6$ to purge RN-1025 for a few minutes.

   e) Leave overpressure in RN-1025 by closing outlet $V6$ before closing inlet $V6$.

   f) Perform alternative vacuum/flush cycles by evacuating the panel and vial lines with the pump, then flushing with UHPN$_2$:

      i Verify $V6$, $V3$, $V9$ and V_{exh} are closed.

      ii Close V_{flux} (coarse and fine) if open.

      iii Initiate the pump and open its vacuum port if closed.

      iv Close the pump's vacuum port, open V_{flux} (coarse) to repressurize.

      v Open V_{exh} to flush.

      vi Iterate as needed (at least 5 times, with overnight flushing, when first time using the system in a while).

   g) Close all panel valves.

2. **Radon loading (no scintillator)**

[1]These last valves ($V8$ and $V9$) will push scintillator back into the flask and a bit into the vial, if no line purging was performed after the completion of a previous source.

a) Prepare beaker with ∼5-cm deep liquid nitrogen (LN2).

b) Open $V4$, $V5$ and V_{exh}.

c) Open $V2$ and V_{flux} through desired fluxmeter (coarse or fine).

d) Close $V4$, open $V6$ and let the RN-1025 flux stabilize.

e) Pull vial adapter needle close to the bottom of the vial (∼1-2 mm separation) by slightly loosening top O-ring fitting (do not let overpressure escape). Re-adjust O-ring fitting.

f) Immerse vial in LN2 until close to the beaker's bottom, without actually touching it.

g) Open $V6$, close $V4$.

h) Open $V7$, close $V5$.

i) Open $V8$ – **Start of radon deposition**.

j) Leave radon loaded UHPN_2 flux until calculated time for deposition has elapsed.

k) Close $V6$ and open $V4$.

l) Close $V7$ and $V8$, open $V5$, verify V_{exh} is open.

3. **Scintillator filling**

a) Retract vial adapter needle to top part of the spherical ampoule for scintillator filling by slightly loosening top O-ring fitting (do not let overpressure escape). Re-adjust O-ring fitting.

b) Pull vacuum on vial by verifying V_{exh} closed, closing $V4$; then opening pump's vacuum port, $V3$, $V5$ and $V7$.

c) Place vial out of LN2 bath.

d) Close pump's vacuum port and all panel valves except $V2$.

e) Open $V9$ (scintillator drawing line) FULLY and close immediately without rushing[2].

f) Pump vacuum and flush all the panel up to V_{exh} with UHPN_2 through V_{flux} (coarse), keeping $V7$ and $V6$ closed, by alternating $V2$ open while $V3$ closed, and viceversa.

g) Finish cycle in overpressure ($V3$ closed while $V2$ open) and close $V2$.

h) **Needle cleaning, pay attention to $V7$ OUT valve**: Re-open $V2$, then open $V7$ **OUTFLOW** (its line is the one coming out the side of the sleeve surrounding the vial filling needle).

i) Open $V9$ to force the remaining scintillator back into the flask. This step can be done near-simultaneously with the opening of $V7$ OUT.

[2]From initiation of valve opening to closure, ∼1-1.5 seconds should have elapsed. This should be enough to fill ∼2/3 of the ampoule without incurring in foaming, which would make it difficult to estimate the actual filling level. With thermal expansion and a few droplets that may fall during the next steps, this amount should be everything that's needed

j) Close $V7$, open V_{exh} and set UHPN_2 flow to 2-3 L/min.

k) Close V_{exh}, open $V7$ IN.

l) Open $V8$, open $V7$ OUT.

m) Retract vial adapter needle to fire-sealing position (above neck constriction) for freezing by slightly loosening top O-ring fitting (overpressure can slightly escape).

n) Re-adjust O-ring fitting and close all panel valves.

4. **Final steps and sealing**

a) Immerse filled vial in LN2 verifying the filling needle is above fire-sealing neck constriction.

b) Pull vacuum by verifying V_{exh} closed, then opening pump vacuum port, $V3$, $V5$, $V7$ IN and $V8$. Wait a few seconds.

c) Close all valves.

d) Prepare propane sealer torch and verify correct flame setting, strength and propane tank has adequate amount of fuel.

e) Wear head mask and cryo gloves.

f) Pull vial out of LN2 bath, doff cryo gloves.

g) Apply flame to neck constriction in as homogeneous a way as possible, while lightly holding the vial's neck just over the ampoule head with the other hand. Try to soften the glass by the same amount on every side around the constriction, while lightly twisting the vial back and forth once it gets soft enough. Eventually the neck space will collapse on itself: keep applying the flame homogeneously and start twisting the neck by a larger amount while very lightly pulling away from the upper remains of the neck. When the glass link is about to separate, twist the vial on its axis to avoid too long a tail that could be fragile or include a capillary channel communicating with the outside. Apply flame to the thinnest strand until after separated, to shorten it without breaking.

WARNING: If the level of the frozen scintillator is beyond 3/4 the capacity of the spherical ampoule head, it is very probable the liquid level will expand to beyond the neck transition once it thaws. *This can happen at any moment*, although it has a higher chance of taking place once fire-sealing is completed. Whenever it happens, it is likely the expansion will blow the softened glass outward or, more likely, make a sealed source explode and send the loaded scintillator spraying isotropically, as well as pulverized sharp quartz fragments.

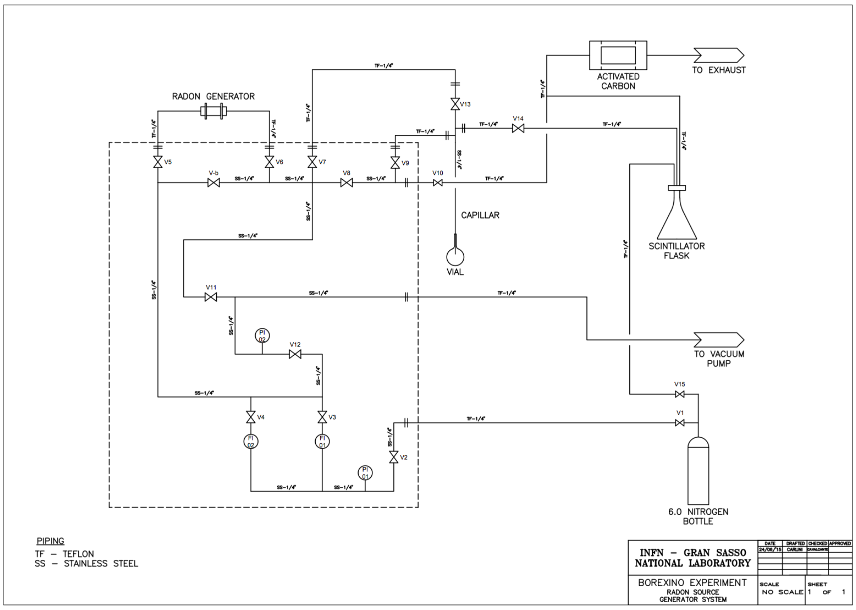

FIGURE A.1: Alternative diagram from the radon loading station, with a different valve naming convention. The procedure outlined above uses the valve naming convention in diagram 5.22

Appendix B

New ^{241}Am^{9}Be source holder technical drawings

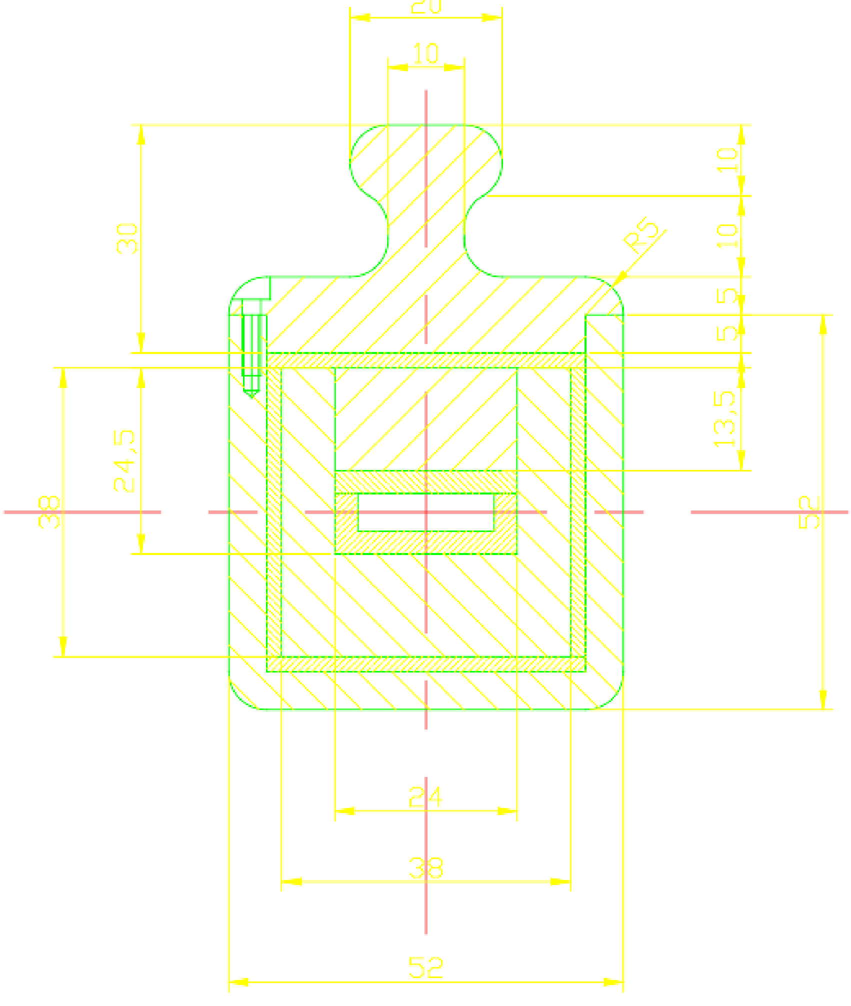

FIGURE B.1: Technical drawing for the final design of the new ^{241}Am^{9}Be neutron source holder, featuring nickel sheets for high-energy γ production.

Appendix C

CrSOX source technical designs

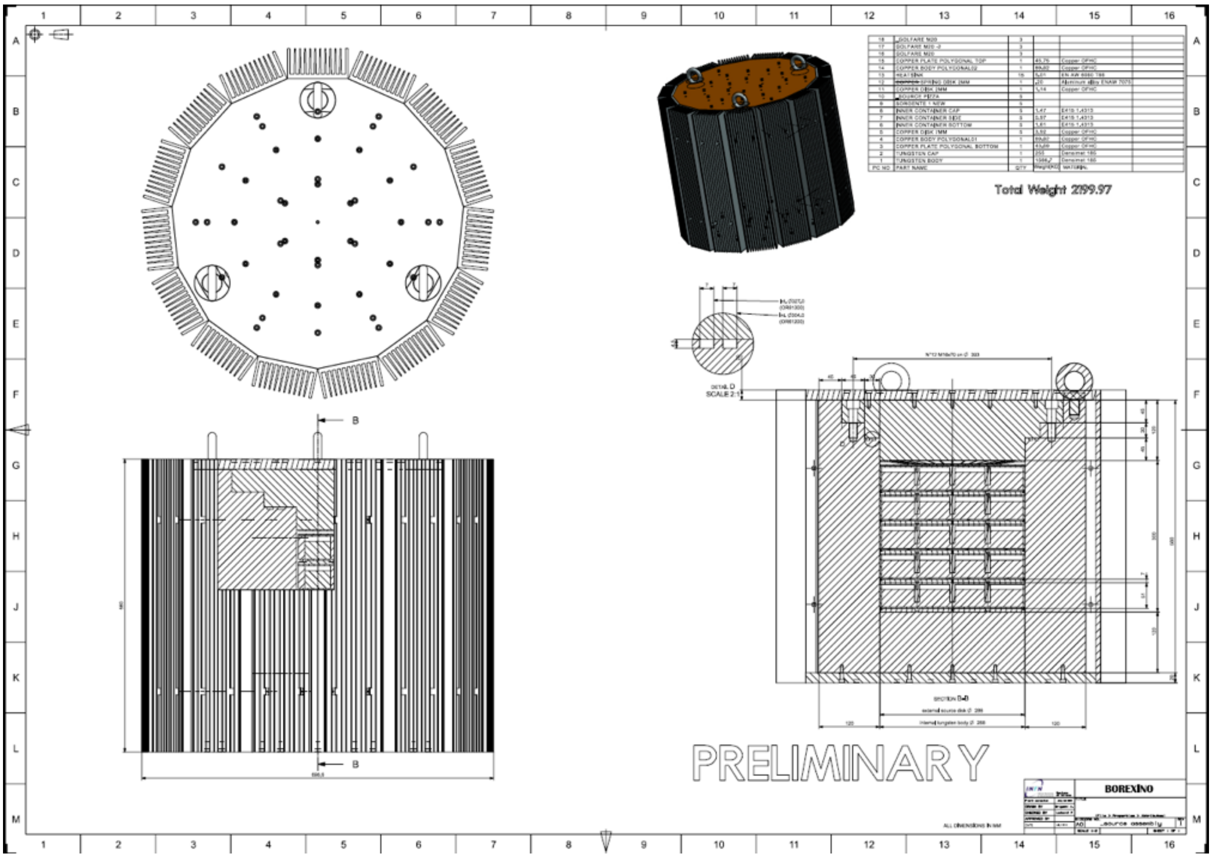

FIGURE C.1: CrSOX source design with the chipped material contained inside five disks with heat-conducting rods for heat management. The finned heat radiators on the outside of the W shielding are also shown attached.

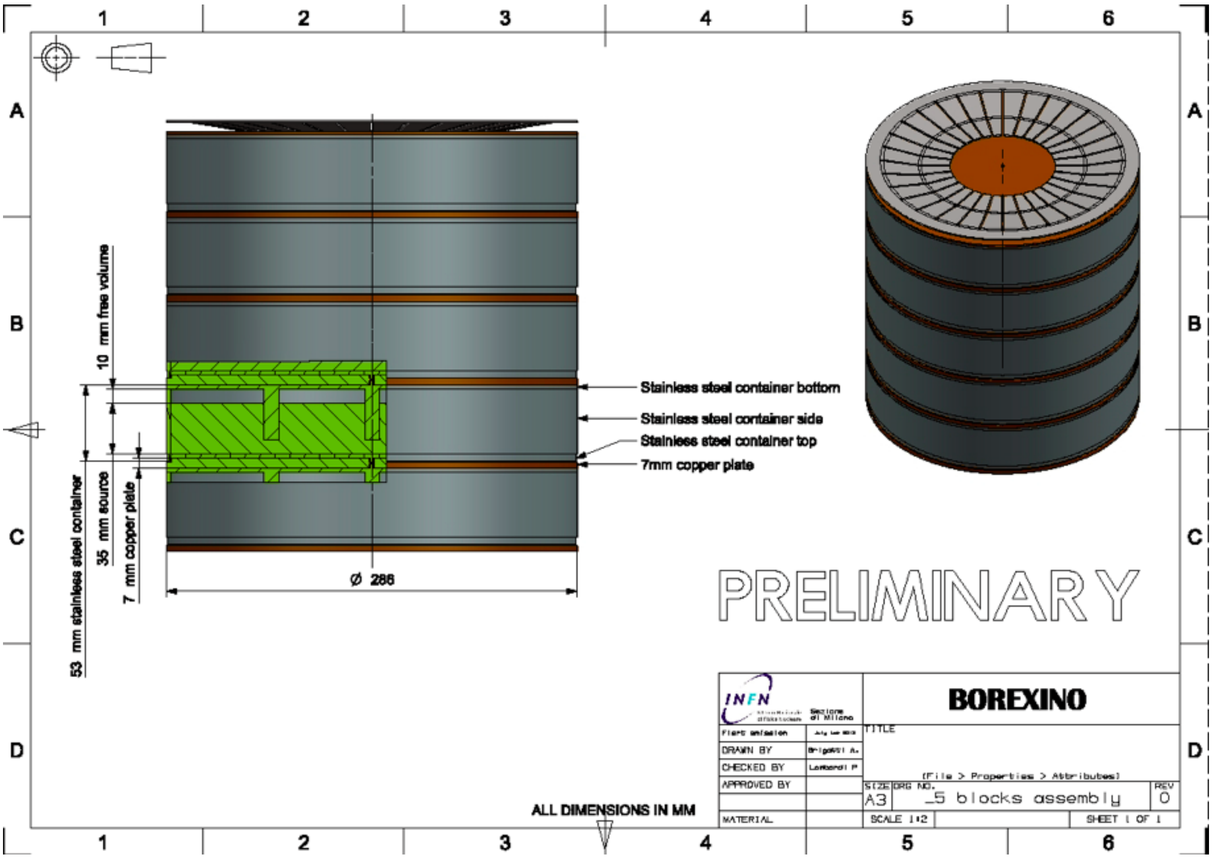

FIGURE C.2: Detailed view of the disk-shaped containers with the chipped material, including the custom-made "spring" that pushes them in place inside the tungsten shielding.

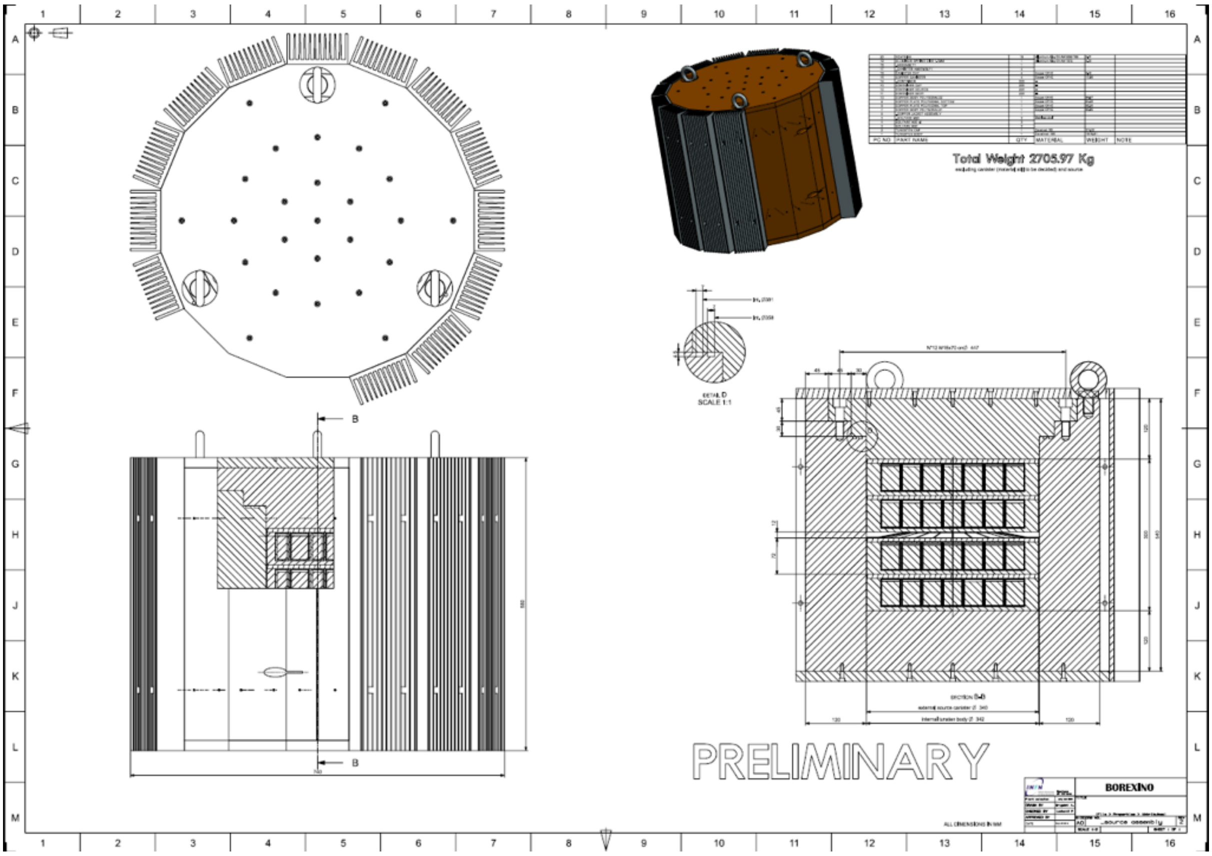

FIGURE C.3: CrSOX source design with the chipped material contained inside 220 small containers distributed in four levels for better material containment and heat transfer. The finned heat radiators on the outside of the W shielding are also shown attached.

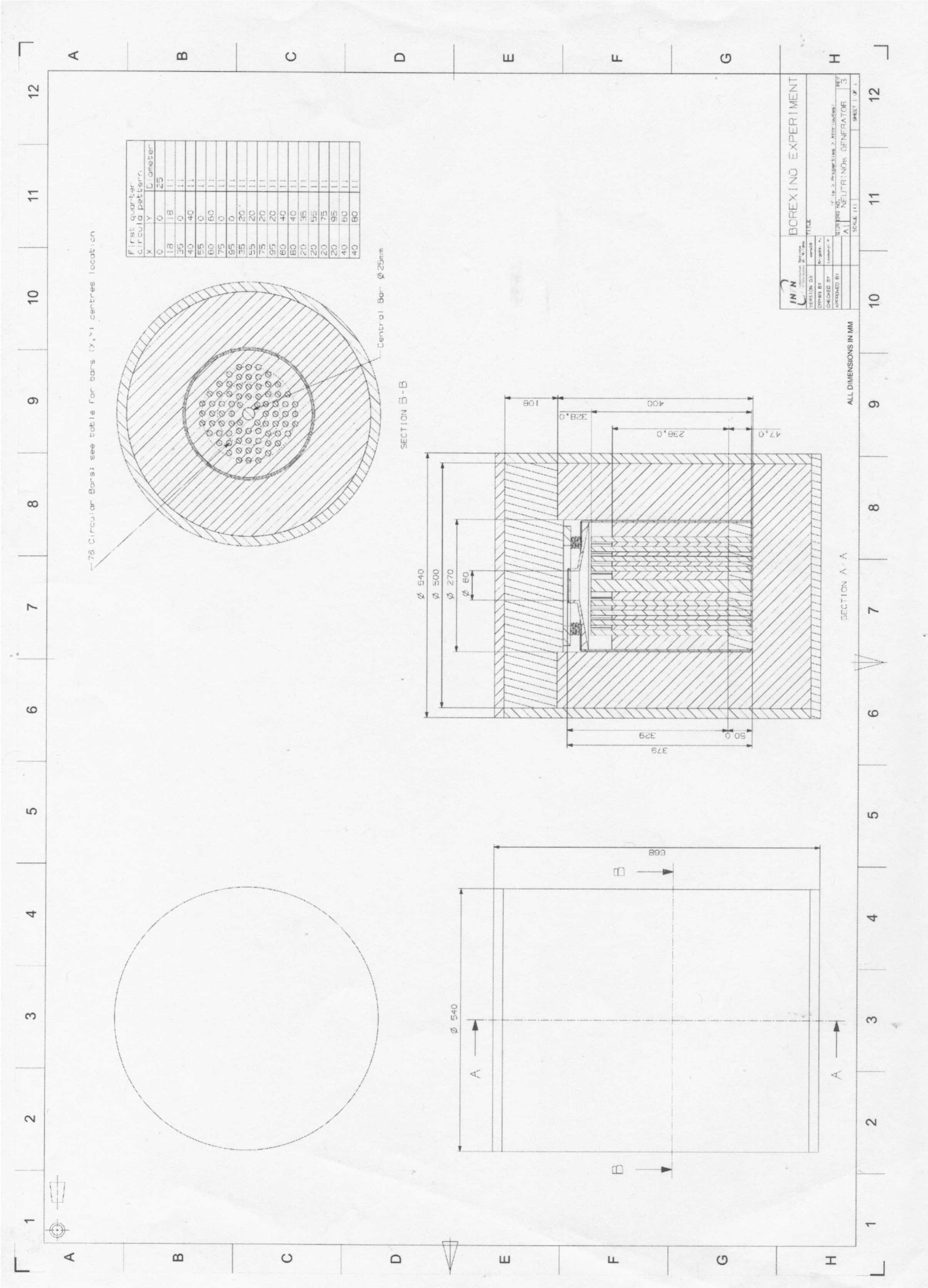

FIGURE C.4: CrSOX source design with the chromium material re-formed into 76 rods (plus a central, wider rod with higher activity, that can be made up of smaller-diameter rods) arranged vertically in a copper or tungsten containment structure.

Appendix D

MCNP simulation results for CrSOX source activity

Sim name	**%^{50}Cr**	**Cr[kg]**	ρ **[g/cm^3]**	**A$_{spc}$ [Ci/g]**	σ_A **[Ci/g]**	**A [MCi]**	σ_A **[MCi]**
Basic homog.	38	35.22	3.0	198.1	0.8	2.651	0.001
Homog. real ρ	38	36.01	3.6	198.1	0.8	2.652	0.002
Basic homog.2x	38	35.22	3.0	277.3	13.6	3.82	0.17
100%^{50}Cr	100	35.22	3.0	93.7	1.3	3.30	0.05
ρ=4	38	46.96	4.0	157.3	1.2	2.81	0.02
ρ=2	38	23.5	2.0	267.8	2.2	2.39	0.02
Highρ 60	60	46.96	4.0	110.0	0.9	3.12	2.5
Lowρ 60	60	46.96	2.0	196.5	1.6	2.77	0.02
Small (H_2O)	38	24.26	3.0	282.4	4.0	2.61	0.03
Small (Be)	38	24.26	3.0	282.4	4.0	2.60	0.03
Small_ext (H_2O)	38	35.25	3	228	3	3.06	0.03
Small_ext real (H_2O)	38	35.26	3.6	224	3	3.01	0.03
NoShadow	38	32.95	3.6	210	2	2.63	0.03
NoShadow mod	38	35.22	3.6	225	2	2.99	0.03
NoShadow 1/3Be	38	33.3	3	219	2	2.77	0.04
NoShadow mod-LVXF	38	35.8	3.6	233	3	2.33	0.04
Containers	38	35.25	3.6	228	3	3.02	0.03
FT	38	0.223	6.9	2653(av)	27	0.14	0.001
Rods SVXF	38	34.6	6.9	230	4	3.04	0.05
Rods opt	38	34.5	6.9	246	5	3.26	0.05
Rods opt+FT	38	34.7	6.9	-	-	3.48	0.05
Rods Temp	38	34.7	6.9	251	7	3.32	0.21

TABLE D.1: Summary of single-cycle MCNP simulation results for CrSOX activity levels, from Section 6.3.

Bibliography

[1] Wolfgang Pauli. Zur alteren und neueren geschichte des neutrinos. *Physik und Erkenntnistheorie*, pages 156–80, 1984.

[2] J. Chadwick. Intensitatsverteilung im magnetischen spektrum der beta-strahlen von radium b + c. *Verhandl. Dtsch. phys. Ges.*, 16:383, 1914.

[3] W. Orhtmann L. Meitner. Uber eine absolute bestimmung der energie der primaren betastrahlen von radium e. *Z. Physik*, 60:143, 1930.

[4] W. A. Wooster C. D. Ellis. The average energy of disintegration of radium e. *Proc. Royal Society (A)*, 117:109, 1922.

[5] J. Chadwick. Possible existence of a neutron. *Nature*, 129:312, 1932.

[6] F. B. Harrison H. W. Kruse C. L. Cowan, F. Reines and A. D. McGuire. Detection of the free neutrino: a confirmation. *Science*, 124:103–104, 1956.

[7] R. Davis Jr. Attempt to detect the antineutrinos from a nulcear reactor by the cl37 (anti-nu,e-) a37 reaction. *Phys. Rev.*, 97:766–769, 1955.

[8] Chris Quigg. The state of the standard model. *arXiv: hep-ph/0001145v2.pdf*, 2000.

[9] CMS collaboration. Observation of a new boson at a mass of 125 gev with the cms experiment at the lhc. *Phys. Lett. B*, 716(1):30–61, September 2012.

[10] S. Willenbrock. Symmetries of the standard models. *arXiv: hep-ph/0410370*, 2008.

[11] B. R. Holstein J. F. Donoghue, E. Golowich. Dynamics of the standard model. *Cambridge Monographs on Particle Physics, Nuclear Physics and Cosmology*, 2, 1992.

[12] E. Kh. Akhmedov. Do charged leptons oscillate? *arXiv: 0706.1216v3*, July 2007.

[13] O. Sumensari D. Bravo-Berguño, C. Ferreira. Z0 to neutrino antineutrino pair oscillations. *Internal report, INSS ICTP-SAIFR*, (22), August 2015.

[14] C. Giunti and Ch. W. Kim. Fundamentals of neutrino physics and astrophysics. *Oxford University Press, ISBN 978 0 19 850871 7*, pages 74, 192, 2007.

[15] Users MissMJ and Eric Drexler. Standard model of elementary particles - elementary particle interactions in the standard model. *https://commons.wikimedia.org/wiki/File:Standard_Model_of_Elementary_Particles.svg - https://commons.wikimedia.org/media/File:Elementary_particle_interactions_in_the_Standard_Model.png*, 2015.

[16] Tatsu Takeuchi. Special relativity. *Encyclopedia of applied high energy and particle physics*, pages 47–94.

[17] R. Davis Jr. Solar neutrinos: Ii. experimental. *Phys. Rev. Lett.*, (12):303, 1964.

[18] J. Bahcall. Solar neutrinos: I. theoretical. *Phys Rev Lett*, 1964.

[19] R. Davis Jr. J. N. Bahcall. An account of the development of the solar neutrino problem. *Essays in Nuclear Astrophysics*, pages 243–285, 1982.

[20] B. Pontecorvo. Mesonium and antimesonium. *Zhurnal Eksperimental'noi i Teoreticheskoi Fiziki, Soviet Physics*, 33:549, 1957.

[21] B. Pontecorvo. Inverse beta processes and nonconservation of lepton charge. *Zhurnal Eksperimentalnoi i Teoreticheskoi Fiziki, Soviet Physics*, 34:247, 1957.

[22] Y. Fukuda et. al. (Kamiokande Collaboration). Study of solar neutrinos at super kamiokande. *Phys. Rev. Lett*, (81):1562, August 1998.

[23] Hampel et al. Gallex solar neutrino observations: results from gallex iv. *Physics Letters B*, 447(1-2):127–133, 1999.

[24] Abdurashitov et al. Measurement of the solar neutrino capture rate by the russian-american gallium solar neutrino experiment during one half of the 22-year cycle of solar activity. *Journal of Experimental and Theoretical Physics*, 95(2):181–193, 2002.

[25] SNO Collaboration. Measurement of the rate of $\nu_e + d \rightarrow p + p + e^-$ interactions provided by ^{8}b solar neutrinos at the sudbury neutrino observatory. *Phys Rev Lett*, 87:071301, 2001.

[26] KamLAND Collaboration. First results from kamland: Evidence for reactor antineutrino disappearance. *Phys Rev Lett*, 90:021802, January 2003.

[27] Super-Kamiokande Collaboration. Evidence for oscillation of atmospheric neutrinos. *Phys Rev Lett*, 81:1562, August 1998.

[28] C. Patrignani et al (Particle Data Group). 2016 review of particle physics. *Chin. Phys. C*, 40, 2016.

[29] Hitoshi Murayama. Oscillation parameter plots. *hitoshi.berkeley.edu/neutrino/*, 2014.

[30] B. Kayser. Neutrino physics. *Phys Rev D*, 24:110, 2004.

[31] S. T. Petkov K. Nakamura. Neutrino mass, mixing and oscillations. http://pdg.lbl.gov/2014/reviews/rpp2014-rev-neutrino-mixing.pdf, August 2014.

[32] S. Nussinov. Solar neutrinos and neutrino mixing. *Phys Lett*, B(63):201–203, 1976.

[33] B. Kaiser. On the quantum mechanics of neutrino oscillation. *Phys Rev D*, 24:110, 1981.

[34] B. J. P. Jones. Sterile neutrinos in cold climates. *Massachusetts Institute of Technology PhD Thesis*, September 2015.

[35] Andre de Gouvea. On neutrino and nucleon decay physics. *Next-generation Nucleon Decay and Neutrino Physics Workshop (Fermilab, IL; USA)*, page 9, October 2012.

[36] K. A. Olive et al. (Particle Data Group). 2014 review of particle physics. *Chinese Physics C*, 38(9), 2014.

[37] Ch. Spiering U. F. Katz. High-energy neutrino astrophysics: status and perspectives. *Prog. Part. Nucl. Phys.*, arXiv:1111.0507(67):651–704, November 2011.

[38] S. M. Manecki. Annual modulation measurement of the low energy solar neutrino flux with the borexino detector. *PhD Thesis, Virginia Tech*, May 2013.

[39] L. Wolfenstein. Neutrino oscillations in matter. *Phys Rev D*, 17:2369, May 1978.

[40] J. Sheiman P. Langacker, J. P. Leveille. On the detection of cosmological neutrinos by coherent scattering. *Phys Rev D*, 27:1228, March 1983.

[41] H. A. Bethe. Possible explanation of the solar neutrino puzzle. *Phys Rev Lett*, 56:1305, 1986.

[42] Borexino Collaboration. Neutrinos from the primary proton-proton fusion process in the sun. *Nature*, 512:383–386, August 2014.

[43] Super-Kamiokande Collaboration. First indication of terrestrial matter effects on solar neutrino oscillation. *Phys Rev Lett*, 112(9):091805, March 2014.

[44] Borexino Collaboration. Absence of a day–night asymmetry in the 7be solar neutrino rate in borexino. *Phys Lett B*, 707(1):22–26, January 2012.

[45] KamLAND Collaboration. Precision measurement of neutrino oscillation parameters with kamland. *Phys Rev Lett*, 100(22), June 2008.

[46] A. Yu. Smirnov J. N. Bahcall, P. I. Krastev. Is a large mixing angle msw effect the solution of the solar neutrino problems? *Phys Rev*, D(60), 1999.

[47] B. W. Carrol and D. A. Ostlie. An introduction to modern astrophysics. *Addison-Wesley*, page 333, 2007.

[48] J. N. Bahcall. Neutrino astrophysics. *Cambridge University Press*, 1989.

[49] Borexino Collaboration. First evidence of pep solar neutrinos by direct detection in borexino. *Phys Rev Lett*, 108:051302, 2012.

[50] Borexino Collaboration. First real-time detection of 7be solar neutrinos with borexino. *Phys Lett B*, 658(4):101–108, January 2008.

[51] Borexino Collaboration. Precision measurement of the ^{7}be solar neutrino interaction rate in borexino. *Phys Rev Lett*, 107:141302, 2011.

[52] Borexino Collaboration. Measurement of the solar 8b neutrino rate with a liquid scintillator target and 3mev energy threshold in the borexino detector. *Phys Rev D*, 82:033006, May 2008.

[53] Super-Kamiokande Collaboration. Solar 8b and hep neutrino measurements from 1258 days of super-kamiokande data. *Phys Rev lett*, 86:5651–5655, March 2001.

[54] H. A. Bethe. Energy production in stars. *Physical Review*, 55(5):434–456, 1939.

[55] A. J. Sauval P. Scott M. Asplund, N. Grevesse. New solar composition: the problem with solar models revisited. *The Astrophysical Journal Letters*, 705(123), 2009.

[56] A. J. Sauval N. Grevesse. Standard solar composition. *Space Sci. Rev.*, 85(161), 1998.

[57] A.M.Serenelli W.C. Haxton, R.G. Hamish Robertson. Solar neutrinos: Status and prospects. *Annual Review Astronomy and Astrophysics*, 51:21–61, June 2013.

[58] R.G.H. Robertson L.C. Stonehill, J.A. Formaggio. Solar neutrinos from cno electron capture. *Phys Rev C*, 69:015801, January 2004.

[59] W. Lin W.C. Haxton. The very low energy solar flux of electron and heavy-flavor neutrinos and antineutrinos. *Phys Lett B*, 486:00764–4, June 2000.

[60] A. Serenelli M. Bergemann. Determination of atmospheric parameters of b, a, f and g-type stars. *Lectures from the School of Spectroscopic Data Analyses Lectures from the School of Spectroscopic Data Analyses*, page 16, March 2014.

[61] F. Delahaye M.H. Pinsonneault F.L. Villante, A.M. Serenelli. The chemical composition of the sun from helioseismic and solar neutrino data. *The Astrophysical Journal*, 12(787), 2013.

[62] A.M. Serenelli F.L. Villante. A quantitative analysis of the solar composition problem. *Physics Procedia*, 61:366–375, 2015.

[63] A.M. Serenelli W.C. Haxton. Cn-cycle solar neutrinos and sun's primordial core metallicity. *The Astrophysical Journal*, 687(1), May 2008.

[64] Werner Maneschg. Low-energy solar neutrino spectroscopy with borexino: towards the detection of the solar pep and cno neutrino flux. *PhD Thesis*, May 2011.

[65] A. Aguilar et. al. Evidence for neutrino oscillations from the observation of electron anti-neutrinos in a muon anti-neutrino beam. *Phys Rev D*, 64:112007, August 2001.

[66] HARP-CDP Group. Revisitig the lsnd anomaly. ii. critique of the data analysis. *Physical Review D*, 85:092009, May 2012.

[67] KARMEN collaboration. Upper limits for neutrino oscillations muon-antineutrino to electron-antineutrino from muon decay at rest. *Phys Rev D*, 65, 2002.

[68] J.N. Abdurashitov et. al. Measurement of the response of a ga solar neutirno experiment to neutrinos from a 37ar source. *Phys Rev C*, 73:045805, December 2006.

[69] M. Laveder C. Giunti. Short-baseline electron-neutrino disappearance, tritium beta decay and neutrinoless double-beta decay. *Phys Rev D*, 82:053005, 2010.

[70] MiniBooNE collaboration. Improved search for $\overline{nu_\mu} \rightarrow \overline{\nu_e}$ oscillations in the miniboone experiment. *Phys Rev Lett (submitted)*, 2013.

[71] MiniBooNE collaboration. Sterile neutrino searches in miniboone and microboone. *Christina M. Ignarra*, FERMILAB-THESIS-2014-31, 2014.

[72] MINOS Collaboration. Active to sterile neutrino mixing limits from neutral-current interactions in minos. *Phys Rev Lett*, 107:011802, July 2011.

[73] MINOS and Daya Bay Collaborations. Limits on active-to-sterile neutrino oscillations from disappearance searches in the minos, daya bay and bugey-3 experiments. *Phys Rev Lett*, 117(151801), 2016.

[74] ICARUS Collaboration. Search for anomalies in the ν_e appearance from a ν_μ beam. *European Physics Journal C*, 73:2599, 2013.

[75] IceCube Collaboration. Searches for sterile neutrinos with the icecube detector. *Phys. Rev. Lett*, 117(071801), 2016.

[76] P. Huber. On the determination of anti-neutrino spectra from nuclear reactors. *Phys Rev C*, 84:024617, January 2012.

[77] T.A. Mueller et. al. Improved predictions of reactor antineutrino spectra. *Phys Rev C*, 83: 054615, 2011.

[78] G. Mention et. al. The reactor antineutrino anomaly. *Phys Rev D*, 83:073006, 2011.

[79] A.C. Hayes et. al. Systematic uncertainties in the analysis of the reactor neutrino anomaly. *Phys Rev Lett*, 112:202501, April 2014.

[80] K.N: Abazajian et al. Light sterile neutrinos: a white paper. *arXiv: 1204.5379*, 2012.

[81] Planck Collaboration. Planck 2013 results. xvi. cosmological parameters. *Astronomy and Astrophysics*, 571, October 2014.

[82] J. Hamann et. al. Sterile neutrinos with ev masses in cosmology – how disfavoured exactly? *JCAP*, 1109:034, 2011.

[83] Y.F. Li H.W. Long C. Giunti, M. Laveder. Pragmatic view of short-baseline neutrino oscillations. *Phys Rev D*, 88:073008, 2013.

[84] F. Dydak et. al. Cern dortmund heidelberg saclay warsaw. *Phys Lett B*, 134:281, 1984.

[85] NOMAD Collaboration. Search for nu(mu) nu(e) oscillations in the nomad experiment. *Phys Lett B*, pages 19–31, June 2003.

[86] L. Borodovsky et. al. Search for muon-neutrino oscillations $\nu_\mu \to \nu_e$ in a wideband neutrino beam. *Phys Rev Lett*, 68, January 1992.

[87] OPERA Collaboration. Search for $\nu_\mu \to \nu_e$ oscillations with the opera experiment in the cngs beam. *JHEP*, 7, 2013.

[88] E.J. Chun K. Choi, K. Hwang. Atmospheric and solar neutrino masses from horizontal u(1) symmetry. *Phys Rev D*, 60:031301, 1999.

[89] J. Jenkins. Model independent explorations of majorana neutrino mass origins. *PhD Thesis, Northwestern university*, arXiv:0805.0303, 2008.

[90] M. Maltoni A. Donini. P. Hernandez, J. Lopez-Pavon. Minimal models with light sterile neutrinos. *JHEP*, 1107:105, 2011.

[91] Borexino Collaboration. The borexino detector at the laboratori nazionali del gran sasso. *Nucl. Instrum. Meth. A*, 600:568–593, 2009.

[92] Davide D'Angelo. Towards the detection of low energy solar neutrinos in borexino: data readout, data reconstruction and background identification. *PhD Thesis*, 2006.

[93] K. A. Olive et al. (Particle Data Group). Neutrino properties. *Chinese Physics C*, 38, 2014.

[94] Richard Saldanha. Precision measurement of the ^{7}be solar neutrino interaction rate in borexino. *PhD Thesis*, pages 80–82, 2012.

[95] R. S. Raghavan et. al. New tools for solving the solar neutrino problem. *Phys Rev Lett*, 57:1801–1804, 1986.

[96] M. Campanella R. S. Raghavan, G. Bellini and D. Giugni. Borexino: A proposal for a real-time detector for solar neutrinos. *INFN, Milano*, 1991.

[97] Borexino Collaboration. A large-scale low background liquid scintillator detector: the counting test facility at gran sasso. *Nucl. Instrum. Meth. A*, 406:411, 1998.

[98] DarkSide Collaboration. Darkside-50: A direct search for dark matter with new techniques for reducing background. *DOE Proposal, Princeton University*, 2008.

[99] Benziger et. al. The nylon scintillator containment vessels for the borexino solar neutrino experiment. *Nucl. Instrum. Meth. A*, 582:509–534, 2007.

[100] Francesco Lombardi. The dynamical fiducial volume (dfv) implementation in bxfilter. *Internal Borexino Report*, January 2015.

[101] J. B. Birks. Photophysics of aromatic molecules. *John Wiley and Sons Ltd. - Wiley Interscience*, 1970.

[102] Borexino Collaboration. Light propagation in a large volume liquid scintillator. *Nucl. Instrum. Meth. A*, 440:360, 2000.

[103] K. B. McCarty. The borexino nylon film and the third counting test facility. *PhD Thesis, Princeton University*, 2006.

[104] CTF collaboration. Pulse-shape discrimination with the countint test facility. *Nucl. Instrum. Meth. A*, 584:93–113, 2008.

[105] E. Gatti and F. deMartini. A new linear method of discrimination between elementary particles in scintillation counters. *Nuclear Electronics*, 2:265–276, 1962.

[106] F. Elisei et. al. Measurements of liquid scintillator properties for the borexino detector. *Nucl. Instrum. Meth. A*, 400(1):53–68, November 1997.

[107] Andrea Pocar. Low background techniques and experimental challenges for borexino and its nylon vessels. *PhD Thesis, Princeton University*, November 2003.

[108] Szymon Manecki. Vessel analysis: volumes and leak rates. *Internal Borexino Report*, March 2010.

[109] Francesco Lombardi. Dynamic fiducial volume - statistical and systematic errors. *Internal Borexino Presentation, Santa Margherita di Pula*, July 2015.

[110] S. Manecki B. Caccianiga, Y. Koshio. Estimation of the fv systematic error. *Internal Borexino Report borex.lngs.infn.it/Doc/memos/2011-06-13_FV_systematics.pdf*, 2011.

[111] G Testera V Lagomarsino. A gateless charge integrator for borexino energy measurements. *NIM A*, 2-3(430):435–466, 1999.

[112] Oleg Smirnov. Energy reconstruction and resolution in borexino: addendum n1 to the echidna report. *Internal Report*, March 2008.

[113] G. Bonfini. Detector stability and trigger re-design. *Internal General Meeting Presentation*, July 2015.

[114] Maksim Gromov. Antineutrino analysis based on the fadc system data in borexino. *LNGS Seminar*, July 2015.

[115] Decay Data Evaluation Project (M.-M. Bé et. al.). Monographie bipm-5 table of radionuclides. *Bureau International des Poids et Mésures*, (http://www.bipm.org/en/publications/scientific-output/monographie-ri-5.html), 1999-2015.

[116] Jochen Ahlswede, Simon Hebel, J. Ole Ross, Robert Schoetter, and Martin B. Kalinowski. Update and improvement of the global krypton-85 emission inventory. *Journal of Environmental Radioactivity*, 115:34 – 42, 2013. ISSN 0265-931X. doi: http://dx.doi.org/10.1016/j.jenvrad.2012.07.006. URL http://www.sciencedirect.com/science/article/pii/S0265931X12001816.

[117] Sandra Zavatarelli. Radon/thoron/krypton. *Milano General Meeting presentation*, February 2016.

[118] R.Löhken H.Resel D.Flothmann, W.Wiesner. *Z. Physik*, 225:164, 1969.

[119] C. Galbiati et. al. Cosmogenic c-11 production and sensitivity of organic scintillator detectors to pep and cno neutrinos. *Phys Rev C*, 055805, 2005.

[120] S. Abe et al. Study of the production of radioactive isotopes through cosmic muon spallation in kamland. *Phys Rev C*, 81(025807):74, 2010.

[121] Stefano Davini. Measurement of the *pep* and cno solar neutrino interaction rates in borexino. *PhD Thesis, Università degli Studi di Genova*, 2012.

[122] A. Pocar. Low background techniques and experimental challenges for borexino and its nylon vessels. *PhD Thesis, Princeton University*, 2003.

[123] MACRO Collaboration. Measurement of the energy spectrum of underground muons at gran sasso with a transition radiation detector. *Astroparticle Physics*, 10:10, arXiv:hep-ex/9807009 1999.

[124] Michael Wurm. Echidna: Muons, neutrons, cosmogenics. *Internal SOX presentation, Data workshop Munich*, November 2014.

[125] R.B Vogelaar, J Benziger, F.P Calaprice, and N Darnton. Removal of cosmogenic 7be from scintillators. *Nuclear Instruments and Methods in Physics Research Section A: Accelerators, Spectrometers, Detectors and Associated Equipment*, 372(1):59 – 62, 1996.

[126] Simone Marcocci. Measurement of solar neutrino fluxes with borexino. *Presentation, Magellan Workshop Connecting Physics and Astronomy*, page 9, March 2016.

[127] Georgy Raikov. Search for solar hep neutrino interactions with carbon $^{12}c(\nu, \nu')^{12}c*$. *Internal Borexino report, LNGS 2016 summer GM*, 2016.

[128] Borexino Collaboration. Measurement of neutrino flux from the primary proton–proton fusion process in the sun with borexino detector. *arXiv:hep-ex/1507.02432*, 2014.

[129] M. Baldoncini et.al. Reference worldwide model for antineutrinos from reactors. *Phys Rev D*, 91:065002, 2015.

[130] G. Bellini, J. Benziger, D. Bick, G. Bonfini, D. Bravo, M. Buizza Avanzini, B. Caccianiga, L. Cadonati, F. Calaprice, P. Cavalcante, A. Chavarria, A. Chepurnov, D. D'Angelo, S. Davini, A. Derbin, A. Empl, A. Etenko, G. Fiorentini, K. Fomenko, D. Franco, C. Galbiati, S. Gazzana, C. Ghiano, M. Giammarchi, M. Goeger-Neff, A. Goretti, L. Grandi, C. Hagner, E. Hungerford, Aldo Ianni, Andrea Ianni, V.V. Kobychev, D. Korablev, G. Korga, Y. Koshio, D. Kryn, M. Laubenstein, T. Lewke, E. Litvinovich, B. Loer, P. Lombardi, F. Lombardi, L. Ludhova, G. Lukyanchenko, I. Machulin, S. Manecki, W. Maneschg, F. Mantovani, G. Manuzio, Q. Meindl, E. Meroni, L. Miramonti, M. Misiaszek, P. Mosteiro, V. Muratova, L. Oberauer, M. Obolensky, F. Ortica, K. Otis, M. Pallavicini, L. Papp, L. Perasso, S. Perasso, A. Pocar, G. Ranucci, A. Razeto, A. Re, B. Ricci, A. Romani, N. Rossi, A. Sabelnikov, R. Saldanha, C. Salvo, S. Schönert, H. Simgen, M. Skorokhvatov, O. Smirnov, A. Sotnikov, S. Sukhotin, Y. Suvorov, R. Tartaglia, G. Testera, D. Vignaud, R.B. Vogelaar, F. von Feilitzsch, J. Winter, M. Wojcik, A. Wright, M. Wurm, J. Xu, O. Zaimidoroga, S. Zavatarelli, and G. Zuzel. Measurement of geo-neutrinos from 1353 days of borexino. *Physics Letters B*, 722(4–5):295 – 300, 2013. doi: http://dx.doi.org/10.1016/j.physletb.2013.04.030.

[131] S.M. Usman et al. Agm2015: Antineutrino global map 2015. *Sci. Rep.*, 5(13945), 2015.

[132] M. Agostini, S. Appel, G. Bellini, J. Benziger, D. Bick, G. Bonfini, D. Bravo, B. Caccianiga, F. Calaprice, A. Caminata, P. Cavalcante, A. Chepurnov, K. Choi, D. D'Angelo, S. Davini, A. Derbin, L. Di Noto, I. Drachnev, A. Empl, A. Etenko, G. Fiorentini, K. Fomenko, D. Franco, F. Gabriele, C. Galbiati, C. Ghiano, M. Giammarchi, M. Goeger-Neff, A. Goretti, M. Gromov, C. Hagner, T. Houdy, E. Hungerford, Aldo Ianni, Andrea Ianni, K. Jedrzejczak, M. Kaiser, V. Kobychev, D. Korablev, G. Korga, D. Kryn, M. Laubenstein, B. Lehnert, E. Litvinovich, F. Lombardi, P. Lombardi, L. Ludhova, G. Lukyanchenko, I. Machulin, S. Manecki, W. Maneschg, F. Mantovani, S. Marcocci, E. Meroni, M. Meyer, L. Miramonti, M. Misiaszek, M. Montuschi, P. Mosteiro, V. Muratova, B. Neumair, L. Oberauer, M. Obolensky, F. Ortica, K. Otis, L. Pagani, M. Pallavicini, L. Papp, L. Perasso, A. Pocar, G. Ranucci, A. Razeto, A. Re, B. Ricci, A. Romani, R. Roncin, N. Rossi, S. Schönert, D. Semenov, H. Simgen, M. Skorokhvatov, O. Smirnov, A. Sotnikov, S. Sukhotin, Y. Suvorov, R. Tartaglia, G. Testera, J. Thurn, M. Toropova, E. Unzhakov, R. B. Vogelaar, F. von Feilitzsch, H. Wang, S. Weinz, J. Winter, M. Wojcik, M. Wurm, Z. Yokley, O. Zaimidoroga, S. Zavatarelli, K. Zuber, and G. Zuzel. Spectroscopy of geoneutrinos from 2056 days of borexino data. *Phys. Rev. D*, 92:031101, Aug 2015. doi: 10.1103/PhysRevD.92.031101.

[133] G. Bellini, J. Benziger, S. Bonetti, M. Buizza Avanzini, B. Caccianiga, L. Cadonati, F. Calaprice, C. Carraro, A. Chavarria, F. Dalnoki-Veress, D. D'Angelo, S. Davini, H. de Kerret, A. Derbin, A. Etenko, G. Fiorentini, K. Fomenko, D. Franco, C. Galbiati, S. Gazzana, C. Ghiano, M. Giammarchi, M. Goeger-Neff, A. Goretti, E. Guardincerri, S. Hardy, Aldo Ianni, Andrea Ianni, M. Joyce, V.V. Kobychev, Y. Koshio, G. Korga, D. Kryn, M. Laubenstein, M. Leung, T. Lewke, E. Litvinovich, B. Loer, P. Lombardi, L. Ludhova, I. Machulin, S. Manecki, W. Maneschg, G. Manuzio, Q. Meindl, E. Meroni, L. Miramonti, M. Misiaszek, D. Montanari, V. Muratova, L. Oberauer, M. Obolensky, F. Ortica, M. Pallavicini, L. Papp, L. Perasso, S. Perasso, A. Pocar, R.S. Raghavan, G. Ranucci, A. Razeto, A. Re, B. Ricci, P. Risso, A. Romani, D. Rountree, A. Sabelnikov, R. Saldanha, C. Salvo, S. Schönert, H. Simgen, M. Skorokhvatov, O. Smirnov, A. Sotnikov, S. Sukhotin, Y. Suvorov, R. Tartaglia, G. Testera, D. Vignaud, R.B. Vogelaar, F. von Feilitzsch, J. Winter, M. Wojcik, A. Wright, M. Wurm, J. Xu, O. Zaimidoroga, S. Zavatarelli, and G. Zuzel. Observation of geo-neutrinos. *Physics Letters B*, 687(4–5):299 – 304, 2010.

[134] Borexino Collaboration. A search for low-energy neutrino and antineutrino signals correlated with gamma-ray bursts with borexino. *http://arxiv.org/abs/1607.05649*, July 2016.

[135] Borexino Collaboration. New experimental limits on the pauli-forbidden transitions in ^{12}C nuclei obtained with 485 days borexino data. *Phys. Rev. C*, 81:034317, Mar 2010. doi: 10.1103/PhysRevC.81.034317.

[136] Borexino Collaboration. Study of solar and other unknown anti-neutrino fluxes with borexino at {LNGS}. *Physics Letters B*, 696(3):191 – 196, 2011. ISSN 0370-2693. doi: http://dx.doi.org/10.1016/j.physletb.2010.12.030.

[137] D. (Borexino Collaboration) D'Angelo. Seasonal modulation in the borexino cosmic muon signal. *32nd International Cosmic Ray Conference*, 2011.

[138] Borexino Collaboration. Search for solar axions produced in the $p(d,^3\mathrm{He})\mathrm{A}$ reaction with borexino detector. *Phys. Rev. D*, 85:092003, May 2012. doi: 10.1103/PhysRevD.85.092003.

[139] Borexino Collaboration. Test of electric charge conservation with borexino. *Phys. Rev. Lett.*, 115:231802, Dec 2015. doi: 10.1103/PhysRevLett.115.231802.

[140] Borexino Collaboration. New limits on heavy sterile neutrino mixing in ^{8}B decay obtained with the borexino detector. *Phys. Rev. D*, 88:072010, Oct 2013. doi: 10.1103/PhysRevD.88.072010.

[141] Borexino CNGS Collaboration. Measurement of cngs muon neutrino speed with borexino. *Physics Letters B*, 716(3–5):401 – 405, 2012. ISSN 0370-2693. doi: http://dx.doi.org/10.1016/j.physletb.2012.08.052.

[142] Richard Saldanha et al. Prospects for pep and cno. *Internal Report*, October 2012.

[143] Richard Saldanha. Cno working group status update. *GM report*, May 2013.

[144] A. Chavarria. Study on pep and cno solar neutrino interaction rates in borexino. *PhD Thesis, Princeton University*, 2012.

[145] M. Misiaszek. Pulse-shape discrimination in bx. *Internal Borexino Presentation, Milano GM*, 2016.

[146] Nicola Rossi. Review and update of 210po analysis. *Internal Borexino Presentation, Santa Margherita di Pula*, 2015.

[147] Nicola Rossi. A ^{210}po update. *Meeting reports for NuSol working group*, 2015.

[148] Gioacchino Ranucci. Borexino status report. *Internal Report*, April 2015.

[149] Werner Maneschg. Internal communication email. 2015.

[150] Paolo Cavalcante. Probes calibration. *Internal Report*, November 2014.

[151] David Bravo. Destination calibration. *Internal General Meeting Presentation*, December 2014.

[152] M. Carlini. Borexino bottom heat transfer - temperature data-based calculation. *Internal Borexino Report*, January 2015.

[153] Federico Gabriele. Status of the thermal insulation work. *Internal Borexino Presentation, Santa Margherita di Pula*, July 2015.

[154] ANSYS. Ansys fluent theory guide. *Program user guide*, (Release 15.0), November 2013.

[155] David Bravo-Bergu no. Latitudinal temperature probes system (water tank and outer buffer internal system) report. *Internal Borexino Report*, May 2015.

[156] David Bravo-Bergu no and Riccardo Mereu. Fluent-based simulations for borexino: conduction-only case. *Internal Borexino Report*, (1), March 2016.

[157] S.H.Yin. Natural convection flow patterns in spherical annuli. *Int.J. Heat Mass Transfer*, 16:1785–1795, 1973.

[158] T.H. Kuehn and R.J. Goldstein. An experimental study of natural convection heat transfer in concentric and eccentric horizontal cylindrical annuli. *Journal of Heat Transfer*, 100: 635–640, 1978.

[159] V.K. Garg. Natural convection between concentric spheres. *Int.J. Heat Mass Transfer*, 35 (8):1935–1945, 1992.

[160] Borexino Collaboration. Borexino calibrations: Hardware, methods, and results. *JINST*, 7:10018, 2012.

[161] S. Hardy. Measuring the 7be neutrino flux from the sun: Calibration of the borexino solar neutrino detector. *PhD Thesis, Virginia Tech*, March 2010.

[162] H. O. Back. Internal radioactive source calibration of the borexino solar neutrino experiment. *PhD Thesis, Virginia Tech*, September 2004.

[163] Department of Defense US Government. Mil-std-1246c. 1994.

[164] OSRAM Opto-Semiconductors Company. Oslon black series (850 nm) - 150° - sfh 4716s. *Product Datasheet*, Version 1.5, January 2016.

[165] Aleksander Chernupov and Maksim Gromov. The current state of the fadc offline and online calibrations. *Internal Borexino report, LNGS summer GM*, 2016.

[166] Pylon Electronics Inc. Radioactive sources: model rn-1025/th-1025/rnc. *Commercial document (`pylonelectronics.com`)*, Datasheet 123, Rev 3.

[167] G. Ranucci A. Romani P. Lombardi, F. Ortica. Decay time and pulse-shape discrimination of liquid scintillators based on novel solvents. *Nucl. Instrum. Meth. A*, (701):133–144, 2013.

[168] Gioacchino Ranucci, Patrizia Ullucci, Silvia Bonetti, Istvan Manno, Emanuela Meroni, and Anna Preda. Scintillation decay time and pulse shape discrimination of binary organic liquid scintillators for the borexino detector. *Nuclear Instruments and Methods in Physics Research Section A: Accelerators, Spectrometers, Detectors and Associated Equipment*, 350(1):338 – 350, 1994. ISSN 0168-9002. doi: http://dx.doi.org/10.1016/0168-9002(94)91183-5. URL http://www.sciencedirect.com/science/article/pii/0168900294911835.

[169] Selvakumaran T S Mohapatra D K Raja E A Subbaiah K V Baskaran R. Pujala U, Thilagam L. Analysis of neutron streaming through the trenches at linac based neutron generator facility, igcar. *Radiat Prot Environ [serial online]*, 34:262–6, 2011.

[170] B. Reinhold for the DS-50 Collaboration. The darkside-50 ^{241}am^{13}c source. *Internal report, DS-50 Collaboration*, March 4 2016.

[171] B. Ricci N. Ferrari, G. Fiorentini. The ^{51}cr neutrino source and borexino: a desirable marriage. *Phys Lett*, B(387):427–431, July 1996.

[172] Borexino Collaboration. Sox: Short distance neutrino oscillations with borexino. *J. High Energ. Phys*, 2013(38), 2013.

[173] F. Cavanna. Studio della sensibilitá di borexino per la ricerca di neutrini sterili. *PhD Thesis, Genova University*, 2012.

[174] M. Cribier et.al. Production of a 62 pbq ^{51}cr low-energy neutrino source for gallex. *Nucl. Instrum. Meth.*, A(378):233–250, 28 February 1996.

[175] V.N.Kornoukhov. Calibration of solar neutrino detectors with artificial ^{51}cr and ^{75}se neutrino sources. *Physics of Atomic Nuclei (Yadernaya Fizika)*, 63(12):2205–2208, 2000.

[176] P. Vilain et.al. Precision measurement of electroweak parameters from the scattering of muon-neutrinos on electrons. *Phys. Lett. B*, (335):246, 1994.

[177] R.A. Forrest INDC (IAEA): J.-Ch. Sublet, J.A. Simpson and D. Nierop. Atlas of neutron capture cross sections. *IAEA Nuclear Data Section*, 28(20):43–45, April 1997.

[178] M. Cribier et.al. Study of a high-intensity 746 kev neutrino source for the calibration of solar neutrino detectors. *Nucl. Instrum. Meth.*, A(265):574–586, 23 September 1988.

[179] E. Bellotti et.al. Measurement of the gamma activity induced by neutron activation in the gallex neutrino source. *Nucl. Instrum. Meth.*, B(100):199–203, 30 December 1995.

[180] F.X. Hartmann and R.L. Hahn. The enriched chromium neutrino source for gallex. *US DoE, Brookhaven National Lab (BNL)*, 52281(DE91 010298), 1991.

[181] Matthieu Vivier. Effect of source extension on sensitivity contours. *Internal Presentation*, Oct 2016.

[182] Mikko Meyer. Monte carlo simulations and sensitivity studies for sox. *Internal Borexino Presentation*, 2014.

[183] M. Pallavicini. Icp-ms ^{50}cr sample analysis. *Internal Borexino Presentation*, 2014.

[184] T. Germain A. Bevilacqua. Chromium source: Qualifying irradiation. *Internal GALLEX presentation, General Meeting*, 1993.

[185] B.P.Koruchov et.al. A possibility for 300 pbq ^{51}cr-based neutrino source production in russian heavy-water reactor l-2: Preprint itep 37-98. *Institut Teoreticheskoi i eksperimentalnoi fiziki, Moskva (Moskow's Theoretical and Experimental Physics Insitute)*, 1998.

[186] M. Wurm D. Franco, G. Ranucci. Studies on sox sensitivity. *Internal Borexino Presentation, Sestri Levante*, 2014.

[187] International Association for the Properties of Water and Steam. Revised release on the iapws industrial formulation 1997 for the thermodynamic properties of water and steam (region 5 to 50 mpa). `http://www.iapws.org/relguide/IF97-Rev.pdf`, 1997.

[188] Konrad Altenmüller. Analysis and results of the blind measurement. *Internal Borexino Presentation, Milano GM*, 2016.

[189] Vasily Kornoukhov. Production of ^{51}cr neutrino and ^{144}ce antineutrino generators for sox and celand experiments. *13th International Conference on Topics in Astroparticle and Underground Physics*, 2013.

[190] J.A.Setaro. Phase i - ^{51}cr solar neutrino project. *ORNL Central Files (ORNL internal) number ORNL/CF-82/307*, 1982.

[191] C.W.Alexander. Cr-51 production at hfir. *Internal ORNL presentation*, December 2013.

[192] J.M.Link. Calculation of ^{51}cr production scaling from gallex. *Virginia Tech's Center for Neutrino Physics (CNP) memo*, February 2013.

[193] US Department of Energy Office of Science. Ornl's neutron hfir website. `neutrons.ornl.gov/hfir/`, 2016.

[194] N. Xuobi and T. Primm. Modeling of the high flux isotope reactor cycle 400. *Research Reactors Division of Oak Ridge National Laboratory (ORNL/TM-2004/251)*, 2004.

[195] X-5 Monte Carlo Team. Mcnp – a general monte carlo n-particle transport code, version 5. *Los Alamos National Laboratory documentation, LA-UR-03-1987*, 2003 (revised 2008).

[196] T. Lasserre. Cesox ce-ang. *Internal Borexino Presentation, LNGS GM*, June 2016.

[197] B. Neumair. Updated sensitivity plots. *Internal Borexino Presentation, LNGS GM*, 2016.